

Tensor network methods for low-dimensional quantum systems

Jheng-Wei Li



Munich 2022

Tensor network methods for low-dimensional quantum systems

Jheng-Wei Li

A dissertation submitted
to the Faculty of Physics at the
Ludwig–Maximilians–Universität München
for the degree of
DOCTOR RERUM NATURALIUM



Munich, August 24, 2022

First referee: Prof. Dr. Jan von Delft
Second referee: Prof. Dr. Frank Pollmann
Day of submission: August 24, 2022
Day of the oral examination: October 21, 2022

Summary

This thesis contributes to developing and applying tensor network methods to simulate correlated many-body quantum systems.

Numerical simulations of correlated quantum many-body systems are challenging. To describe a many-body wavefunction, the required number of parameters grows exponentially with respect to the system size. This exponential wall fundamentally limits our progress on correlated quantum systems in low dimensions. Tensor network methods in recent years have proven to be a useful framework to understand, control and possibly reduce this intrinsic complexity.

The basic idea of tensor network methods is to decompose a many-body wave function as a network of small, multi-index tensors. A one-dimensional (1D) tensor network factorizes a wave function into a train of three-index tensors. This 1D tensor network ansatz is called a matrix product state (MPS) or a tensor train. A two-dimensional (2D) tensor network state is called a projected entangled-pair state (PEPS). This peculiar name PEPS comes from a quantum information perspective, where each local tensor is interpreted as a projector and correlates with the rest of the tensor network through (auxiliary) maximally entangled pairs.

In the first part, we consider MPSs to study 1D and quasi-2D quantum systems. The key parameter of an MPS is its bond dimension, which controls the numerical accuracy. How large a bond dimension can be reached highly depends on the algorithms employed. The contemporary algorithms, although widely used, have to limit the bond dimension due to their high numerical costs. We develop a controlled bond expansions (CBE) scheme that allows us to grow the bond dimensions with marginal computational efforts. This CBE scheme stems from a geometric point of view to parametrize the variational space of an MPS and can be applied in various contexts. Here, we focus on applying the CBE scheme to two types of problems. The first are optimization problems, like solving the extremal eigenvalue problem. This is relevant for the ground state search, and we show that CBE can accelerate the convergence of MPS in terms of CPU time. The second is to solve ordinary differential equations, such as the time-dependant Schrödinger equation. With the help of CBE, it becomes feasible to use MPS to simulate long-time dynamics that could not be accurately computed hitherto.

In the second part, we employ PEPS to simulate 2D quantum systems. PEPS is an expensive but powerful tool to simulate 2D lattices directly in the thermodynamic limit. The PEPS on infinite lattices is acronymed iPEPS. For completeness, a pedagogical review of iPEPS based on Benedikt Bruognolo's PhD work, which I helped polish for publication in Scipost, is included to cover the algorithmic details. Using iPEPS methods, we study the two-dimensional t - J model on square lattices at the small doping. In this work, we uncover the importance of spin rotational symmetry. Our numerics suggest that by allowing spontaneous spin-symmetry breaking or not, we can suppress or permit the emergence of superconducting order in the thermodynamic limit. This finding provides useful insight to cuprate materials. Also, we use iPEPS to investigate the ground state nature of the honeycomb Kitaev- Γ model. Through a joint effort of classical and iPEPS simulations, we identify an

exotic magnetic order in the parameter regime relevant to α - RuCl_3 materials.

In the third and final part, we study the parton construction of tensor network states. Here, we do not simulate the ground state of a given many-body Hamiltonian. Instead, we take an indirect route that first constructs a parton state in an enlarged Hilbert space, and then applies the Gutzwiller projection to return to the original physical Hilbert space. Such a parton approach has been an important theoretical technique to treat electron-electron correlations nonperturbatively in condensed matter physics. Its marriage with tensor network methods furthers its influence. Various properties of parton wave functions, which are difficult to compute previously, can now be easily accessed. We first use the parton approach to construct MPSs that harbor $\text{SU}(N)$ chiral topological orders. The MPS representation of these Gutzwiller projected parton states allows us to compute entanglement spectra, which hold crucial information to characterize different chiral topological orders. We also develop a method to construct parton states using PEPSs. In this project, we use PEPS to approximate parton states of the π -flux models that host $\text{U}(1)$ -Dirac spin liquids. Our approach enables us to compute the critical exponent of the spin-spin correlations for the spin-half system, whose value is still currently under debate.

Publications

This dissertation is based on the following journal articles, ordered as they appear in this thesis.

- P1** *Controlled bond expansion for DMRG ground state search at single-site costs*
 Andreas Gleis, **Jheng-Wei Li**, and Jan von Delft
 Sec. 2.2 / [arXiv:2207.14712](#)
- P2** *Time-dependent variational principle with controlled bond expansion for matrix product states*
Jheng-Wei Li, Andreas Gleis, and Jan von Delft
 Sec. 2.3 / [arXiv:2208.10972](#)
- P3** *Projector formalism for kept and discarded spaces of matrix product states*
 Andreas Gleis, **Jheng-Wei Li** and Jan von Delft
 Sec. 2.4 / [arXiv:2207.13161](#)
- P4** *A beginner's guide to non-abelian iPEPS for correlated fermions*
 Benedikt Bruognolo, **Jheng-Wei Li**, Jan von Delft, Andreas Weichselbaum
 Sec. 3.2 / [arXiv:2006.08289](#) [SciPost Phys. Lect. Notes 25 \(2021\)](#)
- P5** *Study of spin symmetry in the doped t - J model using infinite projected entangled pair states*
Jheng-Wei Li, Benedikt Bruognolo, Andreas Weichselbaum and Jan von Delft
 Sec. 3.3 / [arXiv:2006.08323](#) [Phys. Rev. B 103, 075127 \(2021\)](#)
- P6** *Tangle of Spin Double Helices in the Honeycomb Kitaev- Γ Model*
Jheng-Wei Li, Nihal Rao, Jan von Delft, Lode Pollet, and Ke Liu
 Sec. 3.4 / [arXiv:2206.08946](#)
- P7** *Abelian $SU(N)_1$ chiral spin liquids on the square lattice*
 Ji-Yao Chen, **Jheng-Wei Li**, Pierre Nataf, Sylvain Capponi, Matthieu Mambri, Keisuke Totsuka, Hong-Hao Tu, Andreas Weichselbaum, Jan von Delft, Didier Poilblanc
 Sec. 4.2 / [arXiv:2106.02115](#) [Phys. Rev. B 104, 235104 \(2021\)](#)
- P8** *$U(1)$ -symmetric Gaussian fermionic projected entangled-paired states and their Gutzwiller projection*
Jheng-Wei Li, Jan von Delft, and Hong-Hao Tu
 Sec. 4.3 / [arXiv:2208.04623](#)

Contents

Summary	i
Publications	iii
1 Introduction	1
1.1 Matrix Product States	2
1.2 Projected entangled-paired states	8
1.3 Parton construction for tensor network states	10
2 Matrix Product States	15
2.1 Overview	15
2.2 Publication: <i>Controlled bond expansion for DMRG ground state search at single-site costs</i>	16
2.3 Publication: <i>Time-dependent variational principle with controlled bond expansion for matrix product states</i>	29
2.4 Publication: <i>Projector formalism for kept and discarded spaces of matrix product states</i>	39
3 Projected Entangled-Paired States	53
3.1 Overview	53
3.2 Publication: <i>A beginner's guide to non-abelian iPEPS for correlated fermions</i>	54
3.3 Publication: <i>Study of spin symmetry in the doped t-J model using infinite projected entangled pair states</i>	115
3.4 Publication: <i>Tangle of Spin Double Helices in the Honeycomb Kitaev-Γ Model</i>	128
4 Parton construction of tensor network states	139
4.1 Overview	139
4.2 Publication: <i>Abelian $SU(N)_1$ chiral spin liquids on the square lattice</i>	140
4.3 Publication: <i>U(1)-symmetric Gaussian fermionic projected entangled-paired states and their Gutzwiller projection</i>	174
5 Conclusion and outlook	185
Bibliography	187
Acknowledgements	199

1 Introduction

The challenge of quantum many-body problems comes from the number of degrees of freedom one has to deal with to represent a quantum state. For example, in quantum spin-1/2 systems, each spin is described by two components, i.e., spin-up and spin-down states, but to represent a quantum state of N spins, the total number of components becomes 2^N . In three dimensions and beyond, single-particle theories, such as Landau’s Fermi-liquid theory, have much success in decoupling such immense degrees of freedom to reduce the problem’s complexity. However, in one and two dimensions, the spatial constriction effectively enhances the mutual interactions between quantum entities (being either spins or itinerant fermions). This makes the problem difficult to handle in framework of the single-particle approximation or its related perturbative approaches. Many experimental phenomena, including Mott transitions [Mot68], high- T_c superconductivity [Gro89, Dag94, LNW06] and the fractional quantum Hall effect [TSG82, STG99], can only be explained by explicitly taking the electron-electron interactions into account.

Due to the absence of effective single-particle theories, interacting quantum systems in low dimensions to large extent need to be solved by numerical means. This thesis works on developing and applying tensor network methods to computationally solve quantum many-body problems in one and two dimensions. The quantum many-body problems we are concerned with are model Hamiltonians defined on discrete lattices. They contain far less degrees of freedom than real-world materials, aiming to capture the low-energy physics pertaining to experimental observations. Albeit with drastic simplification, solving model Hamiltonians that are “interesting” remains a daunting task.

The two-dimensional one-band Hubbard model [Edi13, And07] is one of the textbook examples. The Hamiltonian under second quantization reads

$$H = -t \sum_{\langle i,j \rangle} \sum_{\sigma=\uparrow,\downarrow} (c_{i,\sigma}^\dagger c_{j,\sigma} + \text{h.c.}) + U \sum_i c_{i,\uparrow}^\dagger c_{i,\uparrow} c_{i,\downarrow}^\dagger c_{i,\downarrow}, \quad (1.1)$$

with $c_{i,\sigma}^\dagger$ and $c_{i,\sigma}$ the fermionic creation and annihilation operators of spin σ electrons on lattice site i , and $\langle i,j \rangle$ enumerating all nearest-neighbor sites. The first term describes the kinetics, the hopping of fermions with amplitude t , and the second term is the on-site Coulomb interaction of strength U that describes the repulsion between spin-up and spin-down electrons at the same site. Since its first appearance in 1963 [Hub63], numerous concepts and journal articles have been dedicated to this simple-looking model. For example, on the square lattice, at half-filling, for small U , the system is metallic; with sufficient large U , the system becomes a Mott insulator undergoing a Mott transition [Koh64, Mot68, IFT98]. Slightly away from half-filling with a sizable U , the physics is most interesting. Its ground state has been speculated to be a doped chiral spin liquid, a d -wave superconductor, or a spin stripe [Sch89, ZG89, LNW06]. To these days, its phase diagram as well as its spectral properties close to half-filling remain unclear. This thesis is essentially developing tensor network methods that may lead to answering the above question someday.

Tensor network methods have been undergoing active development over the past thirty years. The unifying feature of these methods is their capability to describe weakly-entangled states efficiently, and therefore provide an accurate parametrization to simulate low-lying states of short-range Hamiltonians. In this thesis, we study two types of tensor network Ansätze: matrix product states (MPS) and projected entangled-pair states (PEPS). We use them to solve model Hamiltonians, such as the Hubbard model, Hubbard-like models, and frustrated spin models in one and two dimensions. To set the scene, we below briefly introduce (i) MPS which will be studied in Chapter 2, (ii) PEPS in Chapter 3, and (iii) the use of MPS and PEPS to represent projected parton wave functions in Chapter 4.

1.1 Matrix Product States

The matrix product state (MPS) is a one-dimensional tensor network ansatz. It represents a quantum many-body state as follows:

$$|\Psi\rangle = \sum_{\sigma_1\sigma_2\dots\sigma_{\mathcal{L}}} \sum_{a_1\dots a_{\mathcal{L}-1}} M_{1a_1}^{\sigma_1} M_{a_1a_2}^{\sigma_2} \dots M_{a_{\mathcal{L}-1}1}^{\sigma_{\mathcal{L}}} |\sigma_1\sigma_2\dots\sigma_{\mathcal{L}}\rangle. \quad (1.2)$$

Here $M_{a_{\ell-1}a_{\ell}}^{\sigma_{\ell}}$ is a rank-3 tensor, where σ_{ℓ} enumerates all states in its local computational basis, such as $|\uparrow\rangle$ and $|\downarrow\rangle$ for a spin-1/2, and $a_{\ell-1}$ and a_{ℓ} , the so-called *virtual* indices, connect to the left and right tensors respectively.

Compactly, we can read the summation over a_{ℓ} as matrix-matrix multiplications, i.e.,

$$|\Psi\rangle = \sum_{\sigma_1\sigma_2\dots\sigma_{\mathcal{L}}} M^{\sigma_1} M^{\sigma_2} \dots M^{\sigma_{\mathcal{L}}} |\sigma_1\sigma_2\dots\sigma_{\mathcal{L}}\rangle, \quad (1.3)$$

where M^{σ_1} , $M^{\sigma_{\ell}}$, and $M^{\sigma_{\mathcal{L}}}$ are $1 \times D_1$, $D_{\ell-1} \times D_{\ell}$ and $D_{\mathcal{L}-1} \times 1$ matrices. By that, the evaluation of $|\Psi\rangle$ becomes a matter of calculating the products of those matrices. Hence the name matrix product state. This simple rewriting turns out to be an effective way to parametrize a certain class of quantum states. Most importantly, the curse of dimensionality becomes irrelevant if the maximal rank, or the *bond dimension*, of M matrices, $D = \max\{D_1, D_2, \dots, D_{\mathcal{L}-1}\}$, can be made much smaller than $(\dim(\sigma))^{\mathcal{L}/2}$. This insight had a great impact on the course of simulations of correlated quantum systems.

The density-matrix renormalization group

As is understood nowadays, MPSs are a class of variational Ansätze underlying the density matrix renormalization group (DMRG) [Sch11]. The connection between MPS and DMRG, however, was not entirely obvious in the first place.

The density-matrix renormalization group (DMRG) method was conceived by Steven White back in 1992 [Whi92]. White's seminal paper was published under the title: *Density Matrix Formulation for Quantum Renormalization Groups*, as a technical advance to fix the numerical renormalization group (NRG) when solving quantum lattice problems in real space. NRG works well for quantum impurity problems, such as the single impurity Anderson model, where an interacting fermionic site (impurity) is coupled to the non-interacting conduction electrons (bath) [Wil75]. During the RG flow, as the energy scale is well-separated, NRG needs only to retain the lowest energy states at every iteration, and truncates the rest to avoid

the exponential blow-up of the dimensionality. This turns out to work poorly for one-dimensional spin chains [WN92].

White's key insight is that, instead of keeping the lowest-energy states, one can use the reduced density matrix to identify the relevant states one should retain. The idea is as follows. Let us take a bipartite system composed of two blocks of spins \mathcal{L} and \mathcal{R} . Then its wave function $|\Psi\rangle$ can be expressed as

$$|\Psi\rangle = \sum_i \sum_j \Phi_{ij} |i\rangle_{\mathcal{L}} |j\rangle_{\mathcal{R}}; \quad (1.4)$$

and accordingly, the reduced density matrix of \mathcal{L} is $\rho_{\mathcal{L}} = \text{Tr}_{\mathcal{R}}(|\Psi\rangle\langle\Psi|) = \sum_i |i\rangle_{\mathcal{L}} \langle i|_{\mathcal{L}} \Phi_{ij} \Phi_{ji}^*$. To approximate $|\Psi\rangle$ by truncation is to find a $|\Psi'\rangle$ by keeping only $D < N_{\mathcal{L}}$ states that minimize $\| |\Psi'\rangle - |\Psi\rangle \|$. This can be done by choosing $|i\rangle_{\mathcal{L}}$ as the eigenvectors of $\rho_{\mathcal{L}}$ that correspond to its D largest eigenvalues. This density matrix formulation for real space RG relished its swift success. Its high numerical accuracy at solving low-lying states for the 1D $S = 1$ Heisenberg model was most astonishing [WH93]. Two years after White's first paper, DMRG became the standard jargon.

Historically, MPSs antedate DMRG. They were a class of states introduced by Affleck, Kennedy, Lieb, and Tasaki (AKLT) in 1987, under the name of *finitely correlated state*, as an analytical ansatz to study certain types of spin models [AKLT87]. Hitherto, DMRG and MPS have appeared to be two unrelated concepts. It was Stellan Östlund and Stefan Rommer, three years after White's breakthrough, that first identified the conceptual link in Ref. [OR95]. This is important because MPS, which can thus be optimized via DMRG, has become a flexible variational ansatz, with the widened prospect of numerically tackling low-dimensional quantum systems.

In this vein, a surge of progress in ironing out the MPS simulability was later sparked by Guifre Vidal in the early 2000s. He pointed out in Ref. [Vid03] that the DMRG truncation in Eq. (1.4) can be readily understood as a Schmidt decomposition. To simplify, suppose that $|i\rangle_{\mathcal{L}}$ and $|j\rangle_{\mathcal{R}}$ form orthonormal bases of \mathcal{L} and \mathcal{R} partitions respectively. Then, the DMRG truncation of $|\Psi\rangle$ is equivalent to first performing the singular value decomposition (SVD), i.e., $\Phi_{ij} = U_{i\alpha} \lambda_{\alpha} V_{\alpha j}^{\dagger}$, and then keeping only the largest D singular values,

$$|\Psi\rangle \approx \sum_i \sum_j \sum_{\alpha=1}^D U_{i\alpha} S_{\alpha} V_{\alpha j}^{\dagger} |i\rangle_{\mathcal{L}} |j\rangle_{\mathcal{R}} = \sum_{\alpha=1}^D S_{\alpha} |\alpha\rangle_{\mathcal{L}} |\alpha\rangle_{\mathcal{R}}. \quad (1.5)$$

Here, U (or V^{\dagger}) is the left (or right) isometric matrix projecting $|i\rangle_{\mathcal{L}}$ (or $|i\rangle_{\mathcal{R}}$) into the truncated Schmidt basis.

Furthermore, the rank D now acquires a clear meaning as a measure of the entanglement entropy between blocks \mathcal{L} and \mathcal{R} :

$$S_{\mathcal{L}|\mathcal{R}} = -\text{Tr}(\rho_{\mathcal{L}} \log \rho_{\mathcal{L}}) = -\text{Tr}(\rho_{\mathcal{R}} \log \rho_{\mathcal{R}}) = \sum_{\alpha=1}^D S_{\alpha}^2 \log S_{\alpha}^2. \quad (1.6)$$

With that, we could see at a given bond dimension D , the entanglement entropy that can be encoded in a MPS is always bounded, below a length-independent constant, $\log(D)$.

Hence, given a finite bond dimension, the MPS simulability is restricted. This observation was quickly refined by M. Hastings, F. Verstraete, J.I. Cirac, F. Pollmann, F. Brandao, M. Horodecki, and many others [Has07, VC06, PMTM09, PTBO10,

[ECP10, BH14]. We thus arrive at the current understanding — MPS can simulate ground states faithfully for any gapped local one-dimensional Hamiltonian, as these ground states satisfy the entanglement area law, which bounds the entanglement entropy between any bi-partitions to be below a certain constant regardless of the system size.

Canonical forms

In the previous subsection, we have assumed that $|i\rangle_{\mathcal{L}}$ and $|j\rangle_{\mathcal{R}}$ in Eq. (1.5) are orthonormal bases known a priori. However, it indeed requires a little work to go from Eq. (1.3) to Eq. (1.5).

To that end, we have to recognize that the definition in Eq. (1.3) is not unique. The state remains unchanged after a gauge transformation between two adjacent matrices, M^{σ_ℓ} and $M^{\sigma_{\ell+1}}$, such as

$$M^{\sigma_\ell} \rightarrow M^{\sigma_\ell} X, \quad M^{\sigma_{\ell+1}} \rightarrow X^{-1} M^{\sigma_{\ell+1}}, \quad (1.7)$$

for every σ_ℓ and $\sigma_{\ell+1}$, where X is an invertible matrix.

Exploiting this non-uniqueness, we can fix the MPS gauge to our convenience. An SVD of M^{σ_ℓ} , as $M_{(a_{\ell-1}, \sigma_\ell), a_\ell} = ASV^\dagger$, gives us a *left-normalized* MPS tensor $A_{a_{\ell-1} a_\ell}^{\sigma_\ell}$, following

$$|a_\ell\rangle = \sum_{a_{\ell-1}, \sigma_\ell} A_{a_{\ell-1} a_\ell}^{\sigma_\ell} |a_{\ell-1}\rangle |\sigma_\ell\rangle, \quad (1.8)$$

with $\sum_{a_{\ell-1}, \sigma_\ell} A_{a_{\ell-1} a_\ell}^{\sigma_\ell} (A_{a_{\ell-1} a'_\ell}^{\sigma_\ell})^* = \delta_{a_\ell a'_\ell}$ and $X = SV^\dagger$ to be absorbed to the next tensor. Similarly, we could also obtain a *right-normalized* MPS tensor B via $M_{a_{\ell-1}, (\sigma_\ell, a_\ell)} = USB$, such that

$$|a_{\ell-1}\rangle = \sum_{\sigma_\ell, a_\ell} B_{a_{\ell-1} a_\ell}^{\sigma_\ell} |\sigma_\ell\rangle |a_\ell\rangle, \quad (1.9)$$

and $\sum_{\sigma_\ell, a_\ell} B_{a_{\ell-1} a_\ell}^{\sigma_\ell} (B_{a'_{\ell-1} a_\ell}^{\sigma_\ell})^* = \delta_{a_{\ell-1} a'_{\ell-1}}$.

Applying a sequence of recursive SVD starting from the left and right boundaries, it is always possible to bring an MPS into some particular *canonical form*. For instance, the site- ℓ canonicalized MPS reads,

$$|\Psi\rangle = \sum_{\substack{\sigma_1 \sigma_2 \dots \sigma_L \\ a_1, \dots, a_{L-1}}} A_{1a_1}^{\sigma_1} \dots C_{a_{\ell-1} a_\ell}^{\sigma_\ell} B_{a_\ell a_{\ell+1}}^{\sigma_{\ell+1}} \dots B_{a_{L-1} 1}^{\sigma_L} |\sigma_1 \sigma_2 \dots \sigma_L\rangle \quad (1.10)$$

$$= \sum_{a_{\ell-1} \sigma_\ell a_\ell} \left(\sum_{\substack{\sigma_1 \dots \sigma_{\ell-1} \\ a_1 \dots a_{\ell-2}}} A_{1a_1}^{\sigma_1} \dots A_{a_{\ell-2} a_{\ell-1}}^{\sigma_{\ell-1}} |\sigma_1 \dots \sigma_{\ell-1}\rangle \right) C_{a_{\ell-1} a_\ell}^{\sigma_\ell} |\sigma_\ell\rangle \quad (1.11)$$

$$\left(\sum_{\substack{\sigma_{\ell+1} \dots \sigma_L \\ a_\ell \dots a_{L-1}}} B_{a_\ell a_{\ell+1}}^{\sigma_{\ell+1}} \dots B_{a_{L-1} 1}^{\sigma_L} |\sigma_{\ell+1} \dots \sigma_L\rangle \right) \\ = \sum_{a_{\ell-1} \sigma_\ell a_\ell} C_{a_{\ell-1} a_\ell}^{\sigma_\ell} |a_{\ell-1}\rangle |\sigma_\ell\rangle |a_\ell\rangle. \quad (1.12)$$

Due to the isometric property of left-normalized A tensors (or right-normalized B tensors), the collective states $|a_{\ell-1}\rangle$ (or $|a_\ell\rangle$) consequently form an orthonormal basis

representing the left (or right) blocks of sites, which is of the same form as Eq. (1.5).

Tensor diagram notations

To avoid hairy-index equations as we have just seen, it is convenient to introduce tensor diagram notations [Sch11, BC17, STG⁺19, CPGSV21]. Here, we follow the notation introduced in Ref. [P3].

A general tensor is represented by a circle with legs sticking out, each representing a tensor index. For example,

$$[C_\ell]_{a_{\ell-1}a_\ell}^{\sigma_\ell} = \begin{array}{c} C_\ell \\ \circlearrowleft \\ a_{\ell-1} \quad a_\ell \\ \sigma_\ell \end{array}. \quad (1.13)$$

As for left-normalized A and right-normalized B tensors, we distinguish them with triangles [P3],

$$[A_\ell]_{a_{\ell-1}a_\ell}^{\sigma_\ell} = \begin{array}{c} A_\ell \\ \lrcorner \\ a_{\ell-1} \quad a_\ell \\ \sigma_\ell \end{array}, \quad [B_\ell]_{a_{\ell-1}a_\ell}^{\sigma_\ell} = \begin{array}{c} B_\ell \\ \rceil \\ a_{\ell-1} \quad a_\ell \\ \sigma_\ell \end{array}. \quad (1.14)$$

And the tensor contraction, or the summing over tensor indices, is denoted by connecting the corresponding legs between two tensors. With that, the tensor diagram of Eq. (1.10) reads,

$$|\Psi\rangle = \begin{array}{c} A_1 \quad A_{\ell-1} \quad C_\ell \quad B_{\ell+1} \quad B_{\mathcal{L}} \\ \lrcorner \quad \lrcorner \quad \circlearrowleft \quad \rceil \quad \rceil \\ \sigma_1 \quad \sigma_{\ell-1} \quad \sigma_\ell \quad \sigma_{\ell+1} \quad \sigma_{\mathcal{L}} \end{array}. \quad (1.15)$$

Also, the isometric condition of A_ℓ and B_ℓ tensors [see Eq. (1.8)-(1.9)] can be depicted as following,

$$A_\ell^\dagger A_\ell = \begin{array}{c} A_\ell \\ \lrcorner \\ A_\ell^* \end{array} = \left(\begin{array}{c} \mathbb{1}_\ell \end{array} \right), \quad B_\ell B_\ell^\dagger = \begin{array}{c} B_\ell \\ \rceil \\ B_\ell^* \end{array} = \left(\begin{array}{c} \mathbb{1}_{\ell-1} \end{array} \right), \quad (1.16)$$

with a single line to represent the identity matrix.

Tangent space methods

Meanwhile, a rather different approach to work with MPSs was developed separately by mathematicians. The general idea is to confine the variational space of a wave function $|\Psi\rangle$ to a vector space spanned by the first order variations of its given parameters [Dir30, McL64, BLKL88, MMC90, HLW06]. This vector space is called the tangent space of $|\Psi\rangle$. As the tangent space is a rather small subspace embedded in the full Hilbert space, imposing tangent space approximations to a MPS leads to efficient numerical implementation. [KL07, KL10, HCO⁺11, LO13, UV20]. They were first used to study real-time evolution [LRSV13, LOV15, ZMPR15, HLO⁺16, LPB⁺17, Wu20], and then quickly found its wide application in ground state search, computing low-energy excitations and spectral functions [HOV13, Van17, ZSVF⁺18, VDVH⁺21]. Overall, the crucial ingredient for all the tangent space methods is the design of the tangent space projector, which helps us to project an arbitrary state onto the tangent space of an MPS.

Given an MPS of the form Eq. (1.15), under the fixed rank (bond dimension) approximation [Lub15, HLO⁺16], the tangent space projector reads,

$$\mathcal{P}^{1s} = \sum_{\ell=1}^{\mathcal{L}} \mathcal{P}_{\ell}^{1s} - \sum_{\ell=1}^{\mathcal{L}-1} \mathcal{P}_{\ell}^b = \sum_{\ell=1}^{\mathcal{L}} \begin{array}{c} \triangleleft \\ \diagdown \\ \text{---} \\ \diagup \\ \triangleright \end{array} \dots \begin{array}{c} \triangleleft \\ \diagdown \\ \text{---} \\ \diagup \\ \triangleright \end{array} \bigg| \begin{array}{c} \triangleleft \\ \diagdown \\ \text{---} \\ \diagup \\ \triangleright \end{array} \dots \begin{array}{c} \triangleleft \\ \diagdown \\ \text{---} \\ \diagup \\ \triangleright \end{array} - \sum_{\ell=1}^{\mathcal{L}-1} \begin{array}{c} \triangleleft \\ \diagdown \\ \text{---} \\ \diagup \\ \triangleright \end{array} \dots \begin{array}{c} \triangleleft \\ \diagdown \\ \text{---} \\ \diagup \\ \triangleright \end{array} \begin{array}{c} \triangleleft \\ \diagdown \\ \text{---} \\ \diagup \\ \triangleright \end{array} \dots \begin{array}{c} \triangleleft \\ \diagdown \\ \text{---} \\ \diagup \\ \triangleright \end{array}, \quad (1.17)$$

where each term, \mathcal{P}_{ℓ}^{1s} or \mathcal{P}_{ℓ}^b , is composed of a train of fixed A/B isometries. This additive decomposition is tremendously useful. As we will see later, it allows us to project the MPS into separate local parameter spaces, which makes it possible to formulate efficient one-site algorithms.

Tangent space construction

To motivate Eq. (1.17), we here outline the construction of the tangent space projector for a two-site MPS, following Ref. [LO13, P3]. The key here is to see that, given $\Psi = A\Lambda B$, its variation, $\delta\Psi$, under the fixed rank approximation, can be expressed as a sum of one-derivatives of local tensors, each of the same rank as the original MPS. In other words, each tangent vector $\delta\Psi$ is of the form $(\delta A)\Lambda B + A(\delta\Lambda)B + A\Lambda(\delta B)$.

Furthermore, we can always decompose $\delta A\Lambda$ as $A\Lambda' + \bar{A}\bar{\Lambda}'$, where \bar{A} is the orthogonal complement of A . And likewise, $\Lambda\delta B = \Lambda''B + \bar{\Lambda}''\bar{B}$, with \bar{B} the orthogonal complement of B . With a little reshuffling, we then arrive at

$$\delta\Psi = \frac{\bar{A}\bar{\Lambda}'B}{\sqrt{}} + \frac{A\tilde{\Lambda}B}{\sqrt{}} + \frac{A\bar{\Lambda}''\bar{B}}{\sqrt{}}, \quad (1.18)$$

where $\tilde{\Lambda} = \Lambda' + \delta\Lambda + \Lambda''$, and we use gray triangles to denote the orthogonal complements of A and B .

It is important to note that the three terms on the right of Eq. (1.18) are mutually orthogonal to each other. Because of that, the parametrization of $\delta\Psi$ in terms of orthogonal projectors that are *additive* becomes straightforward. We can indeed project onto the first term by $\bar{A}\bar{A}^\dagger(\delta\Psi)B^\dagger B$; the second by $AA^\dagger(\delta\Psi)B^\dagger B$; and the third by $AA^\dagger(\delta\Psi)\bar{B}^\dagger\bar{B}$. Diagrammatically, these three projectors together read

$$\mathcal{P}_{\Psi} = \begin{array}{c} \triangleleft \\ \diagdown \\ \text{---} \\ \diagup \\ \triangleright \end{array} \begin{array}{c} \triangleleft \\ \diagdown \\ \text{---} \\ \diagup \\ \triangleright \end{array} + \begin{array}{c} \triangleleft \\ \diagdown \\ \text{---} \\ \diagup \\ \triangleright \end{array} \begin{array}{c} \triangleleft \\ \diagdown \\ \text{---} \\ \diagup \\ \triangleright \end{array} + \begin{array}{c} \triangleleft \\ \diagdown \\ \text{---} \\ \diagup \\ \triangleright \end{array} \begin{array}{c} \triangleleft \\ \diagdown \\ \text{---} \\ \diagup \\ \triangleright \end{array}. \quad (1.19)$$

Moreover, with \mathcal{P}_{Ψ} in hand, we can project any arbitrary vector, say Φ , into the tangent space of Ψ , simply via $\mathcal{P}_{\Psi}\Phi$. This projection is indeed an approximation, as it omits the term $(\bar{A}\bar{A}^\dagger)\Phi(\bar{B}^\dagger\bar{B})$, which is a vector living outside of the tangent space manifold.

We can generalize the above observation to arbitrary lengths of MPS. To do so, let us first consider variations of MPS in Eq. (1.10) on a single bond, ℓ , i.e., $A_{\ell}C_{\ell+1} = A_{\ell}\Lambda_{\ell}B_{\ell+1}$, while the other tensors remain fixed. Following the previous argument, we have the tangent space projector for $A_{\ell}\Lambda_{\ell}B_{\ell+1}$ as follows:

$$\begin{aligned} \mathcal{P}_{\ell} &= \begin{array}{c} \triangleleft \\ \diagdown \\ \text{---} \\ \diagup \\ \triangleright \end{array} \dots \begin{array}{c} \triangleleft \\ \diagdown \\ \text{---} \\ \diagup \\ \triangleright \end{array} \begin{array}{c} \triangleleft \\ \diagdown \\ \text{---} \\ \diagup \\ \triangleright \end{array} \begin{array}{c} \triangleleft \\ \diagdown \\ \text{---} \\ \diagup \\ \triangleright \end{array} \dots \begin{array}{c} \triangleleft \\ \diagdown \\ \text{---} \\ \diagup \\ \triangleright \end{array} + \begin{array}{c} \triangleleft \\ \diagdown \\ \text{---} \\ \diagup \\ \triangleright \end{array} \dots \begin{array}{c} \triangleleft \\ \diagdown \\ \text{---} \\ \diagup \\ \triangleright \end{array} \begin{array}{c} \triangleleft \\ \diagdown \\ \text{---} \\ \diagup \\ \triangleright \end{array} \begin{array}{c} \triangleleft \\ \diagdown \\ \text{---} \\ \diagup \\ \triangleright \end{array} \dots \begin{array}{c} \triangleleft \\ \diagdown \\ \text{---} \\ \diagup \\ \triangleright \end{array} + \begin{array}{c} \triangleleft \\ \diagdown \\ \text{---} \\ \diagup \\ \triangleright \end{array} \dots \begin{array}{c} \triangleleft \\ \diagdown \\ \text{---} \\ \diagup \\ \triangleright \end{array} \begin{array}{c} \triangleleft \\ \diagdown \\ \text{---} \\ \diagup \\ \triangleright \end{array} \begin{array}{c} \triangleleft \\ \diagdown \\ \text{---} \\ \diagup \\ \triangleright \end{array} \dots \begin{array}{c} \triangleleft \\ \diagdown \\ \text{---} \\ \diagup \\ \triangleright \end{array} \\ &= \begin{array}{c} \triangleleft \\ \diagdown \\ \text{---} \\ \diagup \\ \triangleright \end{array} \dots \begin{array}{c} \triangleleft \\ \diagdown \\ \text{---} \\ \diagup \\ \triangleright \end{array} \begin{array}{c} \triangleleft \\ \diagdown \\ \text{---} \\ \diagup \\ \triangleright \end{array} \begin{array}{c} \triangleleft \\ \diagdown \\ \text{---} \\ \diagup \\ \triangleright \end{array} \dots \begin{array}{c} \triangleleft \\ \diagdown \\ \text{---} \\ \diagup \\ \triangleright \end{array} + \begin{array}{c} \triangleleft \\ \diagdown \\ \text{---} \\ \diagup \\ \triangleright \end{array} \dots \begin{array}{c} \triangleleft \\ \diagdown \\ \text{---} \\ \diagup \\ \triangleright \end{array} \begin{array}{c} \triangleleft \\ \diagdown \\ \text{---} \\ \diagup \\ \triangleright \end{array} \bigg| \begin{array}{c} \triangleleft \\ \diagdown \\ \text{---} \\ \diagup \\ \triangleright \end{array} \dots \begin{array}{c} \triangleleft \\ \diagdown \\ \text{---} \\ \diagup \\ \triangleright \end{array}, \quad (1.20) \end{aligned}$$

where the second equality exploits the completeness relation, that is

$$\begin{array}{c} \triangleleft \\ \times \\ \times \\ \times \\ \triangleleft \end{array} + \begin{array}{c} \triangleleft \\ \times \\ \times \\ \times \\ \triangleleft \end{array} = \begin{array}{|c} \hline \times \\ \hline \end{array} \quad , \quad \begin{array}{c} \triangleleft \\ \times \\ \times \\ \times \\ \triangleleft \end{array} + \begin{array}{c} \triangleleft \\ \times \\ \times \\ \times \\ \triangleleft \end{array} = \begin{array}{|c} \hline \times \\ \hline \end{array} . \quad (1.21)$$

Moving to the next bond, $\ell' = \ell + 1$, we again apply the same construction and have

$$\begin{aligned} \mathcal{P}_{\ell'} &= \begin{array}{c} \times \\ \times \\ \times \\ \times \\ \times \\ \times \end{array} \begin{array}{c} \triangleleft \\ \times \\ \times \\ \times \\ \triangleleft \end{array} \cdots \begin{array}{c} \times \\ \times \\ \times \\ \times \\ \triangleleft \end{array} \begin{array}{c} \triangleleft \\ \times \\ \times \\ \times \\ \triangleleft \end{array} \begin{array}{c} \triangleleft \\ \times \\ \times \\ \times \\ \triangleleft \end{array} \begin{array}{c} \times \\ \times \\ \times \\ \times \\ \times \\ \times \end{array} + \begin{array}{c} \times \\ \times \\ \times \\ \times \\ \times \\ \times \end{array} \begin{array}{c} \triangleleft \\ \times \\ \times \\ \times \\ \triangleleft \end{array} \cdots \begin{array}{c} \times \\ \times \\ \times \\ \times \\ \triangleleft \end{array} \begin{array}{c} \triangleleft \\ \times \\ \times \\ \times \\ \triangleleft \end{array} \begin{array}{c} \triangleleft \\ \times \\ \times \\ \times \\ \triangleleft \end{array} \begin{array}{c} \times \\ \times \\ \times \\ \times \\ \times \\ \times \end{array} + \begin{array}{c} \times \\ \times \\ \times \\ \times \\ \times \\ \times \end{array} \begin{array}{c} \triangleleft \\ \times \\ \times \\ \times \\ \triangleleft \end{array} \cdots \begin{array}{c} \times \\ \times \\ \times \\ \times \\ \triangleleft \end{array} \begin{array}{c} \triangleleft \\ \times \\ \times \\ \times \\ \triangleleft \end{array} \begin{array}{c} \triangleleft \\ \times \\ \times \\ \times \\ \triangleleft \end{array} \begin{array}{c} \times \\ \times \\ \times \\ \times \\ \times \\ \times \end{array} \\ &= \begin{array}{c} \times \\ \times \\ \times \\ \times \\ \times \\ \times \end{array} \begin{array}{c} \triangleleft \\ \times \\ \times \\ \times \\ \triangleleft \end{array} \cdots \begin{array}{c} \times \\ \times \\ \times \\ \times \\ \triangleleft \end{array} \begin{array}{c} \triangleleft \\ \times \\ \times \\ \times \\ \triangleleft \end{array} \begin{array}{|c} \hline \times \\ \hline \end{array} \begin{array}{c} \triangleleft \\ \times \\ \times \\ \times \\ \triangleleft \end{array} \begin{array}{c} \times \\ \times \\ \times \\ \times \\ \times \\ \times \end{array} + \begin{array}{c} \times \\ \times \\ \times \\ \times \\ \times \\ \times \end{array} \begin{array}{c} \triangleleft \\ \times \\ \times \\ \times \\ \triangleleft \end{array} \cdots \begin{array}{c} \times \\ \times \\ \times \\ \times \\ \triangleleft \end{array} \begin{array}{c} \triangleleft \\ \times \\ \times \\ \times \\ \triangleleft \end{array} \begin{array}{c} \triangleleft \\ \times \\ \times \\ \times \\ \triangleleft \end{array} \begin{array}{c} \times \\ \times \\ \times \\ \times \\ \times \\ \times \end{array} . \quad (1.22) \end{aligned}$$

However, the two tangent spaces associated with projector \mathcal{P}_ℓ and $\mathcal{P}_{\ell'}$ are not mutually orthogonal to each other. This can be clearly seen by comparing the second lines of Eq. (1.20) and (1.22); noticing that the second term in the second line of Eq. (1.20) is the same as the first term in the second line of Eq. (1.22). To build a composite projector for the joint tangent spaces of $A_\ell \Lambda_\ell B_{\ell+1}$ and $A_{\ell+1} \Lambda_{\ell+1} B_{\ell+2}$, we should consider this term only once to avoid double counting. Therefore, only the last term of Eq. (1.22) should be included. The same argument goes for $\ell' = \ell + 2 \dots \mathcal{L}$ on the right, that only the last terms of $\mathcal{P}_{\ell'}$, involving $\bar{B}_{\ell+1}$, need to be taken into account. In the exact same fashion, we can apply the argument again for $\ell' = 1 \dots \ell - 1$ bonds on the left, where only the first terms of $\mathcal{P}_{\ell'}$, involving $\bar{A}_{\ell'}$, are to be considered.

Overall, we arrive at the tangent space projector under the fixed rank approximation that reads,

$$\begin{aligned} \mathcal{P}^{1s} &= \sum_{\ell'=1}^{\ell-1} \begin{array}{c} \times \\ \times \\ \times \\ \times \\ \times \\ \times \end{array} \begin{array}{c} \triangleleft \\ \times \\ \times \\ \times \\ \triangleleft \end{array} \cdots \begin{array}{c} \times \\ \times \\ \times \\ \times \\ \triangleleft \end{array} \begin{array}{c} \triangleleft \\ \times \\ \times \\ \times \\ \triangleleft \end{array} \begin{array}{c} \triangleleft \\ \times \\ \times \\ \times \\ \triangleleft \end{array} \begin{array}{c} \times \\ \times \\ \times \\ \times \\ \times \\ \times \end{array} + \begin{array}{c} \times \\ \times \\ \times \\ \times \\ \times \\ \times \end{array} \begin{array}{c} \triangleleft \\ \times \\ \times \\ \times \\ \triangleleft \end{array} \cdots \begin{array}{c} \times \\ \times \\ \times \\ \times \\ \triangleleft \end{array} \begin{array}{c} \triangleleft \\ \times \\ \times \\ \times \\ \triangleleft \end{array} \begin{array}{c} \triangleleft \\ \times \\ \times \\ \times \\ \triangleleft \end{array} \begin{array}{c} \times \\ \times \\ \times \\ \times \\ \times \\ \times \end{array} \begin{array}{|c} \hline \times \\ \hline \end{array} \begin{array}{c} \triangleleft \\ \times \\ \times \\ \times \\ \triangleleft \end{array} \begin{array}{c} \times \\ \times \\ \times \\ \times \\ \times \\ \times \end{array} \\ &+ \sum_{\ell'=\ell+1}^{\mathcal{L}} \begin{array}{c} \times \\ \times \\ \times \\ \times \\ \times \\ \times \end{array} \begin{array}{c} \triangleleft \\ \times \\ \times \\ \times \\ \triangleleft \end{array} \cdots \begin{array}{c} \times \\ \times \\ \times \\ \times \\ \triangleleft \end{array} \begin{array}{c} \triangleleft \\ \times \\ \times \\ \times \\ \triangleleft \end{array} \begin{array}{c} \triangleleft \\ \times \\ \times \\ \times \\ \triangleleft \end{array} \begin{array}{c} \times \\ \times \\ \times \\ \times \\ \times \\ \times \end{array} , \quad (1.23) \end{aligned}$$

which is essentially identical to Eq. (1.17).

One-site algorithms

To be concrete, let us here consider how to use the tangent space projector \mathcal{P}^{1s} to approximately solve the time-dependent Schrödinger equation.

The principle idea of the tangent space approach is to restrict the variational space of MPS within its tangent space, \mathbb{V}^{1s} . For a time-dependent problem, say given a state $|\Psi(t)\rangle$ at time t , the time evolution which is governed by a Hamiltonian H , will inevitably lead to a state $H|\Psi(t)\rangle$ out of the tangent space of $|\Psi(t)\rangle$. Therefore, to stay within \mathbb{V}^{1s} , what we have to do is to approximate $H|\Psi(t)\rangle$ by its *orthogonal projection* onto this tangent space. This approximation can be easily implemented via the tangent space projector, \mathcal{P}^{1s} :

$$|\dot{\Psi}(t)\rangle = -iH|\Psi\rangle \approx -i\mathcal{P}^{1s}H|\Psi\rangle . \quad (1.24)$$

The important step that leads to an efficient one-site algorithm is to utilize the fact that the projector \mathcal{P}^{1s} admits an additive decomposition. As shown in Eq. (1.17), we can always split \mathcal{P}^{1s} into a set of orthogonal projectors, \mathcal{P}_ℓ^{1s} and \mathcal{P}_ℓ^b . By further

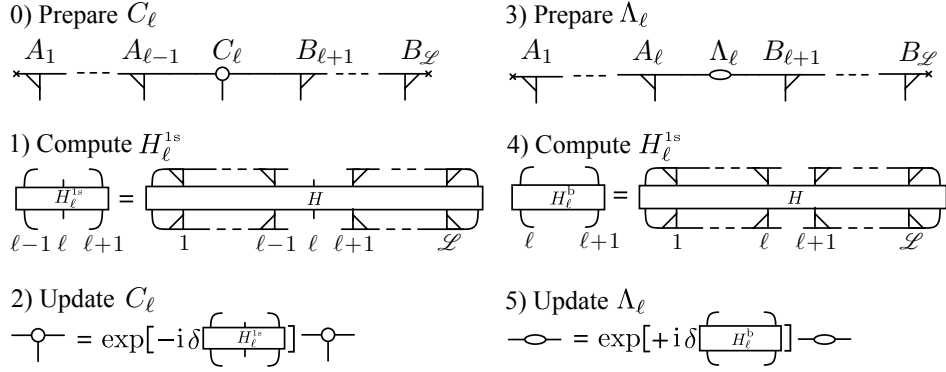


Figure 1.1 The substeps of the one-site algorithm for time integrating an MPS with a Hamiltonian H and time step δ .

invoking the Lie-Trotter approximation, Eq. (1.24) can then be solved by integrating a set of local differential equations sequentially. For example, upon applying $+\mathcal{P}_\ell^{1s}$, we obtain a local equation where only a single tensor C_ℓ needs to be explicitly integrated, as shown in Step. (2) of Fig. 1.1. And by applying $-\mathcal{P}_\ell^b$, we similarly arrive at a local equation where only a matrix Λ_ℓ is involved, as shown in Step (5) of Fig. 1.1. The whole scheme can be implemented very efficiently, if these equations are to be solved from left to right (or from right to left). As there is at most one physical index involved during the local updates, this is hence called the one-site algorithm.

Going beyond the fixed-rank approximation

While the tangent space approach outlined above leads to an efficient one-site implementation, the accuracy is not very well controlled. This is especially true when applying \mathcal{P}^{1s} leads to a significant deviation from the unprojected one [HOV13, YW20, DC21, CKL22]. For real time evolution, one can estimate the inaccuracy through the projection error, $\|(H - \mathcal{P}^{1s}H)|\Psi\rangle\|$. In Chapter 2, we developed a method, controlled bond expansion (CBE), to adjust the tangent space dynamically to reduce the projection error. Combining CBE with the standard one-site algorithms, we eventually achieve an efficient and accurate implementation that is useful for both ground state search and real-time evolution.

1.2 Projected entangled-paired states

Projected entangled-paired states (PEPS) are generalization of matrix product states (MPS) for parametrizing wave functions on quantum lattices with dimensions higher than one [VWPGC06, VMC08]. For an MPS, the wave function is factorized into a train of three-leg tensors $M_{l,r}^\sigma$, where each local physical site (σ) is connected to its nearest neighboring ones on the left and right through indices l and r . Those tensor indices, l and r , not enumerating the local physical states, are called *virtual* indices. They are degrees of freedom, delineating the entanglement between the local physical site and the rest of the system.

The same design principle applies to the local tensor parametrization of PEPS. For example, on a two-dimensional (2D) square lattice, each local PEPS tensor has five legs $M_{l,u,d,r}^\sigma$, which connect the local physical site (σ) to its nearest neighbors in four different directions, left (l), up (u), down (d) and right (r) [see Fig. 1.2(a)]. Such a tensor network factorization, following the lattice geometry, allows PEPS to carry

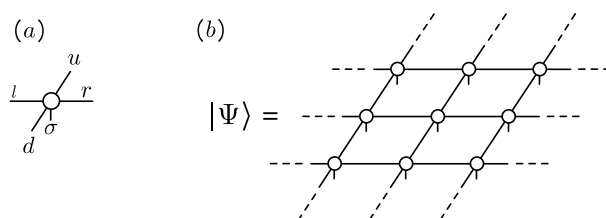


Figure 1.2 (a) The rank-5 PEPS tensor associates with each lattice site on a square lattice. The tensor leg pointing down enumerates the local physical states, while the others connect to neighboring tensors in the wave function. (b) The infinite PEPS to parametrize a 2D quantum state.

the entanglement through *virtual* indices in a more natural way. With its increased connectivity, we expect PEPS to offer a more efficient parametrization than MPS to tackle 2D quantum lattice problems.

Indeed, the generalization to PEPS allows us to simulate bona fide 2D quantum states. This is in contrast to the MPS, which is restricted to simulate states for one-dimensional or narrow-width cylinder systems. Research along this direction has been fruitful [JOV⁺08, OV09, COBV10, BCOT11, LCBn14, PBT⁺15, ZCC⁺17, PCC19, ZP20, SSB⁺20, LZP21, LGL⁺22]. Particularly, the ground-state search via PEPS on infinite lattices, hence called infinite PEPS (iPEPS), provides unique insights to resolve competitive low-lying states that are close in energy [CRT14, LXC⁺17, LKC⁺20]. Being able to work directly in the thermodynamic limit, iPEPS has become a powerful tool to study the phase diagrams of 2D frustrated spins and interacting fermions.

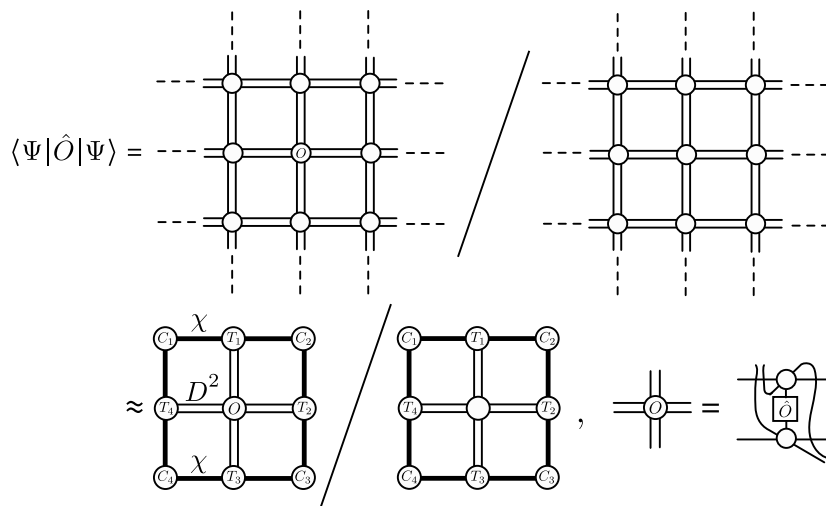


Figure 1.3 Schematics for computing $\langle \Psi | \hat{O} | \Psi \rangle$ via CTMRG to approximate the environment of iPEPS. The environmental tensors C s and T s are assumed to have bond dimensions χ .

However, iPEPS is much harder to handle computationally than the MPS. This is because, when computing local expectation values of local tensors, such as the energy density, we have to first evaluate the so-called *environment*, which is the reduced density matrix representing the bulk part of the state. As iPEPS has no canonical form to exploit as in the case of MPS, the evaluation of the environment needs to be carried out explicitly. The exact evaluation of the environment scales exponentially with respect to the number of lattice sites. By introducing some RG schemes, it

is possible to essentially achieve an iPEPS algorithm with polynomial complexity [see Fig. 1.3]. Among several proposals, in this thesis we adopt the corner transfer matrix renormalization group (CTMRG) method [NO96, NO97, OV09], which is most numerically stable, and easy to extend when considering iPEPS with a large unit-cell.

Furthermore, to simulate the ground state of a local Hamiltonian H , we perform imaginary time evolution, $|\Psi\rangle \approx \frac{e^{-\tau H}|\Psi_0\rangle}{\|e^{-\tau H}|\Psi_0\rangle\|}$, where $|\Psi_0\rangle$ is some initial state. The imaginary time evolution of iPEPS can be combined with different levels of crudity in approximating the iPEPS environment. This in turn gives us three different optimization schemes: *simple-update*, *fast-full-update* and *full-update* methods. The simple-update is computationally cheap [JWX08]. However, because of its gross simplification of the environmental tensors, simple-update often fails to give full account of the physics, especially when close to the phase transition. On the other hand, the full-update [JOV⁺08, COBV10] is notoriously expensive due to the slow convergence of the CTMRG scheme. The fast-full-update improves upon this by accelerating the convergence with a better initialization, but cannot reduce computational complexity further [PBT⁺15].

In Chapter. 3, we first expatiate the detail of iPEPS algorithms mentioned above. The long review article [P4] is largely based on Benedikt Bruognolo's PhD thesis. I have only helped in polishing the manuscript at its final stage and had no contribution to any numerical calculations. It is included here to cover the algorithmic details used in [P5] and [P6]. There we use iPEPS to investigate the ground states for the 2D t-J model on the square lattice and the Kitaev- Γ model on the honeycomb lattice.

1.3 Parton construction for tensor network states

Tensor network methods have provided valuable numerical insights into correlated quantum systems. This owes much not only to the fact that tensor network parametrizations are efficient to describe lowly-entangled states, but also to the strenuous efforts made so far mostly focusing on bringing the computational cost under control. In a sense, tensor network methods have become a powerful numerical grinding machine, when mean-field or perturbative theories become unreliable due to the strong interactions. However, the versatility of tensor network methods is not limited to only this.

The new angle here is to use tensor network states to represent the so-called parton wave functions. Parton wave functions have a long history originally conceived in particle physics. In condensed matter physics, the construction of parton wave functions has also developed into a vital technique to describe collective phenomena emerging from the interactions.

In particular, the parton construction is a powerful approach to study quantum spin-liquids [Gut63, AA88, Wen91a, AM88, RS91]. The basic idea is to rewrite the spins in terms of bosons or fermions with enlarged Hilbert spaces subject to certain constraints. For example, a spin-1/2 operator can be represented by Abrikosov fermions,

$$\mathbf{S} = \frac{1}{2}c_{\alpha}^{\dagger}\boldsymbol{\sigma}_{\alpha\beta}c_{\beta}, \quad (1.25)$$

where c_{α}^{\dagger} is a fermionic creation operator with spin index $\alpha = \uparrow, \downarrow$, and $\boldsymbol{\sigma}$ is the vector of Pauli matrices. The parton construction introduces spurious degrees of freedom (empty and doubly occupied states), which must be removed to fulfill the

local constraint, $\sum_{\alpha} c_{\alpha}^{\dagger} c_{\alpha} = 1$.

A remarkable feature of the parton construction is that, though introduced artificially, these partons might indeed become the true quasiparticles that govern the low-energy behaviors of the spin systems. Its success relies on physical intuition to engineer suitable parton Hamiltonians that (i) are easy to solve and (ii) nonetheless capture the desired physics phenomenologically after projecting out the spurious states. The second step, the implementation of local projections to fix the particle number on each lattice site, turns out to be problematic. For example, in variational Monte Carlo and functional renormalization group approaches, typically only the average particle number can be controlled through Lagrangian multipliers. This makes it unreliable to use parton construction to study the energetics of competing low-lying states. By contrast, using tensor network representations of parton states in the real space, we can implement these local constraints exactly.

Parton construction for MPS

In this thesis, we work on spin models where partons can be chosen to be fermions. Generalizing Eq. (1.25), we use a fermionic parton representation of the $SU(N)$ spin operators [Wen91b], $\mathbf{S} = \sum_{\sigma\sigma'} c_{\sigma}^{\dagger} \mathbf{T}_{\sigma\sigma'} c_{\sigma'}$, where $\mathbf{T}_{\sigma\sigma'}$ are matrix representations of the $SU(N)$ generators in the fundamental representation, and $c_{\ell\sigma}^{\dagger}$ is the fermionic creation operator. Then, we construct some fermionic quadratic Hamiltonian H_{parton} that is exactly solvable and its ground state is a Slater determinant. The strong interactions, which bring out the correlation, are approximated ad hoc by the Gutzwiller projection, P_G^m , to have exactly m fermions per site everywhere [Gut63].

Overall, the projected parton wave function reads,

$$|\Psi\rangle = P_G^m \prod_{q=1}^Q \prod_{\sigma} d_{q\sigma}^{\dagger} |0\rangle, \quad (1.26)$$

where $|0\rangle$ is the fermionic vacuum, and $d_{q\sigma}^{\dagger}$ are the single-particle orbitals of the partons. These single-particle orbitals are composed of local operators $d_{q\sigma}^{\dagger} = \sum_{\ell} A_{\ell}(q) c_{\ell\sigma}^{\dagger}$, with $A(q)$ the eigenmodes of H_{parton} in its single-particle basis. The Gutzwiller projector is $P_G^m = \prod_{\ell=1}^{\mathcal{L}} \prod_{p \neq m} \frac{\hat{n}_{\ell} - p}{m - p}$, where p runs over all values from 0 to N except $p = m$.

This operation projects out any state that has the particle number per site differed from m , and can be trivially implemented in tensor networks.

On the other hand, to express the Slater determinant as a tensor network requires some approximation. For an MPS, how to achieve this optimally has been ironed out in Ref. [WWT20]. The important observation is that each single particle orbital $d_{k\sigma}^{\dagger}$ can be written as a matrix product operator (MPO) of a bond dimension $D = 2$ [see Fig. 1.4] [SRF⁺13, WWT20]. Compactly, the MPO, whose entries viewed as matrices with respect to their virtual indices, reads,

$$d_{q\sigma}^{\dagger} = \begin{pmatrix} 0 & 1 \end{pmatrix} \left[\prod_{j=1}^{\mathcal{L}} \begin{pmatrix} \mathbb{1}_{\ell} & 0 \\ A_{\ell}(q) c_{\ell\sigma}^{\dagger} & F_{\ell} \end{pmatrix} \right] \begin{pmatrix} 1 \\ 0 \end{pmatrix}. \quad (1.27)$$

Here, $c_{\ell\sigma}^{\dagger}$ is the local fermionic creation operator, $\mathbb{1}_{\ell}$ the local identity operator, and F_{ℓ} is the local parity operator introduced to account for the anticommutation relation across different sites. With this, it becomes straightforward to compute Eq. (1.26).

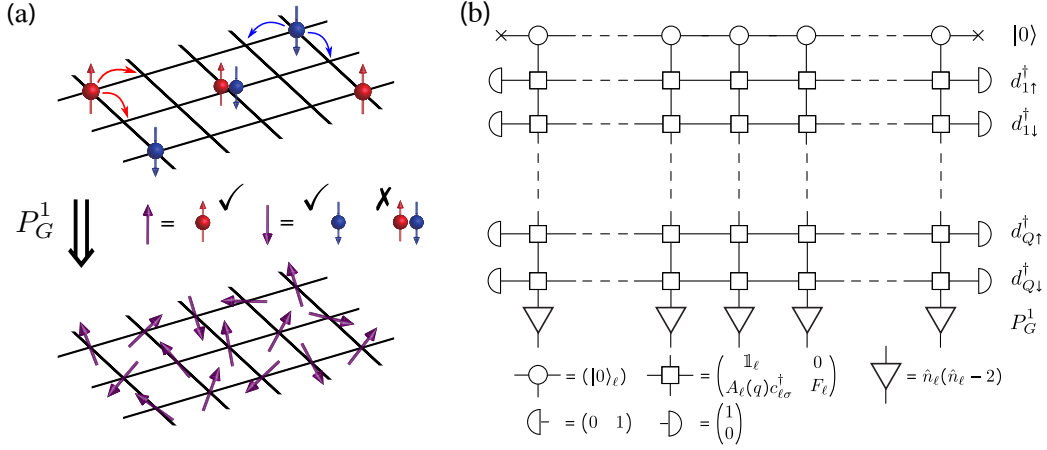


Figure 1.4 (a) Schematics of the projected parton state construction for spin 1/2 model (figure modified from Ref. [WWT20]). (b) The MPO–MPS approach to obtain $|\Psi\rangle = P_G^1 \prod_q \prod_{\sigma=\uparrow\downarrow} d_{k\sigma}^\dagger |0\rangle$.

Starting from the fermionic vacuum, which is a MPS of $D = 1$, we sequentially apply $d_{q\sigma}^\dagger$ to it. The contraction of an MPO with $D = 2$ to an MPS generates a new MPS with a doubled bond dimension. Without any truncation, this will eventually lead to a MPS of $D = 2^{2Q}$. In another word, the contraction of a stack of MPOs, which can also be regarded as a contraction of a two-dimensional tensor network (see Fig. 1.4), has been known to be exponentially difficult. It is thus imperative to apply some approximation. To thwart such exponential growth, we restrict the maximal bond dimension of the MPS by truncating away small singular values during the MPO–MPS evolution. Accepting the truncation error, we in the end attain an approximate Slater determinant as an MPS. In [P7], we will use the MPO–MPS method to generate projected parton states to study $SU(N)$ chiral spin liquids.

Parton construction for PEPS

Another different route is to resort to PEPS to represent the Slater determinant and its Gutzwiller projected state. While the general idea is the same as that of MPS, the formulation is slightly different, due to the difference in tensor network topology and the assumption of translational invariance.

In [P8], we develop an approach to construct Gutzwiller projected parton states using particle-number-conserved PEPSs that exploit the $U(1)$ symmetry. As an example, we here consider the $U(1)$ -symmetric PEPS on a square lattice. On each lattice site \mathbf{r} , we have P physical fermionic (parton) modes, with creation operators $c_{\mathbf{r},\mu}^\dagger$ ($\mu = 1, \dots, P$). In the PEPS framework, we further introduce M virtual fermionic modes, along each edge, with creation operators $c_{\mathbf{r},\nu,\alpha}^\dagger$ ($\nu = l, r, d, u$ and $\alpha = 1, \dots, M$), where l, r, d, u denote left, right, down, and up directions, respectively. And these virtual fermions are maximally entangled to their counterparts on the nearest neighbor sites:

$$|I\rangle = \prod_{\mathbf{r}} \hat{I}_{\mathbf{r}}(x) \hat{I}_{\mathbf{r}}(y) |0\rangle_{\mathbf{v}} = \prod_{\mathbf{r}} \prod_{\alpha=1}^M \frac{c_{\mathbf{r},r,\alpha}^\dagger + c_{\mathbf{r}+\mathbf{x},l,\alpha}^\dagger}{\sqrt{2}} \frac{c_{\mathbf{r},u,\alpha}^\dagger + c_{\mathbf{r}+\mathbf{y},d,\alpha}^\dagger}{\sqrt{2}} |0\rangle_{\mathbf{v}}, \quad (1.28)$$

where $|0\rangle_{\mathbf{v}}$ is the vacuum of virtual fermions, and on a $L \times L$ torus, we have created $N_{\mathbf{v}} = 2ML^2$ virtual fermions.

On the other hand, the physical fermions on different lattice sites are not directly entangled with one another, but indirectly through the entangled virtual modes via a linear map on each site (local PEPS projector),

$$\hat{T}_{\mathbf{r}} = \sum_{\{m_{\mu}\}, \{n_{\nu, \alpha}\}} T(\mathbf{r})^{\{m_{\mu}\}_{\{n_{\nu, \alpha}\}}} \times \left[\prod_{\mu=1}^P (c_{\mathbf{r}, \mu}^{\dagger})^{m_{\mu}} \right] \left[\prod_{\nu=l, r, d, u} \prod_{\alpha=1}^M (c_{\mathbf{r}, \nu, \alpha}^{\dagger})^{n_{\nu, \alpha}} \right]. \quad (1.29)$$

The overall PEPS projector then reads,

$$|T\rangle = \prod_{\mathbf{r}} \hat{T}_{\mathbf{r}} |0\rangle_{\text{p,v}}, \quad (1.30)$$

where $|0\rangle_{\text{p,v}}$ is the joint vacuum state of physical and virtual fermions. The fermionic parton wave function is defined by $|\Psi\rangle = \langle I|T\rangle$, by which the virtual degrees of freedom are entirely contracted out [see Fig 1.5].

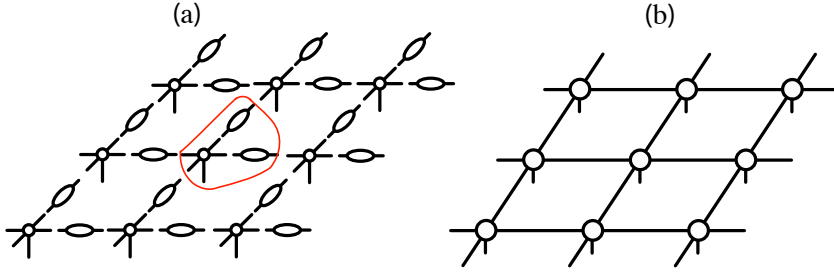


Figure 1.5 (a) Schematics for U(1) PEPS, where $T_{\mathbf{r}}$ is the local rank-5 PEPS projector depicted by circles and the virtual maximally entangled-paired bonds in oval shapes. By appropriately combining local PEPS projector and virtual bonds, we can return to the typical PEPS formalism drawn in (b) introduced in Sec. 1.2.

For the purpose of describing a fermionic parton state with a fixed particle number, we can first impose the U(1) particle number constraint to the PEPS projector $|T\rangle$. Second, to further simplify, we assume that $T(\mathbf{r})$ in Eq. (1.29) is \mathbf{r} -independent, and we have henceforth a translational invariant PEPS. Moreover, since we are only concerned with quadratic parton Hamiltonians, the local PEPS projector $\hat{T}_{\mathbf{r}}$ can eventually be parametrized as a local Slater determinant,

$$\hat{T}_{\mathbf{r}} = \prod_{q=1}^Q d_{\mathbf{r}, q}^{\dagger}, \quad (1.31)$$

where the single-particle orbitals, $d_{\mathbf{r}, q}^{\dagger}$, are linear combinations of local physical modes $c_{\mathbf{r}, \mu}^{\dagger}$ and virtual modes $c_{\mathbf{r}, \nu, \alpha}^{\dagger}$ at the same site. On a $L \times L$ square lattice, we thus obtain a parton state for PEPS, $|\Psi\rangle = \langle I|T\rangle$ with a fixed total particle number $(Q - 2M)L^2$.

The above simplification, namely taking $\hat{T}_{\mathbf{r}}$ to be both translationally invariant and also a Slater determinant, has consequences. It gives rise to certain restrictions on the types of band structure we can simulate. This is more transparent to understand in the momentum space, with $c_{\mathbf{r}}^{\dagger} = \frac{1}{L} \sum_{\mathbf{k}} c_{\mathbf{k}}^{\dagger} e^{-i\mathbf{k} \cdot \mathbf{r}}$ for both physical and virtual fermions. The Fourier transformation of the PEPS projector is trivial, as its local terms are

decoupled,

$$|T\rangle = \prod_{\mathbf{k}} \prod_{q=1}^Q d_{\mathbf{k},q}^\dagger |0\rangle_{\text{p,v}}. \quad (1.32)$$

As for the virtual modes, the nearest-neighboring hopping yields a k dependent phase, and we have

$$|I\rangle = \prod_{\mathbf{k}} \prod_{\alpha=1}^M \frac{1}{2} (c_{\mathbf{k},r,\alpha}^\dagger + c_{\mathbf{k},l,\alpha}^\dagger e^{-ik_x}) (c_{\mathbf{k},u,\alpha}^\dagger + c_{\mathbf{k},d,\alpha}^\dagger e^{-ik_y}) |0\rangle_{\text{v}}. \quad (1.33)$$

Importantly, both $|T\rangle$ and $|I\rangle$ are k -separable, and so does the overall PEPS. That is,

$$|\Psi\rangle = \prod_{\mathbf{k}} \left[\prod_{q=1}^Q \prod_{\alpha=1}^M \langle 0|_{\text{v}} \frac{1}{2} (c_{\mathbf{k},r,\alpha} + c_{\mathbf{k},l,\alpha} e^{+ik_x}) (c_{\mathbf{k},u,\alpha} + c_{\mathbf{k},d,\alpha} e^{+ik_y}) d_{\mathbf{k},q}^\dagger |0\rangle_{\text{p,v}} \right]. \quad (1.34)$$

From the above Eq. (1.34), it becomes clear that each k -point must have the same number of physical fermions, $Q - 2M$. Therefore, we expect that our parton construction for PEPS can only describe systems with completely filled bands, either a band insulator with a finite energy gap, or a semimetal having Dirac cones or quadratic band touching points.

In [P8], we will explain how to numerically optimize the introduced fermionic parton ansatz for PEPS, and we will demonstrate its performance with the π -flux model on square lattices and the $[0, \pi]$ -flux model on kagome lattices.

2 Matrix Product States

2.1 Overview

To these days, matrix product states (MPS) have become the de facto standard tool to study frustrated spins and interacting fermions on one-dimensional lattices and narrow-width cylinders and ladders. MPS can simulate ground states via the density matrix renormalization group (DMRG) and real-time evolution via the time-dependent variational principle (TDVP). Both DMRG and TDVP are algorithms run in polynomial time scale, $\mathcal{O}(\mathcal{L}D^3d^n)$. Here \mathcal{L} is the number of lattice sites, D is the MPS bond dimension and d is the dimension of the local physical Hilbert space. And n is an integer, determining the number of physical sites to be simultaneously updated during optimization.

One-site update The one-site update scheme with complexity $\mathcal{O}(\mathcal{L}D^3d)$ is the cheapest among all. However, it leads to poor accuracy for both DMRG and TDVP. The important ingredient that is missing compared to multi-site update schemes is the possibility to increase the MPS bond dimensions D when necessary.

This problem was first addressed by Steven White in 2005 by adding *noise* to DMRG [Whi05]. The noise refers to small random numbers added to the reduced density matrices before diagonalization, which helps to bump DMRG out of local minima when the initial guess is poor and far away from the true ground state. This perturbative approach was refined later by Hubig et al. in 2015 [HMSW15] and was widely implemented. An exemplary application is the study of the two-dimensional Hubbard model on width-6 cylinders [QCS+20], where unprecedented large bond dimension DMRG calculations were carried out. However, this perturbative approach requires extra care during the calculations, and its numerical cost is not yet optimal.

For real-time evolution, we are facing a similar issue again. It is widely known that the one-site TDVP, without changing the bond dimension, guarantees energy and norm conservation [HCO+11, LO13, LRSV13]. This merit however does not say anything about other physical quantities, nor does it ensure the numerical accuracy in the long time [GD19, CSZ20, MB20]. When the MPS bond dimension is overly restricted, TDVP induces projection errors and the accompanied inaccuracy is hard to control.

To simulate accurate dynamics, some scheme to adaptively increase the bond dimension to accommodate the entanglement growth in time is necessary. In 2020, Yang and White first proposed a global bond expansion scheme [YW20]. Later, several local bond expansion schemes have also been put forward [DRV21, DC21, CKL22, EOS22, XXX+22]. All these attempts are shown to improve the accuracy of the one-site TDVP to some extent. Nonetheless, a method that achieves optimal efficiency and numerical accuracy in the long-time is still in need.

Controlled bond expansion Using tangnet space methods, we develop a unified approach, controlled bond expansion (CBE), that works for both the one-site DMRG and the one-site TDVP. For typical one-site algorithms, the parameter space that

one can work with is confined, as these algorithms only evolve the MPS within its one-site tangent space manifold and cannot go beyond. To improve the accuracy, we use CBE that aims to enlarge the MPS bond dimension, such that it explores the variational space beyond its one-site subspace. CBE inspects the full two-site tangent space manifold, but only enriches the MPS with the relevant portion distilled from that. Therefore, CBE manages to achieve two-site accuracy with one-site costs.

For concrete applications, we show that both CBE-DMRG and CBE-TDVP can achieve accuracy comparable to the typical two-site update scheme at single-site costs. In [P1], we benchmarked the numerical cost of CBE-DMRG, which evidences the linear scaling of d in time complexity. In [P2], we illustrate the performance of CBE-TDVP with several numerical examples on finite quantum lattices. We then close this chapter with a discussion [P3] on generalizing the tangent space construction to a multi-site scenario (up to now only one- and two-site formulas exist), and its potential application in the future.

- P1** *Controlled bond expansion for DMRG ground state search at single-site costs*
Andreas Gleis, **Jheng-Wei Li**, and Jan von Delft
[arXiv:2207.14712 \(2022\)](#)

- P2** *Time-dependent variational principle with controlled bond expansion for matrix product states*
Jheng-Wei Li, Andreas Gleis, and Jan von Delft
[arXiv:2208.10972 \(2022\)](#)

- P3** *Projector formalism for kept and discarded spaces of matrix product states*
Andreas Gleis, **Jheng-Wei Li** and Jan von Delft
[arXiv:2207.13161 \(2022\)](#)

Controlled bond expansion for DMRG ground state search at single-site costs

Andreas Gleis,¹ Jheng-Wei Li,¹ and Jan von Delft¹

¹Arnold Sommerfeld Center for Theoretical Physics, Center for NanoScience, and Munich Center for Quantum Science and Technology, Ludwig-Maximilians-Universität München, 80333 Munich, Germany

(Dated: August 1, 2022)

DMRG ground state search algorithms employing symmetries must be able to expand virtual bond spaces by adding or changing symmetry sectors if these lower the energy. Traditional single-site DMRG does not allow bond expansion; two-site DMRG does, but at much higher computational costs. We present a controlled bond expansion (CBE) algorithm that yields two-site accuracy and convergence per sweep, at single-site costs. Given a matrix product state Ψ defining a variational space, CBE identifies parts of the orthogonal space carrying significant weight in $H\Psi$ and expands bonds to include only these. CBE-DMRG uses no mixing parameters and is fully variational.

DOI:

Introduction.— A powerful tool for studying ground state properties of one- and two-dimensional quantum systems is the density matrix renormalization group (DMRG) [1–7]. Prominent two-dimensional applications include the t - J [8–11] and Hubbard [12–18] models, and quantum magnets [19–22]. Due to their high numerical costs, such studies are currently limited to either small finite-sized systems or cylinders with small circumference. Progress towards computationally cheaper DMRG ground state search algorithms would clearly be welcome.

In this paper, we address this challenge. A DMRG ground state search explores a variational space spanned by matrix product states. If symmetries are exploited, the algorithm must be able to expand the auxiliary spaces associated with virtual bonds by adjusting symmetry sectors if this lowers the energy. Traditional single-site or one-site (1s) DMRG, which variationally updates one site at a time, does not allow such bond expansions. As a result, it often gets stuck in metastable configurations having quantum numbers different from the actual ground state. Two-site (2s) DMRG naturally leads to bond expansion, but carries much higher computational costs.

Hence, schemes have been proposed for achieving bond expansions at sub-2s costs, such as density matrix perturbation [23] or subspace expansion [24]. However, in these schemes, the degree of subspace expansion per local update is controlled by a heuristic mixing factor. Depending on its value, some subspace expansion updates increase, rather than decrease, the energy.

Here, we present a controlled bond expansion (CBE) algorithm which lowers the energy with each step and yields 2s accuracy and convergence per sweep, at 1s costs. Given a matrix product state Ψ defining a variational space, our key idea is to identify parts of the 2s orthogonal space that carry significant weight in $H\Psi$, and to include only these parts when expanding the virtual bonds of a 1s Hamiltonian. Remarkably, these parts can be found via a projector that can be constructed at 1s costs.

MPS basics.— We briefly recall some standard MPS concepts [5], adopting the diagrammatic conventions of

Ref. 25. Consider an \mathcal{L} -site system with an open boundary MPS wavefunction Ψ having dimensions d for physical sites and D for virtual bonds. Ψ can be written in bond-canonical form w.r.t. to any bond ℓ ,

$$\Psi = \begin{array}{c} A_1 \quad A_2 \quad \dots \quad A_\ell \quad \Lambda_\ell \quad B_{\ell+1} \quad \dots \quad B_{\mathcal{L}-1} \quad B_{\mathcal{L}} \\ \text{---} \text{---} \text{---} \text{---} \text{---} \text{---} \text{---} \text{---} \text{---} \text{---} \\ \text{---} \text{---} \text{---} \text{---} \text{---} \text{---} \text{---} \text{---} \text{---} \text{---} \end{array} \quad (1)$$

The tensors Λ_ℓ (\circ), A_ℓ (∇) and B_ℓ (∇) are variational parameters. They are linked by gauge relations, $A_\ell \Lambda_\ell = \Lambda_{\ell-1} B_\ell$, useful for shifting the bond tensor Λ_ℓ to neighboring bonds. A_ℓ and B_ℓ are left and right-sided isometries, respectively, projecting Dd -dimensional *parent* (p) spaces to D -dimensional *kept* (k) image spaces [25]; they satisfy

$$A_\ell^\dagger A_\ell = \left(\bigcap_{A_\ell^*} = \left(= \mathbb{1}_k, \quad B_\ell B_\ell^\dagger = \left(\bigcap_{B_\ell^*} = \right) = \mathbb{1}_{k-1}. \quad (2)$$

The Hamiltonian can similarly be expressed as a matrix product operator (MPO) with virtual bond dimension w ,

$$H = \begin{array}{c} W_1 \quad W_2 \quad \dots \quad W_\ell \quad W_{\mathcal{L}-1} \quad W_{\mathcal{L}} \\ \text{---} \text{---} \text{---} \text{---} \text{---} \text{---} \\ \text{---} \text{---} \text{---} \text{---} \text{---} \text{---} \end{array} \quad (3)$$

For 2s or 1s DMRG, the energy of Ψ is lowered by projecting H to a local variational space associated with sites $(\ell, \ell+1)$ or ℓ , respectively, and using its ground state (GS) within that space to locally update Ψ . The corresponding 2s and 1s Hamiltonians can be computed recursively using

$$H_\ell^{2s} = \left(\begin{array}{c} D \\ \text{---} \text{---} \text{---} \text{---} \\ \ell-1 \quad \ell \quad \ell+1 \quad \ell+2 \end{array} \right)^D = \left(\begin{array}{c} \text{---} \text{---} \text{---} \text{---} \\ \text{---} \text{---} \text{---} \text{---} \\ 1 \quad \ell-1 \quad \ell \quad \ell+1 \quad \ell+2 \quad \mathcal{L} \end{array} \right), \quad (4a)$$

$$H_\ell^{1s} = \left(\begin{array}{c} D \\ \text{---} \text{---} \\ \ell-1 \quad \ell \quad \ell+1 \end{array} \right)^D = \left(\begin{array}{c} \text{---} \text{---} \\ \text{---} \text{---} \\ \ell-2 \quad \ell-1 \quad \ell \quad \ell+1 \end{array} \right) = \left(\begin{array}{c} \text{---} \text{---} \\ \text{---} \text{---} \\ \ell-1 \quad \ell \quad \ell+1 \quad \ell+2 \end{array} \right). \quad (4b)$$

To perform 2s or 1s updates, one replaces $\psi_\ell^{2s} = A_\ell \Lambda_\ell B_{\ell+1}$ or $\psi_\ell^{1s} = C_\ell = A_\ell \Lambda_\ell$ (∇) by the GS solutions of

$$(H_\ell^{2s} - E)\psi_\ell^{2s} = 0, \quad \left(\begin{array}{c} \text{---} \text{---} \text{---} \text{---} \\ \text{---} \text{---} \text{---} \text{---} \\ \ell-1 \quad \ell \quad \ell+1 \quad \ell+2 \end{array} \right) = E \left(\begin{array}{c} \text{---} \text{---} \\ \text{---} \text{---} \\ \ell \quad \ell+1 \end{array} \right), \quad (5a)$$

$$(H_\ell^{1s} - E)\psi_\ell^{1s} = 0, \quad \left(\begin{array}{c} \text{---} \text{---} \\ \text{---} \text{---} \\ \ell-1 \quad \ell \quad \ell+1 \end{array} \right) = E \left(\begin{array}{c} \text{---} \\ \text{---} \\ \ell \end{array} \right). \quad (5b)$$

Updating site by site, one sweeps back and forth through the MPS until the GS energy converges.

The local variational space is larger for 2s than 1s DMRG by a factor d , $\mathcal{O}(D^2 d^2)$ vs. $\mathcal{O}(D^2 d)$. This enables 2s DMRG to increase (“expand”) the bond dimension during updates by including new states (and symmetry sectors!) from the 2s space. 1s DMRG cannot do this, and hence often fails to yield accurate GS energies. The better performance of 2s vs. 1s has its price: much higher numerical costs, $\mathcal{O}(D^3 d^3 + D^3 d^2 w)$ vs. $\mathcal{O}(D^3 dw)$ [5].

Discarded spaces.— To track those parts of 2s spaces not contained in 1s spaces, we introduce orthogonal complements of A_ℓ and B_ℓ , denoted $\bar{A}_\ell(\nabla)$ and $\bar{B}_\ell(\nabla)$. These isometries have image spaces, called *discarded* (D) spaces [25], of dimension $\bar{D}=D(d-1)$, orthogonal to the kept images of A_ℓ and B_ℓ . Thus $A_\ell^\perp(\nabla) = A_\ell \oplus \bar{A}_\ell$ and $B_\ell^\perp(\nabla) = B_\ell \oplus \bar{B}_\ell$ are unitaries on their parent spaces, with

$$\frac{A_\ell}{D \nabla D} \oplus \frac{\bar{A}_\ell}{D \nabla \bar{D}} = \frac{A_\ell^\perp}{D \nabla D}, \quad \frac{B_\ell}{D \nabla D} \oplus \frac{\bar{B}_\ell}{D \nabla \bar{D}} = \frac{B_\ell^\perp}{D \nabla D}. \quad (6)$$

The unitarity conditions for A_ℓ^\perp and B_ℓ^\perp imply orthonormality and completeness relations complementing Eq. (2),

$$\left[\begin{array}{c} \text{---} \\ \text{---} \\ \text{---} \end{array} \right]_\ell = \left(= \mathbb{1}_\ell^D, \quad \left[\begin{array}{c} \text{---} \\ \text{---} \\ \text{---} \end{array} \right]_\ell = 0, \quad \left[\begin{array}{c} \text{---} \\ \text{---} \\ \text{---} \end{array} \right]_\ell = \right) = \mathbb{1}_{\ell-1}^D, \quad \left[\begin{array}{c} \text{---} \\ \text{---} \\ \text{---} \end{array} \right]_\ell = 0 \quad (7a)$$

$$\left[\begin{array}{c} \text{---} \\ \text{---} \\ \text{---} \end{array} \right]_\ell + \left[\begin{array}{c} \text{---} \\ \text{---} \\ \text{---} \end{array} \right]_\ell = \left[\begin{array}{c} \text{---} \\ \text{---} \\ \text{---} \end{array} \right]_\ell = \mathbb{1}_\ell^D, \quad \left[\begin{array}{c} \text{---} \\ \text{---} \\ \text{---} \end{array} \right]_\ell + \left[\begin{array}{c} \text{---} \\ \text{---} \\ \text{---} \end{array} \right]_\ell = \left[\begin{array}{c} \text{---} \\ \text{---} \\ \text{---} \end{array} \right]_\ell = \mathbb{1}_{\ell-1}^D. \quad (7b)$$

If the unitary maps $A_\ell^{\perp\dagger}$ and $B_{\ell+1}^{\perp\dagger}$ of Eq. (6) are applied to some of the open indices of $H_\ell^{1s} \psi_\ell^{1s}$, $H_{\ell+1}^{1s} \psi_{\ell+1}^{1s}$ and $H_\ell^{2s} \psi_\ell^{2s}$ as indicated below, they map the diagrams of Eqs. (5) to

$$\begin{aligned} H_\ell^{1s} \psi_\ell^{1s} &\rightarrow \left[\begin{array}{c} \text{---} \\ \text{---} \\ \text{---} \end{array} \right]_{\ell, \ell+1} = \left[\begin{array}{c} \text{---} \\ \text{---} \\ \text{---} \end{array} \right]_{\ell, \ell+1} = \left[\begin{array}{c} \text{---} \\ \text{---} \\ \text{---} \end{array} \right]_{\ell, \ell+1} \oplus \left[\begin{array}{c} \text{---} \\ \text{---} \\ \text{---} \end{array} \right]_{\ell, \ell+1}, \\ H_{\ell+1}^{1s} \psi_{\ell+1}^{1s} &\rightarrow \left[\begin{array}{c} \text{---} \\ \text{---} \\ \text{---} \end{array} \right]_{\ell, \ell+1} = \left[\begin{array}{c} \text{---} \\ \text{---} \\ \text{---} \end{array} \right]_{\ell, \ell+1} = \left[\begin{array}{c} \text{---} \\ \text{---} \\ \text{---} \end{array} \right]_{\ell, \ell+1} \oplus \left[\begin{array}{c} \text{---} \\ \text{---} \\ \text{---} \end{array} \right]_{\ell, \ell+1}, \\ H_\ell^{2s} \psi_\ell^{2s} &\rightarrow \left[\begin{array}{c} \text{---} \\ \text{---} \\ \text{---} \end{array} \right]_{\ell, \ell+1} \oplus \left[\begin{array}{c} \text{---} \\ \text{---} \\ \text{---} \end{array} \right]_{\ell, \ell+1} \oplus \left[\begin{array}{c} \text{---} \\ \text{---} \\ \text{---} \end{array} \right]_{\ell, \ell+1} \oplus \left[\begin{array}{c} \text{---} \\ \text{---} \\ \text{---} \end{array} \right]_{\ell, \ell+1}. \end{aligned}$$

The first three terms from the third line also appear in the first two lines, but the fourth, involving $\blacktriangleleft \blacktriangleright$, does not. Let DD denote the image of the orthogonal complements $\bar{A}_\ell \otimes \bar{B}_{\ell+1}(\nabla \otimes \nabla)$, then DD is orthogonal to the variational space explored by 1s DMRG on sites $(\ell, \ell+1)$. DD is much larger than the latter, of dimension $\bar{D}^2 = D^2(d-1)^2$ vs. $2D^2 d$, and (importantly!) may contain new symmetry sectors. Thus DD is the 2s ingredient lacking in 1s schemes.

This can also be seen considering the energy variance $\Delta_E = \|(H-E)\Psi\|^2$. By expanding it into contributions involving orthogonal projections on one, two, or more sites [26], $\Delta_E = \Delta_E^{1\perp} + \Delta_E^{2\perp} + \dots$, one obtains [25]

$$\Delta_E^{1\perp} = \sum_{\ell=1}^{\mathcal{L}} \left\| \left[\begin{array}{c} \text{---} \\ \text{---} \\ \text{---} \end{array} \right]_{\ell} \right\|^2, \quad \Delta_E^{2\perp} = \sum_{\ell=1}^{\mathcal{L}-1} \left\| \left[\begin{array}{c} \text{---} \\ \text{---} \\ \text{---} \end{array} \right]_{\ell, \ell+1} \right\|^2. \quad (8)$$

1s DMRG minimizes only $\Delta_E^{1\perp}$, 2s minimizes $\Delta_E^{1\perp}$ and $\Delta_E^{2\perp}$. We thus seek to expand the κ image of ∇ or ∇ at the

expense of the D image of ∇ or ∇ . This transfers weight from $\Delta_E^{2\perp}$ to $\Delta_E^{1\perp}$, making it accessible to 1s minimization.

Controlled bond expansion.— The CBE algorithm rests on two new insights, substantiated by the quality of its results. The first insight is that the subspace of DD relevant for lowering the GS energy is relatively small: it is the subspace on which $H_\ell^{2s} \psi_\ell^{2s}$ and hence $\Delta_E^{2\perp}$ have significant weight. When expanding a bond, it thus suffices to add only this small subspace (hence the moniker *controlled bond expansion*), or only part of it, to be called relevant DD (rDD). Since DD is the image of $\bar{A}_\ell \otimes \bar{B}_{\ell+1}(\nabla \otimes \nabla)$, rDD can be viewed as the image of $\tilde{A}_\ell^{\text{tr}} \otimes \tilde{B}_{\ell+1}^{\text{tr}}(\nabla \otimes \nabla)$ or $\bar{A}_\ell \otimes \tilde{B}_{\ell+1}^{\text{tr}}(\nabla \otimes \nabla)$, where the isometries $\tilde{A}_\ell^{\text{tr}}(\nabla)$ or $\tilde{B}_{\ell+1}^{\text{tr}}(\nabla)$ are *truncated* versions of \bar{A}_ℓ or $\bar{B}_{\ell+1}$ and have image dimensions \tilde{D} , say. It turns out that one may choose $\tilde{D} < D$, independent of d , thus rDD, of dimension $\tilde{D}\bar{D}$, is indeed much smaller than DD. The second insight is that $\tilde{A}_\ell^{\text{tr}}$ or $\tilde{B}_{\ell+1}^{\text{tr}}$ can be constructed at 1s costs using a novel scheme explained in Figs. 1 and 2. We call it *shrewd selection* since it is cheap, efficient and practical, though not strictly optimal (that would require 2s costs).

Based on these insights, a CBE update of bond ℓ proceeds in four substeps. We describe them for a right-to-left sweep for building $\tilde{A}_\ell^{\text{tr}}$ and updating $C_{\ell+1}$ (left-to-right sweeps, building $\tilde{B}_{\ell+1}^{\text{tr}}$ and updating C_ℓ , are analogous).

(i) Compute $\tilde{A}_\ell^{\text{tr}}(\nabla)$ using shrewd selection.

(ii) Expand bond ℓ from dimension D to $D+\tilde{D}$ by replacing A_ℓ by an expanded isometry $A_\ell^{\text{ex}}(\nabla) = A_\ell \oplus \tilde{A}_\ell^{\text{tr}}$, and $C_{\ell+1}$ by an expanded tensor initialized as $C_{\ell+1}^{\text{ex},i}(\nabla)$, defined such that $A_\ell^{\text{ex}} C_{\ell+1}^{\text{ex},i} = A_\ell C_{\ell+1}$:

$$\frac{A_\ell}{D \nabla D} \oplus \frac{\tilde{A}_\ell^{\text{tr}}}{D \nabla \tilde{D}} = \frac{A_\ell^{\text{ex}}}{D \nabla (D+\tilde{D})} \frac{C_{\ell+1}^{\text{ex},i}}{D \nabla D} = \left[\begin{array}{c} \text{---} \\ \text{---} \\ \text{---} \end{array} \right]_{\ell, \ell+1}. \quad (9)$$

Also construct an expanded *one-site* Hamiltonian, defined in a variational space of dimension $D(D+\tilde{D})d$:

$$H_{\ell+1}^{1s, \text{ex}} = \left[\begin{array}{c} \text{---} \\ \text{---} \\ \text{---} \end{array} \right]_{\ell+1} = \left[\begin{array}{c} \text{---} \\ \text{---} \\ \text{---} \end{array} \right]_{\ell+1}^{D+\tilde{D}}. \quad (10)$$

(iii) Update $C_{\ell+1}^{\text{ex}}$ variationally by using an iterative eigensolver, as usual in DMRG, to find the GS solution of $(H_{\ell+1}^{1s, \text{ex}} - E)C_{\ell+1}^{\text{ex}} = 0$, starting from $C_{\ell+1}^{\text{ex},i}$. (We employ a Lanczos eigensolver.) This has costs of $\mathcal{O}(D^3 dw)$. Thus, $C_{\ell+1}^{\text{ex}}$ can be updated at 1s costs, while including only the most relevant 2s information via the contribution of $\tilde{A}_\ell^{\text{tr}}$.

(iv) Shift the isometry center from site $\ell+1$ to site ℓ using a singular value decomposition (SVD) and truncate (*trim*) bond ℓ from dimension $D+\tilde{D}$ back to D , removing low-weight states. The discarded weight, say ξ , of this bond trimming serves as error measure. It can be used for extrapolations, e.g. of GS energy versus ξ , just as for 2s DMRG. This yields GS energies comparable in accuracy to 2s DMRG or 2s variance extrapolations [26] (see below), though computing ξ requires only 1s costs.

$$C_1 = \left\| \begin{array}{c} \text{---} \text{---} \text{---} \\ \text{---} \text{---} \text{---} \\ \text{---} \text{---} \text{---} \end{array} \right\|, \quad C_2 = \left\| \begin{array}{c} \text{---} \text{---} \text{---} \\ \text{---} \text{---} \text{---} \\ \text{---} \text{---} \text{---} \end{array} \right\|, \quad C_3 = \left\| \begin{array}{c} \text{---} \text{---} \text{---} \\ \text{---} \text{---} \text{---} \\ \text{---} \text{---} \text{---} \end{array} \right\|.$$

FIG. 1. During a right-to-left CBE sweep, bond ℓ is expanded from $A_\ell(\nabla)$ to $A_\ell \oplus \tilde{A}_\ell^{\text{tr}}(\nabla \oplus \nabla)$, where $\tilde{A}_\ell^{\text{tr}}(\nabla)$, with image dimension \tilde{D} , is a truncation of $\bar{A}_\ell(\nabla)$, with image dimension $\bar{D} = D(d-1)$. This expansion will reduce Δ_E^{2s} significantly if $\tilde{A}_\ell^{\text{tr}} \oplus \bar{B}_{\ell+1}(\nabla \otimes \nabla)$ targets rDD, a $\tilde{D}\bar{D}$ -dimensional subspace of the \bar{D}^2 -dimensional space DD on which $H_\ell^{2s}\psi_\ell^{2s}$ has significant weight. Ideally, $\tilde{A}_\ell^{\text{tr}}$ should minimize the cost function C_1 , the difference between applying the projectors $\bar{A}_\ell \bar{A}_\ell^\dagger$ or $\tilde{A}_\ell^{\text{tr}} \tilde{A}_\ell^{\text{tr}\dagger}$ to $H_\ell^{2s}\psi_\ell^{2s} \bar{B}_{\ell+1}^\dagger \bar{B}_{\ell+1}$. However, exact minimization of C_1 would involve 2s costs (feasible if d, w and D are comparatively small, but in general undesirable). To maintain 1s costs, $\mathcal{O}(D^3 dw)$, we instead use *shrewd selection*, involving two separate truncations (explained in Fig. 2, depicted schematically in Fig. 3). The first truncation (*preselection*) truncates the central MPS bond from $D \rightarrow D'$ (specified below) in the presence of its environment by minimizing C_2 ; this replaces the full complement by a preselected complement, $\bar{A}_\ell \nabla \rightarrow \hat{A}_\ell^{\text{pr}} \nabla$, with reduced image dimension, $\bar{D} \rightarrow \hat{D} = D'w$ [27]. The second truncation (*final selection*) minimizes C_3 with central MPO bond closed as appropriate for $H_\ell^{2s}\psi_\ell^{2s}$: it further truncates \hat{A}_ℓ^{pr} to yield the final truncated complement, $\tilde{A}_\ell^{\text{tr}} \nabla \rightarrow \nabla$, $\hat{D} \rightarrow \tilde{D} < D$. To ensure 1s costs for final selection we need $\hat{D} = D$, and thus choose $D' = D/w$ for preselection. Though shrewd selection involves severe bond reductions, it yields rDDs suitable for efficiently lowering the GS energy (in step (iii)). Section S-2 in [28] illustrates this by analysing singular value spectra.

The energy minimization based on $H_{\ell+1}^{1s, \text{ex}}$ is variational, hence each CBE update strictly lowers the GS energy. Moreover, although CBE explores a much smaller variational space than 2s DMRG, it still converges at the same rate (as shown below), since it focuses on the subspace that really matters for energy reduction.

We remark that bond expansion using a truncated DD has been proposed before [24, 29]. But our choice of $A_\ell^{\text{ex}}(\nabla)$ is more optimal than for the subspace expansion of Ref. [24], which requires a heuristic mixing factor and yields updates that sometimes raise the energy; and our method of finding $A_\ell^{\text{ex}}(\nabla)$ at 1s costs is cheaper than that used in [29] (for the variational uniform MPS algorithm [30]), which uses an SVD requiring 2s costs.

Sweeping.— Our computations exploit non-Abelian symmetries [31, 32], where bond dimensions, denoted D^* , count symmetry multiplets (D counts states). Usually, D^* is increased with each update during sweeping, from an initial D_1^* to a final $D_f^* = \alpha D_1^*$, with $\alpha > 1$. To achieve this with using CBE, we (i,ii) use $D^* \simeq D_f^*/w^*$, $\hat{D}^* = D_f^*$ (cf. Fig. 2) and expand from D_1^* to

$$D_1^* + \tilde{D}^* = D_f^*(1 + \delta), \quad (11)$$

(iii) call the iterative eigensolver, and (iv) truncate back

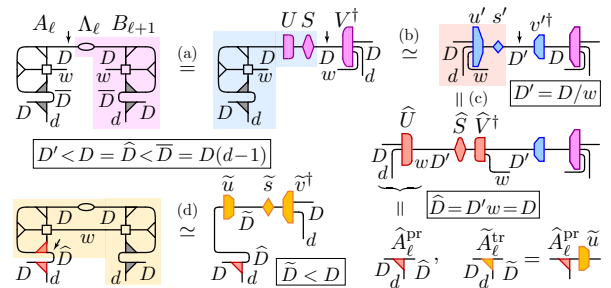


FIG. 2. Shrewd selection: Computation of (a-c) the preselected complement $\hat{A}_\ell^{\text{pr}}(\nabla)$ to minimize C_2 , and (d) the final truncated complement $\tilde{A}_\ell^{\text{tr}}(\nabla)$ to minimize C_3 , using four SVDs, all with at most 1s costs. For each, an arrow indicates a bond being opened before doing the SVD, shading and symbols in matching colors indicate the SVD input and output, and the latter is written as USV^\dagger or usv^\dagger when involving no or some truncation, respectively. Importantly, we express $\bar{A}_\ell \bar{A}_\ell^\dagger$ and $\bar{B}_{\ell+1}^\dagger \bar{B}_{\ell+1}$ (grey) as $\mathbb{1}_\ell - A_\ell A_\ell^\dagger$ and $\mathbb{1}_\ell - B_{\ell+1}^\dagger B_{\ell+1}$ (Eq. (7b)), avoiding the computation of \bar{A}_ℓ and $\bar{B}_{\ell+1}$. (a) The first SVD canonicalizes the right side of the diagram, assigning its weights to the central MPS bond. (b) The second SVD and truncation reduces the dimension of this bond, $D \rightarrow D' = D/w$. (c) The third SVD regroupes indices to combine the truncated MPS bond and the MPO bond into a composite bond of dimension $\hat{D} = D'w = D$, yielding the preselected complement $\hat{A}_\ell^{\text{pr}} = \hat{U}(\nabla)$. Nominally, step (c) would require no truncation if exact arithmetic were used, but in practice (numerically) zero singular values, of order $\mathcal{O}(10^{-16})$, may arise; these must be discarded to ensure $A_\ell^\dagger \hat{A}_\ell^{\text{pr}} = 0$. (d) The fourth SVD and truncation yields the final truncated complement $\tilde{A}_\ell^{\text{tr}} = \hat{A}_\ell^{\text{pr}} \tilde{u}(\nabla)$, with bond reduction $\hat{D} \rightarrow \tilde{D} < D$.

to D_f^* when shifting the isometry center. We use $\alpha = \sqrt{2}$ and $\delta = 0.1$ (for CBE), unless stated otherwise. For the CBE and 2s DMRG comparisons shown below, we use the same initial state: a $D_1^* = 1$ valence bond state with one fermion per site, uniform density and total spin 0.

Results.— We now benchmark CBE-DMRG for free fermions in one dimension (1D), then illustrate its performance for computationally challenging models: the 1D Hubbard-Holstein model and the 2D Hubbard and Kondo-Heisenberg-Holstein models on cylinders. We choose not to discuss their rich physics, aiming here only to demonstrate the feasibility of studying them with CBE-DMRG.

All CPU time measurements were done on a single core of an Intel Core i7-9750H processor.

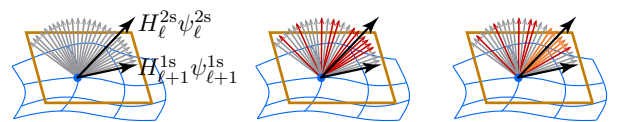


FIG. 3. The projection $H_\ell^{2s}\psi_\ell^{2s} \xrightarrow{A_\ell^\dagger} H_{\ell+1}^{1s}\psi_{\ell+1}^{1s}$ to the tangent space (yellow) of the MPS manifold (blue) discards information from DD (depicted by grey arrows for DD basis vectors). Relevant information is recovered at 1s cost by constructing rDD through preselection (red), then final selection (orange).

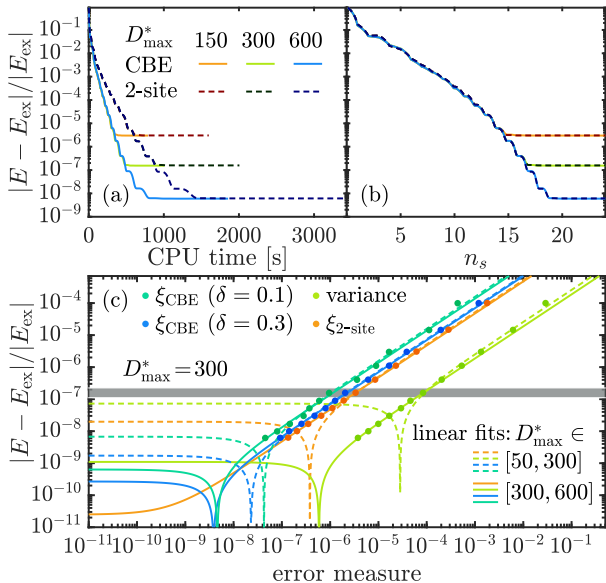


FIG. 4. Relative error in GS energy vs. (a) CPU time and (b) number of half-sweeps n_s , for CBE and 2s DMRG. E_{ex} is the exact GS energy. (c) Quality of linear extrapolation of the GS energy using various error measures. Dashed (solid) lines show linear fits to data points lying on or above (on or below) the grey bar, computed using $D_{\text{max}}^* \leq 300$ (≥ 300), representing intermediate (high) accuracy calculations; when these lines touch zero, the extrapolated error changes sign.

Free fermions.— To benchmark our CBE scheme, we consider a chain of spinful free fermions, exactly solvable but non-trivial for DMRG, with Hamiltonian $H_{\text{ff}} = -\sum_{i=1}^{\mathcal{L}-1} \sum_{\sigma} (c_{i\sigma}^{\dagger} c_{i+1\sigma} + \text{h.c.})$ and $\mathcal{L} = 100$ sites. We exploit $U(1)_{\text{ch}} \otimes SU(2)_{\text{sp}}$ charge and spin symmetry, with local dimension $d^*[d] = 3[4]$. The MPO dimension is $w^*[w] = 4[6]$. We seek the GS in the sector with total spin $S=0$, at half-filling, with particle number $N = \mathcal{L}$.

Figure 4(a) plots the relative error in energy vs. CPU time for different D_{max}^* for both CBE and 2s schemes; Fig. 4(b) plots it vs. the number of half-sweeps n_s . While convergence with n_s is comparable for CBE and 2s, CBE requires less CPU time than 2s by a factor of $\simeq 2$. (This speedup factor is less than $d^* = 3$, since d^* is quite small and steps not involving the iterative eigensolver have the same numerical cost for both CBE and 2s schemes.)

Figure 4(c) shows linear-fit extrapolations of the energy in terms of the discarded weight ξ and the 2s variance (the latter computed following Ref. [26]). The quality of the extrapolations is comparable for all considered methods: they all reduce the error in energy by roughly one order compared to the most accurate data point considered, as expected [23, 26]. The error is smaller for $\delta = 0.3$ than for $\delta = 0.1$, and its dependence on discarded weight slightly less noisy (though this hardly affects the extrapolation).

Hubbard-Holstein model (chain).— As a more challenging application, we consider interacting spinful electrons on a 1D chain coupled to phonons [33–37], described

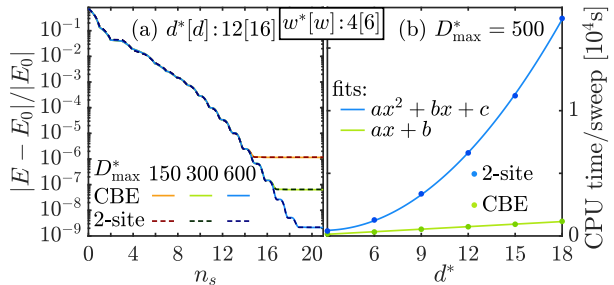


FIG. 5. Hubbard-Holstein model: (a) Convergence of the GS energy versus number of half-sweeps n_s at fixed $d^* = 3(N_{\text{ph}}^{\text{max}} + 1)$. E_0 was obtained by linear ξ -extrapolation of data from $D_{\text{max}}^* \in [1000, 1200]$. (b) CPU time per sweep for different d^* at fixed D_{max}^* , showing d^* vs. d^{*2} scaling for the CBE vs. 2s algorithms.

by the Hamiltonian $H_{\text{HH}} = -\sum_{i\sigma} (c_{i\sigma}^{\dagger} c_{i+1\sigma} + \text{h.c.}) + U \sum_i n_{i\uparrow} n_{i\downarrow} + \omega_{\text{ph}} \sum_i b_i^{\dagger} b_i + g \sum_i (n_{i\uparrow} + n_{i\downarrow} - 1)(b_i^{\dagger} + b_i)$. We chose $U = 0.8$, $g = \sqrt{0.2}$, $\omega_{\text{ph}} = 0.5$, $\mathcal{L} = N = 50$ half-filled sites, total spin $S=0$, and restricted the maximum local number of excited phonons to $N_{\text{ph}}^{\text{max}}$. Then, $d^*[d] = 3(N_{\text{ph}}^{\text{max}} + 1)[4(N_{\text{ph}}^{\text{max}} + 1)]$ and $w^*[w] = 4[6]$.

Figure 5(a) shows the relative error in energy vs. number of half-sweeps n_s for different D_{max}^* at fixed $d^* = 12$, comparing CBE and 2s schemes. The convergence with n_s is again similar for CBE and 2s. Figure 5(b) compares the CPU time per sweep for CBE and 2s for different d^* at fixed D_{max}^* . Linear and quadratic fits confirm the expected d^* or d^{*2} scaling, respectively, showing unambiguously that CBE indeed has 1s scaling.

Fermionic models on cylinders.— To check the ability of CBE-DMRG to deal with very challenging models, we have also tested it on fermionic models on 10×4 cylinders, exploiting $U(1)_{\text{ch}} \otimes SU(2)_{\text{sp}}$ charge and spin symmetries. As a benchmark, we have considered the Hubbard model up to $D^* = 12000$ where we find good agreement with data from Ref. 26. We then considered a more challenging Kondo-Heisenberg-Holstein model, which features physical and MPO bond-dimensions from $d^*[d] = 4[8]$ and $w^*[w] = 10[16]$ (up to $D^* = 15000$) up to $d^*[d] = 16[32]$ and $w^*[w] = 14[30]$ (up to $D^* = 7000$), respectively. More information and data demonstrating stable convergence of CBE-DMRG is shown in the supplemental material [28].

Summary and outlook.— CBE expands bonds by adding subspaces on which Δ_E^{2s} , the 2s contribution to the energy variance, has significant weight, thus making these subspaces accessible to 1s energy minimization. The above results show that CBE yields 2s accuracy and convergence per sweep, at 1s costs. In contrast to previous 1s methods, CBE avoids mixing parameters and is fully variational (up to bond trimming when shifting the isometry center). It has 1s costs, since the variational space is only slightly expanded relative to 1s DMRG. 2s convergence is achieved since the bond expansion is *controlled*, targeting only highly relevant parts of the 2s variational

space contributing strongly to the energy variance Δ_E^{2s} . Using *shrewd selection*, these can be identified at 1s costs.

Due to its significant costs savings, CBE opens the door to studying challenging models of current interest at higher accuracy (larger D) than previously possible, or tackling more complex models, with d or w so large that they were hitherto out of reach. Examples are multi-band models with several different type of couplings, in particular in two-dimensional settings, models involving bosonic excitations, and quantum-chemical applications.

More generally, CBE can be used in any context requiring variational optimization of an MPS. Apart from energy minimization, an example is approximating a given Ψ by a Ψ' with smaller bond dimension through minimization of $\|\Psi' - \Psi\|$. CBE can also be used to build Krylov spaces with 2s accuracy at 1s costs, thus impacting all of the large variety of MPS methods relying on Krylov methods. For example, in a follow-up paper [38] we focus on MPS time evolution using the time-dependent variational principle (TDVP), and use CBE to achieve dramatic improvements in performance. Finally, analogous statements hold for contexts involving the variational optimization or the time evolution of MPOs. We thus expect that CBE will be widely used and become an indispensable tool in the MPS/MPO toolbox.

We thank Andreas Weichselbaum for stimulating discussions, and Seung-Sup Lee, Juan Espinoza, Matan Lotem, Jeongmin Shim and Andreas Weichselbaum for helpful comments on our manuscript. Our numerical simulations employed the QSpace tensor library [31, 32]. This research was funded in part by the Deutsche Forschungsgemeinschaft under Germany's Excellence Strategy EXC-2111 (Project No. 390814868), and is part of the Munich Quantum Valley, supported by the Bavarian state government with funds from the Hightech Agenda Bayern Plus.

-
- [1] S. R. White, Density matrix formulation for quantum renormalization groups, *Phys. Rev. Lett.* **69**, 2863 (1992).
- [2] S. R. White, Density-matrix algorithms for quantum renormalization groups, *Phys. Rev. B* **48**, 10345 (1993).
- [3] F. Verstraete, D. Porras, and J. I. Cirac, Density matrix renormalization group and periodic boundary conditions: A quantum information perspective, *Phys. Rev. Lett.* **93**, 227205 (2004).
- [4] U. Schollwöck, The density-matrix renormalization group, *Rev. Mod. Phys.* **77**, 259 (2005).
- [5] U. Schollwöck, The density-matrix renormalization group in the age of matrix product states, *Annals of Physics* **326**, 96 (2011).
- [6] S. R. White, Spin gaps in a frustrated Heisenberg model for cav_4o_9 , *Phys. Rev. Lett.* **77**, 3633 (1996).
- [7] E. Stoudenmire and S. R. White, Studying two-dimensional systems with the density matrix renormalization group, *Ann. Rev. Cond. Mat. Phys.* **3**, 111 (2012).
- [8] S. R. White and D. J. Scalapino, Density matrix renormalization group study of the striped phase in the $2d$ $t - J$ model, *Phys. Rev. Lett.* **80**, 1272 (1998).
- [9] S. R. White and D. J. Scalapino, Checkerboard patterns in the $t-j$ model, *Phys. Rev. B* **70**, 220506 (2004).
- [10] S. R. White and D. J. Scalapino, Pairing on striped $t-t'-J$ lattices, *Phys. Rev. B* **79**, 220504 (2009).
- [11] S. Jiang, D. J. Scalapino, and S. R. White, Ground-state phase diagram of the $t-t'-J$ model, *Proceedings of the National Academy of Sciences* **118**, e2109978118 (2021).
- [12] J. P. F. LeBlanc, A. E. Antipov, F. Becca, I. W. Bulik, G. K.-L. Chan, C.-M. Chung, Y. Deng, M. Ferrero, T. M. Henderson, C. A. Jiménez-Hoyos, E. Kozik, X.-W. Liu, A. J. Millis, N. V. Prokof'ev, M. Qin, G. E. Scuseria, H. Shi, B. V. Svistunov, L. F. Tocchio, I. S. Tupitsyn, S. R. White, S. Zhang, B.-X. Zheng, Z. Zhu, and E. Gull (Simons Collaboration on the Many-Electron Problem), Solutions of the two-dimensional Hubbard model: Benchmarks and results from a wide range of numerical algorithms, *Phys. Rev. X* **5**, 041041 (2015).
- [13] G. Ehlers, S. R. White, and R. M. Noack, Hybrid-space density matrix renormalization group study of the doped two-dimensional Hubbard model, *Phys. Rev. B* **95**, 125125 (2017).
- [14] B.-X. Zheng, C.-M. Chung, P. Corboz, G. Ehlers, M.-P. Qin, R. M. Noack, H. Shi, S. R. White, S. Zhang, and G. K.-L. Chan, Stripe order in the underdoped region of the two-dimensional Hubbard model, *Science* **358**, 1155 (2017), arXiv:1701.00054 [cond-mat.str-el].
- [15] E. W. Huang, C. B. Mendl, H.-C. Jiang, B. Moritz, and T. P. Devereaux, Stripe order from the perspective of the Hubbard model, *npj Quantum Materials* **3**, 22 (2018).
- [16] M. Qin, C.-M. Chung, H. Shi, E. Vitali, C. Hubig, U. Schollwöck, S. R. White, and S. Zhang (Simons Collaboration on the Many-Electron Problem), Absence of superconductivity in the pure two-dimensional Hubbard model, *Phys. Rev. X* **10**, 031016 (2020).
- [17] Y.-F. Jiang, J. Zaanen, T. P. Devereaux, and H.-C. Jiang, Ground state phase diagram of the doped Hubbard model on the four-leg cylinder, *Phys. Rev. Research* **2**, 033073 (2020).
- [18] H.-C. Jiang and S. A. Kivelson, Stripe order enhanced superconductivity in the Hubbard model, *PNAS* **119**, e2109406119 (2022).
- [19] S. Yan, D. A. Huse, and S. R. White, Spin-liquid ground state of the $S = 1/2$ kagome Heisenberg antiferromagnet, *Science* **332**, 1173 (2011).
- [20] S. Depenbrock, I. P. McCulloch, and U. Schollwöck, Nature of the spin-liquid ground state of the $S = 1/2$ Heisenberg model on the kagome lattice, *Phys. Rev. Lett.* **109**, 067201 (2012).
- [21] F. Kolley, S. Depenbrock, I. P. McCulloch, U. Schollwöck, and V. Alba, Phase diagram of the J_1 - J_2 Heisenberg model on the kagome lattice, *Phys. Rev. B* **91**, 104418 (2015).
- [22] Y.-C. He, M. P. Zaletel, M. Oshikawa, and F. Pollmann, Signatures of dirac cones in a DMRG study of the kagome Heisenberg model, *Phys. Rev. X* **7**, 031020 (2017).
- [23] S. R. White, Density matrix renormalization group algorithms with a single center site, *Phys. Rev. B* **72**, 180403 (2005).
- [24] C. Hubig, I. P. McCulloch, U. Schollwöck, and F. A. Wolf, Strictly single-site DMRG algorithm with subspace expansion, *Phys. Rev. B* **91**, 155115 (2015).
- [25] A. Gleis, J.-W. Li, and J. von Delft, Projector formalism

- for kept and discarded spaces of matrix product states, [arXiv:2207.13161 \[quant-ph\]](https://arxiv.org/abs/2207.13161) (2022).
- [26] C. Hubig, J. Haegeman, and U. Schollwöck, Error estimates for extrapolations with matrix-product states, *Phys. Rev. B* **97**, 045125 (2018).
- [27] We could achieve the desired reduction $\bar{D} \rightarrow \tilde{D}$ already during preselection by choosing $D' = \tilde{D}/w$ there, so that $\hat{D} = \tilde{D}$; however, that would neglect the information that in $H^{2s}\psi^{2s}$ the central MPO bond is closed. Final selection serves to include that information.
- [28] See Supplemental Material at [url] for an analysis of singular value spectra obtained from shrewd selection; numerical results for fermionic models defined on cylinders; and a pseudocode for shrewd selection. The Supplemental Material includes Refs. [13, 26, 39–43].
- [29] V. Zauner-Stauber, L. Vanderstraeten, M. T. Fishman, F. Verstraete, and J. Haegeman, Variational optimization algorithms for uniform matrix product states, *Phys. Rev. B* **97**, 045145 (2018).
- [30] L. Vanderstraeten, J. Haegeman, and F. Verstraete, Tangent-space methods for uniform matrix product states, *SciPost Phys. Lect. Notes* **7** (2019).
- [31] A. Weichselbaum, Non-abelian symmetries in tensor networks: A quantum symmetry space approach, *Ann. of Phys.* **327**, 2972 (2012).
- [32] A. Weichselbaum, X-symbols for non-abelian symmetries in tensor networks, *Phys. Rev. Research* **2**, 023385 (2020).
- [33] E. Jeckelmann and S. R. White, Density-matrix renormalization-group study of the polaron problem in the Holstein model, *Phys. Rev. B* **57**, 6376 (1998).
- [34] M. Tezuka, R. Arita, and H. Aoki, Phase diagram for the one-dimensional Hubbard-Holstein model: A density-matrix renormalization group study, *Phys. Rev. B* **76**, 155114 (2007).
- [35] H. Fehske, G. Hager, and E. Jeckelmann, Metallicity in the half-filled Holstein-Hubbard model, *E. J. Phys.* **84**, 57001 (2008).
- [36] S. Ejima and H. Fehske, DMRG analysis of the sdw-cdw crossover region in the 1d half-filled Hubbard-Holstein model, *J. Phys.: Conference Series* **200**, 012031 (2010).
- [37] T. E. Reinhard, U. Mordovina, C. Hubig, J. S. Kretzmer, U. Schollwöck, H. Appel, M. A. Sentef, and A. Rubio, Density-matrix embedding theory study of the one-dimensional Hubbard-Holstein model, *J. Chem. Theory and Comp.* **15**, 2221 (2019).
- [38] J.-W. Li, A. Gleis, and J. von Delft, Time-dependent variational principle with controlled bond expansion for matrix product states, to be published (2022).
- [39] J. Motruk, M. P. Zaletel, R. S. K. Mong, and F. Pollmann, Density matrix renormalization group on a cylinder in mixed real and momentum space, *Phys. Rev. B* **93**, 155139 (2016).
- [40] P. Coleman, Heavy fermions: Electrons at the edge of magnetism, in *Handbook of Magnetism and Advanced Magnetic Materials*, Vol. 1, edited by H. Kronmüller and S. Parkin (Wiley, 2007) pp. 95–148.
- [41] M. Ye, H.-H. Kung, P. F. S. Rosa, E. D. Bauer, K. Haule, and G. Blumberg, Anisotropy of Kondo-lattice coherence in momentum space for CeCoIn₅, [arXiv:2202.09642 \[cond-mat.str-el\]](https://arxiv.org/abs/2202.09642) (2022).
- [42] P. Coleman, C. Pépin, Q. Si, and R. Ramazashvili, How do Fermi liquids get heavy and die?, *J. Phys. Cond. Mat.* **13**, R723 (2001).
- [43] J. M. Luttinger, Fermi surface and some simple equilibrium properties of a system of interacting fermions, *Phys. Rev.* **119**, 1153 (1960).

Supplemental material: Controlled bond expansion for DMRG ground state search at single-site costs

Andreas Gleis,¹ Jheng-Wei Li,¹ and Jan von Delft¹

¹*Arnold Sommerfeld Center for Theoretical Physics, Center for NanoScience, and Munich Center for Quantum Science and Technology, Ludwig-Maximilians-Universität München, 80333 Munich, Germany*
(Dated: August 1, 2022)

This supplement offers additional material on three issues: in Sec. S-1, a detailed analysis of preselection and final selection; in Sec. S-2, numerical results illustrating the performance of CBE-DMRG for very challenging models (the Hubbard model and the Kondo-Heisenberg-Holstein model, both defined on a cylinder); and in Sec. S-3, a pseudocode for constructing the truncated complement using shrewd selection.

S-1. SHREWD SELECTION

Figures 1 and 2 in the main text discuss a novel scheme, called *shrewd selection*, needed for CBE. It involves two separate truncations, called *preselection* and *final selection*. In this section we discuss these in more detail, and illustrate their effects on the properties of various singular value spectra and singular vectors. We here write bond dimensions with *, indicating numbers of multiplets (not states), since these determine computational complexities and truncation thresholds and are the quantities shown in the figures. Relations such as $\hat{D} = D'w$, exact for Abelian symmetries where all symmetry multiplets have dimension 1, become approximate, $\hat{D}^* \simeq D'^*w^*$, when written for non-Abelian symmetries.

A. Options for preselection and final selection

The key idea of CBE is to expand the isometry $A_\ell(\nabla)$, whose image (the kept space) initially has dimension D_1^* , through a direct sum with a so-called truncated complement, an isometry with image dimension $\tilde{D}^* (< D_1^*)$. The latter is obtained through a suitable truncation of the full complement, $\bar{A}_\ell(\nabla)$, whose image (the discarded space) initially has dimension $\bar{D}^* \simeq D_1^*(d^* - 1)$. Figure 1 defines three cost functions, \mathcal{C}_1 , \mathcal{C}_2 and \mathcal{C}_3 , relevant for constructing the truncated complement. The optimal choice for the truncated complement, to be denoted $\bar{A}_\ell^{\text{tr}}(\nabla)$ here, is obtained by exact minimization of \mathcal{C}_1 , but that requires 2s costs. Therefore, the main text proposes an alternative two-step strategy, requiring only 1s costs. First perform preselection: obtain a preselected complement $\hat{A}_\ell^{\text{pr}}(\nabla)$, with image dimension $\hat{D}^* \simeq D'^*w^*$, through minimization of \mathcal{C}_2 (Fig. 2, steps (a-c)). Then perform final selection: obtain the desired truncated complement, denoted $\tilde{A}_\ell^{\text{tr}}(\nabla)$, through minimization of \mathcal{C}_3 (Fig. 2, step (d)).

The minimization of the cost functions \mathcal{C}_1 and \mathcal{C}_3 defined in Fig. 1 involves performing SVDs and truncations of the following two tensors, respectively:

$$\bar{M}^{\text{full}} = \begin{array}{c} \text{---} \bar{U} \text{---} \bar{S} \text{---} \bar{V}^\dagger \\ \text{---} \bar{D}^* \text{---} \text{---} \bar{D}^* \\ \text{---} \bar{D}^* \text{---} \text{---} \bar{D}^* \end{array} \simeq \begin{array}{c} \text{---} \bar{u} \text{---} \bar{s} \text{---} \bar{v}^\dagger \\ \text{---} \bar{D}^* \text{---} \text{---} \bar{D}^* \\ \text{---} \bar{D}^* \text{---} \text{---} \bar{D}^* \end{array}, \quad (\text{S1a})$$

$$\hat{M}^{\text{pr}} = \begin{array}{c} \text{---} \tilde{U} \text{---} \tilde{S} \text{---} \tilde{V}^\dagger \\ \text{---} \tilde{D}^* \text{---} \text{---} \tilde{D}^* \\ \text{---} \tilde{D}^* \text{---} \text{---} \tilde{D}^* \end{array} \simeq \begin{array}{c} \text{---} \tilde{u} \text{---} \tilde{s} \text{---} \tilde{v}^\dagger \\ \text{---} \tilde{D}^* \text{---} \text{---} \tilde{D}^* \\ \text{---} \tilde{D}^* \text{---} \text{---} \tilde{D}^* \end{array}. \quad (\text{S1b})$$

They differ only in one ingredient, $\bar{A}_\ell^\dagger(\blacktriangle)$ vs. $\hat{A}_\ell^{\text{pr}\dagger}(\blacktriangle)$, but since these have vastly different open leg dimensions, \bar{D}^* vs. \hat{D}^* , the SVD costs differ vastly too, 2s vs. 1s. The isometries \bar{u} (yellow) or \tilde{u} (orange) obtained from the above SVDs and truncations, both with image dimension \tilde{D}^* , can then be used to construct $\bar{A}_\ell^{\text{tr}}(\nabla)$ or $\tilde{A}_\ell^{\text{tr}}(\nabla)$ as follows:

$$\frac{\bar{A}_\ell^{\text{tr}}}{D^* \nabla \bar{D}^*} = \frac{\bar{A}_\ell}{\nabla} \bar{u}, \quad (\text{S2a})$$

$$\frac{\tilde{A}_\ell^{\text{tr}}}{D^* \nabla \tilde{D}^*} = \frac{\hat{A}_\ell^{\text{pr}}}{\nabla} \tilde{u}. \quad (\text{S2b})$$

Both $\bar{A}_\ell^{\text{tr}}(\nabla)$ and $\tilde{A}_\ell^{\text{tr}}(\nabla)$ have image dimension \tilde{D}^* ; the former serves as reference (equivalent to using no preselection, $D'^* = D^*$, the latter is an approximation to the former. An even cruder approximation is obtained if one performs preselection without final selection: for that, truncate $\tilde{U} \simeq \hat{u}$ in step (c) of Fig. 2 using $\hat{D}^* = \tilde{D}^*$ (not D'^*w^*), and use the resulting isometry, $\hat{A}_\ell^{\text{tr}}(\nabla) = \hat{u}$, as approximation for $\bar{A}_\ell^{\text{tr}}(\nabla)$, omitting step (d) altogether:

$$\frac{\hat{A}_\ell^{\text{tr}}}{D^* \nabla \tilde{D}^*} = \frac{\hat{u}}{\nabla}. \quad (\text{S2c})$$

To illustrate the effects of preselection, we will compare four settings: (I) the reference, $\bar{A}_\ell^{\text{tr}}(\nabla)$; or three versions of preselection with $D'^* = D_f^*/w^*$, $0.1D_f^*/w^*$ or 1, to be called (II) *moderate*, (III) *severe* or (IV) *extreme* preselection, respectively, all followed by final selection, yielding three versions of $\tilde{A}_\ell^{\text{tr}}(\nabla)$. Here, D_f^* is the final bond dimension after an update, obtained by expanding

the bond from dimension D_i^* to $D_i^* + \tilde{D}^* = D_i^*(1 + \delta)$, then trimming it back to D_i^* . To illustrate the importance of final selection we also consider a fifth setting: (V) moderate preselection and $\hat{U} \simeq \hat{u}$ truncation, without final selection, yielding $\hat{A}_\ell^{\text{tr}}(\nabla)$.

In the main text, we recommended performing CBE updates using moderate preselection followed by final selection. We showed (Fig. 4(a)) that this yields equally fast convergence per sweep for the GS energy as 2s update. Below, we elucidate why moderate preselection works so well. To this end, we analyze various singular value spectra (Sec. S-1 B) and left singular vectors (Sec. S-1 C), with $D_i^* = D_{\text{max}}^*$ fixed. We also show that severe and even extreme preselection likewise yield full convergence, albeit at slower rates, by comparing various convergence rates per sweep while increasing D_i^* (Sec. S-1 D).

B. Singular values

We start by comparing the singular values of the tensors $\overline{M}^{\text{full}}$ and \overline{M}^{Pr} , i.e. the diagonal elements of the diagonal matrices $\overline{S}(\blacklozenge)$ and $\tilde{S}(\blacklozenge)$ in Eqs. (S1), denoted \overline{s}_i ($i = 1, \dots, \overline{D}^*$) and \tilde{s}_i ($i = 1, \dots, \tilde{D}^*$), respectively. They differ strongly in number, but if the largest \tilde{s}_i values roughly mimic the largest \overline{s}_i values, serving as reference, then preselection is “efficient”, in that it yields essentially optimal results for the dominant singular values.

Figure S-1 compares \overline{s}_i (grey) and \tilde{s}_i (orange: moderate or brown: severe preselection) for bond $\ell = \mathcal{L}/2$ of both the least and most challenging models considered in this work: (a,b) the free fermion chain of Fig. 3, and (c,d) the KHH cylinder of Fig. S-5. Here, we consider the case that D_i^* has reached D_{max}^* and is not grown further, and hence choose $\tilde{D}^* = D_i^* \delta$ (with $\delta = 0.1$), so that $D_i^* = \tilde{D}_i^*$.

For (II) moderate preselection ($D^{*'} = D_i^*/w^*$) the \tilde{s}_i (orange) and \overline{s}_i (grey) values coincide quite well in the range where they are largest, and eventually drift apart as they get smaller. Especially for the largest $\tilde{D}^* = D_i^* \delta$ ($\delta = 0.1$) singular values, i.e. the ones that survive final selection and are used for bond expansion, the agreement is rather good (Figs. S-1 (b,d)). This is a very important finding—it indicates that moderate preselection is efficient. By contrast, (III) severe preselection ($D^{*'} = 0.1D_i^*/w^*$), shown only in Fig. S-1 (a,b), yields \tilde{s}_i (brown) values that differ substantially from their \overline{s}_i (grey) counterparts, even in the range of largest values. Therefore, in this case preselection is too severe to be very efficient.

(We note in passing that when using severe preselection, the corresponding final selection involves almost no further truncation, since \tilde{D}^* (given by $\simeq D^{*'} w^* = 0.1D^*$) is almost equal to \tilde{D}^* (given by $D^* \delta$). For the present example, we have $\tilde{D}^* = 63$ and $\tilde{D}^* = 60$.)

In Figs. S-1 (a,b), the length of the grey vs. orange lines visually illustrates the main rationale for our CBE strat-

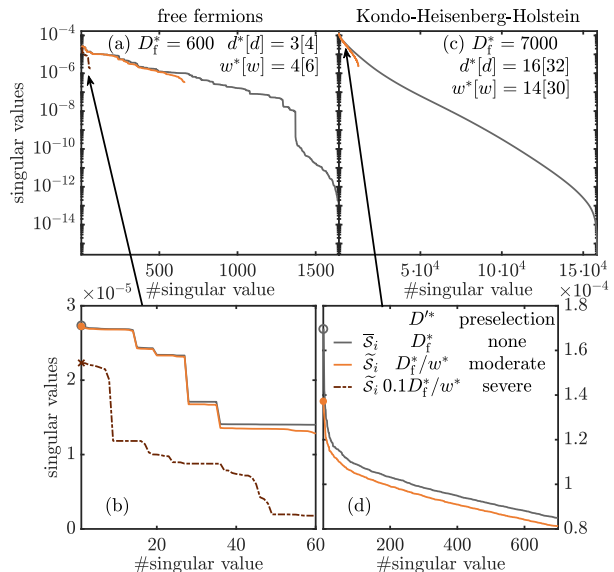


FIG. S-1. Comparison of singular values for three truncation settings (I-III) defined in Sec. S-1 A: the singular values \overline{s}_i of the tensor $\overline{M}^{\text{full}}$, obtained (I) without preselection (reference, grey); and the singular values \tilde{s}_i of the tensor \overline{M}^{Pr} , obtained using (II) moderate preselection ($D^{*'} = D_i^*/w^*$, orange) and (III) severe preselection ($D^{*'} = 0.1D_i^*/w^*$, brown), all followed by final selection with $\tilde{D}^* = 0.1D_i^*$. They are all computed for bond $\ell = \mathcal{L}/2$ of (a,b) the free fermion chain of Fig. 3, and (c,d) the KHH cylinder of Fig. S-5(d). (b,d) Subsets of the data from (a,c), shown on linear scales, focusing on the range of the largest $\tilde{D}^* = D_i^* \delta$ singular values \overline{s}_i and \tilde{s}_i (with $\delta = 0.1$). This range contains all singular vectors comprising the truncated complement $\hat{A}_\ell^{\text{tr}}(\nabla)$ obtained after final selection and used for bond expansion. The singular values found with moderate (orange) or no (grey) preselection agree rather well, but those from severe preselection (brown) differ significantly from these.

egy: the number of \overline{s}_i values is generally very much larger than needed for successful bond expansion, $\overline{D}^* \gg D^*$. Thus, the 2s full complement subspace (obtained by excluding the 1s variational space from the 2s variational space), is likewise much larger than needed for energy minimization—only a small subspace thereof really matters. CBE aims to identify parts of that small subspace; shrewd selection offers a cheap way of doing so, yielding a notable speedup when computing the truncated complement.

C. Singular vectors

We next turn to a comparison of singular vectors to further quantify the benefits of using (II) moderate rather than (III) severe preselection, and of using final selection.

For the latter purpose, we consider a truncation scheme (V) involving moderate preselection but no final selec-

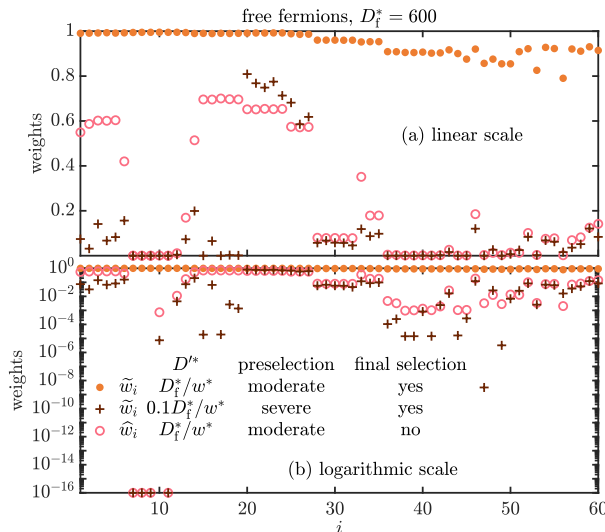


FIG. S-2. Comparison of weights (S3) with which reference singular vectors \tilde{s}_i from $\tilde{A}_\ell^{\text{tr}}(\nabla)$ are supported in truncated spaces obtained with three truncation settings (II–IV) defined in Sec. S-1 A: \tilde{w}_i gives the weight of $|\tilde{s}_i\rangle$ in $\text{span}\{|\tilde{s}_j\rangle\}$, the image of $\tilde{A}_\ell^{\text{tr}}(\nabla)$, computed through shrewd selection, using either (II) moderate (orange dots) or (III) severe (brown crosses) preselection; and \hat{w}_i gives the weight of $|\tilde{s}_i\rangle$ in $\text{span}\{|\tilde{s}_j\rangle\}$, the image of $\hat{A}_\ell^{\text{pr}}(\nabla)$, computed using (IV) moderate preselection without final selection (pink circles). Both panels show the same data, on (a) a linear and (b) a log scale.

tion: after the minimization of the cost function \mathcal{C}_2 (see Fig. 2(c)), we directly truncate $\tilde{U}\tilde{S}\tilde{V}^\dagger \simeq \hat{u}\hat{s}\hat{v}^\dagger$ from \tilde{D}^* to \hat{D}^* , and define the truncated complement as $\hat{A}_\ell^{\text{tr}} = \hat{u}(\nabla)$, with singular vectors $|\hat{s}_i\rangle$.

To compare singular vectors we compute the weights

$$\tilde{w}_i = \sum_{j=1}^{\tilde{D}^*} |\langle \tilde{s}_j | \tilde{s}_i \rangle|^2 = \left(\text{Diagram of } \tilde{w}_i \right), \quad (\text{S3a})$$

$$\hat{w}_i = \sum_{j=1}^{\hat{D}^*} |\langle \hat{s}_j | \tilde{s}_i \rangle|^2 = \left(\text{Diagram of } \hat{w}_i \right). \quad (\text{S3b})$$

Here, \tilde{w}_i is the weight with which a singular vector $|\tilde{s}_i\rangle$ (ordered by size of corresponding singular value) from the image of $\tilde{A}_\ell^{\text{tr}}(\nabla)$ is supported in the subspace $\text{span}\{|\tilde{s}_j\rangle\}$, the image of $\tilde{A}_\ell^{\text{tr}}(\nabla)$; and \hat{w}_i gives its weight in $\text{span}\{|\hat{s}_j\rangle\}$, the image of $\hat{A}_\ell^{\text{tr}}(\nabla)$. In less technical terms, the weights characterize how well reference singular vectors can be represented in these truncated spaces.

These weights are shown in Fig. S-2 for the free fermion data corresponding to Fig. S-1(a). For (II) moderate preselection plus final selection (\tilde{w}_i , orange dots), all weights are close to one. Thus, this truncation scheme almost perfectly captures that part of the 2s subspace most relevant for minimizing the GS energy. By contrast, for both (III)

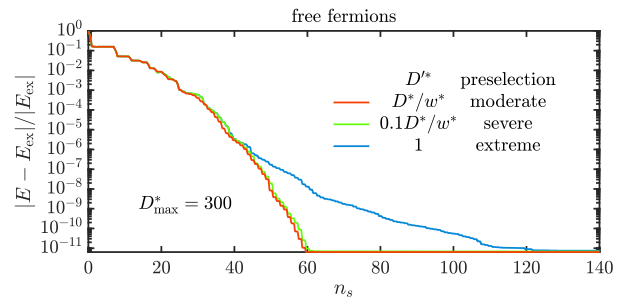


FIG. S-3. Influence of preselection on CBE-DMRG convergence rate, for a half-filled free-fermion chain ($\mathcal{L} = N = 20$). The GS energy is plotted as function of the number of half-sweeps, n_s , for three values of D^* , used for preselection. We start from a $D_i^* = 1$ valence bond state, set $\delta = 0.1$, increase D^* using $\alpha = 1.1$ until $D^* = 300$ is reached, and continue sweeping with $\alpha = 1$ thereafter.

severe preselection plus final selection (\tilde{w}_i , brown crosses) and (V) moderate preselection without final selection (\hat{w}_i , pink circles), most weights are significantly smaller than 1; four are numerically zero. Thus, both these schemes discard a significant part of the space relevant for minimizing the GS energy.

D. Convergence rate per sweep

The weights obtained for severe preselection ($D^* = \delta D^*/w^*$) in Fig. S-2 pose the question whether D^* can be too small to give converged results. In this case, preselection would not only be inefficient, but actually unsuccessful. To explore this, Fig. S-3 compares the CBE-DMRG convergence rate for several choices of D^* , corresponding to (II) moderate (red), (III) severe (green), and (IV) extreme (blue) preselection.

As expected, convergence slows down with smaller D^* . Remarkably, however, once convergence has been reached, the converged results agree (even for $D^* = 1$, a truly extreme choice!). In this sense, the preselection strategy is robust—converged results don’t depend on D^* . Note, though, that the computation time does not depend significantly on D^* (provided it is clearly smaller than D^*). On the other hand, it obviously does depend on the number of sweeps, and the time per sweep can be very large for expensive models. Therefore, D^* should not be chosen too small, to avoid a time-costly increase in the number of sweeps.

To summarize: a bond expansion is *efficient*, yielding a significant reduction in GS energy and therefore quick convergence, if D^* is large enough that the “most important” states $|\tilde{s}_i\rangle$, i.e. those with the largest singular values \tilde{s}_i , are well represented in the expanded space, i.e. have weights $\tilde{w}_i \simeq 1$.

However, even if D^* is so small that most of the im-

portant states $|\tilde{S}_i\rangle$ are represented with small weights, a bond expansion can nevertheless be *successful*, in the sense of adding some relevant new states, provided that these weights are non-zero, $\tilde{w}_i \neq 0$. The reason is that the states $|\tilde{S}_i\rangle$ added to $A_\ell(\nabla)$ contain information about the optimal states $|\bar{S}_i\rangle$ with finite \tilde{w}_i , i.e. those $|\tilde{S}_i\rangle$ are not orthogonal to the expanded kept space. As long as this information is available, subsequent 1s updates will optimize the kept sector accordingly; the states $|\tilde{S}_i\rangle$ just offer a somewhat less optimal starting point for that than the $|\bar{S}_i\rangle$.

Note that it is of utmost importance for successful bond expansion that information on the *most important* $|\bar{S}_i\rangle$ is included. Since only a small set of states is in the end used for expansion, the most important states must be prioritized; otherwise, inferior information is included in the kept space, rendering the bond expansion unsuccessful: Subsequent 1s updates may then optimize towards a suboptimal kept sector, as the optimal one may not be available to the 1s update, e.g. due to symmetry constraints. The energy will still decrease due to the unsuccessful bond expansion plus 1s update, but not as much as if the correct information on the most important $|\bar{S}_i\rangle$ is correctly included. The result will be a suboptimal final state at the desired finite bond dimension D_{\max}^* , i.e. we have wasted resources.

Fig. S-3 shows that CBE-DMRG correctly includes information on the most optimal states when expanding the bond, independent of D^* . Even with extreme preselection ($D^* = 1$), it does not get stuck with some sub-optimal state at $D_{\max}^* = 300$, but eventually converges (albeit slowly) to the same GS as found with larger choices of D_{\max}^* .

S-2. FERMIONIC MODELS ON CYLINDERS

In this section, we show that our CBE-DMRG methods works well also for rather challenging fermionic models on 10×4 cylinders. We first show that for the Hubbard model on a 10×4 cylinder, we obtain results in line with Ref. 26. Then, we show results for a Kondo-Heisenberg-Holstein (KHH) model on a 10×4 cylinder, featuring huge physical and MPO bond dimensions up to $d^*[d]=16$ [32] and $w^*[w]=14$ [30], respectively. Our intention is to show that CBE-DMRG is stable for models at the edge of what is possible with current DMRG techniques, not to discuss their rich physics.

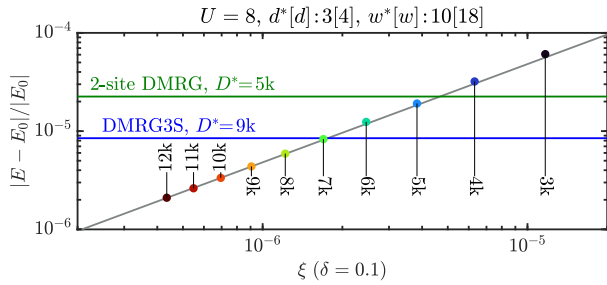


FIG. S-4. Error in GS energy versus discarded weight for the Hubbard model on a 10×4 cylinder. The reference energy $E_0 = -27.8816942$ is obtained by linear ξ -extrapolation to $\xi=0$ (grey line) using the largest four D^* values. D^* values are shown next to their corresponding data point. The horizontal lines show the most accurate computations with 2s DMRG and DMRG3S from Ref. 26, table I as reference values.

A. Hubbard model

The Hubbard model on a 10×4 cylinder is described by the Hamiltonian

$$H_H = - \sum_{\sigma=\uparrow,\downarrow} \sum_{\langle \ell, \ell' \rangle} (c_{\ell\sigma}^\dagger c_{\ell'\sigma} + h.c.) + U \sum_{\ell} n_{\ell\uparrow} n_{\ell\downarrow}. \quad (\text{S4})$$

where $\ell = (x, y)$ is a 2D site index, $\sum_{\langle \ell, \ell' \rangle}$ a sum over nearest-neighbors, $c_{\ell\sigma}^\dagger$ are fermionic creation operators at site ℓ with spin σ and $n_{\ell\sigma} = c_{\ell\sigma}^\dagger c_{\ell\sigma}$ are the corresponding number operators. Following Ref. 26, we choose $U = 8$, and search for the GS in the sector with total filling $N = 36$, i.e. 10% hole doping, and total spin $S = 0$. We exploit $U(1)_{\text{ch}} \otimes SU(2)_{\text{sp}}$ charge and spin symmetries. The MPO is implemented in real space, snaking around the cylinder (in contrast to Ref. 26, where a hybrid-space implementation was used).

Our CBE-DMRG results, shown in Fig. S-4 show nice convergence with D^* , indicated by the linear ξ scaling of the energy. We obtain comparable GS energies as in Ref. 26, but for given D^* reach slightly lower energies. We attribute this difference to the different MPO implementations used (real-space vs. hybrid-space)[13, 39].

B. Kondo-Heisenberg-Holstein model

As an even more challenging application of CBE-DMRG, we compute the GS of a Kondo-Heisenberg-Holstein (KHH) model on a 10×4 cylinder.

The KHH model consists of conduction electron, local magnetic moment and Holstein-phonon degrees of freedom, described by the Hamiltonian

$$H_{\text{KHH}} = - \sum_{\sigma=\uparrow,\downarrow} \sum_{\langle \ell, \ell' \rangle} (c_{\ell\sigma}^\dagger c_{\ell'\sigma} + h.c.) \quad (\text{S5})$$

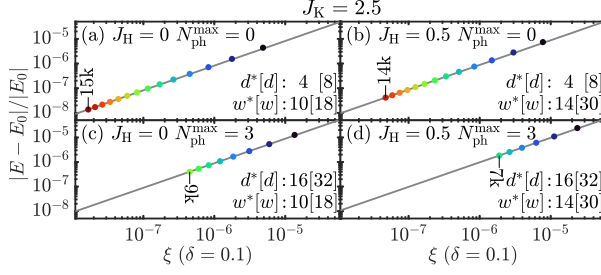


FIG. S-5. Error in GS energy versus discarded weight for the KHH model on a 10×4 cylinder, with (a) only Kondo coupling, (b) Kondo and Heisenberg coupling, (c) Kondo and Holstein coupling and (c) Kondo, Heisenberg and Holstein coupling. Legends state our choices for J_H and $N_{\text{ph}}^{\text{max}}$, and corresponding values of $d^*[d]$ and $w^*[w]$. For each panel, E_0 was obtained by linear ξ -extrapolation to $\xi = 0$ (grey line) using the four largest D^* values. The very largest D^* is shown next to its data point; D^* changes by 1k between adjacent data points.

$$\begin{aligned}
 & + 2J_K \sum_{\ell} \mathbf{S}_{\ell} \cdot \mathbf{s}_{\ell} + J_H \sum_{\langle \ell, \ell' \rangle} \mathbf{S}_{\ell} \cdot \mathbf{S}_{\ell'} \\
 & + \omega_{\text{ph}} \sum_{\ell} b_{\ell}^{\dagger} b_{\ell} + g \sum_{\ell} (n_{\ell\uparrow} + n_{\ell\downarrow} - 1) (b_{\ell}^{\dagger} + b_{\ell}).
 \end{aligned}$$

We use the same notation for fermion operators $c_{\ell\sigma}^{\dagger}$ on a cylinder as in Eq. (S4) for the Hubbard model. Moreover, $\mathbf{s}_{\ell} = \frac{1}{2} \sum_{ss'} c_{\ell s}^{\dagger} \boldsymbol{\sigma}_{ss'} c_{\ell s'}$ is the conduction electron spin operator, \mathbf{S}_{ℓ} the spin operator of a spin $\frac{1}{2}$ local moment, and b_{ℓ}^{\dagger} a phonon creation operator, all for site ℓ .

To deal with the infinite local phonon Hilbert space, we restrict the maximum number of local phonon excitations to $N_{\text{ph}}^{\text{max}}$ (specified below) in our DMRG calculations.

The KHH model is relevant for heavy-fermion materials, which consist of itinerant conduction electrons, hybridiz-

ing with localized f orbitals [40]. At low energies, only the spin degree of freedom of the f electrons remain, leading to a Kondo-Heisenberg (KH) model, which is the KHH model at $N_{\text{ph}}^{\text{max}} = 0$. While the inclusion of optical phonon degrees of freedom, which leads to the KHH model, is rather scarce in the literature, there is experimental data available suggesting these may play a role in heavy-fermion physics [41].

Heavy-fermion materials feature many interesting phenomena. One of the not so well understood ones is the so-called Kondo breakdown quantum critical point. When the system is tuned across this critical point, the FS volume abruptly changes [42], leading to a violation of Luttinger's theorem [43] and strange metal behavior at finite temperatures. Here, our goal is just to showcase the ability of CBE-DMRG to deal with the KHH model; we leave the discussion of its rich physics to future work.

In our CBE-DMRG calculations, we use Kondo-coupling $J_K = 2.5$, Holstein-coupling $g = 0.5$ to the phonons and optical phonon frequency $\omega_{\text{ph}} = 0.5$. Two different values for $N_{\text{ph}}^{\text{max}} \in \{0, 3\}$ and the Heisenberg coupling $J_H \in \{0, 0.5\}$ are considered, respectively.

We performed GS searches for $N = \mathcal{L}(1 + \frac{1}{4}) = 50$ and $S = 0$, i.e. at 25% electron doping. Figure S-5 shows the energy error vs. ξ for four parameter combinations (see legends). The linear ξ -dependence of E demonstrates proper convergence of CBE-DMRG. Very large D^* values are achievable despite the rather huge values of d and w . This is remarkable especially for $J_H = 0.5$ and $N_{\text{ph}}^{\text{max}} = 3$ (Fig. S-5(d)), where 2s schemes become excessively costly.

S-3. PSEUDOCODE FOR SHREWD SELECTION

Below, we provide a pseudocode for computing the truncated complement during CBE using shrewd selection.

Algorithm 1 Computation of truncated complement using shrewd selection

Input: 2s Hamiltonian $H_\ell^{2s} = L_{\ell-1}W_\ell W_{\ell+1}R_{\ell+2}$, 2s wavefunction $\psi^{2s} = A_\ell \Lambda_\ell B_{\ell+1}$ in bond-canonical form, preselection bond-dimension D' , truncated complement dimension \tilde{D}

Output: truncated complement $\tilde{A}_\ell^{\text{tr}}$ (∇)

- 1: **function** GETRORTH($R_{\ell+2}, W_{\ell+1}, B_{\ell+1}, \Lambda_\ell$)
 - 2: Compute $R_{\ell+1}^{\text{tmp}} = \Lambda_\ell B_{\ell+1} W_{\ell+1} R_{\ell+2}$
 - 3: Compute $R_{\ell+1}^{\text{orth}} = R_{\ell+1}^{\text{tmp}} - R_{\ell+1}^{\text{tmp}} B_{\ell+1}^\dagger B_{\ell+1}$
 - 4: **return** $R_{\ell+1}^{\text{orth}}$
 - 5: **end function**
 - 6: (Fig. 2(a)): SVD ℓ -bond of $R_{\ell+1}^{\text{orth}} = USV^\dagger$
 - 7: **function** GETLORTH($L_{\ell-1}, W_\ell, A_\ell, U, S$)
 - 8: Compute $L_\ell^{\text{tmp}} = L_{\ell-1} W_\ell U S$
 - 9: Compute $L_\ell^{\text{orth}} = L_\ell^{\text{tmp}} - A_\ell A_\ell^\dagger L_\ell^{\text{tmp}}$
 - 10: **return** L_ℓ^{orth}
 - 11: **end function**
 - 12: (Fig. 2(b)): SVD $L_\ell^{\text{orth}} = U' S' V'^\dagger$ and truncate all except the largest D' singular values in S' : $U' S' V'^\dagger \xrightarrow{\text{trunc}} u' s' v'^\dagger$
 - 13: (Fig. 2(c)): Redirect the MPO-leg of $u' s'$ and perform an SVD on its combined MPO- and ℓ -bond, $u' s' = \tilde{U} \tilde{S} \tilde{V}^\dagger$. Truncate all singular values in \tilde{S} which are numerically zero to ensure $A_\ell^\dagger \tilde{U} = 0$. \triangleright **warning:** $A_\ell^\dagger \tilde{U} = 0$ is crucial and *must* be ensured!
 - 14: (Optional): safety orthogonalization of \tilde{U} by SVD on $\tilde{U} - A_\ell A_\ell^\dagger \tilde{U}$ plus truncation of small singular values.
 - 15: Assign $\hat{A}_\ell^{\text{pr}} = \tilde{U}$ (∇)
 - 16: **function** GETCORTH($L_{\ell-1}, W_\ell, W_{\ell+1}, R_{\ell+2}, A_\ell, \Lambda_\ell, B_{\ell+1}, \hat{A}_\ell^{\text{pr}}$)
 - 17: Compute $L_\ell^{\text{pr}} = (\hat{A}_\ell^{\text{pr}})^\dagger L_{\ell-1} W_\ell A_\ell$
 - 18: Compute $C_{\ell+1}^{\text{tmp}} = L_\ell^{\text{pr}} \Lambda_\ell B_{\ell+1} W_{\ell+1} R_{\ell+2}$
 - 19: Compute $C_{\ell+1}^{\text{orth}} = C_{\ell+1}^{\text{tmp}} - C_{\ell+1}^{\text{tmp}} B_{\ell+1}^\dagger B_{\ell+1}$
 - 20: **return** $C_{\ell+1}^{\text{orth}}$
 - 21: **end function**
 - 22: (Fig. 2(d)): SVD $C_{\ell+1}^{\text{orth}} = \tilde{U} \tilde{S} \tilde{V}^\dagger$ and truncate all except the largest \tilde{D} singular values: $\tilde{U} \tilde{S} \tilde{V}^\dagger \xrightarrow{\text{trunc}} \tilde{u} \tilde{s} \tilde{v}^\dagger$
 - 23: Compute $\tilde{A}_\ell^{\text{tr}} = \hat{A}_\ell^{\text{pr}} \tilde{u}$ (∇)
-

TABLE I. Pseudocode for computing the truncated complement $\tilde{A}_\ell^{\text{tr}}$ using shrewd selection.

Time-dependent variational principle with controlled bond expansion for matrix product states

Jheng-Wei Li,¹ Andreas Gleis,¹ and Jan von Delft¹

¹*Arnold Sommerfeld Center for Theoretical Physics, Center for NanoScience, and Munich Center for Quantum Science and Technology, Ludwig-Maximilians-Universität München, 80333 Munich, Germany*

(Dated: August 24, 2022)

We present a controlled bond expansion (CBE) approach to simulate quantum dynamics based on the time-dependent variational principle (TDVP) for matrix product states. Our method alleviates the numerical difficulties of the standard, fixed-rank one-site TDVP integrator by increasing bond dimensions on the fly to reduce the projection error. This is achieved in an economical, local fashion, requiring only minor modifications of standard one-site TDVP implementations. We illustrate the performance of CBE–TDVP with several numerical examples on finite quantum lattices.

DOI:

Introduction.— The time-dependent variational principle (TDVP) [1–4] is a standard tool for time-evolving the Schrödinger equation on a constrained manifold parametrizing the wave function. Tensor networks (TN) offer efficient parametrizations based on low-rank approximations [5–12]. Their combination, TN–TDVP, holds much potential for studying the dynamics of quantum lattice models [13–32], quantum field theories [33, 34], and quantum chemistry problems [35–40].

Here, we focus on matrix product states (MPSs), an elementary class of TN states. Their time evolution, pioneered in Refs. [41–43], can be treated using a variety of methods, reviewed in Refs. [8, 44]. Among these, MPS–TDVP [15, 18–22], which uses Lie–Trotter decomposition to integrate a train of tensors sequentially, arguably gives the best results regarding both physical accuracy and performance [44]: it (i) is applicable for long-ranged Hamiltonians, and its one-site (1s) version (1TDVP) ensures (ii) unitary time evolution, (iii) energy conservation [15, 45] and (iv) numerical stability [18, 21, 23].

A drawback of 1TDVP, emphasized in Refs. 46–48, is use of a *fixed*-rank integration scheme. This offers no way of dynamically adjusting the MPS rank (or bond dimension), as needed to track the entanglement growth typically incurred during MPS time evolution. For this, a rank-adaptive two-site (2s) TDVP (2TDVP) algorithm can be used [22], but it has much higher computational costs and in practice does not ensure properties (ii–iii).

To remedy this drawback, we introduce a rank-adaptive integrator for 1TDVP that is more efficient than previous ones [49–52]. It ensures properties (i–iv) at the same numerical costs as 1TDVP, with marginal overhead. Our key idea is to control the TDVP projection error [22, 49, 53] by adjusting MPS ranks on the fly via the controlled bond expansion (CBE) scheme of Ref. [54]. CBE finds and adds subspaces missed by 1s schemes but containing significant weight from $H\Psi$. When used for DMRG ground state searches, CBE yields 2s accuracy with faster convergence per sweep, at 1s costs [54]. CBE–

TDVP likewise comes at essentially 1s costs.

MPS basics.— Let us recall some MPS basics, adopting the notation of Refs. 54 and 55. For an \mathcal{L} -site system an open boundary MPS wave function Ψ having dimensions d for physical sites and D for virtual bonds can always be written in site-canonical form,

$$\Psi = \begin{array}{c} A_1 \quad A_2 \quad \dots \quad A_{\ell-1} \quad C_\ell \quad B_{\ell+1} \quad \dots \quad B_{\mathcal{L}-1} \quad B_{\mathcal{L}} \\ \text{---} \quad \text{---} \quad \text{---} \quad \text{---} \quad \text{---} \quad \text{---} \quad \text{---} \quad \text{---} \\ \text{---} \quad \text{---} \quad \text{---} \quad \text{---} \quad \text{---} \quad \text{---} \quad \text{---} \quad \text{---} \\ \text{---} \quad \text{---} \quad \text{---} \quad \text{---} \quad \text{---} \quad \text{---} \quad \text{---} \quad \text{---} \end{array} \cdot \quad (1)$$

The tensors $C_\ell(\mathcal{V})$, $A_\ell(\mathcal{V})$ and $B_\ell(\mathcal{V})$ are variational parameters. A_ℓ and B_ℓ are left and right-sided isometries, respectively, projecting Dd -dimensional *parent* (\mathcal{P}) spaces to D -dimensional *kept* (\mathcal{K}) images spaces; they obey

$$A_\ell^\dagger A_\ell = \left(\bigcap_{A_\ell^*} \right) = \left(= \mathbb{1}_\ell^\mathcal{K}, \quad B_\ell B_\ell^\dagger = \left(\bigcap_{B_\ell^*} \right) = \right) = \mathbb{1}_{\ell-1}^\mathcal{K}. \quad (2)$$

The gauge relations $C_\ell = A_\ell \Lambda_\ell = \Lambda_{\ell-1} B_\ell$ ensure that Eq. (1) remains unchanged when moving the orthogonality center C_ℓ from one site to another.

The Hamiltonian can likewise be expressed as a matrix product operator (MPO) with virtual bond dimension w ,

$$H = \begin{array}{c} W_1 \quad W_2 \quad \dots \quad W_\ell \quad \dots \quad W_{\mathcal{L}-1} \quad W_{\mathcal{L}} \\ \text{---} \quad \text{---} \quad \text{---} \quad \text{---} \quad \text{---} \quad \text{---} \quad \text{---} \\ \text{---} \quad \text{---} \quad \text{---} \quad \text{---} \quad \text{---} \quad \text{---} \quad \text{---} \\ \text{---} \quad \text{---} \quad \text{---} \quad \text{---} \quad \text{---} \quad \text{---} \quad \text{---} \end{array} \cdot \quad (3)$$

Its projection to the effective local state spaces associated with site ℓ or bond ℓ yields effective one-site or zero-site Hamiltonians, respectively, computable recursively via

$$H_\ell^{1s} = \left(\begin{array}{c} D \\ \ell-1 \quad \ell \quad \ell+1 \end{array} \right) = \left(\begin{array}{c} d \\ 1 \quad \ell-1 \quad \ell \quad \ell+1 \end{array} \right) = \left(\begin{array}{c} D \\ \ell-1 \quad \ell \quad \ell+1 \end{array} \right), \quad (4a)$$

$$H_\ell^b = \left(\begin{array}{c} D \\ \ell \quad \ell+1 \end{array} \right) = \left(\begin{array}{c} D \\ \ell-1 \quad \ell \quad \ell+1 \end{array} \right) = \left(\begin{array}{c} D \\ \ell \quad \ell+1 \quad \ell+2 \end{array} \right). \quad (4b)$$

These act on 1s or bond representations of the wave function, $\psi_\ell^{1s} = C_\ell(\mathcal{V})$ or $\psi_\ell^b = \Lambda_\ell(\infty)$, respectively.

Let $\bar{A}_\ell(\mathcal{V})$ and $\bar{B}_\ell(\mathcal{V})$ be isometries that are orthogonal complements of A_ℓ and B_ℓ , with *discarded* (\mathcal{D}) image spaces of dimension $\bar{D} = D(d-1)$, obeying orthonormality and completeness relations complementing Eq. (2) [54]:

$$\begin{array}{c} \text{---} \\ \text{---} \\ \text{---} \\ \text{---} \\ \text{---} \end{array} = \left(= \mathbb{1}_\ell^p, \quad \begin{array}{c} \text{---} \\ \text{---} \\ \text{---} \\ \text{---} \\ \text{---} \end{array} = 0, \quad \begin{array}{c} \text{---} \\ \text{---} \\ \text{---} \\ \text{---} \\ \text{---} \end{array} = \right) = \mathbb{1}_{\ell-1}^p, \quad \begin{array}{c} \text{---} \\ \text{---} \\ \text{---} \\ \text{---} \\ \text{---} \end{array} = 0, \quad (5a)$$

$$\begin{array}{c} \text{---} \\ \text{---} \\ \text{---} \\ \text{---} \\ \text{---} \end{array} + \begin{array}{c} \text{---} \\ \text{---} \\ \text{---} \\ \text{---} \\ \text{---} \end{array} = \begin{array}{c} \text{---} \\ \text{---} \\ \text{---} \\ \text{---} \\ \text{---} \end{array} = \mathbb{1}_\ell^p, \quad \begin{array}{c} \text{---} \\ \text{---} \\ \text{---} \\ \text{---} \\ \text{---} \end{array} + \begin{array}{c} \text{---} \\ \text{---} \\ \text{---} \\ \text{---} \\ \text{---} \end{array} = \begin{array}{c} \text{---} \\ \text{---} \\ \text{---} \\ \text{---} \\ \text{---} \end{array} = \mathbb{1}_{\ell-1}^p. \quad (5b)$$

Tangent space projector.— Next, we recapitulate the TDVP strategy. It aims to solve the Schrödinger equation, $i\dot{\Psi} = H\Psi$, constrained to the manifold \mathcal{M} of all MPSs of the form (1), with *fixed* bond dimensions. Since $H\Psi$ typically has larger bond dimensions than Ψ and hence does not lie in \mathcal{M} , the TDVP aims to minimize $\|i\dot{\Psi} - H\Psi\|$ within \mathcal{M} . This leads to

$$i\dot{\Psi}(t) = \mathcal{P}^{1s}(t)H\Psi(t), \quad (6)$$

where $\mathcal{P}^{1s}(t)$ is the projector onto the tangent space of \mathcal{M} at $\Psi(t)$, i.e. the space of all 1s variations of $\Psi(t)$:

$$\begin{aligned} \mathcal{P}^{1s} &= \sum_{\ell'=1}^{\mathcal{L}} \begin{array}{c} \text{---} \\ \text{---} \\ \text{---} \\ \text{---} \\ \text{---} \end{array} \Big|_{\ell'} \begin{array}{c} \text{---} \\ \text{---} \\ \text{---} \\ \text{---} \\ \text{---} \end{array} - \sum_{\ell'=1}^{\mathcal{L}-1} \begin{array}{c} \text{---} \\ \text{---} \\ \text{---} \\ \text{---} \\ \text{---} \end{array} \Big|_{\ell'} \begin{array}{c} \text{---} \\ \text{---} \\ \text{---} \\ \text{---} \\ \text{---} \end{array} \quad (7) \\ &= \sum_{\ell=1}^{\mathcal{L}} \begin{array}{c} \text{---} \\ \text{---} \\ \text{---} \\ \text{---} \\ \text{---} \end{array} \Big|_{\ell} \begin{array}{c} \text{---} \\ \text{---} \\ \text{---} \\ \text{---} \\ \text{---} \end{array} + \begin{array}{c} \text{---} \\ \text{---} \\ \text{---} \\ \text{---} \\ \text{---} \end{array} \Big|_{\ell} \begin{array}{c} \text{---} \\ \text{---} \\ \text{---} \\ \text{---} \\ \text{---} \end{array} + \sum_{\ell=\ell+1}^{\mathcal{L}} \begin{array}{c} \text{---} \\ \text{---} \\ \text{---} \\ \text{---} \\ \text{---} \end{array} \Big|_{\ell} \begin{array}{c} \text{---} \\ \text{---} \\ \text{---} \\ \text{---} \\ \text{---} \end{array}. \end{aligned}$$

The form in the first line was derived by Lubich, Oseledts, and Vandereycken [21] (Theorem 3.1), and transcribed into MPS notation in Ref. [22]. For further explanations of its form, see Refs. [55, 56]. The second line, valid for any $\ell=1, \dots, \mathcal{L}-1$, follows via Eq. (5b); Eq. (5a) implies that all its terms conveniently are mutually orthogonal, and that the projector property $(\mathcal{P}^{1s})^2 = \mathcal{P}^{1s}$ holds [55].

One-site TDVP.— The 1TDVP algorithm [21, 22] represents Eq. (6) by $2\mathcal{L}-1$ coupled equations, $i\dot{C}_\ell = H_\ell^{1s}C_\ell$ and $i\dot{\Lambda}_\ell = -H_\ell^b\Lambda_\ell$, stemming, respectively, from the \mathcal{L} single-site and $\mathcal{L}-1$ bond projectors of \mathcal{P}^{1s} (Eq. (7), first line). Evoking a Lie-Trotter decomposition, they are then decoupled and for each time step solved sequentially, for C_ℓ or Λ_ℓ (with all other tensors fixed). For a time step from t to $t'=t+\delta$ one repeatedly performs four substeps, e.g. sweeping right to left: (1) Integrate $i\dot{C}_{\ell+1} = H_{\ell+1}^{1s}C_{\ell+1}$ from t to t' ; (2) QR factorize $C_{\ell+1}(t') = \Lambda_\ell(t')B_{\ell+1}(t')$; (3) integrate $i\dot{\Lambda}_\ell = -H_\ell^b\Lambda_\ell$ from t' to t ; and (4) update $A_\ell(t)C_{\ell+1}(t) \rightarrow C_\ell(t)B_{\ell+1}(t')$, with $C_\ell(t) = A_\ell(t)\Lambda_\ell(t)$.

1TDVP has two leading errors. One is the Lie-Trotter decomposition error. It can be reduced by higher-order integration schemes [45, 57]; we use a third-order integrator with error $\mathcal{O}(\delta^3)$ [58]. The second error is the projection error from projecting the Schrödinger equation into the tangent space of \mathcal{M} at $\Psi(t)$, quantified by $\Delta_P = \|(\mathbb{1} - \mathcal{P}^{1s})H\Psi(t)\|^2$. It can be reduced brute force by increasing the bond dimension, as happens when using 2TDVP [22, 44, 47], or through global subspace expansion [50]. Here, we propose a local approach, similar in spirit to that of Ref. [52], but more efficient, with 1s costs, and without stochastic ingredients, in contrast to [40].

Controlled bond expansion.— Our key idea is to use CBE to reduce the 2s contribution in Δ_P , given by $\Delta_P^{2\perp} = \|\mathcal{P}^{2\perp}H\Psi\|^2$, where $\mathcal{P}^{2\perp} = \mathcal{P}^{2s}(1 - \mathcal{P}^{1s})$. Here, \mathcal{P}^{2s} is the projector onto 2s variations of Ψ , and $\mathcal{P}^{2\perp}$ its component

orthogonal to the tangent space projector (see also [55]):

$$\mathcal{P}^{2s} = \sum_{\ell=1}^{\mathcal{L}-1} \begin{array}{c} \text{---} \\ \text{---} \\ \text{---} \\ \text{---} \\ \text{---} \end{array} \Big|_{\ell} \begin{array}{c} \text{---} \\ \text{---} \\ \text{---} \\ \text{---} \\ \text{---} \end{array} - \sum_{\ell=2}^{\mathcal{L}-1} \begin{array}{c} \text{---} \\ \text{---} \\ \text{---} \\ \text{---} \\ \text{---} \end{array} \Big|_{\ell} \begin{array}{c} \text{---} \\ \text{---} \\ \text{---} \\ \text{---} \\ \text{---} \end{array}, \quad (8a)$$

$$\mathcal{P}^{2\perp} = \sum_{\ell=1}^{\mathcal{L}-1} \begin{array}{c} \text{---} \\ \text{---} \\ \text{---} \\ \text{---} \\ \text{---} \end{array} \Big|_{\ell} \begin{array}{c} \text{---} \\ \text{---} \\ \text{---} \\ \text{---} \\ \text{---} \end{array}, \quad \Delta_P^{2\perp} = \sum_{\ell=1}^{\mathcal{L}-1} \left\| \begin{array}{c} \text{---} \\ \text{---} \\ \text{---} \\ \text{---} \\ \text{---} \end{array} \Big|_{\ell} \begin{array}{c} \text{---} \\ \text{---} \\ \text{---} \\ \text{---} \\ \text{---} \end{array} \right\|^2. \quad (8b)$$

Now note that $\Delta_P^{2\perp}$ is equal to $\Delta_E^{2\perp} = \|\mathcal{P}^{2\perp}(H-E)\Psi\|^2$, the 2s contribution to the energy variance [53–55]. In Ref. [54], discussing ground state searches via CBE-DMRG, we showed how to minimize $\Delta_E^{2\perp}$ at 1s costs: each bond ℓ can be expanded in such a manner that the added subspace carries significant weight from $\mathcal{P}^{2\perp}H\Psi$. This expansion removes that subspace from the image of $\mathcal{P}^{2\perp}$, thus reducing $\Delta_E^{2\perp}$ significantly. Consider, e.g., a right-to-left sweep and let $\tilde{A}_\ell^{\text{tr}}(\nabla)$ be a truncation of $\tilde{A}_\ell(\nabla)$ having an image spanning such a subspace, of dimension \tilde{D} , say. To expand bond ℓ from D to $D + \tilde{D}$, we replace $A_\ell(\nabla)$ by $A_\ell^{\text{ex}}(\nabla)$, $C_{\ell+1}(\nabla)$ by $C_{\ell+1}^{\text{ex}}(\nabla)$ and $H_{\ell+1}^{1s}$ by $H_{\ell+1}^{1s,\text{ex}}$, with expanded tensors defined as

$$\frac{A_\ell}{d} \Big|_D \oplus \frac{\tilde{A}_\ell^{\text{tr}}}{d} \Big|_{\tilde{D}} = \frac{A_\ell^{\text{ex}}}{d} \Big|_{(D+\tilde{D})} \frac{C_{\ell+1}^{\text{ex}}}{d} \Big|_D = \begin{array}{c} \text{---} \\ \text{---} \\ \text{---} \\ \text{---} \\ \text{---} \end{array} \Big|_{\ell+1}, \quad (9)$$

$$H_{\ell+1}^{(1,\text{ex})} = \begin{array}{c} \text{---} \\ \text{---} \\ \text{---} \\ \text{---} \\ \text{---} \end{array} \Big|_{\ell+1} = \begin{array}{c} \text{---} \\ \text{---} \\ \text{---} \\ \text{---} \\ \text{---} \end{array} \Big|_{\ell+1}^{D+\tilde{D}}. \quad (10)$$

Note that Ψ remains unchanged, $A_\ell^{\text{ex}}C_{\ell+1}^{\text{ex}} = A_\ell C_{\ell+1}$.

Similarly, the projection error $\Delta_P^{2\perp}$ can be minimized through a suitable choice of the truncated complement $\tilde{A}_\ell^{\text{tr}}(\nabla)$ [54]. We find $\tilde{A}_\ell^{\text{tr}}$ using the so-called *shrewd selection* strategy of Ref. [54] (Figs. 1 and 2 there); it avoids computation of $\nabla, \bar{\nabla}$ and has 1s costs regarding CPU and memory, thus becoming increasingly advantageous for large D and d . Shrewd selection involves two truncations ($D \rightarrow D'$ and $\tilde{D} \rightarrow \tilde{D}'$ in Ref. [54]). Here, we choose these to respect singular value thresholds of $\epsilon' = 10^{-4}$ and $\tilde{\epsilon} = 10^{-6}$, respectively; empirically, these yield good results in the benchmark studies presented below.

CBE-TDVP.— It is straightforward to incorporate CBE into the 1TDVP algorithm: simply expand each bond ℓ from $D \rightarrow D + \tilde{D}$ before time-evolving it. Concretely, when sweeping right-to-left, we add step (0): expand $A_\ell, C_{\ell+1}, H_{\ell+1}^{1s} \rightarrow A_\ell^{\text{ex}}, C_{\ell+1}^{\text{ex}}, H_{\ell+1}^{1s,\text{ex}}$ following Eq. (9) (and by implication also $\Lambda_\ell, H_\ell^b \rightarrow \Lambda_\ell^{\text{ex}}, H_\ell^{b,\text{ex}}$). The other steps remain as before, except that in (2) we replace the QR factorization by an SVD. This allows us to reduce (trim) the bond dimension from $D + \tilde{D}$ to a final value D_f , as needed in two situations [49, 51, 59]: First, while standard 1TDVP requires keeping and even padding small singular values in order to retain a fixed bond dimension [13, 18], that is not necessary here. Instead, for bond trimming, we discard small singular values below an empirically determined threshold $\epsilon = 10^{-12}$. This keeps the MPS rank as low as possible, without impacting the accuracy [49]. Second, once $D + \tilde{D}$ exceeds

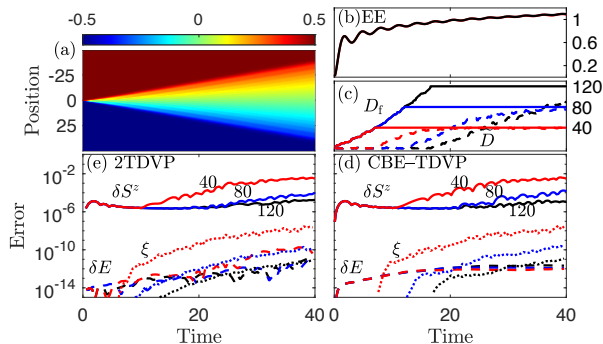


FIG. 1. 100-site XX spin chain: Time evolution of a domain wall, computed with time step $\delta = 0.05$ and $U(1)$ spin symmetry. (a) Local magnetization profile $S_\ell^z(t)$. (b) Entanglement entropy $EE(t)$ between the left and the right half of the chain. (c) Bond dimension $D_f(t)$ and its pre-trimming expansion $\tilde{D}(t)$ per time step, for $D_{\max} = 120$. (d,e) Error analysis: magnetization $\delta S^z(t)$ (solid line), i.e., the maximum deviation (over ℓ) of $S_\ell^z(t)$ from the exact result, energy $\delta E(t)$ (dashed line), and discarded weight $\xi(t)$ (dotted line) for $D_{\max} = 40$ (red), 80 (blue) and 120 (black), computed with (d) CBE-TDVP or (e) 2TDVP. Remarkably, the errors are comparable in size, although CBE-TDVP has much smaller computational costs.

D_{\max} , we trim it back down to D_{\max} aiming to limit computational costs. The trimming error is characterized by its discarded weight, $\xi(t)$, which we either control or monitor. The TDVP properties of (ii) unitary evolution and (iii) energy conservation [51] hold to within order $\xi(t)$.

Results.— We now benchmark CBE-TDVP for three spin models, then illustrate its performance for large d using the Peierls-Hubbard model with $d = 36$. Our benchmark comparisons track the time evolution of the entanglement entropy $EE(t)$ between the left and right halves of a chain, the bond dimensions $D_f(t)$ and $\tilde{D}(t)$, the discarded weight $\xi(t)$, the deviations from exact results of spins expectation values, $\delta S(t)$, and the energy change, $\delta E(t)$, which should vanish for unitary time evolution.

XX model: domain wall motion.— We consider a spin chain with Hamiltonian $H_{XX} = \sum_\ell (S_\ell^x S_{\ell+1}^x + S_\ell^y S_{\ell+1}^y)$. We compute the time evolution of the local magnetization profile $S_\ell^z(t) = \langle \Psi(t) | \hat{S}_\ell^z | \Psi(t) \rangle$, initialized with a sharp domain wall, $|\Psi(0)\rangle = |\uparrow\uparrow\dots\uparrow\downarrow\dots\downarrow\rangle$. For comparison, the analytical solution for $\mathcal{L} \rightarrow \infty$ reads [60] $S_\ell^z(t) = -1/2 \sum_{n=1-\ell}^{\ell-1} J_n(t)^2$, for $\ell \geq 1$ (right half) and $S_\ell^z = -S_{1-\ell}^z$ otherwise, where $J_n(t)$ is the Bessel function of the first kind. The domain wall spreads with time [Fig. 1(a)], entailing a steady growth of the entanglement entropy (EE) between the left and right halves of the spin chain [Fig. 1(b)]. $D(t)$ and $\tilde{D}(t)$ [Fig. 1(c)] start from 1 and 0. Initially, \tilde{D} remains remarkably small ($\lesssim 10$), while D_f increases in steps of \tilde{D} until reaching D_{\max} . Thereafter \tilde{D} increases noticeably, but remains below D_{\max} for all times shown here. This reflects CBE

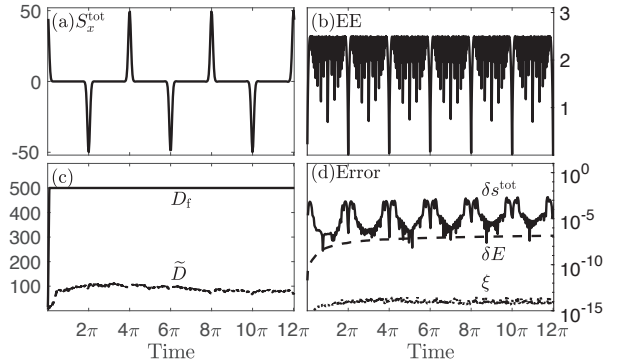


FIG. 2. 100-site one-axis twisting model: Time evolution of an initially x -polarized spin state, computed using $\delta = 0.01$ and \mathbb{Z}_2 spin symmetry. (a) Total spin $S_x^{\text{tot}}(t)$, (b) entanglement entropy, and (c) bond dimensions. (d) Error analysis: error in total spin density $\delta s_x^{\text{tot}}(t)$ (solid line), energy $\delta E(t)$ (dashed line), and discarded weight $\xi(t)$ (dotted line), for $D_{\max} = 500$.

frugality—bonds are expanded only as much as needed.

Figure 1(d) illustrates the effects of changing D_{\max} , following the error analysis of Ref. 61. The leading error is quantified by $\delta S^z(t)$ (solid line), the maximum deviation (over ℓ) of $S_\ell^z(t)$ from the exact result. Comparing the data for $D_{\max} = 40, 80, 120$, we observe a finite bond dimension effect: The error δS^z increases appreciably once the discarded weight ξ (dotted line) becomes larger than 10^{-11} . By contrast, the energy change (dashed line) stays small irrespective of the choice of D_{\max} . (For more discussion of error accumulation, see Ref. [56].) Figure 1(e) shows a corresponding error analysis for 2TDVP, computed using $D = D_{\max}$; its errors are comparable to those of CBE-TDVP, though the latter is much cheaper.

One-axis twisting (OAT) model: quantum revivals.— The OAT model has a very simple Hamiltonian, $H_{\text{OAT}} = (\sum_\ell S_\ell^z)^2/2$, but its long-range interactions are a challenge for tensor network methods using real-space parametrizations. We study the evolution of $S_x^{\text{tot}}(t) = \langle \Psi(t) | \sum_\ell \hat{S}_\ell^x | \Psi(t) \rangle$, for an initial $|\Psi(0)\rangle$ having all spins x -polarized (an MPS with $D = 1$). The exact result, $S_x^{\text{tot}}(t) = (L/2)\cos^{L-1}(t/2)$, exhibits periodic collapses and revivals [62]. Yang and White [50] have studied the short-time dynamics using TDVP with global subspace expansion, reaching times $t \leq 0.5$. CBE-TDVP is numerically stable for much longer times [Fig. 2(a)]; it readily reached $t = 12\pi$, completing three cycles. (More would have been possible with *linear* increase in computation time.) This stability is remarkable, since the rapid initial growth of the entanglement entropy, the finite time-step size, and the limited bond dimension [Fig. 2(b,c)] cause some inaccuracies, which remain visible throughout [Fig. 2(d)]. However, such numerical noise evidently does not accumulate over time and does not spoil the long-time dynamics: CBE-TDVP retains the treasured properties (i-iv) of 1TDVP, up to the trun-

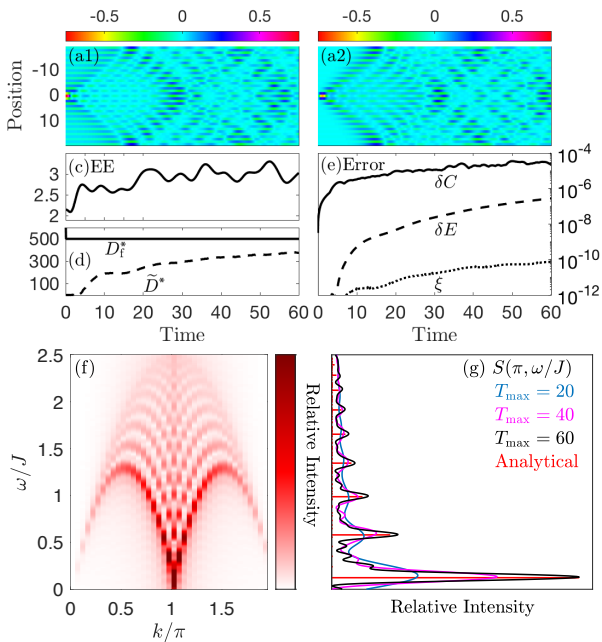


FIG. 3. 40-site SU(2) Haldane-Shastry model: (a-d) Time evolution of a spin excitation, computed with $\delta = 0.05$ and SU(2) spin symmetry. (a1,a2) Real and imaginary parts of $C(x, t)$, (b) entanglement entropy, and (c) bond dimensions. (d) Error analysis: $\delta C(t)$, the maximum of $\delta C(x, t)$ over x (solid line), energy $\delta E(t)$ (dashed line) and discarded weight $\xi(t)$ (dotted line), for $D_{\max} = 500$. (f) Normalized spectral function $S(k, \omega)/S(\pi, 0)$, obtained using $t_{\max} = 60$. (g) $S(\pi, \omega)/S(\pi, 0)$, obtained using $t_{\max} = 20, 40, 60$; red lines indicate exact peak heights.

cation tolerance governed by ξ .

SU(2) Haldane-Shastry model: spectral function.— Our final benchmark example is the SU(2) Haldane-Shastry model on a ring of length \mathcal{L} , with Hamiltonian

$$H_{\text{HS}} = J \sum_{\ell < \ell' \leq \mathcal{L}} \frac{\pi^2 \mathbf{S}_{\ell} \cdot \mathbf{S}_{\ell'}}{\mathcal{L}^2 \sin^2 \frac{\pi}{\mathcal{L}} (\ell - \ell')}. \quad (11)$$

Its ground state correlator, $C(x, t) = \langle \Psi_0 | \hat{\mathbf{S}}_x(t) \hat{\mathbf{S}}_0 | \Psi_0 \rangle$, is related by discrete Fourier transform to its spectral function, $S(k, \omega)$, given by ($0 < \ell' < \ell \leq \mathcal{L}/2$) [63, 64]

$$S\left(2(\ell + \ell') \frac{\pi}{\mathcal{L}}, \frac{\pi^2}{\mathcal{L}^2} ((\ell + \ell') \mathcal{L} - 2(\ell^2 + \ell'^2) + \ell - \ell')\right) \quad (12)$$

$$= \frac{2\ell - 2\ell' - 1}{(2\ell - 1)(\mathcal{L} - 2\ell' - 1)} \prod_{\bar{\ell}=\ell'+1}^{\ell-1} \frac{2\bar{\ell}(\mathcal{L} - 2\bar{\ell})}{(2\bar{\ell} - 1)(\mathcal{L} - 2\bar{\ell} - 1)}.$$

Figures 3(a,b) show the real and the imaginary parts of $C(x, t)$, computed using CBE–TDVP. For early times ($t \leq 20$), the local excitation introduced at $\ell = 0$, $t = 0$ spreads ballistically, as reported previously [28, 65, 66]. Once the counter-propagating wavefronts meet on the ring, an interference pattern emerges. Our numerical results remain accurate throughout, as shown by the error analysis in Fig. 3(e). Figure 3(f) shows the corresponding spectral function $S(k, \omega)$, obtained by discrete Fourier

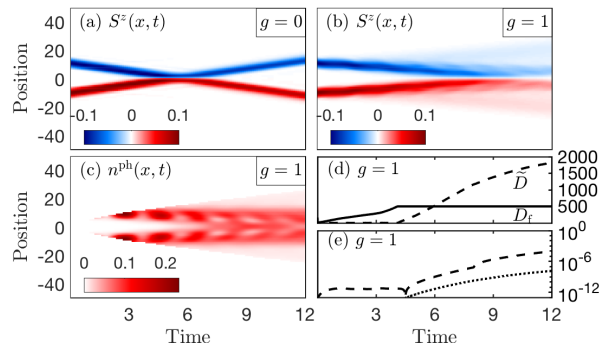


FIG. 4. Peierls–Hubbard model: Real-space scattering of two electron wave packets, for $U=10$ and $\omega_{\text{ph}}=3$, computed with $\delta = 0.05$, $n_{\max}^{\text{ph}} = 8$ and U(1) spin symmetry. (a,b) Spin magnetic moment $S^z(x, t)$ for $g=0$ and $g=1$. (c) Phonon density $n^{\text{ph}}(x, t)$, (d) bond dimensions, and (e) error analysis: energy $\delta E(t)$ (dashed line) and discarded weight $\xi(t)$ (dotted line), all computed for $g=1$, with $D_{\max} = 500$.

transform of $C(x, t)$ using a maximum simulation time of t_{\max} . Figure 3(g) shows a cut along $k = \pi$: peaks can be well resolved by increasing t_{\max} , with relative heights in excellent agreement with the exact Eq. (12).

Peierls–Hubbard model: scattering dynamics.— Finally, we consider the scattering dynamics of interacting electrons coupled to phonons. This interaction leads to non-trivial low-energy physics involving polarons [67–79]; the numerical study of polaron dynamics is currently attracting increasing attention [69, 80–84]. Here, we consider the 1-dimensional Peierls–Hubbard model,

$$H_{\text{PH}} = \sum_{\ell} U n_{\ell \uparrow} n_{\ell \downarrow} + \sum_{\ell} \omega_{\text{ph}} b_{\ell}^{\dagger} b_{\ell} \quad (13)$$

$$+ \sum_{\ell \sigma} (c_{\ell \sigma}^{\dagger} c_{\ell+1 \sigma} + \text{h.c.}) (-t + b_{\ell}^{\dagger} + b_{\ell} - b_{\ell+1}^{\dagger} - b_{\ell+1}).$$

Spinful electrons with onsite interaction strength U and hopping amplitude $t = 1$, and local phonons with frequency ω_{ph} , are coupled with strength g through a Peierls term modulating the electron hopping.

We consider two localized wave packets with opposite spins, average momenta $k = \pm \pi/2$ and width W [85, 86], initialized as $|\Psi_{\pm}\rangle = \sum_{\ell} A e^{-\left(\frac{x_{\ell} \mp x_0}{W}\right)^2} e^{-ikx_{\ell}} c_{\ell \pm}^{\dagger} |0\rangle$, where $|0\rangle$ describes an empty lattice. Without electron-phonon coupling [$g = 0$, Fig. 4(a)], there is little dispersion effect through the time of flight, and the strong interaction causes an elastic collision. By contrast, for a sizable coupling in the nonperturbative regime [77, 79] [$g = 1$, Figs. 4(b-e)], phonons are excited by the electron motion [Fig. 4(c)]. After the two electrons have collided, they show a tendency to remain close to each other (though a finite distance apart, since U is large) [Fig. 4(b)]; they thus seem to form a bi-polaron, stabilized by a significant phonon density in the central region [Fig. 4(c)].

We limited the phonon occupancy to $n_{\max}^{\text{ph}} = 8$ per site. Then, $d = 4(n_{\max}^{\text{ph}} + 1) = 36$, and $\bar{D} = 35D_f$ is so large that 2TDVP would be utterly unfeasible. By contrast, CBE–

TDVP requires a comparatively small bond expansion of only $\tilde{D}(t) \leq 4D_{\max}$ for the times shown; after that, the discarded weight $\xi(t)$ becomes substantial [Figs. 4(d,e)].

Conclusions and outlook.— Among the schemes for MPS time evolution, 1TDVP has various advantages (see introduction), but its projection error is uncontrolled. 2TDVP remedies this, albeit at 2s costs, $\mathcal{O}(d^2wD^3)$, and is able to simulate dynamics reliably [44]. CBE–TDVP at 1s costs, $\mathcal{O}(dwD^3)$ achieves the same accuracy as 2TDVP. Moreover, CBE–TDVP comes with significantly slower growth of bond dimensions D in time, which speeds up the calculations further (see Ref. [56]).

Our benchmark tests of CBE–TDVP, on three exactly solvable spin models (two with long-range interactions), demonstrate its reliability. Our results on the Peierls–Hubbard model suggest that bi-polarons form during electron scattering—an effect not previously explored numerically. This illustrates the potential of CBE–TDVP for tracking complex dynamics in computationally very challenging models.

For applications involving the time evolution of MPSs defined on “doubled” local state spaces, with effective local bond dimensions $d_{\text{eff}} = d^2$, the cost reduction of CBE–TDVP vs. 2TDVP, $\mathcal{O}(d^2wD^3)$ vs. $\mathcal{O}(d^4wD^3)$, will be particularly dramatic. Examples are finite temperature properties, treated by purification of the density matrix [87] or dissipation-assisted operator evolution [88]; and the dynamics of open quantum systems [89], described by Liouville evolution of the density matrix [90–92] or by an influence matrix approach [93].

We thank Andreas Weichselbaum and Frank Pollmann for stimulating discussions, and Seung-Sup Lee, Juan Espinoza, Matan Lotem, Jeongmin Shim and Andreas Weichselbaum for helpful comments on our manuscript. Our computations employed the QSpace tensor library [94, 95]. This research was funded in part by the Deutsche Forschungsgemeinschaft under Germany’s Excellence Strategy EXC-2111 (Project No. 390814868), and is part of the Munich Quantum Valley, supported by the Bavarian state government through the Hightech Agenda Bayern Plus.

-
- [1] P. A. M. Dirac, Note on exchange phenomena in the Thomas atom, *Math. Proc. Camb. Philos. Soc.* **26**, 376 (1930).
- [2] A. McLachlan, A variational solution of the time-dependent Schrödinger equation, *Molecular Physics* **8**, 39 (1964).
- [3] H.-D. Meyer, U. Manthe, and L. Cederbaum, The multi-configurational time-dependent Hartree approach, *Chem. Phys. Lett.* **165**, 73 (1990).
- [4] E. Deumens, A. Diz, R. Longo, and Y. Öhrn, Time-dependent theoretical treatments of the dynamics of electrons and nuclei in molecular systems, *Rev. Mod. Phys.* **66**, 917 (1994).
- [5] F. Verstraete, V. Murg, and J. Cirac, Matrix product states, projected entangled pair states, and variational renormalization group methods for quantum spin systems, *Adv. Phys.* **57**, 143 (2008).
- [6] J. I. Cirac and Frank Verstraete, Renormalization and tensor product states in spin chains and lattices, *J. Phys. A Math.* **42**, 504004 (2009).
- [7] J. Eisert, M. Cramer, and M. B. Plenio, Colloquium: Area laws for the entanglement entropy, *Rev. Mod. Phys.* **82**, 277 (2010).
- [8] U. Schollwöck, The density-matrix renormalization group in the age of matrix product states, *Ann. Phys.* **326**, 96 (2011).
- [9] E. Stoudenmire and S. R. White, Studying two-dimensional systems with the density matrix renormalization group, *Annu. Rev. Condens. Matter Phys.* **3**, 111 (2012).
- [10] J. C. Bridgeman and C. T. Chubb, Hand-waving and interpretive dance: an introductory course on tensor networks, *J. Phys. A Math.* **50**, 223001 (2017).
- [11] R. Orús, Tensor networks for complex quantum systems, *Nat. Rev. Phys.* **1**, 538 (2019).
- [12] P. Silvi, F. Tschirsich, M. Gerster, J. Jünemann, D. Jaschke, M. Rizzi, and S. Montangero, The tensor networks anthology: Simulation techniques for many-body quantum lattice systems, *SciPost Phys. Lect. Notes*, **8** (2019).
- [13] O. Koch and C. Lubich, Dynamical low-rank approximation, *SIAM J. Matrix Anal. Appl.* **29**, 434 (2007).
- [14] O. Koch and C. Lubich, Dynamical tensor approximation, *SIAM J. Matrix Anal. Appl.* **31**, 2360 (2010).
- [15] J. Haegeman, J. I. Cirac, T. J. Osborne, I. Pižorn, H. Verschelde, and F. Verstraete, Time-dependent variational principle for quantum lattices, *Phys. Rev. Lett.* **107**, 070601 (2011).
- [16] T. Koffel, M. Lewenstein, and L. Tagliacozzo, Entanglement entropy for the long-range Ising chain in a transverse field, *Phys. Rev. Lett.* **109**, 267203 (2012).
- [17] P. Hauke and L. Tagliacozzo, Spread of correlations in long-range interacting quantum systems, *Phys. Rev. Lett.* **111**, 207202 (2013).
- [18] C. Lubich and I. V. Oseledets, A projector-splitting integrator for dynamical low-rank approximation, *BIT Numer. Math.* **54**, 171 (2013).
- [19] C. Lubich, T. Rohwedder, R. Schneider, and B. Vandereycken, Dynamical approximation by hierarchical Tucker and tensor-train tensors, *SIAM J. Matrix Anal. Appl.* **34**, 470 (2013).
- [20] J. Haegeman, T. J. Osborne, and F. Verstraete, Post-matrix product state methods: To tangent space and beyond, *Phys. Rev. B* **88**, 075133 (2013).
- [21] C. Lubich, I. V. Oseledets, and B. Vandereycken, Time integration of tensor trains, *SIAM J. Numer. Anal.* **53**, 917 (2015).
- [22] J. Haegeman, C. Lubich, I. Oseledets, B. Vandereycken, and F. Verstraete, Unifying time evolution and optimization with matrix product states, *Phys. Rev. B* **94**, 165116 (2016).
- [23] E. Kieri, C. Lubich, and H. Walach, Discretized dynamical low-rank approximation in the presence of small singular values, *SIAM J. Numer. Anal.* **54**, 1020 (2016).
- [24] V. Zauner-Stauber, L. Vanderstraeten, M. T. Fishman, F. Verstraete, and J. Haegeman, Variational optimization algorithms for uniform matrix product states, *Phys. Rev.*

- B **97**, 045145 (2018).
- [25] L. Vanderstraeten, J. Haegeman, and F. Verstraete, Tangent-space methods for uniform matrix product states, *SciPost Phys. Lect. Notes*, **7** (2019).
- [26] D. Bauernfeind and M. Aichhorn, Time Dependent Variational Principle for Tree Tensor Networks, *SciPost Phys.* **8**, 24 (2020).
- [27] M. M. Rams and M. Zwolak, Breaking the entanglement barrier: Tensor network simulation of quantum transport, *Phys. Rev. Lett.* **124**, 137701 (2020).
- [28] P. Secular, N. Gourianov, M. Lubasch, S. Dolgov, S. R. Clark, and D. Jaksch, Parallel time-dependent variational principle algorithm for matrix product states, *Phys. Rev. B* **101**, 235123 (2020).
- [29] B. Kloss, D. R. Reichman, and Y. B. Lev, Studying dynamics in two-dimensional quantum lattices using tree tensor network states, *SciPost Phys.* **9**, 70 (2020).
- [30] G. Ceruti, C. Lubich, and H. Walach, Time integration of tree tensor networks, *SIAM J. Numer. Anal.* **59**, 289 (2021).
- [31] L. Kohn and G. E. Santoro, Efficient mapping for Anderson impurity problems with matrix product states, *Phys. Rev. B* **104**, 014303 (2021).
- [32] M. Van Damme, R. Vanhove, J. Haegeman, F. Verstraete, and L. Vanderstraeten, Efficient matrix product state methods for extracting spectral information on rings and cylinders, *Phys. Rev. B* **104**, 115142 (2021).
- [33] A. Milsted, J. Haegeman, and T. J. Osborne, Matrix product states and variational methods applied to critical quantum field theory, *Phys. Rev. D* **88**, 085030 (2013).
- [34] E. Gillman and A. Rajantie, Topological defects in quantum field theory with matrix product states, *Phys. Rev. D* **96**, 094509 (2017).
- [35] F. A. Y. N. Schröder and A. W. Chin, Simulating open quantum dynamics with time-dependent variational matrix product states: Towards microscopic correlation of environment dynamics and reduced system evolution, *Phys. Rev. B* **93**, 075105 (2016).
- [36] J. del Pino, F. A. Y. N. Schröder, A. W. Chin, J. Feist, and F. J. Garcia-Vidal, Tensor network simulation of non-Markovian dynamics in organic polaritons, *Phys. Rev. Lett.* **121**, 227401 (2018).
- [37] Y. Kurashige, Matrix product state formulation of the multiconfiguration time-dependent Hartree theory, *J. Chem. Phys.* **149**, 194114 (2018).
- [38] B. Kloss, D. R. Reichman, and R. Tempelaar, Multiset matrix product state calculations reveal mobile Franck-Condon excitations under strong Holstein-type coupling, *Phys. Rev. Lett.* **123**, 126601 (2019).
- [39] X. Xie, Y. Liu, Y. Yao, U. Schollwöck, C. Liu, and H. Ma, Time-dependent density matrix renormalization group quantum dynamics for realistic chemical systems, *J. Chem. Phys.* **151**, 224101 (2019).
- [40] Y. Xu, Z. Xie, X. Xie, U. Schollwöck, and H. Ma, Stochastic adaptive single-site time-dependent variational principle, *JACS Au* **2**, 335 (2022).
- [41] G. Vidal, Efficient simulation of one-dimensional quantum many-body systems, *Phys. Rev. Lett.* **93**, 040502 (2004).
- [42] A. J. Daley, C. Kollath, U. Schollwöck, and G. Vidal, Time-dependent density-matrix renormalization-group using adaptive effective Hilbert spaces, *J. Stat. Mech.: Theor. Exp.* **P04005** (2004).
- [43] S. R. White and A. E. Feiguin, Real-time evolution using the density matrix renormalization group, *Phys. Rev. Lett.* **93**, 076401 (2004).
- [44] S. Paeckel, T. Köhler, A. Swoboda, S. R. Manmana, U. Schollwöck, and C. Hubig, Time-evolution methods for matrix-product states, *Ann. Phys.* **411**, 167998 (2019).
- [45] E. Hairer, C. Lubich, and G. Wanner, *Geometric Numerical Integration* (Springer-Verlag, 2006).
- [46] B. Kloss, Y. B. Lev, and D. Reichman, Time-dependent variational principle in matrix-product state manifolds: Pitfalls and potential, *Phys. Rev. B* **97**, 024307 (2018).
- [47] S. Goto and I. Danshita, Performance of the time-dependent variational principle for matrix product states in the long-time evolution of a pure state, *Phys. Rev. B* **99**, 054307 (2019).
- [48] T. Chanda, P. Sierant, and J. Zakrzewski, Time dynamics with matrix product states: Many-body localization transition of large systems revisited, *Phys. Rev. B* **101**, 035148 (2020).
- [49] A. Dektor, A. Rodgers, and D. Venturi, Rank-adaptive tensor methods for high-dimensional nonlinear PDEs, *J. Sci. Comput.* **88**, 36 (2021).
- [50] M. Yang and S. R. White, Time-dependent variational principle with ancillary Krylov subspace, *Phys. Rev. B* **102**, 094315 (2020).
- [51] G. Ceruti, J. Kusch, and C. Lubich, A rank-adaptive robust integrator for dynamical low-rank approximation, *BIT Numer. Math.* (2022).
- [52] A. J. Dunnett and A. W. Chin, Efficient bond-adaptive approach for finite-temperature open quantum dynamics using the one-site time-dependent variational principle for matrix product states, *Phys. Rev. B* **104**, 214302 (2021).
- [53] C. Hubig, J. Haegeman, and U. Schollwöck, Error estimates for extrapolations with matrix-product states, *Phys. Rev. B* **97**, 045125 (2018).
- [54] A. Gleis, J.-W. Li, and J. von Delft, Controlled bond expansion for DMRG ground state search at single-site costs, arXiv:2207.14712 [cond-mat.str-el] (2022).
- [55] A. Gleis, J.-W. Li, and J. von Delft, Projector formalism for kept and discarded spaces of matrix product states, arXiv:2207.13161 [quant-ph] (2022).
- [56] See Supplemental Material at [url] for: (S-1) an explanation of the structure of the tangent space projector \mathcal{P}^{1s} ; (S-2) an analysis of the fidelity of CBE-TDVP: we show that under backward time evolution (implemented by changing the sign of H), the domain wall recontracts to a point; and (S-3) a comparison of the CPU time costs of CBE-TDVP vs. 2TDVP. The Supplemental Material includes Refs. [21, 22, 51].
- [57] R. I. McLachlan, On the numerical integration of ordinary differential equations by symmetric composition methods, *SIAM J. Sci. Comput.* **16**, 151 (1995).
- [58] A first-order integrator, with error $\mathcal{O}(\delta)$, involves a single left-to-right sweep L_δ or right-to-left sweep R_δ through the entire chain. For 1TDVP, L_δ and R_δ are adjoint operations, with $L_{-\delta} \circ R_\delta = \mathbb{1}$, hence higher-order integrators can be obtained through symmetric compositions [57]. We use one of third order (error $\mathcal{O}(\delta^3)$): $L_{\delta/4} \circ R_{\delta/2} \circ L_{\delta/4}$, for one time step, $R_{\delta/4} \circ L_{\delta/2} \circ R_{\delta/4}$ for the next.
- [59] B. Vanhecke, M. V. Damme, J. Haegeman, L. Vanderstraeten, and Frank Verstraete, Tangent-space methods for truncating uniform MPS, *SciPost Phys. Core* **4**, 4 (2021).

- [60] T. Antal, Z. Rácz, A. Rákos, and G. M. Schütz, Transport in the XX chain at zero temperature: Emergence of flat magnetization profiles, *Phys. Rev. E* **59**, 4912 (1999).
- [61] D. Gobert, C. Kollath, U. Schollwöck, and G. Schütz, Real-time dynamics in spin-1/2 chains with adaptive time-dependent density matrix renormalization group, *Phys. Rev. E* **71**, 036102 (2005).
- [62] S. Dooley and T. P. Spiller, Fractional revivals, multiple-Schrödinger-cat states, and quantum carpets in the interaction of a qubit with n qubits, *Phys. Rev. A* **90**, 012320 (2014).
- [63] T. Yamamoto, Y. Saiga, M. Arikawa, and Y. Kuramoto, Exact dynamical structure factor of the degenerate Haldane-Shastry model, *Phys. Rev. Lett.* **84**, 1308 (2000).
- [64] T. Yamamoto, Y. Saiga, M. Arikawa, and Y. Kuramoto, Exact dynamics of the SU(K) Haldane-Shastry model, *J. Phys. Soc. Japan* **69**, 900 (2000).
- [65] F. D. M. Haldane and M. R. Zirnbauer, Exact calculation of the ground-state dynamical spin correlation function of a $s = 1/2$ antiferromagnetic Heisenberg chain with free spinons, *Phys. Rev. Lett.* **71**, 4055 (1993).
- [66] M. P. Zaletel, R. S. K. Mong, C. Karrasch, J. E. Moore, and F. Pollmann, Time-evolving a matrix product state with long-ranged interactions, *Phys. Rev. B* **91**, 165112 (2015).
- [67] J. Bonča, T. Kataršnik, and S. A. Trugman, Mobile bipolaron, *Phys. Rev. Lett.* **84**, 3153 (2000).
- [68] R. T. Clay and R. P. Hardikar, Intermediate phase of the one dimensional half-filled Hubbard-Holstein model, *Phys. Rev. Lett.* **95**, 096401 (2005).
- [69] H. Fehske and S. A. Trugman, Numerical solution of the Holstein polaron problem, in *Polarons in Advanced Materials*, edited by A. S. Alexandrov (Springer Netherlands, Dordrecht, 2007) p. 393.
- [70] J. P. Hague, P. E. Kornilovitch, J. H. Samson, and A. S. Alexandrov, Superlight small bipolarons in the presence of a strong Coulomb repulsion, *Phys. Rev. Lett.* **98**, 037002 (2007).
- [71] R. P. Hardikar and R. T. Clay, Phase diagram of the one-dimensional Hubbard-Holstein model at half and quarter filling, *Phys. Rev. B* **75**, 245103 (2007).
- [72] M. Tezuka, R. Arita, and H. Aoki, Phase diagram for the one-dimensional Hubbard-Holstein model: A density-matrix renormalization group study, *Phys. Rev. B* **76**, 155114 (2007).
- [73] H. Fehske, G. Hager, and E. Jeckelmann, Metallicity in the half-filled Holstein-Hubbard model, *Europhys Lett.* **84**, 57001 (2008).
- [74] D. J. J. Marchand, G. De Filippis, V. Cataudella, M. Berciu, N. Nagaosa, N. V. Prokof'ev, A. S. Mishchenko, and P. C. E. Stamp, Sharp transition for single polarons in the one-dimensional Su-Schrieffer-Heeger model, *Phys. Rev. Lett.* **105**, 266605 (2010).
- [75] M. Hohenadler and F. F. Assaad, Excitation spectra and spin gap of the half-filled Holstein-Hubbard model, *Phys. Rev. B* **87**, 075149 (2013).
- [76] M. Hohenadler, Interplay of site and bond electron-phonon coupling in one dimension, *Phys. Rev. Lett.* **117**, 206404 (2016).
- [77] J. Sous, M. Chakraborty, R. V. Krems, and M. Berciu, Light bipolarons stabilized by Peierls electron-phonon coupling, *Phys. Rev. Lett.* **121**, 247001 (2018).
- [78] T. E. Reinhard, U. Mordovina, C. Hubig, J. S. Kretzmer, U. Schollwöck, H. Appel, M. A. Sentef, and A. Rubio, Density-matrix embedding theory study of the one-dimensional Hubbard-Holstein model, *J. Chem. Theory Comput.* **15**, 2221 (2019).
- [79] A. Nocera, J. Sous, A. E. Feiguin, and M. Berciu, Bipolaron liquids at strong Peierls electron-phonon couplings, *Phys. Rev. B* **104**, L201109 (2021).
- [80] D. Golež, J. Bonča, and L. Vidmar, Dissociation of a Hubbard-Holstein bipolaron driven away from equilibrium by a constant electric field, *Phys. Rev. B* **85**, 144304 (2012).
- [81] P. Werner and M. Eckstein, Phonon-enhanced relaxation and excitation in the Holstein-Hubbard model, *Phys. Rev. B* **88**, 165108 (2013).
- [82] L. Chen, Y. Zhao, and Y. Tanimura, Dynamics of a one-dimensional Holstein polaron with the hierarchical equations of motion approach, *J. Phys. Chem. Lett.* **6**, 3110 (2015).
- [83] J. H. Fetherolf, D. Golež, and T. C. Berkelbach, A unification of the Holstein polaron and dynamic disorder pictures of charge transport in organic crystals, *Phys. Rev. X* **10**, 021062 (2020).
- [84] B. Pandey, G. Alvarez, and E. Dagotto, Excitonic wavepacket evolution in a two-orbital Hubbard model chain: A real-time real-space study, *Phys. Rev. B* **104**, L220302 (2021).
- [85] K. A. Al-Hassanieh, F. A. Reboredo, A. E. Feiguin, I. González, and E. Dagotto, Excitons in the one-dimensional Hubbard model: A real-time study, *Phys. Rev. Lett.* **100**, 166403 (2008).
- [86] A. Moreno, A. Muramatsu, and J. M. P. Carmelo, Charge and spin fractionalization beyond the Luttinger-liquid paradigm, *Phys. Rev. B* **87**, 075101 (2013).
- [87] F. Verstraete, J. J. Garcia-Ripoll, and J. I. Cirac, Matrix product density operators: Simulation of finite-temperature and dissipative systems, *Phys. Rev. Lett.* **93**, 207204 (2004).
- [88] T. Rakovszky, C. W. von Keyserlingk, and F. Pollmann, Dissipation-assisted operator evolution method for capturing hydrodynamic transport, *Phys. Rev. B* **105**, 075131 (2022).
- [89] H. Weimer, A. Kshetrimayum, and R. Orús, Simulation methods for open quantum many-body systems, *Rev. Mod. Phys.* **93**, 015008 (2021).
- [90] G. Lindblad, On the generators of quantum dynamical semigroups, *Comm. Math. Phys.* **48**, 119 (1976).
- [91] F. Verstraete, J. J. Garcia-Ripoll, and J. I. Cirac, Matrix product density operators: Simulation of finite-temperature and dissipative systems, *Phys. Rev. Lett.* **93**, 207204 (2004).
- [92] M. Zwolak and G. Vidal, Mixed-state dynamics in one-dimensional quantum lattice systems: A time-dependent superoperator renormalization algorithm, *Phys. Rev. Lett.* **93**, 207205 (2004).
- [93] A. Lerose, M. Sonner, and D. A. Abanin, Influence matrix approach to many-body floquet dynamics, *Phys. Rev. X* **11**, 021040 (2021).
- [94] A. Weichselbaum, Non-Abelian symmetries in tensor networks: A quantum symmetry space approach, *Ann. Phys.* **327**, 2972 (2012).
- [95] A. Weichselbaum, X-symbols for non-Abelian symmetries in tensor networks, *Phys. Rev. Res.* **2**, 023385 (2020).

Supplemental material: Time-dependent variational principle with controlled bond expansion for matrix product states

Jheng-Wei Li,¹ Andreas Gleis,¹ and Jan von Delft¹

¹*Arnold Sommerfeld Center for Theoretical Physics, Center for NanoScience, and Munich Center for Quantum Science and Technology, Ludwig-Maximilians-Universität München, 80333 Munich, Germany*

(Dated: August 24, 2022)

S-1. SINGLE SITE (FIXED RANK) TANGENT SPACE PROJECTOR

The structure (7) of the tangent space projector \mathcal{P}^{1s} can be motivated by the following short-cut argument (equivalent to invoking gauge invariance [21, 22]). If Ψ is represented as an MPS, then its tangent vectors $\delta\Psi$ under the fixed-rank approximation can be expressed as a sum of MPSs each containing one derivative of a local tensor. This representation is not unique, but its gauge redundancy can be easily removed. To do so, let us first consider the variation of MPS in Eq. (1) on a single bond ℓ , i.e., $A_\ell C_{\ell+1} = A_\ell \Lambda_\ell B_{\ell+1}$, while the other tensors remain fixed (and hence are not depicted below). Its first order variation then gives us $\delta A_\ell \Lambda_\ell B_{\ell+1} + A_\ell \delta \Lambda_\ell B_{\ell+1} + A_\ell \Lambda_\ell \delta B_{\ell+1}$. By further rewriting $\delta A_\ell \Lambda_\ell$ as $A_\ell \tilde{\Lambda}'_\ell + \tilde{\Lambda}''_\ell \Lambda'_\ell$ and $\Lambda_\ell \delta B_{\ell+1}$ as $\tilde{\Lambda}''_\ell B_{\ell+1} + \tilde{\Lambda}'_\ell \tilde{B}_{\ell+1}$, we obtain the following unique decomposition,

$$\delta \left(\begin{array}{c} A_\ell \Lambda_\ell B_{\ell+1} \\ \diagdown \quad \diagup \\ \text{---} \end{array} \right) = \begin{array}{c} \tilde{A}_\ell \tilde{\Lambda}'_\ell B_{\ell+1} \\ \diagdown \quad \diagup \\ \text{---} \end{array} + \begin{array}{c} A_\ell \tilde{\Lambda}''_\ell B_{\ell+1} \\ \diagdown \quad \diagup \\ \text{---} \end{array} + \begin{array}{c} A_\ell \tilde{\Lambda}''_\ell \tilde{B}_{\ell+1} \\ \diagdown \quad \diagup \\ \text{---} \end{array}, \quad (\text{S1})$$

with $\tilde{\Lambda}_\ell = \tilde{\Lambda}'_\ell + \delta \Lambda_\ell + \tilde{\Lambda}''_\ell$. The three terms on the right are mutually orthogonal to each other. Each of them belongs to the image space of one of the following three orthogonal projectors:

$$\begin{array}{c} \diagdown \quad \diagup \\ \text{---} \end{array}, \begin{array}{c} \diagdown \quad \diagup \\ \text{---} \end{array}, \begin{array}{c} \diagdown \quad \diagup \\ \text{---} \end{array}; \quad (\text{S2})$$

their sum is a tangent space projector for $A_\ell \Lambda_\ell B_{\ell+1}$. Repeating the same argument for all the bonds, while avoiding double counting, i.e., including every term only once, we readily obtain \mathcal{P}^{1s} given by the second line of Eq. (7).

Therefore, given an MPS of the form (1), \mathcal{P}^{1s} is indeed the orthogonal projector onto its tangent space under the fixed-rank approximation. For real-time evolution, applying the Hamiltonian to $|\Psi\rangle$ leads the state out of its tangent space. In the 1TDVP scheme, $H|\Psi\rangle$ is approximated by $\mathcal{P}^{1s}H|\Psi\rangle$, its orthogonal projection onto the tangent space, leading to Eq. (6).

S-2. ANALYSIS OF CBE-TDVP ERROR PROPAGATION

The TDVP time evolution of an MPS under the fixed-rank approximation is unitary, with energy conservation if the Hamiltonian is time-independent. Expanding the

tangent space does not spoil these desirable properties, provided that no truncations are performed. However, then the bond dimension would keep growing with time, which is not practical for studies of long-time dynamics.

With our CBE approach, we instead restrict the bond dimension growth by bond trimming using $\epsilon = 10^{-12}$, and also stopping the increase of D_f once it has reached a specified maximal value D_{\max} . Due to these truncations, the desirable TDVP properties are no longer satisfied exactly. However, *for each time step* they do hold within the truncation error, as shown by Ceruti, Kusch, and Lubich [51]. Thus, the time evolution per time step is almost unitary. Nevertheless, errors can accumulate with time, hence it is unclear *a priori* to what extent the desirable TDVP properties survive over long times.

To investigate this, we revisit our first benchmark example for the domain wall motion of the XX model. We use CBE-TDVP (while exploiting $U(1)$ spin symmetry) to compute the forward-backward fidelity [Fig. S-1(a)]

$$F(\bar{t}) = |\langle \Psi_-(\bar{t}) | \Psi_+(t) \rangle|^2, \quad \bar{t} = t_{\max} - t \in [0, t_{\max}]. \quad (\text{S3})$$

Here, $|\Psi_+(t)\rangle = e^{-iHt} |\Psi(0)\rangle$ is obtained through forward evolution for time t , and $|\Psi_-(\bar{t})\rangle = e^{iH\bar{t}} |\Psi_+(t_{\max})\rangle$ through forward evolution until time $t = t_{\max}$, then back-evolution for $\bar{t} = t_{\max} - t$ to get back to time t . The deviation of the fidelity from unity, $\delta F(\bar{t}) = 1 - F(\bar{t})$, equals zero for unitary evolution; increases with \bar{t} if time evolution is computed using truncations; and tends to 1 for $\bar{t} \rightarrow t_{\max}$ if truncations are too severe.

Figure 1(b) shows the back-evolution of the domain wall described by $|\Psi_-(\bar{t})\rangle$ as \bar{t} increases from 0 to $t_{\max} = 40$, where both $|\Psi_+(t)\rangle$ and $|\Psi_-(\bar{t})\rangle$ were computed using CBE-TDVP with the truncation parameters stated in the main text, namely $\tilde{\epsilon} = 10^{-6}$ and $D_{\max} = 120$. The corresponding $\delta F(\bar{t})$ (Fig. 1(d), black dashes) shows initial transient growth, but then *saturates* at a remarkably small plateau value of 6.7×10^{-5} . Moreover, the corresponding bond expansion per update, $\tilde{D}(\bar{t})$ (Fig. 1(e), black dots), increases only fairly slowly. For these truncation settings, the CBE-TDVP errors are thus clearly under good control and do not accumulate rapidly, so that long-time evolution can be computed accurately.

The fidelity becomes worse ($\delta F(\bar{t})$ increases) if the singular-value threshold for bond expansion, $\tilde{\epsilon}$, is raised (Fig. 1(d), dashed lines). Nevertheless, even for $\tilde{\epsilon}$ as large as 10^{-2} we find long-time plateau behavior for $\delta F(\bar{t})$, implying that the errors remain controlled. This illustrates

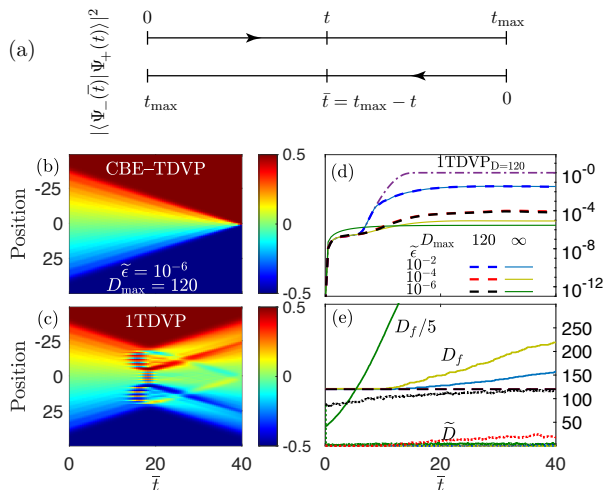


FIG. S-1. (a) Forward-backward time evolution for the computation of $F(t)$. (b,c) Back-evolution of the domain wall, described by $|\Psi_-(\bar{t})\rangle$, computed using (b) CBE-TDVP and (c) 1TDVP. (d) Time evolution of $\delta F(\bar{t}) = 1 - F(\bar{t})$, computed via 1TDVP with $D = 120$ (dash-dotted line), and via CBE-TDVP using three values of $\tilde{\epsilon}$, and either with $D_{\max} = 120$ (dashed lines) or $D_{\max} = \infty$ (solid lines). (e) Time evolution of the corresponding bond dimensions $D_f(\bar{t})$ (solid lines) and $\tilde{D}(\bar{t})$ (dots). (The solid green curve shows $D_f/5$.)

the robustness of CBE-TDVP. The plateau value can be decreased by increasing D_{\max} , but the reduction becomes significant only if $\tilde{\epsilon}$ is sufficiently small. Even for $D_{\max} = \infty$ (Fig. 1(d), solid lines) the plateau reduction relative to $D_{\max} = 120$ is modest, whereas the corresponding growth in D_f (Fig. 1(e), solid lines) becomes so rapid that this setting is not recommended in practice.

Finally, Figs. 1(c) and 1(d) (dash-dotted, purple line) also show 1TDVP results, computed with $D = 120$: the domain wall fails to recontract to a point, and the fidelity reaches zero ($\delta F(\bar{t})$ reaches 1). This occurs even though 1TDVP uses no truncations besides the tangent space projection, and hence yields unitary time evolution. This poor performance illustrates a key limitation of 1TDVP when exploiting symmetries (as here): time evolution involves transitions to sectors having quantum numbers not yet present, but 1TDVP cannot include these, due to the fixed-rank nature of its tangent space projection. CBE-TDVP by construction lifts this restriction.

S-3. COMPARISON OF CPU TIME FOR CBE-TDVP AND 2TDVP

In this section, we compare the CPU time for CBE-TDVP and 2TDVP. As a demonstration, we use the one-axis twisting (OAT) model discussed in *Results* in the main text. All CPU time measurements were done on a single core of an Intel Core i7-9750H processor.

First, we compare the early-time behavior of CBE-TDVP and 2TDVP. From $t = 0$ to 1.5, both methods yield good accuracy as shown in Fig. S-2(a). The CPU

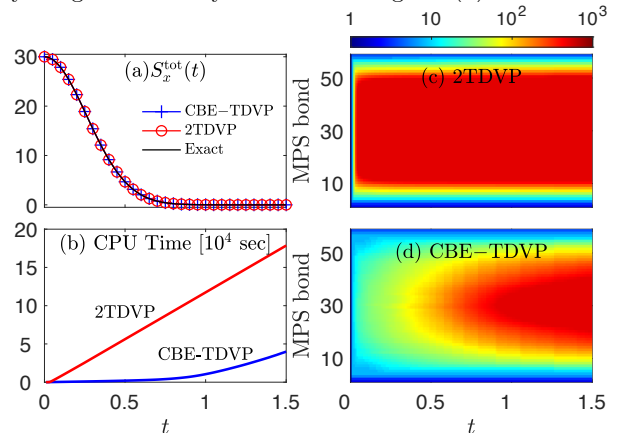


FIG. S-2. 60-site one-axis twisting model for spin $S = 1/2$: Time evolution of an initially x -polarized spin state, computed using $\delta = 0.01$, $D_{\max} = 500$, and \mathbb{Z}_2 spin symmetry. (a) Total spin $S_x^{\text{tot}}(t)$ for CBE-TDVP (blue), 2TDVP (red) and the exact solution (black). (b) CPU time for CBE-TDVP (blue) and 2TDVP (red). (c,d) Color scale plot of the bond dimension as a function of time for all MPS bonds, for (c) 2TDVP and (d) CBE-TDVP.

time spent to achieve this, however, is quite different. In Fig. S-2(b), we see that while the 2TDVP takes about two days, CBE-TDVP accomplishes the same time span overnight.

The main reason for this difference does not lie in the 1s vs. 2s scaling of CBE-TDVP vs. 2TDVP (discussed below), because $d = 2$ (for $S = 1/2$) is small, and CBE involves some algorithmic overhead for determining the truncated complement $\tilde{A}_\ell^{\text{tr}}(\nabla)$. Instead, the difference reflects the fact that the growth in MPS bond dimension $D(t)$ with time is much slower for CBE-TDVP than 2TDVP. This implies dramatic cost savings, since both methods have time complexity proportional to D^3 . Figure S-2(c,d) show the time evolution of bond dimensions for all MPS bonds for CBE-TDVP and 2TDVP respectively. For 2TDVP [Fig. S-2(c)], the bond dimensions grow almost exponentially and quickly saturate to their specified maximal value, here $D_{\max} = 500$. This saturation is reflected by the early onset of linear growth in the CPU time in Fig. S-2(b). By contrast, the bond dimensions of CBE-TDVP show a much slower growth [Fig. S-2(d)], yielding a strong reduction in CPU time compared to 2TDVP.

Second, we demonstrate that when D is fixed, the time complexity of CBE-TDVP vs. 2TDVP scales as d vs. d^2 , implying 1s vs. 2s scaling. Figure S-3 shows this by displaying the CPU time per sweep for the OAT model for several different values of the spin S , with the MPS bond dimension fixed at $D_{\max} = 500$.

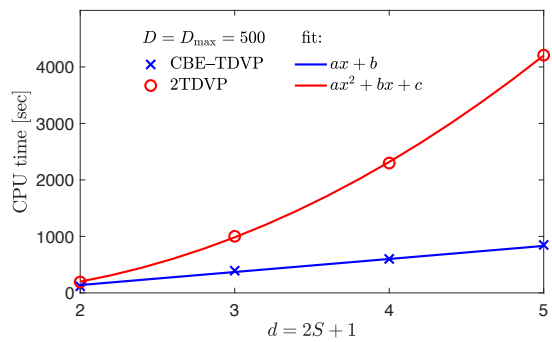


FIG. S-3. CPU time per sweep for the 20-site one-axis twisting model, computed for several values of S , at $D_{\max} = 500$.

Projector formalism for kept and discarded spaces of matrix product states

Andreas Gleis,¹ Jheng-Wei Li,¹ and Jan von Delft¹

¹*Arnold Sommerfeld Center for Theoretical Physics, Center for NanoScience, and Munich Center for Quantum Science and Technology, Ludwig-Maximilians-Universität München, 80333 Munich, Germany*

(Dated: July 28, 2022)

Any matrix product state $|\Psi\rangle$ has a set of associated kept and discarded spaces, needed for the description of $|\Psi\rangle$, and changes thereof, respectively. These induce a partition of the full Hilbert space of the system into mutually orthogonal spaces of irreducible n -site variations of $|\Psi\rangle$. Here, we introduce a convenient projector formalism and diagrammatic notation to characterize these n -site spaces explicitly. This greatly facilitates the formulation of MPS algorithms that explicitly or implicitly employ discarded spaces. As an illustration, we derive an explicit expression for the n -site energy variance and evaluate it numerically for a model with long-range hopping. We also describe an efficient algorithm for computing low-lying n -site excitations above a finite MPS ground state.

DOI:

I. INTRODUCTION

Matrix product states (MPS) are widely used for the numerical description of quantum systems defined on one- or two-dimensional lattices. Well-known MPS-based algorithms include ground state searches and time evolution using the density matrix renormalization group (DMRG and tDMRG) [1–6], time-evolving block decimation (TEBD) methods [7–9], or the time-dependent variational principle (TDVP) [10–14]; and the computation of spectral information using the numerical renormalization group (NRG) [15–17], DMRG [18–21], or so-called post-MPS approaches [14, 22]; see Refs. [23–25] for reviews.

All such algorithms involve update steps: a quantum state of interest, $|\Psi\rangle$, is represented in MPS form, and its constituent tensors are updated, e.g. during optimization or time evolution. During an update, highly relevant information is *kept* (κ) and less relevant information *discarded* (\mathfrak{D}). A sequence of updates thereby endows the full Hilbert space of the system, \mathbb{V} , with a structure of intricately nested κ or \mathfrak{D} subspaces, changing with each update, containing states from \mathbb{V} which either do (κ) or do not (\mathfrak{D}) contribute to the description of $|\Psi\rangle$.

The nested structure of \mathbb{V} is rarely made explicit in the formulation of MPS algorithms. A notable exception is NRG, where \mathfrak{D} states are used to construct a complete basis [26] of approximate energy eigenstates for \mathbb{V} , facilitating the computation of time evolution or spectral information [16, 17]. For the computation of local multipoint correlators [27] using NRG, it has proven useful to elucidate the structure of κ and \mathfrak{D} subspaces by introducing projectors having these subspaces as their images. The orthogonality properties of κ and \mathfrak{D} projectors bring structure and clarity to the description of rather complex algorithmic strategies.

Inspired by the convenience of κ and \mathfrak{D} projectors in the context of NRG, we here introduce an analogous but more general κ, \mathfrak{D} projector formalism and diagrammatic conventions suitable for the description of arbitrary MPS algorithms. In particular, our κ, \mathfrak{D} projectors offer a

natural language for the formulation of algorithms that explicitly or implicitly employ discarded spaces; this includes algorithms evoking the notion of tangent spaces [10, 12–14, 22] and generalizations thereof, as will be described later.

To formulate the goals of this paper, we here briefly indicate how the nested subspaces mentioned above come about. Concrete constructions follow in later sections.

An MPS $|\Psi\rangle$ written in canonical form is defined by a set of isometric tensors [23]. The image space of an isometric tensor, its *kept* space, is needed for the description of $|\Psi\rangle$. The orthogonal complement of the kept space, its *discarded* space, is not needed for $|\Psi\rangle$ itself, but for the description of changes of $|\Psi\rangle$ due to an update step, e.g. during variational optimization, time evolution, or the computation of excitations above the ground state. Any such change can be assigned to one of the subspaces \mathbb{V}^{ns} in the nested hierarchy

$$\mathbb{V}^{0s} \subset \mathbb{V}^{1s} \subset \mathbb{V}^{2s} \subset \dots \subset \mathbb{V}^{\mathcal{L}s} = \mathbb{V}, \quad (1)$$

where \mathbb{V} is the full Hilbert space of a system of \mathcal{L} sites, \mathbb{V}^{ns} the subspace spanned by all n -site (ns) variations of $|\Psi\rangle$, and $\mathbb{V}^{0s} = \text{span}\{|\Psi\rangle\}$ the one-dimensional space spanned by the reference MPS itself. The orthogonality of kept and discarded spaces induces a partition of each \mathbb{V}^{ns} into nested orthogonal subspaces [6, 28], such that

$$\mathbb{V}^{ns} = \bigoplus_{n'=0}^n \mathbb{V}^{n'\perp}, \quad (2)$$

where $\mathbb{V}^{n\perp}$ is the subspace of \mathbb{V}^{ns} spanned by all irreducible ns variations not expressible through n' 's variations with $n' < n$, and $\mathbb{V}^{0\perp} = \mathbb{V}^{0s}$. In particular, the full Hilbert space can be represented as $\mathbb{V} = \bigoplus_{n=0}^{\mathcal{L}} \mathbb{V}^{n\perp}$.

The subspaces defined above underlie, implicitly or explicitly, all MPS algorithms. \mathbb{V}^{1s} is the so-called tangent space of $|\Psi\rangle$, i.e. the space of all one-site ($1s$) variations of $|\Psi\rangle$. It plays an explicit role in numerous recent MPS algorithms, such as TDVP time-evolution, or the description of translationally invariant MPS and their excitations [13, 14, 28]. It also features implicitly in MPS algorithms

formulated using 1s update schemes, such as the 1s formulation of DMRG [23], because 1s updates explore states from \mathbb{V}^{1s} . Likewise, the space \mathbb{V}^{2s} implicitly underlies all 2s MPS algorithms such as 2s DMRG ground state search, 2s time-dependent DMRG (tDMRG), or 2s TDVP, in that 2s updates explore states from \mathbb{V}^{2s} . Moreover, $\mathbb{V}^{1\perp}$ and $\mathbb{V}^{2\perp}$ are invoked explicitly when computing the 2s energy variance, an error measure for MPS ground state searches introduced in Ref. [6]. Finally, \mathbb{V}^{ns} is implicitly invoked in MPS algorithms defining excited states of translationally invariant MPS through linear combinations of local excitations defined on n sites [22].

The construction of a basis for \mathbb{V}^{ns} and $\mathbb{V}^{n\perp}$ is well known for $n = 1$ [12], and for $n = 2$ it is outlined in Ref. [6]. However, we are not aware of a general, explicit construction for $n > 2$, as needed, e.g., to compute the ns energy variance. Here, we explicitly construct projectors, \mathcal{P}^{ns} and $\mathcal{P}^{n\perp}$, having \mathbb{V}^{ns} and $\mathbb{V}^{n\perp}$ as images, respectively. For $n = 1$, this amounts to a construction of a basis for the tangent space \mathbb{V}^{1s} . More generally, our κ, D projector formalism used to construct \mathcal{P}^{ns} and $\mathcal{P}^{n\perp}$ greatly facilitates the formulation of MPS algorithms that explicitly or implicitly employ discarded spaces. As an illustration, we derive an explicit expression for the n -site energy variance, generalizing the error measure proposed in Ref. [6], and evaluate it numerically for a model with long-range hopping, the Haldane-Shastry model. We also show how the multiparticle ns excitations proposed in Ref. [22] are formulated in our scheme, and propose a strategy for computing them explicitly, for any n .

We expect that the κ, D projector formalism developed here will be particularly useful for improving the efficiency of MPS algorithms by incorporating information from $\mathbb{V}^{n\perp}$ into suitably expanded versions of $\mathbb{V}^{(n' < n)s}$ without fully computing $\mathbb{V}^{n\perp}$. For example, we have recently developed a scheme, called controlled bond expansion, which incorporates 2s information into 1s updates for DMRG ground state search [29] and TDVP time evolution [30], in a manner requiring only 1s costs.

This paper is structured as follows. In Sec. II we collect some well-known facts about MPSs, and formally define the associated kept and discarded spaces and corresponding projectors. Section III, the heart of this paper, describes the construction of the \mathcal{P}^{ns} and $\mathcal{P}^{n\perp}$ projectors for general n . As applications of our projector formalism, we compute the ns energy variance of the Haldane-Shastry model in Sec. IV, and describe the construction and computation of ns excitations in Sec. V. We end with a brief outlook in Sec. VI.

II. MPS BASICS

This section offers a concise, tutorial-style summary of MPS notation and the associated diagrammatics. Moreover, we formalize the notion of kept spaces, needed to describe an MPS $|\Psi\rangle$, and discarded spaces, needed to describe changes to it at specified sites. We also recapit-

ulate the definition of local bond, 1s and 2s projectors routinely used in 1s and 2s MPS algorithms.

A. Basic MPS notation

Consider a quantum chain with sites labeled $\ell = 1, \dots, \mathcal{L}$. Let each site be represented by a d -dimensional Hilbert space, \mathbb{v}_ℓ , with local basis states $|\sigma_\ell\rangle$, $\sigma_\ell = 1, \dots, d$. The full Hilbert space is $\mathbb{V} = \prod_{\otimes \ell} \mathbb{v}_\ell = \text{span}\{|\boldsymbol{\sigma}\rangle\}$, with basis states $|\boldsymbol{\sigma}\rangle = |\sigma_1\rangle|\sigma_2\rangle\cdots|\sigma_{\mathcal{L}}\rangle$. Any state $|\Psi\rangle = |\boldsymbol{\sigma}\rangle\Psi^\boldsymbol{\sigma} \in \mathbb{V}$ can be written as an open boundary MPS, with wavefunction of the form

$$\begin{aligned} \Psi^\boldsymbol{\sigma} &= [M_1]_{1\alpha_1}^{\sigma_1} [M_2]_{\alpha_1\alpha_2}^{\sigma_2} \cdots [M_{\mathcal{L}}]_{\alpha_{\mathcal{L}-1}}^{\sigma_{\mathcal{L}}} \\ &= \begin{array}{c} M_1 \quad M_2 \quad \quad \quad \quad \quad M_{\mathcal{L}} \\ \times \quad \circ \quad \circ \quad \circ \quad \circ \quad \circ \quad \circ \quad \times \\ \downarrow \quad \downarrow \quad \downarrow \quad \downarrow \quad \downarrow \quad \downarrow \quad \downarrow \\ 1 \quad \sigma_1 \quad \alpha_1 \quad \sigma_2 \quad \alpha_2 \quad \quad \quad \quad \alpha_{\mathcal{L}-1} \quad \sigma_{\mathcal{L}} \quad 1 \end{array} \end{aligned} \quad (3)$$

(This diagram depicts both the wavefunction Ψ and the corresponding state $|\Psi\rangle$.) Sums over repeated indices are implied throughout, and depicted diagrammatically by bonds. Each M_ℓ is a three-leg tensor with elements $[M_\ell]_{\alpha_{\ell-1}\alpha_\ell}^{\sigma_\ell}$. Its physical and virtual bond indices, σ_ℓ and $\alpha_{\ell-1}$, α_ℓ , have dimensions d and $D_{\ell-1}$, D_ℓ , respectively. The outermost bonds, to dummy sites represented by crosses, have $D_0 = D_{\mathcal{L}} = 1$. The bond dimensions D_ℓ are adjustable parameters, controlling the amount of entanglement an MPS can encode. (In the literature, it is common practice to drop the subscript on D_ℓ for brevity, understanding that D can nevertheless vary from bond to bond.) Likewise, a Hamiltonian acting within \mathbb{V} , $\mathcal{H} = |\boldsymbol{\sigma}\rangle H^{\boldsymbol{\sigma}\boldsymbol{\sigma}'} \langle \boldsymbol{\sigma}'|$, can be expressed as an MPO, with

$$\begin{aligned} H^{\boldsymbol{\sigma}\boldsymbol{\sigma}'} &= [W_1]_{1\nu_1}^{\sigma_1\sigma'_1} [W_2]_{\nu_1\nu_2}^{\sigma_2\sigma'_2} \cdots [W_{\mathcal{L}}]_{\nu_{\mathcal{L}-1}}^{\sigma_{\mathcal{L}}\sigma'_{\mathcal{L}}}, \\ &= \begin{array}{c} \sigma'_1 W_1 \quad \sigma'_2 W_2 \quad \quad \quad \quad \quad \sigma'_{\mathcal{L}} W_{\mathcal{L}} \\ \times \quad \square \quad \square \quad \square \quad \square \quad \square \quad \times \\ \downarrow \quad \downarrow \quad \downarrow \quad \downarrow \quad \downarrow \quad \downarrow \\ 1 \quad \sigma_1 \quad \nu_1 \quad \sigma_2 \quad \nu_2 \quad \quad \quad \quad \nu_{\mathcal{L}-1} \quad \sigma_{\mathcal{L}} \quad 1 \end{array} \end{aligned} \quad (4)$$

where the four-leg tensors W_ℓ have elements $[W_\ell]_{\nu_{\ell-1}\nu_\ell}^{\sigma_\ell\sigma'_\ell}$, and the virtual bond indices ν_ℓ have dimensions w_ℓ .

Any MPS wavefunction can be brought into canonical form w.r.t. an ‘‘orthogonality center’’ at site $\ell \in [1, \mathcal{L}]$, or w.r.t. bond $\tilde{\ell}$ connecting sites ℓ and $\ell + 1$,

$$\Psi^\boldsymbol{\sigma} = \begin{array}{c} A_1 \quad \quad \quad A_{\tilde{\ell}-1} \quad C_{\tilde{\ell}} \quad B_{\tilde{\ell}+1} \quad B_{\mathcal{L}} \\ \times \quad \downarrow \quad \downarrow \quad \downarrow \quad \downarrow \quad \downarrow \quad \downarrow \quad \times \\ \sigma_1 \quad \quad \quad \sigma_{\tilde{\ell}-1} \quad \sigma_{\tilde{\ell}} \quad \sigma_{\tilde{\ell}+1} \quad \sigma_{\mathcal{L}} \end{array}, \quad (5)$$

where we indicated some of the bond dimensions. Here, $A_{\tilde{\ell}}$ and $B_{\tilde{\ell}'}$ (with $1 \leq \tilde{\ell} < \ell < \tilde{\ell}' \leq \mathcal{L}$) satisfy the relations

$$\begin{aligned} [A_{\tilde{\ell}}^\dagger]_{\alpha\tilde{\alpha}}^\sigma [A_{\tilde{\ell}}]_{\tilde{\alpha}\alpha'}^\sigma &= [\mathbb{1}_{\tilde{\ell}}^\kappa]_{\alpha\alpha'}, \quad [B_{\tilde{\ell}'}]_{\alpha\tilde{\alpha}}^\sigma [B_{\tilde{\ell}'}^\dagger]_{\tilde{\alpha}\alpha'}^\sigma = [\mathbb{1}_{\tilde{\ell}'-1}^\kappa]_{\alpha\alpha'}, \\ \alpha \begin{array}{c} A_{\tilde{\ell}} \\ \square \\ A_{\tilde{\ell}}^* \end{array} \alpha' &= \left(\begin{array}{c} \alpha' \\ \alpha \end{array} \begin{array}{c} \alpha \\ \alpha' \end{array} \begin{array}{c} \alpha \\ \alpha' \end{array} \right) = [\mathbb{1}_{\tilde{\ell}'-1}^\kappa]_{\alpha\alpha'}, \quad (6) \end{aligned}$$

or $A_{\tilde{\ell}}^\dagger A_{\tilde{\ell}} = \mathbb{1}_{\tilde{\ell}}^\kappa$, $B_{\tilde{\ell}'} B_{\tilde{\ell}'}^\dagger = \mathbb{1}_{\tilde{\ell}'-1}^\kappa$ for short, where $\mathbb{1}_{\tilde{\ell}}^\kappa$ denotes a $D_{\tilde{\ell}} \times D_{\tilde{\ell}}$ unit matrix. (The superscript κ stands

for “kept”, for reasons explained below.) The open triangles representing $A_{\tilde{\ell}}$ and $B_{\tilde{\ell}'}$ are oriented such that their diagonals face left or right, respectively. The orthogonality center can be shifted left or right by using singular value decomposition (SVD) to express it as $C_{\ell} = U_{\ell-1}S_{\ell-1}B_{\ell}$ or $C_{\ell} = A_{\ell}S_{\ell}V_{\ell}^{\dagger}$:

$$\begin{array}{c} A_{\ell-1} \quad C_{\ell} \\ \diagdown \quad \diagup \\ \hline \\ \diagup \quad \diagdown \\ C_{\ell} \quad B_{\ell+1} \end{array} = \begin{array}{c} A_{\ell-1} \quad U_{\ell-1} \quad S_{\ell-1} \quad B_{\ell} \\ \diagdown \quad \square \quad \square \quad \diagup \\ \hline \\ \diagup \quad \square \quad \square \quad \diagdown \\ A_{\ell} \quad S_{\ell} \quad V_{\ell}^{\dagger} \quad B_{\ell+1} \end{array} = \begin{array}{c} C_{\ell-1} \quad B_{\ell} \\ \diagdown \quad \diagup \\ \hline \\ \diagup \quad \diagdown \\ A_{\ell} \quad C_{\ell+1} \end{array}, \quad (7)$$

Here $U_{\ell-1}$, V_{ℓ}^{\dagger} , $S_{\ell-1}$, S_{ℓ} are square matrices, the former two unitary, the latter two diagonal and containing SVD singular values. (Shifting can be combined with truncation, if desired, by discarding some small singular values and correspondingly reducing the bond dimension.) By renaming $V_{\ell}^{\dagger}B_{\ell+1}$ as $B_{\ell+1}$ and defining $\Lambda_{\ell} = S_{\ell}$, we can also express Ψ^{σ} in “bond-canonical” form w.r.t. bond ℓ :

$$\begin{array}{c} A_1 \\ \diagdown \\ \hline \\ \diagup \\ A_{\ell-1} \quad A_{\ell} \quad \Lambda_{\ell} \quad B_{\ell+1} \quad B_{\mathcal{L}} \\ \diagdown \quad \diagdown \quad \diagup \quad \square \quad \diagdown \quad \diagdown \quad \diagup \\ \hline \\ \diagup \quad \diagup \quad \diagdown \quad \square \quad \diagup \quad \diagup \quad \diagdown \\ A_1 \quad A_{\ell-1} \quad A_{\ell} \quad \Lambda_{\ell} \quad B_{\ell+1} \quad B_{\mathcal{L}} \end{array}. \quad (8)$$

The fact that the same MPS can be written in many different but equivalent ways reflects the gauge freedom of MPS representations.

B. Kept spaces

Given an MPS $|\Psi\rangle$ in canonical form, its constituent tensors can be used to define a set of state spaces defined on parts of the chain, and a sequence of isometric maps between these state spaces. Let us make this explicit to reveal the underlying structures.

The $A_{\tilde{\ell}}$ tensors for sites 1 to $\tilde{\ell}$ can be used to define a set of left *kept* (κ) states $|\Psi_{\tilde{\ell}\alpha}^{\kappa}\rangle$, and the $B_{\tilde{\ell}'}$ tensors for sites $\tilde{\ell}'$ to \mathcal{L} can be used to define right κ states $|\Phi_{\tilde{\ell}'\alpha'}^{\kappa}\rangle$, with wavefunctions of the form

$$\Psi_{\tilde{\ell}\alpha}^{\kappa} = \begin{array}{c} A_1 \quad A_{\tilde{\ell}} \\ \diagdown \quad \diagup \\ \hline \\ \diagup \quad \diagdown \\ \alpha \end{array}, \quad \Phi_{\tilde{\ell}'\alpha'}^{\kappa} = \begin{array}{c} B_{\tilde{\ell}'} \quad B_{\mathcal{L}} \\ \diagdown \quad \diagup \\ \hline \\ \diagup \quad \diagdown \\ \alpha' \end{array}. \quad (9)$$

These states are called *kept*, since they are building blocks of $|\Psi\rangle$. Their spans define left and right κ spaces,

$$\mathbb{V}_{\tilde{\ell}}^{\kappa} = \text{span}\{|\Psi_{\tilde{\ell}\alpha}^{\kappa}\rangle\} \subset \mathbb{v}_1 \otimes \dots \otimes \mathbb{v}_{\tilde{\ell}}, \quad (10)$$

$$\mathbb{W}_{\tilde{\ell}'}^{\kappa} = \text{span}\{|\Phi_{\tilde{\ell}'\alpha'}^{\kappa}\rangle\} \subset \mathbb{v}_{\tilde{\ell}'} \otimes \dots \otimes \mathbb{v}_{\mathcal{L}}, \quad (11)$$

of dimension $D_{\tilde{\ell}}$ and $D_{\tilde{\ell}'-1}$, respectively. The dummy sites 0 and $\mathcal{L}+1$ are represented by one-dimensional spaces, \mathbb{V}_0^{κ} and $\mathbb{W}_{\mathcal{L}+1}^{\kappa}$.

Each $A_{\tilde{\ell}}$ and $B_{\tilde{\ell}'}$ tensor defines an isometric map, from a *parent* (P) space involving a direct product of a κ space and a local space, to an adjacent κ space:

$$\begin{aligned} A_{\tilde{\ell}}: \mathbb{V}_{\tilde{\ell}-1}^{\kappa} \otimes \mathbb{v}_{\tilde{\ell}} &\rightarrow \mathbb{V}_{\tilde{\ell}}^{\kappa}, & |\Psi_{\tilde{\ell}-1,\alpha}^{\kappa}\rangle |\sigma_{\tilde{\ell}}\rangle [A_{\tilde{\ell}}]_{\alpha\alpha'}^{\sigma_{\tilde{\ell}}} &= |\Psi_{\tilde{\ell}\alpha'}^{\kappa}\rangle, \\ B_{\tilde{\ell}'}: \mathbb{v}_{\tilde{\ell}'} \otimes \mathbb{W}_{\tilde{\ell}'+1}^{\kappa} &\rightarrow \mathbb{W}_{\tilde{\ell}'}^{\kappa}, & [B_{\tilde{\ell}'}]_{\alpha\alpha'}^{\sigma_{\tilde{\ell}'}} |\sigma_{\tilde{\ell}'}\rangle |\Phi_{\tilde{\ell}'+1,\alpha'}^{\kappa}\rangle &= |\Phi_{\tilde{\ell}'\alpha'}^{\kappa}\rangle. \end{aligned}$$

(To connect sites 1 and \mathcal{L} to their neighboring dummy sites, we define $\Psi_{0,1}^{\kappa} = 1$, $\Phi_{\mathcal{L}+1,1}^{\kappa} = 1$.) We orient the triangles depicting $A_{\tilde{\ell}}$ and $B_{\tilde{\ell}'}$ such that equal-length legs point to parent spaces and 90-degree angles to kept spaces. The dimensions of left or right kept and parent spaces satisfy $D_{\tilde{\ell}} \leq D_{\tilde{\ell}-1}d$ or $D_{\tilde{\ell}'-1} \leq dD_{\tilde{\ell}'}$, respectively. If a kept space is smaller than its parent space, it has an orthogonal complement, called *discarded* (D) space, discussed in Sec. IID below. The fact that the maps $A_{\tilde{\ell}}$ and $B_{\tilde{\ell}'}$ are *isometries* follows from Eqs. (6). These ensure that the left and right κ basis states form orthonormal sets,

$$\begin{aligned} \langle \Psi_{\tilde{\ell}\alpha}^{\kappa} | \Psi_{\tilde{\ell}\alpha'}^{\kappa} \rangle &= [\mathbb{1}_{\tilde{\ell}}^{\kappa}]_{\alpha\alpha'}, & \langle \Phi_{\tilde{\ell}'\alpha}^{\kappa} | \Phi_{\tilde{\ell}'\alpha'}^{\kappa} \rangle &= [\mathbb{1}_{\tilde{\ell}'-1}^{\kappa}]_{\alpha\alpha'}, \\ \begin{array}{c} \diagdown \quad \diagup \\ \hline \\ \diagup \quad \diagdown \\ 1 \quad \tilde{\ell} \end{array} &= \left(\begin{array}{c} \diagdown \quad \diagup \\ \hline \\ \diagup \quad \diagdown \\ \tilde{\ell}' \quad \mathcal{L} \end{array} \right) &= \left(\begin{array}{c} \diagdown \quad \diagup \\ \hline \\ \diagup \quad \diagdown \\ \tilde{\ell}'-1 \end{array} \right). \end{aligned} \quad (12)$$

The basis states can be used to build projectors onto the left or right κ spaces $\mathbb{V}_{\tilde{\ell}}^{\kappa}$ or $\mathbb{W}_{\tilde{\ell}'}^{\kappa}$, depicted as

$$\mathcal{P}_{\tilde{\ell}}^{\kappa} = \sum_{\alpha} |\Psi_{\tilde{\ell}\alpha}^{\kappa}\rangle \langle \Psi_{\tilde{\ell}\alpha}^{\kappa}| = \begin{array}{c} \diagdown \quad \diagup \\ \hline \\ \diagup \quad \diagdown \\ 1 \quad \tilde{\ell} \end{array}, \quad (13a)$$

$$\mathcal{Q}_{\tilde{\ell}'}^{\kappa} = \sum_{\alpha'} |\Phi_{\tilde{\ell}'\alpha'}^{\kappa}\rangle \langle \Phi_{\tilde{\ell}'\alpha'}^{\kappa}| = \begin{array}{c} \diagdown \quad \diagup \\ \hline \\ \diagup \quad \diagdown \\ \tilde{\ell}' \quad \mathcal{L} \end{array}, \quad (13b)$$

with $\mathcal{P}_0^{\kappa} = 1$, $\mathcal{Q}_{\mathcal{L}+1}^{\kappa} = 1$, and $(\mathcal{P}_{\tilde{\ell}}^{\kappa})^2 = \mathcal{P}_{\tilde{\ell}}^{\kappa}$, $(\mathcal{Q}_{\tilde{\ell}'}^{\kappa})^2 = \mathcal{Q}_{\tilde{\ell}'}^{\kappa}$:

$$\begin{array}{c} \diagdown \quad \diagup \\ \hline \\ \diagup \quad \diagdown \\ 1 \quad \tilde{\ell} \end{array} \begin{array}{c} \diagdown \quad \diagup \\ \hline \\ \diagup \quad \diagdown \\ \tilde{\ell}' \quad \mathcal{L} \end{array} = \begin{array}{c} \diagdown \quad \diagup \\ \hline \\ \diagup \quad \diagdown \\ 1 \quad \tilde{\ell} \end{array} \begin{array}{c} \diagdown \quad \diagup \\ \hline \\ \diagup \quad \diagdown \\ \tilde{\ell}' \quad \mathcal{L} \end{array}, \quad \begin{array}{c} \diagdown \quad \diagup \\ \hline \\ \diagup \quad \diagdown \\ \tilde{\ell}' \quad \mathcal{L} \end{array} \begin{array}{c} \diagdown \quad \diagup \\ \hline \\ \diagup \quad \diagdown \\ \tilde{\ell}' \quad \mathcal{L} \end{array} = \begin{array}{c} \diagdown \quad \diagup \\ \hline \\ \diagup \quad \diagdown \\ \tilde{\ell}' \quad \mathcal{L} \end{array}. \quad (14)$$

C. Bond, 1s and 2s projectors

The above projectors can, in turn, be used to construct bond, 1s and 2s projectors acting on the full chain,

$$\mathcal{P}_{\ell}^b = \mathcal{P}_{\ell}^{\kappa} \otimes \mathcal{Q}_{\ell+1}^{\kappa} = \begin{array}{c} \diagdown \quad \diagup \\ \hline \\ \diagup \quad \diagdown \\ \ell \quad \ell+1 \end{array}, \quad (15a)$$

$$\mathcal{P}_{\ell}^{1s} = \mathcal{P}_{\ell-1}^{\kappa} \otimes \mathbb{1}_d \otimes \mathcal{Q}_{\ell+1}^{\kappa} = \begin{array}{c} \diagdown \quad \diagup \\ \hline \\ \diagup \quad \diagdown \\ \ell-1 \quad \ell \quad \ell+1 \end{array}, \quad (15b)$$

$$\mathcal{P}_{\ell}^{2s} = \mathcal{P}_{\ell-1}^{\kappa} \otimes \mathbb{1}_d \otimes \mathbb{1}_d \otimes \mathcal{Q}_{\ell+2}^{\kappa} = \begin{array}{c} \diagdown \quad \diagup \\ \hline \\ \diagup \quad \diagdown \\ \ell-1 \quad \ell \quad \ell+1 \quad \ell+2 \end{array}, \quad (15c)$$

defined for $\ell \in [0, \mathcal{L}]$, $\ell \in [1, \mathcal{L}]$ and $\ell \in [1, \mathcal{L}-1]$, respectively. They mutually commute and satisfy $(\mathcal{P}_{\ell}^{\kappa})^2 = \mathcal{P}_{\ell}^{\kappa}$, as follows from Eqs. (12) and (14). For example:

$$(\mathcal{P}_{\ell}^b)^2 = \begin{array}{c} \diagdown \quad \diagup \\ \hline \\ \diagup \quad \diagdown \\ \ell \quad \ell \end{array} \begin{array}{c} \diagdown \quad \diagup \\ \hline \\ \diagup \quad \diagdown \\ \ell \quad \ell \end{array} = \begin{array}{c} \diagdown \quad \diagup \\ \hline \\ \diagup \quad \diagdown \\ \ell \quad \ell \end{array} \begin{array}{c} \diagdown \quad \diagup \\ \hline \\ \diagup \quad \diagdown \\ \ell \quad \ell \end{array} = \mathcal{P}_{\ell}^b.$$

The projectors \mathcal{P}^b , \mathcal{P}^{1s} and \mathcal{P}^{2s} map the full \mathbb{V} into the subspaces $\mathbb{V}_{\ell}^{\kappa} \otimes \mathbb{W}_{\ell+1}^{\kappa}$, $\mathbb{V}_{\ell-1}^{\kappa} \otimes \mathbb{v}_{\ell} \otimes \mathbb{W}_{\ell+1}^{\kappa}$ and $\mathbb{V}_{\ell-1}^{\kappa} \otimes$

$\mathbb{V}_\ell \otimes \mathbb{V}_{\ell+1} \otimes \mathbb{W}_{\ell+2}^K$. These spaces offer three equivalent representations of the same state $|\Psi\rangle$, in bond-, 1s- or 2s-canonical form,

$$|\Psi\rangle = |\Psi_{\ell\alpha}^K\rangle |\Phi_{\ell+1,\alpha'}^K\rangle [\psi_\ell^b]_{\alpha\alpha'} \quad (16a)$$

$$= |\Psi_{\ell-1,\alpha}^K\rangle |\sigma_\ell\rangle |\Phi_{\ell+1,\alpha'}^K\rangle [\psi_\ell^{1s}]_{\alpha\alpha'}^{\sigma_\ell} \quad (16b)$$

$$= |\Psi_{\ell-1,\alpha}^K\rangle |\sigma_\ell\rangle |\sigma_{\ell+1}\rangle |\Phi_{\ell+2,\alpha'}^K\rangle [\psi_\ell^{2s}]_{\alpha\alpha'}^{\sigma_\ell\sigma_{\ell+1}}, \quad (16c)$$

$$\psi_\ell^b = \Lambda_\ell, \quad \psi_\ell^{1s} = C_\ell, \quad \psi_\ell^{2s} = A_\ell \Lambda_\ell B_{\ell+1}. \quad (16d)$$

These forms emphasize the tensors describing bond ℓ , site ℓ or sites $(\ell, \ell+1)$ and the bond in between, respectively. For example, Eqs. (16a) and (16b) are depicted as

$$\Psi = \underbrace{\underbrace{A_1}_{\Psi_{\ell\alpha}^K} \underbrace{A_\ell \Lambda_\ell}_{\Phi_{\ell+1,\alpha'}^K} \underbrace{B_{\ell+1}}_{\sigma_\ell} \underbrace{B_{\ell+2}}_{\sigma_{\ell+1}}}_{\Psi_{\ell-1,\alpha}^K} = \underbrace{\underbrace{A_1}_{\Psi_{\ell-1,\alpha}^K} \underbrace{A_{\ell-1} C_\ell}_{\sigma_\ell} \underbrace{B_{\ell+1}}_{\sigma_{\ell+1}} \underbrace{B_{\ell+2}}_{\sigma_{\ell+2}}}_{\Phi_{\ell+1,\alpha'}^K}.$$

The projections of the Hamiltonian into these spaces, $\mathcal{H}_\ell^x = \mathcal{P}_\ell^x \mathcal{H} \mathcal{P}_\ell^x$, have matrix elements of the form

$$H_\ell^b = \left[\begin{array}{c} \text{---} \\ \text{---} \\ \text{---} \end{array} \right]_{\ell \quad \ell+1}, \quad H_\ell^{1s} = \left[\begin{array}{c} \text{---} \\ \text{---} \\ \text{---} \end{array} \right]_{\ell-1 \quad \ell \quad \ell+1}, \quad H_\ell^{2s} = \left[\begin{array}{c} \text{---} \\ \text{---} \\ \text{---} \end{array} \right]_{\ell-1 \quad \ell \quad \ell+1 \quad \ell+2}, \quad (17)$$

with left and right environments for sites $\ell \pm 1$ given by

$$L_\ell = \left[\begin{array}{c} \text{---} \\ \text{---} \\ \text{---} \end{array} \right]_{\ell} = \left[\begin{array}{c} \text{---} \\ \text{---} \\ \text{---} \end{array} \right]_{\ell} = \left[\begin{array}{c} \text{---} \\ \text{---} \\ \text{---} \end{array} \right]_{L_{\ell-1} \quad \ell}, \quad (18a)$$

$$R_\ell = \left[\begin{array}{c} \text{---} \\ \text{---} \\ \text{---} \end{array} \right]_{\ell} = \left[\begin{array}{c} \text{---} \\ \text{---} \\ \text{---} \end{array} \right]_{\ell} = \left[\begin{array}{c} \text{---} \\ \text{---} \\ \text{---} \end{array} \right]_{\ell \quad R_{\ell+1}}. \quad (18b)$$

Here the first equalities define L_ℓ and R_ℓ , the second equalities show how they can be computed recursively, starting from $L_0 = 1$, $R_{\mathcal{L}+1} = 1$. The open triangles on L_ℓ and R_ℓ signify that they are computed using left- or right-normalized A or B tensors.

The above matrix elements are standard ingredients in numerous MPS algorithms. To give a specific example, we briefly recall their role in DMRG ground state searches. These seek approximate ground state solutions to $\mathcal{H}|\Psi\rangle = E|\Psi\rangle$ through a sequence of local optimization steps. Focusing on bond ℓ , or site ℓ , or sites $(\ell, \ell+1)$, one updates Λ_ℓ , or C_ℓ , or $A_\ell \Lambda_\ell B_{\ell+1}$, by finding the ground state solution of, respectively,

$$(H_\ell^b - E)\psi_\ell^b = 0, \quad \left[\begin{array}{c} \text{---} \\ \text{---} \\ \text{---} \end{array} \right]_{\ell \quad \ell+1} = E \text{---} \text{---}, \quad (19a)$$

$$(H_\ell^{1s} - E)\psi_\ell^{1s} = 0, \quad \left[\begin{array}{c} \text{---} \\ \text{---} \\ \text{---} \end{array} \right]_{\ell-1 \quad \ell \quad \ell+1} = E \text{---} \text{---}, \quad (19b)$$

$$(H_\ell^{2s} - E)\psi_\ell^{2s} = 0, \quad \left[\begin{array}{c} \text{---} \\ \text{---} \\ \text{---} \end{array} \right]_{\ell-1 \quad \ell \quad \ell+1 \quad \ell+2} = E \text{---} \text{---}. \quad (19c)$$

One then uses Eq. (7) to shift the orthogonality center to the neighboring bond or site, optimizes it, and sweeps back and forth through the chain until the ground state

energy has converged. These three schemes are known as 0s or bond DMRG, 1s and 2s DMRG, respectively. They differ regarding their flexibility for increasing (“expanding”) virtual bond dimensions, which increases the size of the variational ground state energy. 0s and 1s DMRG offer no way of doing this, because the tensors Λ_ℓ or C_ℓ have the same dimensions after the update as before. By contrast, 2s DMRG does offer a way of expanding bond dimensions: the bonds connecting the updated tensors A_ℓ , Λ_ℓ and $B_{\ell+1}$ have dimensions $d \min(D_{\ell-1}, D_{\ell+1})$, which is $\geq D_\ell$; one may thus expand bond ℓ by retaining more than D_ℓ singular values in Λ_ℓ . However, this comes at a price. The numerical cost is $\mathcal{O}(D^3 d^2 w)$ for applying H^{2s} to ψ_ℓ^{2s} during the iterative solution of the eigenvalue problem Eq. (19c), and $\mathcal{O}(D^3 d^3)$ for SVDing the resulting eigenstate to identify the updated A , Λ , and B . By contrast, for 1s DMRG the costs are lower: $\mathcal{O}(D^3 d w)$ for applying H^{1s} to C , and $\mathcal{O}(D^3 d)$ for SVDing C to shift to the next site. Various schemes have been proposed for achieving 2s accuracy at 1s costs, see Refs. [4, 5, 29].

D. Discarded spaces

In this section, we define discarded spaces as the orthogonal complements of kept spaces, and introduce their corresponding isometries and discarded space projectors.

As mentioned above, the kept spaces \mathbb{W}_ℓ^K and $\mathbb{W}_{\ell'}^K$ have dimensions smaller than the parent spaces $\mathbb{W}_{\ell-1}^K \otimes \mathbb{V}_\ell$ and $\mathbb{V}_{\ell'} \otimes \mathbb{W}_{\ell'+1}^K$ from which they are constructed. Their orthogonal complements are the above-mentioned discarded spaces, to be denoted \mathbb{V}_ℓ^D and $\mathbb{W}_{\ell'}^D$, respectively, of dimension $D_{\ell-1}d - D_\ell$ and $D_{\ell'}d - D_{\ell'-1}$. By definition, $\text{span}\{\mathbb{W}_\ell^K, \mathbb{V}_\ell^D\}$ and $\text{span}\{\mathbb{W}_{\ell'}^K, \mathbb{W}_{\ell'}^D\}$ yield the full parent spaces, respectively. Let \bar{A}_ℓ and $\bar{B}_{\ell'}$ be isometries from the parent to the discarded spaces,

$$\bar{A}_\ell: \mathbb{W}_{\ell-1}^K \otimes \mathbb{V}_\ell \rightarrow \mathbb{V}_\ell^D, \quad |\Psi_{\ell-1,\alpha}^K\rangle |\sigma_\ell\rangle [\bar{A}_\ell]_{\alpha\alpha'}^{\sigma_\ell} = |\Psi_{\ell\alpha}^D\rangle, \\ \bar{B}_{\ell'}: \mathbb{V}_{\ell'} \otimes \mathbb{W}_{\ell'+1}^K \rightarrow \mathbb{W}_{\ell'}^D, \quad [\bar{B}_{\ell'}]_{\alpha\alpha'}^{\sigma_{\ell'}} |\Phi_{\ell'+1,\alpha'}^K\rangle \otimes \mathbb{V}_{\ell'} = |\Phi_{\ell'\alpha}^D\rangle.$$

Then $A_\ell \oplus \bar{A}_\ell$ and $B_{\ell'} \oplus \bar{B}_{\ell'}$ are unitary maps on the parent spaces, and Eq. (6) is complemented by relations expressing orthonormality and completeness:

$$\bar{A}_\ell^\dagger \bar{A}_\ell = \mathbb{1}_\ell^D, \quad A_\ell^\dagger \bar{A}_\ell = 0, \quad \bar{B}_{\ell'} \bar{B}_{\ell'}^\dagger = \mathbb{1}_{\ell'-1}^D, \quad \bar{B}_{\ell'} B_{\ell'}^\dagger = 0, \\ \mathbb{Q}_\ell = \left(\begin{array}{c} \text{---} \\ \text{---} \\ \text{---} \end{array} \right)_\ell = \mathbb{1}_\ell^D, \quad \mathbb{Q}_\ell = 0, \quad \mathbb{P}_\ell = \left(\begin{array}{c} \text{---} \\ \text{---} \\ \text{---} \end{array} \right)_\ell = \mathbb{1}_{\ell-1}^D, \quad \mathbb{P}_\ell = 0, \quad (20)$$

$$A_\ell A_\ell^\dagger + \bar{A}_\ell \bar{A}_\ell^\dagger = \mathbb{1}_\ell^P, \quad B_{\ell'}^\dagger B_{\ell'} + \bar{B}_{\ell'}^\dagger \bar{B}_{\ell'} = \mathbb{1}_{\ell'-1}^P, \\ \left[\begin{array}{c} \text{---} \\ \text{---} \\ \text{---} \end{array} \right]_\ell + \left[\begin{array}{c} \text{---} \\ \text{---} \\ \text{---} \end{array} \right]_\ell = \text{---} \text{---} = \mathbb{1}_\ell^P, \quad \left[\begin{array}{c} \text{---} \\ \text{---} \\ \text{---} \end{array} \right]_{\ell'} + \left[\begin{array}{c} \text{---} \\ \text{---} \\ \text{---} \end{array} \right]_{\ell'} = \text{---} \text{---} = \mathbb{1}_{\ell'-1}^P. \quad (21)$$

Here, left- or right-oriented grey triangles denote the complements \bar{A}_ℓ and $\bar{B}_{\ell'}$ associated with discarded spaces. The orthogonality relations (6) and (20) state that K meeting K or D meeting D yield unity, whereas K meeting

\mathbb{D} yields zero. We will use them often below. For the completeness relations (21), $\mathbb{1}_\ell^{\mathbb{P}} = \mathbb{1}_{\ell-1}^{\mathbb{K}} \otimes \mathbb{1}_d$ and $\mathbb{1}_{\ell-1}^{\mathbb{P}} = \mathbb{1}_d \otimes \mathbb{1}_{\ell-1}^{\mathbb{K}}$ are identity matrices on the parent spaces, with $\mathbb{1}_d$ a $d \times d$ unit matrix. In numerical practice, it is desirable to avoid the explicit computation of $\overline{A}_\ell \overline{A}_\ell^\dagger$ or $\overline{B}_\ell \overline{B}_\ell^\dagger$, since these are huge objects. Instead, one can always use Eq. (21) to express them as $\mathbb{1}_\ell^{\mathbb{P}} - A_\ell A_\ell^\dagger$ or $\mathbb{1}_{\ell-1}^{\mathbb{P}} - B_\ell B_\ell^\dagger$.

Equations (21) imply additional identities that will likewise be useful below:

$$\circlearrowleft |c\rangle = \begin{array}{c} \diagup \\ \diagdown \end{array} c + \begin{array}{c} \diagdown \\ \diagup \end{array} c = \circlearrowright c + \circlearrowleft c, \quad (22a)$$

$$\circlearrowleft |c\rangle |c\rangle = \begin{array}{c} \diagup \\ \diagdown \end{array} \begin{array}{c} \diagdown \\ \diagup \end{array} c + \begin{array}{c} \diagdown \\ \diagup \end{array} \begin{array}{c} \diagup \\ \diagdown \end{array} c + \begin{array}{c} \diagup \\ \diagdown \end{array} \begin{array}{c} \diagup \\ \diagdown \end{array} c + \begin{array}{c} \diagdown \\ \diagup \end{array} \begin{array}{c} \diagdown \\ \diagup \end{array} c, \quad (22b)$$

$$\begin{array}{c} \diagup \\ \diagdown \end{array} \begin{array}{c} \diagdown \\ \diagup \end{array} c = \circlearrowleft |c\rangle - \circlearrowright |c\rangle - \begin{array}{c} \diagdown \\ \diagup \end{array} \begin{array}{c} \diagup \\ \diagdown \end{array} c + \begin{array}{c} \diagup \\ \diagdown \end{array} \begin{array}{c} \diagdown \\ \diagup \end{array} c. \quad (22c)$$

The first two lines can be used to express 1s or 2s projectors through bond projectors, as elaborated below. The third line follows from the first two. The two equivalent forms on the right of Eq. (22a) arise from combining the physical state space of site ℓ with virtual state spaces on either the left or the right, yielding either left- or right-normalized parent spaces.

In complete analogy to Eqs. (9) to (13), the complement isometries can be used to define orthonormal bases states for the left and right discarded spaces $\mathbb{V}_\ell^{\mathbb{D}}$ and $\mathbb{W}_\ell^{\mathbb{D}}$,

$$\Psi_{\ell\alpha}^{\mathbb{D}} = \begin{array}{c} A_1 \\ \diagdown \\ \diagup \\ \diagdown \\ \diagup \end{array} \overline{A}_\ell \alpha, \quad \Phi_{\ell'\alpha'}^{\mathbb{D}} = \alpha' \begin{array}{c} \overline{B}_{\ell'} \\ \diagup \\ \diagdown \\ \diagup \\ \diagdown \end{array} B_{\mathcal{Z}}, \quad (23)$$

satisfying the orthonormality relations

$$\begin{array}{c} \circlearrowleft \\ \circlearrowright \end{array} \begin{array}{c} \diagup \\ \diagdown \\ \diagup \\ \diagdown \end{array} \begin{array}{c} \diagdown \\ \diagup \\ \diagdown \\ \diagup \end{array} = \begin{pmatrix} \circlearrowleft, & \begin{array}{c} \diagup \\ \diagdown \\ \diagup \\ \diagdown \end{array} \\ \circlearrowright, & \begin{array}{c} \diagdown \\ \diagup \\ \diagdown \\ \diagup \end{array} \end{pmatrix}, \quad (24a)$$

$$\begin{array}{c} \circlearrowleft \\ \circlearrowright \end{array} \begin{array}{c} \diagup \\ \diagdown \\ \diagup \\ \diagdown \end{array} \begin{array}{c} \diagdown \\ \diagup \\ \diagdown \\ \diagup \end{array} = 0, \quad \begin{array}{c} \circlearrowleft \\ \circlearrowright \end{array} \begin{array}{c} \diagdown \\ \diagup \\ \diagdown \\ \diagup \end{array} \begin{array}{c} \diagup \\ \diagdown \\ \diagup \\ \diagdown \end{array} = 0. \quad (24b)$$

The corresponding projectors are defined as

$$\mathcal{P}_\ell^{\mathbb{D}} = \sum_{\alpha} |\Psi_{\ell\alpha}^{\mathbb{D}}\rangle \langle \Psi_{\ell\alpha}^{\mathbb{D}}| = \begin{array}{c} \diagup \\ \diagdown \\ \diagup \\ \diagdown \end{array}, \quad (25)$$

$$\mathcal{Q}_{\ell'}^{\mathbb{D}} = \sum_{\alpha'} |\Phi_{\ell'\alpha'}^{\mathbb{D}}\rangle \langle \Phi_{\ell'\alpha'}^{\mathbb{D}}| = \begin{array}{c} \diagdown \\ \diagup \\ \diagdown \\ \diagup \end{array}, \quad (26)$$

with $\mathcal{P}_0^{\mathbb{D}} = \mathcal{Q}_{\mathcal{Z}+1}^{\mathbb{D}} = 0$. They obey orthonormality relations,

$$\mathcal{P}_\ell^{\mathbb{X}} \mathcal{P}_\ell^{\mathbb{Y}} = \delta^{\mathbb{X}\mathbb{Y}} \mathcal{P}_\ell^{\mathbb{X}}, \quad \mathcal{Q}_{\ell'}^{\mathbb{X}} \mathcal{Q}_{\ell'}^{\mathbb{Y}} = \delta^{\mathbb{X}\mathbb{Y}} \mathcal{Q}_{\ell'}^{\mathbb{X}}, \quad (27)$$

where here and henceforth, $\mathbb{X}, \mathbb{Y} \in \{\mathbb{K}, \mathbb{D}\}$. Moreover, Eq. (21) implies the completeness relations

$$\mathcal{P}_\ell^{\mathbb{K}} + \mathcal{P}_\ell^{\mathbb{D}} = \mathcal{P}_{\ell-1}^{\mathbb{K}} \otimes \mathbb{1}_d, \quad \mathcal{Q}_{\ell'}^{\mathbb{K}} + \mathcal{Q}_{\ell'}^{\mathbb{D}} = \mathbb{1}_d \otimes \mathcal{Q}_{\ell'+1}^{\mathbb{K}}, \quad (28)$$

stating that the kept and discarded projectors of a given site together form a projector for their parent space. These will play a crucial role in subsequent sections.

To conclude this section, we apply the projector identity (22b) to the open legs of the state $\mathcal{H}_\ell^{2s} \psi_\ell^{2s}$ appearing in the 2s Schrödinger (19c). We obtain:

$$\begin{array}{c} \ell-1 \ell \ell+1 \ell+2 \\ \begin{array}{c} \circlearrowleft \\ \circlearrowright \end{array} \begin{array}{c} \diagup \\ \diagdown \\ \diagup \\ \diagdown \end{array} + \begin{array}{c} \ell \ell+1 \\ \begin{array}{c} \circlearrowleft \\ \circlearrowright \end{array} \begin{array}{c} \diagup \\ \diagdown \\ \diagup \\ \diagdown \end{array} + \begin{array}{c} \ell \ell+1 \\ \begin{array}{c} \circlearrowleft \\ \circlearrowright \end{array} \begin{array}{c} \diagdown \\ \diagup \\ \diagdown \\ \diagup \end{array} + \begin{array}{c} \ell \ell+1 \\ \begin{array}{c} \circlearrowleft \\ \circlearrowright \end{array} \begin{array}{c} \diagdown \\ \diagup \\ \diagdown \\ \diagup \end{array} \\ = \begin{array}{c} \ell \ell+1 \\ \begin{array}{c} \circlearrowleft \\ \circlearrowright \end{array} \begin{array}{c} \diagup \\ \diagdown \\ \diagup \\ \diagdown \end{array} + \begin{array}{c} \ell \ell+1 \\ \begin{array}{c} \circlearrowleft \\ \circlearrowright \end{array} \begin{array}{c} \diagdown \\ \diagup \\ \diagdown \\ \diagup \end{array} + \begin{array}{c} \ell \ell+1 \\ \begin{array}{c} \circlearrowleft \\ \circlearrowright \end{array} \begin{array}{c} \diagup \\ \diagdown \\ \diagup \\ \diagdown \end{array} + \begin{array}{c} \ell \ell+1 \\ \begin{array}{c} \circlearrowleft \\ \circlearrowright \end{array} \begin{array}{c} \diagdown \\ \diagup \\ \diagdown \\ \diagup \end{array} \end{array} \quad (29)$$

If only the first term is retained, the 2s Schrödinger Eq. (19c) reduces to the bond Schrödinger Eq. (19a), sandwiched between A_ℓ and $B_{\ell+1}$:

$$A_\ell (H_\ell^{\mathbb{D}} - E) \Lambda_\ell B_{\ell+1} = 0. \quad (30a)$$

The first term together with the second or third term reduces to the 1s Schrödinger Eq. (19b) for sites $\ell+1$ or ℓ , left- or right-contracted with A_ℓ and $B_{\ell+1}$, respectively:

$$A_\ell (H_{\ell+1}^{1s} - E) C_{\ell+1} = 0 \quad (30b)$$

$$(H_\ell^{1s} - E) C_\ell B_{\ell+1} = 0. \quad (30c)$$

All four terms together of course give the full 2s Schrödinger Eq. (19c),

$$(H_\ell^{2s} - E) A_\ell \Lambda_\ell B_{\ell+1} = 0. \quad (30d)$$

Evidently, the fourth term in Eq. (29), involving a DD projector pair, is beyond the reach of 1s schemes. A strategy for nevertheless computing its most important contributions with 1s costs, called controlled bond expansion, has recently been formulated in Ref. [29].

III. CONSTRUCTION OF \mathcal{P}^{ns} AND $\mathcal{P}^{n\perp}$

As discussed in the introduction, each site of an MPS $|\Psi\rangle$ induces a splitting of the local Hilbert space into \mathbb{K} and \mathbb{D} sectors. This induces a partition of the full vector space \mathbb{V} into intricately nested orthogonal subspaces [6]. It is useful to identify orthogonal projectors for these subspaces. Gauge invariance—the existence of many equivalent representations of $|\Psi\rangle$ —makes this a nontrivial task. It can be accomplished systematically by Gram-Schmidt orthogonalization, formulated in projector language. The following three sections are devoted to this endeavor.

In the present section, we define a set of projectors, $\mathcal{P}_{\ell\bar{\ell}}^{\mathbb{X}\bar{\mathbb{X}}}$, $\mathbb{X}, \bar{\mathbb{X}} \in \{\mathbb{K}, \mathbb{D}\}$, involving kept and/or discarded sectors at sites $\ell, \bar{\ell}$. These serve as building blocks for all projectors introduced thereafter. Then, in Sec. III B, we define generalized *local* n -site (ns) projectors, \mathcal{P}_ℓ^{ns} , describing variations of $|\Psi\rangle$ involving up to n contiguous sites. In Sec. III C, we add them up to obtain *global* ns projectors, \mathcal{P}^{ns} ; and in Sec. III D we orthogonalize these

to obtain *irreducible* global ns projectors, $\mathcal{P}^{n\perp}$, not expressible through combinations of variations on subsets of $n' < n$ sites. They are useful for various purposes, including the computation of the energy variance [6], and the formulation of MPS algorithms based on the notion of tangent spaces [11–14, 30] and generalizations thereof. Throughout, we concisely summarize the properties of the various projectors encountered along the way.

A. Projectors for kept and discarded sectors, $\mathcal{P}_{\ell\bar{\ell}}^{\times\bar{\times}}$

We start by introducing kept and discarded space projectors defined on the full Hilbert space \mathbb{V} . To this end, we supplement \mathcal{P}_ℓ^\times and \mathcal{Q}_ℓ^\times by right or left environments (E) comprising the entire rest of the chain, and define

$$\mathcal{P}_\ell^{\times\text{E}} = \mathcal{P}_\ell^\times \otimes \mathbb{1}_d^{\otimes \mathcal{L}-\ell}, \quad \mathcal{P}_\ell^{\text{E}\times} = \mathbb{1}_d^{\otimes \ell-1} \otimes \mathcal{Q}_\ell^\times, \quad (31)$$

$$\begin{aligned} \mathcal{P}_\ell^{\text{KE}} &= \left[\begin{array}{c} \text{---} \times \text{---} \\ \text{---} \times \text{---} \\ \text{---} \times \text{---} \\ \text{---} \times \text{---} \end{array} \right]_{\mathcal{L}} \Big| \Big| \Big|_{\mathcal{L}}^{\times}, & \mathcal{P}_\ell^{\text{EK}} &= \times \Big| \Big| \Big|_{\ell} \left[\begin{array}{c} \text{---} \times \text{---} \\ \text{---} \times \text{---} \\ \text{---} \times \text{---} \\ \text{---} \times \text{---} \end{array} \right], \\ \mathcal{P}_\ell^{\text{DE}} &= \left[\begin{array}{c} \text{---} \times \text{---} \\ \text{---} \times \text{---} \\ \text{---} \times \text{---} \\ \text{---} \times \text{---} \end{array} \right]_{\mathcal{L}} \Big| \Big| \Big|_{\mathcal{L}}^{\times}, & \mathcal{P}_\ell^{\text{ED}} &= \times \Big| \Big| \Big|_{\ell} \left[\begin{array}{c} \text{---} \times \text{---} \\ \text{---} \times \text{---} \\ \text{---} \times \text{---} \\ \text{---} \times \text{---} \end{array} \right]. \end{aligned}$$

with $\ell \in [0, \mathcal{L}]$ for $\mathcal{P}_\ell^{\times\text{E}}$ and $\ell \in [1, \mathcal{L}+1]$ for $\mathcal{P}_\ell^{\text{E}\times}$. Equations (12) and (24) imply orthogonality relations for projectors with E on the same side (both right or both left):

$$\mathcal{P}_\ell^{\times\text{E}} \mathcal{P}_\ell^{\bar{\times}\text{E}} = \delta^{\ell < \bar{\ell}} \delta_{\times\bar{\times}} \mathcal{P}_\ell^{\bar{\times}\text{E}} + \delta^{\ell\bar{\ell}} \delta_{\times\bar{\times}} \mathcal{P}_\ell^{\bar{\times}\text{E}} + \delta^{\ell > \bar{\ell}} \mathcal{P}_\ell^{\times\text{E}} \delta_{\times\bar{\times}}, \quad (32a)$$

$$\mathcal{P}_\ell^{\text{E}\times} \mathcal{P}_\ell^{\text{E}\bar{\times}} = \delta^{\ell < \bar{\ell}} \mathcal{P}_\ell^{\text{E}\times} \delta_{\times\bar{\times}} + \delta^{\ell\bar{\ell}} \delta_{\times\bar{\times}} \mathcal{P}_\ell^{\text{E}\bar{\times}} + \delta^{\ell > \bar{\ell}} \delta_{\times\bar{\times}} \mathcal{P}_\ell^{\text{E}\bar{\times}}. \quad (32b)$$

The δ symbols indicate that the first, second, and third terms contribute only for $\ell < \bar{\ell}$, $\ell = \bar{\ell}$, and $\ell > \bar{\ell}$, respectively. Thus, same-site projectors are orthonormal; different-site products with Es on the same side, of the type $\mathcal{P}_\ell^{\times\text{E}} \mathcal{P}_\ell^{\bar{\times}\text{E}}$ (or $\mathcal{P}_\ell^{\text{E}\times} \mathcal{P}_\ell^{\text{E}\bar{\times}}$), vanish if the earlier (later) site hosts a D; if it hosts a K, they yield the projector from the other site. We depict two cases of Eq. (32a) below:

$$\begin{aligned} \mathcal{P}_\ell^{\text{DE}} \mathcal{P}_\ell^{\text{DE}} &= \left[\begin{array}{c} \text{---} \times \text{---} \\ \text{---} \times \text{---} \\ \text{---} \times \text{---} \\ \text{---} \times \text{---} \end{array} \right]_{\ell} \Big| \Big| \Big|_{\ell}^{\times} = \left[\begin{array}{c} \text{---} \times \text{---} \\ \text{---} \times \text{---} \\ \text{---} \times \text{---} \\ \text{---} \times \text{---} \end{array} \right]_{\ell} \Big| \Big| \Big|_{\ell}^{\times} = \mathcal{P}_\ell^{\text{DE}}. \\ \mathcal{P}_\ell^{\text{KE}} \mathcal{P}_\ell^{\text{DE}} &= \left[\begin{array}{c} \text{---} \times \text{---} \\ \text{---} \times \text{---} \\ \text{---} \times \text{---} \\ \text{---} \times \text{---} \end{array} \right]_{\ell} \Big| \Big| \Big|_{\ell}^{\times} = \left[\begin{array}{c} \text{---} \times \text{---} \\ \text{---} \times \text{---} \\ \text{---} \times \text{---} \\ \text{---} \times \text{---} \end{array} \right]_{\ell} \Big| \Big| \Big|_{\ell}^{\times} = \mathcal{P}_\ell^{\text{DE}}. \end{aligned}$$

Equation (32a) was first written down in that form in Ref. [27], Eq. (29), in the context of NRG. There, one deals exclusively with left-normalized states, and sites to the right of the orthogonality center are treated purely as environmental degrees of freedom, described by product states. Equation (32b) is the counterpart of (32a) for right-normalized states.

Projector products with Es in the middle, $\mathcal{P}_\ell^{\times\text{E}} \mathcal{P}_{\bar{\ell}}^{\text{E}\bar{\times}}$, and $\ell < \bar{\ell}$, again yield projectors. We denote them by

$$\mathcal{P}_{\ell\bar{\ell}}^{\times\bar{\times}} = \mathcal{P}_\ell^{\times\text{E}} \mathcal{P}_{\bar{\ell}}^{\text{E}\bar{\times}} \quad (0 \leq \ell < \bar{\ell} \leq \mathcal{L}+1), \quad (33)$$

$$\begin{aligned} \mathcal{P}_{\ell\bar{\ell}}^{\text{KK}} &= \left[\begin{array}{c} \text{---} \times \text{---} \\ \text{---} \times \text{---} \\ \text{---} \times \text{---} \\ \text{---} \times \text{---} \end{array} \right]_{\ell} \Big| \Big| \Big|_{\bar{\ell}} \left[\begin{array}{c} \text{---} \times \text{---} \\ \text{---} \times \text{---} \\ \text{---} \times \text{---} \\ \text{---} \times \text{---} \end{array} \right]_{\bar{\ell}}, & \mathcal{P}_{\ell\bar{\ell}}^{\text{KD}} &= \left[\begin{array}{c} \text{---} \times \text{---} \\ \text{---} \times \text{---} \\ \text{---} \times \text{---} \\ \text{---} \times \text{---} \end{array} \right]_{\ell} \Big| \Big| \Big|_{\bar{\ell}} \left[\begin{array}{c} \text{---} \times \text{---} \\ \text{---} \times \text{---} \\ \text{---} \times \text{---} \\ \text{---} \times \text{---} \end{array} \right]_{\bar{\ell}}, \\ \mathcal{P}_{\ell\bar{\ell}}^{\text{DK}} &= \left[\begin{array}{c} \text{---} \times \text{---} \\ \text{---} \times \text{---} \\ \text{---} \times \text{---} \\ \text{---} \times \text{---} \end{array} \right]_{\ell} \Big| \Big| \Big|_{\bar{\ell}} \left[\begin{array}{c} \text{---} \times \text{---} \\ \text{---} \times \text{---} \\ \text{---} \times \text{---} \\ \text{---} \times \text{---} \end{array} \right]_{\bar{\ell}}, & \mathcal{P}_{\ell\bar{\ell}}^{\text{DD}} &= \left[\begin{array}{c} \text{---} \times \text{---} \\ \text{---} \times \text{---} \\ \text{---} \times \text{---} \\ \text{---} \times \text{---} \end{array} \right]_{\ell} \Big| \Big| \Big|_{\bar{\ell}} \left[\begin{array}{c} \text{---} \times \text{---} \\ \text{---} \times \text{---} \\ \text{---} \times \text{---} \\ \text{---} \times \text{---} \end{array} \right]_{\bar{\ell}}. \end{aligned}$$

They have local unit operators on $n = \bar{\ell} - (\ell + 1)$ contiguous sites, sandwiched between any combination of K and D projectors to the left and right. In this sense, they generalize Eqs. (15) and will be called generalized *local ns* projectors. They fulfill numerous orthogonality relations following directly from Eqs. (32). For example:

$$\mathcal{P}_{\ell\bar{\ell}}^{\times\bar{\times}} \mathcal{P}_{\ell'\bar{\ell}'}^{\times'\bar{\times}'} = \delta^{\times\times'} \delta^{\bar{\times}\bar{\times}'} \mathcal{P}_{\ell\bar{\ell}}^{\times\bar{\times}}, \quad (34a)$$

$$\forall \ell < \ell': \mathcal{P}_{\ell\bar{\ell}}^{\times\bar{\times}} \mathcal{P}_{\ell'\bar{\ell}'}^{\times'\bar{\times}'} = 0, \quad \forall \bar{\ell} < \bar{\ell}': \mathcal{P}_{\ell\bar{\ell}}^{\times\bar{\times}} \mathcal{P}_{\ell'\bar{\ell}'}^{\times'\bar{\times}'} = 0, \quad (34b)$$

$$\mathcal{P}_{\ell\bar{\ell}}^{\text{D}\bar{\times}} \mathcal{P}_{\ell'\bar{\ell}'}^{\text{D}\bar{\times}'} \sim \delta_{\ell\ell'}, \quad \mathcal{P}_{\ell\bar{\ell}}^{\text{D}\bar{\times}} \mathcal{P}_{\ell'\bar{\ell}'}^{\text{D}\bar{\times}'} \sim \delta_{\bar{\ell}\bar{\ell}'}. \quad (34c)$$

Thus, two projectors having the same site indices are orthonormal; projector products involving a D on a site earlier or later than all other indexed sites vanish; those involving two Ds on the same side but different sites vanish, too. Some of these relations are illustrated below:

$$\begin{aligned} \mathcal{P}_{\ell\bar{\ell}}^{\text{DK}} \mathcal{P}_{\ell\bar{\ell}}^{\text{DK}} &= \left[\begin{array}{c} \text{---} \times \text{---} \\ \text{---} \times \text{---} \\ \text{---} \times \text{---} \\ \text{---} \times \text{---} \end{array} \right]_{\ell} \Big| \Big| \Big|_{\bar{\ell}} \left[\begin{array}{c} \text{---} \times \text{---} \\ \text{---} \times \text{---} \\ \text{---} \times \text{---} \\ \text{---} \times \text{---} \end{array} \right]_{\bar{\ell}} = \left[\begin{array}{c} \text{---} \times \text{---} \\ \text{---} \times \text{---} \\ \text{---} \times \text{---} \\ \text{---} \times \text{---} \end{array} \right]_{\ell} \Big| \Big| \Big|_{\bar{\ell}} = \mathcal{P}_{\ell\bar{\ell}}^{\text{DK}}, \\ \mathcal{P}_{\ell\bar{\ell}}^{\text{DK}} \mathcal{P}_{\ell'\bar{\ell}'}^{\text{KK}} &= \left[\begin{array}{c} \text{---} \times \text{---} \\ \text{---} \times \text{---} \\ \text{---} \times \text{---} \\ \text{---} \times \text{---} \end{array} \right]_{\ell} \Big| \Big| \Big|_{\bar{\ell}} \left[\begin{array}{c} \text{---} \times \text{---} \\ \text{---} \times \text{---} \\ \text{---} \times \text{---} \\ \text{---} \times \text{---} \end{array} \right]_{\ell'} = 0, \\ \mathcal{P}_{\ell\bar{\ell}}^{\text{DK}} \mathcal{P}_{\ell\bar{\ell}}^{\text{DD}} &= \left[\begin{array}{c} \text{---} \times \text{---} \\ \text{---} \times \text{---} \\ \text{---} \times \text{---} \\ \text{---} \times \text{---} \end{array} \right]_{\ell} \Big| \Big| \Big|_{\bar{\ell}} \left[\begin{array}{c} \text{---} \times \text{---} \\ \text{---} \times \text{---} \\ \text{---} \times \text{---} \\ \text{---} \times \text{---} \end{array} \right]_{\bar{\ell}} = \left[\begin{array}{c} \text{---} \times \text{---} \\ \text{---} \times \text{---} \\ \text{---} \times \text{---} \\ \text{---} \times \text{---} \end{array} \right]_{\ell} \Big| \Big| \Big|_{\bar{\ell}} = \mathcal{P}_{\ell\bar{\ell}}^{\text{DD}}. \end{aligned}$$

Eq. (28) implies another useful property (for $\bar{\ell} - \ell > 1$),

$$\mathcal{P}_{\ell\bar{\ell}}^{\times\bar{\times}} = \mathcal{P}_{\ell+1, \bar{\ell}}^{\times\bar{\times}} + \mathcal{P}_{\ell+1, \bar{\ell}}^{\text{D}\bar{\times}}, \quad \mathcal{P}_{\ell\bar{\ell}}^{\text{K}\bar{\times}} = \mathcal{P}_{\ell, \bar{\ell}-1}^{\text{K}\bar{\times}} + \mathcal{P}_{\ell, \bar{\ell}-1}^{\text{D}\bar{\times}}, \quad (35)$$

reflecting Eq. (22b). Thus, a K on a given site ℓ (or $\bar{\ell}$) can be decomposed into K and D on the inner neighboring site $\ell+1$ (or $\bar{\ell}-1$), thereby expressing one projector through two that both target one less site. This decomposition will be used repeatedly below.

B. Local n -site projectors, \mathcal{P}_ℓ^{ns}

The KK projectors merit special attention. For $\bar{\ell} - \ell = 1$, 2 or 3, they correspond to the bond, 1s and 2s projectors introduced in Eqs. (15). These can be expressed as

$$\mathcal{P}_\ell^{\text{b}} = \mathcal{P}_{\ell, \ell+1}^{\text{KK}}, \quad \mathcal{P}_\ell^{\text{1s}} = \mathcal{P}_{\ell-1, \ell+1}^{\text{KK}}, \quad \mathcal{P}_\ell^{\text{2s}} = \mathcal{P}_{\ell-1, \ell+2}^{\text{KK}}. \quad (36)$$

Generalizing the notation of (36), we define a set of local ns projectors (for $n \geq 0$ and $\ell \in [1, \mathcal{L}+1-n]$) as:

$$\mathcal{P}_\ell^{ns} = \mathcal{P}_{\ell-1, \ell+n}^{\text{KK}} = \left[\begin{array}{c} \text{---} \times \text{---} \\ \text{---} \times \text{---} \\ \text{---} \times \text{---} \\ \text{---} \times \text{---} \end{array} \right]_{\ell-1} \Big| \Big| \Big|_{\ell+n} \left[\begin{array}{c} \text{---} \times \text{---} \\ \text{---} \times \text{---} \\ \text{---} \times \text{---} \\ \text{---} \times \text{---} \end{array} \right]_{\ell+n}. \quad (37)$$

Then $\mathcal{P}_\ell^{0s} = \mathcal{P}_{\ell-1}^b$, and for $n \geq 1$, these projectors span the spaces of variations of $|\Psi\rangle$ on n contiguous sites from ℓ to $\ell + n - 1$. However, projectors \mathcal{P}_ℓ^{ns} and $\mathcal{P}_{\ell'}^{ns}$ with $\ell \neq \ell'$ are not orthogonal. Instead, the following relations hold for all $\ell < \ell'$,

$$\mathcal{P}_\ell^{ns} \mathcal{P}_{\ell'}^{ns} = \mathcal{P}_{\ell+1}^{(n-1)s} \mathcal{P}_{\ell'}^{ns} = \mathcal{P}_\ell^{ns} \mathcal{P}_{\ell'}^{(n-1)s} = \mathcal{P}_{\ell+1}^{(n-1)s} \mathcal{P}_{\ell'}^{(n-1)s}, \quad (38)$$

as can be verified using Eqs. (32). For example, for

we obtain the same result in both cases. In particular, for $n \geq 1$, two ns projectors mismatched by one site yield an $(n-1)$ -site projector,

$$\mathcal{P}_\ell^{ns} \mathcal{P}_{\ell+1}^{ns} = \mathcal{P}_{\ell+1}^{(n-1)s} \quad (39)$$

Orthogonalized versions of the \mathcal{P}_ℓ^{ns} projectors will be constructed in the next subsection. Here, we collect some properties, following from Eq. (32), that will be needed for that purpose:

$$\forall \ell < \ell': \quad \mathcal{P}_{\ell\ell}^{\text{D}\bar{\text{X}}} \mathcal{P}_{\ell'}^{ns} = 0, \quad (40a)$$

$$\forall (\ell+n) \leq \ell': \quad \mathcal{P}_\ell^{ns} \mathcal{P}_{\ell'\ell'}^{\text{X}'\text{D}} = 0. \quad (40b)$$

Thus, \mathcal{P}_ℓ^{ns} is annihilated by a left D on its left or a right D on its right. For example,

$$\mathcal{P}_\ell^{ns} \mathcal{P}_{\ell'}^{\text{KD}} = 0.$$

Using Eq. (35), \mathcal{P}_ℓ^{ns} can be expressed through two $(n-1)$ s projectors:

$$\begin{aligned} \mathcal{P}_\ell^{ns} &= \mathcal{P}_{\ell,\ell+n}^{\text{KK}} + \mathcal{P}_{\ell,\ell+n}^{\text{DK}} = \mathcal{P}_{\ell-1,\ell+n-1}^{\text{KK}} + \mathcal{P}_{\ell-1,\ell+n-1}^{\text{KD}} \\ &= \mathcal{P}_{\ell+1}^{(n-1)s} + \mathcal{P}_{\ell,\ell+n}^{\text{DK}} = \mathcal{P}_\ell^{(n-1)s} + \mathcal{P}_{\ell-1,\ell+n-1}^{\text{KD}} \quad (41) \\ &= \text{Diagram 1} + \text{Diagram 2} \\ &= \text{Diagram 3} + \text{Diagram 4} \end{aligned}$$

The existence of two different decompositions of \mathcal{P}_ℓ^{ns} , mimicking Eq. (22a), reflects the gauge freedom of MPSs. This can be exploited to write $\mathcal{P}_{\ell,\ell+n}^{\text{DK}}$ as $\mathcal{P}_\ell^{(n-1)s} + \mathcal{P}_{\ell-1,\ell-1+n}^{\text{KD}} - \mathcal{P}_{\ell+1}^{(n-1)s}$, converting DK to KD, or vice versa. Repeated use yields an identity that will be useful below:

$$\sum_{\ell=\bar{\ell}}^{\ell'} \mathcal{P}_{\ell,\ell+n}^{\text{DK}} = \mathcal{P}_{\bar{\ell}}^{(n-1)s} + \sum_{\ell=\bar{\ell}}^{\ell'} \mathcal{P}_{\ell-1,\ell-1+n}^{\text{KD}} - \mathcal{P}_{\ell'+1}^{(n-1)s}. \quad (42)$$

C. Global ns projectors, \mathbb{V}^{ns}

We now are ready to define the ns spaces \mathbb{V}^{ns} . For $n = 0$, we define $\mathbb{V}^{0s} = \text{span}\{|\Psi\rangle\}$. For $n \geq 1$, we define \mathbb{V}^{ns} as the span of $|\Psi\rangle$ and all states $|\Psi'\rangle$ differing from it on at most n contiguous sites:

$$\mathbb{V}^{ns} = \text{span}\left\{ \text{Diagram} \mid \ell \in [1, \mathcal{L} + 1 - n] \right\}. \quad (43)$$

For $n = 1$, \mathbb{V}^{1s} is the tangent space of $|\Psi\rangle$. More concretely, \mathbb{V}^{ns} is defined as the image of all local ns projectors:

$$\mathbb{V}^{ns} = \text{span}\left\{ \text{im}(\mathcal{P}_1^{ns}), \text{im}(\mathcal{P}_2^{ns}), \dots, \text{im}(\mathcal{P}_{\mathcal{L}+1-n}^{ns}) \right\}. \quad (44)$$

For any $n' \leq n$, the image $\text{im}(\mathcal{P}_{\ell'}^{n's})$ is by construction fully contained in the image $\text{im}(\mathcal{P}_\ell^{ns})$, hence $\mathbb{V}^{n's}$ is a subspace of \mathbb{V}^{ns} , implying the nested hierarchy (1).

Let \mathcal{P}^{ns} be the projector having \mathbb{V}^{ns} as image; then, $\text{im}(\mathcal{P}^{ns})$ contains $\text{im}(\mathcal{P}_\ell^{ns})$ for all $\ell \in [1, \mathcal{L} + 1 - n]$. Formally, \mathcal{P}^{ns} has the defining properties

$$(\mathcal{P}^{ns})^2 = \mathcal{P}^{ns}, \quad \mathcal{P}^{ns} \mathcal{P}_\ell^{ns} = \mathcal{P}_\ell^{ns}, \quad (45a)$$

$$\mathcal{P}_\ell^{ns} |\Phi\rangle = 0 \quad \forall \ell \implies \mathcal{P}^{ns} |\Phi\rangle = 0. \quad (45b)$$

Moreover, the nested structure of the \mathbb{V}^{ns} s implies

$$\forall n' < n: \quad \mathcal{P}^{ns} \mathcal{P}^{n's} = \mathcal{P}^{n's}. \quad (46)$$

Let us construct \mathcal{P}^{ns} explicitly. Simply summing up the local projectors \mathcal{P}_ℓ^{ns} does not yield a projector because the images of \mathcal{P}_ℓ^{ns} and $\mathcal{P}_{\ell'}^{ns}$ are not orthogonal. A set of mutually orthogonal local projectors can be obtained by projecting out the overlap between \mathcal{P}_ℓ^{ns} and $\mathcal{P}_{\ell\pm 1}^{ns}$. We thus define

$$\mathcal{P}_{\ell \leq}^{ns} = \mathcal{P}_\ell^{ns} (\mathbb{1}_V - \mathcal{P}_{\ell\pm 1}^{ns}), \quad (47)$$

so that $\mathcal{P}_{\ell \leq}^{ns} \mathcal{P}_{\ell'}^{ns} = 0$ holds for neighboring ℓ, ℓ' with $\ell \leq \ell'$. It suffices to orthogonalize ns projectors mismatched by one site, since from these we can select a set of projectors mutually orthogonal on all sites. Indeed, Eqs. (39) and (41) yield $(n-1)$ -site projectors containing DS ,

$$\mathcal{P}_{\ell <}^{ns} = \mathcal{P}_\ell^{ns} - \mathcal{P}_{\ell+1}^{(n-1)s} = \mathcal{P}_{\ell,\ell+n}^{\text{DK}}, \quad (48a)$$

$$\mathcal{P}_{\ell >}^{ns} = \mathcal{P}_\ell^{ns} - \mathcal{P}_{\ell-1}^{(n-1)s} = \mathcal{P}_{\ell-1,\ell-1+n}^{\text{KD}}, \quad (48b)$$

and the ds ensure the orthonormality relations (cf. (34))

$$\mathcal{P}_{\ell \leq}^{ns} \mathcal{P}_{\ell' \leq}^{ns} = \delta_{\ell \ell'} \mathcal{P}_{\ell \leq}^{ns}, \quad (49a)$$

$$\forall \ell < \ell': \quad \mathcal{P}_{\ell <}^{ns} \mathcal{P}_{\ell' >}^{ns} = 0, \quad (49b)$$

$$\forall \ell \leq \ell': \quad \mathcal{P}_{\ell \leq}^{ns} \mathcal{P}_{\ell' \leq}^{ns} = 0. \quad (49c)$$

These equations have a remarkable implication: for any choice of $\ell' \in [1, \mathcal{L} - n + 1]$, the projectors $\mathcal{P}_{\ell <}^{ns}$ for $\ell \in [1, \ell' - 1]$, $\mathcal{P}_{\ell'}^{ns}$, and $\mathcal{P}_{\ell >}^{ns}$ for $\ell \in [\ell' + 1, \mathcal{L} + 1 - n]$ form an orthonormal set, and this set contains a \mathcal{P}_{ℓ}^{ns} (in projected form) for every $\ell \in [1, \mathcal{L} + 1 - n]$. We define the global ns projector as their sum,

$$\begin{aligned} \mathcal{P}^{ns} &= \sum_{\ell=1}^{\ell'-1} \mathcal{P}_{\ell <}^{ns} + \mathcal{P}_{\ell'}^{ns} + \sum_{\ell=\ell'+1}^{\mathcal{L}+1-n} \mathcal{P}_{\ell >}^{ns} \quad (50) \\ &= \sum_{\ell=1}^{\ell'-1} \begin{array}{c} \leftarrow \leftarrow \leftarrow \\ \leftarrow \leftarrow \leftarrow \end{array} \Big| \Big| \Big| \begin{array}{c} \leftarrow \leftarrow \leftarrow \\ \leftarrow \leftarrow \leftarrow \end{array} + \begin{array}{c} \leftarrow \leftarrow \leftarrow \\ \leftarrow \leftarrow \leftarrow \end{array} \Big| \Big| \Big| \begin{array}{c} \leftarrow \leftarrow \leftarrow \\ \leftarrow \leftarrow \leftarrow \end{array} \\ &+ \sum_{\ell=\ell'+1}^{\mathcal{L}+1-n} \begin{array}{c} \leftarrow \leftarrow \leftarrow \\ \leftarrow \leftarrow \leftarrow \end{array} \Big| \Big| \Big| \begin{array}{c} \leftarrow \leftarrow \leftarrow \\ \leftarrow \leftarrow \leftarrow \end{array}. \end{aligned}$$

Here, ℓ' may be chosen freely as convenience dictates; different choices are equivalent, being related by Eqs. (41). The orthogonality relations (49) ensure the properties (45a). For example,

$$\mathcal{P}^{ns} \mathcal{P}_{\ell'}^{ns} = 0 + \mathcal{P}_{\ell'}^{ns} \mathcal{P}_{\ell'}^{ns} + 0 = \mathcal{P}_{\ell'}^{ns}. \quad (51)$$

The property (45b) is ensured by orthogonalizing \mathcal{P}_{ℓ}^{ns} w.r.t. each other and thus never including states with $\mathcal{P}_{\ell}^{ns} |\Phi\rangle = 0 \forall \ell$. This confirms that $\text{im}(\mathcal{P}^{ns})$ contains $\text{im}(\mathcal{P}_{\ell}^{ns})$ for all $\ell \in [1, \mathcal{L} + 1 - n]$; thus, \mathcal{P}^{ns} indeed is the desired projector having \mathbb{V}^{ns} as image. Evaluating Eq. (50) using the middle expressions from (48), we obtain

$$\begin{aligned} \mathcal{P}^{ns} &= \sum_{\ell=1}^{\mathcal{L}+1-n} \mathcal{P}_{\ell}^{ns} - \sum_{\ell=1}^{\mathcal{L}-n} \mathcal{P}_{\ell+1}^{(n-1)s} \quad (52a) \\ &= \sum_{\ell=1}^{\mathcal{L}+1-n} \begin{array}{c} \leftarrow \leftarrow \leftarrow \\ \leftarrow \leftarrow \leftarrow \end{array} \Big| \Big| \Big| \begin{array}{c} \leftarrow \leftarrow \leftarrow \\ \leftarrow \leftarrow \leftarrow \end{array} - \sum_{\ell=1}^{\mathcal{L}-n} \begin{array}{c} \leftarrow \leftarrow \leftarrow \\ \leftarrow \leftarrow \leftarrow \end{array} \Big| \Big| \Big| \begin{array}{c} \leftarrow \leftarrow \leftarrow \\ \leftarrow \leftarrow \leftarrow \end{array}, \end{aligned}$$

expressing \mathcal{P}^{ns} through local ns and $(n-1)s$ projectors in a manner manifestly independent of ℓ' , and not involving any \mathbb{D} sectors. The occurrence of the first term, a sum over all \mathcal{P}_{ℓ}^{ns} , is no surprise; the nontrivial part of the above construction was establishing the form of the second term, needed to ensure that \mathcal{P}^{ns} is a projector. Note that Eq. (52a) directly implies property (45b). Alternatively, we can use the rightmost forms of (48) in (50) to obtain

$$\mathcal{P}^{ns} = \sum_{\ell=1}^{\ell'} \mathcal{P}_{\ell, \ell+n}^{\text{DK}} + \mathcal{P}_{\ell', \ell'+n}^{\text{KK}} + \sum_{\ell=\ell'}^{\mathcal{L}-n} \mathcal{P}_{\ell, \ell+n}^{\text{KD}}, \quad (52b)$$

now expressed purely through $(n-1)s$ projectors, with all but one involving \mathbb{D} sectors.

For $n = 1$, Eqs. (52) reproduce the well-known tangent space projector,

$$\begin{aligned} \mathcal{P}^{1s} &= \sum_{\ell=1}^{\mathcal{L}} \mathcal{P}_{\ell}^{1s} - \sum_{\ell=1}^{\mathcal{L}-1} \mathcal{P}_{\ell}^{\text{b}} \quad (53a) \\ &= \sum_{\ell=1}^{\mathcal{L}} \begin{array}{c} \leftarrow \leftarrow \leftarrow \\ \leftarrow \leftarrow \leftarrow \end{array} \Big| \Big| \Big| \begin{array}{c} \leftarrow \leftarrow \leftarrow \\ \leftarrow \leftarrow \leftarrow \end{array} - \sum_{\ell=1}^{\mathcal{L}-1} \begin{array}{c} \leftarrow \leftarrow \leftarrow \\ \leftarrow \leftarrow \leftarrow \end{array} \Big| \Big| \Big| \begin{array}{c} \leftarrow \leftarrow \leftarrow \\ \leftarrow \leftarrow \leftarrow \end{array}, \\ &= \sum_{\ell=1}^{\ell'} \mathcal{P}_{\ell, \ell+1}^{\text{DK}} + \mathcal{P}_{\ell', \ell'+1}^{\text{KK}} + \sum_{\ell=\ell'}^{\mathcal{L}-1} \mathcal{P}_{\ell, \ell+1}^{\text{KD}} \quad (53b) \\ &= \sum_{\ell=1}^{\ell'} \begin{array}{c} \leftarrow \leftarrow \leftarrow \\ \leftarrow \leftarrow \leftarrow \end{array} \Big| \Big| \Big| \begin{array}{c} \leftarrow \leftarrow \leftarrow \\ \leftarrow \leftarrow \leftarrow \end{array} + \begin{array}{c} \leftarrow \leftarrow \leftarrow \\ \leftarrow \leftarrow \leftarrow \end{array} \Big| \Big| \Big| \begin{array}{c} \leftarrow \leftarrow \leftarrow \\ \leftarrow \leftarrow \leftarrow \end{array} \\ &+ \sum_{\ell=\ell'}^{\mathcal{L}-1} \begin{array}{c} \leftarrow \leftarrow \leftarrow \\ \leftarrow \leftarrow \leftarrow \end{array} \Big| \Big| \Big| \begin{array}{c} \leftarrow \leftarrow \leftarrow \\ \leftarrow \leftarrow \leftarrow \end{array}. \end{aligned}$$

These expressions are widely used in MPS algorithms based on tangent space concepts, such as time evolution using the time-dependent variational principle (TDVP) [11–14, 30]. The form (53a), or (53b) with the choice $\ell' = \mathcal{L} - 1$, was first given Lubich, Oseledts and Vandereycken [11] (Theorem 3.1), and transcribed into MPS notation in Ref. [12]. In these works it was derived in a different manner than here, using arguments invoking gauge invariance. Our derivation has the advantage that it generalizes directly to ns projectors. For $n = 2$, our expression (52a) for \mathcal{P}^{2s} reproduces the projector proposed in Ref. [12] for 2s TDVP:

$$\mathcal{P}^{2s} = \sum_{\ell=1}^{\mathcal{L}-1} \begin{array}{c} \leftarrow \leftarrow \leftarrow \\ \leftarrow \leftarrow \leftarrow \end{array} \Big| \Big| \Big| \begin{array}{c} \leftarrow \leftarrow \leftarrow \\ \leftarrow \leftarrow \leftarrow \end{array} - \sum_{\ell=2}^{\mathcal{L}-1} \begin{array}{c} \leftarrow \leftarrow \leftarrow \\ \leftarrow \leftarrow \leftarrow \end{array} \Big| \Big| \Big| \begin{array}{c} \leftarrow \leftarrow \leftarrow \\ \leftarrow \leftarrow \leftarrow \end{array}. \quad (54)$$

D. Irreducible global ns projectors, $\mathcal{P}^{n\perp}$

Our final step is to orthogonalize the global \mathcal{P}^{ns} projectors to obtain mutually *orthogonal* global ns projectors, $\mathcal{P}^{n\perp}$. This step is inspired by the observation, made in Ref. 6, that a given MPS $|\Psi\rangle$ induces a decomposition of the full Hilbert space into mutually orthogonal subspaces,

$$\mathbb{V} = \bigoplus_{n=0}^{\mathcal{L}} \mathbb{V}^{n\perp}, \quad (55)$$

where $\mathbb{V}^{0\perp}$ is spanned by $|\Psi\rangle$, and for $n \geq 1$ each $\mathbb{V}^{n\perp}$ is the complement of $\mathbb{V}^{(n-1)s}$ in $\mathbb{V}^{ns} = \mathbb{V}^{(n-1)s} \oplus \mathbb{V}^{n\perp}$. Each $\mathbb{V}^{n\perp}$ is *irreducible*, comprising variations of $|\Psi\rangle$ defined on n contiguous sites that are not expressible through variations on subsets of $n' < n$ sites.

The decomposition (55) induces a decomposition of the identity on \mathbb{V} into a sum of irreducible, mutually orthogonal projectors, $\mathcal{P}^{n\perp}$, each with a $\mathbb{V}^{n\perp}$ as image:

$$\mathbb{1}_{\mathbb{V}} = \mathbb{1}_d^{\otimes \mathcal{L}} = \sum_{n=0}^{\mathcal{L}} \mathcal{P}^{n\perp}, \quad \mathcal{P}^{n\perp} \mathcal{P}^{n'\perp} = \delta^{nn'} \mathcal{P}^{n\perp}. \quad (56)$$

are manifestly mutually orthogonal if $n \neq n'$. This can be checked via Eqs. (24), e.g. for $\mathbb{V}^{0\perp}$ and $\mathbb{V}^{1\perp}$:

$$\langle \text{Diagram 1} | \text{Diagram 2} \rangle = 0, \quad \langle \text{Diagram 3} | \text{Diagram 4} \rangle = 0. \quad (63)$$

States of the form (62) yield a complete basis for \mathbb{V} . This is ensured by our Gram-Schmidt construction; but for $\mathcal{P}^{1\perp}$, the completeness is not self-evident. For example, consider a state $|\Psi'\rangle$ of the following form:

$$\begin{aligned} |\Psi'\rangle &= \text{Diagram 5} \quad \Psi = \text{Diagram 6}, \\ \langle \Psi | \Psi' \rangle &= \text{Diagram 7} = 0. \end{aligned} \quad (64)$$

It differs from $|\Psi\rangle$ only in the κ space of bond of ℓ' , having a bond matrix $\Lambda'_{\ell'}$ orthogonal to the $\Lambda_{\ell'}$ of $|\Psi\rangle$. Since $|\Psi'\rangle$ is orthogonal to $|\Psi\rangle$ it does not lie in $\mathbb{V}^{0\perp}$, but it is not immediately apparent that it lies in $\text{im}(\mathcal{P}^{1\perp})$. To see that it does, we rewrite Eq. (59b) such that it contains DKs to the left of site ℓ and Ks to its right, using Eq. (42) (with $\bar{\ell}, \ell'$ there replaced by $\ell' + 1, \mathcal{L}$):

$$\mathcal{P}^{1\perp} = \sum_{\ell=1}^{\ell'-1} \mathcal{P}_{\ell, \ell+1}^{\text{DK}} + \mathcal{P}_{\ell'}^{\text{1s}} + \sum_{\ell=\ell'+1}^{\mathcal{L}} \mathcal{P}_{\ell-1, \ell}^{\text{KD}} - \mathcal{P}_{\mathcal{L}, \mathcal{L}+1}^{\text{KK}}. \quad (65)$$

When evaluating $\mathcal{P}^{1\perp}|\Psi'\rangle$ using this form, and recalling that $\mathcal{P}_{\mathcal{L}, \mathcal{L}+1}^{\text{KK}} = |\Psi\rangle\langle\Psi|$, we find that all terms but the second yield zero, and the second yields $|\Psi'\rangle$, as claimed above. In this manner, one sees that the image of $\mathcal{P}^{1\perp}$ indeed contains all single-site and single-bond variations of $|\Psi\rangle$ that are orthogonal to $|\Psi\rangle$.

To conclude this section, we remark that the nested structure of \mathbb{V} is an integral part for (thermo)dynamical computations using the NRG [16, 17, 24], although a slightly different structure from $\mathcal{P}^{n\perp}$ is used to systematically span the full Hilbert space. While the chain considered in NRG is in principle semi-infinite, this chain is in practice cut off naturally by thermal weights [17, 24]. The resulting chain length \mathcal{L} increases logarithmically with decreasing temperature. In NRG, the so-called Anders-Schiller basis [26] is routinely used, which decomposes the full identity as follows:

$$\mathbb{1}_{\mathbb{V}} = \sum_{\ell=1}^{\mathcal{L}} \text{Diagram 8} \Big| \Big| \Big|_{\mathcal{L}}^{\times}. \quad (66)$$

Here, all states of the parent space associated with the last site, \mathcal{L} , are considered discarded, i.e. the kept space of site \mathcal{L} has dimension 0. The projectors occurring in Eq. (66) are constructed from approximate eigenstates of the Hamiltonian, so that this decomposition of unity can be used, e.g., to explicitly construct time-evolution operators [26], full thermal density matrices [17, 24] or evaluate Lehmann representations for two-point [17] or recently even multi-point [27, 31] spectral functions.

IV. ENERGY VARIANCE

The decomposition of the identity $\mathbb{1}_{\mathbb{V}}$ into mutually orthogonal n -site projections can be used to similarly split the energy variance, $\Delta_E = \|(H-E)\Psi\|^2$, of a state with average energy $E = \langle\Psi|H|\Psi\rangle$ into n -site contributions. For $n = 1$ and 2, these were given in Ref. [6]. Here, we extend their analysis to general n :

$$\Delta_E = \sum_{n=0}^{\mathcal{L}} \langle\Psi|(H-E)\mathcal{P}^{n\perp}(H-E)|\Psi\rangle = \sum_{n=1}^{\mathcal{L}} \Delta_E^{n\perp}, \quad (67a)$$

$$\Delta_E^{n\perp} = \|\mathcal{P}^{n\perp}H\Psi\|^2 \quad (67b)$$

$$= \begin{cases} \sum_{\ell=1}^{\mathcal{L}} \|\mathcal{P}_{\ell, \ell+1}^{\text{DK}}H\Psi\|^2 & (n=1), \\ \sum_{\ell=1}^{\mathcal{L}+1-n} \|\mathcal{P}_{\ell, \ell+n-1}^{\text{DD}}H\Psi\|^2 & (n \geq 2). \end{cases} \quad (67c)$$

In the first line, we used (56), $\mathbb{1}_{\mathbb{V}} = \sum_{n=0}^{\mathcal{L}} \mathcal{P}^{n\perp}$; since $\mathcal{P}^{0\perp} = |\Psi\rangle\langle\Psi|$ and $\mathcal{P}^{(n>0)\perp}|\Psi\rangle = 0$, the potentially large contributions linear and quadratic in E drop out. This convenient feature, emphasized in Ref. [6], significantly improves the accuracy of the determination of Δ_E . The cumulative ns variance is defined as $\Delta_E^{ns} = \sum_{n'=1}^n \Delta_E^{n'\perp}$.

Expressed diagrammatically, the 1s and ns variance are

$$\Delta_E^{1\perp} = \sum_{\ell=1}^{\mathcal{L}} \left\| \text{Diagram 9} \right\|^2 = \sum_{\ell=1}^{\mathcal{L}} \left\| \text{Diagram 10} \right\|^2, \quad (68a)$$

$$\Delta_E^{(n \geq 2)\perp} = \sum_{\ell=1}^{\mathcal{L}-(n-1)} \left\| \text{Diagram 11} \right\|^2. \quad (68b)$$

To compute these expressions in practice, the D projectors are expressed through κ projectors using Eq. (21), e.g.

$$\Delta_E^{1\perp} = \sum_{\ell=1}^{\mathcal{L}} \left\| \text{Diagram 12} - \text{Diagram 13} \right\|^2. \quad (69)$$

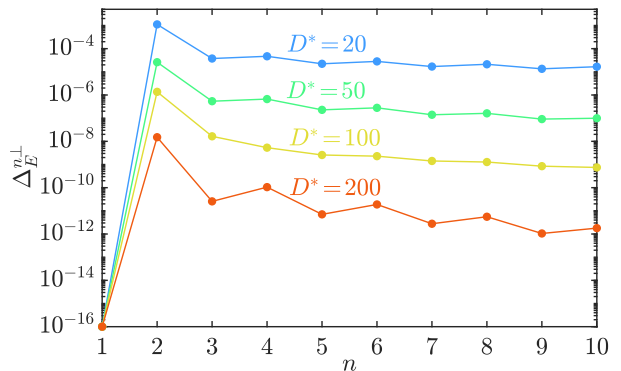


FIG. 1. The n -site variance, $\Delta_E^{n\perp}$, of the $\mathcal{L} = 40$ Haldane-Shastry model for different D^* . $\Delta_E^{1\perp}$ is numerically zero (i.e. $\Delta_E^{1\perp} \lesssim 10^{-16}$) when DMRG is converged properly, plotted here symbolically at $\Delta_E^{1\perp} = 10^{-16}$.

If the Hamiltonian contains only local and nearest-neighbor terms, all contributions with $n > 2$ are zero [6], i.e. $\Delta_E = \Delta_E^{2s}$. However, it has been argued in Ref. 6 that even if long-range terms are present, Δ_E^{2s} is a reliable error measure. Here, we confirm this for the case of the spin- $\frac{1}{2}$ Haldane-Shastry model on a ring of length $\mathcal{L} = 40$, with Hamiltonian

$$\mathcal{H}_{\text{HS}} = \sum_{\ell < \ell' \leq \mathcal{L}} \frac{\pi^2 \mathbf{S}_\ell \cdot \mathbf{S}_{\ell'}}{\mathcal{L}^2 \sin^2 \frac{\pi}{\mathcal{L}} (\ell - \ell')}. \quad (70)$$

Figure 1 shows $\Delta_E^{n\perp}$ for $n \in \{1, 2, \dots, 10\}$ and four choices of D^* . In all cases, $\Delta_E^{n\perp}$ is largest for $n = 2$, and smaller by an order magnitude or more for $n > 2$, with the decrease being stronger the larger D^* . For this model, therefore, $\Delta_E^{2\perp}$ by itself suffices to reliably estimate the energy error.

V. n -SITE EXCITATIONS

The ns projectors can be used as an Ansatz to compute low energy excitations. This so-called excitation Ansatz has been very successful in infinite systems [14, 22, 28, 32] and lately also shown to be reliable on finite lattices [33]. Using our diagrammatic notation, we generalize the 1s Ansatz for finite systems used in Ref. 33 to n sites, similar to the ns Ansatz for infinite systems [22, 28].

In the ns excitation Ansatz, the wavefunctions for the excitations are parametrized as

$$|\Psi_{\text{ex}}^{ns}\rangle = \sum_{\ell=1}^{\mathcal{L}-n+1} \star \left[\begin{array}{c} T_1^\ell \quad T_n^\ell \\ \ell \quad \ell+n-1 \end{array} \right] \star, \quad (71)$$

where $T_{i>1}^\ell$ ($\hat{\Psi}$) are generic tensors of rank 3 and T_1^ℓ ($\hat{\Psi}$) are tensors of the form

$$T_1^\ell = \hat{\Psi} = \left[\begin{array}{c} \circ \\ \circ \\ \circ \end{array} \right] + \delta_{\ell, \mathcal{L}-n+1} \left[\begin{array}{c} \circ \\ \circ \\ \circ \end{array} \right]. \quad (72)$$

The construction (71) is such that it can represent any state in the image of \mathcal{P}^{ns} , i.e. $\mathcal{P}^{ns}|\Psi_{\text{ex}}^{ns}\rangle = |\Psi_{\text{ex}}^{ns}\rangle$.

It seems that $|\Psi_{\text{ex}}^{ns}\rangle$ cannot be efficiently computed, since it involves a sum over $\mathcal{L} - n + 1$ (i.e. many!) terms, and performing MPS sums explicitly leads to increased bond dimensions. However, that can be avoided here. The isometries A_ℓ (∇) and B_ℓ (∇) flanking the modified sites reappear in every summand and only need to be saved once; hence only the tensors T_i^ℓ need to be saved. In the case of $n = 1$ for example, we have to save \mathcal{L} tensors of dimensions $D \times d \times D$, i.e. the same memory requirement as for an MPS with bond dimension D .

Second, due to Eq. (72), all summands are by construction mutually orthogonal, facilitating the computation of overlaps. Consider $|\Psi_{\text{ex}}^{ns}\rangle$ and $|\Psi_{\text{ex}}'^{ns}\rangle$, characterized by T_i^ℓ and $T_i'^\ell$, respectively. Their overlap is then given by

$$\langle \Psi_{\text{ex}}'^{ns} | \Psi_{\text{ex}}^{ns} \rangle = \sum_{\ell=1}^{\mathcal{L}-n+1} \left[\begin{array}{c} T_1^\ell \quad T_n^\ell \\ T_1'^\ell \quad T_n'^\ell \end{array} \right], \quad (73)$$

while the computation of sums or differences can be done on the level of the T_i^ℓ , i.e.

$$|\Psi_{\text{ex}}^{ns}\rangle + a|\Psi_{\text{ex}}'^{ns}\rangle \rightarrow \forall \ell: \left[\begin{array}{c} T_1^\ell \quad T_n^\ell \\ \ell \quad \ell+n-1 \end{array} \right] + a \left[\begin{array}{c} T_1'^\ell \quad T_n'^\ell \\ \ell \quad \ell+n-1 \end{array} \right]. \quad (74)$$

If $\prod_{i=1}^n T_i^\ell$ and $\prod_{i=1}^n T_i'^\ell$ are represented as MPSs, Eq. (74) in effect involves a sum of two ns MPSs; this is manageable if n is not too large. In the case $n = 1$, there is only T_1^ℓ and $T_1'^\ell$, i.e. in this case, no MPS sums are required.

To determine the tensors T_i^ℓ for $|\Psi_{\text{ex}}^{ns}\rangle$ explicitly, one projects the Hamiltonian onto the space \mathbb{V}^{ns} and solves for low-energy states of

$$\mathcal{P}^{ns} H \mathcal{P}^{ns} |\Psi_{\text{ex}}^{ns}\rangle = E_{\text{ex}}^{ns} |\Psi_{\text{ex}}^{ns}\rangle \quad (75)$$

that are orthogonal to the ground state. This can be done using some iterative eigensolver like the Lanczos method, initialized by some appropriate initial wavefunction. Explicit orthogonalization w.r.t. to the ground state is required, since our Ansatz space \mathcal{P}^{ns} contains the ground state, whose kept and discarded spaces span the image of \mathcal{P}^{ns} .

To run an iterative eigensolver, a scheme is needed for efficiently applying the projected Hamiltonian $\mathcal{P}^{ns} H \mathcal{P}^{ns}$ to the state $|\Psi_{\text{ex}}^{ns}\rangle$. The resulting state, say $|\tilde{\Psi}_{\text{ex}}^{ns}\rangle = \mathcal{P}^{ns} H \mathcal{P}^{ns} |\Psi_{\text{ex}}^{ns}\rangle$, will again be of the form (71), but described by tensors \tilde{T}_i^ℓ . To find these, we compute the tensors

$$\tilde{T}_1^\ell \tilde{T}_2^\ell \tilde{T}_n^\ell = \sum_{\ell'=1}^{\mathcal{L}-n+1} \left[\begin{array}{c} T_1^{\ell'} \quad T_n^{\ell'} \\ \ell' \quad \ell'+n-1 \end{array} \right], \quad (76)$$

and project \tilde{T}_1^ℓ to the discarded space to obtain \bar{T}_1^ℓ ,

$$\bar{T}_1^\ell = \tilde{T}_1^\ell - (1 - \delta_{\ell, \mathcal{L}-n+1}) \left[\begin{array}{c} \tilde{T}_1^\ell \\ A_\ell^* \\ \nabla A_\ell \end{array} \right], \quad (77)$$

such that Eq. (72) is fulfilled.

To evaluate Eq. (76), we split the sum $\sum_{\ell'}$ into terms with $\ell' < \ell$ and $\ell' \geq \ell$, and express these as follows:

$$\begin{aligned} \tilde{T}_1^\ell \tilde{T}_2^\ell \tilde{T}_n^\ell &= \sum_{m=1}^n \left[\begin{array}{c} T_{m+1}^{\ell-m} \quad T_n^{\ell-m} \\ \mathcal{L}_{\ell-1}^m \quad R_{\ell+n} \end{array} \right] \\ &+ \sum_{m=0}^n \left[\begin{array}{c} T_1^{\ell+m} \quad T_{n-m}^{\ell+m} \\ L_{\ell-1} \quad \mathcal{R}_{\ell+n}^m \end{array} \right]. \end{aligned} \quad (78)$$

Next to the left and right environments L_ℓ and R_ℓ defined in Eq. (18), these expressions contain another set of environments, denoted by \mathcal{L}_ℓ^m and \mathcal{R}_ℓ^m , each involving those m of the $T_i^{\ell'}$ tensors in Eq. (76) that do not face open physical legs. For $m = 0$, $m \in \{1, \dots, n-1\}$ or $m = n$, they are defined by the left equalities below; the right

equalities show how for each m , $\mathcal{L}_{\ell+1}^m$ and $\mathcal{R}_{\ell-1}^m$ can be computed recursively from \mathcal{L}_ℓ^m and \mathcal{R}_ℓ^m , initialized with $\mathcal{L}_0^0 = 1$, $\mathcal{L}_0^{m>0} = 0$, $\mathcal{R}_{\mathcal{L}+1}^0 = 1$, $\mathcal{R}_{\mathcal{L}+1}^{m>0} = 0$:

$$\mathcal{L}_\ell^0 = \left\langle \right\rangle = \left\langle \right\rangle = \left\langle \right\rangle, \quad (79a)$$

$$\mathcal{L}_\ell^m = \left\langle \right\rangle = \left\langle \right\rangle = \left\langle \right\rangle,$$

$$\mathcal{L}_\ell^n = \left\langle \right\rangle = \sum_{\ell'=1}^{\ell-n+1} \left\langle \right\rangle = \left\langle \right\rangle + \left\langle \right\rangle,$$

$$\mathcal{R}_\ell^0 = \left\langle \right\rangle = \left\langle \right\rangle = \left\langle \right\rangle, \quad (79b)$$

$$\mathcal{R}_\ell^m = \left\langle \right\rangle = \left\langle \right\rangle = \left\langle \right\rangle,$$

$$\mathcal{R}_\ell^n = \left\langle \right\rangle = \sum_{\ell'=\ell}^{\mathcal{L}-n+1} \left\langle \right\rangle = \left\langle \right\rangle + \left\langle \right\rangle.$$

The solution of Eq. (75) using an iterative eigensolver has costs scaling with $\mathcal{O}(D^3 d^n w)$, the same as ns DMRG. However, because the Ansatz Eq. (71) is built from a sum over $\mathcal{L} - n + 1$ MPSs, states can be captured which would need significantly larger bond dimensions if represented in standard fashion as an MPS. Because there are n summands in Eq. (71) which differ from the ground state at site ℓ (with corresponding tensors $T_1^\ell, \dots, T_n^{\ell-n+1}$ at site ℓ), an MPS representation would need bond dimension $D(1+n)$, assuming A_ℓ, B_ℓ and T_i^ℓ are tensors of dimension $D \times d \times D$. Optimizing such an MPS with ns DMRG comes with $\mathcal{O}(D^3(n+1)^3 d^n w)$ costs, larger by $(n+1)^3$ than the costs for optimizing the Ansatz Eq. (71). Of course, the latter Ansatz is much more restrictive than a generic MPS of bond dimension $D(1+n)$. However, that should not be a limitation if the physics of interest involves single- or few-particle excitations, as is the case, e.g., when computing correlations functions of single- or few-particle operators.

We test the ns excitation Ansatz on a Haldane-Shastry model on a ring of length $\mathcal{L} = 40$ (see Eq. (70) for the Hamiltonian), for which we seek to compute the lowest energy excitation with total spin $S = 1$ above the total spin $S = 0$ ground state. For comparison, we have also computed this state by performing a DMRG ground state search in the $S = 1$ sector.

Fig. 2 shows the corresponding relative errors in energy versus the bond dimension D^* . As reference values, we use the exact energies $E_{\text{exact}}^{S=0} = -\pi^2(\mathcal{L} + 5/\mathcal{L})/24$ and $E_{\text{exact}}^{S=1} = -\pi^2(\mathcal{L} - 7/\mathcal{L})/24$ for the ground state and excited state [34–36], respectively. Remarkably, we find

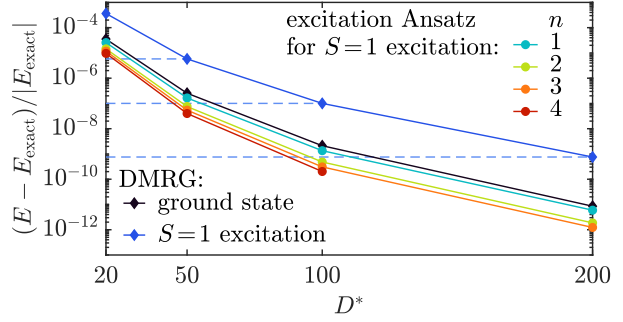


FIG. 2. Relative error in energy of the lowest-lying $S = 1$ excited state of the Haldane-Shastry model, computed using the n -site excitation Ansatz (circles), or using DMRG (blue diamonds). Black diamonds show DMRG results for the $S = 0$ ground state. The dashed blue lines are guides to the eye.

that for the same D^* , the $n = 1$ site excitation Ansatz yields an $S = 1$ excitation energy that is more accurate than that obtained from DMRG by one to two orders of magnitude, even though the computational cost of both approaches at the same D^* is comparable. In fact, the relative error obtained by the excitation Ansatz for the $S = 1$ state is comparable to (even slightly lower than) that obtained by DMRG for the $S = 0$ ground state.

The reason for the high accuracy of the excitation Ansatz is that the first excited state is essentially a superposition of local spin excitations, i.e. it fits Ansatz (71). The excitation Ansatz avoids representing this superposition as a single MPS, which would require about twice the bond dimension. Instead, it exploits the fact that each local excitation differs from the ground state only locally. This leads to a more economic Ansatz compared to DMRG, which needs about twice the bond dimension. This can also be seen in Fig. 2, where the relative error in energy of the 1s excitation Ansatz at some D^* almost coincides with the corresponding error of DMRG at $2D^*$. The latter error is slightly smaller than the former, because the $2D^*$ MPS Ansatz used by DMRG is less restrictive than the D^* excitation Ansatz, though this improvement is rather marginal.

The capability of the excitation Ansatz can be further improved by considering $n > 1$, leading to a reduction of the relative error in energy compared to $n = 1$, see Fig. 2. This reduction is rather small and further improvements seem to become ever smaller for ever larger n . However, with increasing n the costs for this Ansatz increase exponentially, as $\sim d^n$. Therefore, including information beyond $n = 1$ by brute force, i.e. by just going to $n > 1$, is not advisable. Nevertheless, we believe that valuable improvements of the Ansatz may be achievable, while circumventing the exponential d^n scaling, by including only the those parts of the $n > 1$ sectors that contribute to the excited state with significant weight. It should be possible to identify these parts by generalizing the strategy proposed in our recent work on controlled bond expansion in both DMRG ground state search [29] and

TDVP time evolution [30]. We leave this as a topic for future study.

More generally, we believe that the diagrammatics for the n -site excitation Ansatz and the projector formalism developed in this work will provide a solid foundation to construct systematic improvements to the 1-site excitation Ansatz without a significant increase in computational costs.

VI. SUMMARY AND OUTLOOK

We have developed a projector formalism for kept and discarded spaces of MPS, together with a convenient diagrammatic notation. We use it to derive explicit expressions for global n -site projectors \mathcal{P}^{ns} and irreducible n -site projectors $\mathcal{P}^{n\perp}$. We then use our results to derive explicit formulas for the n -site variance and evaluate it for the Haldane-Shastry model, showing that indeed the 2-site contribution is the most dominant one. Further, we derive explicit diagrammatic formulas to perform excited state computations based on the n -site excitation Ansatz for finite, non-translation invariant MPS.

The κ, D projector formalism and diagrammatic notation developed here proved very convenient for the applications considered in this work. More generally, we expect them to provide a convenient tool for the development of new MPS algorithms that explicitly or implicitly utilize the properties of discarded spaces. The information contained in these is a *resource*, useful for

describing changes or variations of a given MPS, and for algorithms exploiting this resource, the κ, D projector formalism facilitates book-keeping thereof. Indeed, we have developed the formalism presented here while working out a controlled bond expansion algorithm to perform both DMRG ground-state searches [29] and time evolutions using the time-dependent variational principle [30] with 2-site accuracy at 1-site computational cost. Moreover, our formalism provides the tools needed to efficiently implement the perspectives outlined in Refs. 14 and 22 for post-MPS applications, that build on a given MPS to compute low energy excitation spectra.

As a final remark, we note that though we focused on MPSs in this work, our formalism should be generalizable to any tensor network for which canonical forms are available, such as tensor networks without loops.

ACKNOWLEDGEMENTS

We thank Andreas Weichselbaum for stimulating discussions, and Seung-Sup Lee, Juan Espinoza, Matan Lotem, Jeongmin Shim and Andreas Weichselbaum for helpful comments on the manuscript. Our numerical simulations employed the QSpace tensor library [37, 38]. This research was funded in part by the Deutsche Forschungsgemeinschaft under Germany's Excellence Strategy EXC-2111 (Project No. 390814868), and is part of the Munich Quantum Valley, supported by the Bavarian state government with funds from the Hightech Agenda Bayern Plus.

-
- [1] S. R. White, Density matrix formulation for quantum renormalization groups, *Phys. Rev. Lett.* **69**, 2863 (1992).
 - [2] S. R. White, Density-matrix algorithms for quantum renormalization groups, *Phys. Rev. B* **48**, 10345 (1993).
 - [3] A. J. Daley, C. Kollath, U. Schollwöck, and G. Vidal, Time-dependent density-matrix renormalization-group using adaptive effective hilbert spaces, *J. Stat. Mech.: Theor. Exp.* **P04005** (2004).
 - [4] S. R. White, Density matrix renormalization group algorithms with a single center site, *Phys. Rev. B* **72**, 180403 (2005).
 - [5] C. Hubig, I. P. McCulloch, U. Schollwöck, and F. A. Wolf, Strictly single-site dmrg algorithm with subspace expansion, *Phys. Rev. B* **91**, 155115 (2015).
 - [6] C. Hubig, J. Haegeman, and U. Schollwöck, Error estimates for extrapolations with matrix-product states, *Phys. Rev. B* **97**, 045125 (2018).
 - [7] G. Vidal, Efficient classical simulation of slightly entangled quantum computations, *Phys. Rev. Lett.* **91**, 147902 (2003).
 - [8] G. Vidal, Efficient simulation of one-dimensional quantum many-body systems, *Phys. Rev. Lett.* **93**, 040502 (2004).
 - [9] G. Vidal, Classical simulation of infinite-size quantum lattice systems in one spatial dimension, *Phys. Rev. Lett.* **98**, 070201 (2007).
 - [10] J. Haegeman, J. I. Cirac, T. J. Osborne, I. Pižorn, H. Verschelde, and F. Verstraete, Time-dependent variational principle for quantum lattices, *Phys. Rev. Lett.* **107**, 070601 (2011).
 - [11] C. Lubich, I. V. Oseledets, and B. Vandereycken, Time integration of tensor trains, *SIAM J. Numer. Anal.* **53**, 917 (2015).
 - [12] J. Haegeman, C. Lubich, I. Oseledets, B. Vandereycken, and F. Verstraete, Unifying time evolution and optimization with matrix product states, *Phys. Rev. B* **94**, 165116 (2016).
 - [13] V. Zauner-Stauber, L. Vanderstraeten, M. T. Fishman, F. Verstraete, and J. Haegeman, Variational optimization algorithms for uniform matrix product states, *Phys. Rev. B* **97**, 045145 (2018).
 - [14] L. Vanderstraeten, J. Haegeman, and F. Verstraete, Tangent-space methods for uniform matrix product states, *SciPost Phys. Lect. Notes* **7** (2019).
 - [15] K. G. Wilson, The renormalization group: Critical phenomena and the Kondo problem, *Rev. Mod. Phys.* **47**, 773 (1975).
 - [16] R. Peters, T. Pruschke, and F. B. Anders, Numerical renormalization group approach to Green's functions for quantum impurity models, *Phys. Rev. B* **74**, 245114 (2006).
 - [17] A. Weichselbaum and J. von Delft, Sum-rule conserving spectral functions from the numerical renormalization group, *Phys. Rev. Lett.* **99**, 076402 (2007).
 - [18] K. A. Hallberg, Density-matrix algorithm for the calculation of dynamical properties of low-dimensional systems,

- 52**, 9827(R) (1995).
- [19] T. D. Kühner and S. R. White, Dynamical correlation functions using the density matrix renormalization group, *Phys. Rev. B* **60**, 335 (1999).
- [20] E. Jeckelmann, Dynamical density-matrix renormalization-group method, *Phys. Rev. B* **66**, 045114 (2002).
- [21] A. Holzner, A. Weichselbaum, I. P. McCulloch, U. Schollwöck, and J. von Delft, Chebyshev matrix product state approach for spectral functions, *Phys. Rev. B* **83**, 195115 (2011).
- [22] J. Haegeman, T. J. Osborne, and F. Verstraete, Post-matrix product state methods: To tangent space and beyond, *Phys. Rev. B* **88**, 075133 (2013).
- [23] U. Schollwöck, The density-matrix renormalization group in the age of matrix product states, *Annals of Physics* **326**, 96 (2011).
- [24] A. Weichselbaum, Tensor networks and the numerical renormalization group, *Phys. Rev. B* **86**, 245124 (2012).
- [25] S. Paeckel, T. Köhler, A. Swoboda, S. R. Manmana, U. Schollwöck, and C. Hubig, Time-evolution methods for matrix-product states, *Annals of Physics* **411**, 167998 (2019).
- [26] F. B. Anders and A. Schiller, Real-time dynamics in quantum-impurity systems: A time-dependent numerical renormalization-group approach, *Phys. Rev. Lett.* **95**, 196801 (2005).
- [27] S.-S. B. Lee, F. B. Kugler, and J. von Delft, Computing local multipoint correlators using the numerical renormalization group, *Phys. Rev. X* **11**, 041007 (2021).
- [28] J. Haegeman, S. Michalakis, B. Nachtergaele, T. J. Osborne, N. Schuch, and F. Verstraete, Elementary excitations in gapped quantum spin systems, *Phys. Rev. Lett.* **111**, 080401 (2013).
- [29] A. Gleis, J.-W. Li, and J. von Delft, Controlled bond expansion for DMRG ground state search at single-site costs, to be published (2022).
- [30] J.-W. Li, A. Gleis, and J. von Delft, Time-dependent variational principle with controlled bond expansion for matrix product states, to be published (2022).
- [31] F. B. Kugler, S.-S. B. Lee, and J. von Delft, Multipoint correlation functions: Spectral representation and numerical evaluation, *Phys. Rev. X* **11**, 041006 (2021).
- [32] J. Haegeman, B. Pirvu, D. J. Weir, J. I. Cirac, T. J. Osborne, H. Verschelde, and F. Verstraete, Variational matrix product ansatz for dispersion relations, *Phys. Rev. B* **85**, 100408 (2012).
- [33] M. Van Damme, R. Vanhove, J. Haegeman, F. Verstraete, and L. Vanderstraeten, Efficient matrix product state methods for extracting spectral information on rings and cylinders, *Phys. Rev. B* **104**, 115142 (2021).
- [34] T. Yamamoto, Y. Saiga, M. Arikawa, and Y. Kuramoto, Exact dynamical structure factor of the degenerate Haldane-Shastry model, *Phys. Rev. Lett.* **84**, 1308 (2000).
- [35] T. Yamamoto, Y. Saiga, M. Arikawa, and Y. Kuramoto, Exact dynamics of the SU(K) Haldane-Shastry model, *Journal of the Physical Society of Japan* **69**, 900 (2000).
- [36] Y.-H. Wu, L. Wang, and H.-H. Tu, Tensor network representations of parton wave functions, *Phys. Rev. Lett.* **124**, 246401 (2020).
- [37] A. Weichselbaum, Non-abelian symmetries in tensor networks: A quantum symmetry space approach, *Ann. of Phys.* **327**, 2972 (2012).
- [38] A. Weichselbaum, X-symbols for non-abelian symmetries in tensor networks, *Phys. Rev. Research* **2**, 023385 (2020).

3 Projected Entangled-Paired States

3.1 Overview

For two-dimensional quantum systems, the infinite projected entangled-pair state (iPEPS) is a useful tool to directly simulate ground states in the thermodynamic limit. iPEPS, however, comes with demanding computational costs both in memory and time. An important technical aspect of iPEPS is to exploit continuous symmetries to improve its performance. In [P4], we discuss the implementation details to achieve that.

The t - J model In [P5], we use iPEPS to study the doped t - J model on square lattices [GJR87, DR92]. The t - J model is related to the one-band Hubbard model in the strong-coupling limit. When $U/t \rightarrow \infty$, the double occupancies are energetically unfavoured and suppressed. Their contribution to the low energies is only through the virtual hopping processes. Particularly, the two-site virtual hoppings produce the superexchange antiferromagnetic interactions with $J = 4t^2/U$. At small hole doping, the t - J model is commonly regarded as the minimal model of the cuprate materials [ZR88].

The t - J model is well understood at certain parameter regimes. First, at exact half-filling, the t - J model reduces to the Heisenberg model. Its ground state has long-range anti-ferromagnetic order; exotic phases postulated analytically, such as resonant valence bond states [KRS87] or flux phases [AM88], were dispelled by numerics [RY88, DM88, San97]. Second, at the single hole limit, the string picture gives a succinct description of the hole motion [Tru88, GKNB+18, GZSD18, GP20, JXK+21], where the mobile hole creates a ferromagnetic bubble, often called a Nagaoka polaron [Nag66]. However, at finite doping, the nonperturbative nature of the hole-hole interactions immediately puts the string picture in a difficult ground [DW89, SCW96, WSCT97, EBHA02]. Third, at large J/t , the ground state undergoes a phase separation into a hole-rich and a hole-poor region [RY89, KEL90, EKL90, EBHA02]. The regime of large J/t is only of academic interest, since the physical relevant regime with a large U corresponds to a small value of J/t .

For $J/t \lesssim 0.5$, the ground state nature of the t - J model at small but finite doping remains controversial. One possibility is a spatially uniform superconductivity [KL88, HM99, CS00]. Another is a tendency towards phase separation [EKL90, HM97, PKH98]. The third one is stripe order with periodic spin and charge modulations in the real space [Sch89, ZG89, PcvZ93, WS98]. The discovery of stripe order appears to be a theoretical success, as it rationalizes an anomaly observed in $\text{La}_{2-x}\text{Ba}_x\text{CuO}_4$ materials, in which superconductivity is sharply suppressed at doping $x = 1/8$. Nonetheless, we have to bear in mind that these numerics did not give account for the origin of d -wave superconducting order. Besides the insulated stripe order just mentioned, a stripe with modulated superconductivity has also been considered [BFK+07] and supported by recent tensor network calculations [CRT14, JWK18].

In short, the physics of t - J model at the physical relevant regime is far from clear. Here, we revisited this old problem using symmetric iPEPS. Exploiting the

continuous symmetries within iPEPS has two advantages. First, the sparse tensor implementation reduces the computational cost. Second, this gives us a numerical knob to turn on and off certain global symmetries to target low-energy states that belong to different symmetry sectors. We demonstrated how by allowing or disallowing the breaking of the spin rotational symmetry affects the superconductivity and the stripe order that are competing with each other at small doping.

The Kitaev- Γ model Ever since Kitaev’s proposal of spin liquids on honeycomb lattices [Kit06], its experimental realization has been unflaggingly pursued. The prime candidate material is α -RuCl₃. At low energies, spectroscopic experiments reveal fractionalized excitations, hinting towards proximate spin liquid behavior [BBY⁺16, BYK⁺17]. Even so, its phase diagram, complicated by significant non-Kitaev interactions, is not well understood to date. The minimal microscopic model to clarify the physics of α -RuCl₃ includes not only the Kitaev (K) interactions, but also the off-diagonal symmetric (Γ) interactions.

When Γ and K are roughly of equal strength, whether there exists a quantum Kitaev- Γ spin liquid for $S = 1/2$ is a heated debate. Early calculations using exact diagonalization [CYW⁺18] and infinite DMRG [GWY⁺18] suggested an extended spin liquid phase away from the Kitaev limit. Such optimism was quickly refuted. Careful inspections reveal unexpected ramifications of having the Γ interactions. A zig-zag ordering was identified via the variational Monte Carlo [WNL19]. Also, incommensurate order, nematic order, and complicated magnetic order found by different tensor network methods [JDJ19, GCKK20, LKC⁺20] can not be excluded.

In [P6], we use iPEPS to study the Kitaev- Γ model. For quantum spins $S = 1/2$, our iPEPS simulations find an unusual magnetic order at $\Gamma/|K| \sim 1$. It breaks the translational symmetry and forms an 18-sublattice pattern. Guided by classical Monte Carlo simulations performed by Ke Liu, we trace the origin of this exotic quantum magnetic order to its classical counterpart.

P4 *A beginner’s guide to non-abelian iPEPS for correlated fermions*

Benedikt Bruognolo, **Jheng-Wei Li**, Jan von Delft, Andreas Weichselbaum
[SciPost Phys. Lect. Notes 25 \(2021\)](#)

P5 *Study of spin symmetry in the doped t - J model using infinite projected entangled pair states*

Jheng-Wei Li, Benedikt Bruognolo, Andreas Weichselbaum and Jan von Delft
[Phys. Rev. B 103, 075127 \(2021\)](#)

P6 *Tangle of Spin Double Helices in the Honeycomb Kitaev- Γ Model*

Jheng-Wei Li, Nihal Rao, Jan von Delft, Lode Pollet, and Ke Liu
[arXiv:2206.08946](#)

A beginner's guide to non-abelian iPEPS for correlated fermions

Benedikt Bruognolo¹, Jheng-Wei Li¹, Jan von Delft¹ and Andreas Weichselbaum^{1,2*}

¹ Arnold Sommerfeld Center for Theoretical Physics, Center for NanoScience,
and Munich Center for Quantum Science and Technology,
Ludwig-Maximilians-Universität München, 80333 Munich, Germany

² Department of Condensed Matter Physics and Materials Science,
Brookhaven National Laboratory, Upton, NY 11973-5000, USA

* weichselbaum@bnl.gov

Abstract

Infinite projected entangled pair states (iPEPS) have emerged as a powerful tool for studying interacting two-dimensional fermionic systems. In this review, we discuss the iPEPS construction and some basic properties of this tensor network (TN) ansatz. Special focus is put on (i) a gentle introduction of the diagrammatic TN representations forming the basis for deriving the complex numerical algorithm, and (ii) the technical advance of fully exploiting non-abelian symmetries for fermionic iPEPS treatments of multi-band lattice models. The exploitation of non-abelian symmetries substantially increases the performance of the algorithm, enabling the treatment of fermionic systems up to a bond dimension $D = 24$ on a square lattice. A variety of complex two-dimensional (2D) models thus become numerically accessible. Here, we present first promising results for two types of multi-band Hubbard models, one with 2 bands of spinful fermions of $SU(2)_{\text{spin}} \otimes SU(2)_{\text{orb}}$ symmetry, the other with 3 flavors of spinless fermions of $SU(3)_{\text{flavor}}$ symmetry.



Copyright B. Bruognolo *et al.*

This work is licensed under the Creative Commons

[Attribution 4.0 International License](https://creativecommons.org/licenses/by/4.0/).

Published by the SciPost Foundation.

Received 18-06-2020

Accepted 04-02-2021

Published 25-02-2021

doi:[10.21468/SciPostPhysLectNotes.25](https://doi.org/10.21468/SciPostPhysLectNotes.25)



Check for updates

Contents

1	Introduction	1
2	Tensor network diagrams and convention	3
3	Infinite projected entangled pair states	4
3.1	PEPS ansatz and properties	4
3.2	iPEPS	6
3.3	Contractions	7
3.3.1	Corner transfer matrix scheme	9
3.4	Expectation value	16
3.5	Ground state search	17
3.5.1	Bond projection	18
3.5.2	Simple update	19

3.5.3	Full update	22
3.5.4	Alternative approaches	24
3.5.5	Gauge fixing	24
4	Fermionic tensor networks	25
4.1	Parity conservation	26
4.2	Fermionic swap gates	27
4.3	Fermionic operators	27
4.4	Fermionic PEPS implementation	28
4.5	Fermionic iPEPS implementation	29
5	Implementation of symmetries	32
5.1	Abelian symmetries	32
5.2	Non-abelian symmetries	32
5.3	Outer multiplicity	33
5.4	PEPS with symmetries	34
5.5	Technicalities	35
5.5.1	Global symmetry sector	36
5.5.2	Arrow convention	36
5.5.3	Efficient contractions	36
6	Examples	39
6.1	Spinful two-band Hubbard model	40
6.2	Three-flavor Hubbard model	45
7	Conclusion	48
A	Constructing tensors with symmetry	48
A.1	SU(2) spin algebra	49
A.2	Tensor product decomposition	49
A.3	Irreducible tensor operator	50
A.4	PEPS tensor construction	51
	References	52

1 Introduction

Ever since the discovery of high- T_c superconductivity, there is a great need for developing and improving numerical approaches for studying one-band and multi-band fermionic many-body systems in two spatial dimensions. Quantum Monte-Carlo (QMC) is an excellent candidate for this challenge [1]. However, the presence of the fermionic sign problem in these systems at finite doping often restricts the applicability of QMC to special points in the phase diagram close to half filling.

Tensor network techniques represent a promising alternative to QMC to successfully deal with complex systems of itinerant fermions. In particular, the density matrix renormalization group (DMRG) applied to two-dimensional clusters has provided us with some remarkable insights. Examples include the discovery of the spin-liquid ground state of the Kagome Heisenberg model [2,3] or the first observation of stripe states in the hole-doped t - J model [4]. More

recently, also the infinite projected entangled pair state (iPEPS) approach was successfully used for a detailed study of the t - J model [5, 6], as well as for clarifying the spin-liquid nature of the spin-half Kagome Heisenberg model [7, 8]. In addition, a combined iPEPS and DMRG study, supported by other numerical methods, led to a consensus regarding the existence of stripe order in the hole-doped Hubbard model [9].

A PEPS can be constructed by considering a lattice system where the entanglement of each site to the rest of the system is encoded via virtual degrees of freedom (entangled pairs) associated with the lattice bonds connecting that site to its neighbors. Projecting all virtual degrees of freedom associated with a given site to the physical Hilbert space of that site generates a PEPS tensor for that site [10]. Such a tensor network representation can be considered as a generalization of Affleck, Kennedy, Lieb and Tasaki (AKLT) states or tensor product states, which date back to even earlier literature [11–14]. In short, many tensor network algorithms to simulate many-body states in 2D are based on the PEPS representation, including the tensor renormalization group (TRG) [15, 16], the second renormalization group (SRG) [17], the higher-order tensor renormalization group [18], tensor network renormalization [19, 20], DMRG-like ground-state optimization [21, 22] and promising extensions to excited states by means of tangent space methods [23].

Despite many interesting developments, PEPS has not yet reached its full potential in application to frustrated and fermionic 2D systems. This is mostly due to the technical complexity of the algorithm, especially when dealing with fermionic signs [24] and when implementing symmetries explicitly [25–33]. Nevertheless, PEPS has recently proven its competitiveness and, for instance, provided new insights for underdoped Hubbard model [9, 34, 35] and t - J models [5, 6, 36], for spin- $\frac{1}{2}$ [7, 8] and spin-1 Kagome-Heisenberg models [37], as well as for the Shastry-Sutherland model [38, 39]. At the same time, PEPS is still in its infancy and there is much room for technical progress boosting the performance of the method [40–42].

In this work, we consider the PEPS method applied to translationally invariant systems, the so-called iPEPS ansatz [43], and focus on an aspect where further technical progress is certainly possible – the exploitation of symmetries. If the Hamiltonian is invariant under some symmetry group, its energy eigenstates can be grouped into multiplets transforming as irreducible representations (irreps) under symmetry transformations. Correspondingly, a tensor network for such a system can be constructed from tensors whose legs (both physical and virtual) carry irrep labels. Keeping track of this multiplet structure can reduce computational costs tremendously, since tensors acquire block substructures. Moreover, for non-abelian symmetries the relevant bond dimension is reduced from D , the number of individual states per bond, to D^* , the number of multiplets per bond. Computational costs scaling as D^α can thus effectively be reduced by a factor of $(D/D^*)^\alpha$. Also, memory requirements, the primary bottleneck for iPEPS calculations, can be significantly reduced. However, the tensor block structure entails overhead in the code complexity and performance, which requires some special care, specifically so if many, individually small blocks arise. With $\alpha \gtrsim 12$ for iPEPS and $D/D^* \simeq 3$ for $SU(2)$ symmetry or larger for $SU(N > 2)$, the potential benefits of exploiting symmetries are evidently enormous. In practice, however, keeping track of symmetry labels requires codes with an additional layer of complexity, in particular for symmetry groups having outer multiplicity > 1 , such as $SU(N > 2)$. While the exploitation of abelian symmetries in PEPS codes is becoming fairly routine by now, the number of applications of non-abelian PEPS can still be counted on one hand [33, 37, 44], all involving $SU(2)$ symmetry.

Believing that non-abelian PEPS nevertheless holds great promise, we devote this tutorial review to a detailed exposition of its key ingredients. We offer a pedagogical review of the most important aspects of the PEPS representation and the iPEPS algorithm, mainly following the work of Philippe Corboz and coworkers [5, 6, 24, 45–47]. In particular, we discuss how to perform contractions [Sec. 3.3], how to keep track of fermionic minus signs, and how to per-

form tensor optimization via imaginary-time evolution [Sec. 3.5], including the gauge fixing for iPEPS [47, 48]. Additionally, we go beyond the scope of Corboz’ work by explaining how arbitrary non-abelian symmetries can explicitly incorporated in the fermionic iPEPS ansatz in a generic manner, based on the QSpace [30] tensor library. A pedagogical discussion of SU(2) iPEPS was recently given in Ref. [49], with benchmarking computations on spin systems reported in Ref. [50]. Our treatment of symmetries represents a fully alternative approach to theirs, which permits us to deal with non-trivial outer multiplicities (OM) on a general footing. While OM is not present for SU(2) for rank-3 tensors, it already also occurs for SU(2) for tensors of rank $r > 3$. For larger symmetries, such as SU($N > 2$), OM already occurs generically even at the elementary level of rank-3 tensors.

A first application of our non-abelian fermionic iPEPS code, published concurrently with this tutorial review, is a study of the 2D fermionic t - J model [51] – by exploiting either U(1) or SU(2) symmetry to allow or forbid spontaneous spin symmetry breaking, we elucidate the interplay between antiferromagnetic order, stripe formation and pairing correlations. In the present work, we further illustrate the power of non-abelian iPEPS by presenting some exemplary results for two 2D fermionic Hubbard models of higher complexity: a model with two degenerate bands of spinful fermions, featuring SU(2)_{spin} \otimes SU(2)_{orb} symmetry, and a model with three degenerate bands of spinless fermions, featuring SU(3)_{flavor} symmetry.

2 Tensor network diagrams and convention

As implied by their name, tensor network techniques typically involve a large number of tensors of various rank that are iteratively manipulated. These manipulation steps may vary in their complexity and, for example, include matrix multiplication, or decomposition techniques such as singular value or eigenvalue decompositions. In order to simplify the lengthy mathematical expressions which describe these steps and typically involve large sums over multiple indices, we heavily rely on using a diagrammatic representation for tensor network states. Analogous to the role of Feynman diagrams in quantum field theories, these tensor network diagrams are pictorial representation of mathematical expressions and help a great deal grasping the essence a TN algorithm. Since we extensively employ this pictorial language in this review, we here give a brief summary of our conventions together with an explanation on how to understand these diagrams in the following.

Each TN diagram consists of one or multiple extended objects (squares, circles, ...), which are connected by lines. Objects and lines represent tensors and indices, respectively. In the following, we give a few simple examples. For instance, a matrix or rank-2 tensor A has two indices α, β ,

$$A_{\alpha\beta} = \overset{\alpha}{\text{---}} \bigcirc \overset{A}{\text{---}} \underset{\beta}{\text{---}}. \tag{1}$$

The number of values that an index can take is called its dimension.

The next expression, illustrating a matrix multiplication

$$\sum_{\beta} A_{\alpha\beta} B_{\beta\gamma} = \overset{\alpha}{\text{---}} \bigcirc \overset{A}{\text{---}} \underset{\beta}{\text{---}} \bigcirc \overset{B}{\text{---}} \underset{\gamma}{\text{---}}, \tag{2}$$

involves the sum over the common index β of A and B . This contraction is indicated by a line connecting A and B .

In addition to the simple expressions shown above, we often have to deal with diagrams containing multiple sums and open indices, such as

$$\sum_{\alpha,\gamma} A_{\alpha\delta} B_{\alpha\beta\gamma} C_{\gamma\epsilon} = \text{Diagram} \quad (3)$$

It holds generally true, that the diagrammatic representation becomes more beneficial, the more complex the expression and the larger the number of tensors involved since the logic of reading and understanding these diagrams remains the same.

For more evolved topics, such as fermionic TN descriptions and symmetric TNs, the diagrams will contain extra features. We will introduce these features in detail at the appropriate parts of this review.

3 Infinite projected entangled pair states

Projected entangled pair states (PEPS) present the natural generalization of the well-known MPS ansatz to higher spatial dimensions [10]. Analogously to their 1D counterpart, a PEPS consists of a set of high-ranked tensors which are connected by virtual bonds along the physical directions of the corresponding lattice system. In addition, PEPS satisfy the area law of the entanglement entropy in two dimensions [52], thus being able to faithfully represent physical states in gapped lattice models.

In this section, we give a pragmatic introduction to the PEPS construction from the point of view of numerical practitioners. To this end, we only briefly elaborate the ansatz and its properties before discussing numerical details of contraction, optimization, fermionic systems, and the implementation of symmetries.

3.1 PEPS ansatz and properties

To give a practical example, we consider a generic many-body wavefunction $|\psi\rangle$ on a 3×3 cluster. In its most general form, the wavefunction can be expressed in terms of the rank-9 coefficient tensor $\Psi_{\sigma_1^1 \sigma_2^1 \dots \sigma_3^3}$ acting in the local Fock space $|\sigma_y^x\rangle$,

$$|\psi\rangle = \sum_{\sigma_1^1 \sigma_2^1 \dots \sigma_3^3} \Psi_{\sigma_1^1 \sigma_2^1 \dots \sigma_3^3} |\sigma_1^1\rangle |\sigma_2^1\rangle \dots |\sigma_3^3\rangle, \quad (4)$$

where the integer indices x and y enumerate sites in the horizontal and vertical direction. The local or physical index $\sigma_y^x \in 1, \dots, d$ labels states in the local Hilbert space at site $\mathbf{r} = (x, y)$. Obviously, this generic representation suffers from an exponential system-size scaling, which is reflected in the fact that the number of elements of Ψ is equal to the total Hilbert space $d^N = d^9$. Here N denotes the total number of sites and the local dimension d describes the total number of quantum states per site. Typical values are $d = 2$ for a spin- $\frac{1}{2}$ system or spinless fermions, $d = 3$ for spin-1, and $d = 4$ for spinful fermions.

The key idea of the PEPS construction is to circumvent the exponential scaling in system size by decomposing Ψ into a set of high-ranked tensors (in the following denoted M tensors).

A PEPS representation for the wavefunction in Eq. (4) requires a total of nine M tensors,

$$|\psi\rangle = \sum_{\substack{\sigma_1^1 \sigma_2^1 \dots \sigma_3^3 \\ \alpha_1 \alpha_2 \dots \alpha_6 \\ \gamma_1 \gamma_2 \dots \gamma_6}} M_{\alpha_1 \gamma_1}^{\sigma_1^1} M_{\alpha_2 \gamma_1 \gamma_2}^{\sigma_2^1} \dots M_{\alpha_6 \gamma_6}^{\sigma_3^3} |\sigma_1^1 \sigma_2^1 \dots \sigma_3^3\rangle. \quad (5)$$

Each tensor M has a set of virtual indices, α_i for horizontal bonds and γ_i for vertical bonds, connecting each M to its counterparts on up to four neighboring sites, according to the lattice geometry. Following Sec. 2, the diagrammatic representation can be easily derived by introducing the diagram for a rank-5 “bulk” tensor

$$M_{\alpha\beta\gamma\rho}^{\sigma_y^x} = \begin{array}{c} \gamma \\ \circlearrowleft M_y^x \\ \alpha \quad \beta \\ \rho \\ \sigma_y^x \end{array}. \quad (6)$$

The boundary tensors of a finite-size PEPS contain fewer legs. Since we focus on the translationally invariant formulation of PEPS in the following, we refrain from a detailed discussion of various boundary conditions and the corresponding tensors [48].

In general, the number of M tensors in the PEPS representation is equal to the number of sites in the system, e.g., $N = L \times L$ tensors for a square lattice of $L \times L$ sites. Starting from Eq. (6), the diagrammatic representation of the full wavefunction $|\psi\rangle$ in Eqs. (4) and (5) follows immediately,

$$\Psi = \begin{array}{c} \text{Diagrammatic representation of } |\psi\rangle \text{ as a contraction of } M \text{ tensors on a } 3 \times 3 \text{ lattice.} \end{array} \quad (7)$$

In principle, one can perform such a decomposition exactly for any arbitrary many-body wavefunction. For larger systems, however, the dimension of the virtual indices has to be increased exponential which, for numerical purposes, is not practicable. Therefore, one limits the dimension of the virtual bonds of each PEPS tensor to some upper cutoff D [53]. Thus adding an additional site (or row/column of sites) only leads to a polynomial increase in the number of coefficients of the wavefunction. In numerical practice, D is used as a control parameter for the numerical accuracy. It is typically restricted to $D \leq 8-16$, depending on the model and lattice geometry, because for larger values the numerical costs become unfeasibly high.

Restricting the bond dimension of the M tensors comes at a price: only a subset of states can efficiently be represented by a PEPS, since D also limits the maximum amount of entanglement that can be captured by the construction. Fortunately, this is perfectly in line with the area law of the entanglement entropy in 2D, which is fully satisfied by a PEPS representation. Hence, PEPS are ideally suited to approximate low-energy states, including the ground state of local gapped Hamiltonians in two dimensions. Although this statement cannot yet be put on such a mathematically rigorous foundation as 1D, it is strongly supported by numerical evidence [54].

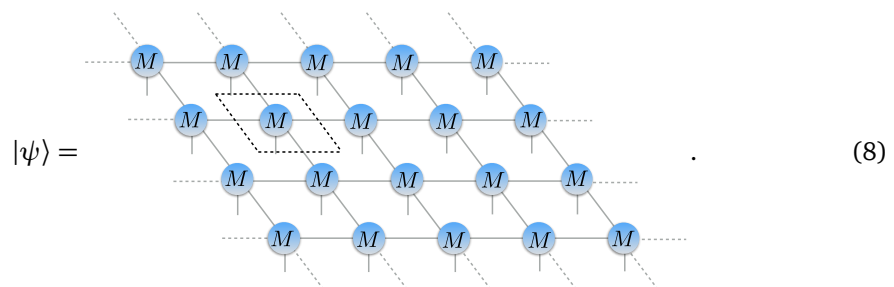
Moreover, the PEPS representation has the remarkable property that, in contrast to MPS, it is capable of faithfully representing algebraically decaying correlation functions, which are

characteristic for gapless models. This can easily be shown for the example of the partition function of the 2D Ising model [52]. Therefore, the PEPS ansatz is in principle able to also treat critical ground state wavefunctions. In practice, however, this does not help substantially in the context of 2D quantum criticality (the above mentioned example deals with classical and not quantum criticality). Based on the quantum-to-classical correspondence, one would require a 3D PEPS construction to faithfully approximate a critical 2D quantum system. Thus, in reality PEPS faces the same challenges in the context of gapless 2D systems as MPS treating critical 1D models: Both TN frameworks may yield results ranging from excellent to moderate quality depending on the “severeness” of the area-law violation in a particular system [53].

3.2 iPEPS

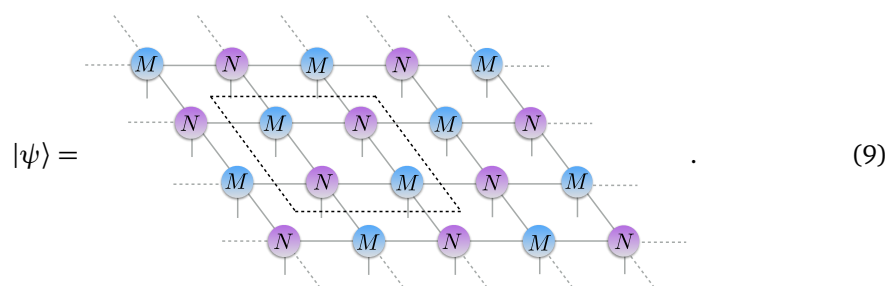
For finite-size PEPS simulations, each M tensor is typically chosen to be different (similar to MPS applications for finite systems). Alternatively, it is possible to exploit the translational invariance of a system and directly work in the thermodynamic limit (of course, this approach also works for MPS [55]). In this way, finite-size and boundary effects can be completely eliminated.

In order to construct an infinite PEPS (iPEPS) [43], we first choose a fixed unit cell of a certain size, and repeat it periodically to cover the entire infinitely large lattice. The size of the fundamental unit cell directly translates into the number of different M tensors required for the iPEPS representation. For instance, one can impose strict translational invariance and choose a unit cell of size 1×1 ,

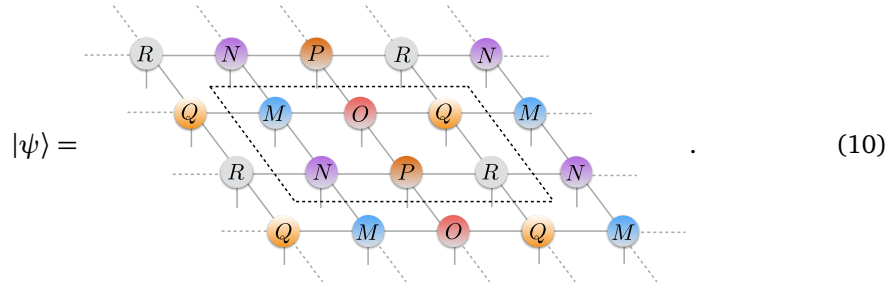


The resulting iPEPS representation of $|\psi\rangle$ then requires only a single M tensor.

However, ordered ground states often break translational invariance to some degree. An iPEPS ansatz of type (8) cannot capture this behavior. Therefore, it is advisable to relax the translational invariance to some extent by choosing a larger unit cell. For example, the following ansatz is fully compatible with an antiferromagnetic ground-state order using two different M tensors in a 2×2 unit cell:



In principle, unit-cells of arbitrary size can be considered, e.g.,



The numerical costs scale linearly with the number of tensors in the unit cell, meaning that large unit cells become numerically expensive. A natural guideline to evaluate which unit-cell sizes should be considered in a simulation is to remember that the unit cell should be compatible with the actual ground-state order. Otherwise, one does not obtain the actual ground state from an iPEPS calculation. Instead, one ends up with the lowest-energy state for the system constrained to the corresponding unit-cell geometry and, therefore, is restricted to specific orders.

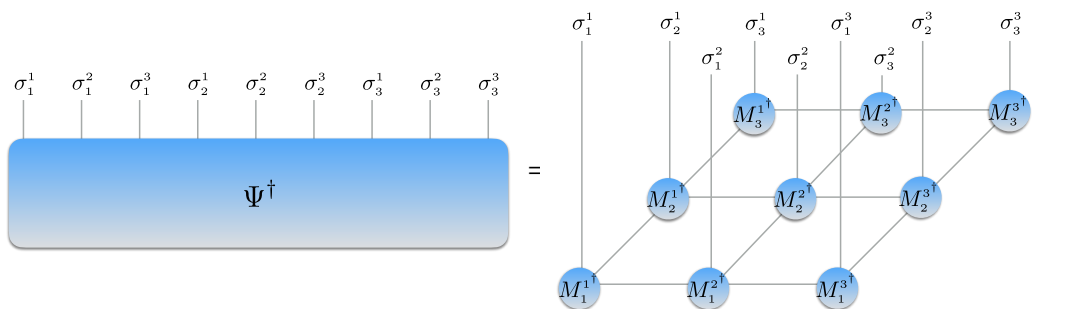
When studying systems with competing low-energy orders, the flexible unit-cell setup of the iPEPS algorithm actually becomes a big advantage. By probing different unit cells, it is possible to stabilize wavefunctions with competing orders independently. Comparing the energies obtained from the corresponding simulations, one may then determine which order survives in the ground state of the system [5, 6].

3.3 Contractions

To extract local observables, perform overlaps, or to actually optimize the tensors, the (i)PEPS framework requires contracting an (infinitely) large tensor network. This turns out to be much more challenging than in context of MPS where, for example, overlaps can be evaluated exactly with only polynomial costs in system size. For a PEPS tensor network, however, the calculation of an exact overlap represents an exponentially hard problem [56] and cannot be performed efficiently. Fortunately, there exist a variety of approximate schemes to deal with this issue.

In this review, we focus on the corner transfer matrix method (CTM) [57, 58], which is particularly well suited for iPEPS applications on square-lattice geometries. Alternatively, it is also possible to rely on an infinite MPS technique for the purpose of this work [43, 59, 60]. Other contraction schemes based on renormalization ideas, such as the tensor renormalization group [15, 16], or tensor network renormalization [19, 20], do have some technical disadvantages (e.g., environmental recycling [47, 61] is not possible, and difficulties arise when calculating longer-ranged correlators, ect.), rendering them unsuitable for our purposes.

Before discussing the details of the CTM scheme for evaluating the scalar product $\langle \psi | \psi \rangle$, we first introduce the corresponding diagram of $\langle \psi |$ for the 3×3 square-lattice toy example,



(11)

which is a mirror image of Eq. (7). The contraction of $\langle\psi|\psi\rangle$ can be done site by site using so-called reduced tensor $m = M_y^{x\dagger}M_y^x$, which is obtained by tracing over the joint physical index of $M_y^{x\dagger}M_y^x$,

$$\begin{aligned}
 m_{\gamma(\alpha\alpha')(\beta\beta')(\gamma\gamma')(\rho\rho')}^x &= \sum_{\sigma_y^x} M_{\rho\gamma\beta\alpha}^{\sigma_y^{x\dagger}} M_{\alpha'\beta'\gamma'\rho'}^{\sigma_y^x} = \\
 &= \frac{\alpha'}{\alpha} \frac{\beta'}{\beta} \frac{\gamma'}{\gamma} \frac{\rho'}{\rho} = \frac{(\alpha\alpha')}{(\rho\rho')} \frac{(\beta\beta')}{(\gamma\gamma')} m_y^x, \quad (12)
 \end{aligned}$$

where the double indices (e.g., $\alpha\alpha'$) have dimension D^2 , as indicated by their increased line thickness. In the second line, we redrew the lines representing indices γ and ρ in such a way that pairs of corresponding primed and unprimed indices match up. This diagrammatically performed “index bending” exploits the non-uniqueness of the graphical representation for a tensor network [45]. This modification is completely trivial for bosonic iPEPS but will add additional complications in the context of fermions [see Sec. 4].

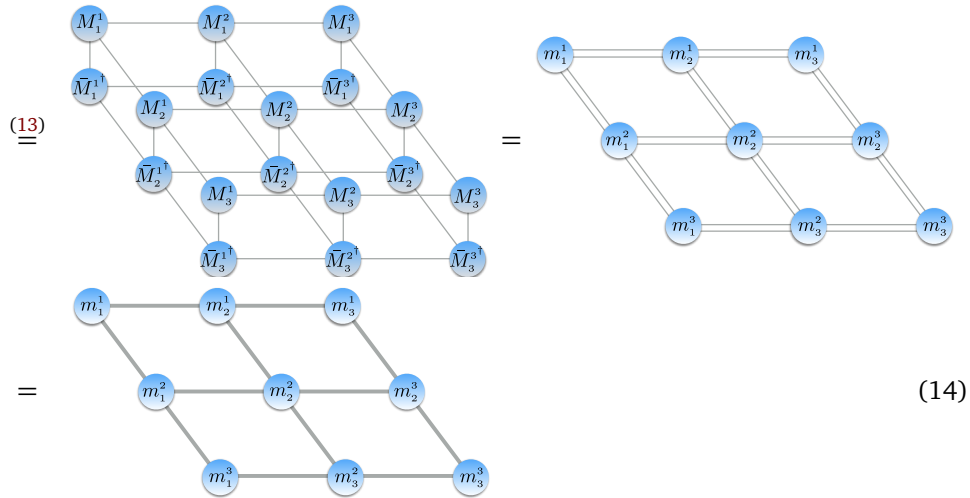
To reduce the complexity of the TN diagrams appearing in the following, we introduce a modified version of the conjugate tensor that automatically accounts for the index bending discussed in Eq. (12):

$$\text{Diagram of } M_y^{x\dagger} \text{ with bent lines} = \text{Diagram of } \bar{M}_y^{x\dagger} \text{ with straight lines}. \quad (13)$$

This distinction may seem unnecessary at this point, since $\bar{M}_y^{x\dagger}$ and $M_y^{x\dagger}$ are mathematically equivalent objects in the context of bosons. However, this is not the case for fermionic systems [c.f. Eq. (61)]. Therefore, we emphasize the importance of this modification already here.

The scalar product $\langle\psi|\psi\rangle$ for this simple example is obtained by contracting all physical and virtual index of the nine m tensors,

$$\langle\psi|\psi\rangle = \text{Diagram of 9 } m \text{ tensors} = \text{Diagram of 9 } m \text{ tensors with index bending}$$



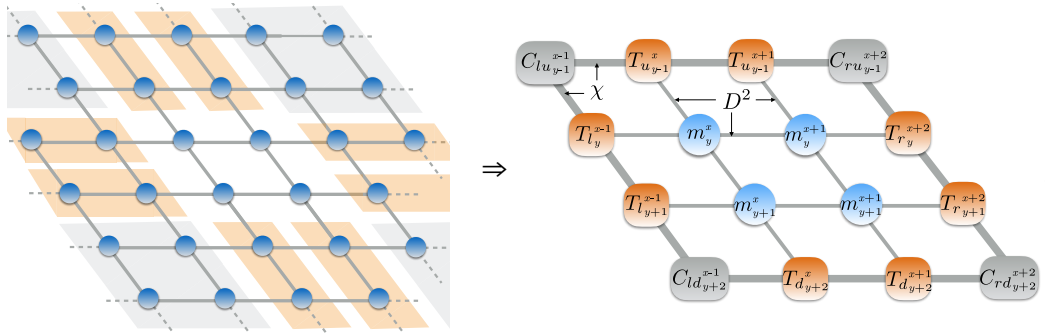
Note that the second step (\equiv^*) also exploits the non-uniqueness of the diagrammatic representation by employing a number of so-called “jump-moves” [45]. In these operations, it is possible to drag a line over a tensor without changing the corresponding TN. For example, the line connecting M_3^2 and M_3^3 was dragged downward across $M_2^{3\dagger}$. Again, this modification is trivial in context of bosonic PEPS, but nontrivial for fermionic PEPS [see Sec. 4].

Studying the small tensor networks in Eq. (14), it becomes obvious that the exact contraction of the expression scales exponential with system sizes. No matter in which order one decides to contract the tensors, i.e., which “contraction pattern” one uses, one always generates an object with a number of open indices scaling with L (here $L = 3$).

3.3.1 Corner transfer matrix scheme

Since it is not possible to perform the exact calculation of a scalar product efficiently in the PEPS nor in the iPEPS framework, one has to rely on approximate approaches. A particularly powerful contraction scheme is based on ideas of the corner transfer matrix (CTM) renormalization group proposed by Nishino and Okunishi [57]. Their idea was later adapted by Orús and Vidal [58] in the context of quantum systems to efficiently evaluate an iPEPS tensor network contraction.

The key insight of the approach is to represent the infinitely large tensor network by a small number of tensors, zooming into a 1×1 or 2×2 window of sites (in general, this might be only a subset of the full unit cell, which in general has the size $L_x \times L_y$). The rest of the system, the so-called “environment”, is represented by a set of corner matrices C and transfer tensors T . For the 2×2 subset embedded in the environment, this takes the form



where the environmental tensor network is represented by a set of four corner matrices ($C_{lu}, C_{ld}, C_{ru}, C_{rd}$ with subscripts denoting the spatial location, i.e., l, r, u, d stand for left,

right, up, down, respectively), and eight transfer tensors (two tensors for each direction, T_l, T_r, T_u, T_d , respectively). In this representation, a new set of virtual indices is introduced connecting tensors of the environment only. As we discuss below, the dimension χ of these indices acts as additional parameter controlling the accuracy of the environmental approximation (reasonable choices are $\chi \geq D^2$).

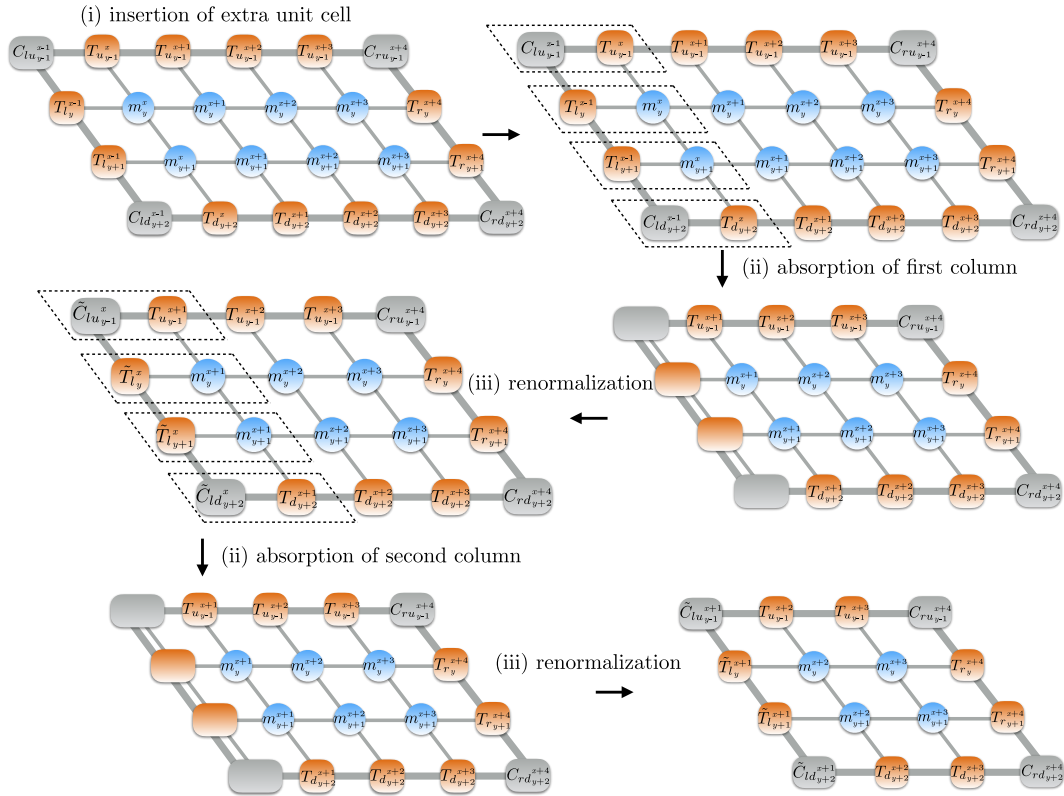


Figure 1: CTM coarse graining move to the left lattice direction: (i) extra unit cell is first inserted, and then column-wise integrated into the left part of the environment by performing two subsequent (ii) absorption and (iii) renormalization steps.

CTM protocol.– The environmental tensors are obtained by performing directional coarse graining moves in each direction of the lattice. Each coarse graining move consists of three different steps: (i) *insertion* of an extra unit cell; (ii) *absorption* of a single row or column of the unit-cell tensors into the set of environmental tensors in one lattice direction, leading to an enlarged environmental bond dimension χD^2 ; (iii) *renormalization* (or truncation/compression) of the enlarged environmental tensors to their original size. Steps (ii) and (iii) are repeated until the inserted unit cell has been fully absorbed into the set of environmental tensors in the one particular direction. Next, an additional unit cell is inserted next to the original unit cell in one of the other directions, and the move is carried out with respect to another direction of the lattice. A full coarse graining step is completed after one move in each of the four lattice directions (left, right, top, bottom) has been performed.

In the following, we illustrate this procedure for an iPEPS representation with a 2×2 unit cell, using four M tensors that all have the property $M_y^x = M_y^{x+2} = M_{y+2}^x = M_{y+2}^{x+2}$ (as in Eq.9). A directional move to the left then includes the steps illustrated in Fig. 1. Note that

the extra unit cell has been inserted horizontally on the left (this is also the case for a move to the right). Moreover, two absorption and renormalization steps are carried out, at the end of which the inserted unit cell has been fully integrated into the left part of the environment. This set of operations yields an updated set of environmental tensors for the direction of the coarse graining step.

We also sketch in Fig. 2 a coarse graining move towards the top of the lattice. In this case,

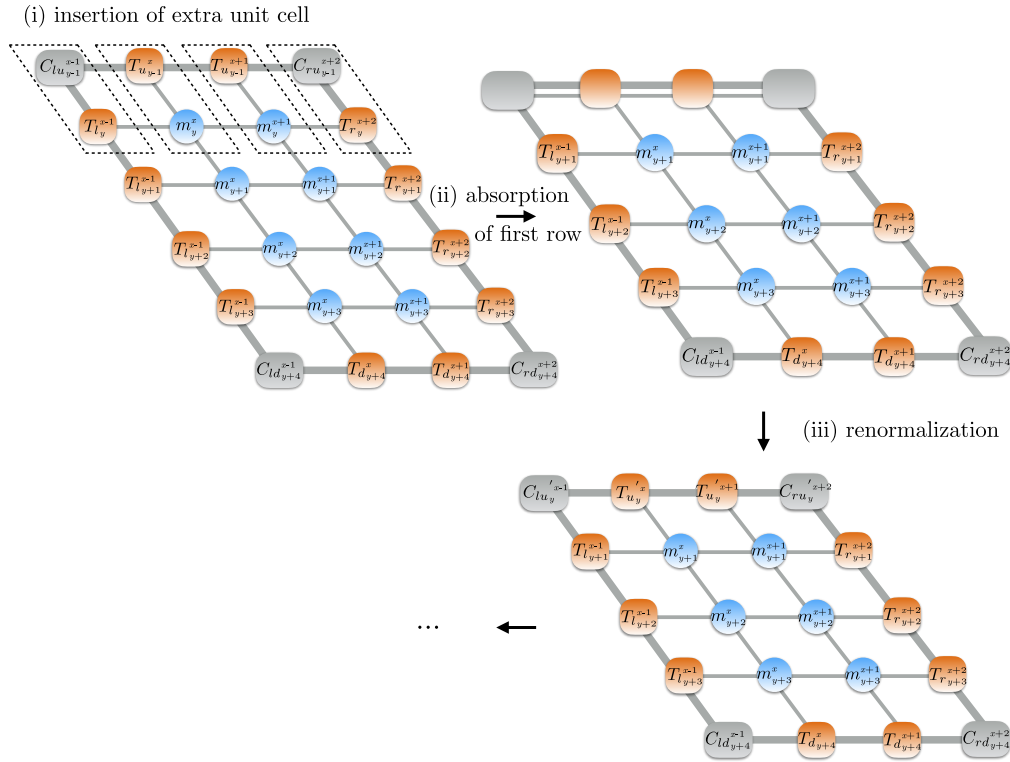


Figure 2: CTM coarse graining move to the top of the lattice: (i) extra unit cell is first inserted, and then row-wise integrated into the upper part of the environment by performing two subsequent (ii) absorption and (iii) renormalization steps (only first step is shown).

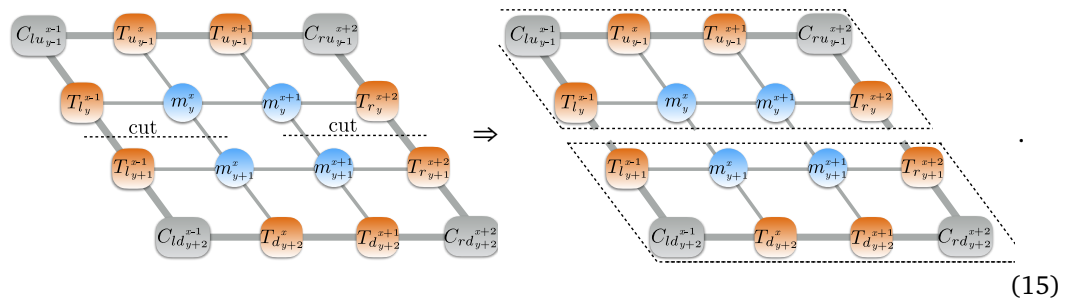
the unit cell is inserted vertically. Then we follow the same protocol as for the left move. Only the direction of the absorption and renormalization steps differs. After also carrying out these coarse graining moves with respect to the other two lattice directions, a full coarse graining step has been completed. The full cycle is typically repeated multiple times depending on the correlation length in the system. For example, for a gapped system a few (~ 10) steps may be sufficient to obtain converged results. However, for a critical system, due to the absence of the energy gap, the number of steps required to reach convergence in local observables can be significantly larger, up to $\gtrsim 100$ steps.

Renormalization.— In addition to the number of steps performed, the convergence of the results also strongly depends on the implementation of the renormalization step, which truncates the environmental tensors after the absorption step. The renormalization is crucial for the performance of the CTM scheme. However, its implementation details are not very straightforward, and currently there seems to be ample room for future improvement. The ambiguity of implementation details is mostly caused by the lack of an exact canonical representation for

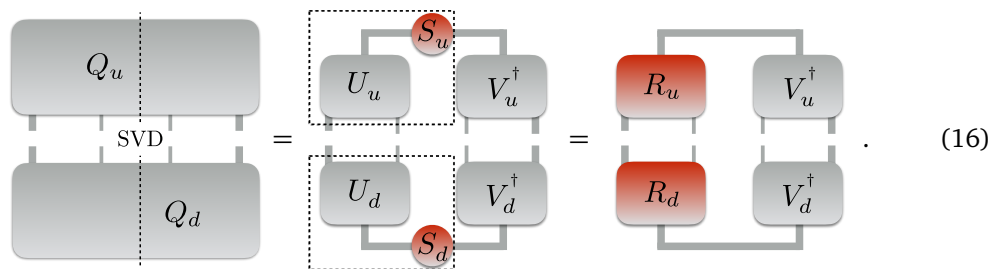
a PEPS TN, which implies that there is no obvious optimal way of performing the truncation (in contrast to an MPS tensor network, which can be truncated optimally even in the context of translationally invariant systems [60]).

We list and comment on a number of different renormalization schemes. One corresponds to the directional updated scheme proposed by Orús and Vidal in Ref. [58], which we found to work well only in the context of very homogenous wavefunctions. This method takes only small subsets of the environment into account and implicitly assumes full translational invariance when generating the projectors (or isometries) to perform the truncation. This ultimately yields a very biased truncation pattern for inhomogeneous systems, where this method is bound to fail. The second approach is based on the original CTMRG of Nishino and Okunishi [57] and was first employed by Corboz, Jordan and Vidal Ref. [24] in the context of iPEPS. In this case, the full environment is taken into account in each truncation step, which presents a crucial advantage for simulating inhomogeneous states. On the other hand, it is severely limited by machine precision, making it unstable for large values of environmental bond dimension χ . This is far from ideal since it is desirable to use χ as additional control parameter. To overcome these shortcomings, Corboz, Rice and Troyer Ref. [6] introduced a third CTM variant that shows strongly improved convergence properties in comparison to the original CTMRG scheme and, at the same time, overcomes the inhomogeneity issues of the directional updated scheme. In the following, we sketch how to obtain the projectors used to reduce the sizes of the environmental tensors after an absorption step in the left direction, following Ref. [6]. The protocol works similarly for the other spatial directions of the lattice.

In the first step, we enforce two cuts in the tensor network consisting of the 2×2 unit-cell subset embedded in the effective environment as follows



Our goal is to obtain projectors (or isometries) that are inserted after an absorption step at a specific bond to “project” (or truncate/compress) the enlarged environmental Hilbert space $D^2\chi$ back to its original size χ . In this example, we specifically aim for the projectors to be inserted into the two bonds split by the left cut.¹ To this end, we contract the two upper and lower parts of the tensor network, leading to rank-4 tensors Q_u and Q_d . By applying a singular value (or QR) decomposition to both of these tensors, we obtain



¹Analogously, we could use (15) to obtain the projectors for the two split bonds on the right. This becomes necessary when performing a CTM move into the right direction of the lattice.

The product $R_u R_d$ is then subjected to an additional SVD where only the χ largest singular values are kept,

$$\begin{array}{c} R_u \\ R_d \end{array} = \text{SVD} \approx \begin{array}{c} U \\ S \\ V^\dagger \end{array} \Rightarrow \begin{array}{c} R_d^{-1} \\ R_u^{-1} \end{array} \approx \begin{array}{c} V \\ S^{-1} \\ U^\dagger \end{array} \quad (17)$$

Using the inverse matrices R_u^{-1} and R_d^{-1} , we generate the projectors P_y^x, \tilde{P}_y^x that are inserted at the left cut of the tensor network (15):

$$\mathbb{I} = \begin{array}{c} R_d \\ R_d^{-1} \\ R_u^{-1} \\ R_u \end{array} \approx \begin{array}{c} R_d \\ V \\ \sqrt{S^{-1}} \\ \sqrt{S^{-1}} \\ U^\dagger \\ R_u \end{array} = \begin{array}{c} \tilde{P}_y^x \\ P_y^x \end{array} \quad (18)$$

The protocol is repeated for the entire row of the unit cell to be absorbed into the environment during this particular coarse graining step (i.e., L_y times). In our example of an 2×2 unit cell, we therefore also obtain P_{y+1}^x and \tilde{P}_{y+1}^x (or alternatively P_{y-1}^x and \tilde{P}_{y-1}^x due to translational invariance) by considering the tensor network and repeating the procedure sketched above,

$$\begin{array}{c} C_{lu_y}^{x-1} \quad T_{u_y}^x \quad T_{u_y}^{x+1} \quad C_{ru_y}^{x+2} \\ T_{y+1}^{x-1} \quad m_{y+1}^x \quad m_{y+1}^{x+1} \quad T_{y+1}^{x+2} \\ \text{--- cut ---} \\ T_{y+2}^x \quad m_{y+2}^x \quad m_{y+2}^{x+1} \quad T_{y+2}^{x+2} \\ C_{ld_{y+3}}^{x-1} \quad T_{d_{y+3}}^x \quad T_{d_{y+3}}^{x+1} \quad C_{rd_{y+3}}^{x+2} \end{array} \Rightarrow \begin{array}{c} \tilde{P}_{y+1}^x \\ P_{y+1}^x \end{array} = \begin{array}{c} \tilde{P}_{y-1}^x \\ P_{y-1}^x \end{array} \quad (19)$$

Now we are fully equipped to renormalize the entire set of environmental tensor which are

subject to truncation during an absorption step to the left,

$$\begin{array}{c}
 C l_{y-1}^{x-1} \quad T u_{y-1}^x \\
 \downarrow \tilde{P}_{y-1}^x \\
 \tilde{P}_{y-1}^x \\
 \downarrow T l_y^{x-1} \quad m_y^x \\
 \tilde{P}_y^x \\
 \tilde{P}_y^x \\
 \downarrow T l_{y+1}^{x-1} \quad m_{y+1}^x \\
 \tilde{P}_{y+1}^x \\
 \tilde{P}_{y+1}^x \\
 \downarrow C l_{y+2}^{x-1} \quad T d_{y+2}^x \\
 \tilde{C} l_{y-1}^x \\
 \tilde{T} l_y^x \\
 \tilde{T} l_{y+1}^x \\
 \tilde{C} l_{y+2}^x
 \end{array} = \dots \tag{20}$$

What has been achieved is a scheme that compressed the bond dimensions of the environmental tensors along the left row in a way that encodes information from the full environment. Thus we can appropriately deal with translational symmetry breaking in the iPEPS wavefunction. At the same time, this procedure leads to numerically stable results since we can eliminate spurious parts of the SVD spectrum during the intermediate SVD decompositions in Eq. (16) by discarding very small singular values (e.g., $< 10^{-7}$). This helps to reduce the influence of numerical noise in the subsequent steps.

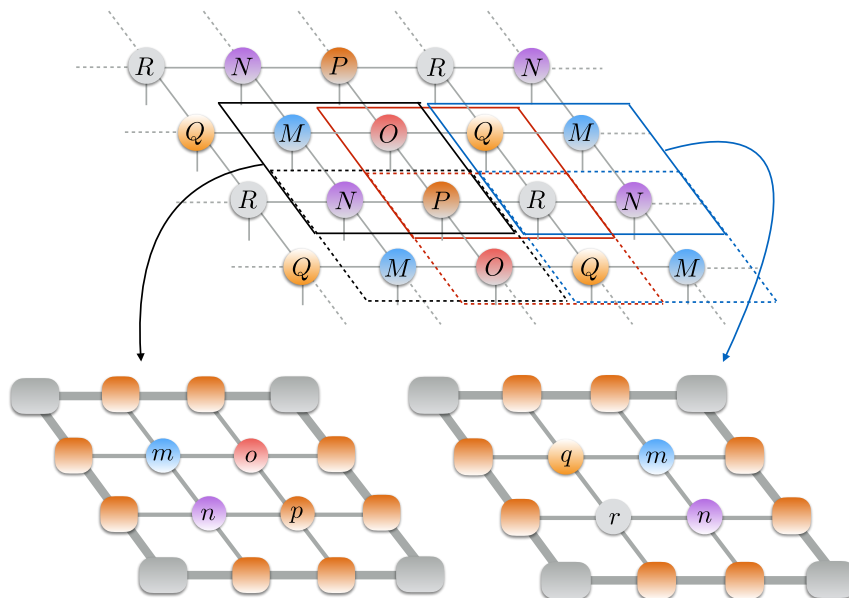


Figure 3: A unit cell of size 3×2 consists of six different M tensors (here denoted $M, N, O, P, Q,$ and R). For each of the six relative coordinates in the unit cell, we have to obtain a 2×2 CTM representation (indicated by the solid and dashed squares, and explicitly illustrated for two examples). Therefore, the CTM scheme here requires storing 24 corner matrices and 24 transfer tensors in total.

Larger unit cells.– The CTM scheme can also deal with rectangular unit cells of arbitrary

sizes containing $L_x \times L_y = N$ different M tensors, where the relative position of each tensor in the unit cell is labeled by its coordinate $\mathbf{r} = (x, y)$. To this end, we assign one set of corner matrices and transfer tensors to *each* coordinate, requiring a total number of $4N$ corner matrices and $4N$ transfer tensors to be stored independently. We illustrate this approach for a 3×2 unit cell in Fig. 3. After initialization (see below), the environmental tensors are then iteratively updated by performing coarse graining moves in all four lattice directions, as outlined above. However, an entire CTM cycle now includes L_x coarse graining steps to the left and right, respectively, as well as L_y coarse graining steps to the top and L_y to the bottom of the lattice. Note that using a larger zooming window is not an option, since the numerical costs quickly become unfeasible.

Initialization.– While covering the coarse graining procedure to obtain the converged environmental tensors, we have not yet discussed the initialization of the CTM scheme. In principle, one could start from an arbitrary set of corner matrices and transfer tensors. However, choosing a completely random set can significantly increase the number of coarse graining steps required for obtaining a stable environment TN and sometimes even cause numerical instabilities. In practice, we found that optimal convergence is achieved by starting from an environmental tensor set formed by the corresponding M_y^x tensors and their conjugates, which previously have been generated by means of ground-state optimization [see Sec. 3.5]. We illustrate this initialization procedure for two examples,

$$C_{l_y^x} = \text{network of } M_y^x \text{ and } M_y^{x\dagger}, \quad T_{l_y^x} = \text{network of } M_y^x \text{ and } M_y^{x\dagger}. \quad (21)$$

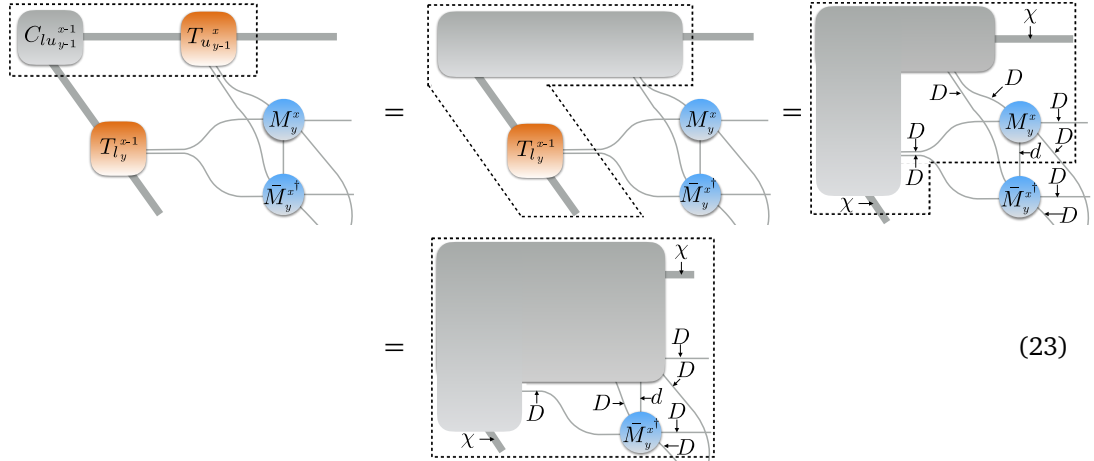
Effective contraction pattern.– The numerical costs of implementing the square-lattice CTM scheme presented above scales as $\mathcal{O}(D^6 \chi^3)$, with iPEPS bond dimension D and environmental bond dimension χ . Note that these costs are equivalent to those of the infinite MPS method from Ref. [43]. Assuming that $\chi = \mathcal{O}(D^2)$, we end up with a total cost scaling of $\mathcal{O}(D^{12})$ for the iPEPS algorithm. The underlying assumption behind this cost scaling is that all contractions are carried out as efficiently as possible, which forces us to pay some attention to the contraction patterns. In particular, we cannot directly work with the reduced tensors m_y^x , but rather need to perform contractions involving M_y^x and its conjugate $M_y^{x\dagger}$ sequentially.

This is illustrated below for contracting a part of the diagram in Eq. (15). First consider the case explicitly using the reduced tensor m_y^x ,

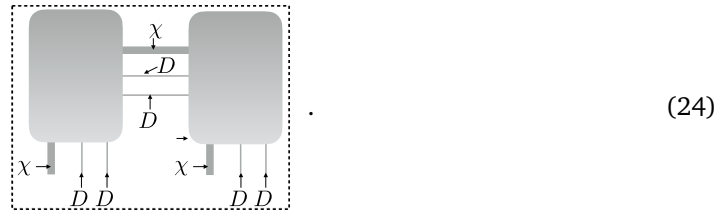
$$\text{network of } C_{l_{y-1}^{x-1}}, T_{l_{y-1}^x}, T_{l_y^{x-1}}, m_y^x = \text{intermediate contraction} = \text{L-shaped block with } \chi, D^2. \quad (22)$$

Counting the involved indices in the dashed box, it becomes clear that the last contraction step scales rather unfavorably as $\mathcal{O}(D^8 \chi^2)$.

If we want to achieve the optimal scaling $\mathcal{O}(D^6 \chi^2 d)$ in this step, we have to contract over M_y^x and $M_y^{x\dagger}$ sequentially,



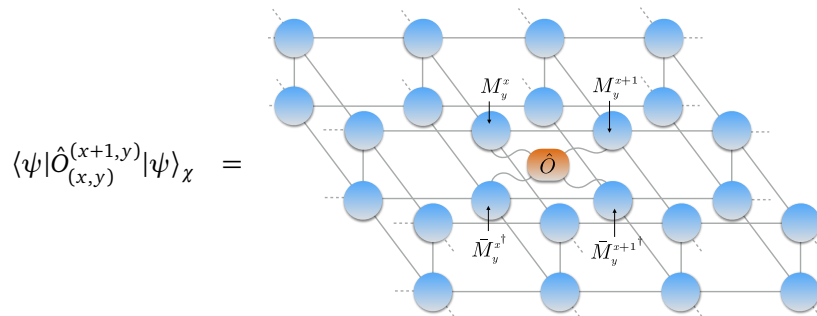
The same applies to contraction orders of other TN such as, for example, the one shown in Eq. (20) and many others. It pays off to constantly pay attention and ensuring that the optimal contraction pattern is used when implementing an iPEPS algorithm. Otherwise, the backlash of an inefficient iPEPS implementation will quickly become apparent, since simulations with moderate to large D will not be feasible. Note that the most expensive steps of the CTM algorithm occur when generating the projectors. To obtain the tensor Q_u in Eq. (16), for instance, one has to perform the contraction,



This always yields a cost scaling of $\mathcal{O}(\chi^3 D^6)$ which cannot be reduced further.

3.4 Expectation value

The CTM scheme enables us to evaluate observables within the iPEPS framework. For this case, we consider a simple two-site observable $\hat{O}_{(x,y)}^{(x+1,y)}$ which, for example, represents a spin-spin correlation function involving two neighboring sites. To compute an approximation for the expectation value $\langle \hat{O}_{(x,y)}^{(x+1,y)} \rangle = \langle \psi | \hat{O}_{(x,y)}^{(x+1,y)} | \psi \rangle / \langle \psi | \psi \rangle$, we represent the environment of the two contiguous sites $\mathbf{r} = (x, y)$ and $\mathbf{r}' = (x, y + 1)$ in terms of the corner matrices and transfer tensors encountered in the last section,



The contraction of the final tensor network, consisting of the six environmental tensors E_1, \dots, E_6 , the two M tensors, their conjugates, and the operator \hat{O} can be carried out efficiently. It produces an approximation of $\langle \psi | \hat{O}_{(x,y)}^{(x+1,y)} | \psi \rangle \approx \langle \psi | \hat{O}_{(x,y)}^{(x+1,y)} | \psi \rangle_\chi$ which is generally expected to deviate from the exact value due to the non-exact representation of the full tensor network. The correct value of $\langle \psi | \hat{O}_{(x,y)}^{(x+1,y)} | \psi \rangle / \langle \psi | \psi \rangle \approx \langle \psi | \hat{O}_{(x,y)}^{(x+1,y)} | \psi \rangle_\chi / \langle \psi | \psi \rangle_\chi$ should be recovered in the limit $\chi \rightarrow \infty$. In practice, one evaluates Eq. (25) for a number of different values of $\chi = 10, 20, \dots, 100, 150, \dots$ until the observable shows no more significant dependence on χ . The required value for χ to obtain converged results strongly varies depending on the physical properties of the corresponding system and the employed iPEPS bond dimension D . If one is already well within the relevant low-energy critical regime, it can therefore be useful to extrapolate observables towards $1/\chi \rightarrow 0$ and $1/D \rightarrow 0$ [62, 63]. A theoretical justification for such an approach is based on the theory of finite entanglement scaling, which has been well analyzed in the one-dimensional scenario [64–67].

3.5 Ground state search

An iPEPS is an approximate representation for the ground-state wavefunction of a local Hamiltonian on a two-dimensional lattice. Having addressed the contraction issue by means of the CTM scheme [see previous Sec. 3.3], the remaining open question concerns finding the ground-state iPEPS representation, given some Hamiltonian \hat{H} with only nearest-neighbor interactions. (Albeit technical more complicated, iPEPS can also treat longer-ranged interactions, for more details see Ref. [24, 38].)

Here we follow the strategy proposed in the original iPEPS formulation by Jordan, Orús, Vidal, Verstraete and Cirac [43], and use the imaginary time evolution to target the ground state,

$$|\psi_0\rangle = \lim_{\tau \rightarrow \infty} \frac{e^{-\tau \hat{H}} |\psi\rangle}{\|e^{-\tau \hat{H}} |\psi\rangle\|}. \tag{26}$$

The time-evolution operator $e^{-\tau \hat{H}}$ is further decomposed by Suzuki-Trotter decomposition,

$$e^{-\hat{H}\tau} \approx \prod_{j=1}^{N_b} e^{-\hat{h}_{y,y'}^{x,x'} \tau} + \mathcal{O}(\tau^2), \tag{27}$$

where $\hat{h}_{y,y'}^{x,x'}$ describes the local interaction terms acting on a pair of nearest-neighbor sites in the unit cell, and $\hat{H} = \sum_{((x,y),(x',y'))} \hat{h}_{y,y'}^{x,x'}$. The two-site gates, $e^{-\hat{h}_{y,y'}^{x,x'}\tau}$, are subsequently applied to the corresponding pairs of M tensors, M_y^x and $M_{y'}^{x'}$. As in the case of MPS, the resulting tensor has to be truncated accordingly to restore the original form of the iPEPS representation.

In the MPS framework, the truncation can be implemented in an optimal way using the canonical form of the MPS and employing a single singular value decomposition. In the context of iPEPS, this step turns out to be more evolved. Due to the lack of an exact canonical form for the iPEPS, one has to rely on approximate techniques to account for the effects of the environment when employing the truncation. This can be done using several different optimization schemes, such as the *simple update* [68] and the *full update* [43]. We discuss both of these approaches extensively in the rest of this section.

Although not employed in the context of this review, we also note that two groups recently introduced alternative optimization schemes, which do not rely on imaginary time evolution [21, 22]. Instead, they implement a variational update method,

$$\min_{\{M_y^x\}} [E_0] = \frac{\langle \psi_0 | \hat{H} | \psi_0 \rangle}{\langle \psi_0 | \psi_0 \rangle}. \quad (28)$$

The major technical challenge of these newly developed schemes is to find an approximate, yet accurate, representation for the full Hamiltonian \hat{H} . Corboz [21] achieves this based on a modified CTM scheme, while Vanderstraeten, Haegeman, Corboz and Verstraete [22] build on MPS techniques. In addition, it is still unclear how to optimally translate the local update performed on a pair of tensors to the iPEPS representation in the infinite system. Despite these issues, both variational optimization techniques already obtain very impressive results, illustrating that the iPEPS formalism will continuously improve and become more competitive in the near future.

3.5.1 Bond projection

In this work, we only consider the optimization via imaginary-time evolution based on two-site Trotter gates, which implies that we constantly have to update two neighboring M tensors at once (i.e., there is no one-site version of this algorithm). Hence, it is essential to perform the tensor updates as efficiently as possible. Treating the full M tensors in this context turns out to be numerically very inefficient (i.e., numerical costs of $\mathcal{O}(D^{12})$ in the context of the full update). Instead, it is always advisable to perform the tensor update on two subtensors with lower rank which are easily obtained by a bond projection [69], leading to a significant cost reduction (i.e., $\mathcal{O}(D^6 d^3)$) [47]. Note that this scheme does not introduce further approximations since the two-site Trotter gate only changes properties of the corresponding bond but leaves the remaining bonds of the iPEPS tensors unchanged.

The bond projection is obtained by performing two exact SVD (or QR) decompositions:

$$\begin{aligned}
 & \begin{array}{c} \text{---} \\ | \sigma_y^x \rangle \\ \text{---} \end{array} M_y^x \begin{array}{c} \text{---} \\ | \sigma_y^{x+1} \rangle \\ \text{---} \end{array} M_y^{x+1} \\
 &= \begin{array}{c} \text{---} \\ | \sigma_y^x \rangle \\ \text{---} \end{array} M_y^x \begin{array}{c} \text{---} \\ | \sigma_y^{x+1} \rangle \\ \text{---} \end{array} M_y^{x+1} \\
 &= \begin{array}{c} \text{---} \\ | \sigma_y^x \rangle \\ \text{---} \end{array} \text{SVD} \text{---} \text{SVD} \begin{array}{c} \text{---} \\ | \sigma_y^{x+1} \rangle \\ \text{---} \end{array} \\
 &= \begin{array}{c} \text{---} \\ | \sigma_y^x \rangle \\ \text{---} \end{array} X_y^x \begin{array}{c} \text{---} \\ | \sigma_y^x \rangle \\ \text{---} \end{array} v_y^x \begin{array}{c} \text{---} \\ | \sigma_y^{x+1} \rangle \\ \text{---} \end{array} w_y^{x+1} \begin{array}{c} \text{---} \\ | \sigma_y^{x+1} \rangle \\ \text{---} \end{array} Y_y^{x+1} \text{---} . \quad (29)
 \end{aligned}$$

The tensor optimization now only affects the subtensors v_y^x and w_y^{x+1} , whereas the remaining bonds are shifted into the subtensors X_y^x and Y_y^{x+1} , which can be treated as parts of the environment tensor network during the optimization.

Each tensor update is initialized by applying the corresponding Trotter gate in the bond projection,

$$\begin{aligned}
 e^{-\hat{h}_{y,y}^{x,x+1}\tau} |\psi\rangle &= \text{Diagram 1} \\
 &= \text{Diagram 2} \\
 &= \text{Diagram 3} = |\psi(\tilde{v}, \tilde{w})\rangle. \quad (30)
 \end{aligned}$$

The Trotter gate increases the initial bond dimension D of the subtensors v_y^x and w_y^{x+1} . Restoring the original representation exactly yields a pair of enlarged subtensors \tilde{v}_y^x and \tilde{w}_y^{x+1} with bond dimension dD (illustrated by the increased line thickness in Eq. (30)). In a next step, we have to find an appropriate truncation scheme to obtain a pair of subtensors v_y^x and w_y^{x+1} with the original bond dimension D to prevent an exponential blowup of the iPEPS tensors.

In the following, we present two different truncation methods: (i) the simple update [68], a numerically very efficient and fast approach which, however, relies on a strong simplification of the environmental tensor network and thus carries out the truncation in a suboptimal way; (ii) the full update scheme [43] which leads to an optimal truncation by incorporating the effects of the entire wavefunction appropriately. However, the full update comes at the price of requiring significantly more numerical resources.

3.5.2 Simple update

The simple update, introduced by Jiang, Weng and Xiang Ref. [68] is formulated in a slightly modified iPEPS representation. So far, we only dealt with M tensors located directly at sites of the lattice. For the simple update we put an extra set of tensors on the bonds of the iPEPS tensor network. These tensors, here labeled λ_y^x for horizontal and $\tilde{\lambda}_y^x$ for vertical bonds, are diagonal matrices similar to those used in Vidal’s TEBD and iTEBD formulation for time-evolving matrix product states [59, 70].

Starting from the standard iPEPS representation that has been adopted in this review, so

far, it requires only a minor adaption to translate into this modified representation,

$$M_y^x = \Gamma_y^x \begin{matrix} \lambda_{y-1}^{x-1/2} \\ \lambda_y^{x-1/2} \\ \lambda_y^{x+1/2} \\ \lambda_{y+1}^{x+1/2} \end{matrix}, \quad (31)$$

where Γ_y^x in combination with the roots of all four bond tensors yields the original M_y^x tensor. The key idea of the simplified update is to approximate the full environment of two neighboring sites, $\mathbf{r} = (x, y)$ and $\mathbf{r}' = (x + 1, y)$, by only the diagonal tensors surrounding this pair of sites. This procedure is adopted from MPS-based time evolution via the iTEBD algorithm.

To perform the simple update explicitly, we switch first into the bond projection to carry out the optimization more efficiently. We illustrate the projection here explicitly since different tensors are involved in the modified iPEPS representation,

$$\begin{aligned} & \left[\Gamma_y^x \right] \left[\Gamma_y^{x+1} \right] = \left[\tilde{\Gamma}_y^x \right] \left[\tilde{\Gamma}_y^{x+1} \right] \\ & = \left[X_y^x \right] \left[v_y^x \right] \left[w_y^{x+1} \right] \left[Y_y^{x+1} \right]. \quad (32) \end{aligned}$$

Now the Trotter gate is applied to the subtensors on the bond, adding entanglement and potentially increasing the bond dimension to dD . To obtain the pair of subtensors $v_y^{x'}$ and $w_y^{x'+1}$ with the original bond dimension D , the simple update relies on a simple SVD,

$$\begin{aligned} & \left[\Gamma_y^x \right] \left[\Gamma_y^{x+1} \right] e^{-\hat{h}_{y,y}^{x,x+1} \tau} = \left[X_y^x \right] \left[v_y^x \right] \left[w_y^{x+1} \right] \left[Y_y^{x+1} \right] e^{-\hat{h}_{y,y}^{x,x+1} \tau} \\ & = \left[X_y^x \right] \left[\text{SVD} \right] \left[Y_y^{x+1} \right] \\ & = \left[X_y^x \right] \left[v_y^{x'} \right] \left[w_y^{x'+1} \right] \left[Y_y^{x+1} \right] \\ & = \left[Q_y^x \right] \left[\lambda_y^{x'} \right] \left[Q_y^{x+1} \right]. \quad (33) \end{aligned}$$

No extra iteration or optimization is required to complete the update (hence, the name “simple” update). The updated diagonal bond matrix $\lambda_y^{x'}$ contains the D largest singular values, the optimized subtensors are obtained from $v_y^{x'} = U$ and $w_y^{x'+1} = V^\dagger$.

To restore the form of the iPEPS tensors from Q_y^x and Q_y^{x+1} , we apply the inverse of the additional bond tensors, which have not been altered by this optimization step,

$$\Gamma'_y{}^x = \text{diag}(\lambda_y^{x-1}) \circ Q_y^x \circ \text{diag}(\lambda_y^{x-1}), \quad \Gamma'_y{}^{x+1} = \text{diag}(\lambda_y^{x-1}) \circ Q_y^{x+1} \circ \text{diag}(\lambda_y^{x-1}). \quad (34)$$

The simple update is particularly appealing due to its low complexity and high numerical efficiency; the truncation based on a plain SVD in Eq. (33) only scales with $\mathcal{O}(D^3 d^6)$ operations. Yet, the truncation itself cannot be considered optimal in the context of iPEPS. It would have been optimal if we had gauged the surrounding bonds in such a way that they exclusively contain orthonormal basis sets. Unfortunately, this is only possible if the environment is separable, as in the case of MPS or other tensor networks *without loops*. In fact, one can show that a tensor optimization performed in this way presents an optimal update for an infinite tensor network on a Bethe lattice [69].

Any iPEPS representation on a standard 2D lattice, however, does feature loops, which means that we cannot separate the environment into two blocks and find a gauge with orthonormal basis sets on all surrounding bonds. Hence, the simple update introduces a systematic error, as it does not properly account for the full environment of the bond during the optimization. The magnitude of this error turns out to be less severe than one might expect. Especially for systems in gapped phases, the simple update leads to excellent results [45]. Moreover, its numerical efficiency often allows simulations with larger bond dimensions compared to the full update; thus it can give access to complex systems which remain out of reach for full-update calculations.

We conclude this section with a few practical comments concerning the implementation of the simple update:

- For a generic unit cell, the simple update is employed sequentially on all bonds in the system. One can easily work with a second-order Trotter decomposition by reversing the application order of the gates in every second step.
- The normalization of the tensor network can be conveniently achieved on the fly by normalizing the trace of each updated diagonal bond matrix λ_y^x to unity. This procedure leads to a numerically fully stable algorithm.
- To obtain a meaningful representation of the ground state by means of imaginary-time evolution, we start from a random set of tensors and use a fairly large time step $\tau = \mathcal{O}(10^{-1})$. A large initial time step is important since it minimizes the risk of getting stuck in a local energy minimum and, in case of symmetric iPEPS implementation, it enables us to dynamically adapt the symmetry sectors on the bonds (starting from a very small time step, one can get stuck in the initial symmetry configuration and not reach all relevant sectors). To decrease the effect of the Trotter error, we then gradually reduce τ as soon as we observe convergence with respect to the SVD spectra (typically after a few hundred or thousand time steps). After reaching a time step of the order $\mathcal{O}(10^{-5})$, the ground-state wavefunction is typically converged.
- Measurements of observables are performed with the converged iPEPS representation, obtained from the simple update, as input for the CTM scheme. Relying on CTM, this leads to a total numerical cost scaling of $\mathcal{O}(\chi^3 D^6)$, which is, in principle, equivalent to the cost scaling of the full update. In the latter, however, the full environment has to be calculated in every step and not just at the end to perform measurements.

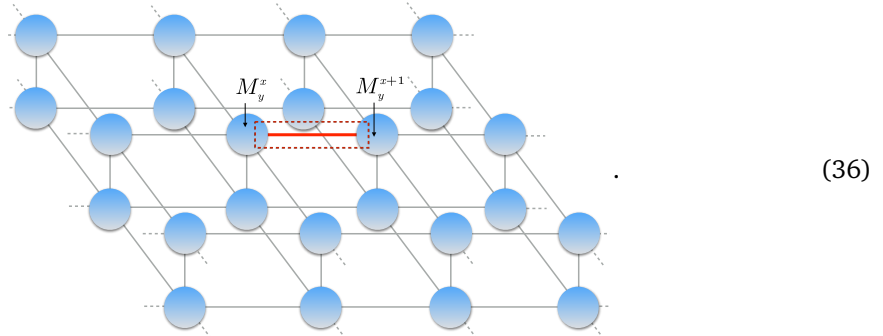
3.5.3 Full update

The full update introduced by Jordan, Orús, Vidal, Verstraete and Cirac [43] represents a clean and accurate protocol for performing the tensor update during imaginary-time evolution. Its name is derived from the fact that the effects of the entire wavefunction on the bond tensors are considered, including the full environmental TN. The only approximation stems from the non-exact contraction of the environmental TN, which we carry out based on the CTM scheme [see Sec. 3.3.1].

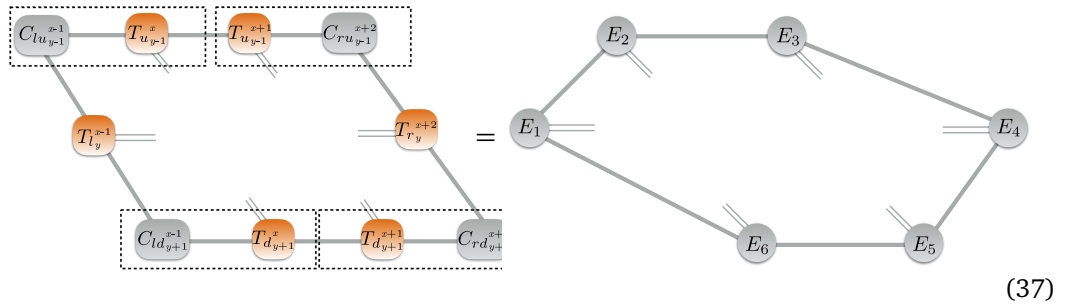
After the application of the Trotter gate in Eq. (30), the full update generates the optimized pair of subtensors v_y^x and w_y^{x+1} with bond dimension D by minimizing the squared norm between $|\psi(v', w')\rangle$ and the wavefunction $|\psi(\tilde{v}, \tilde{w})\rangle$ containing the exact subtensors \tilde{v}_y^x and \tilde{w}_y^{x+1} with enlarged bond dimension dD ,

$$d(\tilde{v}, \tilde{w}, v', w') = \left\| |\psi(v', w')\rangle - |\psi(\tilde{v}, \tilde{w})\rangle \right\|^2. \quad (35)$$

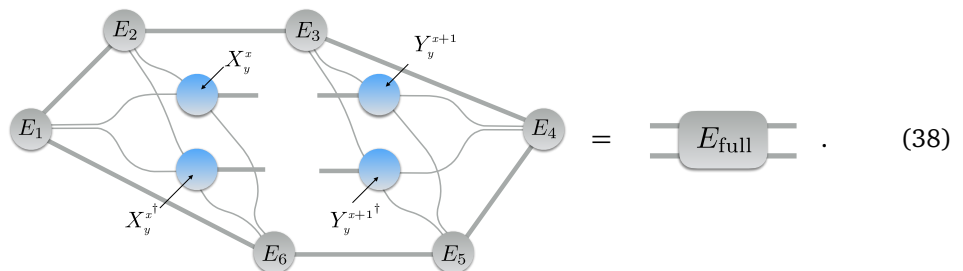
To minimize Eq. (35) with respect to v_y^x and w_y^{x+1} , we first have to obtain an effective representation of the environment with respect to the bond to be updated (marked red):



This is achieved via the CTM scheme, leading to an approximate representation of the environment in terms of corner matrices and transfer tensors,



As in the case of the simple update, we carry out the tensor update for efficiency reasons in the bond projection, as discussed above. In order to generate the full environment in this representation, we have to account for the subtensors X_y^x and Y_y^{x+1} as well as their conjugates, and multiply them to the effective environment shown in Eq. (37), obtaining



In this way, it is possible to represent the cost function (35) diagrammatically,

$$\begin{aligned}
 & d(\tilde{v}, \tilde{w}, v', w') \\
 &= \langle \psi(v', w') | \psi(v', w') \rangle + \langle \psi(\tilde{v}, \tilde{w}) | \psi(\tilde{v}, \tilde{w}) \rangle - \langle \psi(v', w') | \psi(\tilde{v}, \tilde{w}) \rangle - \langle \psi(\tilde{v}, \tilde{w}) | \psi(v', w') \rangle \\
 &= \begin{array}{c} \begin{array}{c} \begin{array}{c} v'_y{}^x \quad w'_y{}^{x+1} \\ \text{---} \\ E_{\text{full}} \\ \text{---} \\ v'_y{}^{x\dagger} \quad w'_y{}^{x+1\dagger} \end{array} \\ + \\ \begin{array}{c} \begin{array}{c} \tilde{v}_y{}^x \quad \tilde{w}_y{}^{x+1} \\ \text{---} \\ E_{\text{full}} \\ \text{---} \\ \tilde{v}_y{}^{x\dagger} \quad \tilde{w}_y{}^{x+1\dagger} \end{array} \end{array} \\ - \\ \begin{array}{c} \begin{array}{c} \tilde{v}_y{}^x \quad \tilde{w}_y{}^{x+1} \\ \text{---} \\ E_{\text{full}} \\ \text{---} \\ v'_y{}^{x\dagger} \quad w'_y{}^{x+1\dagger} \end{array} \\ - \\ \begin{array}{c} \begin{array}{c} v'_y{}^x \quad w'_y{}^{x+1} \\ \text{---} \\ E_{\text{full}} \\ \text{---} \\ \tilde{v}_y{}^{x\dagger} \quad \tilde{w}_y{}^{x+1\dagger} \end{array} \end{array} \end{array} \quad (39)
 \end{aligned}$$

$d(\tilde{v}, \tilde{w}, v', w')$ is a quadratic function of the tensors $v'_y{}^x$ and $w'_y{}^{x+1}$. Thus, the optimized subtensors can be found using an alternating least-square algorithm [43].

To this end, we can first optimize $v'_y{}^x$ while keeping $w'_y{}^{x+1}$ fixed. Analogous to the MPS compression, we form the partial derivative of Eq. (39) with respect to $v'_y{}^{x\dagger}$,

$$\frac{\partial}{\partial v'^{\dagger}} d(\tilde{v}, \tilde{w}, v', w') \stackrel{!}{=} 0 \Rightarrow \begin{array}{c} \begin{array}{c} \boxed{v'_y{}^x} \quad w'_y{}^{x+1} \\ \text{---} \\ E_{\text{full}} \\ \text{---} \\ w'_y{}^{x+1\dagger} \end{array} \begin{array}{c} R \\ \text{---} \\ \end{array} = \begin{array}{c} \begin{array}{c} \tilde{v}_y{}^x \quad \tilde{w}_y{}^{x+1} \\ \text{---} \\ E_{\text{full}} \\ \text{---} \\ w'_y{}^{x+1\dagger} \end{array} \begin{array}{c} S \\ \text{---} \\ \end{array} \end{array} \quad (40)$$

The solution for $v'_y{}^x$ in Eq. (40) is found by inverting R . Using the bond projection, the inversion can be computed exactly with moderate numerical effort $\mathcal{O}(d^3 D^6)$. The full M tensor representation, on the other hand, leads to an unfeasible costs of $\mathcal{O}(D^{12})$ for the exact inversion, and $\mathcal{O}(D^8)$ employing approximation methods.

After obtaining the optimized subtensor $v'_y{}^x$, we next update $w'_y{}^{x+1}$ while keeping $v'_y{}^x$ fixed by forming the partial derivative of Eq. (39) with respect to $w'_y{}^{x+1\dagger}$,

$$\frac{\partial}{\partial w'^{\dagger}} d(\tilde{v}, \tilde{w}, v', w') \stackrel{!}{=} 0 \Rightarrow \begin{array}{c} \begin{array}{c} v'_y{}^x \quad \boxed{w'_y{}^{x+1}} \\ \text{---} \\ E_{\text{full}} \\ \text{---} \\ v'_y{}^{x\dagger} \end{array} \begin{array}{c} R \\ \text{---} \\ \end{array} = \begin{array}{c} \begin{array}{c} \tilde{v}_y{}^x \quad \tilde{w}_y{}^{x+1} \\ \text{---} \\ E_{\text{full}} \\ \text{---} \\ v'_y{}^{x\dagger} \end{array} \begin{array}{c} S \\ \text{---} \\ \end{array} \end{array} \quad (41)$$

The solution for w_y^{x+1} is again computed by matrix inversion of R .

This alternation process is repeated until the subtensors v_y^x and w_y^{x+1} converge. Monitoring the cost function $d(\tilde{v}, \tilde{w}, v', w')$ after every iteration step i , the convergence is detected by means of a fidelity measure which, following Phien, Bengua, Tuan, Corboz and Orús [47], can be defined as

$$f_d = |d_{i+1} - d_i|/d_0. \tag{42}$$

The alternating optimization is stopped in case f_d drops below some small threshold $\epsilon_d = \mathcal{O}(10^{-10})$ while showing no sign of large fluctuations.

Equipped with the converged subtensors v_y^x and w_y^{x+1} , the original iPEPS form is then restored,

The diagram shows two tensor equations. The first equation is $M'_y^x = X_y^x v_y^x$, where M'_y^x is a blue circle with four legs, X_y^x is a blue circle with two legs, and v_y^x is a blue rectangle with two legs. The second equation is $M'_y^{x+1} = w_y^{x+1} Y_y^{x+1}$, where M'_y^{x+1} is a blue circle with four legs, w_y^{x+1} is a blue rectangle with two legs, and Y_y^{x+1} is a blue circle with two legs. The equations are separated by a comma.

so that we can apply the next Trotter gate and repeat the full update optimization.

3.5.4 Alternative approaches

By accounting for the entire many-body wavefunction of the infinite system, the full update provides an optimization scheme that is free from the systematic error plaguing the simple update. Only the CTM representation of the effective environment induces some approximate character to the algorithm. The high accuracy of the method, however, comes at the price of drastically enhanced numerical costs since the full effective environment, in principle, has to be calculated after the application of every single Trotter gate (i.e., typically thousands of times). The fast-full update [47], where one updates the effective environment and site tensors simultaneously, offers an immediate improvement to this problem. Another possibility is the cluster update [71, 72], a hybrid version of the simple and the full update, which takes into account an improved, yet not complete version of the effective environment. Also, we note that it may be possible to achieve improvements in accuracy when computing the environment by properly removing the short-range entanglement residing in loops. To this end, it may be fruitful to combine the CTM method with other entanglement filtering algorithms, such as the Loop-TNR algorithm [73], graph-independent local truncation [74], full environment truncation [75], or entanglement branching [76].

Besides imaginary time evolution based algorithms, gradient-based energy minimization algorithms have also been found to be useful [22, 77, 78]. In particular, an automatic differentiation (AD) approach can be applied to reduce the complexity of the implementation, as the evaluation of gradients involves a huge number of summation of tensor environments [77, 79–83], which always needs to be done iteratively in any case. The prescription is generic, and may therefore also be attractive when combining AD techniques with non-abelian iPEPS in the future.

3.5.5 Gauge fixing

A well-known technical fact in the context of MPS is that the gauge degree of freedom on the bond indices can be efficiently exploited to generate a canonical representation [84]. Through the correct gauge, the effective environment of a specific bond, or rather its tensor network representation, can be replaced by identity matrices, ensuring numerical precision and stability of the MPS framework. The success of this scheme is closely linked to the fact that the environmental tensor network of an MPS is separable, such that the left and right block can be gauged independently. In the case of PEPS and iPEPS, the environment no longer factorizes

into different blocks, due to the presence of loops in the tensor network. In other words, cutting the TN at a single bond does not yield a bipartition of the system (as in the case of MPS), and therefore no full canonical PEPS or iPEPS representation exists.

Nevertheless, it is still possible to exploit the gauge degree of freedom on the bonds to improve the stability of the algorithm. Inspired by the 1D gauging protocol, Lubasch, Cirac, and Bañuls [48] recently introduced a gauge-fixing prescription for finite PEPS calculations that was later adapted in the context of iPEPS by Ref. [47]. It yields a significantly better conditioned effective environment and thus strongly improves the stability of the tensor optimization during the full update.

The gauge protocol [48] starts from the effective environment in the bond projection (38) which, after symmetrization, is subject to an eigenvalue decomposition,

$$\begin{array}{c}
 \text{---} \\
 | \\
 \text{---} \\
 E_{\text{full}} \\
 \text{---} \\
 | \\
 \text{---}
 \end{array}
 =
 \begin{array}{c}
 \text{---} \\
 | \\
 \text{---} \\
 W \\
 | \\
 \text{---} \\
 \epsilon \\
 | \\
 \text{---} \\
 W^\dagger \\
 | \\
 \text{---}
 \end{array}
 \approx
 \begin{array}{c}
 \text{---} \\
 | \\
 \text{---} \\
 W \\
 | \\
 \text{---} \\
 \epsilon_+ \\
 | \\
 \text{---} \\
 W^\dagger \\
 | \\
 \text{---}
 \end{array}
 =
 \begin{array}{c}
 \text{---} \\
 | \\
 \text{---} \\
 Z \\
 | \\
 \text{---} \\
 Z^\dagger \\
 | \\
 \text{---}
 \end{array}
 . \tag{44}$$

During this process, we remove the contributions from small negative eigenvalues to restore the positivity of E_{full} . Next we independently apply a QR and LQ decomposition to the tensor Z ,

$$\begin{array}{c}
 \text{---} \\
 | \\
 \text{---} \\
 Z \\
 | \\
 \text{---}
 \end{array}
 =
 \begin{array}{c}
 \text{---} \\
 | \\
 \text{---} \\
 Q_R \\
 | \\
 \text{---}
 \end{array}
 R
 =
 \begin{array}{c}
 \text{---} \\
 | \\
 \text{---} \\
 L \\
 | \\
 \text{---}
 \end{array}
 Q_L
 , \tag{45}$$

and insert two identities LL^{-1} and $R^{-1}R$, into the left and right bond indices of the effective environment, respectively. This yields a renormalized pair of subtensors \bar{v}_y^x and \bar{w}_y^{x+1} and a modified environment \bar{E}_{full} :

$$\begin{array}{c}
 \text{---} \\
 | \\
 \text{---} \\
 L \\
 | \\
 \text{---} \\
 v_y^x \\
 | \\
 \text{---} \\
 w_y^{x+1} \\
 | \\
 \text{---} \\
 R \\
 | \\
 \text{---} \\
 L^{-1} \\
 | \\
 \text{---} \\
 E_{\text{full}} \\
 | \\
 \text{---} \\
 R^{-1} \\
 | \\
 \text{---} \\
 L^{-1\dagger} \\
 | \\
 \text{---} \\
 R^{-1\dagger} \\
 | \\
 \text{---} \\
 L^\dagger \\
 | \\
 \text{---} \\
 v_y^{x\dagger} \\
 | \\
 \text{---} \\
 w_y^{x+1\dagger} \\
 | \\
 \text{---} \\
 R^\dagger \\
 | \\
 \text{---}
 \end{array}
 =
 \begin{array}{c}
 \text{---} \\
 | \\
 \text{---} \\
 \bar{v}_y^x \\
 | \\
 \text{---} \\
 \bar{w}_y^{x+1} \\
 | \\
 \text{---} \\
 \bar{E}_{\text{full}} \\
 | \\
 \text{---} \\
 \bar{v}_y^{x\dagger} \\
 | \\
 \text{---} \\
 \bar{w}_y^{x+1\dagger} \\
 | \\
 \text{---}
 \end{array}
 . \tag{46}$$

Moreover, one also has to apply the inverse L^{-1} , R^{-1} to the subtensors X_y^x and Y_y^{x+1} , respectively, so that the full M tensors can be restored properly after the tensor update [c.f. Eq. (43)],

$$\begin{array}{c}
 \text{---} \\
 | \\
 \text{---} \\
 \bar{X}_y^x \\
 | \\
 \text{---}
 \end{array}
 =
 \begin{array}{c}
 \text{---} \\
 | \\
 \text{---} \\
 X_y^x \\
 | \\
 \text{---} \\
 L^{-1} \\
 | \\
 \text{---}
 \end{array}
 , \quad
 \begin{array}{c}
 \text{---} \\
 | \\
 \text{---} \\
 \bar{Y}_y^{x+1} \\
 | \\
 \text{---}
 \end{array}
 =
 \begin{array}{c}
 \text{---} \\
 | \\
 \text{---} \\
 R^{-1} \\
 | \\
 \text{---} \\
 Y_y^{x+1} \\
 | \\
 \text{---}
 \end{array}
 . \tag{47}$$

4 Fermionic tensor networks

For the tensor network representations discussed so far, we implicitly restricted our discussion to bosonic quantum many-body models. However, some of the most challenging and

interesting open questions with respect to the physics of strongly correlated systems involve fermions. Especially in two dimensions, the t - J model, the Hubbard model, and its multi-band extensions continuously attract much attention, since they are believed to play an important role for understanding of high- T_c superconductivity and quantum criticality. Due to the lack of alternative approaches (QMC is particularly limited by the sign problem in this context), much hope is set on tensor network techniques to treat these complex fermionic models under controlled conditions.

TN representations can incorporate fermionic statistics in any spatial dimension, and several different approaches have been developed for its efficient implementation, being mathematically all equivalent [45, 46, 85–89]. The most useful point of view for practitioners is that taken by Corboz and Vidal [85], adapted to the iPEPS by Corboz, Orús, Bauer and Vidal [45]. It fully implements the fermionic exchange rules in terms of modifications to the tensor network diagrams. In the following, we briefly review the main ingredients for fermionic tensor networks, mostly following [45], although not with the same formal rigor, to keep the presentation compact. We refer to Sec. 4.4 for technical details on the fermionic iPEPS implementation in combination with non-abelian symmetries.

For simplicity, we focus on a lattice of spinless fermions with a local Hilbert space dimension $d = 2$ on every site (though everything can easily be generalized to fermions with $d > 2$ [45]). The fermionic statistic of this model is typically treated at the level of operators, specifically by the anticommutation relations of the fermionic annihilation and creation operators, \hat{c}_j and \hat{c}_j^\dagger ,

$$\{\hat{c}_j, \hat{c}_{j'}^\dagger\} = \delta_{jj'} \quad \{\hat{c}_j, \hat{c}_{j'}\} = 0. \quad (48)$$

In addition, one always imposes some fermionic ordering of the sites, such that a fully occupied state on the lattice containing N sites can be expressed by means of second quantization using the vacuum state $|0_1\rangle|0_2\rangle \dots |0_N\rangle$ and an ordered sequence of creation operators,

$$|1_1\rangle|1_2\rangle \dots |1_N\rangle = \hat{c}_1^\dagger \hat{c}_2^\dagger \hat{c}_3^\dagger \dots \hat{c}_N^\dagger |0_1\rangle|0_2\rangle \dots |0_N\rangle. \quad (49)$$

Starting from the techniques discussed in the context of bosonic systems, how can we incorporate the fermionic statistic into the framework of tensor networks? One possibility is to employ a Jordan-Wigner transformation to represent the fermionic operators in terms of Pauli matrices. In this way, the fermionic operator \hat{c}_j is expressed in terms of bosonic operators in a non-local form, which can be described by a so-called *Jordan-Wigner string* acting on all sites $j' < j$ that appear “earlier” in the fermionic order of Eq. (49) [90]. These strings can be treated efficiently in the MPS framework, where it is always possible to choose the fermionic order j equivalent to the position of a site in the MPS chain mapping. However, it leads to severe complications in the context of PEPS, where two nearest-neighbor sites $\mathbf{r} = (x, y)$ and $\mathbf{r}' = (x + 1, y)$ on the lattice might appear far apart in terms of their fermionic order j and j' [45].

To retain the “locality” of the iPEPS algorithm as well, we here adopt a different approach for the treatment of fermionic statistic in the tensor network language. This formulation builds on two simple “fermionization” rules discussed below, that were pioneered in the context of fermionic MERA by Refs. [85] and [46], and later adapted to the PEPS and iPEPS framework [45].

4.1 Parity conservation

A Fermionic Hamiltonian typically preserves the *parity* of the particle number of the state it acts on, defined to be $p = 1$ or -1 for an even or an odd number of particles, respectively.

This \mathbb{Z}_2 parity symmetry enables us to define wavefunctions and operators in terms of a well-defined parity quantum number p , resulting in a block structure in the tensor network. In particular, every index of a tensor can be assigned a well-defined parity.

The first fermionization rule enforces parity conservation in a TN representation. To this end, all tensors have to be chosen to be parity preserving. Taking a generic element of some M tensor as example, it means that

$$M_{\alpha\beta\gamma\rho}^{[\sigma_y^x]} = 0 \quad \text{if} \quad p(\alpha)p(\beta)p(\gamma)p(\rho)p(\sigma_y^x) = -1, \quad (50)$$

with $p(\alpha) \in \{-1, 1\}$ describing the parity of the state labeled by the index α [45]. This immediately has the consequence that operators changing the parity number of a state, such as \hat{c}_j have to be encoded with an additional index (see below). Parity conservation does not directly capture the fermionic statistic. However, it is crucial in order to track the fermionic signs, since we are able to distinguish states containing an even or odd number of fermions.

4.2 Fermionic swap gates

The second fermionization rule of [85] incorporates the fermionic statistics into the tensor network formalism. It implies that each line crossing in the TN is replaced by a fermionic swap gate,

$$\hat{S}_{\beta'\alpha'}^{\alpha\beta} = \delta_{\alpha\beta'}\delta_{\beta\alpha'} S(\alpha, \beta) = \begin{array}{c} \alpha \quad \beta \\ \diagdown \quad \diagup \\ \blacklozenge \\ \diagup \quad \diagdown \\ \alpha' \quad \beta' \end{array}, \quad (51)$$

with $S(\alpha, \beta) = -1$ if $p(\alpha) = p(\beta) = -1$ and $S(\alpha, \beta) = 1$ otherwise.

Why do the swap gates mimic the anticommutation relations of the fermions? Each line of the TN diagrams corresponds to a fermionic degree of freedom representing either physical (site indices) or virtual particles (bond indices). Any line crossing then corresponds to a particle exchange [85]. The implication of such an exchange depends on the nature of the particles. In the case of bosons such a swap is a trivial operation without any consequence. In the context of other particles, such as fermions, the underlying particle statistic does yield non-trivial consequences. For instance, additional factors of -1 have to be multiplied to the tensor network when swapping two states with odd fermionic parity number. Thus, the fermionic statistic of any tensor network can be captured by adding swap gates of type (51) to the diagrammatic representation. As a prerequisite, one has to be able to read out the parity of every index in the TN (hence, the first rule).

We emphasize that the fermionization rules can be readily implemented into any standard bosonic TN algorithm *without* altering the leading numerical costs, since the swap gates can typically be absorbed into a single tensor [85]. All steps can be performed completely analogously. In our iPEPS implementation we were able to recycle most parts of our code for bosonic systems by simply adding swap gates at the appropriate lines.

4.3 Fermionic operators

Another prerequisite to capture the fermionic statistic in a TN representation relates to the proper definition of local fermionic operators. Consider a generic two-site operator \hat{O}_{ij} acting on sites i and j , with $j > i$ not necessarily labeling contiguous sites in terms of the imposed fermionic order. Applied to a generic wavefunction, the resulting TN diagram contains a number of fermionic swap gates (illustrated in detail for MPS and iPEPS below). The impact of these gates on the wavefunction can be interpreted as swapping the physical index of site i such that it becomes contiguous to j with respect to the fermionic order. But this alone does

not fully account for the fermionic statistics. In addition, the fermionic order of the local two-site Hilbert space generated by sites i and j has to be properly incorporated on the level of the operators, which leads to factors of -1 for some matrix elements.

While easily generalizable to arbitrary systems [45], we illustrate this briefly for the simple example of spinless fermions, where the operator is expanded in the two-site basis $|\sigma_i\sigma_j\rangle = (c_i^\dagger)^{\sigma_j}(c_j^\dagger)^{\sigma_j}|0_i0_j\rangle$, with $\sigma_j \in \{0, 1\}$:

$$\hat{O} = \sum_{\substack{\sigma'_i\sigma'_j \\ \sigma_i\sigma_j}} O_{\sigma_i\sigma_j}^{\sigma'_i\sigma'_j} |\sigma_i\sigma_j\rangle\langle\sigma'_i\sigma'_j|. \quad (52)$$

The coefficients $O_{\sigma_i\sigma_j}^{\sigma'_i\sigma'_j}$ are given by

$$O_{\sigma_i\sigma_j}^{\sigma'_i\sigma'_j} = \langle\sigma_i\sigma_j|\hat{O}|\sigma'_i\sigma'_j\rangle = \langle 0_i0_j|(\hat{c}_i)^{\sigma_i}(\hat{c}_j)^{\sigma_j}\hat{O}(\hat{c}_i^\dagger)^{\sigma'_i}(\hat{c}_j^\dagger)^{\sigma'_j}|0_i0_j\rangle. \quad (53)$$

If the operator describes a pairing term, $\hat{O} = \hat{c}_i\hat{c}_j$, the only non-vanishing coefficient is

$$O_{0_i0_j}^{1_i1_j} = \langle 0_i0_j|\hat{c}_i\hat{c}_j\hat{c}_i^\dagger\hat{c}_j^\dagger|0_i0_j\rangle = -1. \quad (54)$$

A standard hopping term $\hat{O} = \hat{c}_i^\dagger\hat{c}_j$ also has only a single nonzero element,

$$O_{1_i0_j}^{0_i1_j} = \langle 0_j0_j|\hat{c}_i\hat{c}_i^\dagger\hat{c}_j\hat{c}_j^\dagger|0_i0_j\rangle = 1. \quad (55)$$

We conclude this part with an additional comment on operators that change the parity of a state, such as $\hat{O} = \hat{c}_j$. The first fermionization rule restricts our TN description to parity preserving tensors, as defined in Eq. (50). Naively, this would imply that simple annihilation or creation operators could not be properly described by fermionic TNs, since their tensor representation does not conserve fermionic parity. However, any parity changing tensor can be represented by a parity conserving tensor just by adding an additional single-valued index δ with $p(\delta) = -1$ [45]. For instance, the diagrammatic form \hat{c}_j is then given by

$$(\hat{c})_{\sigma_j,\delta}^{\sigma'_j} = \begin{array}{c} \sigma'_j \\ | \\ \textcircled{\hat{c}_j} \text{---} \delta \\ | \\ \sigma_j \end{array}, \quad (56)$$

where the red line indicates that δ only takes a single value, i.e., represents a singleton dimension in a rank-3 tensor. This representation ensures that the only nonzero element, $(\hat{c})_{0_j,\delta}^{1_j}$, now satisfies Eq. (50):

$$p(1_j)p(0_j)p(\delta) = (-1)(+1)(-1) = 1. \quad (57)$$

4.4 Fermionic PEPS implementation

To enter this discussion, we return to our finite-size PEPS example on a 3×3 square-lattice cluster used in the beginning of Sec. 3.1. Recall that each site is labeled according to its coordinate in space, $\mathbf{r} = (x, y)$, so that the local basis states are denoted by $|\sigma_y^x\rangle$. In addition, we now have to decide on a specific fermionic order and use an additional label j , running from 1 to 9, to enumerate all sites of the system, $|\sigma_{y,j}^x\rangle$ (the red color of the fermionic index acts as guide for the eyes). Thus, a specific state in the Fock space can be expressed as

$$|\sigma_{1,1}^1\rangle|\sigma_{2,2}^1\rangle\dots|\sigma_{3,9}^3\rangle = (\hat{c}_1^\dagger)^{\sigma_1^1}(\hat{c}_2^\dagger)^{\sigma_2^1} \dots (\hat{c}_9^\dagger)^{\sigma_3^3}|0_{1,1}^1\rangle|0_{1,2}^1\rangle\dots|0_{1,9}^3\rangle. \quad (58)$$

Diagrammatically, this ordering *always* corresponds to the order in which the open indices of the wavefunction $|\psi\rangle$ are drawn, and directly affects the specific appearance of the PEPS TN,

(59)

We emphasize that a different fermionic order automatically leads to a different diagrammatic representation, where the swap gates (black diamonds) potentially act on a different set of bonds. In this work, we only consider the fermionic ‘zig-zag’ order of Eq. (59) which (i) can also easily be applied to an infinite lattice system and (ii) enables us to recycle all bosonic iPEPS diagrams depicted in Sec. 3.1. For an explicit example of imposing another fermionic order, see Ref. [45].

After obtaining the proper diagrammatic form of the PEPS, all subsequent operations follow in complete analogy from the bosonic case. The only additional feature are the swap gates, which are put on every line crossing. For instance, an overlap calculation $\langle\psi|\psi\rangle$, derived in Eq. (14) for the bosonic PEPS by performing a number of jump moves, is carried out similarly for a fermionic system,

(60)

To reduce the complexity of the diagram, we again introduced a modified representation $\bar{M}_y^{x\dagger}$ of the conjugate tensors in the second step of Eq. (60). In contrast to the bosonic case, where $\bar{M}_y^{x\dagger}$ and $M_y^{x\dagger}$ are mathematically equivalent objects [see Eq. (13)], we emphasize that $\bar{M}_y^{x\dagger}$ here includes two fermionic swap gates that are absorbed into the tensor, according to

(61)

4.5 Fermionic iPEPS implementation

Considering fermions in an infinite lattice system, the protocol of imposing a zig-zag fermionic order on the lattice can be adopted in a very straightforward manner [45]. In hindsight, we already implied this kind of ordering when drawing the iPEPS diagrams in Sec. 3.1. The

extensions from the bosonic to the fermionic case is easily achieved by the presence of the fermionic swap gates at line crossings.

In most iPEPS applications, the modified definition of the conjugate tensor $\bar{M}_y^{x\dagger}$, (61), and the fermionic version of the reduced tensor m_y^x

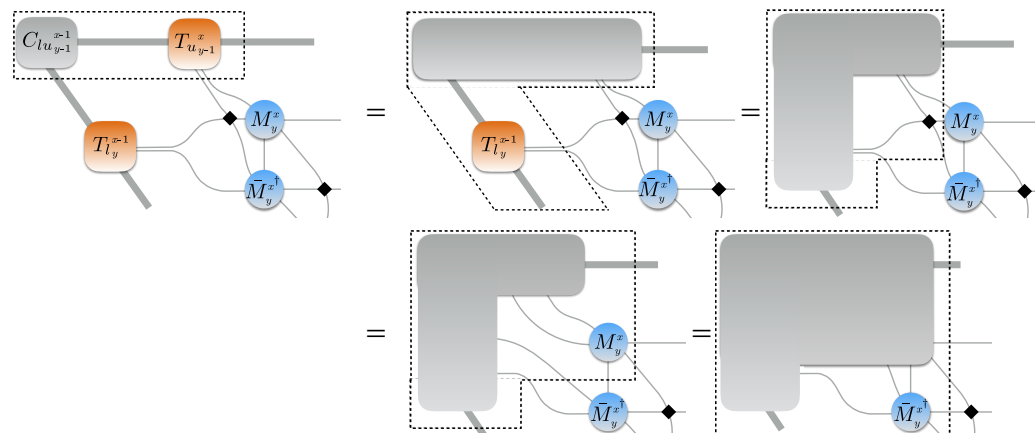
$$m_y^x = \begin{array}{c} M_y^x \\ \bar{M}_y^{x\dagger} \end{array} \quad (62)$$

simplify the algorithm by a great deal. For instance, the calculation of an overlap $\langle \psi | \psi \rangle$ can even be represented diagrammatically without any swap gates present,

$$\text{[Diagrammatic representation of tensor network simplification]} \quad (63)$$

In principle, this would also enable us to carry out the coarse graining steps in the CTM calculation exactly in the same way as in bosonic iPEPS in terms of the reduced m tensors. To perform the algorithm with an efficient cost scaling, however, the M tensors and their conjugates have to be kept separated [see Sec. 3.3]. This typically leads to the presence of four additional swap gates for each site (only two when using $\bar{M}_y^{x\dagger}$).

The strategy of incorporating the swap gates appearing in a TN is to absorb them into one single tensor [85]. Depending on the TN, this is not always possible in the very first contraction step. Nevertheless, every swap gate can typically be absorbed at some intermediate contraction step. We illustrate this procedure for the contraction of parts of the CTM environment,



$$= \text{[Diagram of a gray rectangular tensor with four legs and a central dot]} \quad (64)$$

Swap gates also appear in the context of tensor optimization and the evaluation of a two-site operator, such as,

$$\langle \psi | \hat{O} | \psi \rangle = \text{[Diagram of a tensor network with nodes } E_1, E_2, E_3, E_4, E_5, E_6 \text{ and tensors } M_y^x, \bar{M}_y^{x\dagger}, M_y^{x+1}, \bar{M}_y^{x+1\dagger} \text{ and operator } \hat{O}] \quad (65)$$

We conclude this section by pointing out the modifications to the full-update protocol in the context of fermions. Again, most of the steps are exactly the same as in the bosonic version of the algorithm. In particular, the actual tensor optimization does not contain any swap gates due to the absence of line crossings in Eq. (39). However, the initialization slightly differs since one has to account for the presence of swap gates when performing the bond projection,

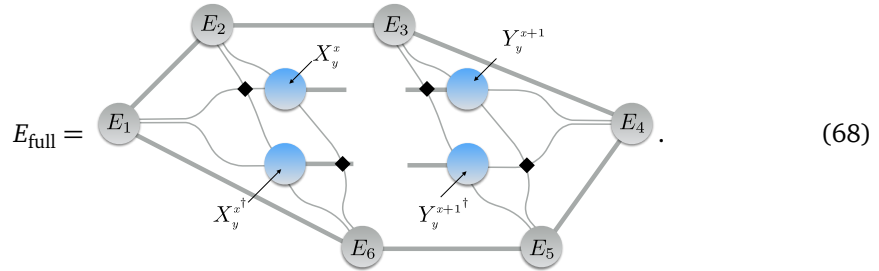
$$\begin{aligned} & \text{[Diagram showing } M_y^x \text{ and } M_y^{x+1} \text{ tensors with a swap gate]} \\ &= \text{[Diagram showing } M_y^x \text{ and } M_y^{x+1} \text{ tensors with SVD lines]} \\ &= \text{[Diagram showing } X_y^x, v_y^x, w_y^{x+1}, Y_y^{x+1} \text{ tensors]} \end{aligned} \quad (66)$$

Importantly, the swap gate acts differently on the conjugate tensors, so that the conjugate subtensors have to be generated by two independent SVD or QR decompositions,

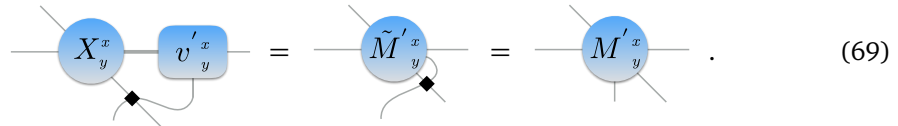
$$\begin{aligned} & \text{[Diagram showing } \bar{M}_y^{x\dagger} \text{ and } \bar{M}_y^{x+1\dagger} \text{ tensors with a swap gate]} \\ &= \text{[Diagram showing } \bar{M}_y^{x\dagger} \text{ and } \bar{M}_y^{x+1\dagger} \text{ tensors with SVD lines]} \\ &= \text{[Diagram showing } X_y^{x\dagger}, v_y^{x\dagger}, w_y^{x+1\dagger}, Y_y^{x+1\dagger} \text{ tensors]} \end{aligned} \quad (67)$$

The tensor network representation of the effective environment also contains an additional set

of swap gates,



Whereas the tensor optimization does not differ from the bosonic formulation, the restoration of the actual iPEPS representation after the update works in a slightly modified way,



Compared to the bosonic case in Eq. (43), we have to account for the additional swap gate.

5 Implementation of symmetries

The exploitation of symmetries, where available, is very important for writing efficient tensor network codes. In this Section we address various aspects of this issue.

5.1 Abelian symmetries

For a lattice model with abelian symmetries, quantum states can be labeled $|ql\rangle$, where q is an abelian “charge” quantum number, and l distinguishes different states with the same charge. Consider the simplest non-trivial example of a rank-3 tensor A , which fuses the tensor product of two elementary state spaces with abelian symmetry, $|q'm\rangle$ and $|q''n\rangle$, into the combined tensor product space $|ql\rangle$. This operation can be expressed as

$$|ql\rangle = \sum_{q'l'} \sum_{q''l''} |q'l'\rangle |q''l''\rangle (A_{q'q''}^q)_{l'l''}^l. \tag{70}$$

To reflect the system’s abelian symmetry, the A tensor carries a q -label for the symmetry sector of each of the indices l, l' and l'' . From a numerical perspective this introduces additional bookkeeping effort. At the same time, symmetry-specific selection rules enforce a large number of elements of A to be exactly zero [for the example of $U(1)$ particle conservation, the selection rule takes the form $q = q' + q''$]. Keeping only the nonzero elements leads to sparse tensor structures and, hence, results in significant computational speed-up and reduced memory requirements.

5.2 Non-abelian symmetries

Let us now consider the same example in the context of non-abelian symmetries. Then quantum states can be organized into irreducible symmetry multiplets (irreps) that carry an additional label q_z that specifies the internal structure of an individual multiplet, e.g. $|ql\rangle \rightarrow |ql; q_z\rangle$. The decomposition of a direct product of two irreps into a direct sum of irreps is fully defined by the Clebsch-Gordan coefficients (CGCs) of the symmetries present. In this description, the

coefficients of the A tensor in Eq. (70) factorize into tensor products of reduced matrix elements and CGCs, so that Eq. (70) generalizes to

$$|ql; q_z\rangle = \sum_{q'l'q'_z} \sum_{q''l''q''_z} |q'l'; q'_z\rangle |q''l''; q''_z\rangle \cdot \|A_{q'q''}^q\|_{l'l''}^l \cdot (C_{q'q''}^q)_{q'_zq''_z}^{q_z} \quad (71)$$

Here $(C_{q'q''}^q)_{q'_zq''_z}^{q_z} \equiv \langle qq'; q_z q'_z | q''; q''_z \rangle$ represent CGCs, and $\|A_{q'q''}^q\|_{l'l''}^l$ denote reduced matrix elements of the basis transformation [30]. This allows one to *compress* the nonzero data blocks of the tensors, further reducing the numerical requirements, yet at the price of a significantly increased bookkeeping effort.

The same structure as in Eq. (71) also carries over to the coefficients of arbitrary operators $\hat{O}_{q'l'q'_z}$ that acts in a given (local) state space $|ql; q_z\rangle$, where the latter itself is already properly organized w.r.t. given symmetries. Clearly, if one wants to exploit symmetries in numerical simulations, these symmetries must be well-defined throughout at every step and, in particular, for each individual tensorial object under consideration. Hence one also needs to know how operators transform under given symmetries. That is, all operators can be reduced to or built from irreducible tensor operators (irrops). These elementary objects consist of a set of operators (like a spinor) that under symmetry operation are transformed into each other completely analogously to the states of a particular irreducible multiplet q' , in which case q'_z labels the individual operators in the set. The intimate relation to states becomes apparent when the irrop acts on a scalar state $|0\rangle$, i.e., a singlet in all symmetries having $q = 0$ like a vacuum state. Then $\hat{O}_{q'l'q'_z}|0\rangle \equiv |q'l'q'_z\rangle$ associates an irrop with an irrep, up to normalization and assuming the state is not destroyed. Both of them transform according to the irrep q' . Generally then, a *particular* irrop with multiplet index $l' (= 1)$, can be expressed in a factorized form exploiting the Wigner-Eckart theorem,

$$\langle ql; q_z | \hat{O}_{q'l'q'_z} | q''l''; q''_z \rangle \equiv \langle ql; q_z | \cdot (\hat{O}_{q'l'q'_z} | q''l''; q''_z \rangle) = \|O_{q'q''}^q\|_{l'l''}^l \cdot (C_{q'q''}^q)_{q'_zq''_z}^{q_z}, \quad (72)$$

with CGCs $C_{q'q''}^q$ and reduced matrix elements $\|O_{q'q''}^q\|_{l'l''}^l$. The latter describe transitions between multiplets ql and $q''n$ within a given Hilbert space induced by the irrop $\hat{O}_{q'l'}$.

The conceptual structure of the tensor describing a basis transformation or operator matrix elements is thus the same. With focus on the tensor alone, i.e., skipping the ket states contracted with the tensor in Eq. (71), the tensor itself may be written more compactly in the generic form [31],

$$A = \bigoplus_q \|A\|_q \otimes C_q, \quad (73)$$

where q now is the full collection of symmetry labels for all indices (legs) in a particular block realization. For example for the cases above, $q \leftarrow (q', q''; q)$ where, by convention, e.g., subscript indices are grouped and listed before superscript indices. This demonstrates that each tensor acquires a block structure (collected via the outer sum), and that for each such block, Clebsch-Gordan tensors are split off in a tensor-product structure. The tensor product involves a reduced matrix element tensor (RMT) and a corresponding generalized Clebsch-Gordon coefficient tensor (CGT) with the same tensor rank. This *reduces* the actual number of freely choosable matrix elements, and thus the effective dimensionality of the tensor, $A \rightarrow \|A\|_q$, e.g., going from D states on a given index (leg) to $D^* \leq D$ multiplets. For abelian symmetries there is no reduction, $D^* = D$, whereas for $SU(N)$, one empirically finds an effective average dimensional reduction of $D^* \sim D/3^{N-1} \ll D$.

The conceptual framework described above forms the basis for the QSpace tensor library [30, 31] for building many-body state spaces in the presence of symmetries [Eq. (71)] and for

describing the actions of operators therein [Eq. (72)]. It allows one to construct a tensor network and its constituent tensors step by step in an iterative fashion. For a tutorial illustration of its underlying ideas, see App. A.

5.3 Outer multiplicity

When dealing with non-abelian symmetries, one generically also encounters outer multiplicity, i.e. direct sums in which the same irrep or irrop (or the same combination of several of them) occurs more than once. Consider, for example, an SU(2) rank-4 CGT having two incoming and two outgoing legs with symmetry labels (S_1, S_2) and (S'_1, S'_2) , respectively. Then, there are several different possibilities to fuse (S_1, S_2) to an intermediate irrep \bar{S} and to subsequently split the latter into (S'_1, S'_2) :

The diagram shows a rank-4 CGT on the left with two incoming legs labeled S_1 and S_2 , and two outgoing legs labeled S'_1 and S'_2 . This is equal to a direct sum over an intermediate irrep \bar{S} of CGTs where the two incoming legs first fuse into \bar{S} , which then splits into the two outgoing legs. The equation is labeled (74).

In this sense, the *outer multiplicity* (OM) of the rank-4 CGT on the left is larger than one. Each of the terms in the direct sum on the right corresponds to an *independent* CGT within a set of *orthogonal* CGTs C_q^μ , all carrying the same external symmetry labels $q \equiv (S_1, S_2; S'_1, S'_2)$, but distinguished by an outer multiplicity label μ (here given by \bar{S}). For example, if $S_1 = S_2 = S'_1 = S'_2 = S$, then the outer multiplicity label $\mu = \bar{S}$ can take the values $0, 1, \dots, 2S$. Since the outer multiplicity label is being summed over on the right, it is no longer *visible* at the level of the rank-4 CGT on the left.

SU(2) CGTs generically have OM larger than 1 once their rank is $r \geq 4$. For general non-abelian symmetries such as SU($N \geq 3$), OM larger than 1 already also occurs at the level of rank-3 CGTs, e.g., in the standard state space decomposition as in Eq. (71). There, the same q on the l.h.s. can arise in several different ways, which needs to be distinguished through an outer multiplicity index μ :

$$|q(l\mu); q_z\rangle = \sum_{q'l'q''} \sum_{q''l''q''_z} |q'l'; q'_z\rangle |q''l''; q''_z\rangle \cdot \|A_{q'l'q''}^q\|_{l'l''}^{l\mu} \cdot (C_{q'l'q''}^{q\mu})_{q'_zq''_z}^{q_z}, \quad (75)$$

where $\tilde{l} \equiv (l\mu)$ just labels the overall multiplets on the l.h.s., whereas the multiplicity index μ on the r.h.s. constitutes an additional dimension of the RMT $\|A\|$ within its particular symmetry sector tied to the CGT $C_{q'l'q''}^{q\mu}$. In the presence of OM, the tensor representation in Eq. (73) generalizes to

$$A = \bigoplus_q \left[\sum_\mu \|A\|_q^\mu \otimes C_q^\mu \right], \quad (76)$$

with a *regular* summation over the multiplicity index μ here. OM evidently also increases the effective dimension of the reduced matrix element tensors $\|A\|_{q\mu}$. In general, OM needs to be properly accounted for (once and for all) at the level of rank-3 CGTs [30]. Moreover, to ensure overall consistency, OM needs to be tracked meticulously not only when performing direct product decompositions into direct sums, but also when performing (iterative pairwise) contractions of tensors [31].

5.4 PEPS with symmetries

Building on the fusion rules for different state spaces in Eq. (71), one can generate symmetric tensor networks consisting of higher-rank tensors. This can be easily understood from the perspective of contracting multiple A tensors to some larger-ranked object. The resulting tensor

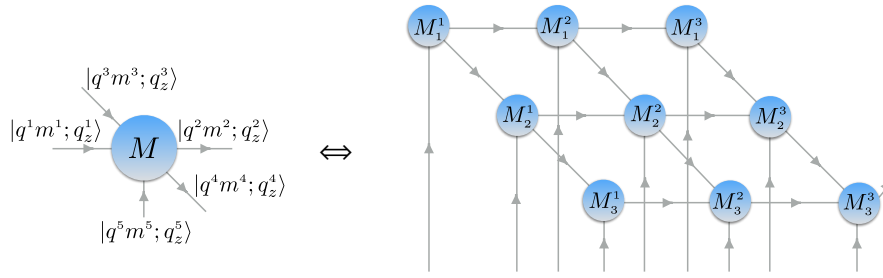


Figure 4: Schematic construction of a PEPS tensor network state. The elementary tensor M associated with each site (left panel) is tiled in a translational invariant fashion into a PEPS (right panel). The index order of its five legs is arbitrary but fixed. Here we use the order $(l, r, t, b, \sigma) \equiv (1, 2, 3, 4, 5)$ for left, right, top, bottom, and local state spaces, respectively. When exploiting symmetries, every individual index (i.e., leg of a tensor or line) represents a state space that must be expressed in terms of symmetry subspaces, throughout. For non-abelian symmetries, a given index describes a state space s that is organized as $|s\rangle \equiv |qn; q_z\rangle$, where q specifies a symmetry sector, n a specific multiplet within the symmetry sector q , whereas q_z indexes the internal multiplet structure which can be split off as a tensor product with a generalized CGTs [30].

then represents a tensor product of several state spaces. Setting up a symmetric PEPS tensor network, for example, follows exactly this pattern, leading to the diagrammatic representations in Fig. (4) for a single tensor (left) and a contraction of several such tensors (right): The symmetrized M tensors contain additional arrows on the index lines to indicate which state spaces are incoming and outgoing (i.e., which (group of) state spaces are fused into which, according to Eq. (71)). We have some freedom in fixing the direction of these arrows and some choices might be more convenient to implement than others. Note that the extra index of M_3^3 determines the global symmetry state of a specific PEPS representation. Of course, the symmetric PEPS also guarantees that the corresponding quantum state is symmetric, i.e., forms a well-defined symmetry multiplet.

Symmetry-induced selection rules cause a large number of matrix elements to be exactly zero, thus bringing the Hamiltonian into a block-diagonal structure and subdividing tensors into well-defined symmetry sectors. Keeping only the nonzero elements, we can achieve tremendous improvement in speed and accuracy in numerical simulations by the incorporation of symmetries. In the context of non-abelian symmetries, the nonzero data blocks are not independent of each other and can be further compressed using reduced matrix elements together with the Clebsch-Gordan algebra for multiplet spaces.

The special ingredient of our fermionic iPEPS implementation, that sets our work apart from that of other iPEPS practitioners, concerns the explicit incorporation of non-abelian symmetries, such as $SU(2)_{\text{spin}} \otimes SU(N)_{\text{orb}}$ with the fermionic \mathbb{Z}_2 parity symmetry in the particle sector. The non-abelian symmetries are fully encoded in the QSpace [30] tensor library, which automatically handles the symmetry-induced fusion rules of both the reduced matrix elements and the Clebsch-Gordan space.

Non-abelian iPEPS was pioneered by Liu, Li, Weichselbaum, von Delft and Su [37] for the case of the spin-1 Kagome Heisenberg antiferromagnet, which illustrated an $SU(2)_{\text{spin}}$ symmetric iPEPS representation in terms of a “projection” picture. Following ideas of $SU(2)$ invariant iPEPS representations for the spin- $\frac{1}{2}$ resonating valence-bond state [91, 92] and the spin-1 resonating AKLT state [93], the symmetric iPEPS tensors can be understood as emerging from

sets of “virtual particles” associated with each site that are pairwise maximally entangled along each virtual bond with their nearest neighbor sites, and then projected into the local degrees of freedom of the corresponding site. Starting from such an SU(2) invariant iPEPS, eventually one only specifies the effective bond dimension D^* , and lets the tensor optimization dynamically determine the relevant symmetry sectors on each bond. The number of multiplets D^* translates into a significantly larger actual number of states, D , associated with each bond (note that D may vary for the same D^* depending on the actual multiplets being used). In practice, the maximal feasible values for D^* correspond to retaining an actual number of states D which typically lies out of reach of standard iPEPS calculations incorporating abelian symmetries only.

5.5 Technicalities

In the remainder of this section we briefly point out some important technicalities when implementing non-abelian iPEPS.

5.5.1 Global symmetry sector

Ref. [37] states that the projection picture is dense, in the sense that it can cover the full Hilbert space and generate any symmetry eigenstate. Whereas this is true for finite-size PEPS, we emphasize that for translational invariant systems where the iPEPS is tiled with the *same* M tensor, by construction, there cannot be a “drift” in average value of a quantum number along any line of M tensors. In the case of non-abelian symmetries this implies that the global symmetry label of the iPEPS is *always* constrained to the singlet sector. This is conceptually similar to the case of U(1) symmetries in iPEPS, where states are restricted to a global symmetry sector corresponding to the quantum number zero, i.e., $q = 0$ (see Ref. [94], referred as ‘identity charge’ therein).

We note, however, that for abelian U(1) symmetries such as charge, any local filling can be realized based on the simple observation that U(1) symmetry labels are additive. Hence one is free to shift them locally and scale them globally at will. Specifically, one may shift the charge labels associated with the local state space of each site relative to the targeted mean local occupation \bar{q} , i.e., $q \rightarrow q - \bar{q}$. By this simple relabeling trick, average charges associated with the virtual bonds can fluctuate around $q = 0$. For non-abelian symmetries, however, such a relabeling scheme appears ill-suited, so that, by construction, our iPEPS implementation represents a global singlet. For our results below at finite doping, we still also only use \mathbb{Z}_2 charge parity even though charge itself is conserved.

5.5.2 Arrow convention

When exploiting symmetries, every index represents a state space with a particular symmetry multiplet. Now when fusing state spaces across tensors, this naturally introduces the concept of state spaces that ‘enter’ a given tensor, and state spaces that ‘emerge’ from it. For tensors this implies in a graphical depiction that one has to distinguish *ingoing* and *outgoing legs*, i.e., every leg acquires a direction, specified by an arrow [e.g., see Fig. 4]. Mathematically, this is equivalent to distinguishing between co- and contravariant indices (a notational convention not used here) [31]. The action of raising or lowering indices then corresponds to reverting arrows, as schematically depicted in Fig. 5. This is an operation that represents gauge-transformations of tensor network states, leaving the physical properties of the individual states unaffected [95]. Importantly, within a tensor network state, a summed over, i.e., *contracted* index connecting a pair of tensors, where it is outgoing from one tensor, and incoming to the other.

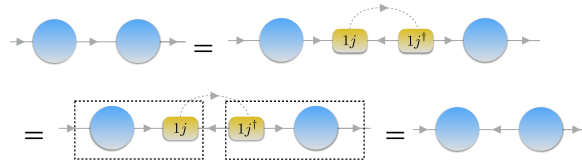


Figure 5: Arrow inversion. An identity, $\mathbb{I} = U^\dagger U$, is inserted on a bond (here the center bond) where up to normalization the unitary U represents a $1j$ symbol [31], i.e., a (degenerate) rank-3 tensor which combines two state spaces, q and its dual \bar{q} into a scalar singlet state. Upon absorbing U and U^\dagger on opposite sides with the neighboring tensors, effectively, the arrow on the center bond has been reverted. The singlet index (dashed line) can be omitted in the end.

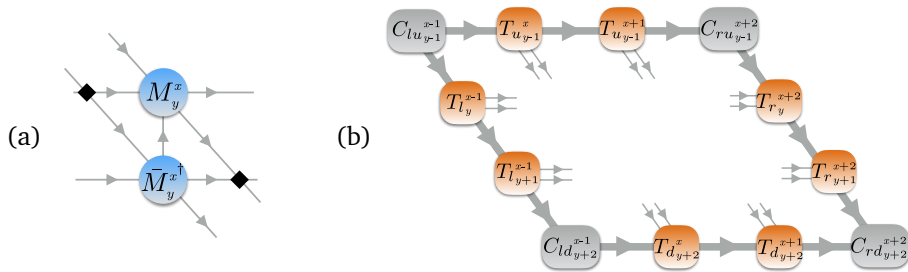


Figure 6: Arrow convention for M tensor (panel a) as they enter inside the corner transfer matrix (CTM) setup in (panel b). The latter combines bra and ket state as required for the minimization of the total energy $E = \langle \psi | H | \psi \rangle$ when truncating [58]. From the perspective of an individual site, this “double layer” tensor network translates into $\langle M | \dots | M \rangle$. For this, note that we have reverted the bond indices of the ‘bra-tensor’ $M \rightarrow \bar{M}$ such that they point in the *same* direction as the corresponding indices of M . Only then one can fuse the ‘double bond index’ into a single *fat* index. This greatly simplifies many fusion steps during the CTM procedure. The black diamonds in (a) indicate fermionic swap gates [45, 85].

When setting up a symmetric iPEPS representation, we therefore have to choose an “arrow convention” for all iPEPS tensors. On a square lattice, when a single M tensor with four virtual bond indices tiles an entire 2D iPEPS, this necessarily implies that two virtual bond indices must be ingoing and two outgoing [cf. Fig. 4(b)].

For compactness and readability of the code, we want to minimize the number of steps in the algorithm that involve reverting arrows as in Fig. 5. To this end, we establish the arrow convention for M tensors as well as the corner transfer matrices as shown in Fig. 6. Thus the quantum labels on all virtual bonds always “flow” from the upper left to the lower right corner of the tensor network.

5.5.3 Efficient contractions

The standard procedure when contracting tensors *in the absence of any symmetries* is to reshape a contraction into an effective matrix product [96] where efficient libraries can be utilized. That is, for any tensor in a contraction, the indices that are contracted as well as the ones that are kept, are grouped, i.e., permuted into order, and then fused into hyperindices.

This strategy also carries over when implementing symmetries, abelian and non-abelian alike. In principle, one has the option of matching symmetry sectors first, and then do the

contractions for every match in the above spirit. However, for abelian and non-abelian symmetries alike, this would cause a significant proliferation of symmetry sectors with increasing rank already for an individual tensor, yet also for matching symmetry combinations when contracting a pair of tensors. Roughly, if there are on average m symmetry sectors associated with each of the r legs of a given rank- r tensor, one may expect up to m^r possible symmetry combinations. The situation is worse still for non-abelian symmetries, where the tensor products of two multiplets can give rise to many different multiplets. Therefore a computation of a contraction is slowed down by (exponentially) many combinations with increasing rank of the involved tensors. Yet the individual contractions of matching symmetry sectors often involve only small effective block matrices. As a consequence, the above strategy becomes prohibitively inefficient strongly with increasing rank of the tensors. For an efficient way to proceed, one therefore *first* needs to merge indices into hyperindices (respecting fusion rules in the presence of non-abelian symmetries), and then do the contraction.

An efficient non-abelian iPEPS implementation therefore must fuse indices in contractions prior to the actual contraction, while being aware that only legs that point in the same direction can be fused [e.g. see Fig. 6]. After the contraction, the remaining open indices must be given back their original structure. In the presence of non-abelian symmetries, the fusion is effectively taken care of by an additional contraction with unitary tensors, which need to be reapplied on the open indices. This is an extra layer of complication that concerns each and every contraction that involve tensors with rank $r \gtrsim 4$.

To be specific, we consider the the two-band Hubbard model (discussed in Sec. 6.1 below) with $\mathbb{Z}_2 \otimes \text{SU}(2)_{\text{spin}} \otimes \text{SU}(2)_{\text{orb}}$, retaining $D^* = 6$ multiplets on each bond. Already the M tensors of rank 5 are complicated objects. However, the numerically most demanding tensors appear during the CTM coarse graining. Here, we typically have to deal with rank-6 and rank-7 tensors, and it depends strongly on the implementation details whether the CTM procedure is still feasible. Let us focus on a typical rank-6 tensor appearing several times in a CTM step, obtained by contracting the following TN diagram,

(77)

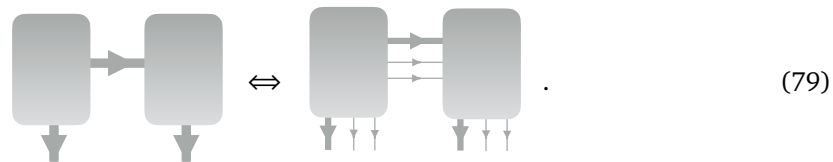
Each thin line corresponds to a single-layer bond index of dimension D^* , while the thick lines are environmental bond indices of dimension $\chi^* = 80$. The resulting tensor on the r.h.s of Eq. (77) requires only 390 MB of memory for the reduced matrix elements, as compared to an estimated 883 GB without symmetries. This highlights the efficiency of the non-abelian symmetries, where here we gain more than factor of 2,000 only in terms of storage requirement! At the same time, its QSpace consists of about 430,000(!) individual symmetry blocks. Numerically, this number corresponds to $(0.61 \chi^*)^2 (0.61 D^*)^4$, in agreement with an expected exponential proliferation of symmetry blocks with increasing rank. The sizes of the symmetry blocks, of course, are comparatively small, on average containing only $100 = 10^2$ individual coefficients.

To reduce the rank of this tensor, it is possible to fuse the three indices pointing to the left and to the bottom, respectively. This yields the rank-2 matrix representation,

(78)

with size $28,000 \times 28,000$ on the multiplet level. Being a rank-2 object, it must be block-diagonal. The matrix only contains 37 symmetry blocks of larger size (on average, each block consists of 750^2 coefficients). Remarkably, the reduced matrix elements of the latter matrix require *slightly less* memory (350 MB) than those of the original rank-6 tensor. To a very minor extent, this may be attributed to overhead for organizing the long lists of symmetry blocks in the tensor. More importantly, the rank-6 tensor has significant outer multiplicity [30, 31], which is absent in the rank-2 tensor. Most importantly, however, this simple comparison strongly suggests that the symmetry blocks in the rank-2 matrix representation are densely populated by the entries in the rank-6 tensor.

Now how do the two different representations perform in terms of contraction speed? To compare them, we consider the next step of the CTM scheme, which requires forming the upper part of the environment, by contraction the following tensor network, both in the rank-6 and rank-2 representation



The speed of the contraction vastly differs. Contracting two rank-2 objects results in 37 contractions of the block-diagonal rank-2 objects, which is performed with QSpace [30] in about one second of CPU time. In contrast, we had to terminate the contraction of the rank-6 tensors after four hours (!) of calculation time. In the latter case, 10^9 individual contractions are allowed by symmetry. Although the effort for each of these contractions is minimal, having to process their vast number step by step leads to a significant overhead, and thus to a drastic decrease in numerical efficiency.

6 Examples

Our main goal here is to illustrate the potential of non-abelian iPEPS, discussing both the benefits and limitations of exploiting non-abelian symmetries, by showing exemplary results for symmetric two and three band Hubbard models. A full analysis of the intricate physics of each of these systems goes beyond the scope of this work and is left for future studies.

Whereas the one-band Hubbard model already features important aspects of strongly correlated materials, such as the Mott insulator transition or the emergence of d -wave superconducting pairing, for a multi-band Hubbard model a number of fascinating phenomena emerge from the interplay of different electron orbitals which cannot be captured by an effective model with a single band. Both intra-atomic Coulomb exchange or the presence of crystal field splitting can give rise to a number of intriguing effects, such as the existence of an orbital-selective Mott insulating phase, where only one orbital becomes insulating while the other retains its metallic properties [97–101]. In order to understand this physics from a theoretical perspective, it is clearly necessary to go beyond a single-band system and study multi-band generalizations of the Hubbard model.

In addition to perspectives in strongly correlated materials, multi-band high-symmetry models, such as $SU(N)$ Hubbard models or related Heisenberg models give rise to fascinating new types of quantum states including exotic magnetically ordered phases. These are not only of general academic interest but recently have also become experimentally accessible in the context of cold atoms [102, 103].

The exponentially large quantum many-body Hilbert space and the ensuing strong electronic correlations pose an extreme challenge to numerical approaches. Besides, one also

has to deal with an enlarged parameter space that substantially adds to the complexity of these systems. For instance, the spinful symmetric two-band Hubbard model with only on-site interactions already contains additional parameters such as Hund’s interaction energy in comparison to its single-band version. Therefore, wide regions of the phase diagram of these models remain blank and there is a compelling need for developing numerical methods that can reliably deal with such systems in an unbiased way.

6.1 Spinful two-band Hubbard model

In this section, we demonstrate that fermionic iPEPS enhanced with non-abelian symmetries is a valuable ansatz to deal with symmetric complex multi-band systems in 2D. As a first example, we consider the repulsive Hubbard model with $M = 2$ bands and spin and orbital degeneracy on the square lattice. Specifically, we consider the Hamiltonian [104],

$$\hat{H} = \sum_{\langle ij \rangle} \sum_{m\sigma} (-t \hat{c}_{im\sigma}^\dagger \hat{c}_{jm\sigma} + \text{H.c.}) + \frac{U}{2} \sum_i \hat{n}_i(\hat{n}_i - 1) \quad (80a)$$

$$\hat{H}_\mu = \hat{H} - (\underbrace{\mu + \frac{3U}{2}}_{\equiv \mu_0}) \sum_i \hat{n}_i, \quad (80b)$$

with hopping amplitude t between nearest-neighbor sites $\langle ij \rangle$, spin index $\sigma \in \{\uparrow, \downarrow\}$, orbital index $m = 1, \dots, M$, and site occupation $\hat{n}_i \equiv \sum_{m\sigma} \hat{n}_{im\sigma}$. We take $t := 1$ as unit of energy, throughout. We tune the average occupation via the chemical potential μ in Eq. (80b). But when computing the ground state energies, we compute the expectation values of the Hamiltonian in Eq. (80a), otherwise. The chemical potential in Eq. (80b) was offset by μ_0 such that $\mu = 0$ corresponds to half-filling in the presence of a finite onsite Coulomb energy U . Overall, the Hamiltonian in (80) features both an $SU(2)_{\text{spin}}$ and $SU(2)_{\text{orbital}}$ symmetry, which we exploit in our iPEPS implementation. We ignore local Hund’s coupling. Therefore spin and orbital index become interchangeable, resulting in 4 equivalent flavors. Overall, this actually leads to an enlarged $SU(4)$ symmetry of 4 spinless flavors (not exploited here). Also, we exploit only charge *parity* conservation rather than $U(1)$ charge, and tune the filling via a chemical potential. The reason for this is partly technical, in that by being interested in finite doping we do not necessarily have integer filling in our unit cell. As a benefit, by just tracking charge parity, this immediately also permits the study of superconducting correlations.

For the ground state of a given average filling $n = n(\mu)$, set via Eq. (80b), we define the ground state energy per site e_0 , the bond energy e_0^{ij} , and the generalized spin-singlet pairing amplitude Δ^{ij} as the expectation values

$$e_0 \equiv \frac{1}{N} \langle \hat{H} \rangle \quad (81a)$$

$$e_0^{ij} \equiv \left\langle -t \sum_{m\sigma} (\hat{c}_{im\sigma}^\dagger \hat{c}_{jm\sigma} + \text{H.c.}) + \frac{U}{8} [\hat{n}_i(\hat{n}_i - 1) + \hat{n}_j(\hat{n}_j - 1)] \right\rangle \quad (81b)$$

$$\Delta^{ij} \equiv \frac{1}{\sqrt{2}} \sum_m \langle \hat{c}_{im\uparrow} \hat{c}_{jm\downarrow} - \hat{c}_{im\downarrow} \hat{c}_{jm\uparrow} \rangle, \quad (81c)$$

with N the (fictitious total) number of sites. Here the ‘bond energy’ includes the Coulomb interaction energy $U/2$ of each of its associated pair of sites, weighted by $1/z$ with $z = 4$ the coordination number on the square lattice. Therefore, the average bond energy of all nearest neighbor bonds, $\overline{e_0^{ij}} = \frac{1}{4} \sum_{j \in [\text{n.n. of } i]} e^{ij}$, is related to the average energy per site, e_0 , by $\overline{e_0^{ij}} = \frac{e_0}{2}$, since on average there are two bonds associated with each site.

Table 1: Typical multiplet configurations on the auxiliary bonds obtained from symmetric iPEPS simulations on the square lattice with two symmetric spinful orbitals. The rows show the results for varying multiplet bond dimension D^* (left column) at half filling. The corresponding state space dimension D is listed in the right column. In the multiplet listing on the left, the notation $(\cdot)^m$ indicates m multiplets in the symmetry sector (\cdot) , with $m = 1$ if not specified. For better readability, we also adopt the QSpace [30] convention of specifying $SU(2)$ multiplets through the integer number $2S$ (i.e., the number of boxes in the corresponding Young tableaux).

D^*	multiplets in symmetry sectors ($\mathbb{Z}_2, SU(2)_{\text{spin}}, SU(2)_{\text{orb}}$)	D
3	$(1, 0, 0) \oplus (-1, 1, 1) \oplus (1, 2, 0)$	$1 + 4 + 3 = 8$
4	$(1, 0, 0) \oplus (-1, 1, 1)^2 \oplus (1, 2, 0)$	$1 + 8 + 3 = 12$
5	$(1, 0, 0) \oplus (-1, 1, 1)^2 \oplus (1, 2, 0) \oplus (1, 2, 2)$	$1 + 8 + 3 + 9 = 21$
6	$(1, 0, 0) \oplus (-1, 1, 1)^2 \oplus (1, 2, 0) \oplus (1, 0, 2) \oplus (1, 2, 2)$	$1 + 8 + 3 + 3 + 9 = 24$

We study the Hamiltonian (80) for finite hole hopping by tuning $\mu \leq 0$ (which is equivalent by particle-hole transformation to particle doping $\mu \geq 0$). To our knowledge, the phase diagram of this system is largely unknown away from integer filling. However, some interesting results are available for certain points in parameter space.

At half-filling $\langle n \rangle = 2$, several studies based on a sign-problem-free determinant quantum Monte-Carlo method addressed the magnetic properties of the model [105–107]. Their findings support the existence of long-ranged antiferromagnetic (AF) order for larger interactions $U \geq 2$ [106]. Interestingly, the AF order does not show a monotonic behavior with respect to U ; instead, it exhibits a maximum around $U \approx 8$ and then decreases again towards larger interactions strengths. Whether or not the long-ranged AF order persists in the limit $U \rightarrow \infty$ remains an open question. A previous QMC study of the corresponding Heisenberg model found no AF order but potentially a gapless spin-liquid phase in this regime [108]. Another recent work based on variational QMC [109] addressed the Mott transition of the half-filled Hubbard model, finding a critical coupling $U_c \approx 11$ for the case of degenerate bands (their ansatz is rather biased, however, as it only accounts for a non-magnetic solutions).

In the quarter-filled case $\langle n \rangle = 1$ at infinite U , the Hamiltonian (80) can be mapped on an $SU(4)$ -symmetric Heisenberg model, which was studied in Ref. [110]. Their combined iPEPS and ED study finds a rather exotic Neel-like order with dimers alternating between pairs of flavors, pointing towards a spontaneously broken $SU(4)$ symmetry with an enlarged unit cell.

In this section, we present a first step towards a systematic iPEPS study of the symmetric two-band Hubbard model (80) that, in addition to half- and quarter filling, also investigates arbitrary doping regimes. The main challenge for iPEPS in the context of such a two-band model is the strongly enlarged local Hilbert space. In total, we need to deal with four different flavors of fermions ($2 \text{ spins} \times 2 \text{ orbitals}$) resulting in a local state space dimension $d = 16$ per site, larger by a factor of four relative to the $d = 4$ in the one-band version.

To treat systems with a large local state space within iPEPS (or other TN approaches) one can follow two different strategies, as illustrated in Fig. 7: (a) either one keeps a lattice as a single unit with a large local state space (and hence preserves its symmetry), or (b) artificially splits it, for the sake of the iPEPS simulation, into smaller sublattices. Strategy (a) is hardly feasible for standard iPEPS techniques, even when incorporating all abelian symmetries of the system. For (b), a natural choice is to split the lattice into two interleaved sublattices, one for each orbital. The drawback, besides an artificially broken lattice symmetry, is that iPEPS then has to handle longer-ranged interactions and correlations in its ansatz. This necessitates

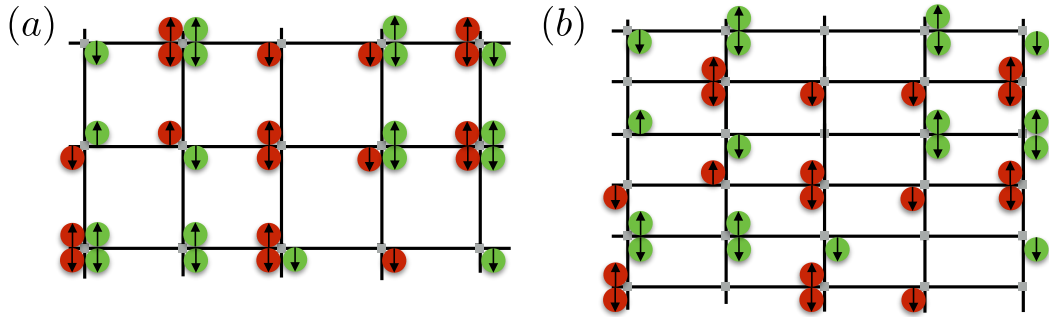


Figure 7: Schematic depiction of two-band setups for a spinful Hubbard model, with the two bands depicted by the different colors red and green. In setup (a) all four fermionic flavors still reside on a given lattice site, leading to an enlarged Hilbert space of $d = 4^2$. This setup respects flavor symmetry, which thus may be exploited. Setup (b) avoids the enlarged local Hilbert space by splitting the lattice into two sublattice, one for each band. This comes at the cost of introducing an additional set of sites, causing interaction terms to become longer-ranged.

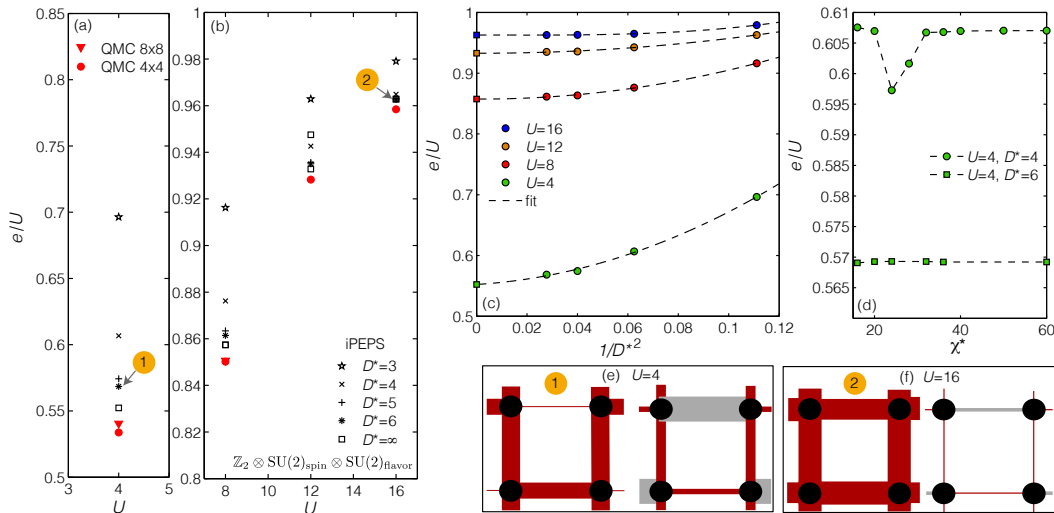


Figure 8: Non-abelian iPEPS results for the two-band Hubbard model with a 2×2 unit cell using simple update at half-filling $\langle n \rangle = 2$. Panels (a) and (b) display the normalized ground-state energy per site e_0/U as a function of U from iPEPS for various multiplet bond dimensions D^* (black symbols) in comparison to QMC data (red symbols). The iPEPS energies were obtained by extrapolation vs. $1/D^{*2} \rightarrow 0$ (squares), with the extrapolations shown in (c). The convergence of the energy with the environmental bond dimension χ^* is shown in (d), where the maximum $\chi^* = 60$ roughly corresponds to $\chi = 200$. Labels (1) and (2) in panels (a) and (b) point to individual iPEPS wavefunctions characterized in panels (e) and (f). There the diameter of the black dots is proportional to the average local occupation, and the bond width to the bond energy e_0^{ij} [Eq. (81b)]. To better illustrate the breaking of translational invariance in the unit cell, the right subpanels in (e) and (f) depict the same wavefunctions, but with bond energies shifted relative to their mean, $e_0^{ij} \rightarrow e_0^{ij} - (e_0/2)$. Here red (gray) bond correspond to positive (negative) values, respectively.

swap gates in the implementation of imaginary time evolution, which generates an additional source of error.

Here we follow strategy (a) because this preserves the orbital $SU(2)$ symmetry, where we can fully exploit all available non-abelian symmetry. Specifically, with finite doping in mind, we incorporate $\mathbb{Z}_2 \otimes SU(2)_{\text{spin}} \otimes SU(2)_{\text{orb}}$ symmetry. This way, the local state space with $d = 16$ is reduced to an effective multiplet dimension $d^* = 6$. At the same time this enables us to retain up to $D^* = 6$ multiplets on each virtual bond, which corresponds to an effective bond dimension of $D = 24$ states [cf. Table. 1]. This enables us to run simple-update simulations for a wide regime of parameters, the results of which are presented in the following.

We start with the half-filled case $\langle n \rangle = 2$, i.e., $\mu = 0$ in (80b), to benchmark against existing determinant projector QMC data [111]. The results of this analysis are summarized in Fig. 8. Panels (a,b) show the normalized ground-state energies per site versus the interaction strength U obtained from a simple-update iPEPS simulation on a 2×2 unit cell. The various bond dimensions $D^* = 3, 4, 5, 6$ in Fig. 8(a,b) are made up of dominant multiplets which emerge dynamically from the iPEPS simulations for each D^* . They are listed in Table 1, for completeness. The extrapolated energies for $1/(D^*)^2 \rightarrow 0$ are empirically determined by polynomial fits as depicted in Fig. 8(c). The convergence of our data with respect to the environmental bond dimension χ^* is shown in Fig. 8(d). We attach no significance to the bump seen at small χ^* , since our focus is on the large- χ^* convergence. Note that QMC simulates finite-size systems with periodic BC, hence its ground state energy, specifically so in Fig. 8(a), is expected to still increase with increasing system size, as it converges from below. Nevertheless, we find good agreement, to within 1%, of our extrapolated energies with the QMC results, confirming the reliability of our approach.

At half filling, following the work of Ref. [106], we expect the presence of long-ranged AF order for all values of U considered in Fig. 8. This is also supported by the Mott plateau seen in Fig. 9(b,d) at half-filling. Since by construction our iPEPS is $SU(2)_{\text{spin}}$ invariant, however, a direct measurement of the local magnetization is not possible. Nevertheless, we expect that the symmetry-breaking AF order still to be present, yet *symmetrized* and hence only accessible via static spin-spin correlations over longer distances.

In the context of symmetric iPEPS simulations for a spin- $\frac{1}{2}$ Heisenberg model, we have observed (not shown) that the two-fold degeneracy in the AF ground state manifests itself as a spontaneous formation of row or column stripes which, in agreement with the AF state itself, breaks translational symmetry within the unit cell. Interestingly, we here also observe such an effect in the iPEPS wavefunctions in the 2-band Hubbard model as shown in Figs. 8(e,f). For $U = 4$ [Fig. 8(e)], we clearly observe that two out of eight independent bonds in the unit cell carry a substantially reduced energy. This suggests (at least) a 4-fold degenerate ground state.

Based on this loose connection, we will refer to the symmetry-broken regime as the AF regime where the strength of the spatial symmetry breaking in our simulations may roughly correlate with the AF magnetic moment. For $U = 10$ [Fig. 8(f)] the “AF order” is weaker than at $U = 4$, consistent with the finding of Ref. [106] that the strength of AF order decrease for $U \rightarrow \infty$. Ultimately, of course, the precise AF nature needs to be studied via long-ranged spin-spin correlations. This is left for future work.

Next we turn to the case of arbitrary filling away from half-filling, which is equally accessible to iPEPS, but not to QMC. We focus on small to intermediate interactions, $U = 4$ and $U = 8$. By symmetry, it is sufficient to consider only the case of finite hole doping, $\delta \equiv 2 - \langle n \rangle > 0$, i.e., $\langle n \rangle < 2$. For the 2-band case, this regime has not been explored in detail by other methods so far. Figure 9 summarizes our iPEPS results as a function of filling, tuned by means of a chemical potential [cf. Eq. (80b)]. Figures 9(a,c) show the ground-state energy per site, e_0/U , as a function of δ for $D^* = 5$ and 6.

The dependence of the filling $\langle n \rangle = 2 - \delta$ on the chemical potential is shown in Figs. 9(b,d).

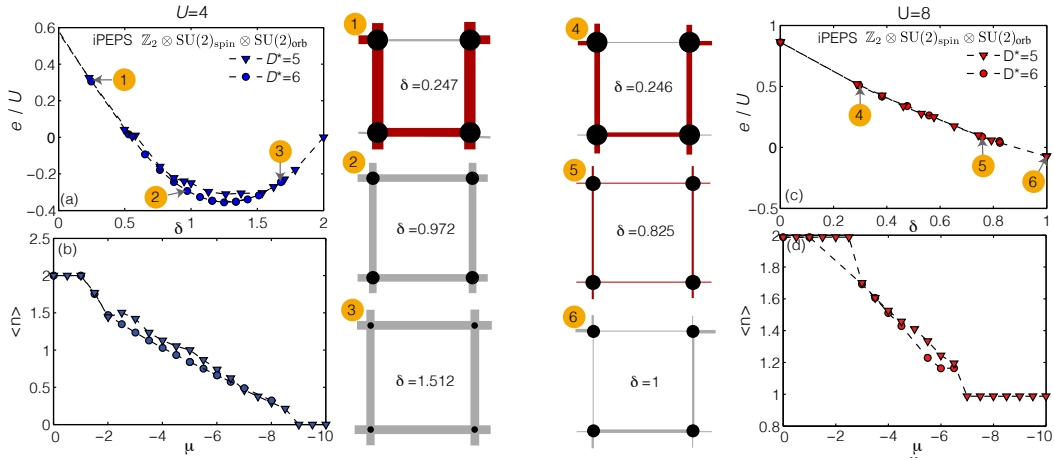


Figure 9: Non-abelian iPEPS results for the two-band Hubbard model away from half filling for $U = 4$ (left panels) and $U = 8$ (right panels). Panels (a) and (c) display the normalized ground-state energy e_0/U as a function of doping δ for multiplet bond dimensions $D^* = 5, 6$. (b) and (d) show the filling $\langle n \rangle$ as a function of the chemical potential μ . (In contrast to Figs. 8(a,b), no QMC data are available for comparison here, hence no $1/D^{*2}$ extrapolations were performed.) The parameter points (1) to (6) are analyzed in detail in the corresponding panels (1-6) in the center by characterizing the underlying iPEPS wave function. Again, the filling per site and the bond energy are proportional to the diameter of the black dots and the width of the bonds, where red (gray) bond correspond to positive (negative) values, respectively. The bond energies change signs at small doping, which is due to the definition of e_0^{ij} in Eq. (81b), where the Coulomb interaction energy (positive) competes with the kinetic energy (negative).

For either U , the systems are in the AF regime for zero or small doping δ , as inferred from the symmetry-broken states depicted in Figs. 9(1,4). For $U = 4$ we find an energy minimum around $\delta \simeq 1.2$. In this regime, we still observe a significant dependence of the energy on bond dimension D^* , hinting at a strongly entangled ground state. For $U = 8$, for the same range in chemical potential [Fig. 9(b,d)], we reach a smaller range in doping [Fig. 9(c)]. Since here the interaction strength is comparable to the non-interacting bandwidth is $W = 8$, we also see a Mott plateau at $\langle \hat{n} \rangle = 1$ [Fig. 9(d)] that is absent for $U = 4$ [Fig. 9(b)] [112].

At zero filling, i.e. $\delta = 2$, the ground state energy is zero, i.e. with Eq. (81a), $e_0(n = 0) = 0$ [similar as in Fig. 9(a)] irrespective of the strength of U . Therefore the data in Fig. 9(c), already turning negative, will necessarily also reach a minimum somewhere in the regime for $1 < \delta < 2$.

In addition to antiferromagnetism, we also expect superconducting order to play an important role in the two-band Hubbard model at finite hole doping. To check for the presence of d -wave superconductivity, we measure a generalized singlet-pairing amplitude Δ^{ij} [Eq. (81c)]. The results for different values of U and δ are displayed in Fig. 10. We find that, indeed, superconducting order is present for the entire doping range $0 < \delta < 1$ for all considered interaction strengths. Two effects that will require further attention in the future, are the suppression of superconductivity at $\delta = 1$, and the fact that Δ decreases with increasing interaction strength. Both appear justified on intuitive grounds, however: Charge fluctuations are suppressed with increasing interaction strength, specifically so at integer filling. Moreover, for filling $n \lesssim 1$, local double occupancy is strongly suppressed for sizable U , yet double occupancy is required for finite Δ to start with. We also observe strong inhomogeneity of Δ^{ij} across different bonds.

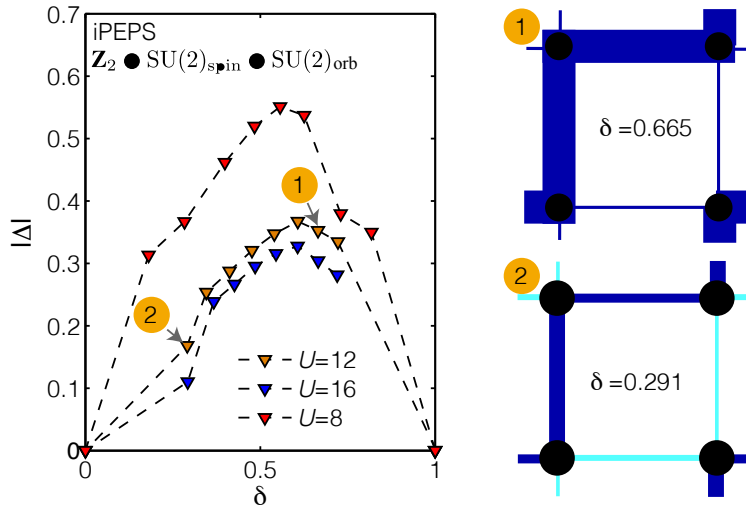


Figure 10: Generalized singlet-pairing amplitude $|\Delta|$ per site, extracted from iPEPS wavefunctions with $D^* = 5$ as a function of the hole doping δ . $|\Delta| \equiv \langle |\Delta^{ij}| \rangle$ is obtained by averaging over the absolute value of Δ^{ij} for each bond in the unit cell. Labels 1 and 2 point to individual iPEPS wavefunctions characterized on the right, where the filling per site and the singlet-pairing amplitude are proportional to the diameter of the black dots and the width of the bonds, respectively [blue (cyan) bond correspond to positive (negative) Δ^{ij}].

This may indicate a tendency toward spontaneous symmetry breaking of the orbital symmetry that is conserved by construction in our iPEPS implementation, or to the fact that the actual ground state breaks translational symmetry in a different way. Simulations on different unit-cell geometries are needed to shed light on this issue.

In conclusion, we have presented first fermionic iPEPS simulations of the two-band Hubbard model, which incorporates spin- and orbital $SU(2)$ symmetry explicitly in the TN ansatz. The excellent agreement of our results found at half-filling with QMC data encouraged us to explore also the hole-doped regime, where our initial results uncover a number of intriguing features. Going forward, much work remains to be done to fully understand the guiding mechanisms and phases in this regime. This includes the study of longer-ranged spin-spin correlators, the comparison to simulations on different unit cells and unveiling the dependencies of various quantities such as energy and d -wave pairing as a function of interaction strength and doping more carefully. Since in the present model spin and orbital flavors are equivalent (e.g., there is no onsite Hund’s coupling J), the efficiency of iPEPS could be further enhanced by exploiting the full $SU(4)_{\text{flavor}}$ symmetry present in the Hamiltonian within QSpace [30]. After fully understanding the phase diagram in this parameter regime, it will be highly interesting to study the effects of finite Hund’s coupling J on the emergence of superconductivity and other competing orders. Moreover, it would also be worthwhile to analyze whether abelian iPEPS simulations are numerically feasible in a modified setup involving separate sublattice for the two bands (c.f. Fig. 7). This would yield a different perspective on the ground-state properties of the model, especially in the context of spontaneous symmetry breaking.

6.2 Three-flavor Hubbard model

In addition to basic $SU(2)$ symmetries, QSpace [30] also provides a convenient framework for the incorporation of more complex non-abelian symmetries such as $SU(N > 2)$. To explore the

potential of this feature within fermionic iPEPS, we consider a symmetric spinless three-flavor Hubbard model where we fully exploit the $SU(3)$ flavor symmetry. Its Hamiltonian has the same form as in (80), except that the composite index (m, σ) is replaced by a single flavor index, $m = 1, 2, 3$. Choosing $\mu_0 = U$ here, this again also ensures that $\mu = 0$ corresponds to half-filling. In contrast to the spinful case, however, the fact that $N = 3$ is odd implies that half-filling is metallic, unless symmetry broken (see below). Only integer filling results in Mott or Heisenberg physics for larger U [112].

Although systems with a total of three symmetric flavors are not naturally realized by the atomic configuration of any real electronic material, $SU(N > 2)$ realizations of the fermionic Hubbard model currently attract a lot of attention in the context of cold-atom experiments based on alkaline earth-like atoms such as ytterbium [102, 103], where such systems have become directly accessible in highly controlled setups. $SU(N)$ symmetric systems feature a number of exotic phases and magnetic properties, which are of interest from a condensed matter perspective. In addition, they are also relevant for other fields, for example in the context of studying lattice gauge theories for quantum chromodynamics [113].

So far, little is known for the spinless $SU(3)$ Hubbard model on the 2D square lattice. Some work has been done for the weak to intermediate coupling limit, where one expects the emergence of a flavor density wave breaking the translational symmetry of the lattice [114]. At half filling in particular, it is expected that two flavors occupy the same lattice site whereas neighboring sites exclusively host the third flavor, such that a bipartite two-sublattice structure emerges. This is motivated by the following consideration: a site with single occupancy transforms in the defining three-dimensional representation $\mathbf{3}$ of $SU(3)$, whereas a doubly filled site is a fully filled site with one hole, which transforms in the conjugate representation $\bar{\mathbf{3}}$. Within the symmetry broken setting above then, neighboring sites could, in principle, bind into a singlet configuration.

At integer filling $n = 1$ and in the strong coupling limit, the model can be mapped onto an $SU(3)$ Heisenberg model in the defining $\mathbf{3}$ representation (physically equivalent, for $n = 2$, this becomes the dual $\bar{\mathbf{3}}$). This is believed to favor a three-sublattice order with finite magnetic moments [115]. On intuitive grounds, note that for an $SU(3)$ Heisenberg model in the $\mathbf{3}$ representation, a multiple of three sites is required to form a singlet. This is not naturally suited to the square lattice, and hence results in frustration, eventually giving rise to a three-sublattice order.

We have again reduced the numerical complexity of our model system by fully incorporating the non-abelian $SU(3)$ symmetry in the fermionic iPEPS ansatz. To this end, the full local fermionic state space, $d = 8$, can be reduced to $d^* = 4$ multiplets. We then performed simple-update calculations with a multiplet bond dimensions up to $D^* = 6$. Again, the symmetry sectors are dynamically adapted during the optimization. We illustrate examples of the relevant multiplet contributions encountered in iPEPS simulations with varying D^* at half filling in Table 2.

We performed iPEPS simulations on both 2×2 and 3×3 unit cells with two and three different tensors, respectively, to slightly bias the emergence of the two- and three-sublattice order expected from the considerations discussed above. Any tendency towards spontaneous symmetry breaking of $SU(3)$, are, however, symmetrized by our setup. Figures 11(a,b) summarize our results for the ground-state energy per site, e_0/U , as a function of filling, $\langle n \rangle$, both at weak coupling $U = 1$ and stronger coupling $U = 6$. In either case, the simulations on both unit-cell geometries surprisingly yield very compatible ground-state energies.

For $U = 1$ at half-filling, which in the present case of $N = 3$ corresponds to half-integer filling on average, we observe a tendency toward translational symmetry breaking in the form of modulation of the occupancy on different sites for both 2×2 and 3×3 clusters (wavefunction 1 and 2). This is in qualitative agreement with Ref. [114], which predicts a phase with

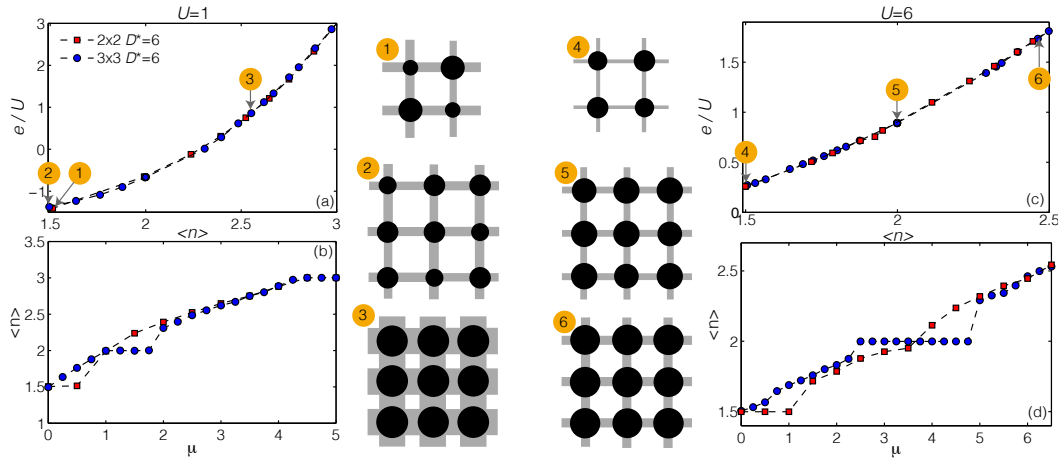


Figure 11: Non-abelian iPEPS results for the three-flavor Hubbard model for $U = 1$ (left panels) and $U = 6$ (right panels). Panels (a) and (c) display the ground-state energy e_0/U as a function of filling $\langle n \rangle$ for iPEPS simulations on a 2×2 and 3×3 unit cell, whereas (b) and (d) show the filling $\langle n \rangle$ as a function of the chemical potential μ . Panels (1) to (6) depict individual iPEPS wavefunctions at the points marked in panels (a,c). The filling per site and the bond energy are proportional to the diameter of the black dots and the width of the bonds, respectively.

Table 2: Typical multiplet configurations on the auxiliary bonds obtained from $SU(3)$ symmetric iPEPS simulations on the square lattice Hubbard model with three equivalent flavors. The different rows show the results for increasing multiplet bond dimension D^* (left column) at half filling. The $SU(3)$ multiplet labels are in Dynkin form, where we adopt the compact QSpace [30] notation. For the center column we use the same notation as in Table 1.

D^*	multiplets in symmetry sectors ($\mathbb{Z}_2, SU(3)_{\text{flavor}}$)	D
4	$(-1, 00) \oplus (-1, 01) \oplus (1, 01) \oplus (1, 10)$	$1 + 3 + 3 + 3 = 10$
5	$(-1, 00) \oplus (-1, 11) \oplus (1, 01) \oplus (1, 10)$	$1 + 8 + 3 + 3 = 16$
6	$(-1, 00) \oplus (-1, 11) \oplus (1, 01)^2 \oplus (1, 10)$	$1 + 8 + 6 + 3 = 19$

two-sublattice order with single and double occupancy on neighboring sites. This is almost realized by wavefunction 1 shown in Fig. 11, with occupancies $N \approx 1.19$ and $N \approx 1.81$ on neighboring sites. For the 2×2 cluster, this also goes hand in hand with a pinning of the occupation at average $\langle n \rangle = 1.5$ [Fig. 11(b,d)], suggesting that the system energetically prefers a translationally symmetry broken state. The density modulation are substantially suppressed on the 3×3 unit cell, where we find two sites having the same occupancy $N \approx 1.58$ while slightly fewer particles occupy the third site $N \approx 1.32$ at essentially no pinning of the average occupation when changing the chemical potential. The density-wave modulation disappears both in the case when the occupation significantly deviates from the half-filled case, and also for stronger interaction, as illustrated by the wave functions 3, 4, 5, and 6 in Fig. 11.

As already pointed out with Figs. 11(b,d), the occupancy is clearly not a smooth increasing function of the chemical potential, which drives the filling. While the 2×2 unit cell shows plateaus – and hence favors – half-filling, this is not the case for the 3×3 unit cells. The situation is completely reverse, however, at integer filling $\langle n \rangle = 2$ as seen in Figs. 11(b,d).

At this filling, a 2×2 unit cell cannot be in a singlet configuration, but has residual spin. Hence there is a certain degree of frustration in this setup. By contrast, the 3×3 unit cell can host a singlet configuration at $\langle n \rangle = 2$. Interestingly, the 3×3 unit cell already shows charge locking for the case of rather smaller $U = 1$, which may be due to frustration in the present case. Eventually, however, this will require a more thorough analysis based on an extrapolation of $D^* \rightarrow \infty$.

Locking of charge at integer filling is typically a signature of Mott physics, which is to some extent also expected in the three-flavor model at $\langle n \rangle = 2$ [112, 116]. However, locking may also occur if the occupation inside an enlarged unit cell changes by integers. This effect may be physical, e.g., as suggested above, in that $\mathbf{3}$ and $\bar{\mathbf{3}}$ bind into singlets, which occurs at half-filling. The effect may also be artificial, in which case it depends on numerical details and should become less pronounced with increasing D^* . This can be observed for the plateau at filling $\langle n \rangle = 1.5$ (data not shown).

In summary, nevertheless, based on the earlier arguments we do expect that in the present case the 2×2 unit cell is more suitable for the half-filled case, whereas the 3×3 unit cell is a better fit for integer filling. Furthermore, it should be possible to reveal additional information about the flavor order by studying (i) longer-ranged correlators and (ii) switching off the $SU(3)$ in favor of two abelian $U(1)$ symmetries and explicitly allowing spontaneous breaking of the flavor symmetry.

7 Conclusion

In this review, we attempt to give an overview of the rapid developments of iPEPS, which has reached a remarkable sophistication over the last few years. A large part of the review, addressed to newcomers to the field, is dedicated to two widely used ground state search methods: simple-update and full-update. Simple-update is very competitive in run-time, while full-update yields highly accurate results that are important to characterize ground states of correlated electrons. Besides that, we present a comprehensive technical detail about using non-abelian symmetry in iPEPS, where a seemingly formidable computational overhead can be avoided by careful implementation. Two non-trivial examples, the two-band Hubbard model and the three-flavor Hubbard model, are included to show how exploiting symmetry can be useful. All in all, we hope that this review will motivate more efforts to the development of 2D tensor network algorithms, which have the potential for achieving crucial advances in computational studies of correlated electrons.

Funding information The Deutsche Forschungsgemeinschaft supported BB, JWL and JvD through the Excellence Cluster “Nanosystems Initiative Munich” and the Excellence Strategy-EXC-2111-390814868. JWL was also supported by DFG WE4819/3-1. AW was supported by the U.S. Department of Energy, Office of Basic Energy Sciences, under Contract No. DE-SC0012704.

A Constructing tensors with symmetry

In this Appendix, we provide a sketch of how to deal with non-abelian symmetry in tensor networks. For simplicity, we use $SU(2)$ as a concrete example. The strategy can be generalized to $SU(N)$ (for more detail, we refer to Ref. 30, 31). The example illustrates the conceptual bottom-up approach underlying the QSpace tensor library [30, 31] for implementing symmetries in tensor networks: construct all ingredients step by step, systematically combining

elementary building blocks into more complex structures.

A.1 SU(2) spin algebra

A group element of SU(2) can be represented by an unitary transformation, $\hat{G} = e^{i\hat{S}}$, in a complex vector space, with \hat{S} an arbitrary Hermitian matrix in that space. This matrix can be parametrized by three independent real numbers φ_a , with $a \in \{x, y, z\}$, such that $\hat{S} = \sum_a \varphi_a \hat{S}^a \equiv \varphi \cdot \hat{\mathbf{S}}$, with \hat{S}^a the generators of the symmetry, satisfying $[\hat{S}^a, \hat{S}^b] = i\epsilon^{abc} \hat{S}^c$. In the defining, two-dimensional representation with spin multiplet label $S = \frac{1}{2}$, the generators can be chosen as $\hat{S}^a \equiv \frac{1}{2} \sigma^a$, with σ^a the Pauli matrices.

This is the smallest non-trivial SU(2) matrix representation. More generally, an SU(2) irreducible representation (irrep) with spin S has dimension $2S + 1$, i.e. the generators \hat{S} are represented by matrices of size $(2S + 1) \times (2S + 1)$.

In general, an irreducible multiplet consists of a set of states that can be labeled by their eigenvalues of the generators that were chosen diagonal, i.e., in the SU(2) context, S_z . For a general non-abelian symmetry, this can be a set of generators, say Q_x , resulting in a tuple of labels q_x . These can be lexicographically sorted, with the *largest*, i.e., the maximum weight state being unique. Its *weights* q_x therefore can be used to label the entire multiplet. In the SU(2) context, $\max(S_z) = S$.

Alternatively, the complete set of Casimir operators also labels a multiplet uniquely. Hence there exists a well-defined polynomial mapping from the maximum weight labels to the Casimir labels. For example, in the case of SU(2), $S \rightarrow S(S + 1)$, with the latter being the eigenvalue of the quadratic Casimir, $\hat{S}^2 \equiv \hat{S}^a \hat{S}_a$, using Einstein summation convention. Other than that, the Casimir operators are not required, and so we do not use them. Instead, we use convenient internal conventions on the normalization of generators, with a subsequent *linear* mapping of the maximum weight labels to standard Dynkin labels. In particular, this implies for SU(2) the symmetry labels $q = 2S$. For one, this is consistent with SU($N > 2$), e.g., in that q is equivalent to the number of boxes in its corresponding Young tableau. Moreover, this also has the advantage that all symmetry labels are integers, which we find more readable and convenient on practical grounds. We use the notation q as label for irreducible multiplets, in order to emphasize that this can be a tuple of labels for an irreducible multiplet for any symmetry.

A.2 Tensor product decomposition

A tensor product of two irreps q_1 and q_2 can be decomposed into a direct sum of irreps,

$$V^{q_1} \otimes V^{q_2} = \bigoplus_q M_{q_1 q_2}^q V^q, \tag{82}$$

where in this symbolic notation, the multiplicity coefficients $M_{q_1 q_2}^q$ are integers encoding the fusion rules. That is, irreps that do occur in the product decomposition have $M_{q_1 q_2}^q > 0$, whereas multiplets q with $M_{q_1 q_2}^q = 0$ do not occur in the decomposition [for SU(2) $M_{q_1 q_2}^q = 1$ for $q = 2S \in |q_1 - q_2|, |q_1 - q_2| + 2, q_1 + q_2$, and $M_{q_1 q_2}^q = 0$ otherwise]. For general non-abelian symmetries as for SU($N \geq 3$), the *same* irrep q can routinely occur multiple times, i.e., having outer multiplicity $M_{q_1 q_2}^q > 1$.

The coupled basis vector $|q, q_z\rangle$ and the direct product basis $|q_1, q_{1z}\rangle \otimes |q_2, q_{2z}\rangle$ are related by a unitary basis transformation matrix, namely,

$$|q_1, q_{1z}\rangle \otimes |q_2, q_{2z}\rangle = \left(\sum_{q, q_z} |q, q_z\rangle \langle q, q_z| \right) |q_1, q_{1z}\rangle \otimes |q_2, q_{2z}\rangle, \tag{83}$$

$$\equiv \underbrace{\left(C_{q_1 q_2}^q \right)_{q_{1z} q_{2z}}^{q_z}}_{\equiv \left(C_{q_1 q_2}^q \right)_{q_{1z} q_{2z}}^{q_z}}$$

where $(C_{q_1 q_2}^q)_{q_1 z q_2 z}^{q_z}$ are the standard Clebsch-Gordan coefficient (CGC) spaces. The notation here emphasizes the tensorial structure, in that the Clebsch-Gordan *tensor* (CGT) $C_{q_1 q_2}^q$ is indexed by the q_z -labels (in the presence of inner multiplicity where degeneracies in the the q_z -labels occur, caveats apply [30]). The rank-3 CGTs above are fundamental building blocks since any higher-rank CGC can be generated from them.

Example: Direct product of two spin-half multiplets The tensor product of the two vector spaces of two spin-half multiplets, having $q_1 = q_2 = 2S = 1$, can be decomposed into a spin-singlet, $q = 0$, and a spin-triplet, $q = 2S = 2$, i.e, $1 \otimes 1 = 0 \oplus 2$.

The unitary basis transformation matrix from the direct product basis to the coupled basis can be read as

(using the familiar labels $\langle S, S_z |$ for the rows and $|S_{1z}, S_{2z}\rangle$ for the columns on the r.h.s.),

$$\begin{pmatrix} C_{q_1 q_2}^0 \\ C_{q_1 q_2}^2 \end{pmatrix} = \begin{matrix} \langle 0, 0 | \\ \langle 1, 1 | \\ \langle 1, 0 | \\ \langle 1, -1 | \end{matrix} \begin{matrix} | \uparrow \uparrow \rangle & | \uparrow \downarrow \rangle & | \downarrow \uparrow \rangle & | \downarrow \downarrow \rangle \\ \begin{pmatrix} 0 & 1/\sqrt{2} & -1/\sqrt{2} & 0 \\ 1 & 0 & 0 & 0 \\ 0 & 1/\sqrt{2} & 1/\sqrt{2} & 0 \\ 0 & 0 & 0 & 1 \end{pmatrix} \end{matrix} . \quad (84)$$

This includes two sets of CGCs concatenated vertically, namely for $q = 0$ and $q = 2$, as indicated by the horizontal lines separating them. These CGCs are fully defined by symmetries. They can be explicitly computed via (generalized) tensor-product decomposition [30], and stored as separate tensors in sparse format in a database.

A.3 Irreducible tensor operator

State spaces and operators are tightly related. For example, if one creates a particle with spin-half on top of a singlet (or vacuum state), $\hat{c}_\sigma^\dagger |0\rangle \equiv |\sigma\rangle$, the operator on the l.h.s. necessarily needs to transform under symmetry like the resulting state on the r.h.s. Symmetry operations on the state to the right translate into commutation relations for the operators on the left, and Clebsch-Gordan coefficients come into play, as also evidenced by the Wigner-Eckart theorem.

For example, in the case of SU(2), the operation of a raising or lowering operator for an irreducible operator (irrop) \hat{T}^{SS_z} , which by notation transforms like a spin- S multiplet, translates into the following relations:

$$[(\hat{S}_x \pm i\hat{S}_y), \hat{T}^{SS_z}] = \sqrt{S(S+1) - S_z(S_z \pm 1)} \hat{T}^{SS_z \pm 1} \quad (85)$$

$$[\hat{S}_z, \hat{T}^{SS_z}] = S_z \hat{T}^{SS_z} . \quad (86)$$

This demonstrates that just as a multiplet $|SS_z\rangle$ is irreducible under a given symmetry, so is the irrop. In particular, an irrop represents a set of operators, here labeled by S_z , which carries a representation of the symmetry group.

Now if an irrop acts on a non-trivial state space that itself transforms like a non-scalar symmetry multiplet, the resulting states correspond to a tensor product of symmetry multiplets, and the rules of tensor product decomposition of multiplets apply. This is manifested in the Wigner Eckart theorem (returning to generic ‘ q -labels’),

$$\langle q_1 q_{1z} | \hat{T}^{q q_z} | q_2 q_{2z} \rangle \equiv \langle q_1 q_{1z} | \cdot \left(\hat{T}^{q q_z} \times | q_2 q_{2z} \rangle \right) = \langle q_1 || \hat{T}^q || q_2 \rangle (C_{q q_2}^{q_1})_{q_1 z q_2 z}^{q_z}, \quad (87)$$

where the *reduced matrix element* $\langle q_1 || \hat{T}^q || q_2 \rangle$ is the only remaining effective matrix element

not determined by symmetry, but depending on the physical action of the operator. Other than that, the Wigner-Eckart theorem demonstrates that the matrix elements of an irrep are not independent of each other, but are highly constrained by symmetry operations, i.e., related by CGCs. In other words, an $SU(2)$ symmetric tensor can be factorized into two parts, *reduced tensor elements* and CGCs. With both state space decomposition and operator representation thus linked to CGTs, this forms a natural framework to build tensors of arbitrary complexity precisely on the basis of tensor network states.

A.4 PEPS tensor construction

Here we demonstrate, based on an instructive example relevant for the present context, how complex tensors can be built from elementary building blocks, making explicit use of rank-3 CGTs. With the focus on iPEPS in this work, the building block of the iPEPS itself is a local rank-5 tensor M , with four virtual bond indices, say L(ef), R(ight), U(p), and D(own), together with a local state space, P(hysical). So how would one build, or even initialize such a tensor while respecting non-abelian symmetries in a generic fashion?

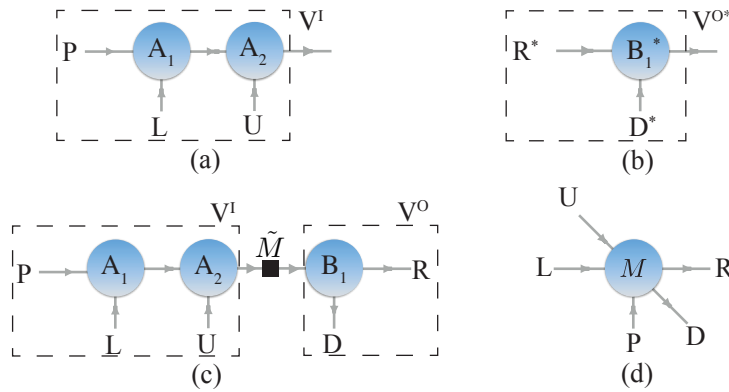


Figure 12: Steps (a)-(c) for building rank-5 PEPS tensor in (d) from elementary rank-3 tensors. (a) Iterative fusion of the “incoming” state spaces, $V^P \otimes V^L \otimes V^U \equiv (V^P \otimes V^L) \otimes V^U \equiv V^I$, first combining the physical states space P with the left bond L via A_1 , then fusing the result with the upper bond U via A_2 . (b) Fusion of the ‘outgoing’ states spaces, $V^{R*} \otimes V^{D*} \equiv V^{O*}$. (c) Fusing together the results of (a) and the *conjugate* [31] of (b) into a global singlet via the bond tensor \tilde{M} . The latter is block-diagonal with trivial CGCs; its reduced matrix elements can be chosen arbitrarily, e.g., such that the overall tensor may satisfy certain lattice symmetries. The indices R and D became outgoing indices in the last step. (d) The final rank-5 PEPS tensor after contracting all tensors in (c). Each leg U, D, L, R and P represents a state space which in the presence of non-abelian symmetries is organized via the generic composite labels $|ql; qz\rangle$ as introduced with Eq. (71).

The prescription to build such a rank-5 PEPS tensor M is summarized in Fig. 12. We assume that the state spaces of each of the constituent bonds are already specified (or have been obtained in some fashion). Importantly, each bond also has a direction, indicating whether an index *enters* or *leaves* the final desired object. As indicated in Fig. 12(d), the tensor M has three incoming indices, (P, L, U) , and two outgoing indices, (R, D) . So one can fuse the state spaces in either case. A set of state spaces, such as (L, U, P) , can be build iteratively by adding one state space at a time, $V^P \otimes V^L \otimes V^U \equiv (V^P \otimes V^L) \otimes V^U \equiv V^I$, where I stands for the combined incoming state space, as depicted in Fig. 12(a). The same can be done for the outgoing state spaces, except that by the very concept of fusing input spaces into output, the tensor product

deals with the opposite direction of R and D , namely also ingoing. Hence the state space in the dual (or conjugate) representation needs to be considered in the fusion itself, as indicated by the asterisk in $V^{R*} \otimes V^{D*} \equiv V^{O*}$ in Fig. 12(b). Here O stands for the combined state spaces of legs eventually leaving the tensor M .

Having fused in- and outgoing state spaces separately and without truncation, the final step is to tie together the two fused state spaces into a global singlet, symbolically written as $V^I \otimes V^{O*} \rightarrow 0$, with $q = 0$ the scalar representation, i.e., a singlet. This sixth index, namely a global singlet state, then corresponds to a singleton dimension that can be skipped. Since for any irrep q only the combination with its dual q^* can result in a singlet, the CGCs for this step are simple ($1j$ symbols in the language of [31]), as one can only link in a 1-to-1 correspondence between V^I and V^{O*} . However, the situation is much simpler still, since one needs to contract the *conjugate* of the V^{O*} above, in order to obtain the final desired index directions. The conjugate of the entire object in Fig. 12(b) can be drawn pictorially as a mirror image [here left-to-right, as in Fig. 12(c)], with all arrows reversed [see [31] for details]. This now can be simply contracted with the tensors in Fig. 12(a) as shown in Fig. 12(c). Since arrow directions are preserved, this implies that the only free choice of tensor coefficients left are in the tensor \tilde{M} in Fig. 12(c) that ties together in- and outgoing state spaces. Via Wigner Eckart theorem, the tensor \tilde{M} is a scalar operator, where with the corresponding singleton dimension of the irrep set skipped, this can be written as a plain block-diagonal tensor, with the corresponding CGTs $C_{0q}^q = 1^q$ being trivial identity matrices in the multiplet space of the respective multiplet q .

The above example reflects the generic transparent guiding principle when working with symmetric tensors, namely: to construct arbitrarily complex tensors from known, manageable, elementary building blocks. In the present case, this included (i) the fusion of pairs of state spaces [via A_i and B_i , as well as the final fusion into a trivial scalar multiplet via \tilde{M} in Figs. 12(a-c)]. This was followed by (ii) the pairwise contraction of symmetric tensors [31] to obtain M in Fig. 12(d). Here, for example, one may have used the nested pairwise grouping $A_1 A_2 \tilde{M} B_1 = ((A_1 * A_2) * (\tilde{M} * B_1))$, where ‘*’ refers to the contraction of a pair tensors on fully connected indices, which simply generalizes matrix multiplication to tensors.

References

- [1] C. Gros, *Physics of projected wavefunctions*, Ann. Phys. **189**, 53 (1989), doi:[10.1016/0003-4916\(89\)90077-8](https://doi.org/10.1016/0003-4916(89)90077-8).
- [2] S. Yan, D. A. Huse and S. R. White, *Spin-liquid ground state of the $S = 1/2$ Kagome Heisenberg antiferromagnet*, Science **332**, 1173 (2011), doi:[10.1126/science.1201080](https://doi.org/10.1126/science.1201080).
- [3] S. Depenbrock, I. P. McCulloch and U. Schollwöck, *Nature of the spin-liquid ground state of the $S=1/2$ Heisenberg model on the Kagome lattice*, Phys. Rev. Lett. **109**, 067201 (2012), doi:[10.1103/PhysRevLett.109.067201](https://doi.org/10.1103/PhysRevLett.109.067201).
- [4] S. R. White and D. J. Scalapino, *Density matrix renormalization group study of the striped phase in the 2D t - J model*, Phys. Rev. Lett. **80**, 1272 (1998), doi:[10.1103/PhysRevLett.80.1272](https://doi.org/10.1103/PhysRevLett.80.1272).
- [5] P. Corboz, S. R. White, G. Vidal and M. Troyer, *Stripes in the two-dimensional t - J model with infinite projected entangled-pair states*, Phys. Rev. B **84**, 041108 (2011), doi:[10.1103/PhysRevB.84.041108](https://doi.org/10.1103/PhysRevB.84.041108).

- [6] P. Corboz, T. M. Rice and M. Troyer, *Competing states in the t - J model: Uniform d -wave state versus stripe state*, Phys. Rev. Lett. **113**, 046402 (2014), doi:[10.1103/PhysRevLett.113.046402](https://doi.org/10.1103/PhysRevLett.113.046402).
- [7] J.-W. Mei, J.-Y. Chen, H. He and X.-G. Wen, *Gapped spin liquid with Z_2 topological order for the Kagome Heisenberg model*, Phys. Rev. B **95**, 235107 (2017), doi:[10.1103/PhysRevB.95.235107](https://doi.org/10.1103/PhysRevB.95.235107).
- [8] H. J. Liao, Z. Y. Xie, J. Chen, Z. Y. Liu, H. D. Xie, R. Z. Huang, B. Normand and T. Xiang, *Gapless spin-liquid ground state in the $S=1/2$ Kagome antiferromagnet*, Phys. Rev. Lett. **118**, 137202 (2017), doi:[10.1103/PhysRevLett.118.137202](https://doi.org/10.1103/PhysRevLett.118.137202).
- [9] B.-X. Zheng et al., *Stripe order in the underdoped region of the two-dimensional Hubbard model*, Science **358**, 1155 (2017), doi:[10.1126/science.aam7127](https://doi.org/10.1126/science.aam7127).
- [10] F. Verstraete and J. I. Cirac, *Renormalization algorithms for quantum-many body systems in two and higher dimensions* (2004), [arXiv:cond-mat/0407066](https://arxiv.org/abs/cond-mat/0407066).
- [11] I. Affleck, T. Kennedy, E. H. Lieb and H. Tasaki, *Rigorous results on valence-bond ground states in antiferromagnets*, Phys. Rev. Lett. **59**, 799 (1987), doi:[10.1103/PhysRevLett.59.799](https://doi.org/10.1103/PhysRevLett.59.799).
- [12] Y. Hieida, K. Okunishi and Y. Akutsu, *Numerical renormalization approach to two-dimensional quantum antiferromagnets with valence-bond-solid type ground state*, New J. Phys. **1**, 7 (1999), doi:[10.1088/1367-2630/1/1/007](https://doi.org/10.1088/1367-2630/1/1/007).
- [13] K. Okunishi and T. Nishino, *Kramers-Wannier approximation for the 3D Ising model*, Progr. Theor. Phys. **103**, 541 (2000), doi:[10.1143/PTP.103.541](https://doi.org/10.1143/PTP.103.541).
- [14] Y. Nishio, N. Maeshima, A. Gendiar and T. Nishino, *Tensor product variational formulation for quantum systems* (2004), [arXiv:cond-mat/0401115](https://arxiv.org/abs/cond-mat/0401115).
- [15] M. Levin and C. P. Nave, *Tensor renormalization group approach to two-dimensional classical lattice models*, Phys. Rev. Lett. **99**, 120601 (2007), doi:[10.1103/PhysRevLett.99.120601](https://doi.org/10.1103/PhysRevLett.99.120601).
- [16] Z.-C. Gu, M. Levin and X.-G. Wen, *Tensor-entanglement renormalization group approach as a unified method for symmetry breaking and topological phase transitions*, Phys. Rev. B **78**, 205116 (2008), doi:[10.1103/PhysRevB.78.205116](https://doi.org/10.1103/PhysRevB.78.205116).
- [17] Z. Y. Xie, H. C. Jiang, Q. N. Chen, Z. Y. Weng and T. Xiang, *Second renormalization of tensor-network states*, Phys. Rev. Lett. **103**, 160601 (2009), doi:[10.1103/PhysRevLett.103.160601](https://doi.org/10.1103/PhysRevLett.103.160601).
- [18] Z. Y. Xie, J. Chen, M. P. Qin, J. W. Zhu, L. P. Yang and T. Xiang, *Coarse-graining renormalization by higher-order singular value decomposition*, Phys. Rev. B **86**, 045139 (2012), doi:[10.1103/PhysRevB.86.045139](https://doi.org/10.1103/PhysRevB.86.045139).
- [19] G. Evenbly and G. Vidal, *Tensor network renormalization*, Phys. Rev. Lett. **115**, 180405 (2015), doi:[10.1103/PhysRevLett.115.180405](https://doi.org/10.1103/PhysRevLett.115.180405).
- [20] G. Evenbly, *Algorithms for tensor network renormalization*, Phys. Rev. B **95**, 045117 (2017), doi:[10.1103/PhysRevB.95.045117](https://doi.org/10.1103/PhysRevB.95.045117).
- [21] P. Corboz, *Variational optimization with infinite projected entangled-pair states*, Phys. Rev. B **94**, 035133 (2016), doi:[10.1103/PhysRevB.94.035133](https://doi.org/10.1103/PhysRevB.94.035133).

- [22] L. Vanderstraeten, J. Haegeman, P. Corboz and F. Verstraete, *Gradient methods for variational optimization of projected entangled-pair states*, Phys. Rev. B **94**, 155123 (2016), doi:[10.1103/PhysRevB.94.155123](https://doi.org/10.1103/PhysRevB.94.155123).
- [23] L. Vanderstraeten, M. Mariën, F. Verstraete and J. Haegeman, *Excitations and the tangent space of projected entangled-pair states*, Phys. Rev. B **92**, 201111 (2015), doi:[10.1103/PhysRevB.92.201111](https://doi.org/10.1103/PhysRevB.92.201111).
- [24] P. Corboz, J. Jordan and G. Vidal, *Simulation of fermionic lattice models in two dimensions with projected entangled-pair states: Next-nearest neighbor Hamiltonians*, Phys. Rev. B **82**, 245119 (2010), doi:[10.1103/PhysRevB.82.245119](https://doi.org/10.1103/PhysRevB.82.245119).
- [25] I. P. McCulloch and M. Gulácsi, *The non-Abelian density matrix renormalization group algorithm*, Europhys. Lett. **57**, 852 (2002), doi:[10.1209/epl/i2002-00393-0](https://doi.org/10.1209/epl/i2002-00393-0).
- [26] I. P. McCulloch, *From density-matrix renormalization group to matrix product states*, J. Stat. Mech. P10014 (2007), doi:[10.1088/1742-5468/2007/10/p10014](https://doi.org/10.1088/1742-5468/2007/10/p10014).
- [27] S. Singh, R. N. C. Pfeifer and G. Vidal, *Tensor network decompositions in the presence of a global symmetry*, Phys. Rev. A **82**, 050301 (2010), doi:[10.1103/PhysRevA.82.050301](https://doi.org/10.1103/PhysRevA.82.050301).
- [28] S. Singh, R. N. C. Pfeifer and G. Vidal, *Tensor network states and algorithms in the presence of a global $U(1)$ symmetry*, Phys. Rev. B **83**, 115125 (2011), doi:[10.1103/PhysRevB.83.115125](https://doi.org/10.1103/PhysRevB.83.115125).
- [29] S. Singh and G. Vidal, *Tensor network states and algorithms in the presence of a global $SU(2)$ symmetry*, Phys. Rev. B **86**, 195114 (2012), doi:[10.1103/PhysRevB.86.195114](https://doi.org/10.1103/PhysRevB.86.195114).
- [30] A. Weichselbaum, *Non-abelian symmetries in tensor networks: A quantum symmetry space approach*, Ann. Phys. **327**, 2972 (2012), doi:[10.1016/j.aop.2012.07.009](https://doi.org/10.1016/j.aop.2012.07.009).
- [31] A. Weichselbaum, *X-symbols for non-Abelian symmetries in tensor networks*, Phys. Rev. Research **2**, 023385 (2020), doi:[10.1103/PhysRevResearch.2.023385](https://doi.org/10.1103/PhysRevResearch.2.023385).
- [32] S. Wouters, W. Poelmans, P. W. Ayers and D. Van Neck, *CheMPS2: A free open-source spin-adapted implementation of the density matrix renormalization group for ab initio quantum chemistry*, Comput. Phys. Commun. **185**, 1501 (2014), doi:[10.1016/j.cpc.2014.01.019](https://doi.org/10.1016/j.cpc.2014.01.019).
- [33] C. Hubig, *Abelian and non-abelian symmetries in infinite projected entangled pair states*, SciPost Phys. **5**, 047 (2018), doi:[10.21468/SciPostPhys.5.5.047](https://doi.org/10.21468/SciPostPhys.5.5.047).
- [34] P. Czarnik, M. M. Rams and J. Dziarmaga, *Variational tensor network renormalization in imaginary time: Benchmark results in the Hubbard model at finite temperature*, Phys. Rev. B **94**, 235142 (2016), doi:[10.1103/physrevb.94.235142](https://doi.org/10.1103/physrevb.94.235142).
- [35] B. Ponsioen, S. S. Chung and P. Corboz, *Period 4 stripe in the extended two-dimensional Hubbard model*, Phys. Rev. B **100**, 195141 (2019), doi:[10.1103/PhysRevB.100.195141](https://doi.org/10.1103/PhysRevB.100.195141).
- [36] P. Corboz, *Improved energy extrapolation with infinite projected entangled-pair states applied to the two-dimensional Hubbard model*, Phys. Rev. B **93**, 045116 (2016), doi:[10.1103/PhysRevB.93.045116](https://doi.org/10.1103/PhysRevB.93.045116).
- [37] T. Liu, W. Li, A. Weichselbaum, J. von Delft and G. Su, *Simplex valence-bond crystal in the spin-1 Kagome Heisenberg antiferromagnet*, Phys. Rev. B **91**, 060403 (2015), doi:[10.1103/PhysRevB.91.060403](https://doi.org/10.1103/PhysRevB.91.060403).

- [38] P. Corboz and F. Mila, *Tensor network study of the Shastry-Sutherland model in zero magnetic field*, Phys. Rev. B **87**, 115144 (2013), doi:[10.1103/PhysRevB.87.115144](https://doi.org/10.1103/PhysRevB.87.115144).
- [39] P. Corboz and F. Mila, *Crystals of bound states in the magnetization plateaus of the Shastry-Sutherland model*, Phys. Rev. Lett. **112**, 147203 (2014), doi:[10.1103/PhysRevLett.112.147203](https://doi.org/10.1103/PhysRevLett.112.147203).
- [40] M. P. Zaletel and F. Pollmann, *Isometric tensor network states in two dimensions*, Phys. Rev. Lett. **124**, 037201 (2020), doi:[10.1103/PhysRevLett.124.037201](https://doi.org/10.1103/PhysRevLett.124.037201).
- [41] R. Haghshenas, M. J. O'Rourke and G. Kin-Lic Chan, *Conversion of projected entangled pair states into a canonical form*, Phys. Rev. B **100**, 054404 (2019), doi:[10.1103/PhysRevB.100.054404](https://doi.org/10.1103/PhysRevB.100.054404).
- [42] L. Vanderstraeten, J. Haegeman and F. Verstraete, *Simulating excitation spectra with projected entangled-pair states*, Phys. Rev. B **99**, 165121 (2019), doi:[10.1103/physrevb.99.165121](https://doi.org/10.1103/physrevb.99.165121).
- [43] J. Jordan, R. Orús, G. Vidal, F. Verstraete and J. I. Cirac, *Classical simulation of infinite-size quantum lattice systems in two spatial dimensions*, Phys. Rev. Lett. **101**, 250602 (2008), doi:[10.1103/PhysRevLett.101.250602](https://doi.org/10.1103/PhysRevLett.101.250602).
- [44] D. Poilblanc and M. Mambrini, *Quantum critical phase with infinite projected entangled paired states*, Phys. Rev. B **96**, 014414 (2017), doi:[10.1103/PhysRevB.96.014414](https://doi.org/10.1103/PhysRevB.96.014414).
- [45] P. Corboz, R. Orús, B. Bauer and G. Vidal, *Simulation of strongly correlated fermions in two spatial dimensions with fermionic projected entangled-pair states*, Phys. Rev. B **81**, 165104 (2010), doi:[10.1103/PhysRevB.81.165104](https://doi.org/10.1103/PhysRevB.81.165104).
- [46] P. Corboz, G. Evenbly, F. Verstraete and G. Vidal, *Simulation of interacting fermions with entanglement renormalization*, Phys. Rev. A **81**, 010303 (2010), doi:[10.1103/PhysRevA.81.010303](https://doi.org/10.1103/PhysRevA.81.010303).
- [47] H. N. Phien, J. A. Bengua, H. D. Tuan, P. Corboz and R. Orús, *Infinite projected entangled pair states algorithm improved: Fast full update and gauge fixing*, Phys. Rev. B **92**, 035142 (2015), doi:[10.1103/PhysRevB.92.035142](https://doi.org/10.1103/PhysRevB.92.035142).
- [48] M. Lubasch, J. I. Cirac and M.-C. Bañuls, *Algorithms for finite projected entangled pair states*, Phys. Rev. B **90**, 064425 (2014), doi:[10.1103/PhysRevB.90.064425](https://doi.org/10.1103/PhysRevB.90.064425).
- [49] P. Schmoll, S. Singh, M. Rizzi and R. Orús, *A programming guide for tensor networks with global $SU(2)$ symmetry*, Ann. Phys. **419**, 168232 (2020), doi:[10.1016/j.aop.2020.168232](https://doi.org/10.1016/j.aop.2020.168232).
- [50] P. Schmoll and R. Orús, *Benchmarking global $SU(2)$ symmetry in two-dimensional tensor network algorithms*, Phys. Rev. B **102**, 241101 (2020), doi:[10.1103/PhysRevB.102.241101](https://doi.org/10.1103/PhysRevB.102.241101).
- [51] J.-W. Li, B. Bruognolo, A. Weichselbaum and J. von Delft, *iPEPS study of spin symmetry in the doped t - J model* (2020), [arXiv:2006.08323](https://arxiv.org/abs/2006.08323).
- [52] F. Verstraete, M. M. Wolf, D. Perez-Garcia and J. I. Cirac, *Criticality, the area law, and the computational power of projected entangled pair states*, Phys. Rev. Lett. **96**, 220601 (2006), doi:[10.1103/PhysRevLett.96.220601](https://doi.org/10.1103/PhysRevLett.96.220601).

- [53] R. Orús, *A practical introduction to tensor networks: Matrix product states and projected entangled pair states*, Ann. Phys. **349**, 117 (2014), doi:[10.1016/j.aop.2014.06.013](https://doi.org/10.1016/j.aop.2014.06.013).
- [54] J. Eisert, *Entanglement and tensor network states* (2013), [arXiv:1308.3318](https://arxiv.org/abs/1308.3318).
- [55] I. P. McCulloch, *Infinite size density matrix renormalization group, revisited* (2008), [arXiv:0804.2509](https://arxiv.org/abs/0804.2509).
- [56] N. Schuch, M. M. Wolf, K. G. H. Vollbrecht and J. I. Cirac, *On entropy growth and the hardness of simulating time evolution*, New J. Phys. **10**, 033032 (2008), doi:[10.1088/1367-2630/10/3/033032](https://doi.org/10.1088/1367-2630/10/3/033032).
- [57] T. Nishino and K. Okunishi, *Corner transfer matrix renormalization group method*, J. Phys. Soc. Jpn. **65**, 891 (1996), doi:[10.1143/JPSJ.65.891](https://doi.org/10.1143/JPSJ.65.891).
- [58] R. Orús and G. Vidal, *Simulation of two-dimensional quantum systems on an infinite lattice revisited: Corner transfer matrix for tensor contraction*, Phys. Rev. B **80**, 094403 (2009), doi:[10.1103/PhysRevB.80.094403](https://doi.org/10.1103/PhysRevB.80.094403).
- [59] G. Vidal, *Classical simulation of infinite-size quantum lattice systems in one spatial dimension*, Phys. Rev. Lett. **98**, 070201 (2007), doi:[10.1103/PhysRevLett.98.070201](https://doi.org/10.1103/PhysRevLett.98.070201).
- [60] R. Orús and G. Vidal, *Infinite time-evolving block decimation algorithm beyond unitary evolution*, Phys. Rev. B **78**, 155117 (2008), doi:[10.1103/PhysRevB.78.155117](https://doi.org/10.1103/PhysRevB.78.155117).
- [61] H. N. Phien, I. P. McCulloch and G. Vidal, *Fast convergence of imaginary time evolution tensor network algorithms by recycling the environment*, Phys. Rev. B **91**, 115137 (2015), doi:[10.1103/PhysRevB.91.115137](https://doi.org/10.1103/PhysRevB.91.115137).
- [62] P. Corboz, P. Czarnik, G. Kapteijns and L. Tagliacozzo, *Finite correlation length scaling with infinite projected entangled-pair states*, Phys. Rev. X **8**, 031031 (2018), doi:[10.1103/PhysRevX.8.031031](https://doi.org/10.1103/PhysRevX.8.031031).
- [63] M. Rader and A. M. Läuchli, *Finite correlation length scaling in Lorentz-Invariant gapless iPEPS wave functions*, Phys. Rev. X **8**, 031030 (2018), doi:[10.1103/PhysRevX.8.031030](https://doi.org/10.1103/PhysRevX.8.031030).
- [64] L. Tagliacozzo, Thiago. R. de Oliveira, S. Iblisdir and J. I. Latorre, *Scaling of entanglement support for matrix product states*, Phys. Rev. B **78**, 024410 (2008), doi:[10.1103/PhysRevB.78.024410](https://doi.org/10.1103/PhysRevB.78.024410).
- [65] F. Pollmann, S. Mukerjee, A. M. Turner and J. E. Moore, *Theory of finite-entanglement scaling at one-dimensional quantum critical points*, Phys. Rev. Lett. **102**, 255701 (2009), doi:[10.1103/PhysRevLett.102.255701](https://doi.org/10.1103/PhysRevLett.102.255701).
- [66] B. Pirvu, G. Vidal, F. Verstraete and L. Tagliacozzo, *Matrix product states for critical spin chains: Finite-size versus finite-entanglement scaling*, Phys. Rev. B **86**, 075117 (2012), doi:[10.1103/PhysRevB.86.075117](https://doi.org/10.1103/PhysRevB.86.075117).
- [67] V. Stojevic, J. Haegeman, I. P. McCulloch, L. Tagliacozzo and F. Verstraete, *Conformal data from finite entanglement scaling*, Phys. Rev. B **91**, 035120 (2015), doi:[10.1103/PhysRevB.91.035120](https://doi.org/10.1103/PhysRevB.91.035120).
- [68] H. C. Jiang, Z. Y. Weng and T. Xiang, *Accurate determination of tensor network state of quantum lattice models in two dimensions*, Phys. Rev. Lett. **101**, 090603 (2008), doi:[10.1103/PhysRevLett.101.090603](https://doi.org/10.1103/PhysRevLett.101.090603).

- [69] W. Li, J. von Delft and T. Xiang, *Efficient simulation of infinite tree tensor network states on the Bethe lattice*, Phys. Rev. B **86**, 195137 (2012), doi:[10.1103/PhysRevB.86.195137](https://doi.org/10.1103/PhysRevB.86.195137).
- [70] G. Vidal, *Efficient simulation of one-dimensional quantum many-body systems*, Phys. Rev. Lett. **93**, 040502 (2004), doi:[10.1103/PhysRevLett.93.040502](https://doi.org/10.1103/PhysRevLett.93.040502).
- [71] L. Wang and F. Verstraete, *Cluster update for tensor network states* (2011), [arXiv:1110.4362](https://arxiv.org/abs/1110.4362).
- [72] M. Lubasch, J. I. Cirac and M.-C. Bañuls, *Unifying projected entangled pair state contractions*, New J. Phys. **16**, 033014 (2014), doi:[10.1088/1367-2630/16/3/033014](https://doi.org/10.1088/1367-2630/16/3/033014).
- [73] S. Yang, Z.-C. Gu and X.-G. Wen, *Loop optimization for tensor network renormalization*, Phys. Rev. Lett. **118**, 110504 (2017), doi:[10.1103/PhysRevLett.118.110504](https://doi.org/10.1103/PhysRevLett.118.110504).
- [74] M. Hauru, C. Delcamp and S. Mizera, *Renormalization of tensor networks using graph-independent local truncations*, Phys. Rev. B **97**, 045111 (2018), doi:[10.1103/PhysRevB.97.045111](https://doi.org/10.1103/PhysRevB.97.045111).
- [75] G. Evenbly, *Gauge fixing, canonical forms, and optimal truncations in tensor networks with closed loops*, Phys. Rev. B **98**, 085155 (2018), doi:[10.1103/PhysRevB.98.085155](https://doi.org/10.1103/PhysRevB.98.085155).
- [76] K. Harada, *Entanglement branching operator*, Phys. Rev. B **97**, 045124 (2018), doi:[10.1103/PhysRevB.97.045124](https://doi.org/10.1103/PhysRevB.97.045124).
- [77] H.-J. Liao, J.-G. Liu, L. Wang and T. Xiang, *Differentiable programming tensor networks*, Phys. Rev. X **9**, 031041 (2019), doi:[10.1103/PhysRevX.9.031041](https://doi.org/10.1103/PhysRevX.9.031041).
- [78] S. P. G. Crone and P. Corboz, *Detecting a Z_2 topologically ordered phase from unbiased infinite projected entangled-pair state simulations*, Phys. Rev. B **101**, 115143 (2020), doi:[10.1103/PhysRevB.101.115143](https://doi.org/10.1103/PhysRevB.101.115143).
- [79] C. Roberts, A. Milsted, M. Ganahl, A. Zalcman, B. Fontaine, Y. Zou, J. Hidary, G. Vidal and S. Leichenauer, *Tensornetwork: A library for physics and machine learning* (2019), [arXiv:1905.01330](https://arxiv.org/abs/1905.01330).
- [80] A. Milsted, M. Ganahl, S. Leichenauer, J. Hidary and G. Vidal, *Tensornetwork on tensorflow: A spin chain application using tree tensor networks* (2019), [arXiv:1905.01331](https://arxiv.org/abs/1905.01331).
- [81] M. Ganahl, A. Milsted, S. Leichenauer, J. Hidary and G. Vidal, *Tensornetwork on tensorflow: Entanglement renormalization for quantum critical lattice models* (2019), [arXiv:1906.12030](https://arxiv.org/abs/1906.12030).
- [82] H. Xie, J.-G. Liu and L. Wang, *Automatic differentiation of dominant eigensolver and its applications in quantum physics*, Phys. Rev. B **101**, 245139 (2020), doi:[10.1103/PhysRevB.101.245139](https://doi.org/10.1103/PhysRevB.101.245139).
- [83] M. Hauru, M. Van Damme and J. Haegeman, *Riemannian optimization of isometric tensor networks* (2020), [arXiv:2007.03638v1](https://arxiv.org/abs/2007.03638v1).
- [84] F. Verstraete, V. Murg and J. I. Cirac, *Matrix product states, projected entangled pair states, and variational renormalization group methods for quantum spin systems*, Adv. Phys. **57**, 143 (2008), doi:[10.1080/14789940801912366](https://doi.org/10.1080/14789940801912366).
- [85] P. Corboz and G. Vidal, *Fermionic multiscale entanglement renormalization ansatz*, Phys. Rev. B **80**, 165129 (2009), doi:[10.1103/PhysRevB.80.165129](https://doi.org/10.1103/PhysRevB.80.165129).

- [86] T. Barthel, C. Pineda and J. Eisert, *Contraction of fermionic operator circuits and the simulation of strongly correlated fermions*, Phys. Rev. A **80**, 042333 (2009), doi:[10.1103/PhysRevA.80.042333](https://doi.org/10.1103/PhysRevA.80.042333).
- [87] C. Pineda, T. Barthel and J. Eisert, *Unitary circuits for strongly correlated fermions*, Phys. Rev. A **81**, 050303 (2010), doi:[10.1103/PhysRevA.81.050303](https://doi.org/10.1103/PhysRevA.81.050303).
- [88] C. V. Kraus, N. Schuch, F. Verstraete and J. I. Cirac, *Fermionic projected entangled pair states*, Phys. Rev. A **81**, 052338 (2010), doi:[10.1103/PhysRevA.81.052338](https://doi.org/10.1103/PhysRevA.81.052338).
- [89] Q.-Q. Shi, S.-H. Li, J.-H. Zhao and H.-Q. Zhou, *Graded projected entangled-pair state representations and an algorithm for translationally invariant strongly correlated electronic systems on infinite-size lattices in two spatial dimensions* (2009), [arXiv:0907.5520](https://arxiv.org/abs/0907.5520).
- [90] A. Weichselbaum, *Tensor networks and the numerical renormalization group*, Phys. Rev. B **86**, 245124 (2012), doi:[10.1103/PhysRevB.86.245124](https://doi.org/10.1103/PhysRevB.86.245124).
- [91] D. Poilblanc, N. Schuch, D. Pérez-García and J. I. Cirac, *Topological and entanglement properties of resonating valence bond wave functions*, Phys. Rev. B **86**, 014404 (2012), doi:[10.1103/PhysRevB.86.014404](https://doi.org/10.1103/PhysRevB.86.014404).
- [92] D. Poilblanc and N. Schuch, *Simplex Z_2 spin liquids on the Kagome lattice with projected entangled pair states: Spinon and vison coherence lengths, topological entropy, and gapless edge modes*, Phys. Rev. B **87**, 140407 (2013), doi:[10.1103/PhysRevB.87.140407](https://doi.org/10.1103/PhysRevB.87.140407).
- [93] W. Li, S. Yang, M. Cheng, Z.-X. Liu and H.-H. Tu, *Topology and criticality in the resonating Affleck-Kennedy-Lieb-Tasaki loop spin liquid states*, Phys. Rev. B **89**, 174411 (2014), doi:[10.1103/PhysRevB.89.174411](https://doi.org/10.1103/PhysRevB.89.174411).
- [94] B. Bauer, P. Corboz, R. Orús and M. Troyer, *Implementing global Abelian symmetries in projected entangled-pair state algorithms*, Phys. Rev. B **83**, 125106 (2011), doi:[10.1103/PhysRevB.83.125106](https://doi.org/10.1103/PhysRevB.83.125106).
- [95] J. I. Cirac and F. Verstraete, *Renormalization and tensor product states in spin chains and lattices*, J. Phys. A: Math. Theor. **42**, 504004 (2009), doi:[10.1088/1751-8113/42/50/504004](https://doi.org/10.1088/1751-8113/42/50/504004).
- [96] U. Schollwöck, *The density-matrix renormalization group in the age of matrix product states*, Ann. Phys. **326**, 96 (2011), doi:[10.1016/j.aop.2010.09.012](https://doi.org/10.1016/j.aop.2010.09.012).
- [97] M. Imada, A. Fujimori and Y. Tokura, *Metal-insulator transitions*, Rev. Mod. Phys. **70**, 1039 (1998), doi:[10.1103/RevModPhys.70.1039](https://doi.org/10.1103/RevModPhys.70.1039).
- [98] Y. Tokura and N. Nagaosa, *Orbital physics in transition-metal oxides*, Science **288**, 462 (2000), doi:[10.1126/science.288.5465.462](https://doi.org/10.1126/science.288.5465.462).
- [99] M. Yi et al., *Observation of temperature-induced crossover to an orbital-selective Mott phase in $A_x\text{Fe}_{2-y}\text{Se}_2$ ($A=\text{K, Rb}$) superconductors*, Phys. Rev. Lett. **110**, 067003 (2013), doi:[10.1103/PhysRevLett.110.067003](https://doi.org/10.1103/PhysRevLett.110.067003).
- [100] M. Yi et al., *Observation of universal strong orbital-dependent correlation effects in iron chalcogenides*, Nat. Commun. **6**, 7777 (2015), doi:[10.1038/ncomms8777](https://doi.org/10.1038/ncomms8777).
- [101] F. B. Kugler, S.-S. B. Lee, A. Weichselbaum, G. Kotliar and J. von Delft, *Orbital differentiation in Hund metals*, Phys. Rev. B **100**, 115159 (2019), doi:[10.1103/PhysRevB.100.115159](https://doi.org/10.1103/PhysRevB.100.115159).

- [102] F. Scazza, C. Hofrichter, M. Höfer, P. C. De Groot, I. Bloch and S. Fölling, *Observation of two-orbital spin-exchange interactions with ultracold $SU(N)$ -symmetric fermions*, Nat. Phys. **10**, 779 (2014), doi:[10.1038/nphys3061](https://doi.org/10.1038/nphys3061).
- [103] C. Hofrichter, L. Riegger, F. Scazza, M. Höfer, D. Rio Fernandes, I. Bloch and S. Fölling, *Direct probing of the Mott crossover in the $SU(N)$ Fermi-Hubbard model*, Phys. Rev. X **6**, 021030 (2016), doi:[10.1103/PhysRevX.6.021030](https://doi.org/10.1103/PhysRevX.6.021030).
- [104] A. Georges, L. de' Medici and J. Mravlje, *Strong correlations from Hund's coupling*, Annu. Rev. Condens. Matter Phys. **4**, 137 (2013), doi:[10.1146/annurev-conmatphys-020911-125045](https://doi.org/10.1146/annurev-conmatphys-020911-125045).
- [105] Z. Cai, H.-H. Hung, L. Wang and C. Wu, *Quantum magnetic properties of the $SU(2N)$ Hubbard model in the square lattice: A quantum Monte Carlo study*, Phys. Rev. B **88**, 125108 (2013), doi:[10.1103/PhysRevB.88.125108](https://doi.org/10.1103/PhysRevB.88.125108).
- [106] D. Wang, Y. Li, Z. Cai, Z. Zhou, Y. Wang and C. Wu, *Competing orders in the 2D half-filled $SU(2N)$ Hubbard model through the pinning-field quantum Monte Carlo simulations*, Phys. Rev. Lett. **112**, 156403 (2014), doi:[10.1103/PhysRevLett.112.156403](https://doi.org/10.1103/PhysRevLett.112.156403).
- [107] Z. Zhou, Z. Cai, C. Wu and Y. Wang, *Quantum Monte Carlo simulations of thermodynamic properties of $SU(2N)$ ultracold fermions in optical lattices*, Phys. Rev. B **90**, 235139 (2014), doi:[10.1103/PhysRevB.90.235139](https://doi.org/10.1103/PhysRevB.90.235139).
- [108] F. E. Assaad, *Phase diagram of the half-filled two-dimensional $SU(N)$ Hubbard-Heisenberg model: A quantum Monte Carlo study*, Phys. Rev. B **71**, 075103 (2005), doi:[10.1103/PhysRevB.71.075103](https://doi.org/10.1103/PhysRevB.71.075103).
- [109] L. F. Tocchio, F. Arrigoni, S. Sorella and F. Becca, *Assessing the orbital selective Mott transition with variational wave functions*, J. Phys.: Condens. Matter **28**, 105602 (2016), doi:[10.1088/0953-8984/28/10/105602](https://doi.org/10.1088/0953-8984/28/10/105602).
- [110] P. Corboz, A. M. Läuchli, K. Penc, M. Troyer and F. Mila, *Simultaneous dimerization and $SU(4)$ symmetry breaking of 4-color fermions on the square lattice*, Phys. Rev. Lett. **107**, 215301 (2011), doi:[10.1103/PhysRevLett.107.215301](https://doi.org/10.1103/PhysRevLett.107.215301).
- [111] Z. Cai, Private communication (2017).
- [112] S.-S. B. Lee, J. von Delft and A. Weichselbaum, *Filling-driven Mott transition in $SU(N)$ Hubbard models*, Phys. Rev. B **97**, 165143 (2018), doi:[10.1103/PhysRevB.97.165143](https://doi.org/10.1103/PhysRevB.97.165143).
- [113] D. Banerjee, M. Bögli, M. Dalmonte, E. Rico, P. Stebler, U.-J. Wiese and P. Zoller, *Atomic quantum simulation of $U(N)$ and $SU(N)$ non-Abelian lattice gauge theories*, Phys. Rev. Lett. **110**, 125303 (2013), doi:[10.1103/PhysRevLett.110.125303](https://doi.org/10.1103/PhysRevLett.110.125303).
- [114] C. Honerkamp and W. Hofstetter, *Ultracold fermions and the $SU(N)$ Hubbard model*, Phys. Rev. Lett. **92**, 170403 (2004), doi:[10.1103/PhysRevLett.92.170403](https://doi.org/10.1103/PhysRevLett.92.170403).
- [115] B. Bauer, P. Corboz, A. M. Läuchli, L. Messio, K. Penc, M. Troyer and F. Mila, *Three-sublattice order in the $SU(3)$ Heisenberg model on the square and triangular lattice*, Phys. Rev. B **85**, 125116 (2012), doi:[10.1103/PhysRevB.85.125116](https://doi.org/10.1103/PhysRevB.85.125116).
- [116] E. V. Gorelik and N. Blümer, *Mott transitions in ternary flavor mixtures of ultracold fermions on optical lattices*, Phys. Rev. A **80**, 051602 (2009), doi:[10.1103/PhysRevA.80.051602](https://doi.org/10.1103/PhysRevA.80.051602).


Study of spin symmetry in the doped t - J model using infinite projected entangled pair states

Jheng-Wei Li¹, Benedikt Bruognolo^{1,2}, Andreas Weichselbaum^{3,1} and Jan von Delft¹

¹*Arnold Sommerfeld Center for Theoretical Physics, Center for NanoScience, and Munich Center for Quantum Science and Technology, Ludwig-Maximilians-Universität München, 80333 Munich, Germany*

²*Max-Planck-Institut für Quantenoptik, Hans-Kopfermann-Strasse 1, D-85748 Garching, Germany*

³*Department of Condensed Matter Physics and Materials Science, Brookhaven National Laboratory, Upton, New York 11973-5000, USA*

 (Received 18 June 2020; revised 25 January 2021; accepted 29 January 2021; published 15 February 2021)

We study the two-dimensional t - J model on a square lattice using infinite projected entangled pair states (iPEPS). At small doping, multiple orders, such as antiferromagnetic order, stripe order and superconducting order, are intertwined or compete with each other. We demonstrate the role of spin symmetry at small doping by either imposing SU(2) spin symmetry or its U(1) subgroup in the iPEPS ansatz, thereby excluding or allowing spontaneous spin-symmetry breaking, respectively, in the thermodynamic limit. From a detailed comparison of our simulations, we provide evidence that stripe order is pinned by long-range antiferromagnetic order. We also find SU(2) iPEPS, enforcing a spin-singlet state, yields a uniform charge distribution and favors d -wave singlet pairing.

DOI: [10.1103/PhysRevB.103.075127](https://doi.org/10.1103/PhysRevB.103.075127)

I. INTRODUCTION

The discovery of high-temperature superconductivity has triggered intense research on the properties of the one-band t - J model on a square lattice, which has been argued to capture essential low-energy properties of cuprate materials [1]. Despite many analytical and numerical works, full consensus regarding the competing low-energy states with different charge, spin, and superconducting orders of the t - J model has not yet been reached. One category includes so-called stripe states, featuring spin-density waves and charge-density waves [2–24], where some of these states also exhibit co-existing d -wave superconducting order. Another potential candidate for the ground state of the hole-doped t - J model is a superconducting state with uniform hole density [18,25,26]. Recently, Corboz *et al.* [24], using infinite projected entangle pair states (iPEPS), demonstrated the energetically extremely close competition of the uniform state and the stripe state, even for the largest accessible numerical simulations. Similar work on the Hubbard model also pointed towards a striped ground state [27–33]. Nevertheless, the underlying physical mechanism causing these intriguing ground-state properties remains elusive, and refined work in this direction is clearly necessary.

In this paper, we focus on the so-called $\lambda 5$ stripe state, featuring spin and charge modulations with a period of $\lambda = 5$ lattice spacings, which was previously shown to be energetically favorable near hole doping $\delta \simeq 0.1$ at $J/t = 0.4$ (referred to as the W5 stripe in [24]). We use iPEPS (i) to study the evolution of $\lambda 5$ stripe order from its optimal doping $\delta \simeq 0.1$ into the spin and charge uniform phase and (ii) to provide insight into the relation between stripes and long-range antiferromagnetic (AF) order in the thermodynamic limit.

In particular, we show that by implementing either U(1) or SU(2) spin symmetry in the iPEPS ansatz, the relevance of long-range AF order can be directly examined. Our analysis complements the finite-size scaling often used in density matrix renormalization group (DMRG) and quantum Monte Carlo (QMC) simulations, thereby addressing the question of “the fate of the magnetic correlations in the 2D limit” raised in Ref. [34]. Moreover, we show that the SU(2) iPEPS ansatz which, by construction, represents a spin-singlet state, possesses d -wave singlet pairing order. Such SU(2) iPEPS can be interpreted as a generalized resonating valence bond (RVB) state [35–39], and in this sense our finding of d -wave pairing for the SU(2) iPEPS is reminiscent of Anderson’s original RVB proposal [40–42].

II. MODEL AND METHODS

The t - J Hamiltonian is given by

$$\hat{H} = -t \sum_{\langle ij \rangle \sigma} (\tilde{c}_{i\sigma}^\dagger \tilde{c}_{j\sigma} + \text{H.c.}) + J \sum_{\langle ij \rangle} \left(\hat{\mathbf{S}}_i \cdot \hat{\mathbf{S}}_j - \frac{1}{4} \hat{n}_i \hat{n}_j \right), \quad (1)$$

with the spin operators $\hat{\mathbf{S}}_i$, projected fermionic operators $\tilde{c}_{i\sigma} = \hat{c}_{i\sigma} (1 - \hat{c}_{i\bar{\sigma}}^\dagger \hat{c}_{i\bar{\sigma}})$, spin label $\sigma \in \{\uparrow, \downarrow\}$, and $\langle ij \rangle$ indexing all nearest-neighbor sites on a square lattice. To control the doping, we minimize $\hat{H} - \mu \hat{N}$ for a specified choice of chemical potential μ (see the Supplemental Material [62], Sec. S-II.). We set $t = 1$ as the unit of energy and use $J/t = 0.4$ throughout.

We use iPEPS to obtain an approximate ground state for Eq. (1). The iPEPS ground state is a tensor network state consisting of a unit cell of rank-5 tensors, i.e., tensors with five indices or legs, repeated periodically on an infinite

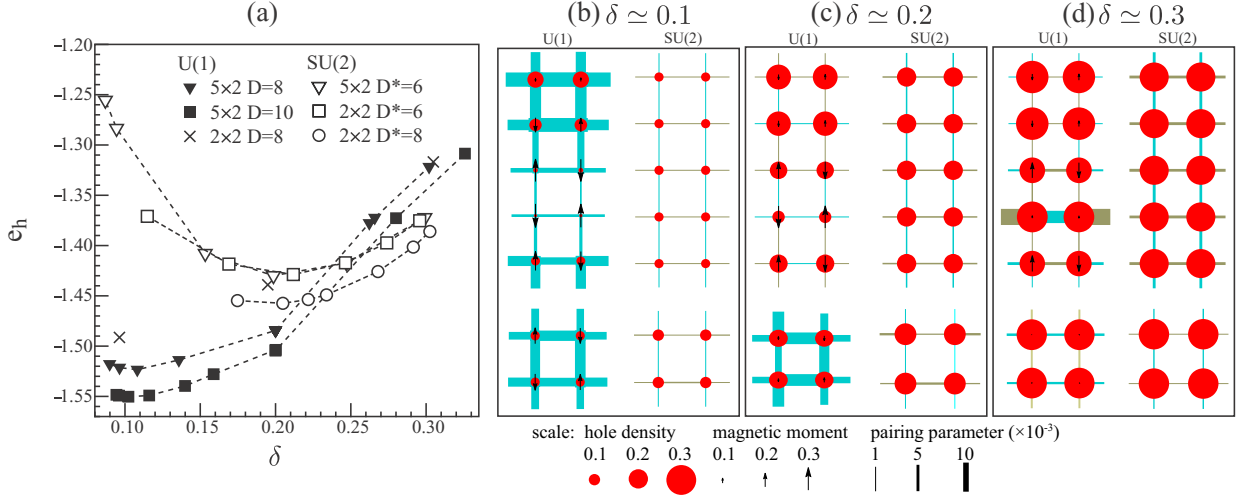


FIG. 1. U(1) and SU(2) iPEPS results for the t - J model at $J/t = 0.4$. (a) The energy per hole e_h as a function of hole doping δ for 5×2 and 2×2 unit cells. (b)–(d) Spin, hole, and singlet pairing amplitude profiles at $\delta \approx 0.1, 0.2$, and 0.3 . U(1) iPEPS ($D = 8$) yields stripes on 5×2 clusters and charge-uniform states on 2×2 clusters; SU(2) iPEPS ($D^* = 6$) yields spin singlets. Symbols and linewidths are drawn to scale as indicated.

square lattice [24,43–48]. Each rank-5 tensor has one physical index and four virtual indices (bonds) connecting to the four nearest-neighboring sites. The accuracy of such a variational ansatz is guaranteed by the area law and can be systematically improved by increasing the bond dimension D .

Using the QSPACE tensor network library [49], we can simply switch between exploiting either U(1) or SU(2) spin symmetries for our iPEPS implementation [50]. This allows us to use sufficiently large bond dimensions to obtain accurate ground state wave functions. With SU(2) iPEPS [35–39,50–55], we push the reduced bond dimension D^* up to 8, where D^* is the number of retained SU(2) multiplets per virtual bond, which corresponds to a full bond dimension of $D \simeq 13$ states. To optimize the iPEPS wave functions via imaginary-time evolution, we use full-update and fast full-update methods [24,45,47,56,57]. The contraction of the two-dimensional infinite lattice is evaluated approximately by the corner transfer matrix method [24,58–61], which generates so-called environment tensors with an environment bond dimension χ . For SU(2) iPEPS, the environment bond dimensions used here are $\chi^* = 144$ ($\chi \simeq 300$) for $D^* = 6$ ($D \simeq 11$) and $\chi^* = 128$ ($\chi \simeq 270$) for $D^* = 8$ ($D \simeq 13$). For U(1) iPEPS, the environment bond dimensions are $\chi = 256$ for $D = 8$ and $\chi = 200$ for $D = 10$.

III. ENERGETICS

In Fig. 1(a), we show the energy per hole, $e_h(\delta) \equiv (e_s - e_0)/\delta$, as a function of hole doping δ , obtained from various iPEPS simulations (plots of $e_s(\delta)$ vs δ are shown in the Supplemental Material [62], Fig. S3). Here e_s is the average ground state energy per site, and $e_0 = -0.467775$ is the numerically exact value for the AF phase at zero doping taken from Ref. [63]. Using U(1) iPEPS on a 5×2 unit cell, we find a minimum at $\delta_c \simeq 0.1$, as previously reported [24]. If phase separation, involving a mixture of AF and stripe orders, sets in with decreasing δ , then δ_c provides an upper bound

for this onset (see the Supplemental Material for details). Increasing the bond dimension from $D = 8$ to $D = 10$ improves the ground state energy consistently for every doping δ considered here. On the other hand, using SU(2) iPEPS ($D^* = 6$), we obtain a spin-singlet state with no stripe feature on a 5×2 unit cell. Moreover, the ground state energy is almost independent of the shape of unit cells (compare 5×2 and 2×2 data). We further improve the ground states using $D^* = 8$ on the 2×2 unit cell. Overall, for $\delta \lesssim 0.2$ in Fig. 1(a), we see that the U(1) $\lambda 5$ stripe state yields a substantially lower ground state energy than the spin-singlet state, while the latter lies below the former for $\delta \gtrsim 0.25$. From a technical perspective, our calculations show that for the non-symmetry-breaking phase favored at $\delta \gtrsim 0.25$, SU(2) iPEPS benefits from the full utilization of the spin-rotational symmetry, even though U(1) iPEPS has a larger number of variational parameters when $D > D^*$.

Next, we take a close look at each individual iPEPS for three values of doping. The stripe states obtained using U(1) iPEPS, shown in the top left parts of Figs. 1(b)–1(d), exhibit modulation of charge and spin densities along the y direction. At $\delta \simeq 0.1$, we find hole doping to be maximal along the top row, implying a site-centered stripe, in agreement with previous work [24]. Note that the spins in the two rows on either side of the top row (rows 2 and 5) are ordered antiferromagnetically (implying a so-called π phase shift across the top row), thereby reducing the energy of transverse hole hopping along the domain wall [10,11,16]. At $\delta \simeq 0.2$, we find hole doping to be maximal between two rows (the first and second), implying a bond-centered stripe, as frequently observed in DMRG, density matrix embedding theory (DMET), and QMC calculations [10,27]. Finally, at $\delta \simeq 0.3$, the hole densities are roughly equal across all sites, with residual charge and spin modulation. Overall, the stripe states we find here are in agreement with previous studies, which concluded that in the t - J model stripe formation is predominantly driven by the competition between the kinetic energy and the exchange

energy [2,3,9,15]. However, the same mechanism can also induce the pairing formation [12,18,26,64]. Therefore, it is *a priori* unclear under what circumstances the system will favor stripe order or pairing at small doping. To clarify this issue, we now turn to our SU(2) iPEPS results.

In contrast to the U(1) iPEPS results, switching on spin-rotational symmetry on the 5×2 unit cell by using SU(2) iPEPS suppresses the AF order and hence the spin modulation, as shown in the top right parts of Figs. 1(b)–1(d). The resulting state no longer shows any spin stripes and instead has the same structure as the uniform state obtained on a 2×2 unit cell at similar doping [see the bottom right parts of Figs. 1(b)–1(d)]. In addition, enforcing SU(2) symmetry also makes charge modulations completely disappear as well. This observation suggests that in the t - J model charge density waves are strongly tied to spin stripes.

We have also examined d -wave superconducting order by computing the singlet pairing amplitude, $\langle \Delta_{ij} \rangle = \frac{1}{\sqrt{2}} \langle \tilde{c}_{i\uparrow} \tilde{c}_{j\downarrow} - \tilde{c}_{i\downarrow} \tilde{c}_{j\uparrow} \rangle$. For the U(1) iPEPS λ 5 stripe states in Figs. 1(b)–1(d), we cannot directly identify a d -wave pairing character, in contrast to Refs. [24,27], which found opposite signs for the amplitude of the bonds along the x and y axes. However, a word of caution is necessary in reading this result when the ground state spontaneously breaks SU(2) spin symmetry because even a trivial term, such as $\langle \tilde{c}_{i\uparrow} \tilde{c}_{j\downarrow} \rangle$, could yield a nonzero contribution to $\langle \Delta_{ij} \rangle$. For a more rigorous diagnosis, one should explicitly study the pair correlation function [34,65–67], which goes beyond the scope of this work. Hence, our results do not exclude the possibility that stripes and d -wave superconducting order could coexist. For example, in the case of the U(1) results of Figs. 1(b)–1(d) we find that local d -wave order including the proper signs is absent at $\delta \simeq 0.1$ and 0.2. However, it is present for the 2×2 U(1) cell at $\delta \simeq 0.3$, where the local magnetization is too small to sustain significant AF order.

On the other hand, the SU(2) iPEPS is a spin-singlet state by construction. It takes into account short-range spin correlations but excludes long-range AF order, which breaks spin-rotational symmetry in the thermodynamic limit (see the Supplemental Material for details). This rules out the aforementioned ambiguity, and the singlet pairing amplitude becomes a robust measure. As shown in Figs. 1(b)–1(d), a d -wave pattern appears on both the 5×2 and 2×2 unit cells. Figure 2 shows the averaged singlet pairing amplitude, $\bar{\Delta} = \frac{1}{N} \sum_{(ij)} f(\mathbf{r}_{ij}) \langle \Delta_{ij} \rangle$, as a function of doping, where N is the number of sites in the unit cells, $\mathbf{r}_{ij} \equiv \mathbf{r}_j - \mathbf{r}_i$, and $f(\mathbf{r})$ is a d -wave form factor, which takes the values $f(\pm\hat{y}) = -1$ and $f(\pm\hat{x}) = 1$, respectively. The error bar indicates the mean absolute deviation of the pairing amplitudes among all bonds. In the 2×2 case, the pronounced deviation is mostly attributed to the difference in pairing amplitudes along the x and y directions. A similar phenomenon was also observed in a recent large-scale DMRG calculation [34], and an almost equal mixture between d -wave and s -wave singlet pairing amplitude was suggested. Upon increasing the bond dimension D^* from 6 to 8, the d -wave pairing order increases. This is different from the previous analysis of charge uniform states using U(1) iPEPS, where pairing is suppressed with increasing D [24]. Furthermore, the 5×2 case also shows a rather uniform d -wave pattern. The magnitude of the pairing

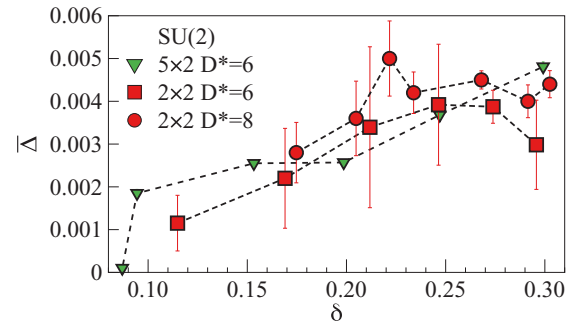


FIG. 2. Averaged singlet pairing amplitude as a function of doping using SU(2) iPEPS. The error bar shows the mean absolute deviation of the pairing amplitudes among all bonds. For the 5×2 unit cell, the error bars are smaller than the symbols.

amplitude in Fig. 2 is small but finite, even if about an order of magnitude smaller than reported in other U(1) iPEPS or DMRG simulations [19,21,24]. This appears consistent with Fig. 1(d) for $\delta \simeq 0.3$, showing d -wave order with an amplitude slightly smaller for 2×2 SU(2) than for 2×2 U(1) or 5×2 SU(2), which are comparable. All in all, our SU(2) iPEPS results show that, if spin rotational symmetry is enforced, the doped t - J model exhibits d -wave superconductivity in the thermodynamic limit, in agreement with an early prediction from mean-field theory [41].

IV. INFLUENCE OF STRIPES ON ANTIFERROMAGNETIC ORDER

In the previous section we showed that stripes can be stabilized as ground states using the U(1) iPEPS at doping $0.1 \lesssim \delta \lesssim 0.2$ on a 5×2 unit cell. By contrast, the SU(2) iPEPS shows no signature of any spatial modulations of spin and charge density. This suggests that the stripes and the AF order are intimately related. While such a viewpoint has been discussed extensively both theoretically and experimentally since the discovery of the so-called $\frac{1}{8}$ anomaly [68–71], direct understanding of how AF order coexists with stripes is still lacking.

To address this, we have computed the staggered spin-spin correlation functions for the ground state,

$$C(i) = \frac{(-1)^{x+y}}{\frac{3}{4}(1-\delta)N} \sum_{j \in \text{unit cell}} \langle \hat{\mathbf{S}}_{j+i} \cdot \hat{\mathbf{S}}_j \rangle, \quad (2)$$

with $i = (x, y)$. The prefactor normalizes the same-site correlator to unity, $C(0) = 1$, given $(1-\delta)N$ spins per unit cell. This facilitates the comparison of different unit cells and doping. In the following, we analyze $C(i)$ along the long (y) and short (x) directions of the unit cell.

First, we study the staggered spin-spin correlations on a 5×2 unit cell at doping $\delta \simeq 0.1, 0.2$, and 0.3, using U(1) iPEPS. In Fig. 3(a), we can clearly identify λ 5 stripe order at $\delta \simeq 0.1$ and 0.2, with staggered spin-spin correlations oscillating around zero, reflecting the pattern already seen in the left panels of Figs. 1(b) and 1(c). The staggered magnetic order undergoes a phase shift of π across the length of the 5×2 unit cell, resulting in a period of $\lambda_m = 10$. At doping $\delta \simeq 0.3$, the correlations decay much more rapidly, with weak residual

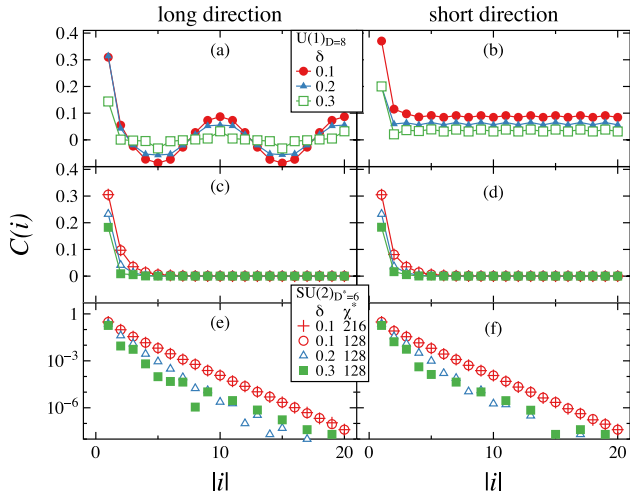


FIG. 3. Normalized staggered spin-spin correlation functions, computed on a 5×2 unit cell along the long (y) direction (left column) and the short (x) direction (right column), using (a) and (b) U(1) iPEPS and (c)–(f) SU(2) iPEPS, on linear and semilogarithmic scales, respectively. Solid symbols indicate the variational state [U(1) or SU(2)] with the lower energy for a given δ .

oscillations remaining at large distances. Given its higher variational energy compared to its SU(2) counterpart, this reflects the numerical inefficiency of using a broken-symmetry ansatz to simulate a spin singlet when many low-energy states are nearly degenerate. By contrast, Fig. 3(b) shows that the correlations along the “short” direction decrease with doping but remain positive at large distances, indicating long-range AF order, i.e., $C(|i| \rightarrow \infty) \neq 0$, although attenuated with increasing δ . Therefore, Figs. 3(a) and 3(b) suggest that stripes along the long direction go hand in hand with long-range AF order along the short direction.

To further elucidate this point, we turn our attention to the SU(2) iPEPS. Again, we have computed the staggered spin-spin correlations on a 5×2 unit cell using SU(2) iPEPS. In Figs. 3(c) and 3(d), the correlations along the long and short directions are nearly identical and rapidly decay to zero, showing no sign of either stripes or the long-range AF order. Note that for SU(2) iPEPS, the instability of a given state towards AF order can be detected by the increase in correlation length with increasing χ^* . (We illustrate this for the Heisenberg model in the Supplemental Material [62], Sec. SI). However, this tendency is not observed at $\delta = 0.1$ [see Figs. 3(e) and 3(f)]. In short, we conclude that stripes emerge only in the presence of long-range AF order.

To strengthen our previous statement, we further consider $L \times 2$ unit cells with $L = 5, 4, 3, 2$ at $\delta \simeq 0.2$ using U(1) iPEPS ($D = 8$). Those could host spin stripes of periods $\lambda = L$ or an AF ordered state for $L = 2$. A previous iPEPS study showed a very close competition between a $\lambda 5$ stripe state and an AF state with uniform charge distribution ($L = 2$) at $\delta \simeq 0.1$ [24]. For a 2×2 unit cell [Fig. 4(a)], the spin-spin correlations along both the long and short directions quickly decay to nearly zero, showing that AF order is weak at $\delta \simeq 0.2$ if a charge-uniform state is assumed. The same charge-uniform state is also favored for a 4×2 unit cell:

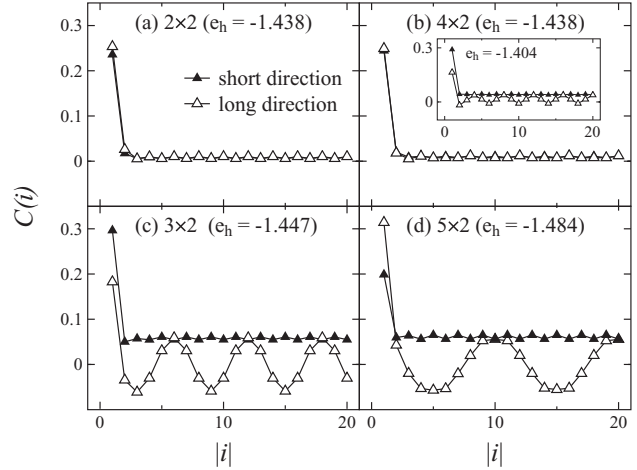


FIG. 4. Comparison of normalized staggered spin-spin correlation functions for $\delta \simeq 0.2$ using U(1) iPEPS at $D = 8$ along the long (y) direction and the short (x) direction on $L \times 2$ unit cells for $L = 2, 3, 4, 5$ in (a)–(d), respectively. The inset in (b) is a $\lambda 4$ stripe state obtained from different initialization.

we obtain this by initializing the 4×2 unit cell of a full-update optimization using two copies of the 2×2 unit cell in Fig. 4(a), which yields a slightly lower energy than a $\lambda 4$ stripe state [inset in Fig. 4(b)] initialized from simple-update results. By contrast, 3×2 and 5×2 unit cells show a clear stripe feature along the long direction, together with nonzero long-range AF order along the short one [Figs. 4(c) and 4(d)], and slightly lower ground state energy than those of 2×2 and 4×2 . However, the bond dimension D used here is not large enough to conclusively resolve the close competition between the different states. Overall, by plotting the correlations along both the short and long directions in the same panel, we see that the amplitude of the stripe modulation is the same as that of attenuated long-range AF correlations. This further confirms that the stripes and the long-range AF order are indeed tied to each other at finite doping.

V. SUMMARY

We have studied the doped t - J model with $J/t = 0.4$ using U(1) and SU(2) iPEPS. For doping $0.1 \lesssim \delta \lesssim 0.2$, the $\lambda 5$ striped charge and spin order with U(1) symmetry is energetically favorable compared to a spin-singlet state with SU(2) symmetry. By contrast, for $\delta \gtrsim 0.25$, the latter is favored. By studying the spin-spin correlations, we find a close link between stripe order and long-range AF order. At small doping, the U(1) iPEPS shows that spin stripes emerge along one spatial direction, while attenuated long-range AF order persists along the other spatial direction. Upon increasing doping, the strength of stripe order decreases hand in hand with long-range AF order. By contrast, the SU(2) iPEPS, which does not break spin rotational symmetry, excludes long-range AF order and hence stripe formation but yields d -wave superconducting order at finite doping. Our study demonstrates the utility and importance of being able to turn on and off the SU(2) spin-rotational symmetry at will—it gives direct insight

into the interplay between regimes with spontaneously broken symmetries and where $SU(2)$ invariance remains intact.

ACKNOWLEDGMENTS

The Deutsche Forschungsgemeinschaft supported B.B., J.-W.L., and J.v.D. through the Excellence Cluster

“Nanosystems Initiative Munich” and the Excellence Strategy-EXC-2111-390814868. J.-W.L. was also supported by German Research Foundation (DFG WE4819/3-1) under Germany’s Excellence Strategy—EXC-2111-390814868. A.W. was supported by the U.S. Department of Energy, Office of Basic Energy Sciences, under Contract No. DE-SC0012704.

-
- [1] F. C. Zhang and T. M. Rice, *Phys. Rev. B* **37**, 3759 (1988).
 [2] D. Poilblanc and T. M. Rice, *Phys. Rev. B* **39**, 9749 (1989).
 [3] J. Zaanen and O. Gunnarsson, *Phys. Rev. B* **40**, 7391 (1989).
 [4] K. Machida, *Physica C (Amsterdam, Neth.)* **158**, 192 (1989).
 [5] H. Schulz, *J. Phys. (Paris)* **50**, 2833 (1989).
 [6] S. R. White, D. J. Scalapino, R. L. Sugar, N. E. Bickers, and R. T. Scalettar, *Phys. Rev. B* **39**, 839 (1989).
 [7] V. J. Emery, S. A. Kivelson, and H. Q. Lin, *Phys. Rev. Lett.* **64**, 475 (1990).
 [8] V. Emery and S. Kivelson, *Physica C (Amsterdam, Neth.)* **209**, 597 (1993).
 [9] C. Nayak and F. Wilczek, *Phys. Rev. Lett.* **78**, 2465 (1997).
 [10] S. R. White and D. J. Scalapino, *Phys. Rev. Lett.* **80**, 1272 (1998).
 [11] S. R. White and D. J. Scalapino, *Phys. Rev. Lett.* **81**, 3227 (1998).
 [12] S. R. White and D. J. Scalapino, *Phys. Rev. B* **60**, R753(R) (1999).
 [13] H. Eskes, O. Y. Osman, R. Grimberg, W. van Saarloos, and J. Zaanen, *Phys. Rev. B* **58**, 6963 (1998).
 [14] L. P. Pryadko, S. A. Kivelson, V. J. Emery, Y. B. Bazaliy, and E. A. Demler, *Phys. Rev. B* **60**, 7541 (1999).
 [15] S. R. White and D. J. Scalapino, *Phys. Rev. B* **61**, 6320 (2000).
 [16] A. L. Chernyshev, S. R. White, and A. H. Castro Neto, *Phys. Rev. B* **65**, 214527 (2002).
 [17] A. Himeda, T. Kato, and M. Ogata, *Phys. Rev. Lett.* **88**, 117001 (2002).
 [18] C.-P. Chou, N. Fukushima, and T. K. Lee, *Phys. Rev. B* **78**, 134530 (2008).
 [19] S. R. White and D. J. Scalapino, *Phys. Rev. B* **79**, 220504(R) (2009).
 [20] K.-Y. Yang, W. Q. Chen, T. M. Rice, M. Sigrist, and F.-C. Zhang, *New J. Phys.* **11**, 055053 (2009).
 [21] P. Corboz, S. R. White, G. Vidal, and M. Troyer, *Phys. Rev. B* **84**, 041108(R) (2011).
 [22] S. Sorella, G. B. Martins, F. Becca, C. Gazza, L. Capriotti, A. Parola, and E. Dagotto, *Phys. Rev. Lett.* **88**, 117002 (2002).
 [23] W.-J. Hu, F. Becca, and S. Sorella, *Phys. Rev. B* **85**, 081110(R) (2012).
 [24] P. Corboz, T. M. Rice, and M. Troyer, *Phys. Rev. Lett.* **113**, 046402 (2014).
 [25] C. S. Hellberg and E. Manousakis, *Phys. Rev. Lett.* **83**, 132 (1999).
 [26] M. Raczkowski, M. Capello, D. Poilblanc, R. Frésard, and A. M. Oleś, *Phys. Rev. B* **76**, 140505(R) (2007).
 [27] B.-X. Zheng, C.-M. Chung, P. Corboz, G. Ehlers, M.-P. Qin, R. M. Noack, H. Shi, S. R. White, S. Zhang, and G. K.-L. Chan, *Science* **358**, 1155 (2017).
 [28] E. W. Huang, C. B. Mendl, H.-C. Jiang, B. Moritz, and T. P. Devereaux, *npj Quantum Mater.* **3**, 22 (2018).
 [29] K. Ido, T. Ohgoe, and M. Imada, *Phys. Rev. B* **97**, 045138 (2018).
 [30] A. S. Darmawan, Y. Nomura, Y. Yamaji, and M. Imada, *Phys. Rev. B* **98**, 205132 (2018).
 [31] H.-C. Jiang and T. P. Devereaux, *Science* **365**, 1424 (2019).
 [32] B. Ponsioen, S. S. Chung, and P. Corboz, *Phys. Rev. B* **100**, 195141 (2019).
 [33] M. Qin, C.-M. Chung, H. Shi, E. Vitali, C. Hubig, U. Schollwöck, S. R. White, and S. Zhang, *Phys. Rev. X* **10**, 031016 (2020).
 [34] H.-C. Jiang, Z.-Y. Weng, and S. A. Kivelson, *Phys. Rev. B* **98**, 140505(R) (2018).
 [35] D. Poilblanc, N. Schuch, D. Pérez-García, and J. I. Cirac, *Phys. Rev. B* **86**, 014404 (2012).
 [36] L. Wang, D. Poilblanc, Z.-C. Gu, X.-G. Wen, and F. Verstraete, *Phys. Rev. Lett.* **111**, 037202 (2013).
 [37] D. Poilblanc, P. Corboz, N. Schuch, and J. I. Cirac, *Phys. Rev. B* **89**, 241106(R) (2014).
 [38] D. Poilblanc and M. Mambri, *Phys. Rev. B* **96**, 014414 (2017).
 [39] J.-Y. Chen and D. Poilblanc, *Phys. Rev. B* **97**, 161107(R) (2018).
 [40] P. W. Anderson, G. Baskaran, Z. Zou, and T. Hsu, *Phys. Rev. Lett.* **58**, 2790 (1987).
 [41] G. Kotliar, *Phys. Rev. B* **37**, 3664 (1988).
 [42] P. W. Anderson, *Science* **316**, 1705 (2007).
 [43] F. Verstraete and J. I. Cirac, *arXiv:cond-mat/0407066*.
 [44] F. Verstraete, M. M. Wolf, D. Perez-Garcia, and J. I. Cirac, *Phys. Rev. Lett.* **96**, 220601 (2006).
 [45] J. Jordan, R. Orús, G. Vidal, F. Verstraete, and J. I. Cirac, *Phys. Rev. Lett.* **101**, 250602 (2008).
 [46] C. V. Kraus, N. Schuch, F. Verstraete, and J. I. Cirac, *Phys. Rev. A* **81**, 052338 (2010).
 [47] P. Corboz, R. Orús, B. Bauer, and G. Vidal, *Phys. Rev. B* **81**, 165104 (2010).
 [48] B. Bauer, P. Corboz, R. Orús, and M. Troyer, *Phys. Rev. B* **83**, 125106 (2011).
 [49] A. Weichselbaum, *Ann. Phys. (NY)* **327**, 2972 (2012).
 [50] B. Bruognolo, J.-W. Li, J. von Delft, and A. Weichselbaum, *arXiv:2006.08289*.
 [51] S. Singh and G. Vidal, *Phys. Rev. B* **86**, 195114 (2012).
 [52] T. Liu, W. Li, A. Weichselbaum, J. von Delft, and G. Su, *Phys. Rev. B* **91**, 060403(R) (2015).
 [53] P. Schmoll, S. Singh, M. Rizzi, and R. Orús, *Ann. Phys. (NY)* **419**, 168232 (2020).
 [54] C. Hubig, *SciPost Phys.* **5**, 47 (2018).
 [55] P. Schmoll and R. Orús, *Phys. Rev. B* **102**, 241101(R) (2020).

- [56] Z. Y. Xie, H. C. Jiang, Q. N. Chen, Z. Y. Weng, and T. Xiang, *Phys. Rev. Lett.* **103**, 160601 (2009).
- [57] H. N. Phien, J. A. Bengua, H. D. Tuan, P. Corboz, and R. Orús, *Phys. Rev. B* **92**, 035142 (2015).
- [58] R. J. Baxter, *J. Stat. Phys.* **19**, 461 (1978).
- [59] T. Nishino, K. Okunishi, and M. Kikuchi, *Phys. Lett. A* **213**, 69 (1996).
- [60] T. Nishino and K. Okunishi, *J. Phys. Soc. Jpn.* **65**, 891 (1996).
- [61] R. Orús and G. Vidal, *Phys. Rev. B* **80**, 094403 (2009).
- [62] See Supplemental Material at <http://link.aps.org/supplemental/10.1103/PhysRevB.103.075127> for discussions of the 2D Heisenberg model, phase separation, d-wave order, symmetries, and some further results of our computations.
- [63] A. W. Sandvik, *Phys. Rev. B* **56**, 11678 (1997).
- [64] S. R. White and D. J. Scalapino, [arXiv:cond-mat/0006071](https://arxiv.org/abs/cond-mat/0006071).
- [65] E. Dagotto, A. Moreo, F. Ortolani, D. Poilblanc, and J. Riera, *Phys. Rev. B* **45**, 10741 (1992).
- [66] E. Dagotto, J. Riera, Y. C. Chen, A. Moreo, A. Nazarenko, F. Alcaraz, and F. Ortolani, *Phys. Rev. B* **49**, 3548 (1994).
- [67] C. Cheng, R. Mondaini, and M. Rigol, *Phys. Rev. B* **98**, 121112(R) (2018).
- [68] J. M. Tranquada, B. J. Sternlieb, J. D. Axe, Y. Nakamura, and S. Uchida, *Nature (London)* **375**, 561 (1995).
- [69] S. A. Kivelson, I. P. Bindloss, E. Fradkin, V. Oganesyan, J. M. Tranquada, A. Kapitulnik, and C. Howald, *Rev. Mod. Phys.* **75**, 1201 (2003).
- [70] M. Vojta, *Adv. Phys.* **58**, 699 (2009).
- [71] N. J. Robinson, P. D. Johnson, T. M. Rice, and A. M. Tsvelik, *Rep. Prog. Phys.* **82**, 126501 (2019).

Supplementary Material – iPEPS study of spin symmetry in the doped t - J model

Jheng-Wei Li,¹ Benedikt Bruognolo,^{1,2} Andreas Weichselbaum,^{1,3} and Jan von Delft¹

¹Arnold Sommerfeld Center for Theoretical Physics, Center for NanoScience, and Munich Center for Quantum Science and Technology, Ludwig-Maximilians-Universität München, 80333 Munich, Germany

²Max-Planck-Institut für Quantenoptik, Hans-Kopfermann-Strasse 1, D-85748 Garching, Germany

³Department of Condensed Matter Physics and Materials Science, Brookhaven National Laboratory, Upton, NY 11973-5000, USA

(Dated: January 25, 2021)

In this Supplementary Material, we include discussions of the 2D Heisenberg model, phase separation, d-wave order, symmetries, and some further results of our computations, detailing how the nature of the iPEPS states studied here change with doping.

S-I. CORRELATIONS OF THE 2D HEISENBERG MODEL

In the main text, we point out the difference between U(1) iPEPS and SU(2) iPEPS in the doped t - J model. Here, we further illustrate that for $\delta = 0$. It is known that, at zero doping, the t - J model reduces to the antiferromagnetic Heisenberg model, and the ground state exhibits spontaneous symmetry breaking. At this critical point, we show that the U(1) iPEPS has finite AF magnetization, and hence rigid long-range order. In contrast, the SU(2) iPEPS can not have long-range order in a given ground state, even though the paramagnetic phase is unstable and the criticality can be inferred by the slow decay of the staggered spin-spin correlation function.

In Table S1 we summarize our results for the 2D AF Heisenberg model obtained from U(1)-symmetric and the SU(2)-symmetric iPEPS calculations, using $J = 1$ as unit of energy. Our U(1) iPEPS variational energy per site, $e_0 = -0.6693$, agrees well with the best estimate from QMC (see Table S1), namely -0.6694 . The SU(2) simulations, by construction, represent a symmetrized state and hence cannot gain energy from spontaneously symmetry breaking. Therefore they yield a slightly higher energy, consistent with previous works [38, 54].

Next, we study how symmetry affects the real-space

TABLE S1. Comparison of the ground state energy per site e_0 , and the square of the local magnetization m_{stag}^2 , for the 2D Heisenberg model between U(1) and SU(2) iPEPS results. We report values obtained at the largest possible CTM environment in the measurement, for U(1) $D = 4$ and 8, $\chi = 512$ and, for SU(2) $D^* = 4$, $\chi^* = 128$.

	e_0	m_{stag}^2
U(1) _{$D=4$}	-0.6686	0.1271
U(1) _{$D=8$}	-0.6693	0.1141
SU(2) _{$D^*=4$ ($D=12$)}	-0.6686	—
QMC [63]	-0.6694	0.0944

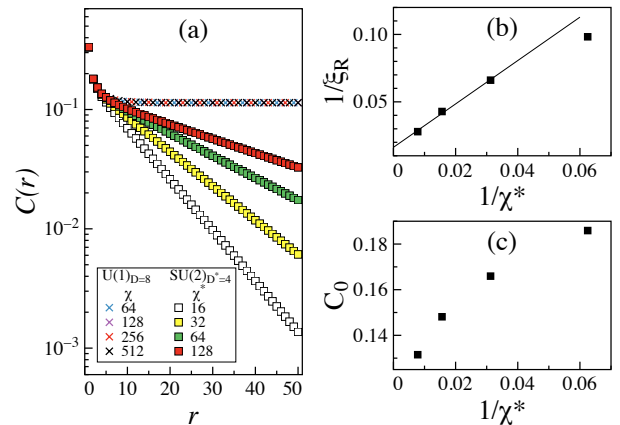


FIG. S1. (a) Staggered spin-spin correlation functions (b) The inverse of correlation length $1/\xi_R$ extracted from the asymptotic large-distance behaviors $C(r) \simeq C_0 e^{-r/\xi_R}$ vs χ^* for SU(2) iPEPS (c) C_0 vs $1/\chi^*$ for SU(2) iPEPS

spin-spin correlations. Fig. S1(a) shows the staggered spin-spin correlations for both U(1) and SU(2) symmetry, for several values of χ , on a semilogarithmic scale. For the U(1) iPEPS, the correlations quickly saturate to a nonzero value with increasing distance, resulting in a finite magnetization $\lim_{r \rightarrow \infty} C(r) = m_{\text{stag}}^2$, and remain almost the same upon increasing χ from 64 to 512. This suggests that these CTM simulations are already well converged with respect to χ for the given finite value of D . The subleading spin-spin correlations on top of this AF background can be extracted by computing $\delta C_{ij} = \langle \hat{\mathbf{S}}_i \cdot \hat{\mathbf{S}}_j \rangle - \langle \hat{\mathbf{S}}_i \rangle \cdot \langle \hat{\mathbf{S}}_j \rangle$ (not shown), which decay exponentially with $r \geq 5$ lattice spacings.

For the case of SU(2) iPEPS, on the other hand, it holds by construction that $\langle \hat{\mathbf{S}}_j \rangle = 0$. Therefore, $C(r)$ itself decays exponentially at sufficiently large distance r . In either case, δC for U(1) or C for SU(2) here, this implies finite gaps induced by the finite bond dimensions D and the finite environment dimensions χ . However, for the case of SU(2), the slope of the exponential decay has a strong dependence on χ . The correlation length increases with increasing χ , and no sign of saturation is found up to $\chi^* = 128$ ($\chi \simeq 500$), as expected for a critical state with no gap (see Fig. S1(b,c)).

Recently, it has also been pointed out that SU(2)

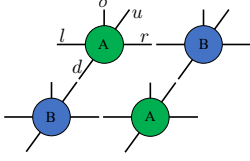


FIG. S2. A pictorial representation of an iPEPS on a 2×2 lattice with an $ABBA$ tiling pattern. σ, l, u, d, r represents the physical index and four virtual indices at left, up, down and right directions, respectively.

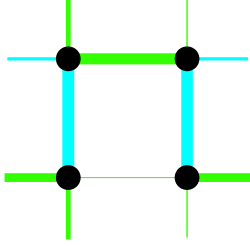


FIG. S3. Plot of $\langle S_i \cdot S_j \rangle - \frac{1}{N_{\text{site}}} \sum_i \langle S_i \cdot S_j \rangle$ to illustrate the breaking of translational symmetry, with blue (green) bonds representing positive (negative) values.

iPEPS is capable of capturing the critical phase in the study of the J_1 - J_2 Heisenberg model [38]. However, we notice a subtle difference regarding the issue of symmetry-breaking between our simulations and theirs. In their SU(2) iPEPS simulations for $D^* = 4$, the CTM approximation at finite χ induces symmetry breaking, and the resulting spurious staggered magnetization only vanishes when $\chi \rightarrow \infty$. In contrast, no such observation of symmetry-breaking appears in our SU(2) iPEPS calculations. We suspect the difference comes from the different setup of the PEPS ansatz. In Ref. 38, a single-site PEPS with C_{4v} rotational symmetry is assumed, and the virtual multiplets occurring in the ansatz are manually preselected. For $D^* = 4$, they are fixed to $\{0, (\frac{1}{2})^3\}$ (here the superscript specifies the multiplicity, i.e., the number of multiplets in a given symmetry sector, resulting in $D = 1 + 3 \cdot 2 = 7$ states total).

Instead, we use a 2×2 unit cell with 4 independent tensors, and we allow the quantum numbers at virtual legs to fluctuate during optimization. In our setup, the converged 2×2 PEPS shows an $ABBA$ tiling pattern (see Fig. S2). The variationally selected virtual space for $D^* = 4$ leads to the multiplets $\{0, 1^2, 2\}$ (i.e., $D = 1 + 2 \cdot 3 + 5 = 12$) for three virtual legs, and $\{(\frac{1}{2})^2, (\frac{3}{2})^2\}$ (i.e., $D = 2 \cdot 2 + 2 \cdot 4 = 12$) for the fourth one. This seems to break the translational and rotational symmetry for a single site (see Fig. S3). However, all bonds have the same total bond dimension of $D = 12$ states. (Note that, if the local state space has half-integer spin, it is not possible to have all-integer or all half-integer spins on all virtual bonds. Of course, the iPEPS tensors could be symmetrized to have a linear combination of integer and half-integer spins on each of the virtual bonds. But *a priori*, having the above configuration with half-integer

spins on only one virtual leg in the SU(2) iPEPS does not necessarily imply that the state is physically anisotropic.)

In short, we have addressed the key difference between U(1) and SU(2) iPEPS for the 2D AF Heisenberg model. U(1) iPEPS ($D = 8$) exhibits long-range AF order, breaking spin rotational symmetry, and the quantum fluctuations are short-ranged. In contrast, SU(2) iPEPS ($D^* = 4$) is critical: at any finite χ , there is no long-range AF order, but the AF spin fluctuations are strong and slowly decaying. Taking $\chi \rightarrow \infty$, we find a diverging correlation length ξ_R , as expected for quantum criticality.

S-II. PHASE SEPARATION

The energy per hole $e_h(\delta)$, related to the energy per site by $e_s = \delta \cdot e_h + e_0$, has often been used to detect the stability of a given phase at small doping relative to the AF phase at the zero doping. [7, 15, 23, 24]. It has been argued that if $e_h(\delta)$ has a minimum at δ_c , the system phase separates for hole densities $0 < \delta < \delta_c$ [24].

Here we point out that this statement holds only in the dilute limit, i.e. for $\delta_c \ll 1$. If δ_c is not very small, the statement has to be refined: then δ_c does not mark the onset of phase separation, but rather provides an upper bound for this onset. This can be seen as follows: For a system to phase separate, the energy per site, e_s , must have a negative curvature, i.e., $e_s''(\delta) < 0$, or, equivalently, $e_s'' = (\delta \cdot e_h + e_0)'' = 2e_h' + \delta e_h'' < 0$. Now, consider lowering δ down to a value δ_c at which $e_h'(\delta_c) = 0$, then $e_s''(\delta_c) = \delta_c e_h''(\delta_c)$. Now as seen in Fig. 1 in the main text, the curvature $e_h''(\delta) > 0$ is positive. Since also $\delta > 0$, this implies that for $e_s''(\delta)$ to vanish and thus phase separation to set in, δ has to be lowered some more. In this sense, δ_c constitutes an upper bound for the onset of phase separation. If $\delta_c e_h''(\delta_c)$ is very small, e.g., by already having $\delta \ll 1$, the upper bound and the actual onset may practically coincide. In general, however, they can differ considerably.

In Ref. [24], Corboz *et al.* found a value of $\delta_c = 0.1$ for U(1) simulations of a $\lambda 5$ system (see Fig. 4 of their supplement, data for W5, $D = 8$). In Fig. 1(a) of our main text, our $\lambda 5$ U(1) data is consistent with their result—we likewise find $\delta_c \simeq 0.1$. Based on the above line of reasoning, we regard this as an upper bound for phase separation. Our $\lambda 5$ SU(2) data in Fig. 1(a) has a minimum at $\delta_c \simeq 0.2$. However, this yields no additional information on phase separation, since at that value of doping, the U(1) data already lies energetically below the SU(2) data.

Our interpretation of $\delta_c \simeq 0.1$ as an upper bound for the onset of phase separation is confirmed by Fig. S5. There we have replotted the data for $e_h(\delta)$ vs. δ from Fig. 1(a) of the main text, but now showing $e_s(\delta)$ vs. δ , instead. In the simulated doping range ($\delta > 0.1$), we find $e_s'' \geq 0$ for both our U(1) and SU(2), i.e., no indication of phase separation, even though the U(1) and SU(2) results for e_h show a clear minima near $\delta \simeq 0.1$ and 0.2 ,

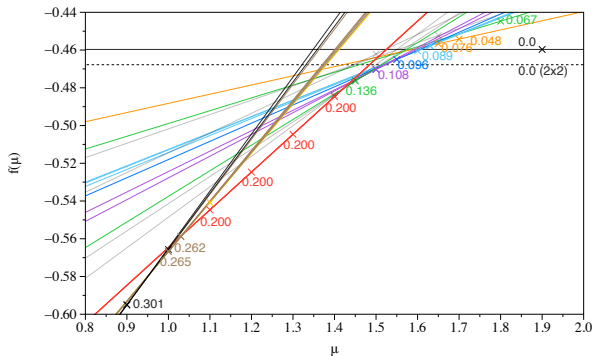


FIG. S4. The grand-canonical energy per site $f_i(\mu)$ of Eq. (S.1), plotted vs. chemical potential μ . Each colored symbol, placed at $(\mu_i, f_i(\mu_i))$, represents a U(1) iPEPS state $|\Psi_i\rangle$, obtained by minimizing $\langle \Psi_i | \hat{H} - \mu_i \hat{N} | \Psi_i \rangle$ on the 5×2 unit cell for a specified value of $\mu = \mu_i$; the color-matched number gives the corresponding value of doping, $\delta_i = 1 - n_i$. A color-matched line through a symbol shows $(\mu, f_i(\mu))$, plotted by varying μ in Eq. (S.1) while keeping e_i and n_i fixed as computed for μ_i . Symbols with the same μ_i but different $f_i(\mu_i)$ values can arise, because iPEPS optimizations starting from different randomized initial states can get stuck in different local minima, corresponding to excited states. For reference, the lower horizontal dashed black line was obtained using a U(1) 2×2 unit cell for the Heisenberg model, having $\delta = 0$ by definition. The latter unit cell is more naturally suited to describe the AF state and hence already well coincides with the thermodynamic limit for large μ [cf. Table S1].

respectively.

To further elucidate the different stability properties of the regimes $\delta \gtrsim 0.1$ or $\lesssim 0.1$, we now describe in more detail how we obtained the data of Fig. 1(a), which shows the energy per hole e_h as a function of δ . To obtain different values of δ , we varied the chemical potential μ as input parameter. Concretely, we picked a specified set of values of the chemical potential, $\{\mu_1, \mu_2, \dots\}$. For each μ_i , we minimized $\langle \Psi_i | \hat{H} - \mu_i \hat{N} | \Psi_i \rangle$ to find an iPEPS state $|\Psi_i\rangle$. We then computed $e_i = \langle \Psi_i | \hat{H} | \Psi_i \rangle / N_{\text{sites}}$, $n_i = \langle \Psi_i | \hat{N} | \Psi_i \rangle / N_{\text{sites}}$, and the doping $\delta_i = 1 - n_i$. The state $|\Psi_i\rangle$ spans a one-dimensional variational space for minimizing the grand-canonical (ground state) energy per site,

$$f_i(\mu) = e_i - \mu(n_i - 1), \quad (\text{S.1})$$

as a function of μ , where e_i and n_i are kept constant as computed for given μ_i . Here we also added a trivial shift $+\mu$ on the r.h.s., such that zero doping (half-filling) gives rise to a horizontal line vs. μ in Fig. S4. For each data point $(\mu_i, f_i(\mu_i))$ depicted by a symbol, we also plot a color-matched line $f_i(\mu)$ vs. μ . By construction, this line always also passes through its corresponding symbol. For a given value of μ , the state $|\Psi_i\rangle$ having the lowest $f_i(\mu)$ may be viewed as the “stable” one. It corresponds to the ground state for the given setting, en-

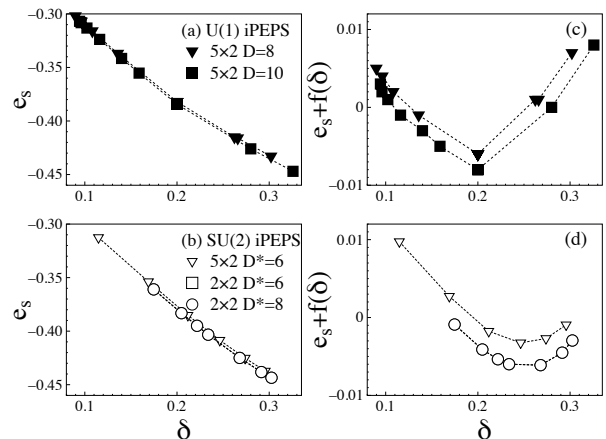


FIG. S5. (a,b) Energy per site, e_s , as a function of hole doping δ for U(1) and SU(2) iPEPS. (c,d) Same data, but relative to a linear fit, i.e., adding $f(\delta) = 0.63\delta + 0.25$ to improve the visibility of the curvature.

tailoring finite-size effects through a combination of the chosen unit-cell geometry and bond dimension. The envelope constructed from the corresponding lowest-lying straight-line segments shows the evolution of the grand-canonical energy $f(\mu)$ with chemical potential. For each μ_i yielding a stable solution, the pair of values δ_i and $e_{h,i} = (e_i - e_0)/\delta_i$ yield a data point in Fig. 1(a).

We find stable solutions for $\delta \gtrsim 0.1$ corresponding to $\mu \lesssim 1.45$, but none for $\delta \lesssim 0.1$. This likely reflects stronger finite-size effects, since $\delta \lesssim 0.1$ describes fillings less than one particle per unit cell here. For example, note that for small doping, $0 < \delta \lesssim 0.07$, the symbols and corresponding lines start to lie above the zero doping case even for the 5×2 unit cell itself (horizontal black solid line, $\delta = 0$). At zero doping, finally, there is a minor finite-size effect, in that the energy for the 5×2 unit cell (solid black line) lies above that of the 2×2 unit cell (dashed solid line), the latter computed for the Heisenberg model. This reflects the incommensurability of the 5×2 unit cell with underlying AF phase.

S-III. D-WAVE PAIRING

In the main text we reported that our U(1) results for the $\lambda 5$ stripe show no evidence for a d-wave pattern, i.e. the local singlet pairing order $\langle \Delta_{ij} \rangle = \frac{1}{\sqrt{2}} \langle \tilde{c}_{i\uparrow} \tilde{c}_{j\downarrow} - \tilde{c}_{i\downarrow} \tilde{c}_{j\uparrow} \rangle$, though non-zero, does not have opposite signs on horizontal and vertical bonds. This finding differs somewhat from previous DMRG and iPEPS studies, which did report d-wave order for U(1) wave functions [19, 24, 27]. To resolve this issue, we have performed a set of U(1) simulations for which we strongly biased our system by adding sizable pairing fields,

$$D_{ij} = h_{ij}(\Delta_{ij} + \Delta_{ij}^\dagger), \quad (\text{S.2})$$

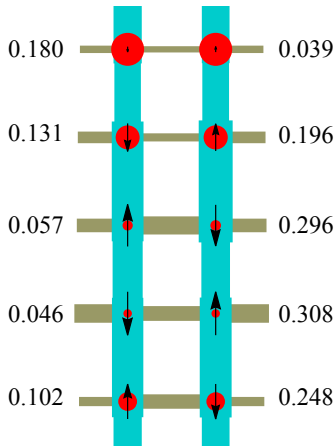


FIG. S6. U(1) iPEPS simulations at $\delta \simeq 0.1$ with a 5×2 unit cell with the pairing fields in Eq. (S.2) to probe sensitivity to d-wave pairing order. The left (right) column of numbers give hole densities (local moments), averaged in terms of absolute value over the two sites in a row.

to the Hamiltonian to stabilize the d-wave pattern [6, 19, 33]. We chose the same amplitudes on all bonds, $|h_{ij}| = 0.10$, but with opposite signs along vertical and horizontal directions. This indeed stabilizes states showing d-wave pairing, with a typical example shown in Fig. S6.

Similar to the analysis in Ref. [33] on the Hubbard model, we find that local observables, such as, hole densities and local moments, change only slightly when introducing pairing pinning fields (compare on-site data in Fig. S6 and upper middle panel in Table S2). This behavior is consistent with previous simulations. The 5×2 unit cell in Fig. S6, by having $(1/\delta) \simeq 2\lambda$, features a so-called *half-filled stripe* [27]. The present calculation therefore shows that a half-filled stripe can coexist with singlet pairing, and that the latter can have a d-wave pattern (albeit here enhanced with the help of pinning fields). This is in stark contrast to a *filled stripe* (i.e., with $\lambda = 1/\delta$), for which a charge gap is present but the pairing amplitude is entirely suppressed. For example, a filled stripe is seen in the main text in the U(1) simulation at $\delta = 0.2$ in Fig. (1c). It shows strongly reduced pairing correlations, in contrast to the non-stripe system in the corresponding SU(2) simulation right next to it.

Our results for simulations using pairing pinning fields, exemplified by Fig. S6, leave open the possibility of coexisting stripe order and d-wave singlet pairing of the type observed previously. What is still unclear is whether the d-wave singlet pairing represents a spontaneous symmetry-broken order or not. Our U(1) iPEPS simulations cannot directly answer this question. This is because without even though the local pairing Δ_{ij} does not display d-wave pairing if the pinning field is switched off, a d-wave pattern might nevertheless be present, though visible only to non-local correlators.

AF order in the U(1) simulations appears to be able to overshadow an underlying d-wave singlet pairing. For example, consider the first column in Table S2 for a 2×2 unit cell which favors the charge uniform state. As δ is increased from 0.1 through 0.2 to 0.3, the local AF moment decreases, and with it also the observed strong pairing expectation values with uniform sign. Eventually, the state approaches a singlet state with a negligible local magnetic moment. At the same time, notably, the d-wave singlet pairing pattern (now with the alternating signs of *d*-wave order) appears without any help of pinning field.

Conversely, one can simply consider an SU(2) singlet state. In this case, the phase of the singlet pairing can be measured locally without the interference of triplet pairing. As seen in Fig. 1(b-d) of the main text, singlet pairing is clearly present, albeit weak, for $\delta = 0.1, 0.2$ and 0.3 . It thus appears that spontaneous symmetry breaking towards singlet pairing is more easily detectable when the symmetry-unbroken state is already a condensate of singlets. From this perspective, our result suggests that the d-wave singlet pairing order does exist.

Assuming that stripe order and d-wave pairing order compete at small doping, our SU(2) results should be considered an upper bound for the d-wave pairing order parameter, since SU(2) enforcement suppresses the stripes. However, a complete analysis of the dependency of d-wave order on the bond dimension D is still lacking.

In summary, we conclude that as long as the ground state is close to a singlet, d-wave pairing is present in the t - J model. If stripe order occurs and the stripe is not filled, the d-wave pairing can possibly coexist with the stripe order. What remains unclear is the precise magnitude of the pairing amplitude, which likely requires simulations with even larger bond dimensions than we have reported here.

S-IV. FURTHER SYMMETRY AND FILLING RELATED TECHNICALITIES

In this section, we document the details of our iPEPS simulations for the doped t - J model with $J/t = 0.4$. In our setup, the total particle number is not conserved, and \mathbb{Z}_2 parity symmetry is used in the charge sector. The average number of holes is controlled by the chemical potential μ . In order to ensure that at $\mu = 0$ the system is half-filled, we add an additional term, $\frac{2t^2}{J} \sum_i (\hat{n}_i - \frac{1}{2})$, to the t - J model [65]. This term is similar to the one used in the Hubbard model, $\frac{U}{2} \sum_i (\hat{n}_i - \frac{1}{2})$, to make the Coulomb interaction particle-hole symmetric. The spin sector, as discussed in the main text, has either U(1) or SU(2) symmetry.

S-V. FURTHER FIGURES

For reference, Tables [S2-S3](#) depict detailed numerical values for the iPEPS states shown in Fig. 1(b-d), and several related states.

TABLE S2. $U(1)$ iPEPS with $D = 8$ and $D = 10$ at doping $\delta \simeq 0.1, 0.2$ and 0.3 . Within each column separated by vertical lines, the left (right) column of numbers give hole densities (local moments), averaged (in terms of absolute value) over the two sites in a row.

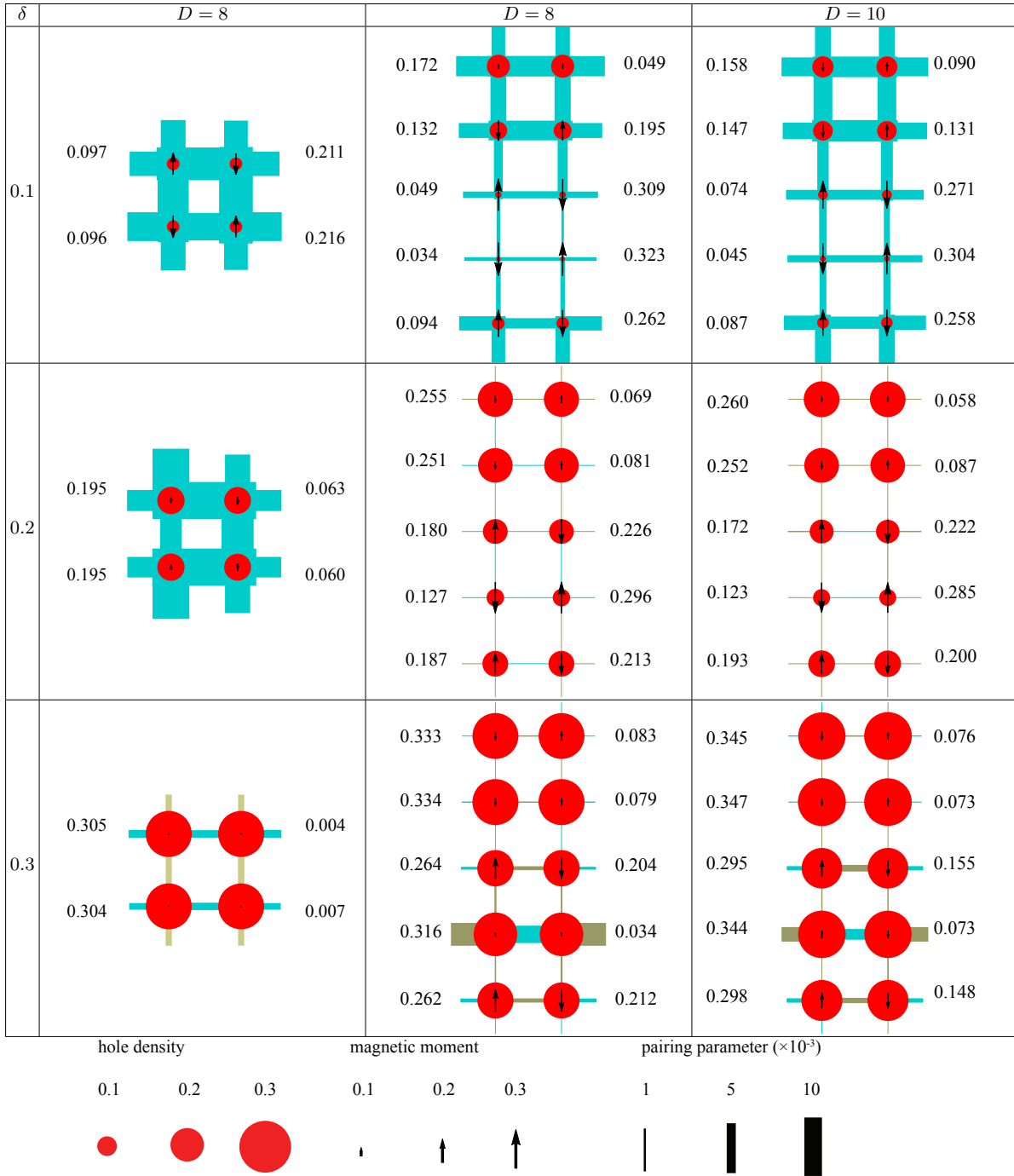
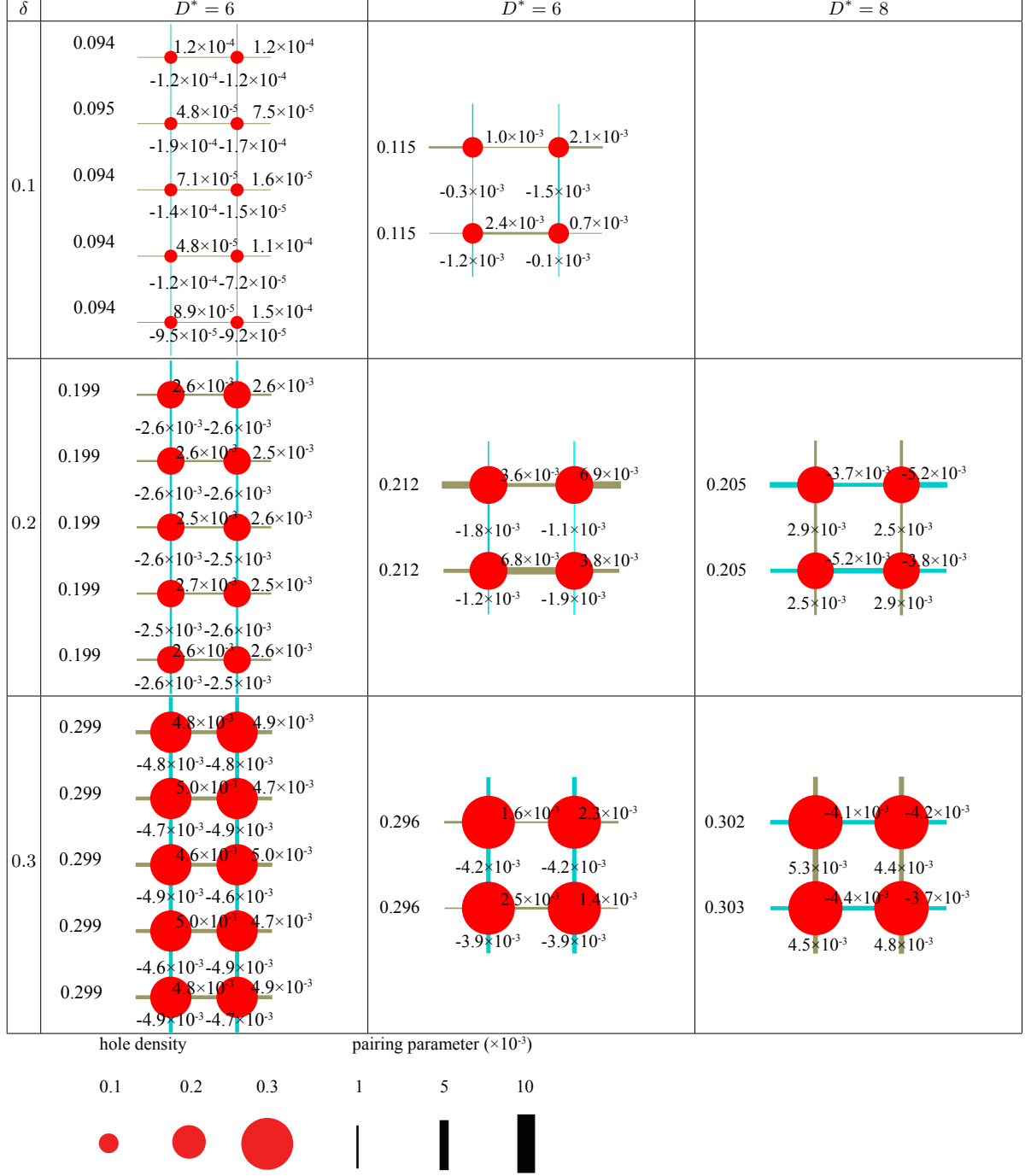


TABLE S3. SU(2) iPEPS with $D^* = 6$ and $D^* = 8$ at doping $\delta \simeq 0.1, 0.2$ and 0.3 . The left column of numbers gives hole densities averaged over the two sites in a row. The number on each bond is the singlet pairing amplitude.



Tangle of Spin Double Helices in the Honeycomb Kitaev- Γ Model

Jheng-Wei Li,^{1,2} Nihal Rao,^{1,2} Jan von Delft,^{1,2} Lode Pollet,^{1,2,3} and Ke Liu^{1,2,*}

¹Arnold Sommerfeld Center for Theoretical Physics, University of Munich, Theresienstr. 37, 80333 München, Germany

²Munich Center for Quantum Science and Technology (MCQST), Schellingstr. 4, 80799 München, Germany

³Wilczek Quantum Center, School of Physics and Astronomy, Shanghai Jiao Tong University, Shanghai 200240, China
(Dated: June 22, 2022)

We investigate the ground-state nature of the honeycomb Kitaev- Γ model in the material-relevant parameter regime through a combination of classical and quantum simulations. The classical model is imprinted with a tangle of highly structured spin double helices. This helix tangle exhibits 18 inequivalent helical axes and features a spontaneous periodicity anisotropy and a $\text{sgn}(\Gamma)$ -determined chirality pattern. Infinite PEPS simulations with clusters up to 36 sites identify hallmarks of this many-body order in the quantum spin-1/2 model. Our findings provide a fresh perspective of the Kitaev- Γ model and enrich the physics of Kitaev magnetism.

Introduction. The honeycomb Kitaev- Γ Hamiltonian is a paradigmatic model for the physics of two-dimensional Kitaev magnets [1–6]. The Kitaev exchange leads to an exactly solvable spin liquid [7] and can be realized in d -electron transition-metal compounds with edge-shared geometry [1]. However, a Γ term generically exists owing to symmetry [3, 4]. Indeed, in the proximate spin-liquid material α -RuCl₃ [8–17], this term has been found to be as large as the Kitaev interaction [18–24]. Theoretical studies further suggest that the Γ exchange can induce exotic phases beyond a Kitaev spin liquid (KSL) [23–40]. Nonetheless, state-of-the-art numerical methods, including exact diagonalization [25, 38], tensor network [26–29], variational Monte Carlo [30], and functional renormalization group [31] techniques, have yielded highly diverse results for the spin-1/2 Kitaev- Γ model, leaving the quantum phase diagram obscure. Consensus exits for a KSL at finite Γ but even its extent is debated.

In this Letter, we conduct large-scale classical and quantum simulations to unravel the ground-state nature of the honeycomb Kitaev- Γ model in the most puzzling yet relevant region for materials. We first demonstrate that the classical ground state imprints a tangle of *spin double helices* (Fig. 1). This helix tangle exhibits a number of distinctive characteristics including a multitude of different helical axes, anisotropic spacial periodicities, and $\text{sgn}(\Gamma)$ -determined chirality patterns [Eq. (5)]. The emergence of such sophisticated helicity poses fundamental challenges to quantum algorithms and may have been the source of non-coherent observations in the literature. Nevertheless, our infinite projected entangled pair states (iPEPS) calculations identify signatures of this unprecedented many-body order, showing that it can survive quantum fluctuations in the spin-1/2 case.

Model and symmetry. The Kitaev- Γ model on a honeycomb lattice comprises two bond-dependent terms: a directional Ising-type interaction and a symmetric off-

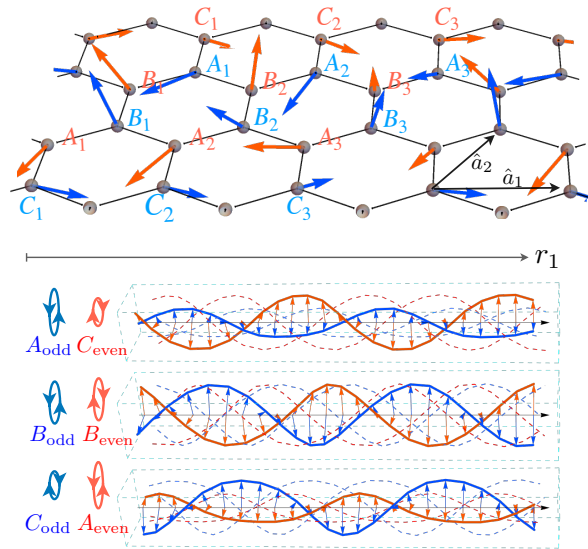


Figure 1. A classical ground state of the honeycomb Kitaev- Γ model at $\Gamma = -K$. The letters A_j, B_j, C_j with $j = 1, 2, 3$ are assigned to distinct rotation axes, and their colors distinguish the odd (blue) and even (orange) honeycomb sublattices, together defining a 3×3 unit cell with 18 sublattices. Spins belonging to the *same* sublattice form helices and swirl about their respective rotation axes. The lower panel illustrates the spiral components of spins along the r_1 direction. Six of the 18 helices specified by a unit cell are highlighted with solid lines, while other twelve are presented as dashed lines. Cycles on the side indicate different spiral strengths, and arrows reflect the opposite chirality on the odd and even honeycomb sublattices. $\hat{a}_{1,2}$ denote the lattice unit vectors. The linear system size is $L = 72$.

diagonal Γ interaction,

$$H = \sum_{\langle ij \rangle_\gamma} K S_i^\gamma S_j^\gamma + \Gamma \left(S_i^\alpha S_j^\beta + S_i^\beta S_j^\alpha \right). \quad (1)$$

Here, γ labels the three different types of bonds, and $\alpha, \beta, \gamma \in \{x, y, z\}$ are mutually exclusive. For example, the local Hamiltonian on a z -bond reads $H_z = K S_i^z S_j^z +$

$\Gamma (S_i^x S_j^y + S_i^y S_j^x)$. For simplicity, we assume the coupling strengths on the three bonds are uniform. Nevertheless, one expects that a small bond anisotropy (e.g., $K_z \neq K_{x,y}$) does not alter the nature of the underlying phases as in the case of a pure Kitaev model [7].

The Hamiltonian Eq. (1) has a hidden global symmetry that intertwines the spacial and spin spaces and leads to an additional two-fold degeneracy. This is easily seen by rewriting the Hamiltonian as $H = \sum_{\langle ij \rangle_\gamma} \mathbf{S}_i \cdot \hat{J}_{ij}^\gamma \mathbf{S}_j$, in terms of three exchange tensors

$$\hat{J}_{ij}^x = \begin{bmatrix} K & & \\ & \Gamma & \\ & & \Gamma \end{bmatrix}, \hat{J}_{ij}^y = \begin{bmatrix} & K & \\ & & \Gamma \\ \Gamma & & \Gamma \end{bmatrix}, \hat{J}_{ij}^z = \begin{bmatrix} \Gamma & & \\ & \Gamma & \\ & & K \end{bmatrix}. \quad (2)$$

One can verify that \hat{J}_{ij}^γ , hence the local environment of spins, is invariant under the transformations

$$\sigma_i^{\alpha\beta} \hat{J}_{ij}^\gamma \sigma_j^{\alpha\beta} = \hat{J}_{ij}^\gamma, \quad (3)$$

$$\sigma_i^{\alpha\gamma} \hat{J}_{ij}^\gamma \sigma_j^{\gamma\beta} = \hat{J}_{ij}^\gamma, \quad (4)$$

where $\sigma_i^{\alpha\beta}$ denotes spin reflections transforming a spin as $\sigma_i^{\alpha\beta} S_i^\gamma = -S_i^\gamma$. These transformations alternate the three spin reflections in accordance with the index rule of Eqs. (3) and (4), until covering the entire lattice (see SM [41] for a concrete example). In contrast to normal global symmetries, such as the time reversal and homogeneous spin rotations, this hidden symmetry can modify correlations in the system and make two *distinct* orders degenerate.

Selected parameter region. The main open problems in constructing the phase diagram of the spin-1/2 Kitaev- Γ model can be viewed from three fronts. First, although mounting numerical evidences suggest an extended KSL regime under a small Γ , different algorithms find different extents of this regime [27–31]. Furthermore, in the large Γ limits, the fate of thermal Γ spin liquids [36, 42, 43] in the spin-1/2 case is unsettled and prone to simulation techniques [44, 45]. Away from these two limits, a diversity of candidate ground states have been suggested, including non-Kitaev spin liquids, quantum paramagnets, incommensurate or spiral orders, and various magnetic states [26–31]. As all these open problems cannot be resolved in a single work, we focus our efforts on the regime where both interactions are sizable and competing, which is of the highest relevance for real materials. For convenience, we parameterize the two interactions using an angle parameter θ as $K = \sin \theta$, $\Gamma = \cos \theta$. We consider the frustrated region with a ferromagnetic K and an antiferromagnetic Γ ($1.5\pi < \theta < 2\pi$), which corresponds to the exchange parameters realized in the d -electron Ir- and Ru-based compounds [22, 24, 46]. Through a mapping $\theta \rightarrow \theta + \pi$ and simultaneously $\mathbf{S}_{2i} \rightarrow \mathbf{S}_{2i}$, $\mathbf{S}_{2i+1} \rightarrow -\mathbf{S}_{2i+1}$ [47], its results also enlighten the physics at $0.5\pi < \theta < \pi$. Other parameter regions with $\theta \in (0, 0.5\pi)$ and $(\pi, 1.5\pi)$ are unfrustrated and understood to develop strong 120°-type magnetic orders [25, 36].

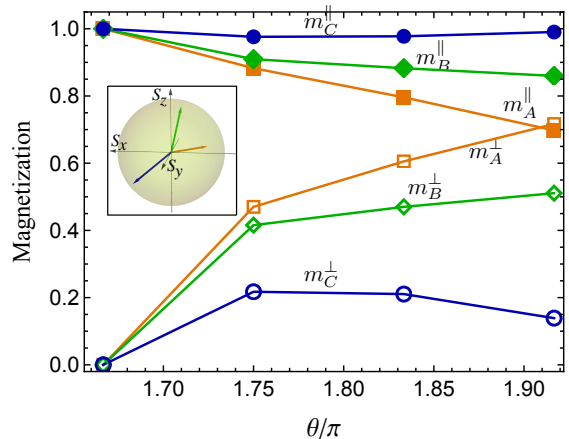


Figure 2. Magnetizations of the classical spin-helix complex with comparable Kitaev and Γ interaction, $K = \sin \theta$, $\Gamma = \cos \theta$. The longitudinal components m_μ^\parallel reflect a long-range order in the helical axes, and the transversal components m_μ^\perp measure the spiral magnitudes. The classical order is fully characterized as the total magnetization $(m_\mu^\parallel)^2 + (m_\mu^\perp)^2 = 1$. The m_μ^\perp component at $\theta \approx 1.67\pi$ is small but non-vanishing (see Fig. 3). The inset exemplifies the orientations of $\mathbf{m}_{A_1}^\parallel$, $\mathbf{m}_{B_1}^\parallel$ and $\mathbf{m}_{C_1}^\parallel$ (indicated by colors) at $\theta = 1.75\pi$.

Tangle of spin helices. We first discuss the classical ground states in the selected parameter regime. The growing interest towards the classical Kitaev- Γ model is not merely a compromise to the quantum complexity but is rewarded with rich physics [34–40]. In particular, two recent works [34, 38] based on analysis of small systems reported various large-unit-cell states including two degenerate 6- and 18-site structures. By examining large systems at temperature $T = 10^{-3}\sqrt{K^2 + \Gamma^2}$, the Tensorial-kernel support vector machine (TKSVM) method [48–50] mapped these two states to a frustrated phase spanning over $1.58\pi \lesssim \theta < 2\pi$ [36]. This phase can be understood by the competition between two classical spin liquids, and its order parameter exhibits an intrinsic undersaturation indicating the lack of perfect translationally invariant order [36].

We now reveal that the missing magnitude in the order parameter encodes a quintessential nature of the classical ground state, which is only manifested at large system sizes and very cold temperatures. We utilize parallel tempering Monte Carlo methods to reach temperatures down to $T = 10^{-5}\sqrt{K^2 + \Gamma^2}$ for systems of linear size up to $L = 72$ and 108. We further cool the system to $T \rightarrow 0$ by eliminating the thermal noise; see the SM [41].

In Fig. 1, we show a representative ground-state configuration at $\Gamma = -K$ ($\theta = 1.75\pi$). First ignoring the subscripts $j = 1, 2, 3$, one can recognize a motif with seemingly repeating $C-A-B-B-A-C$ pattern, which corresponds to the X-phase and the 6-site order in the litera-

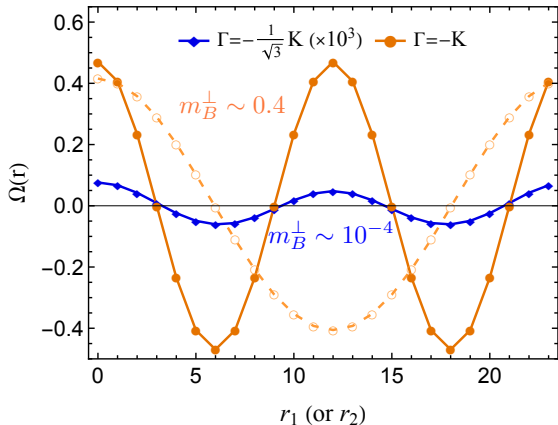


Figure 3. The oscillation parameter $\Omega_\mu(\mathbf{r})$ for B-helices at $\Gamma = -K/\sqrt{3}$ (blue) and $-K$ (orange) ($\theta = 1.67\pi, 1.75\pi$). The oscillation reflects the phase difference between two spins $\mathbf{S}_{\mu, \mathbf{r}_0}$ and $\mathbf{S}_{\mu, \mathbf{r}_0 + \mathbf{r}}$, and the amplitude is proportional to m_μ^\perp . For visibility, the $\Gamma = -K/\sqrt{3}$ curve is rescaled by a factor 10^3 . Filled and open symbols are measured along the r_1 and r_2 directions, respectively, hence exhibit different periodicities. The linear size is $L = 72$, and $r_1, r_2 = 0, 1, \dots, \frac{L}{3} - 1$.

ture [34, 38]. Then applying the transformations Eqs. (3) and (4), it will retrieve the subscripts and enlarge to a 3×3 superstructure containing 18 sublattices. Nevertheless, these motifs are only approximate and the ground states do not have true translational symmetry.

To further illustrate the structure, we define a generic sublattice magnetization $\mathbf{m}_\mu^\parallel = \frac{1}{N_{\text{cell}}} \sum_{\text{cells}} \mathbf{S}_\mu$ by averaging spins over the (approximate) 3×3 unit cell, with $\mu = A_j, B_j, C_j$. Thanks to the hidden symmetry, the resultant \mathbf{m}_μ^\parallel can be discriminated into three categories whose magnitudes are denoted as $m_A^\parallel, m_B^\parallel, m_C^\parallel$. These scalar magnetizations are measured in Fig. 2 in a subregion around $\Gamma = -K$, where one clearly sees the unsaturation and a general suppression with increasing Γ .

In fact, \mathbf{m}_μ^\parallel only captures the rotation axes (or longitudinal components) of an ensemble of highly structured spin helices. To find the spiral (transverse) components, it is convenient to work in local coordinates where $\tilde{\mathbf{m}}_\mu^\parallel = (0, 0, m_\mu^\parallel)$ for each sublattice. The transverse components of a spin can then be characterized by an ansatz

$$\tilde{S}_{\mu, \mathbf{r}}^\perp = m_\mu^\perp \left(\cos \frac{6\pi}{L} (2r_1 + r_2), \text{sgn}(\Gamma)^\eta \sin \frac{6\pi}{L} (2r_1 + r_2), 0 \right). \quad (5)$$

Here, $m_\mu^\perp = \frac{1}{N_{\text{cell}}} \sum_{\text{cells}} |\tilde{S}_\mu^\perp|$ defines a spiral magnetization, $\mathbf{r} = (r_1, r_2)$ with $r_1, r_2 = 0, 1, \dots, \frac{L}{3} - 1$ labels the unit cells, and $\eta = 0, 1$ distinguishes the even and odd honeycomb sublattices. This ansatz is verified in Fig. 2 by measuring a saturated total magnetization $(m_\mu^\parallel)^2 + (m_\mu^\perp)^2 = 1$.

Several prominent features of the classical ground states can now be made explicit. A “unit cell” can only be defined for the longitudinal moments \mathbf{m}_μ^\parallel , which are the source of the long-range magnetic correlations and stable $\frac{2}{3}\mathbf{M}$ magnetic Bragg peaks [34, 36]. Spins in the *same* unit cell form helices and rotate about the respective \mathbf{m}_μ^\parallel . Thus there is a 3×3 modulation in the helical axes, and the system cannot be simplified as rigid clusters rotating about a common axis. The spin helices living on the even and odd honeycomb sublattices develop staggered (uniform) chirality patterns if Γ is anti-ferromagnet (ferromagnet). Therefore, the 18 helices specified in a unit cell can be viewed as nine double helices with their (relative) chirality determined by the sign of Γ , as visualized in Fig. 1.

Moreover, this intricate helicity is an imprinted feature of the entire frustrated phase $1.58\pi \lesssim \theta < 2\pi$, while it may be hardly noticeable for weaker Γ values. This can be demonstrated by introducing an oscillation parameter

$$\Omega_\mu(\mathbf{r}) = \frac{1}{m_\mu^\perp} \left(\mathbf{S}_{\mu, \mathbf{r}_0} \cdot \mathbf{S}_{\mu, \mathbf{r}_0 + \mathbf{r}} - |\mathbf{m}_\mu^\parallel|^2 \right), \quad (6)$$

whose amplitude is proportional to the spiral magnitude m_μ^\perp . In Fig. 3, Ω_μ is measured for B-helices. Despite the extremely small $m_B^\perp \sim 10^{-4}$ at the weaker $\Gamma = -K/\sqrt{3}$, the expected cosine oscillation is still formed.

Also remarkable is the *spontaneous anisotropy* in spacial periodicities: The helix pitch is $\frac{L}{3}$ pitch in the C - A - B modulated direction but is $\frac{L}{6}$ pitch within a A_j, B_j , or C_j chain (the r_1 direction in Fig. 1), which is encoded in the ansatz Eq. (5) and reflected in Fig. 3.

Proximate quantum ground states. The identification of the classical ground state provides a reference for understanding the quantum model. Indeed, strong magnetic orders established in the classical limit often can persist in the quantum spin-1/2 case with a reduced ordering moment and shifted phase boundary. Examples can be found in both Kitaev magnets [25, 37, 51] and other highly frustrated systems such as triangular anti-ferromagnets [52, 53]. In the current problem our full characterization of the helix tangle is especially helpful as the intricacies of this order pose challenges that lie far beyond the capabilities of any state-of-the-art quantum algorithm.

Our hope with the iPEPS is that if Γ , hence the spiral m_μ^\perp , is not too strong, it may capture a consistent longitudinal magnetization. We consider three tensor network ansatzes built from a 4-site, a 16-site, and a 36-site cluster. These clusters cover potential competing orders such as ferromagnetic, Néel, $\sqrt{3} \times \sqrt{3}$, stripy, and zigzag type orders which are commonly found in Kitaev magnets [25, 37, 54]. The 36-site cluster can further fit two unit cells of the classical helical axes. We scan the parameter space through a simple update scheme [55, 56] with a large bond dimension $D = 8$. Typically over 600 initial-

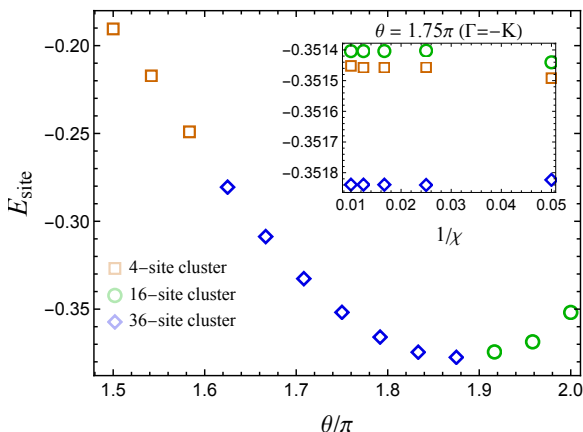


Figure 4. (Proximate) Ground state energies computed with iPEPS. In the regime with comparable Kitaev and Γ interactions ($1.6\pi < \theta < 1.9\pi$), the 36-site cluster systematically gives the lowest energies and develops a magnetic pattern similar to the classical longitudinal magnetization \mathbf{m}_μ^\parallel . At larger Γ ($\theta > 1.9\pi$), the 16-site and 4-site clusters take over and capture a zigzag-type order. Small magnetizations are obtained near the Kitaev corner ($\theta < 1.6\pi$) where the 4-site cluster is preferred. The inset shows the energy convergence with the environmental bond dimension χ .

izations are simulated at each θ value. Physical quantities are measured using a CTMRG method [57, 58] with environmental bond dimensions $\chi > D^2$. For comparison, we have also examined a full update scheme [51, 59] but find the improvements are limited for the symmetry-broken states. See SM for details [41].

We present our iPEPS results in Fig. 4. In the parameter regime $1.6\pi < \theta < 1.9\pi$, the 36-site cluster systematically leads to the lowest energies whose variations in χ are significantly smaller than the energy distinctions between different clusters. This confirms the convergence of our simulations and exclude competing magnetic orders. Remarkably, the quantum magnetic moments \mathbf{m}_μ in the cluster display a very similar sublattice structure as the classical \mathbf{m}_μ^\parallel [41]. Their strengths reduce from the classical values $0.8 \lesssim |\mathbf{m}_{A,B,C}^\parallel| \lesssim 1$ to $0.3S \lesssim |\mathbf{m}_{A,B,C}| \lesssim 0.5S$ but remain sizable to distinguish from paramagnetic states. In Fig. 5, orientations of the quantum \mathbf{m}_μ are inspected and found close to the classical longitudinal magnetization.

The resemblances between the quantum and classical magnetic moments indicate persistence of longitudinal magnetization. In particular for the weaker Γ regime such as $\theta \approx 1.67\pi$, there the helicity emerges with a magnetization in the order of $m_\mu^\perp \sim 10^{-4}$ (Fig. 3). Since the energy is expected to scale with $|m_\mu^\perp|^2$, the iPEPS ansatzes may remain legitimate at such a Γ value. Adding that we do not observe signals of a phase transition at immediately stronger Γ in both quantum and classical cases,

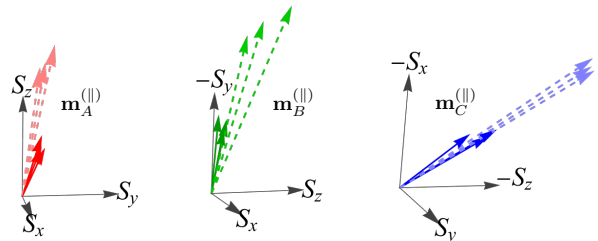


Figure 5. Comparison of quantum (solid arrows) and classical (dashed arrows) sublattice magnetizations at $\theta = 1.67\pi, 1.75\pi, 1.83\pi$ ($\Gamma = -K/\sqrt{3}, -K, -\sqrt{3}K$). Orientations of the quantum magnetic moments are very close to the classical longitudinal magnetizations, while the magnitudes reduce to $0.3S \lesssim |\mathbf{m}_{A,B,C}| \lesssim 0.5S$ from the classical values $0.8 \lesssim |\mathbf{m}_{A,B,C}^\parallel| \lesssim 1$. The axes are rotated for visualization.

the classical order can be anticipated to survive quantum fluctuations at least for a finite extent of moderate Γ values.

In the large Γ regime ($\theta > 1.9\pi$), the 16-site and 4-site clusters take over with indistinguishable energies but both show a clear zigzag type magnetization [41]. Nevertheless, here we expect iPEPS ansatzes to fail due to the underlying strong helicity. The observed zigzag order may reflect a numerical artifact or a consequence of a possible quantum order-by-disorder at the Γ point [44, 45].

Near the Kitaev corner ($\theta < 1.6\pi$) we obtain small magnetizations, which is consistent with the literature [28–30].

Summary and discussion. Understanding the physics of the honeycomb Kitaev- Γ model is crucial for both interpreting experimental observations and exploring novel phases in Kitaev magnets. In this work, we have investigated its ground-state properties through a combination of comprehensive classical and quantum simulations. We discovered a tangle of highly structured spin double helices imprinted in the classical ground states at material-relevant Γ values. This helix tangle stands out among typical spiral magnets [60–63] by its intricate modulation of helical axes, spontaneous periodicity anisotropy, and well regulated chirality pattern. The full characterization of the classical ground state becomes particularly valuable in view of fundamental limitations in state-of-the-art quantum numerical algorithms. Converged iPEPS calculations reproduced magnetic moments resembling the classical longitudinal magnetization and signal persistence of the helix tangle against quantum fluctuations. The emergence of the unconventional helicity may leave fingerprints to dynamical and transport behaviors such as inducing spectrum broadening, long-living currents and anomalous diffusions [64–66].

Acknowledgments. This project is partially funded by the Deutsche Forschungsgemeinschaft (DFG, German Research Foundation) under Germany’s Excellence

Strategy – EXC-2111 – 390814868. The research is also part of the Munich Quantum Valley, which is supported by the Bavarian state government with funds from the Hightech Agenda Bayern Plus. N.R., L.P., and K.L. also acknowledge support from FP7/ERC Consolidator Grant QSIMCORR, No. 771891. Our numerical simulations make use of the QSpace tensor library [67, 68], the TKSVMLibrary [48, 49], and the ALPSCore library [69]. The simulations were performed on the KCS cluster at Leibniz-Rechenzentrum (LRZ) and the ASC cluster at Arnold Sommerfeld Center. The data used in this work will be made available.

* ke.liu@lmu.de

- [1] G. Jackeli and G. Khaliullin, *Phys. Rev. Lett.* **102**, 017205 (2009).
- [2] J. Chaloupka, G. Jackeli, and G. Khaliullin, *Phys. Rev. Lett.* **105**, 027204 (2010).
- [3] J. G. Rau, E. K.-H. Lee, and H.-Y. Kee, *Phys. Rev. Lett.* **112**, 077204 (2014).
- [4] J. G. Rau, E. K.-H. Lee, and H.-Y. Kee, *Annual Review of Condensed Matter Physics* **7**, 195 (2016).
- [5] H. Takagi, T. Takayama, G. Jackeli, G. Khaliullin, and S. E. Nagler, *Nat. Rev. Phys.* **1**, 264 (2019).
- [6] S. M. Winter, A. A. Tsirlin, M. Daghofer, J. van den Brink, Y. Singh, P. Gegenwart, and R. Valentí, *Journal of Physics: Condensed Matter* **29**, 493002 (2017).
- [7] A. Kitaev, *Ann. Phys. (N. Y.)* **321**, 2 (2006), January Special Issue.
- [8] A. Banerjee, C. A. Bridges, J. Q. Yan, A. A. Aczel, L. Li, M. B. Stone, G. E. Granroth, M. D. Lumsden, Y. Yiu, J. Knolle, S. Bhattacharjee, D. L. Kovrizhin, R. Moessner, D. A. Tennant, D. G. Mandrus, and S. E. Nagler, *Nat. Mater.* **15**, 733 (2016).
- [9] A. Banerjee, J. Yan, J. Knolle, C. A. Bridges, M. B. Stone, M. D. Lumsden, D. G. Mandrus, D. A. Tennant, R. Moessner, and S. E. Nagler, *Science* **356**, 1055 (2017).
- [10] J. Zheng, K. Ran, T. Li, J. Wang, P. Wang, B. Liu, Z.-X. Liu, B. Normand, J. Wen, and W. Yu, *Phys. Rev. Lett.* **119**, 227208 (2017).
- [11] Y. Kasahara, T. Ohnishi, Y. Mizukami, O. Tanaka, S. Ma, K. Sugii, N. Kurita, H. Tanaka, J. Nasu, Y. Motome, T. Shibauchi, and Y. Matsuda, *Nature* **559**, 227 (2018).
- [12] T. Yokoi, S. Ma, Y. Kasahara, S. Kasahara, T. Shibauchi, N. Kurita, H. Tanaka, J. Nasu, Y. Motome, C. Hickey, S. Trebst, and Y. Matsuda, *Science* **373**, 568 (2021).
- [13] S. Bachus, D. A. S. Kaib, Y. Tokiwa, A. Jesche, V. Tsurkan, A. Loidl, S. M. Winter, A. A. Tsirlin, R. Valentí, and P. Gegenwart, *Phys. Rev. Lett.* **125**, 097203 (2020).
- [14] P. Czajka, T. Gao, M. Hirschberger, P. Lampen-Kelley, A. Banerjee, J. Yan, D. G. Mandrus, S. E. Nagler, and N. P. Ong, *Nature Physics* **17**, 915 (2021).
- [15] P. Czajka, T. Gao, M. Hirschberger, P. Lampen-Kelley, A. Banerjee, N. Quirk, D. G. Mandrus, S. E. Nagler, and N. Ong, arXiv preprint arXiv:2201.07873 (2022).
- [16] J. A. N. Bruin, R. R. Claus, Y. Matsumoto, N. Kurita, H. Tanaka, and H. Takagi, *Nature Physics* **18**, 401 (2022).
- [17] E. Lefrançois, G. Grissomanche, J. Baglo, P. Lampen-Kelley, J.-Q. Yan, C. Balz, D. Mandrus, S. E. Nagler, S. Kim, Y.-J. Kim, N. Doiron-Leyraud, and L. Taillefer, *Phys. Rev. X* **12**, 021025 (2022).
- [18] K. Ran, J. Wang, W. Wang, Z.-Y. Dong, X. Ren, S. Bao, S. Li, Z. Ma, Y. Gan, Y. Zhang, J. T. Park, G. Deng, S. Danilkin, S.-L. Yu, J.-X. Li, and J. Wen, *Phys. Rev. Lett.* **118**, 107203 (2017).
- [19] R. Yadav, N. A. Bogdanov, V. M. Katukuri, S. Nishimoto, J. van den Brink, and L. Hozoi, *Scientific Reports* **6**, 37925 (2016).
- [20] H.-S. Kim and H.-Y. Kee, *Phys. Rev. B* **93**, 155143 (2016).
- [21] S. M. Winter, Y. Li, H. O. Jeschke, and R. Valentí, *Phys. Rev. B* **93**, 214431 (2016).
- [22] S. M. Winter, K. Riedl, P. A. Maksimov, A. L. Chernyshev, A. Honecker, and R. Valentí, *Nature Communications* **8**, 1152 (2017).
- [23] P. A. Maksimov and A. L. Chernyshev, *Phys. Rev. Research* **2**, 033011 (2020).
- [24] P. Laurell and S. Okamoto, *npj Quantum Materials* **5**, 2 (2020).
- [25] J. Rusnačko, D. Gotfryd, and J. Chaloupka, *Phys. Rev. B* **99**, 064425 (2019).
- [26] Y.-F. Jiang, T. P. Devereaux, and H.-C. Jiang, *Phys. Rev. B* **100**, 165123 (2019).
- [27] J. S. Gordon, A. Catuneanu, E. S. Sørensen, and H.-Y. Kee, *Nature Communications* **10**, 2470 (2019).
- [28] H.-Y. Lee, R. Kaneko, L. E. Chern, T. Okubo, Y. Yamaji, N. Kawashima, and Y. B. Kim, *Nature Communications* **11**, 1639 (2020).
- [29] M. Gohlke, L. E. Chern, H.-Y. Kee, and Y. B. Kim, *Phys. Rev. Research* **2**, 043023 (2020).
- [30] J. Wang, B. Normand, and Z.-X. Liu, *Phys. Rev. Lett.* **123**, 197201 (2019).
- [31] F. L. Buessen and Y. B. Kim, *Phys. Rev. B* **103**, 184407 (2021).
- [32] J. Wang and Z.-X. Liu, *Phys. Rev. B* **102**, 094416 (2020).
- [33] E. S. Sørensen, A. Catuneanu, J. S. Gordon, and H.-Y. Kee, *Phys. Rev. X* **11**, 011013 (2021).
- [34] L. E. Chern, R. Kaneko, H.-Y. Lee, and Y. B. Kim, *Phys. Rev. Research* **2**, 013014 (2020).
- [35] L. E. Chern, F. L. Buessen, and Y. B. Kim, *npj Quantum Materials* **6**, 33 (2021).
- [36] K. Liu, N. Sadoune, N. Rao, J. Greitemann, and L. Pollet, *Phys. Rev. Research* **3**, 023016 (2021).
- [37] N. Rao, K. Liu, M. Machaczek, and L. Pollet, *Phys. Rev. Research* **3**, 033223 (2021).
- [38] P. Lampen-Kelley, L. Janssen, E. Andrade, S. Rachel, J.-Q. Yan, C. Balz, D. Mandrus, S. Nagler, and M. Vojta, arXiv preprint arXiv:1807.06192 (2018).
- [39] A. Rayyan, Q. Luo, and H.-Y. Kee, *Phys. Rev. B* **104**, 094431 (2021).
- [40] K. Chen, Q. Luo, Z. Zhou, S. He, B. Xi, C. Jia, H.-G. Luo, and J. Zhao, arXiv preprint arXiv:2202.02753 (2022).
- [41] See Supplemental Material for details of the classical and iPEPS simulations.
- [42] I. Rousochatzakis and N. B. Perkins, *Phys. Rev. Lett.* **118**, 147204 (2017).
- [43] P. Saha, Z. Fan, D. Zhang, and G.-W. Chern, *Phys. Rev. Lett.* **122**, 257204 (2019).

- [44] Q. Luo, J. Zhao, H.-Y. Kee, and X. Wang, *npj Quantum Materials* **6**, 57 (2021).
- [45] Simulations at the Γ point are prone to boundary conditions and algorithms. Private communications with Hong-Hao Tu and Ji-Ze Zhao.
- [46] R. Yadav, S. Nishimoto, M. Richter, J. van den Brink, and R. Ray, *Phys. Rev. B* **100**, 144422 (2019).
- [47] This is similar to the mapping between the ferromagnetic and anti-ferromagnetic Heisenberg model on a bipartite lattice.
- [48] J. Greitemann, K. Liu, and L. Pollet, *Phys. Rev. B* **99**, 060404(R) (2019).
- [49] K. Liu, J. Greitemann, and L. Pollet, *Phys. Rev. B* **99**, 104410 (2019).
- [50] J. Greitemann, K. Liu, L. D. C. Jaubert, H. Yan, N. Shannon, and L. Pollet, *Phys. Rev. B* **100**, 174408 (2019).
- [51] J. Osorio Iregui, P. Corboz, and M. Troyer, *Phys. Rev. B* **90**, 195102 (2014).
- [52] S. R. White and A. L. Chernyshev, *Phys. Rev. Lett.* **99**, 127004 (2007).
- [53] Y.-D. Li, Y. Shen, Y. Li, J. Zhao, and G. Chen, *Phys. Rev. B* **97**, 125105 (2018).
- [54] J. Chaloupka and G. Khaliullin, *Phys. Rev. B* **92**, 024413 (2015).
- [55] H. C. Jiang, Z. Y. Weng, and T. Xiang, *Phys. Rev. Lett.* **101**, 090603 (2008).
- [56] P. Corboz, R. Orús, B. Bauer, and G. Vidal, *Phys. Rev. B* **81**, 165104 (2010).
- [57] T. Nishino and K. Okunishi, *Journal of the Physical Society of Japan* **65**, 891 (1996).
- [58] R. Orús and G. Vidal, *Phys. Rev. B* **80**, 094403 (2009).
- [59] J. Jordan, R. Orús, G. Vidal, F. Verstraete, and J. I. Cirac, *Phys. Rev. Lett.* **101**, 250602 (2008).
- [60] M. Mostovoy, *Phys. Rev. Lett.* **96**, 067601 (2006).
- [61] T. Kimura, *Annual Review of Materials Research* **37**, 387 (2007).
- [62] D. Khomskii, *Physics* **2**, 20 (2009).
- [63] Y. Tokura and S. Seki, *Advanced Materials* **22**, 1554 (2010).
- [64] V. Popkov and G. M. Schütz, *Phys. Rev. E* **95**, 042128 (2017).
- [65] P. N. Jepsen, J. Amato-Grill, I. Dimitrova, W. W. Ho, E. Demler, and W. Ketterle, *Nature* **588**, 403 (2020).
- [66] M. P. Walsler, C. Reichl, W. Wegscheider, and G. Salis, *Nature Physics* **8**, 757 (2012).
- [67] A. Weichselbaum, *Annals of Physics* **327**, 2972 (2012).
- [68] A. Weichselbaum, *Phys. Rev. Research* **2**, 023385 (2020).
- [69] A. Gaenko, A. Antipov, G. Carcassi, T. Chen, X. Chen, Q. Dong, L. Gamper, J. Gukelberger, R. Igarashi, S. Isakov, M. Könz, J. LeBlanc, R. Levy, P. Ma, J. Paki, H. Shinaoka, S. Todo, M. Troyer, and E. Gull, *Comput. Phys. Commun.* **213**, 235 (2017).
- [70] J. Greitemann, K. Liu, and L. Pollet, tensorial-kernel SVM library, <https://gitlab.physik.uni-muenchen.de/tk-svm/tksvm-op>.
- [71] H. G. Katzgraber, S. Trebst, D. A. Huse, and M. Troyer, *Journal of Statistical Mechanics: Theory and Experiment* **2006**, P03018 (2006).
- [72] L. Janssen, E. C. Andrade, and M. Vojta, *Phys. Rev. Lett.* **117**, 277202 (2016).
- [73] P. Corboz, M. Lajkó, A. M. Läuchli, K. Penc, and F. Mila, *Phys. Rev. X* **2**, 041013 (2012).

— Supplementary Materials —

Tangle of Spin Double Helices in the Honeycomb Kitaev- Γ Model

Jheng-Wei Li^{1,2}, Nihal Rao^{1,2}, Jan von Delft^{1,2}, Lode Pollet^{1,2,3}, and Ke Liu^{1,2}

¹*Arnold Sommerfeld Center for Theoretical Physics, University of Munich, Theresienstr. 37, 80333 München, Germany*

²*Munich Center for Quantum Science and Technology (MCQST), Schellingstr. 4, 80799 München, Germany*

³*Wilczek Quantum Center, School of Physics and Astronomy, Shanghai Jiao Tong University, Shanghai 200240, China*

S.I. CLASSICAL GROUND STATES

A. Details of the classical simulations

Simulating highly frustrated models with large system sizes is in general a challenging task. To ensure we access the correct classical ground states, we first use a parallel tempering Monte Carlo (PTMC) method to generate spin configurations at a low temperature $T = 10^{-5}\sqrt{K^2 + \Gamma^2}$ and then cool the system to $T \rightarrow 0$ by eliminating remnant small thermal noises (see below). We mostly consider lattices with linear spacing $L = 72$ (10,386 spins) on a torus, and have also checked larger lattices up to $L = 108$ (23,328 spins) at particular parameter points. Such large systems sizes and low temperatures are crucial to manifest the spin helices.

We use parallel tempering jointly with heat bath and over-relaxation algorithms to equilibrate the system [70]. $N_T = 256$ logarithmically equidistant temperatures are used to ensure efficient iterations between different temperatures [71]. Typically 10^7 Monte Carlo sweeps are performed in an individual run. All independent runs have converged to the same states, confirming the ergodicity of our simulations.

The PTMC generates spin configurations lying slightly above the classical ground states by an energy scale $\Delta E \sim 10^{-5}$ preset by the lowest simulated temperature. We cool the system to further approach the ground states by iteratively aligning spins along their local molecular fields $\mathbf{B}_i^{\text{loc}}$ [72],

$$\mathbf{S}_i^{\text{new}} = \frac{\mathbf{B}_i^{\text{loc}}}{|\mathbf{B}_i^{\text{loc}}|} |\mathbf{S}_i^{\text{old}}|. \quad (\text{S1})$$

Here $\mathbf{B}_i^{\text{loc}} = \sum_{\langle ij \rangle_\gamma} \hat{J}_{ij}^\gamma \mathbf{S}_j$ and the exchange tensors \hat{J}_{ij}^γ are reproduced for convenience

$$\hat{J}_{ij}^x = \begin{bmatrix} K & & \\ & \Gamma & \\ & & \Gamma \end{bmatrix}, \quad \hat{J}_{ij}^y = \begin{bmatrix} & K & \\ & & \Gamma \\ \Gamma & & \Gamma \end{bmatrix}, \quad \hat{J}_{ij}^z = \begin{bmatrix} & & \Gamma \\ \Gamma & & \\ & \Gamma & K \end{bmatrix}. \quad (\text{S2})$$

We continue to cool the spins until the maximum difference in energies of the spin configurations between successive iterations $|E^{\text{old}} - E^{\text{new}}|_{\text{max}}$ is less than 10^{-14} . Evolutions of energies and magnetizations during the cooling are shown in Fig. S1 for example. At each fixed parameter point, we examine a number of statistically uncorrelated configurations and find identical energies up to the numerical precision, which reaffirm the ergodicity of our simulations.

B. Simulated states vs. magnetic ansatzes

A common strategy for finding magnetic ground states is to assume a small periodic cluster and minimize the local Hamiltonian, while the choice of the cluster can be guided by small-size simulations or knowledge about the spin structure factor. However, this approach will fail in the case of the Kitaev- Γ model due to the emergent helicity which is quintessential for the physics of the classical ground states. Instead, its solutions are magnetic ansatzes manifesting the sublattice (longitudinal) magnetizations of the helical axes.

In Fig. S2, we show two such ansatzes states obtained at $\Gamma = -K$ by enforcing a 3×3 cluster. The two states have a six-site and a 18-site unit cell, respectively, related by the hidden symmetry $\sigma_i^{\alpha\beta} \hat{J}_{ij}^\gamma \sigma_j^{\alpha\beta} = \hat{J}_{ij}^\gamma$ and $\sigma_i^{\alpha\gamma} \hat{J}_{ij}^\gamma \sigma_j^{\gamma\beta} = \hat{J}_{ij}^\gamma$. Both can be reconstructed from three elementary unit-length spins $\tilde{\mathbf{S}}_A, \tilde{\mathbf{S}}_B, \tilde{\mathbf{S}}_C$, where the tilde symbols are used to distinguish from spins \mathbf{S}_μ in a simulation.

The energy of these ansatz states are higher than the simulated energy on a $L = 72$ lattice as compared in Fig. S1. This is because the emergent helicity brings an infinite degeneracy and allows continuous spin orientations that do not fit into small clusters or small lattices.

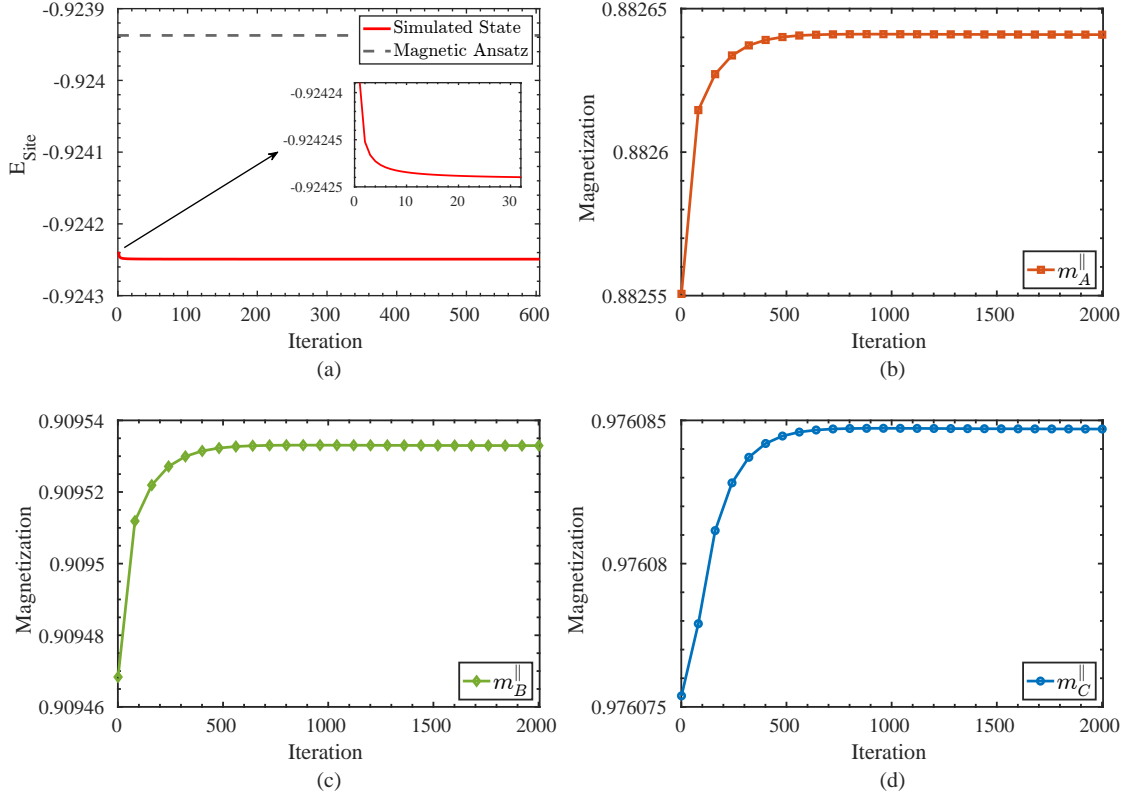


Figure S1. Cooling of a classical state simulated on a $L = 72$ lattice at $\Gamma = -K$ ($\theta = 1.75\pi$), with $|\mathbf{S}_i| = 1$. (a) Convergence of the energy. The energy per spin is $E_{\text{site}} = -0.92423895$ before the cooling and is $E_{\text{site}} = -0.92424917$ after the cooling (solid line); both are lower than the ansatz energy $E_{\text{site}} = -0.92393734$ (dashed line). The inset magnifies the evolution in a short time period. (b-d) Convergence of the sublattice (longitudinal) magnetizations, $m_{A,B,C}^{\parallel}$, of the helical axes. These magnetizations converge to values below unity owing to non-vanishing spiral magnetizations $m_{\bar{A},\bar{B},\bar{C}}$.

Nevertheless, the ansatz states still offer useful information by capturing longitudinal magnetizations of the helical axes. They not only give the correct sublattice structure, but the ansatz spins $\tilde{\mathbf{S}}_{A,B,C}$ also approximate to the simulated sublattice magnetic moments $\mathbf{m}_{\mu}^{\parallel} = \frac{1}{N_{\text{cell}}} \sum_{\text{cells}} \mathbf{S}_{\mu}$ in orientations to high precision.

For a quantitative description, we introduce a cosine de-similarity

$$D_{\mu} = \frac{1}{2} \left(1 - \tilde{\mathbf{S}}_{\mu} \cdot \frac{\mathbf{m}_{\mu}^{\parallel}}{|\mathbf{m}_{\mu}^{\parallel}|} \right) \in [0, 1], \quad (\text{S3})$$

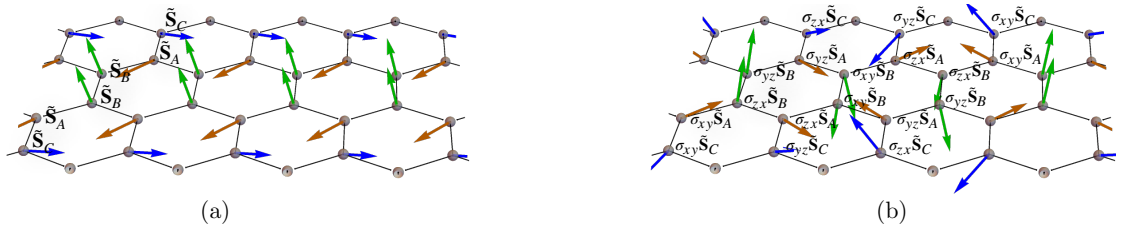


Figure S2. Two degenerate magnetic ansatzes obtained by enforcing a 3×3 periodic cluster at $K = -\Gamma$. (a) The three spin orientations $\tilde{\mathbf{S}}_A, \tilde{\mathbf{S}}_B, \tilde{\mathbf{S}}_C$ form a pattern of $C\text{-}A\text{-}B\text{-}B\text{-}A\text{-}C$ repeating over the lattice. (b) The degenerate configuration can be obtained by applying the hidden symmetry.

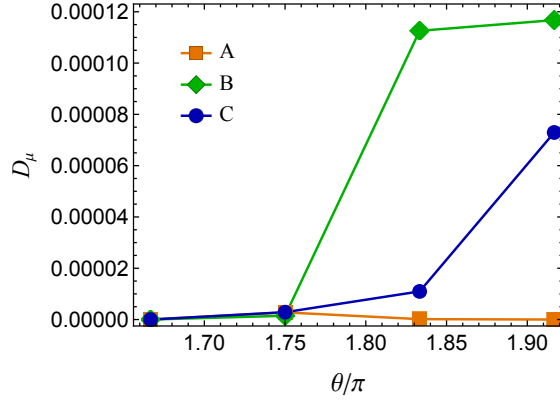


Figure S3. Cosine de-similarity $D_\mu \in [0, 1]$ between the ansatz spin orientations $\mathbf{S}_{A,B,C}$ and the sublattice magnetizations $\mathbf{m}_{A,B,C}^\parallel$ simulated on a $L = 72$ lattice. D_μ generally rises with increasing Γ , which is expected due to the stronger spiral magnitudes. Nevertheless, even at the large Γ value $\theta \approx 1.92\pi$, the de-similarities remain remarkably small, and the magnetic ansatzes can still provide a proximate description of the correct sublattice structure.

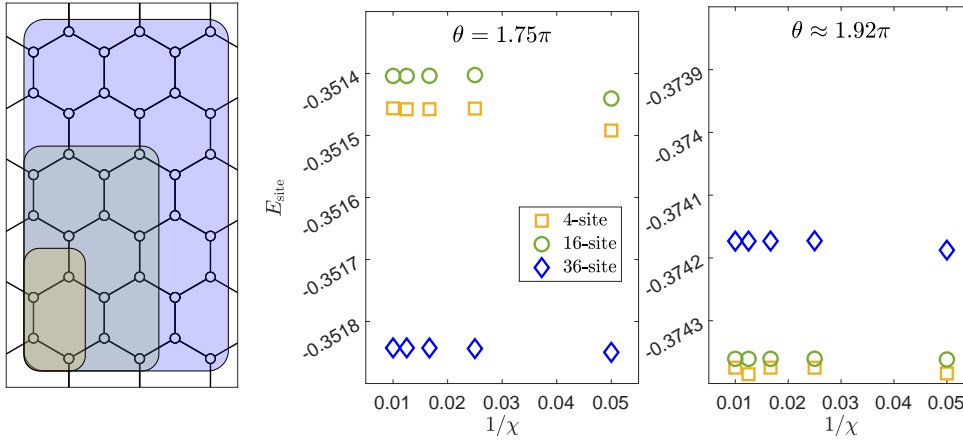


Figure S4. Geometries of the iPEPS ansatzes and energy convergence. The three clusters are indicated by shadings in the left panel. The 36-site cluster leads to the lowest energy at the moderate $\Gamma = -K$ ($\theta = 1.75\pi$), but is superseded by the 16-site and 4-site clusters at a stronger $\Gamma \approx -3.73K$ ($\theta \approx 1.92\pi$).

which measures the orientation difference between $\tilde{\mathbf{S}}_{A,B,C}$ and $\mathbf{m}_{A,B,C}^\parallel$ by ignoring their magnitudes.

As measured in Fig. S3, even in the region where the spiral magnetizations m_μ^\perp have become comparable in magnitude with the longitudinal m_μ^\parallel (see Fig. 2 in the main text), D_μ remains extremely small for all the three elementary orientations. This hence provides a visualization for the classical ground states: the sublattice magnetic moments can be approximately estimated using the magnetic ansatzes, while the actual spins are swirling about those moments and form helices.

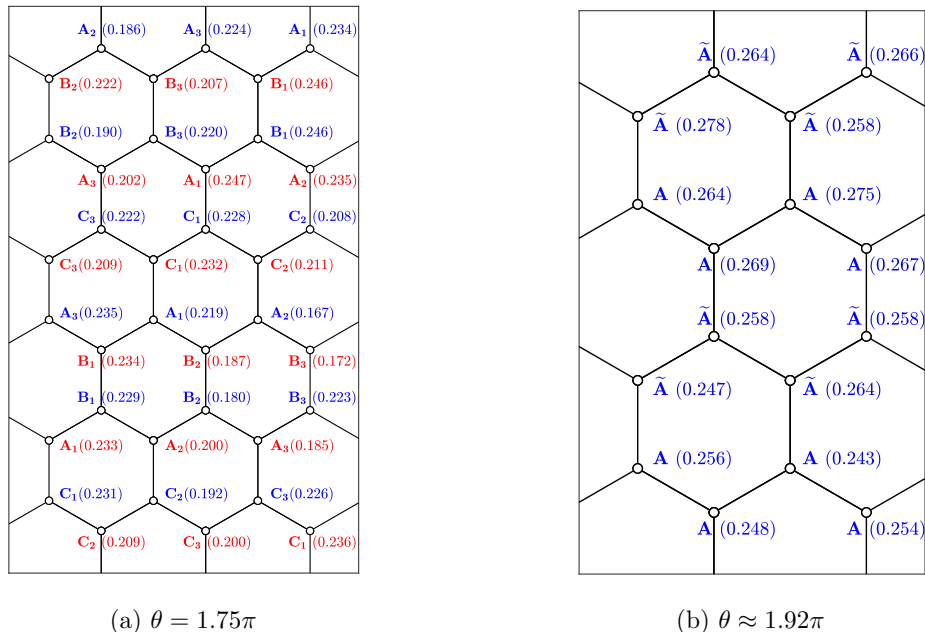


Figure S5. Magnetic structures computed by the iPEPS at $\theta = 1.75\pi, 1.92\pi$ ($\Gamma = -K, -3.73K$), with $S = \frac{1}{2}$. (a) Sites in the 36-site cluster are labeled in a similar way as the 3×3 unit cell of the classical helical axes. A_j, B_j, C_j indicate three elementary orientations of the magnetic moments. The numbers show the strength of the corresponding sublattice magnetization. (b) A zigzag order captured by the 16-site cluster. A and \tilde{A} denote two opposite magnetic moments.

S.II. PROXIMATE QUANTUM GROUND STATES

A. Details of iPEPS simulations

Our iPEPS ansatzes are formulated on a brick-wall lattice which maps onto the honeycomb lattice by introducing a trivial index on each tensor [51, 73]. Three tensor ansatzes with a 4-site, a 16-site, and a 36-site geometry are considered, as illustrated in Fig. S4 (left panel). The former two geometries are chosen to probe ferromagnetic, Néel, stripy, and zigzag-type orders, while the latter can (additionally) capture $\sqrt{3} \times \sqrt{3}$ -type orders as well as the longitudinal sublattice magnetization of the helical axes. We initialize our simulations using both random tensors and the corresponding classical ground states. Typically over 600 initializations are examined for each θ value.

We adopt a simple update scheme [55, 56] to scan the parameter space and run the simulations with a bond dimension $D = 8$. In addition, we have also compared the results with the full update scheme [51, 59] at particular parameter points. Although it has been shown that the full update method can noticeably improve simulations at the Kitaev spin liquid points [51], we nevertheless find that the improvements are limited for the present symmetry-broken states.

We use the corner transfer matrix renormalization group (CTMRG) method [57, 58] to determine the value of physical quantities. Large environmental dimensions $\chi > D^2$ are examined for ensuring the CTMRG convergence as exemplified in Fig. S4 for a moderate and a large Γ value. In the parameter regime $\Gamma, 1.6\pi < \theta < 1.9\pi$ the 36-site cluster provides the best approximation to the ground state and can be clearly distinguished from other two clusters. The 16-site and 4-site clusters lead to the lowest energies for the large Γ regime $\theta > 1.9\pi$ with nearly degenerate values. Their energy difference is comparable to the energy variation due to the finite χ approximation, while convergences of the 16-site cluster appear to be better over this regime. Nevertheless, there we expect the iPEPS to fail because of growing spirality. Hence the change from the 36-site ansatz to the 16-site or 4-site one does not necessarily reflect a phase transition.

B. Comparison of quantum and classical magnetic moments

Very large system sizes are required to represent a helix state, while the situation in the Kitaev- Γ model is especially challenging. In our classical simulations on the $L = 72$ lattice, each helix is “only” formed by 24 spins due to the 3×3 modulation of the helical axes. Faithful simulations of the spin-1/2 Kitaev- Γ model are hence far beyond the capabilities of available quantum algorithms.

Nevertheless, our detailed characterization of the classical helicity provides a possibility to gain insight in the quantum ground states in regimes where the helicity remains mild in strength. As we measured in the main text by the oscillation parameter Ω_μ (Fig. 3), the classical spiral magnetization is about $m_\mu^\perp \sim 10^{-4}$ at $\Gamma = -K/\sqrt{3}$ ($\theta \approx 1.67\pi$). Since this quantity affects the energy of a two-body Hamiltonian in quadratic form, i.e. in a magnitude $\mathcal{O}(10^{-8})$, we expect the iPEPS ansatzes to remain legitimate at such a Γ value despite that the ground state is not translationally invariant. Provided the simulations do not detect signals of a phase transition when slightly increasing Γ , one naturally expects the same physics to manifest for a finite parameter regime. Then by comparing the structures of the classical and quantum moments, we may infer whether the classical order is immediately destroyed by quantum fluctuations.

The magnetic pattern captured by our converged simulations using the 36-site cluster shows remarkable resemblances to the longitudinal magnetization of the classical helical axes. In addition to the orientations of its magnetic moments presented in the main text (Fig. 5.), we show in Fig. S5 the structure and magnitudes of its sublattice magnetizations. The 16-site and 4-site clusters capture a zigzag-type order in the large Γ region, which is also depicted in Fig. S5.

4 Parton construction of tensor network states

4.1 Overview

Using parton construction of tensor network states (TNSs) to study spin liquids involves two steps. We first approximate the parton fermionic state as TNSs, then we apply the Gutzwiller projection that projects the parton fermionic state to single occupancy to obtain the final spin wave function.

SU(N) chiral spin liquids Parton construction of MPSs is useful to characterize topological orders [WWT20]. A topological phase in a gapped system contains a set of nearly degenerate ground states with special properties. They all lie below the bulk gap, but can be neither distinguished by local order parameters, nor smoothly deformed into one another by local unitary transformations. Besides that, these states manifest different patterns of long-range entanglement, and each of them may feature a distinct entanglement spectrum that corresponds to a specific topological sector. Being able to obtain a full set of these nearly degenerate ground states is important for characterizing topological orders.

In this vein, an important notion called minimally entangled state (MES) was first introduced by Zhang Yi et al. [ZGT⁺12]. On cylinders, the MESs define a set of orthogonal states that span the identical space of these degenerate ground states, and they minimize the entanglement entropy through a cut that splits open edges on the left and the right into two disjoint parts. The minimization of this bipartite entanglement entropy also maximizes the topological entanglement entropy [LW06, Kit06]. By doing so, these MESs are in one-to-one correspondence with having different anyonic fluxes threading through the cylinder [ZGT⁺12, ZMP13, CV13, ZMPR15].

Conceptually, the search for MESs on cylinders comes natural for DMRG. In reality, however, using DMRG to find a complete set of MESs is obstructed by the finite size effect. On a finite-width cylinder, the ground state degeneracy is lifted, and a naive DMRG calculation is unlikely to capture states that are being pushed high in energy. This obstruction tinges the search of spin liquids using DMRG with doubt, since with limited access to only one topological sector the topological properties can only be indirectly inferred [JWB12, CCG⁺21]. Empirical approaches have been developed to tackle this issue. For simple cases, such as the Z_2 spin liquids and simplest chiral spin liquids ($\nu = 1/2$ Laughlin state) [KL87, KL89], a trial-and-error approach [CV13, BCK⁺14] and adiabatic flux-insertion [HSC14b, HSC14a] have shown some initial success. However, it is not easy to foresee how to generalize these approaches to more complicated scenarios.

In [P7], we use parton construction to address this difficulty for the SU(N) chiral spin liquids. By engineering suitable parton Hamiltonians, we can manipulate edge modes that control different types of anyonic flux through the cylinder at will. We then express these parton wave functions as MPSs, and the resulting N different projected parton MPSs constitute a complete set of MESs that fully characterizes the SU(N) chiral spin liquids. With the MESs, we further use DMRG to find the

suitable spin Hamiltonian that can stabilize them as ground states. The proposal of such $SU(N)$ spin Hamiltonians with only short-range interactions paves the way for experimentalists to realize chiral spin liquids in the future [CNA⁺11, GLHF14, Aid16].

U(1) Dirac spin liquids In [P8], we develop a Gaussian PEPS approach to represent parton fermionic states as iPEPS on two-dimensional infinite lattices. Specifically, we use iPEPS to approximate ground states for the π -flux model on a square lattice and the $[0, \pi]$ -flux model on a kagome lattice. The ground states for these fermionic parton models have gapless Dirac fermions at half-filling, and their corresponding projected wave functions are believed to describe the gapless U(1) spin liquids.

The progress in validating the parton-constructed gapless spin liquids for $S = 1/2$ has been slow. In the large- N limit, stable spin liquids can be obtained [RW06]. However, for $N = 2$, i.e. the spin one-half, whether such a parton approach indeed leads to gapless spin liquids after the Gutzwiller projection remains questionable. For parton models containing gapless fermions, any small perturbation due to the gauge-field fluctuations may trigger off instabilities towards some spontaneous symmetry breaking upon applying the Gutzwiller projection [Has00]. In recent, two numerical studies for $S = 1/2$ were performed using the DMRG [HZOP17] and the variational Monte Carlo [FPB21] on narrow cylinders. While the results are encouraging, the fate of parton-constructed gapless spin liquids in the thermodynamic limit remains unknown. Using iPEPS, we find tentative evidence towards gapless spin liquids for $S = 1/2$.

P7 *Abelian $SU(N)_1$ chiral spin liquids on the square lattice*

Ji-Yao Chen, **Jheng-Wei Li**, Pierre Nataf, Sylvain Capponi, Matthieu Mambri, Keisuke Totsuka, Hong-Hao Tu, Andreas Weichselbaum, Jan von Delft, Didier Poilblanc






[Phys. Rev. B 104, 235104 \(2021\)](#)

P8 *U(1)-symmetric Gaussian fermionic projected entangled-paired states and their Gutzwiller projection*

Jheng-Wei Li, Jan von Delft, and Hong-Hao Tu

[arXiv:2208.04623](#)

Abelian $SU(N)_1$ chiral spin liquids on the square lattice

Ji-Yao Chen ^{1,2}, Jheng-Wei Li ³, Pierre Nataf,⁴ Sylvain Capponi ⁵, Matthieu Mambriani ⁵, Keisuke Totsuka,⁶
 Hong-Hao Tu ⁷, Andreas Weichselbaum,⁸ Jan von Delft,³ and Didier Poilblanc⁵

¹Max-Planck-Institut für Quantenoptik, Hans-Kopfermann-Straße 1, 85748 Garching, Germany

²Munich Center for Quantum Science and Technology, Schellingstraße 4, 80799 München, Germany

³Arnold Sommerfeld Center for Theoretical Physics, Center for NanoScience, and Munich Center for Quantum Science and Technology, Ludwig-Maximilians-Universität München, 80333 Munich, Germany


⁴Laboratoire de Physique et de Modélisation des Milieux Condensés, Université Grenoble Alpes, CNRS, 38000 Grenoble, France

⁵Laboratoire de Physique Théorique, Fédération Fermi, Université de Toulouse, CNRS, UPS, 31062 Toulouse, France

⁶Yukawa Institute for Theoretical Physics, Kyoto University, Kitashirakawa Oiwake-Cho, Kyoto 606-8502, Japan

⁷Institut für Theoretische Physik, Technische Universität Dresden, 01062 Dresden, Germany

⁸Condensed Matter Physics and Materials Science Department, Brookhaven National Laboratory, Upton, New York 11973, USA

 (Received 12 June 2021; revised 11 October 2021; accepted 15 November 2021; published 3 December 2021)

In the physics of the fractional quantum Hall (FQH) effect, a zoo of Abelian topological phases can be obtained by varying the magnetic field. Aiming to reach the same phenomenology in spin like systems, we propose a family of $SU(N)$ -symmetric models in the fundamental representation, on the square lattice with short-range interactions restricted to triangular units, a natural generalization for arbitrary N of an $SU(3)$ model studied previously where time-reversal symmetry is broken explicitly. Guided by the recent discovery of $SU(2)_1$ and $SU(3)_1$ chiral spin liquids (CSL) on similar models we search for topological $SU(N)_1$ CSL in some range of the Hamiltonian parameters via a combination of complementary numerical methods such as exact diagonalizations (ED), infinite density matrix renormalization group (iDMRG) and infinite Projected Entangled Pair State (iPEPS). Extensive ED on small (periodic and open) clusters up to $N = 10$ and an innovative $SU(N)$ -symmetric version of iDMRG to compute entanglement spectra on (infinitely long) cylinders in all topological sectors provide unambiguous signatures of the $SU(N)_1$ character of the chiral liquids. An $SU(4)$ -symmetric chiral PEPS, constructed in a manner similar to its $SU(2)$ and $SU(3)$ analogs, is shown to give a good variational ansatz of the $N = 4$ ground state, with chiral edge modes originating from the PEPS holographic bulk-edge correspondence. Finally, we discuss the possible observation of such Abelian CSL in ultracold atom setups where the possibility of varying N provides a tuning parameter similar to the magnetic field in the physics of the FQH effect.

DOI: [10.1103/PhysRevB.104.235104](https://doi.org/10.1103/PhysRevB.104.235104)

I. INTRODUCTION

Quantum spin liquids are states of matter of two-dimensional electronic spin systems not showing any sign of spontaneous symmetry breaking down to zero temperature [1–3]. Spin liquids with long-range entanglement may also exhibit topological order [4] such as the spin-1/2 resonating valence bond (RVB) state on the kagome lattice [5]. Among the broad family of spin liquids, chiral spin liquids (CSL) [6–10] form a very special and interesting class [11] exhibiting broken time-reversal symmetry and chiral topological order [4]. Intimately related to FQH states [12], CSL are incompressible quantum fluids (i.e., with a bulk gap) and host both (Abelian or non-Abelian) anyonic quasiparticles in the bulk [13] and chiral gapless modes on the edge [14]. After the original papers, the Kalmeyer-Laughlin CSL lay dormant for many years until an explicit parent Hamiltonian was constructed [15,16] using Laughlin's idea [8]. Later somewhat simpler Hamiltonians were found using different methods [17,18]. An important step towards the goal of finding a chiral spin liquid in realistic systems was taken by examining a

physically motivated model for a Mott insulator (Hubbard model) with broken time-reversal symmetry [19,20]. Then, an Abelian CSL was identified in the (chiral) spin-1/2 Heisenberg model on the triangular lattice [21,22]. Note that CSL hosting non-Abelian excitations (useful for topological quantum computing [23]) have also been introduced in different contexts [24–26].

It was early suggested that, in systems with enhanced $SU(N)$ symmetry, realizable with ultracold alkaline earth atoms loaded in optical lattices [27], CSL can naturally appear [28], although this original proposal on the square lattice remained controversial. Later on, an Abelian CSL was indeed identified on the triangular lattice in $SU(N)$ Heisenberg models with $N > 2$ [29]. The presence of a chiral spin interaction, achievable experimentally via a synthetic gauge field, seems to be a key feature to stabilize $SU(N)$ CSL [30]. Nevertheless, the T and P violation required for a CSL could emerge spontaneously in T-invariant models, as found for $N = 2$ in a spin-1/2 Kagome Heisenberg model [31–33] or, for $N = 3$, in the Mott phase of a Hubbard model on the triangular lattice [34]. Note also that, using optical pumping, it is now

possible to realize (so far in one dimension) strongly correlated liquids of ultracold fermions with a tunable number N of spin components and $SU(N)$ symmetry [35]. This offers the prospect to be able to experimentally tune the system through various topological liquids, as it is realized in the physics of the FQH effect via a tunable external magnetic field. Apart from ultracold atom setups, condensed matter systems may also host $SU(N)$ CSL. For example, it has been proposed very recently that an $SU(4)$ CSL could be realized in double-layer moiré superlattices [36].

In recent years, projected entangled pair states (PEPS) [37] have progressively emerged as a powerful tool to study quantum spin liquids providing variational ground states competitive with other methods [38–40]. PEPS also offer a powerful framework to encode topological order [41–43] and construct chiral Abelian [44] and non-Abelian [45] $SU(2)$ spin liquids. Generically, $SU(2)$ CSL described by PEPS exhibit linearly dispersing chiral branches in the entanglement spectrum (ES) well described by Wess-Zumino-Witten (WZW) $SU(2)_k$ (with the level of the WZW model $k = 1$ for Abelian CSL) conformal field theory (CFT) for one-dimensional edges [46].

Recently, on a square lattice with three-dimensional spin degrees of freedom which transform as the fundamental representation of $SU(3)$ on every site, an Abelian CSL was found as the ground state (GS) of a simple Hamiltonian involving only nearest-neighbor and next-nearest-neighbor (color) permutations and (imaginary) three-site cyclic permutations [47]. Exact diagonalizations (ED) of open finite-size clusters and infinite-PEPS (iPEPS) in the thermodynamic limit (and encoding the full $SU(3)$ symmetry) unambiguously showed the existence of chiral edge modes following the $SU(3)_1$ WZW CFT. Interestingly, these results can be viewed as extending previous results obtained for an $SU(2)$ spin-1/2 (i.e., $N = 2$) chiral Heisenberg model [20,48]. Exactly the same type of Hamiltonian can be defined for N -dimensional spin degrees of freedom transforming according to the fundamental representation of $SU(N)$, for arbitrary integer $N \geq 2$. It is then natural to speculate that, if such $SU(N)$ models also host CSLs for $N > 3$, then the later should also be of the $SU(N)_1$ type. Note however that, although a chiral perturbation necessary induces, from linear response theory, a finite response of the quantum spin system, it, by no means, implies the existence of topological order or the absence of conventional (lattice or magnetic) symmetry breaking, which both characterize a CSL. The emergence of a uniform CSL with protected edge modes is therefore a subtle feature that needs to be investigated on a case by case basis. It is far from clear that the findings for $SU(3)$ generalize to $SU(N > 3)$ bearing in mind that N may be commensurate or incommensurate with the fixed number of nearest neighbors on the square lattice. Then, in this work, we have (i) generalized the chiral Hamiltonians of Refs. [20,47,48] to arbitrary N , (ii) defined a subset of these $SU(N)$ models whose Hamiltonians can be written solely as a sum of S_3 -symmetric operators acting on all triangles within square plaquettes (as in Ref. [47]), and (iii) studied these models up to $N = 10$ using a combination of complementary numerical techniques such as ED, density matrix renormalization group (DMRG) and iPEPS, supplemented by CFT analytical predictions.

We then start by generalizing the $SU(2)$ and $SU(3)$ chiral Hamiltonians by placing, on every site of a square lattice, an N -dimensional spin degree of freedom, which transforms as the fundamental representation of $SU(N)$. As for $N = 3$, we consider the most general $SU(N)$ -symmetric short-range three-site interaction:

$$H = J_1 \sum_{\langle i,j \rangle} P_{ij} + J_2 \sum_{\langle\langle k,l \rangle\rangle} P_{kl} + J_R \sum_{\Delta ijk} (P_{ijk} + P_{ijk}^{-1}) + iJ_I \sum_{\Delta ijk} (P_{ijk} - P_{ijk}^{-1}), \quad (1)$$

where the first (second) term corresponds to two-site permutations over all (next-)nearest-neighbor bonds, and the third and fourth terms are three-site (clockwise) permutations on all triangles of every plaquette. P_{ij} (P_{ijk}) is defined through its action on the local basis states, $P_{ij}|\alpha\rangle_i|\beta\rangle_j = |\beta\rangle_i|\alpha\rangle_j$ ($P_{ijk}|\alpha\rangle_i|\beta\rangle_j|\gamma\rangle_k = |\gamma\rangle_i|\alpha\rangle_j|\beta\rangle_k$, for a fixed orientation of the triangle i, j, k , let's say anticlockwise). To restrict the number of parameters, we have chosen $J_2 = J_1/2$. In that case, the two-body part (J_1 and J_2) on the interacting triangular units becomes S_3 symmetric, hence mimicking the corresponding Hamiltonian on the triangular lattice.¹ We then use the same parametrization as in Ref. [47]:

$$J_1 = 2J_2 = \frac{4}{3} \cos \theta \sin \phi, \quad J_R = \cos \theta \cos \phi, \\ J_I = \sin \theta, \quad (2)$$

and restrict ourselves to *antiferromagnetic* couplings $J_1, J_2 > 0$, i.e., $0 \leq \theta \leq \pi/2$ and $0 \leq \phi \leq \pi$. Note however that, for $\phi > \pi/2$, the amplitude of the (real) three-site permutation J_R becomes ferromagnetic ($J_R < 0$). A detailed analysis of the multiplet structure of a 2×2 plaquette of the Hamiltonian above is given in Appendix A.

For $N = 2$, various forms of the Hamiltonian (1) can be found in the literature [20,48]. In the original formulation [20], a chiral interaction $4J_3 \mathbf{S}_i \cdot (\mathbf{S}_j \times \mathbf{S}_k)$ on all triangular units $\Delta(ijk)$ is introduced, corresponding to the three-site cyclic permutations of (1) with amplitudes $J_R = 0$ and $J_I = J_3$. Also, the two-site exchange interactions are introduced here as spin-1/2 Heisenberg couplings, which is equivalent from the identity $2\mathbf{S}_i \cdot \mathbf{S}_j = P_{ij} - \frac{1}{2}$.² A Hamiltonian including a (pure-imaginary) cyclic permutation $i\lambda_c(P_{ijkl} - P_{ijkl}^{-1})$ on each plaquette $\square(ijkl)$ was also introduced [48]. In fact, the plaquette cyclic permutation $i(P_{ijkl} - \text{H.c.})$ can be rewritten as $\frac{i}{2}(P_{ijk} + P_{jkl} + P_{kli} + P_{lij} - \text{H.c.})$,³ so that this model corresponds also to $J_R = 0$ and we can identify $J_I = J_3 = \lambda_c/2$. An optimum choice of parameters for the stability of the $SU(2)$ CSL phase is found to be (in our notations) $J_2/J_1 \simeq 0.47$ and $J_I/J_1 \simeq 0.21$ [20]. Furthermore, evidence is provided that the

¹The chiral spin liquid phase should also exist away from $J_2 = J_1/2$, due to its gapped nature.

²This can be extended to all fundamental IRREPs of $SU(N)$: $P_{ij} = \mathbf{J}_i \cdot \mathbf{J}_j + \frac{1}{N}$, where J^α are the generators defined in Eq. (C1) of Appendix C. Note, the usual $SU(2)$ spin operators are given by $\mathbf{S} = (1/\sqrt{2})\mathbf{J}$.

³This decomposition holds only for $N = 2$ (in the fundamental representation).

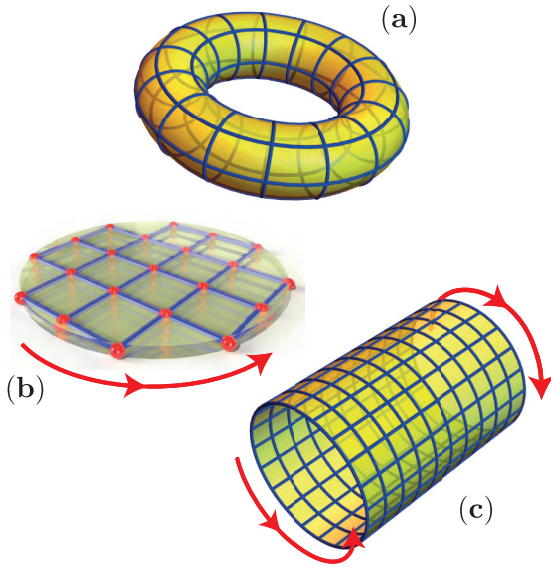


FIG. 1. We considered various system topologies: (a) periodic cluster topologically equivalent to a torus; (b) open cluster topologically equivalent to a disk; (c) cylinder with left and right boundaries. We used (a) and (b) in ED and the infinite-length version of (c) in DMRG and iPEPS. The chiral modes of the CSL are schematically shown on the system edges.

CSL survives in a rather extended zone of parameter space around this point. Also, an $SU(2)$ -symmetric PEPS ansatz [44] provides an accurate representation of the GS at the optimum values of the parameters [48], and of its edge modes [49] following an $SU(2)_1$ WZW CFT.

For $N = 3$, from ED, DMRG and iPEPS simulations, clear evidence of a gapped CSL is found for $J_2 = J_1/2$ and angles like $\theta = \phi = \pi/4$ corresponding to $J_R/J_1 = 0.75$ and $J_1/J_1 \simeq 1.06$ [47], and around these values in a rather extended parameter range (see Supplemental Material of Ref. [47]). In addition, edge modes are found to closely follow the predictions of the $SU(3)_1$ CFT.

In the following, we will investigate model (1) using complementary ED and DMRG techniques, providing overwhelming evidence of a stable topological CSL phase. Various systems of different topology, as shown in Fig. 1, will be used. A torus geometry enables to probe bulk properties while a disk or a cylinder geometry, with one or two edges respectively, provides information on the existence and on the nature of edge modes. More precisely, the topological nature of a CSL phase can be established from (i) the topological GS degeneracy [4] on periodic clusters, (ii) the existence of chiral edge modes [14] both in open systems like Fig. 1(b) and in the entanglement spectra of (quasi)infinite cylinders, and (iii) the content of the edge modes following closely the prediction of some chiral CFT theory. The Abelian CSL expected here should be revealed by exactly N quasidegenerate GS on a closed manifold and by the exact $SU(N)_1$ WZW CFT content of its edge modes. The second goal of the paper, beside establishing the existence of the $SU(N)_1$ CSL phase itself, is to provide its faithful representation in terms of an $SU(N)$ -symmetric PEPS. Following the prescription for $N = 2$ and

TABLE I. List of periodic clusters used here in ED: number of sites N_s , cluster size vectors \mathbf{t}_1 and \mathbf{t}_2 , and point-group symmetry. Eigenstates can be labeled according to discrete momenta in the BZ. At high-symmetry points Γ , X , or M of the BZ, eigenstates can be further labeled by the C_4 -symmetry (C_2 -symmetry) IRREP labels, A , B , E_a , and E_b (A and B)—see Fig. 4.

N_s	\mathbf{t}_1	\mathbf{t}_2	point group
8	(2,2)	(2, -2)	C_{4v}
11	(1,3)	(3, -2)	C_2
12	(1,3)	(4,0)	C_2
13	(2, -3)	(3,2)	C_4
14	(1,4)	(3, -2)	C_2
15	(1,4)	(4,1)	C_{2v}
16	(4,0)	(0,4)	C_{4v}
18	(3,3)	(3, -3)	C_{4v}
19	(1,4)	(4, -3)	C_2
20	(4,2)	(-2, 4)	C_4
21	(1,4)	(5, -1)	C_2

$N = 3$, we shall focus on the $N = 4$ case. Common features observed for PEPS with these three values of N allow us to draw heuristic rules and conclusions for general N .

II. EXACT DIAGONALIZATIONS

A. Exact diagonalizations in the $U(1)$ basis and in the standard Young tableaux (SYT) basis

We start this section by a brief review of the two distinct and complementary exact diagonalization methods used in this work.

First, for periodic clusters (see Table I), we can implement the spatial symmetries (and in particular the translations) which allows us to both reduce the size of the matrix to diagonalize by a factor typically equal to N_s (where N_s is the size of the cluster) and to directly obtain the momenta associated to each eigenenergy.

However, as N increases, EDs performed this way are severely limited by the size of the available clusters since the dimension of the Hilbert space increases exponentially with N_s . A way to overcome such limitations is to implement the $SU(N)$ symmetry and this is the second ED protocol that we have employed here. In particular, when N_s is a multiple of N , the ground state of Hamiltonian (1) is an $SU(N)$ singlet state for a wide range of parameters. The singlet sector has a dimension much smaller than the one of the full Hilbert space. The gain to implement the full $SU(N)$ symmetry and to look for the lowest energy states directly in the singlet sector is huge and increases with N . For instance, for $N = 10$ and $N_s = 20$, the singlet sector has only dimension 16796, while the dimension of the full Hilbert space is 10^{20} . In addition, to write the matrix representing the Hamiltonian in the singlet subspace and in the sectors labeled by higher dimensional $SU(N)$ irreducible representation (IRREP), we have employed the algorithms detailed in Refs. [50,51], which is mainly based on the use of Standard Young Tableaux and on the theory of the representation of the permutation group.

In particular, it allows one to bypass the need for the Clebsch-Gordan coefficients, which can only be calculated with an algorithm whose complexity also increases with N (see Ref. [52]). Typically, for the present problem, through this method, we can address clusters with $N_s \sim 20$ sites for N up to 10. Note that contrary to the first ED method based on the implementation of spatial symmetries, the momenta can only be accessed in a second stage: we first calculate the eigenvectors and then the effect of translation or rotation on them.

B. Periodic clusters: bulk gap and GS manifold

The results for $N = 2$ and $N = 3$ described above suggest that the existence of an Abelian CSL may be generic for arbitrary integer N . To investigate such an appealing scenario, we start by examining, for larger N , the low-energy spectra obtained on N_s -site periodic clusters (see Table I for details about clusters used). For antiferromagnetic and frustrating couplings $J_1 > 0$, $J_2 > 0$, we expect the lowest-energy to belong to the antisymmetric IRREP $\text{aIR}_N(r_0)$ defined by a Young tableau of r_0 vertical boxes, $r_0 = \text{mod}(N_s, N)$. In particular, in the case where N_s is an integer multiple of N ($r_0 = 0$), the low-energy states are expected to belong to the singlet subspace. However, at, e.g., $\theta = \pi/4$, when increasing ϕ beyond $\phi = \pi/2$, J_R changes sign and states belonging to the antisymmetric IRREP are gradually destabilized with respect to the completely symmetric (ferromagnetic) state of energy $E_{\text{ferro}}/N_s = 3J_1 + 8J_R$. In particular, we clearly see at $\theta = \pi/4$ a *macroscopic* energy gain (penalty) of the lowest-energy eigenstate of $\text{aIR}_N(r_0)$ with respect to the ferromagnetic state at $\phi = \pi/2$ ($\phi = \pi$) (see Appendix D). This fact indicates a transition at $\phi = \phi_F$ (somewhere in the range $\pi/2 < \phi_F < \pi$) between one (or several) spin liquid phase(s) and a ferromagnetic phase. Note also that a detailed analysis of the 2×2 plaquette Hamiltonian in Appendix A, shows that the antiferromagnetic states dominate the low energy regime, yet with the ferromagnetic regime in close proximity.

We now focus on the prospective spin liquid region discussed above and consider the case of $N_s = kN$, $k \in \mathbb{N}$, so that no quasiparticle excitations would be populating the GS of a CSL phase. To identify the exact nature(s) of the spin liquid(s), one needs to examine in details the low-energy singlet subspace (gap structure, degeneracies, etc.). A selection of the singlet energy spectra for fixed $\theta = \pi/4$, plotted versus ϕ (for fixed $\phi = \pi/2$, plotted versus θ), is shown in Fig. 2 for N ranging from 2 to 10 (for $N = 4, 7, 8, 9$). For all the values of N studied here, in a broad interval of ϕ ($\phi < \phi_F$) or θ values, a clear gap is observed between a group of degenerate and quasidegenerate states and the rest of the singlet spectrum. Interestingly, for $\theta = \pi/4$ and $N > 3$, we observe level crossings occurring in the singlet subspace at some value of $\phi_{\text{lc}} < \pi/2$, suggesting the existence of two different gapped phases. For $0 \leq \phi < \phi_{\text{lc}}$, we observe a twofold quasidegenerate GS manifold within the singlet subspace which are translationally invariant but which break the lattice point group $\pi/2$ -rotation symmetry.⁴ This could correspond to a nematic valence clus-

ter state as also seen in SU(2) spin-1 models [53,54]. Note that, as a finite-size effect, the ground state of the total spectrum for small ϕ and θ around $\pi/4$ is not necessarily a singlet state when $N_s < N^2$ (see Appendix D). A more careful investigation of this phase, although interesting, is beyond the scope of this work and left for a future study.

We now move to a closer inspection of the gapped spin liquid phase seen for $N = 2, 3$ and $\phi < \phi_F$, and for $N > 3$ and $\phi_{\text{lc}} < \phi < \phi_F$, and identify it as a CSL. Interestingly, we note that $\phi = \pi/2$ —corresponding to a pure imaginary three-site cyclic permutation—is always located within this gapped phase (note, for $N = 3$, $\phi = \pi/4$ instead was chosen in Ref. [47]). This gapped phase is also stable within a significant range of the parameter θ , around $\theta = \pi/4$ and $\phi = \pi/2$, e.g. also at $\theta = \pi/6$. Hence, in the following, we shall mostly report results obtained at fixed $\phi = \pi/2$ (i.e., for a pure imaginary three-site permutation) and for $\theta = \pi/4$ or, occasionally, $\theta = \pi/6$.

To identify the type of (singlet) gapped phase, we now investigate the exact degeneracy and the quantum numbers of the singlet GS manifold. Figure 3 shows a zoom of the low-energy spectra at $\theta = \pi/4$ and $\phi = \pi/2$, with the exact degeneracy of each level below the gap. A simple counting shows that there are exactly N states below the gap. Note that the first excitation defining the gap does not belong to the singlet sector but most often belongs to the adjoint IRREP of dimension $N^2 - 1$, except for some of the largest values of N (like $N = 9$) for which finite size effects are the strongest. This is an extension of the SU(2) case where the first excitation in antiferromagnetic spin liquids are typically spin-1 “magnons.” In the thermodynamic limit, the gap in the singlet sector should be bounded from above by twice the true “magnetic” gap as two isolated “magnons” can fuse into a singlet. If a singlet bound state occurs between two magnons, the singlet gap is then strictly smaller than twice the magnon gap.

The above observation of the N -fold degeneracy of the GS space suggests that the gapped phases indeed correspond to Abelian SU(N)₁ chiral spin liquids. As realized already for $N = 3$ in Ref. [47], it is possible to obtain, for arbitrary N , the exact momenta of the various states in the GS manifold expected for an Abelian SU(N)₁ CSL. This can be inferred from a simple generalized exclusion principle (GEP) [55,56] with clustering rules (see Appendix B for details). As a final check for periodic systems, we then focus on two distinct commensurability relations between the cluster size N_s and N ; either (i) $N_s = kN$, $k \in \mathbb{N}$, for which, as above, the GS contains no quasiparticle or (ii) $N_s = kN - 1$, $k \in \mathbb{N}$, for which, a single quasihole populates the GS. Note that in case (ii), $r_0 = N - 1$ so that the IRREP of the GS manifold is the \bar{N} antifundamental IRREP. The GEP implies a GS (quasi)degeneracy of N and N_s for (i) and (ii), respectively. This is indeed observed as shown in Fig. 4. The predictions of the GEP are even more precise, providing all GS momenta expected for the (Abelian) CSL on every periodic cluster (see Appendix B for details on the way momenta are assigned). We have checked that—in most cases—all GS momenta reported in Fig. 4 match the ones predicted by the heuristic rules. In particular, for $N_s = kN - 1$, the GS manifold is made of exactly one \bar{N} (antifundamental) IRREP at each cluster momentum. Rare failures of the GEP rules (which may be attributed to cluster shapes,

⁴Both states are translationally invariant and have different ± 1 characters under $\pi/2$ -rotation, for C_4 -symmetric clusters.

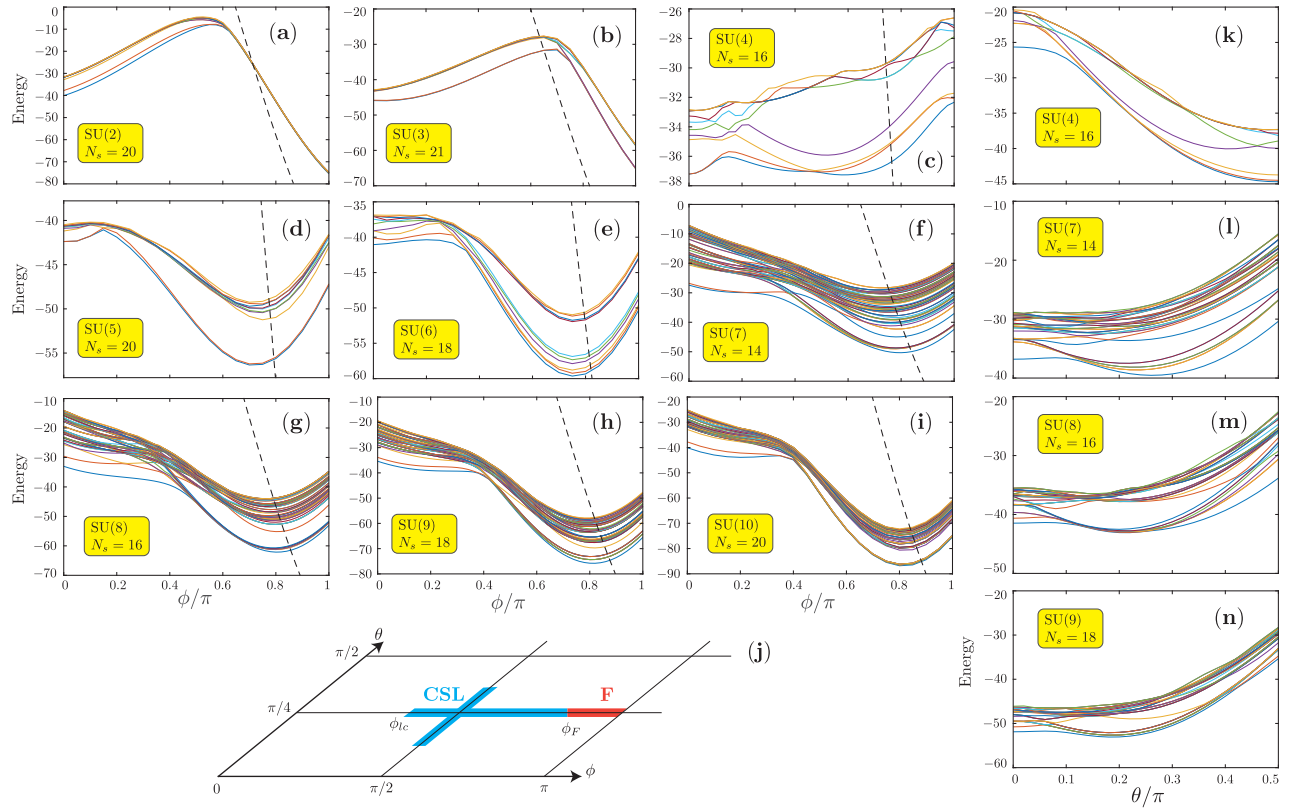


FIG. 2. Low-energy spectra computed by ED in the SYT singlet basis on periodic clusters of $N_s = kN$ sites, $k \in \mathbb{N}$, and [(a)–(i)] for a fixed value of $\theta = \pi/4$ as a function of ϕ , for N ranging from 2 to 10, or [(k)–(n)] for a fixed value of $\phi = \pi/2$ as a function of $\theta \in [0, \pi/2]$, for $N = 4, 7, 8, 9$. Only 10 (40) lowest singlet levels are shown at small N in (a)–(e) and (k) [larger N in (f)–(i) and (l)–(n)]. The ϕ and θ axes being discretized, lines connecting the data points are used as guides to the eye (hence, levels crossings around ϕ_c may look like anticrossings). N degenerate or quasidegenerate singlets (see Figs. 3 and 4 and text) are separated from the higher energy states by a gap, in an extended (ϕ, θ) region around $(\pi/2, \pi/4)$. The energy of the (fully polarized) ferromagnetic state ($E_{\text{ferro}} = 2\sqrt{2}N_s(2\cos\phi + \sin\phi)$), crossing the singlet GS at $\phi = \phi_F$, is shown as a dashed line in (a)–(i). The location of the CSL and ferromagnetic phases along the cuts (c)–(i) and (k)–(n) are schematized in (j). Note that for $N = 2$ and 3 [(a) and (b)] the CSL is expected to extend all the way to $\phi = 0$.

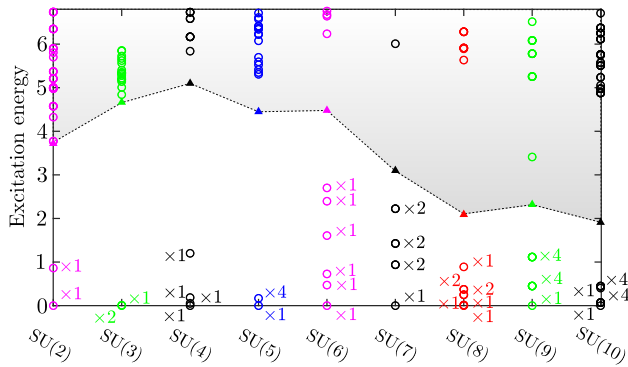


FIG. 3. Zoom of the singlet low-energy spectra at $\theta = \pi/4$ and $\phi = \pi/2$, for N ranging from 2 to 10, and the same cluster sizes as in Fig. 2. The GS energy is subtracted off for better comparison between the various spectra. The exact degeneracy g of each level is indicated on the plot as $\times g$. The first nonsinglet excitation belonging to the adjoint IRREP above the N quasidegenerate low-energy singlets is shown as a filled triangle (see text).

etc.) to predict the correct momenta will be discussed in Appendix B.

Interestingly, the above features predicted and observed in the case of a single quasihole can be understood using a simple physical argument. If the single quasihole would be static, it could be placed on each of the N_s sites of the cluster, and this, for each of the N topological (singlet) sectors, hence spanning a $N_s N$ -dimensional Hilbert space. The effective hopping allows the quasihole states to form a weakly dispersing band below the gap, hence with N states at every momentum. From the $SU(N)$ -symmetry, these N states should form a single multiplet belonging to the \bar{N} (antifundamental) IRREP, as predicted by the GEP and found numerically.

C. Open systems: edge physics and CFT content

The previous results give strong evidence of the CSL nature of the GS of the model, for the parameters chosen, from its bulk properties on periodic systems (topologically equivalent to tori). We complete the identification of the CSL phase by the investigation by ED of open clusters. The existence of a chiral edge mode fulfilling the $SU(N)_1$ WZW CFT should be

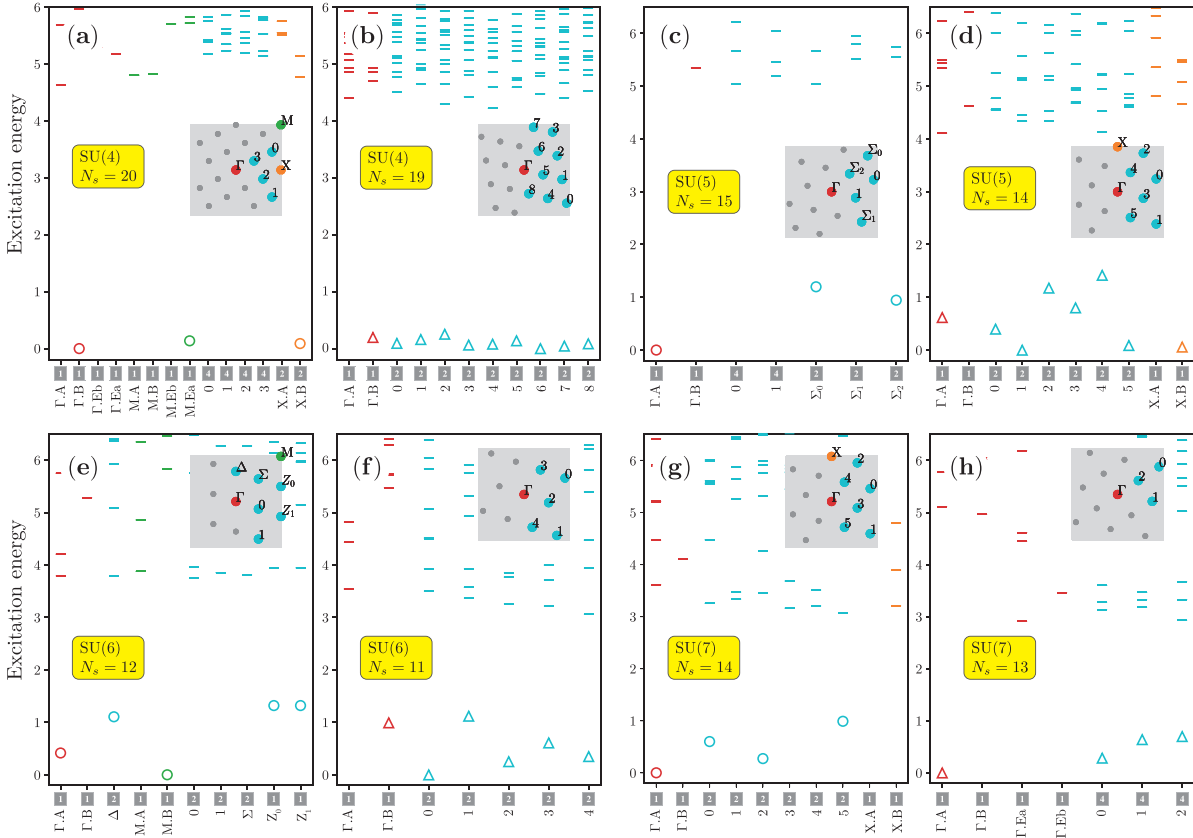


FIG. 4. Low-energy spectra on periodic clusters at fixed $\phi = \pi/2$ and for $\theta = \pi/4$ [(a)–(d)] or $\theta = \pi/6$ (e)–(h)]. Clusters with site numbers $N_s = kN$ (left) or $N_s = kN - 1$ (right), $k \in \mathbb{N}$, are chosen to obtain 0 and 1 quasihole, respectively, in the putative CSL. The respective BZ with the allowed discrete momenta is shown on each plot as a gray square—only nonequivalent momenta are labeled—and the number of equivalent momenta appearing are listed as grayed squared numbers. For $N_s = kN$ (left), the GS manifold is composed of N singlets (open circles). For $N_s = kN - 1$ (right), it is composed of N_s quasidegenerate levels, one level at each cluster momentum. Each level is comprised of N degenerate states forming a \bar{N} antifundamental IRREP (open triangles).

reflected in the precise content of its low-energy spectrum. By choosing finite-size clusters with (i) open boundaries and (ii) C_4 point-group symmetry, we can investigate the low-energy spectrum as a function of the angular momentum, $l = 0, \pm 1, 2 \pmod{4}$ and reveal a single chiral branch linearly dispersing only in one direction, as expected. At a given N , changing the cluster size N_s —whenever such a C_4 -symmetric cluster is available—enables to change the topological sector defined by the integer $r_0 = \text{mod}(N_s, N)$, $r_0 = 0, \dots, N - 1$. Indeed, each topological sector is characterized by the $SU(N)$ IRREP $\text{aIR}_N(r_0)$ (defined by a Young tableau of r_0 vertical boxes), and can then be reached whenever $N_s = kN + r_0$. Note that the dimension of $\text{aIR}_N(r_0)$ is given by $\frac{N!}{(N-r_0)!r_0!}$.

The ED investigation of the chiral edge modes has been carried out on two types of open systems, all exhibiting C_4 symmetry with respect to the cluster center. The first type of clusters is build around a central site by adding successive shells of four sites at 90° angles. The second type of open clusters are built in the same way but from a center 2×2 plaquette. The 13-site, 17-site, and 21-site (16-site) clusters

belongs to the first (second) category, as shown on the right-hand side of Fig. 5. Note that the 17-site cluster is “chiral,” i.e., it breaks reflection symmetry (parity), and spectra for $J_I > 0$ and $J_I < 0$ are expected to be (slightly) different. Here, $J_I > 0$ and the P_{ijk} permutation is assumed counterclockwise. ED spectra obtained on such clusters for $N = 4, 5, 6, 7, 8$ are shown in Fig. 5, for $\phi = \pi/2$ and $\theta = \pi/4$ or $\pi/6$ (as specified in the caption). In all cases, we observed a rather sharply defined low-energy chiral edge mode, i.e., a group of levels (i) well-separated from higher-energy levels by a gap, (ii) following a linear dispersion with respect to the angular momentum, and (iii) with a very precise and nontrivial content in terms of $SU(N)$ multiplets. Each edge mode is characterized by its GS given by the antisymmetric IRREP $\text{aIR}_N(r_0)$. For each pair (N, r_0) occurring in Fig. 5, we have computed the expected “tower of states” (ToS) generated by $\text{aIR}_N(r_0)$, as predicted by the $SU(N)_1$ WZW CFT—see Appendix C. Numerically, one can use $(N - 1)$ $U(1)$ quantum numbers to diagonalize the Hamiltonian and identify the IRREP content for each group of *exactly* degenerate levels. A careful check shows that, generically, the quantum numbers of the chiral

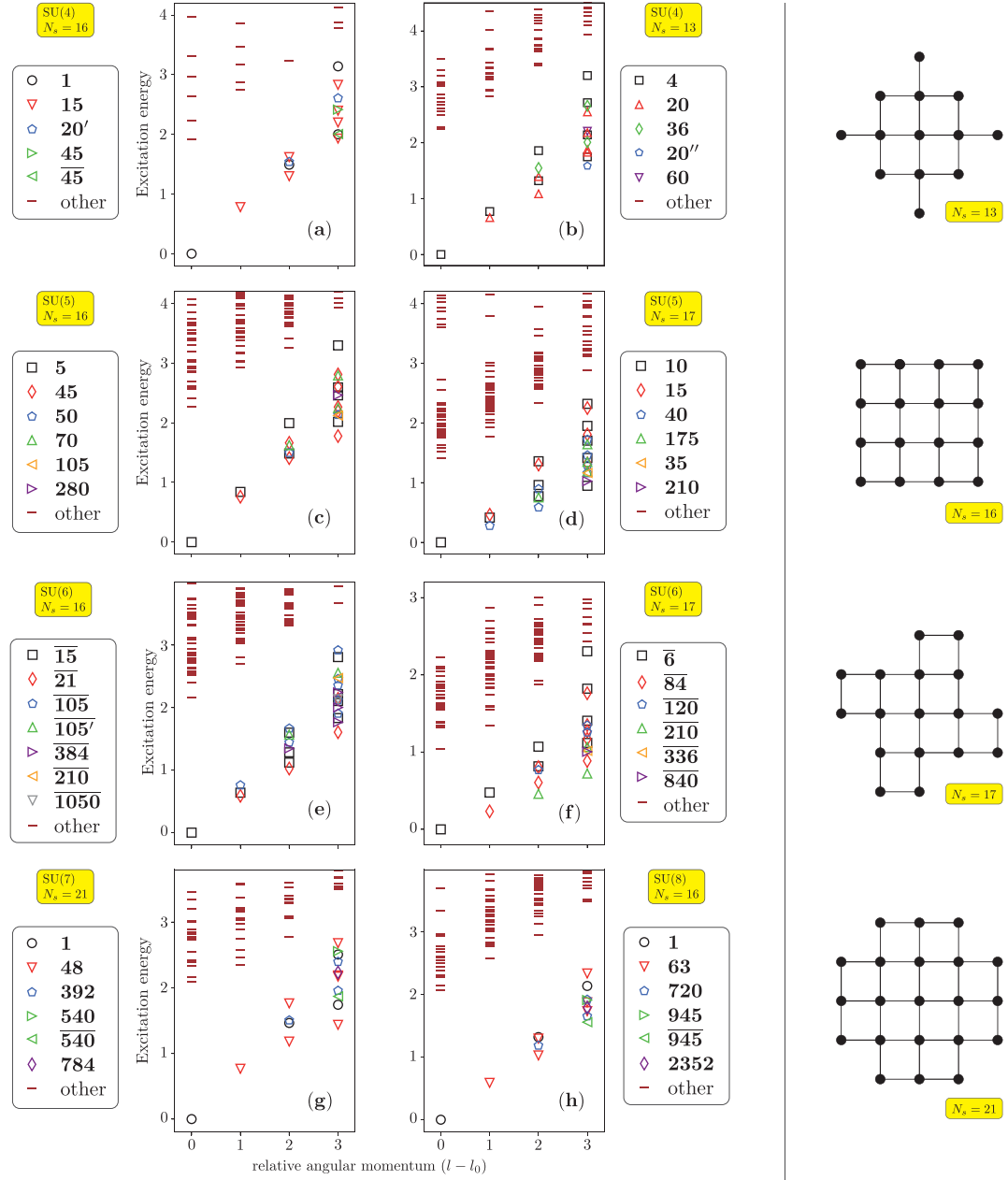


FIG. 5. Low-energy spectra on open C_4 -symmetric clusters depicted on the right-hand side of the figure, as a function of the angular momentum l (with respect to the GS angular momentum l_0), at fixed $\phi = \pi/2$ and for $\theta = \pi/4$ (a)–(d) or $\theta = \pi/6$ [(e)–(h)]. Symbols labeling the various $SU(N)$ IRREPs entering the chiral mode are shown in the legends. The Young diagrams for the corresponding IRREPs can be identified using the tables in Appendix C. The GS IRREPs are fully antisymmetric, and labeled by Young diagrams consisting of a single column of $r_0 = \text{mod}(N_s, N)$ boxes, with degeneracy $\frac{N!}{(N-r_0)!r_0!}$. Identifying $l - l_0$ with the Virasoro level L_0 , all low-energy ToS in (a)–(h) for $0 \leq l - l_0 \leq 3$ follow exactly the WZW CFT predictions of Tables VIII, IX, XII, XIII, XVI, XV, XVII, and XXI, respectively. The only exception is the $SU(6)$ $\overline{15}$ ($SU(8)$ $\overline{1}$) tower, for which two multiplets $\overline{15}$ and $\overline{21}$ ($\overline{1}$ and $\overline{63}$) are missing in the $L_0 = 3$ Virasoro level.

edge mode spectra match exactly the WZW CFT ToS predictions (identifying the angular momentum with the Virasoro level L_0), providing a real hallmark of the CSL phase. For two cases corresponding to the smallest $N_s = 16$ cluster, a small number of multiplets in the CFT predictions are missing in Fig. 5. We have explicitly checked that finite-size effects can indeed lead to incomplete towers.

III. DMRG

For characterizing chiral topological states, the correspondence between the entanglement spectrum and the conformal tower of states is a fingerprint evidence. While DMRG is in principle suited for this purpose, a technical difficulty is that the characterization of topological order requires the full set of

(quasi)degenerate ground states and, furthermore, these states should be combined into the so-called minimally entangled state (MES) basis [57]. In this section, we use a two-step procedure to accomplish this task: (i) build Gutzwiller projected parton wave functions which describe the $SU(N)_1$ CSL, use them to construct the MES basis on the cylinder, and convert them into MPS; ii) initialize DMRG with the parton-constructed MES basis. This strategy allows us to find the full set of N (quasi)degenerate ground states in the MES basis. The parton picture also helps us to identify the correspondence between the entanglement spectrum and the $SU(N)_1$ conformal towers.

A. Parton wave functions

In this section, we outline the parton approach to construct trial wave functions for the $SU(N)$ CSL model. To construct the minimally entangled states (MESS) [57], we use a fermionic parton representation of the $SU(N)$ generators [58–60], $S_i^\mu = \sum_{\sigma\sigma'} c_{i\sigma}^\dagger T_{\sigma\sigma'}^\mu c_{i\sigma'}$, where $T_{\sigma\sigma'}^\mu$ are matrix representations of the $SU(N)$ generators in the fundamental representation, and $c_{i\sigma}^\dagger$ is the creation operator at site i . A local constraint $\sum_{\sigma} c_{i\sigma}^\dagger c_{i\sigma} = 1$ has to be imposed to ensure that singly occupied fermions represent the N states in the $SU(N)$ fundamental representation, i.e., $|\sigma\rangle = c_{i\sigma}^\dagger |0\rangle$ (site index suppressed), with $|0\rangle$ being the vacuum of partons. The $SU(N)$ CSL with $SU(N)_1$ topological order can be constructed by Gutzwiller projecting a fully occupied $C = 1$ Chern band of fermionic partons, where C is the Chern number. To have a systematic construction for all N , we design the following quadratic Hamiltonian for partons on a square lattice:

$$\begin{aligned}
 H_p = & - \sum_{m,n,\sigma} (t_x c_{m+1,n,\sigma}^\dagger c_{m,n,\sigma} + t_y e^{im\varphi} c_{m,n+1,\sigma}^\dagger c_{m,n,\sigma}) \\
 & - \sum_{m,n,\sigma} (t_2 e^{i(m\varphi \pm \pi/N)} c_{m\pm 1, n+1, \sigma}^\dagger c_{m,n,\sigma}) + \text{H.c.} \\
 & - \mu \sum_{m,n,\sigma} c_{m,n,\sigma}^\dagger c_{m,n,\sigma}. \quad (3)
 \end{aligned}$$

The phase φ is chosen to be $2\pi/N$, so that the flux through each square plaquette is $2\pi/N$ and each triangular plaquette is π/N . To minimize finite-size effects, we maximize the band gap by choosing $t_2 = t_y/2$.

The design of the parton Hamiltonian (3) follows a lattice discretization of the Landau level problem, i.e., 2D electrons in a strong magnetic field (with the Landau gauge). Under periodic boundary conditions (torus geometry), the fluxes in the square/triangular plaquette are chosen such that there are N bands with the lowest band having Chern number $C = 1$ (see Fig. 6). The $N = 2$ case has been considered previously in Refs. [57,61–63], which was used to construct Gutzwiller projected wave functions representing the $SU(2)$ CSL of Kalmeyer-Laughlin type. For $N > 2$, the lowest band becomes flat and indeed resembles the lowest Landau level. The trial wave functions for describing the $SU(N)_1$ CSL are obtained by (i) tuning the chemical potential μ such that the lowest band is completely filled and all others empty, yielding a filling of $1/N$ on the lattice when also including the edge mode (see Fig. 7) and (ii) Gutzwiller projecting the Fermi sea with fully occupied lowest band. Strictly speaking, this

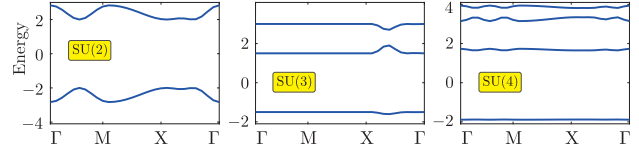


FIG. 6. Band structures of the parton Hamiltonian on the torus along high symmetry directions for $N = 2, 3$ and 4 . We set $t_x = t_y$ for $N = 2$ and 4 , and $t_x = t_y/2$ for $N = 3$.

construction does not depend on the flatness of the $C = 1$ band. Here, our extra requirement of a nearly flat band serves another purpose: the single-particle wave functions of a flat band can be made more localized, which helps to suppress the entanglement growth when converting Gutzwiller projected wave functions into MPS [63]. Last but not the least, this parton Hamiltonian is also designed to support exact zero modes on the cylinder, which, as we shall see, are important for constructing the MES basis.

For our purpose, we shall consider the cylinder geometry (with circumference N_y) rather than the torus geometry, with open boundaries in the x direction and a periodic (or twisted) boundary condition in the y direction. This allows us to characterize the MESS via the entanglement spectrum [61,64], and to use these wave functions to initialize our DMRG simulations [65].

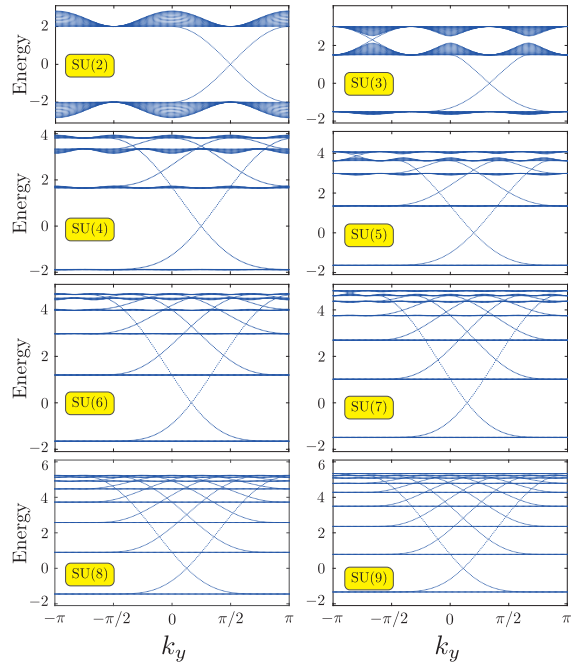


FIG. 7. The parton single-particle levels including the edge states on a wide cylinder for $N = 2$ to 9 . Filling the Fermi sea up to zero energy corresponds to a filling fraction $1/N$. This fully occupies the lowest parton band as well as the edge states up to the degenerate zero modes at the single-particle momentum $k_y = \pi/N$. These exact zero modes, denoted by $d_{L\sigma}$ and $d_{R\sigma}$, are localized at the left and right boundaries of the cylinder, respectively.

By diagonalizing the parton Hamiltonian (3) on the cylinder, we obtain a set of single-particle orbitals composed of local operators, $d_{k\sigma}^\dagger = \sum_{m,n} A_{m,n}(k) c_{m,n,\sigma}^\dagger$. For $N = 2$, it is known that the exact zero modes play an important role in constructing the MESs [61,63]. These exact zero modes, denoted by $d_{L\sigma}$ and $d_{R\sigma}$, localize at the two boundaries of the cylinder. Their occurrence at the single-particle momentum $k_y = \pi/2$ requires that for $\text{mod}(N_y, 4) = 0$ (2), the parton Hamiltonian has periodic (antiperiodic) boundary condition in the y direction. The two MESs with $S_z = 0$ are then written as Gutzwiller projected wave functions, $|\Psi_1\rangle = P_G d_{L\uparrow}^\dagger d_{R\downarrow}^\dagger |\Phi\rangle$ and $|\Psi_2\rangle = P_G d_{L\uparrow}^\dagger d_{L\downarrow}^\dagger |\Phi\rangle$, where P_G imposes the single-occupancy constraint at each site and $|\Phi\rangle$ is the state with all parton modes below the zero modes being fully occupied. In this representation, it is transparent that the zero mode $d_{L(R)\sigma}^\dagger$ creates a semion carrying spin-1/2 (with spin projection σ) at the left (right) boundary of the cylinder. It was found [63] that the entanglement spectra of $|\Psi_1\rangle$ and $|\Psi_2\rangle$ correspond to the conformal towers of states of the chiral $SU(2)_1$ WZW model in its spin-1/2 (semion) and spin-0 (identity) sectors, respectively. To qualify as the (quasi) degenerate ground states of chiral spin liquids, the wave functions should be $SU(2)$ spin singlets. While $|\Psi_2\rangle$ is manifestly a spin singlet, $|\Psi_1\rangle$ needs to be combined with $P_G d_{L\downarrow}^\dagger d_{R\uparrow}^\dagger |\Phi\rangle$ to form a spin singlet $|\tilde{\Psi}_1\rangle = P_G (d_{L\uparrow}^\dagger d_{R\downarrow}^\dagger - d_{L\downarrow}^\dagger d_{R\uparrow}^\dagger) |\Phi\rangle$. However, the entanglement spectrum of $|\tilde{\Psi}_1\rangle$ would then correspond to two copies of spin-1/2 conformal towers due to the entanglement cut of an additional nonlocal singlet formed by a pair of two spin-1/2 semions at the boundaries [66].

This parton construction of MESs for the $SU(2)$ CSL can be naturally generalized to the $SU(N)$ CSL. To allow for exact zero modes, the hopping parameters in Eq. (3) are chosen as $t_x = t_y$ if N is even, and $t_x = t_y \cos(\pi/N)$ otherwise. This ensures that the exact zero modes, $d_{L\sigma}^\dagger$ and $d_{R\sigma}^\dagger$, appear at $k_y = \pi/N$ (see Fig. 7), which is always allowed for a suitably chosen boundary condition (i.e., periodic or twisted) in the y direction. Occupying N of these boundary modes distributed arbitrarily over left and right boundaries ensures that the total momentum of the state in y direction is zero. As such this is then consistent with a width- N cylinder with plain periodic boundary conditions around the cylinder.

With that, MESs belonging to N different topological sectors can be written in analogy to the $SU(2)$ case as

$$|\Psi_p\rangle = P_G (d_{L1}^\dagger \dots d_{Lp}^\dagger d_{R,p+1}^\dagger \dots d_{RN}^\dagger |\Phi\rangle), \quad (4)$$

$p = 0, \dots, N$. Here $d_{L(R)\sigma}^\dagger$ creates an elementary anyon of the chiral $SU(N)_1$ theory and also transforms under the $SU(N)$ fundamental representation. Therefore $p = 0$ (N) corresponds to all N anyons either located, equivalently and respectively, at the left or right boundary. The entanglement spectra of these states $|\Psi_p\rangle$ should be in one-to-one correspondence with the N Kac-Moody conformal towers of the chiral $SU(N)_1$ WZW model, whose N primary fields are labeled by Young diagrams with p vertical boxes, respectively. However, except for $p = 0$ or N , the states above do not yet describe proper $SU(N)$ multiplets. For a more direct comparison with CFT, the N boundary modes need to be antisymmetrized over all flavors into an overall $SU(N)$ singlet. The corresponding $SU(N)$ singlets can

be written as

$$|\tilde{\Psi}_p\rangle = P_G (\varepsilon_{\sigma_1 \dots \sigma_N} d_{L\sigma_1}^\dagger \dots d_{L\sigma_p}^\dagger d_{R\sigma_{p+1}}^\dagger \dots d_{R\sigma_N}^\dagger |\Phi\rangle), \quad (5)$$

where $\varepsilon_{\sigma_1 \dots \sigma_N}$ is the totally antisymmetric Levi-Civita tensor. Eq. (5) indicates that for nonidentity sectors, multiple branches contribute to the entanglement spectrum. The number of branches is $\frac{N!}{(N-p)!p!}$, where $N!$ comes from the Levi-Civita tensor, and the factors $(N-p)!$ and $p!$ account for the antisymmetrization of the anyons on the left or right edge, represented by $N-p$ or p vertical boxes in the corresponding Young tableau, IRREPS \bar{p} and p , respectively. Note that as such this precisely also corresponds to the dimensions $\dim(\text{aIR}_N(p)) = \dim(\text{aIR}_N(N-p))$ [see Sec. II C above].

Using the matrix-product-operator matrix-product-state (MPO-MPS) method of Ref. [63] to implement the parton construction, we can express the filled Fermi sea of the above parton wave function $|\tilde{\Psi}_p\rangle$ as an MPS. The principal idea for that is as follows: (i) the vacuum state $|0\rangle$ is an MPS with bond dimension $D = 1$; (ii) the nonlocal parton operator $d_{k\sigma}^\dagger$, subject to Wannier localization, can be written as an MPO of bond dimension $D = 2$; (iii) the MPOs $d_{k\sigma}^\dagger$ are applied sequentially onto the MPS with possible compression after each step, resulting in an MPS with a finite bond dimension that represents a filled Fermi sea; and (iv) the Gutzwiller projector $P_G = \prod_{\ell=1}^L P_\ell$ is applied to separately enforce the local constraint, $\sum_{\sigma} c_{m,n,\sigma}^\dagger c_{m,n,\sigma} = 1$, on each site to recover the correct local physical subspace.

B. Infinite DMRG

For a cylinder geometry, the N different minimally entangled states of the $SU(N)$ CSLs, each carrying distinct anyonic flux threading through the hole in the annulus, form a complete basis for the N -fold degenerate ground states. Finding such a complete basis numerically for the Hamiltonian of Eq. (1) would be a convincing validation for our short-range CSL proposal.

Numerically the finite system width N_y lifts the N -fold ground-state degeneracy, with an energy gap which decreases with increasing width. If the cylinder is infinitely long, CFT predicts that the energy splittings (with respect to the ground state) are given by $\frac{2\pi v}{N_y}(h_p + \bar{h}_p)$, where v is the velocity of the chiral edge states and h_p, \bar{h}_p are conformal weights of the primary fields (corresponding to the respective anyons at the boundaries). Thus, we expect a power-law splitting $\mathcal{O}(1/N_y)$ for chiral topological phases (rather than exponential, as in the case of nonchiral topological phases with gapped edges [5,23,67]).

This hampers the search for distinct topological sectors via DMRG, a ground-state search algorithm when using cylinders. Previous DMRG works [31,67–72] have shed some light on this, showing that the presumably higher-energy states can still be examined by adopting tailored boundaries, e.g., imposing \mathbb{Z}_N charges.⁵

⁵For $SU(N)_1$ CSL, all topological sectors can be obtained in this way. However, for some topological phases, other types of anyon sectors can appear, such as a “defect line” cutting along the x direc-

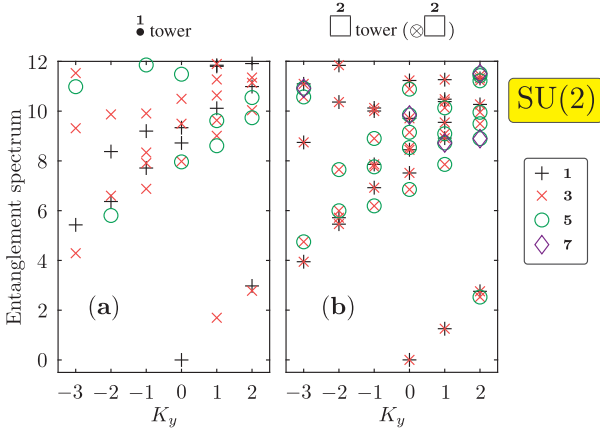


FIG. 8. The entanglement spectra on width-6 cylinders for SU(2) CSLs. (a) Identity sector. (b) Semion sector ($\otimes \frac{1}{2}$). Identifying K_y with the Virasoro level L_0 , the content of the chiral branches agrees exactly with the CFT predictions of Tables IV and II up to $K_y = 4 \pmod{6}$.

Concretely, DMRG is used to optimize the bulk part of the cylinder, while a small portion of spins at the boundaries are engineered to mitigate finite-width effects, thereby favoring different topological sectors if any exist. However, how to engineer the boundary spins and choose suitable lattice orientation remains an elusive undertaking.

Our work here is an extension of the above idea, and the parton approach paves a systematic way to construct the boundary spins for different MESs. For the identity sector, we use typical infinite DMRG (iDMRG) to find the ground state for Eq. (1) [73,74]. For other sectors that are higher in energy, we use the parton approach outlined above to initialize several possible MESs by occupying edge modes in different ways, then use the infinite DMRG algorithm to minimize the (bulk) ground-state energy with respect to the Hamiltonian of Eq. (1) for each. The ED calculations in Sec. II suggest a substantial region of a gapped CSL in the parameter space of $(\theta, \phi) = (\sin^{-1}(J_I), \tan^{-1}(\frac{3}{4}J_I/J_R))$ for each N . Here we focus on only one point within that phase, for $N = 2$ up to 4. While $N = 2$ and 3 have been investigated by ED and iPEPS previously, a thorough DMRG study for them has not been performed. We therefore include them here too, to corroborate the consistency of the model as well as the method for different N . We choose $(\theta, \phi) = (\pi/12, \pi/2)$ for $N = 2$, $(\theta, \phi) = (\pi/6, \pi/2)$ for $N = 3$, and $(\theta, \phi) = (\pi/4, \pi/2)$ for $N = 4$. The widths of the cylinder are chosen to be a multiple of N , so that if N different MESs do exist, all of them they can be found for arbitrary cylinder lengths.

The entanglement spectrum, as the fingerprint of topological order, can be readily extracted from iDMRG wave functions. To enable a comparison with CFT, we identify the entanglement levels by their SU(N) irreps and the momentum $k_y = \frac{2\pi K_y}{N_y}$, $K_y \in \mathbb{N}$ [67], as the converged states should be

tion. This is also very common and appears in, e.g., \mathbb{Z}_2 [5] and Ising topological phases. Then, adopting tailored boundaries in DMRG is not sufficient to detect such topological sectors.

TABLE II. SU(2)₁ WZW model—The direct product of the conformal tower of the spin-1/2 primary (left: see Table V in Appendix C) with a spin-1/2 gives a new tower (right) with a doubling of the number of states in each Virasoro level indexed by L_0 .

L_0	\square tower	\square tower $\otimes \square$
0	\square	$\square \oplus \square$
1	\square	$\square \oplus \square$
2	$\square \oplus \square$	$\square \oplus \square \oplus \square \oplus \square$
3	$\square \oplus \square$	$\square \oplus \square \oplus \square \oplus \square$
4	$\square \oplus \square$	$\square \oplus \square \oplus \square \oplus \square$

translationally invariant along the y direction. They are thus (approximate) eigenstates of the translation operator, with phase factors as eigenvalues, from which we extract the associated momenta k_y . From Fig. 8(a), we see that the identity sector agrees with the SU(2)₁ WZW CFT (see Table IV) for the first few low-lying states. For the semion sector, the ES [see Fig. 8(b)] consists of a new conformal tower containing integer spin multiplets, and twice the number of states expected for the semionic conformal tower. This discrepancy is rooted in the fact that semions carry spin-1/2 quantum numbers and can be best understood from the parton context [63]: the CFT content describes a single edge mode for spin-1/2, while the state in our simulation is a spin-singlet, corresponding to an antisymmetric combination of two spin-1/2 edge modes. In other words, neither of the semion states carrying spin-1/2 at the edges, i.e., $|\Psi_1\rangle = P_G d_{L\uparrow}^\dagger d_{R\downarrow}^\dagger |\Phi\rangle$ or $|\Psi_{1'}\rangle = P_G d_{R\uparrow}^\dagger d_{L\downarrow}^\dagger |\Phi\rangle$, does have a definite total spin. A spin-singlet can be formed, however, via a linear combination of $|\Psi_1\rangle$ and $|\Psi_{1'}\rangle$, which leads to the doubling of the number of states of the conformal towers [75]. This can be easily verified by a direct product of the conformal towers of the spin-1/2 primary of Table V (Appendix C) with a spin-1/2, as shown in Table II. This observation applies also for cases of $N > 2$: for nonidentity sectors, the ESs contain, in each Virasoro level, an integer multiplicity ($\geq N$) of the number of states of a single CFT tower. In general, it is possible to account for such a multiplicity by taking the direct product of each conformal tower with the conjugate of its primary spin (see Tables XXVI, XXVII, and XXVIII in Appendix F as examples). This brings our simulations in overall agreement with CFT as shown in Figs. 9 and 10 for $N = 3$ and $N = 4$, respectively, and a direct comparison with Tables XXVI, XXVII and XXVIII (see Appendix F). Conversely, one also could have “quenched” the edge spins p and \bar{p} in the DMRG simulation by coupling them to an artificial additional physical edge site with spin \bar{p} and p at the left and right boundary, respectively. However, we refrained from doing so.

To summarize: in this section we have shown that a DMRG ground-state search for the Hamiltonian of Eq. (1), initialized with an MPS obtained via Gutzwiller-projected parton construction, yields entanglement spectra in excellent agreement with the expectations for SU(N)₁ CSLs. At a technical level,

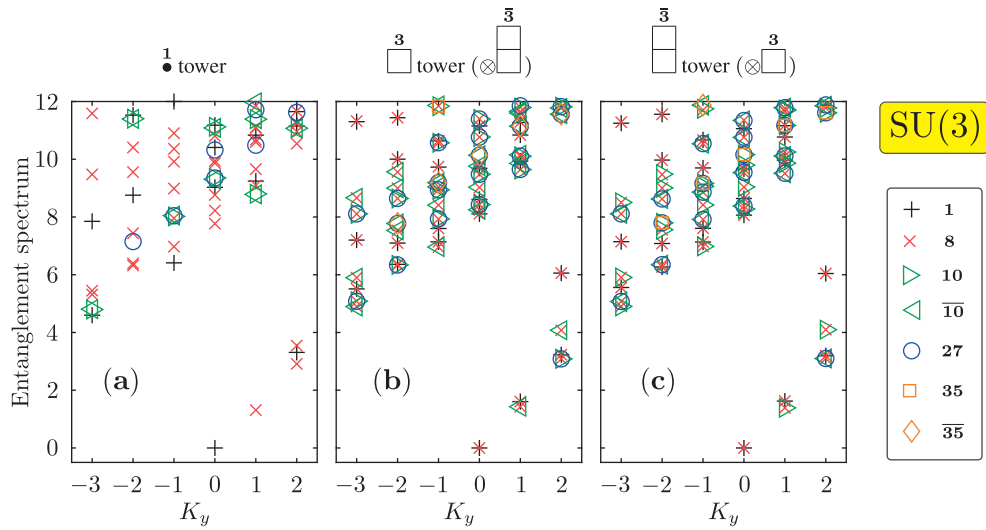


FIG. 9. The entanglement spectra on width-6 cylinders for $SU(3)$ CSLs. (a) Identity sector. (b) $\mathbf{3}$ sector ($\otimes \mathbf{3}$). (c) $\bar{\mathbf{3}}$ sector ($\otimes \bar{\mathbf{3}}$). Identifying K_y with the Virasoro level L_0 , the content of the chiral branches agrees exactly with the CFT predictions of tables VI and XXVI up to $K_y = 3 \pmod{6}$. Note that the towers of the $\mathbf{3}$ and $\bar{\mathbf{3}}$ sectors are identical, apart from an overall conjugation of all IRREPs.

this required the following innovations: (i) the Gutzwiller projected wave functions for $SU(N)_1$ CSLs, including the MES basis on the cylinder, are systematically constructed; (ii) the powerful tensor network library incorporating non-Abelian

symmetry efficiently converts the projected wave functions into MPSs with high fidelity; and (iii) the iDMRG is initialized with the MES basis and preserves the $SU(N)$ symmetry. The combination of these innovative techniques allows us to

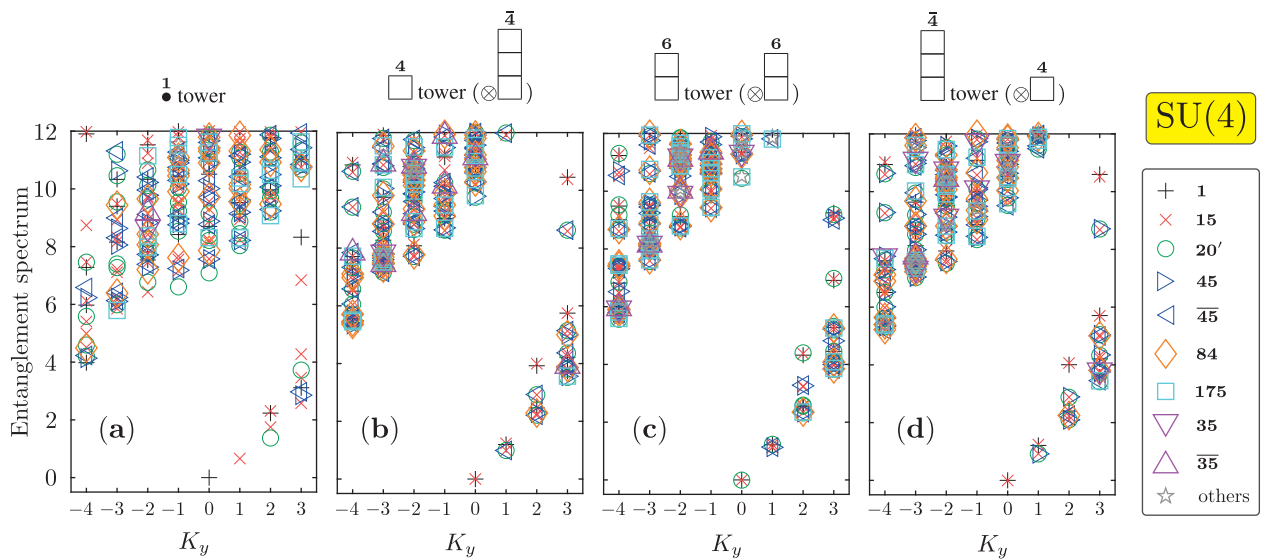


FIG. 10. The entanglement spectra on width-8 cylinders for $SU(4)$ CSLs. (a) Identity sector. (b) $\mathbf{4}$ sector ($\otimes \mathbf{4}$). (c) $\mathbf{6}$ sector ($\otimes \mathbf{6}$). (d) $\bar{\mathbf{4}}$ sector ($\otimes \bar{\mathbf{4}}$). Note that the towers of the $\mathbf{4}$ and $\bar{\mathbf{4}}$ sectors are identical, apart from an overall conjugation of all IRREPs. Identifying K_y with the Virasoro level L_0 , the content of the chiral branches agrees exactly with the CFT predictions of tables VIII, XXVII and XXVIII up to $K_y = 3$.

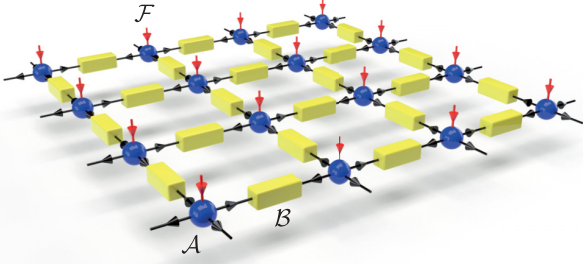


FIG. 11. PEPS on the square lattice involving site \mathcal{A} tensors and bond \mathcal{B} tensors. The bond dimension on the black links is D , up to $D^* = 4$ ($D = 15$), and the vertical red segments correspond to the physical space \mathcal{F} spanned by the $d = N$ ($d^* = 1$) physical degrees of freedom. All indices (i.e., legs or lines) carry arrows which indicate whether legs enter or leave a tensor in terms of state space fusion. This can be translated into co- and contravariant tensor index notation, respectively [76,77]. Note that reverting an arrow also flips all affected IRREPS into their dual representations.

obtain all N degenerate ground states of the $SU(N)_1$ CSL and characterize them from the entanglement spectrum.

IV. IPEPS

The results obtained from ED and iDMRG have shown affirmative evidences for $SU(N)_1$ CSL in a wide range of parameters with arbitrary N . On the other hand, a variational ansatz capturing properties of the CSL phase is also highly desired, especially in terms of symmetric PEPS. Following the implementation of chiral PEPS for $N = 2$ (see Refs. [44,48,49]) and $N = 3$ (see Ref. [47]), we will first outline the general scheme of the construction, with focus on how the relevant symmetries are realized on the local tensors. We then proceed to a variational optimization of the very few parameters. Finally, we investigate the entanglement properties and bulk correlations of the optimized chiral PEPS, confronting the results with general considerations.

A. Symmetric PEPS construction

Let us first extend the construction of chiral PEPS used for $N = 2$ (see Refs. [44,48,49]) and $N = 3$ (see Ref. [47] for more details). The PEPS is obtained by contracting the network represented in Fig. 11, i.e., by summing all virtual indices on the links connecting rank- $(z+1)$ site and rank-2 bond tensors, z being the lattice coordination number, $z = 4$ for the square lattice. The physical space \mathcal{F} on every lattice site is spanned by $d = N$ states transforming according to the fundamental IRREP of $SU(N)$. The choice of the virtual space on the $z = 4$ bonds around each site can be made following heuristic rules valid for all N . In other words, we construct a $SU(N)$ -symmetric PEPS from site/bond tensors with virtual (or bond state) space,

$$\mathcal{V}_N = \bullet \oplus \square \oplus \cdots \oplus \left. \begin{array}{c} \square \\ \square \\ \square \end{array} \right\} N-1, \quad (6)$$

TABLE III. Number of symmetric site-tensors in each class characterized by the IRREP of the C_{4v} point group of the square lattice (rows) and the occupation numbers $\{n_6, n_4, n_{\bar{4}}, n_1\}$ of the $\mathbf{6}$, $\mathbf{4}$, $\bar{\mathbf{4}}$, and $\mathbf{1}$ multiplets on the 4 virtual bonds (columns).

	$\{0, 0, 3, 1\}$	$\{0, 1, 0, 3\}$	$\{1, 0, 1, 2\}$	$\{1, 3, 0, 0\}$	$\{3, 0, 1, 0\}$	$\{0, 2, 1, 1\}$	$\{2, 1, 0, 1\}$	$\{1, 1, 2, 0\}$
A_1		1	2	1	2	3	3	4
A_2	1		1	2	2	3	3	5
B_1		1	2	1	2	3	3	4
B_2	1		1	2	2	3	3	5

where the direct sum contains all N IRREPs defined by single column Young diagrams of 0 up to $N-1$ boxes, consistently with the $N = 2$ and $N = 3$ cases, $\mathcal{V}_2 = \mathbf{1} \oplus \mathbf{2}$ and $\mathcal{V}_3 = \mathbf{1} \oplus \mathbf{3} \oplus \bar{\mathbf{3}}$.⁶ For the $N = 4$ case, we then assume $\mathcal{V}_4 = \mathbf{1} \oplus \mathbf{4} \oplus \mathbf{6} \oplus \bar{\mathbf{4}}$ (with bond dimension $D = 15$). By construction, the bond state (or virtual) space remains the same when the direction of arrow in Fig. 11 is reverted, as \mathcal{V} maps into itself when all IRREPs are flipped into their dual. Note that the site tensor \mathcal{A} can be seen as a linear map (or projection) $(\mathcal{V}_N)^{\otimes z} \rightarrow \mathcal{F}$ onto the physical state space, and the bond tensor \mathcal{B} as fusing bond state spaces into a fully entangled pair singlet state, $(\mathcal{V}_N)^{\otimes 2} \rightarrow \bullet$. As such, the tensors \mathcal{A} and \mathcal{B} explicitly correspond to the ‘‘P’’ and ‘‘EP’’ part in the acronym PEPS, respectively. Up to normalization, the bond tensor \mathcal{B} corresponds to an orthogonal matrix inserted into each bond within the tensor network [76,77]. It is real and defined as a weighted sum of three elementary (reflection-symmetric) tensors representing the three allowed fusion channels $\bullet \otimes \bullet \rightarrow \bullet$, $\mathbf{6} \otimes \mathbf{6} \rightarrow \bullet$ and $\mathbf{4} \otimes \bar{\mathbf{4}} \rightarrow \bullet$. As such, it does not add any variational degrees of freedom.

As for $N = 2$ and 3, we classify the $SU(4)$ -symmetric site-tensors according to (i) the number n_α of α -IRREPs appearing on their $z = 4$ virtual bonds, $n_{\text{occ}} = \{n_6, n_4, n_{\bar{4}}, n_1\}$ ($\sum n_\alpha = z$) and (ii) the (one-dimensional) IRREP of the C_{4v} point group of the square lattice [78] (see Table III). Since the chiral spin liquid only breaks P (parity) and T (time-reversal) but does not break the product PT, the PEPS complex site tensor \mathcal{A} should be invariant (up to a sign) under PT symmetry but acquires a complex conjugation under P or T separately (up to a sign). The simplest adequate ansatz has the following form:

$$\mathcal{A} = \mathcal{A}_R + i\mathcal{A}_I = \sum_{a=1}^{N_R} \lambda_a^R \mathcal{A}_R^a + i \sum_{b=1}^{N_I} \lambda_b^I \mathcal{A}_I^b, \quad (7)$$

where the real elementary tensors \mathcal{A}_R^a and \mathcal{A}_I^b either transform according to the A_1 and A_2 IRREPs, respectively, or according to the B_1 and B_2 IRREPs, respectively, giving rise to two possible families, \mathcal{A}_A and \mathcal{A}_B . $N_R = 16$ and $N_I = 17$ are the numbers of the elementary tensors in each class and λ_a^R and λ_a^I are arbitrary real coefficients of these tensors to be optimized variationally.

⁶To describe non-Abelian $SU(N)_k$ CSL, $k > 1$, we speculate that one should include all IRREPS in \mathcal{V} with up to k columns, consistently with the $SU(2)_2$ case [45].

To contract the infinite (double layer) tensor network, we have used the iPEPS method employing a corner transfer matrix renormalization group (CTMRG) algorithm [79,80] and obtain the fixed-point environment tensors used to compute the variational energy (on a 2×2 plaquette) or the entanglement spectra on infinite cylinders [47,48]. In order to cope with the large bond dimension ($D = 15$), the tensor contractions at each CTMRG step have been performed using the full $SU(N)$ -symmetry, thanks to the QSpace library [76,77]. This changes the description of any vector space \mathcal{V} from state-based to multiplet-based. For numerical efficiency then, importantly, the dimensionality is reduced from $D_{\mathcal{V}}$ states to an effective dimension of $D_{\mathcal{V}}^*$ multiplets, where for $SU(N)$ it typically holds $D_{\mathcal{V}}^* \ll D_{\mathcal{V}}$. As an example, the bond dimension $D^2 = 225$ of the double layer (rank-4) tensor $\mathcal{A}\mathcal{A}^*$ (used in CTMRG) can be reduced to $D^{2*} = 26$ which represents the number of multiplets in the product space:

$$\begin{aligned}
 v_4^{\otimes 2} = & \begin{array}{c} \boxed{4} \oplus \boxed{1} \oplus \boxed{4} \oplus \boxed{4} \oplus \boxed{4} \oplus \boxed{4} \oplus \boxed{4} \oplus \boxed{6} \oplus \boxed{10} \\ \oplus \boxed{10} \oplus \boxed{15} \oplus \boxed{20} \\ \oplus \boxed{20'} \oplus \boxed{20} \end{array} \quad (8)
 \end{aligned}$$

By fully enforcing $SU(N)$ symmetries on all tensors and indices, this automatically implies that singular values within any multiplet are degenerate. Therefore naturally, state space truncation is also always performed based on entire multiplets. Degeneracies across different multiplets, however, can be arbitrarily split depending on the algorithm and overall convergence. For $SU(4)$, we have increased the environment dimension up to $\chi^* = 221$ multiplets (corresponding to $\chi = 1350$ states) to control truncation errors. The optimization of the PEPS (7) with respect to its variational parameters is done within a variational optimization scheme [81]. For $\theta = \pi/4$ and $\phi = \pi/2$, the best variational energy (per site) $e \simeq -2.105$ (close to the DMRG estimate -2.14) is obtained for the \mathcal{A}_B ansatz that we shall consider hereafter.

B. Entanglement spectrum and edge physics

Both ED and DMRG computations have shown overwhelming evidence of $SU(N)_1$ edge modes, both on disk and cylinder geometries, a fingerprint of the Abelian CSL phase. We note that, apart from the trivial (identity) sector, the conformal towers previously obtained using PEPS on cylinders for $N = 2$ and 3 bear some differences with those obtained in DMRG. For example, the spin-1/2 semionic branch of the $SU(2)$ spin-1/2 chiral PEPS corresponds exactly to the $SU(2)_1$ conformal tower—consisting of half-integer spin multiplets—associated to the WZW spin-1/2 primary field and its descendants, but with an exact twofold degeneracy [44,48,49]. For the $SU(3)$ spin- \square chiral PEPS, in the

topological sectors defined by imposing $Q = \pm 1 \mathbb{Z}_3$ charges at the boundaries (strictly speaking, infinitely far away), three chiral branches—instead of a single one—separated in momentum by $2\pi/3$ are observed in the ES, whose level contents follow the prediction of the Virasoro levels of the $SU(3)_1$ WZW CFT [47]. Interestingly, both DMRG and PEPS show the same number of states in each Virasoro level, namely N times the WZW CFT content. These particular features of the PEPS ansatz are now further tested in the case of the $SU(4)$ model in order to draw more general (empirical) statements for $SU(N)$ spin- \square chiral PEPS.

The ES, revealing the topological properties of the PEPS, is computed by placing the optimized $D = 15$ ($D^* = 4$) PEPS on a width-4 infinite cylinder partitioned in two halves. The PEPS holographic bulk-edge correspondence [47,82] enables to compute the ES simply from the (fixed-point) environment tensors. The four topological sectors are selected by imposing a well-defined total \mathbb{Z}_4 charge Q at both ends (strictly speaking at infinity) on the virtual levels. Following the assignment $q_1 = 0, q_4 = 1, q_{\bar{4}} = -1$, and $q_6 = 2$, we have $Q = \sum q_\alpha \text{ mod}[4]$, where the sum runs over the virtual open bonds along the circumference at the boundaries. In practice, this is performed by filtering out the components of the environment tensors used to approximate each halves of the cylinder.

A necessary ingredient for identifying the linear dispersing modes in ES is the momentum quantum number associated with each energy level, which originates from the translation invariance along the circumference of the cylinder. For that purpose, we consider the momentum projection operator P_{k_y} :

$$P_{k_y} = \frac{1}{N_y} \sum_{r=0}^{N_y-1} e^{-ik_y r} T^r, \quad (9)$$

where $k_y = \frac{2\pi}{N_y} K_y$, $K_y = 0, 1, 2, \dots, N_y - 1$, and T is the one-site translation operator acting on the virtual degrees of freedom. Since T commutes with ρ , we can diagonalize $P_{k_y} \rho P_{k_y}$, whose nonzero eigenvalues are also eigenvalues of ρ , and corresponding eigenstates carry momentum quantum number k_y , to obtain ES and momentum quantum number simultaneously. In this setup, the action of translation operator on ρ can be implemented as a permutation of indices of ρ .

In Fig. 12, the ES in the four topological sectors are shown as a function of the momentum k_y along the circumference. For $Q = 2, 0$ and ± 1 , we identify one, two or four linearly dispersing chiral branches, respectively. When two or four branches are seen, the later are equally spaced in momentum, i.e., by $2\pi/2 = \pi$ and by $2\pi/4 = \pi/2$, respectively. Despite the very small circumference ($N_v = 4$), for $Q = 2$ and 0 the expected $SU(4)_1$ counting of the first Virasoro levels is satisfied. For $Q = \pm 1$, due to limited resolution in K -space, the states of the second Virasoro level of each branch are not clearly separated from the continuum above. Although it is difficult to draw definite conclusions on such a thin cylinder, it seems that the $SU(4)$ chiral PEPS reveals, as for the $SU(2)$ and $SU(3)$ cases, a duplication of the chiral branches for most topological sectors. In the $SU(2)$ PEPS this was attributed to the so-called “dressed mirror symmetry” within the virtual degrees of freedom [83]. Note however that there is no exact degeneracy in the $N = 3$ and $N = 4$ cases, in contrast to

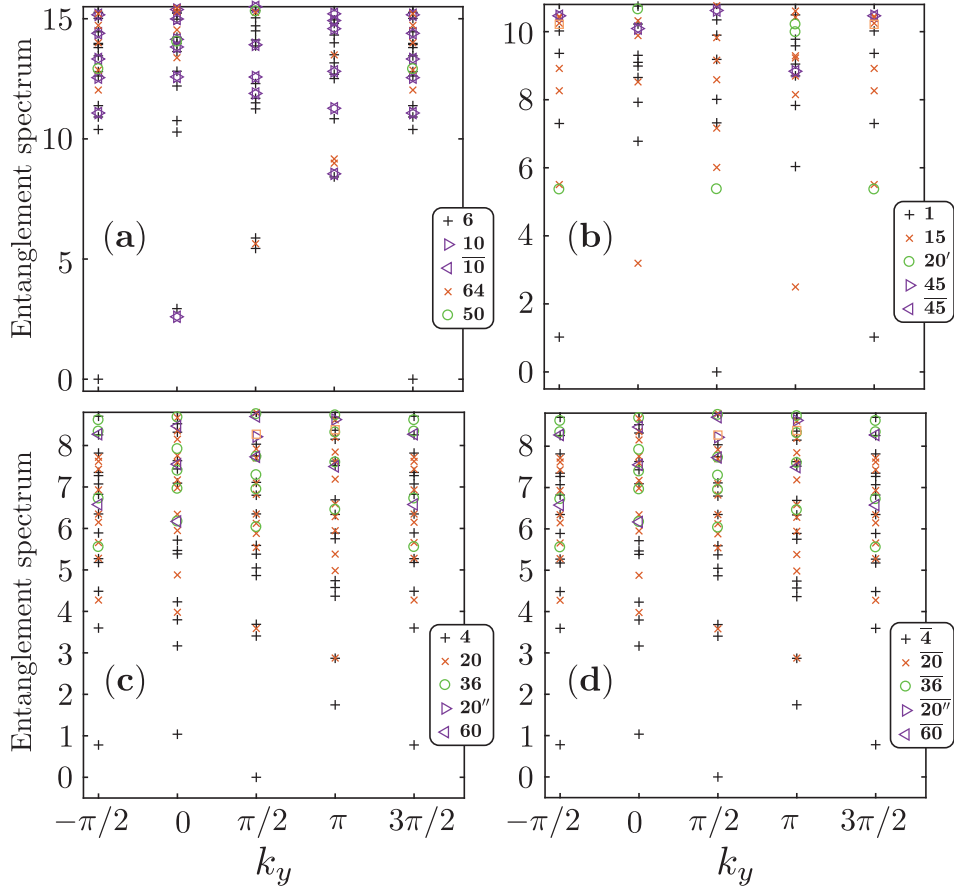


FIG. 12. Entanglement spectra on an infinitely long width-4 cylinder obtained from an $SU(4)$ ($D = 15$) PEPS wave function optimized for $\theta = \pi/4$, $\phi = \pi/2$ and environment dimension $\chi = 1350$. Spectra are plotted vs perimeter momentum k_y , and, to better evidence their chiral nature, the $k_y = -\pi/2$ spectrum is replicated at $k_y = 3\pi/2$. Appropriate \mathbb{Z}_4 charge boundaries $Q = 2, 0$ and ± 1 are set up to select the **6** (a), **1** (b), and $\mathbf{4}/\bar{\mathbf{4}}$ [(c) and (d)] topological sectors, showing one, two and four branches, respectively. Note that the **4** and $\bar{\mathbf{4}}$ spectra are identical apart from an overall charge conjugation of all IRREPs (and small finite- χ numerical errors).

$N = 2$, so that the duplication of the chiral modes may have a different origin here. In any case, as for the DMRG wave function, the duplication of the chiral states in the PEPS is linked to the fact that the ansatz is not a MES but, rather, carry an extra entanglement due to its global singlet nature. However, the manifestation in the ES is different in the two cases.

C. Correlation lengths

It was proven that any short-range quadratic parent Hamiltonian for chiral *noninteracting* PEPS is gapless [84]. This suggests that a fundamental obstruction or “no-go theorem” may prevent to describe a gapped CSL phase with a 2D PEPS (of finite bond dimension D). In fact, the PEPS optimized for the $N = 2$ and $N = 3$ chiral Heisenberg models [47,48] reveal rather long-range correlations and growing correlation lengths with environment dimension χ . It is therefore of much interest to also test this important feature in our $SU(4)$ PEPS. For that purpose, we have computed the leading correlation lengths (associated to the leading correlations in the bulk of the PEPS) from the leading eigenvalues of the transfer matrix

(TM) [44] (with no gauge “vison” flux). These correlation lengths, plotted in Fig. 13, show no sign of saturation with χ^*/D^{2*} , or equivalently with χ/D^2 ($D = 15$)—at least the three largest ones. The latter (shown in orange color) have been obtained from the singlet eigenvalues of the TM and, probably, correspond to dimer correlations. The next two (shown in blue color) correspond to spinon correlations. We note that all correlation lengths remain rather short, even for the largest χ value. However, the data for $N = 2, 3$ and 4 clearly show that all correlation lengths are comparable at the same value of χ/D^2 . For example, the dimer correlation length ranges between 3.5 and 6 for $\chi/D^2 = 6$, weakly dependent on N and on the model parameters. Since the PEPS bond dimension increases significantly with N ($D = 3, 7, 15$ for $N = 2, 3, 4$, respectively) the maximum achievable value of χ/D^2 , and hence of the correlation lengths, decreases strongly with N .

Note that in the $SU(2)$ case, the diverging nature of the correlation lengths was shown to be associated, not to a conventional critical behavior but, rather, to the existence of “long-range tails” (of very small weight) in most correlation functions [48]. We believe such a property also holds for any

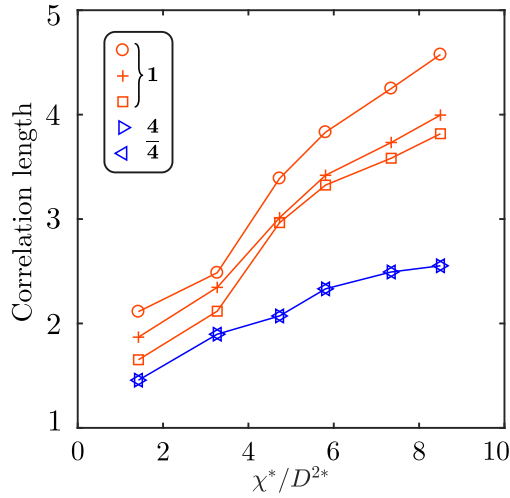


FIG. 13. Leading correlation lengths obtained from the transfer matrix (in the absence of gauge flux) for the case of $SU(4)$ plotted versus the number of multipliants χ^* kept in the environmental tensors, normalized by $D^{2*} = 26$ which represents the number of multipliants in the product space of $D \times D$ states with D fixed. The $SU(4)$ IRREPs associated to these correlation lengths are indicated.

$SU(N)$ CSL, although it could not be established here for $N = 4$ due to the large value of the bond dimension D .

V. CONCLUSION AND OUTLOOK

In this work, the previous family of $SU(3)$ chiral Heisenberg models on the square lattice has been generalized to any $SU(N)$ fundamental IRREP as physical degrees of freedom. The construction follows two steps: the first one consists in building up the most general fully translational, rotational and $SU(N)$ -symmetric model (possibly breaking time-reversal symmetry) whose interactions extend at most to three-sites within the square plaquettes. In a second step, one restricts to a subset of this model family whose Hamiltonians can be written solely as a sum of S_3 -symmetric operators defined on all the triangles within the square plaquettes. By doing so, we expect to mimic some of the physics of the triangular lattice with three-site chiral interactions, although keeping the full C_{4v} point group symmetry of the square lattice. This procedure defines a sub-family of chiral Heisenberg models spanned by two independent parameters (angles) that we have explored in details.

Extensive ED computations bring overwhelming evidence of extended regions of stability of $SU(N)$ CSL phases for all N , up to $N = 10$. The Abelian $SU(N)_1$ topological nature of these phases has been clearly established from the many-body low-energy spectra of periodic (tori) and open (disks) clusters. When the system size N_s is commensurate with N (so that no anyons is present in the GS) a N -fold GS degeneracy is observed on small tori as expected. When the commensurability between N_s and N is such that a single quasihole populates the GS, N_s quasidegenerate GS are found, as expected. Finally, chiral many-body low-energy spectra on open clusters following WZW CFT counting rules provide an even more stringent test of the existence of the $SU(N)_1$ Abelian CSL.

iDMRG computations by enabling to access much larger systems—typically infinitely long broad cylinders—provide most valuable and complementary results for $N = 2, 3, 4$. Gutwiler-projected parton wave functions offer a guide to construct iDMRG ansatz in each topological sector. Due to their $SU(N)$ global singlet nature, the iDMRG wave functions carry larger entanglement than MES (they can be seen as linear combinations of MES, except in the trivial sector) and, hence, show ES with more structure whose complete understanding has been fully provided.

Following the prescriptions for $N = 2$ and $N = 3$, we have constructed a family of chiral $SU(4)$ -symmetric PEPS and, under optimization, a good variational PEPS ansatz is obtained for the chiral $SU(4)$ Heisenberg model. The entanglement spectra obtained in the $N = 4$ topological sectors of an infinitely long cylinder reveal chiral modes. The multiplicity of the chiral modes is attributed to the non-MES nature of the singlet PEPS ansatz in most topological sectors. Finally, growing correlation lengths with environment dimension are consistent with the existence of “long-range tails” (of very small weight) in correlation functions (evidenced explicitly for $N = 2$ [48]). We speculate that these long-range tails would fade away (i.e., their weights would continuously vanish) for increasing D , providing a more and more faithful representation of the GS. If correct, this implies that the no-go theorem [84] does not *practically* prevent an accurate chiral PEPS representation of the topological gapped CSL phase.

We note that the $SU(N)$ CSL is stable in some regime where the three-site interaction is purely imaginary (corresponding to $\phi = \pi/2$), mostly studied here. In fact, this case is relevant in ultracold atom systems which can realize an $SU(N)$ fermionic Hubbard model [27]. In the presence of an artificial gauge field (providing complex amplitudes to the effective hoppings), at $1/N$ filling (one particle per site), the large- U Mott insulating phase [19,29,30] can be approximately described by our Hamiltonian, so that an Abelian $SU(N)$ phase on the square lattice may be seen experimentally if low-enough temperatures could be reached. Experimental setups of ultracold atoms at other fractional fillings like k/N ($k \in \mathbb{N}$ particles/per site) could be also of great interest and be described by new types of $SU(N)$ spin Hamiltonians, like the two-fermion $SU(4)$ model [85] with additional chiral interactions on triangular units, opening the way to observe non-Abelian CSL.

ACKNOWLEDGMENTS

D.P. conceptualized the work. We acknowledge enlightening conversations with Norbert Schuch. We also thank Alexander Wietek for the use of his QuantiPy library and Laurens Vanderstraeten for help on non-Abelian symmetries in tensor networks. J.-Y.C. acknowledges support by the European Union’s Horizon 2020 programme through the ERC Starting Grant WASCOSYS (Grant No. 636201) and the ERC Consolidator Grant SEQUAM (Grant No. 863476), and from the Deutsche Forschungsgemeinschaft (DFG, German Research Foundation) under Germany’s Excellence Strategy (EXC-2111–390814868). K.T. is supported in part by JSPS KAKENHI Grants No. 18K03455 and No. 21K03401. H.-H.T. is supported by the Deutsche Forschungs-

gemeinschaft through project A06 of SFB 1143 (project-id 247310070). J.v.D. acknowledges support from the Deutsche Forschungsgemeinschaft under Germany's Excellence Strategy EXC-2111390814868, through project No. 409562408. D.P. acknowledges support by the TNSTRONG ANR-16-CE30-0025 and TNTOP ANR-18-CE30-0026-01 grants awarded by the French Research Council. J.-W.L. acknowledges support by DFG WE4819/3-1. A.W. was supported by the U.S. Department of Energy, Office of Science, Basic Energy Sciences, Materials Sciences and Engineering Division. This work was granted access to the HPC resources of CALMIP and GENCI supercomputing centers under the allocation 2017-P1231 and A0030500225, respectively, and computations have also been carried out on the TQO cluster of the Max-Planck-Institute of Quantum Optics.

J.-Y.C., J.-W.L., and P.N. contributed equally to this work.

APPENDIX A: ANALYSIS OF 2×2 PLAQUETTE

The focus of the present paper is on chiral spin liquids which have the $SU(N)$ flavor symmetry intact both locally and globally. In particular, the ground state remains an $SU(N)$ singlet in the thermodynamic limit. This suggests that also the low-energy regime of smaller clusters should have a singlet ground state. If that is not possible by finite size, at least, one may expect to have a ground state that is closest to a singlet in the sense that they tend to prefer to fill up full columns in the corresponding Young tableau (YT).

In this spirit, this Appendix analyzes the 2×2 plaquette as an elementary unit of the Hamiltonian. The Hamiltonian (1) on the full 2D square lattice can be rewritten as

$$H = \sum_p H_p, \quad (\text{A1})$$

where H_p is the Hamiltonian for a single square plaquette p of 2×2 sites that combines all terms $i, j, k \in p$ (in order to avoid overcounting along the edge of the plaquette, we set $J_1 \rightarrow \frac{1}{2}J_1$ for H_p , whereas J_2, J_R , and J_I remain the same). Now with H_p the combined set of local operators that can be used to tile the entire 2D Hamiltonian, it is natural to analyze its multiplet structure. Multiplets in H_p that are low in energy are expected to be important in the low energy physics on the 2D lattice itself, whereas multiplets of H_p at higher energies will likely play a minor role. Clearly, the ground state multiplet of H_p also may change when tuning the coupling parameters $\{J_1, J_2, J_R, J_I\}$. This then may signal a qualitative change of the overall low-energy behavior of the 2D system, e.g., a low-order phase transition for similar coupling parameters.

The eigenspectrum of the 2×2 plaquette Hamiltonian H_p is analyzed in Fig. 14 for $N = 2, 3, 4, 5$ in panels (a)–(d), respectively. The $SU(N)$ multiplet structure is fully resolved as indicated with the legend. For the sake of the discussion here, we use Dynkin labels in compact notation to identify symmetry sectors where $q \equiv (q_1 \dots q_{N-1})$ directly specifies to corresponding $SU(N)$ YT via differential length offsets of the number of boxes in subsequent rows of the YT (e.g., see also Appendix A in Ref. [86]). For example, $(10 \dots 0)_{N-1}$ is the fundamental or defining representation also labeled as \mathbf{N} in the main text, and $(10 \dots 01)_{N-1}$ is the adjoint representation. The reverse order $(q_{N-1} \dots q_1) \equiv \bar{q}$ specifies the dual IRREP

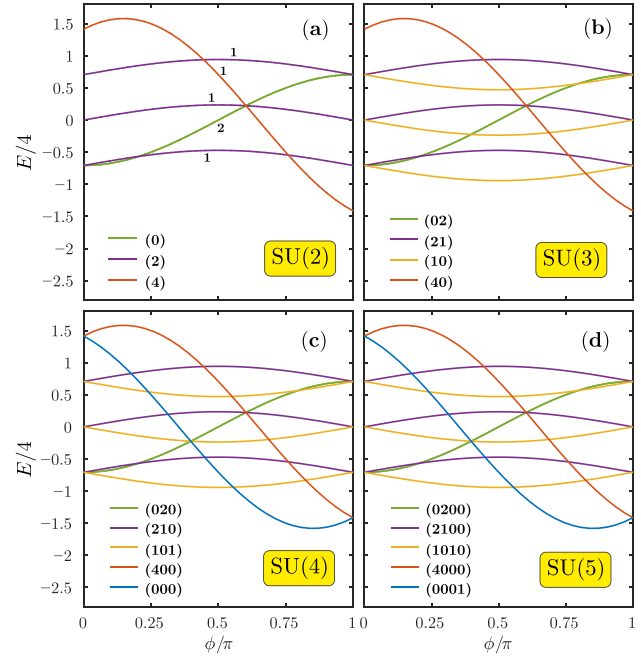


FIG. 14. Eigenspectrum of a 2×2 cluster described by the plaquette Hamiltonian H_p in Eq. (A1) vs ϕ using the parametrization in Eq. (2), with $\theta = \pi/4$ fixed as in the main text [e.g., see Fig. 2]. To focus on energy per site, the energies are divided by the number of sites $N_s = 4$ as indicated. (a)–(d) refer to case of $N = 2, 3, 4, 5$ symmetric flavors, respectively. Colors indicate symmetry sectors as indicated with the legend based on Dynkin labels. The small numbers on top of each line in panel (a) indicate the degeneracy of multiplets which shows that the green line only is twofold degenerate. This also holds for all data in the other panels.

to any $q = (q_1 \dots q_{N-1})$. For the case of $SU(2)$, having a single number (q_1) only, the integer q_1 simply counts the total number of boxes in the YT, and thus corresponds to a spin $S \equiv q_1/2$ multiplet. Its adjoint is given by $S = 1$, i.e., multiplet $q = (2)$.

a. General aspects of $SU(N)$ permutation Hamiltonian

The Hamiltonian (1) and therefore also H_p above is defined via simple permutations of flavors over two or three sites. A direct consequence of this is, that all eigenenergies appearing for $SU(N)$ exactly also must appear for $SU(N' > N)$, as can be clearly observed in Fig. 14. The simple reason is that adding additional flavors $N' - N > 0$ on top of all sites, the Hamiltonian will not make any reference to these when applying it to a state that only contains up to the first N flavors. The multiplet label needs to adapt, though. By using Dynkin labels, this simply concatenates additional trailing numbers q_i . Considering a four-site plaquette here, these extra trailing numbers must all be zero for $N' > 4$, as largely already also observed for $SU(4)$ itself [see legend in Fig. 14(d)]. With this clearly also the degeneracy in terms of states within these multiplets changes as required by the increased Hilbert space. However the eigenenergies themselves remain exactly the same. Therefore given a Hamiltonian that solely consists of permutations of otherwise symmetric flavors, the many-body

eigenspectrum for a given $SU(N)$ is exactly inherited also to all cases $SU(N' > N)$. This is made explicit across the panels in Fig. 14 by choosing matching color coding. For example, what was a singlet in $SU(2)$, i.e., the green line for $q = (0)$, becomes $q = (02)$ for $SU(3)$, and then $q = (020 \dots)$ for larger N still.

When increasing the number of flavors $N \rightarrow N' > N$, however, also new eigenenergies can emerge that were previously absent. For example, in Fig. 14, this is seen as additional lines that appear when going from $N = 2 \rightarrow 3$ (yellow lines) or $N = 3 \rightarrow 4$ (blue line). Given a four-site plaquette with the fundamental IRREP on each site, the number of lines will no longer change for $N' > 4$, as seen by going from $N = 4 \rightarrow 5$, since all YTs with four boxes are already present.

b. Low-energy regimes

Now the analysis in Fig. 14 tracks the eigenvalues vs. ϕ for fixed $\theta = \pi/4$ similar to Fig. 2 in the main text. The red line in Fig. 14 corresponds to the fully symmetric IRREP $q = (40 \dots)_{N-1}$ that is present for all $N \geq 2$. This multiplet crosses over and becomes the ground state for $\phi > \pi$ for $N \geq 4$, and already earlier for $N = 2$ and $N = 3$. This shows that the 2×2 plaquette becomes ferromagnetic around $\phi \gtrsim \pi$ [note that based on Eq. (2), $\phi > \pi$ corresponds to negative, and hence ferromagnetic J_1 and J_2]. As such, this signals the onset of ferromagnetism on the full 2D system, also consistent with the analysis of the larger clusters in Fig. 2.

Finally, with focus on a singlet ground state, on the given four-site plaquette this can only be achieved exactly for $N = 2$ and $N = 4$. Interestingly then, the singlet for $SU(2)$ [green line in Fig. 14(a)] becomes a nonsinglet for $N > 2$, i.e., (02) for $SU(3)$, and $(020 \dots)$ thereafter. Instead, an entirely new singlet shows up for $SU(4)$ in the low-energy regime, and remains an eigenenergy for $N \geq 4$ (blue line). Therefore, while in the case of $SU(2)$ the singlet is favored for small $\phi \in [0, \pi]$, it is favored for larger $\phi \in [0, \pi]$ for $SU(4)$ and onward. What comes closest to a singlet for $SU(3)$ on the 2×2 plaquette, on the other hand, is the multiplet (10) , i.e., the fundamental IRREP. Based on the fusion of the four fundamental IRREPs on the 2×2 plaquette to start with, this already fused three of these into a singlet. As seen by the yellow line in Fig. 14(b), the multiplet (10) is the ground state for a wide range $\phi \in [0, \pi]$, including small but excluding large ϕ where the system becomes ferromagnetic. This is perfectly consistent with the analysis on the larger cluster in Fig. 2(a) in the main text which for $N = 3$ also shows the chiral phase extending all the way down to $\phi = 0$.

The chiral phase was identified in Fig. 2 with the gapped phase around $\phi \gtrsim \pi/2$. However, when reducing ϕ , as seen in Fig. 2 for $N > 3$, this gapped phase closes at finite ϕ . Even more, for certain N it appears to reopen before approaching $\phi = 0$. Hence based on Fig. 2 having the chiral phase identified with the regime of larger $\phi \gtrsim \pi/2$, this is entirely consistent with the regime in the present analysis of the 2×2 plaquette where the system is (or tends towards becoming) a singlet for $N \geq 4$ in Figs. 14(c) and 14(d). Note that for $N > 4$, the blue line in Fig. 14(d) corresponds to the fully

antisymmetric multiplet where four boxes are stacked on top of each other into a single column in the corresponding YT.

In the chiral regime $\phi \gtrsim \pi/2$, also the coupling strength of the real three-site permutation term $H_{ijk}^R \equiv J_R(P_{ijk} + P_{ijk}^{-1})$ turns negative, i.e., having $J_R < 0$. Its effect is revealed by looking at the eigenvalues in the three-site eigenbasis for given triangle (ijk) . One finds for $N \geq 3$ that the completely symmetric multiplet $(30 \dots)$ and the completely antisymmetric multiplet $(001 \dots)$ [equivalent to (00) for $SU(3)$] are eigenstates to the same eigenvalue $+2J_R$, whereas the twofold degenerate multiplets $(110 \dots)$ have eigenvalue $-J_R$ (which are eventually differentiated by the complex term J_I). Hence negative J_R equally favors both, the completely symmetric multiplet (ferromagnetic) as well as the completely antisymmetric multiplet (antiferromagnetic) on any triangle. When considering all triangles within a 2×2 plaquette as analyzed in Fig. 14, the antiferromagnetic states dominate the low energy regime, yet with the ferromagnetic regime in close proximity (both, the blue and red lines move downward with increasing ϕ for $N \geq 4$). Eventually, for $\phi > \pi$ when also the two-site exchange couplings J_1 and J_2 turn negative, the ferromagnetic state takes over.

APPENDIX B: GENERALIZED EXCLUSION PRINCIPLE FOR ABELIAN $SU(N)$ CSL

We provide here complementary details about the heuristics on the content (degeneracy, quantum numbers, etc.) of the GS manifold within the CSL phase on small periodic clusters (of torus geometry).

As realized already for $N = 3$ in Ref. [47], it is possible to obtain, for arbitrary N , the exact momenta of the various states in the GS manifold expected for an Abelian $SU(N)_1$ CSL. This can be inferred from a simple generalized exclusion principle (GEP) known for FQH states [55] or fractional Chern insulators [56] with clustering properties.

For our $SU(N)$ model in the fundamental representation, there are N states per site which can be viewed as a color degree of freedom. The mapping to a bosonic FQH requires to treat them separately: one (arbitrarily chosen) color will correspond to a hole while the remaining $C = N - 1$ will correspond to spinful $SU(C)$ bosons. Hence, Abelian bosonic FQH states can be constructed at a filling $\nu_{FQH} = C/(C + 1) = (N - 1)/N$, corresponding to Halperin states [87–89]. In this terminology, the ground states and quasihole states is given by the number of dressed partitions $(1, 2)_C$, see Ref. [56]. Moreover, the respective momenta can be obtained from the mapping between N_s orbitals obtained when folding the Brillouin zone [90,91].

To be more specific, let us consider for instance $N = 3$ which maps onto $C = 2$ bosons, i.e., spin-1/2 particles. Then, the generalized exclusion principle for the ground-states (for $N_s = kN$) enforces the occupations $(\downarrow, \uparrow, 0, \dots)$ and its translations, i.e., 3 states. This $(1, 2)_2$ exclusion rule simply enforces that identical particles cannot be neighbors but a \downarrow particle can be followed by a \uparrow particle. Such rules can be rephrased in terms of follow-up rules in the string of states, e.g., $0 \rightarrow (0, \downarrow, \uparrow), \uparrow \rightarrow 0, \downarrow \rightarrow (0, \uparrow)$, which defines

a “transfer matrix,”

$$T^{(N=3)} = \begin{bmatrix} 1 & 1 & 1 \\ 1 & 0 & 1 \\ 1 & 0 & 0 \end{bmatrix}, \quad (\text{B1})$$

for $N = 3$.

The transfer matrix above is easy to generalize to any N , with 1's in the first column and above the diagonal and zeros otherwise. For example, one gets

$$T^{(N=5)} = \begin{bmatrix} 1 & 1 & 1 & 1 & 1 \\ 1 & 0 & 1 & 1 & 1 \\ 1 & 0 & 0 & 1 & 1 \\ 1 & 0 & 0 & 0 & 1 \\ 1 & 0 & 0 & 0 & 0 \end{bmatrix}, \quad (\text{B2})$$

for $N = 5$. Note that, in addition to the rules encoded in the transfer matrix (which alone produce a large number of irrelevant configurations), one should also simultaneously enforce a global property relating the total appearance of all colors such that the GS belong to the $SU(N)$ IRREP of smallest possible dimension compatible with system size. More precisely, defining the integer $r_0 = \text{mod}(N_s, N)$, the smallest possible IRREP corresponds to the antisymmetric IRREP with a Young diagram of r_0 vertical boxes (labeled in the text $\text{aIR}_N(r_0)$), and, heuristically, is to be associated to the GS manifold. For instance for $N_s = kN$, all colors should appear exactly k times, i.e., $c_1 = c_2 = \dots = c_N = k$, as the singlet character of the GS manifold implies.

For $N_s = kN - 1$, $k \in \mathbb{N}$, we expect the low-energy states to represent the quasihole excitations, similar to the Laughlin states when inserting a flux in a fractional quantum Hall state on a torus. In particular, the quasihole counting on a finite cluster should be the same as in the thermodynamic limit and is given by a generalized Haldane exclusion principle [90,91]. Moreover, the lattice momenta at which these (quasi) degenerate states sit can be obtained using a heuristic rule by folding the two-dimensional Brillouin zone into a one-dimensional lattice of orbitals [90]. For instance, for all the quasihole examples shown in Fig. 4, since $\text{GCD}(N, N_s) = 1$, we expect to find one low-energy $SU(N)$ multiplet at each momentum (i.e., a total number of quasihole states equal to NN_s), which is exactly what is found numerically.

When $N_s = kN$, we expect N -fold quasidegenerate ground states on a torus. The momenta are given using a similar heuristic rule and are nontrivial. For completeness, here are the predictions corresponding to the values shown in Fig. 4 (see the Brillouin zones as insets for the momenta notations): (i) $N = 4$ and $N_s = 20$: one state at momentum Γ , M and twofold degenerate X ; (ii) $N = 5$ and $N_s = 15$: one state at momentum Γ , $\pm\Sigma_0$, $\pm\Sigma_2$; (iii) $N = 6$ and $N_s = 12$: one state at momentum Γ , Z_1 , $\pm\Delta$, Z_0 , Δ ; and (iv) $N = 7$ and $N_s = 14$: one state at momentum Γ , ± 0 , ± 2 , ± 5 . All these predictions are verified numerically, and the low-energy states are always well separated from the higher excited ones as expected in this topological incompressible gapped phase.

APPENDIX C: WZW $SU(N)_1$ CHIRAL TOWERS OF STATES

We provide here an almost self-contained explanation of the Hilbert-space structure of the $SU(N)$ WZW CFT and

derive the $SU(N)_1$ WZW towers of states for $N = 2$ to 8, which are to be compared with the ED results for $SU(N)$ open clusters investigated and discussed in the main text. This Appendix is organized as follow. In the first part, we recall some basic facts on $\mathfrak{su}(N)$ Lie algebra and its representation theory (see Ref. [92] for a readable introduction to Lie algebras and their representation). In a second part, we briefly present the affine extension of $SU(N)$ and introduce the primary states on which the Hilbert space is constructed. Most of the equations presented in the first two parts are relevant to any (affine) Lie algebras unless otherwise stated. In the last part, we explain how WZW $SU(N)_1$ chiral towers of states for open clusters can be computed using this formalism. The Appendix closes with the tables showing the explicit form of the towers of states relevant for the present study, up to $SU(8)$. This Appendix is not intended to give a mathematical presentation of the field but rather to introduce, without any mathematical proof, the basic tools needed to identify the expected representations in WZW $SU(N)_1$ chiral towers of states.

1. $\mathfrak{su}(N)$ Lie algebra

Group, Generators. The special unitary group $SU(N)$ is the Lie group of $N \times N$ unitary matrices with determinant 1. The Lie algebra $\mathfrak{su}(N)$ associated to the Lie group $SU(N)$ is determined by a set of $N^2 - 1$ traceless hermitian generators J^α satisfying the commutation relations,

$$[J^\alpha, J^\beta] = if_{\alpha\beta\gamma} J^\gamma, \quad (\text{C1})$$

where the real fully antisymmetric tensor f encodes the structure constants. Equation (C1) is a direct consequence of the group structure of $SU(N)$ and the fact that the Lie group and the Lie algebra are related by the exponential map which associate to any element J of $\mathfrak{su}(N)$ an element $\exp(itJ)$ of $SU(N)$.

Cartan Weyl basis, Adjoint representation, roots. The maximal subset $\{H^i\}_{i=1,\dots,r}$ of $\mathfrak{su}(N)$ composed of commuting generators $[H^i, H^j] = 0$ forms the Cartan subalgebra of $\mathfrak{su}(N)$ and plays the role of S^z in $\mathfrak{su}(2)$. Obviously, since all H^i can be diagonalized simultaneously, the rank r of $\mathfrak{su}(N)$ is $N - 1$, which is equal to the maximal number of traceless diagonal $N \times N$ matrices. As $\{H^i\}$ can be simultaneously diagonalized, we can choose the basis vectors in any irreducible representation to be the eigenstates $|\mu\rangle$ of H^i :

$$H^i |\mu\rangle = \mu_i |\mu\rangle. \quad (\text{C2})$$

The $(N - 1)$ -dimensional vector $\mu = (\mu_1, \dots, \mu_{N-1})$ is called the weight. The remaining $N(N - 1)$ off-diagonal generators will be denoted as E^α .

To each generator J^α , we can associate a linear map ad_J from $\mathfrak{su}(N)$ to itself defined as $\text{ad}_J(X) = [J, X]$ for any X in $\mathfrak{su}(N)$. This defines the adjoint representation which can be used to classify the generators E^α as eigenvectors of ad_{H^i} :

$$\text{ad}_{H^i}(E^\alpha) = [H^i, E^\alpha] = \alpha_i E^\alpha \quad (i = 1, \dots, N - 1). \quad (\text{C3})$$

The $(N - 1)$ -dimensional vectors $\alpha = (\alpha_1, \dots, \alpha_{N-1})$ are called the roots and E^α , which play the role of S^\pm , the ladder operators. The Cartan-Weyl basis is $\{H^i, E^\alpha\}_{i \in \{1, \dots, r\}, \alpha \in \Delta}$ where Δ denotes the set of all $N(N - 1)$ roots. Obviously,

only $r = N - 1$ roots are linearly independent. An important remark is the nondegeneracy of roots. Indeed, the existence of a degenerate root would contradict the definition of the Cartan subalgebra (*maximal* set of commuting generators).

It is clear from Eq. (C3) that there is some arbitrariness in the determination of E^α and α as both depend on the choice of a particular basis for the Cartan subalgebra. Nevertheless, some general properties can be established. Once the basis of $r = N - 1$ linearly independent roots is fixed, one can expand any root in this basis. Roots with positive coefficients in this expansion are called *positive* and form the set Δ_+ . A root $\alpha^{(i)}$ ($i = 1, \dots, r$) that cannot be expressed as an integer sum of two positive roots is by definition a *simple root*.

The central role of such $r = N - 1$ simple roots not only lies in the fact they provide a convenient basis for roots but also because the $(N - 1) \times (N - 1)$ matrix A of the scalar products of simple roots (the *Cartan matrix*) completely encode the Lie algebra:

$$A^{ij} = \frac{2\alpha^{(i)} \cdot \alpha^{(j)}}{\alpha^{(j)} \cdot \alpha^{(j)}} = \alpha^{(i)} \cdot \alpha^{(j)\vee}, \quad (\text{C4})$$

with $\alpha^{(i)\vee} = 2\alpha^{(i)}/|\alpha^{(i)}|^2$ (*coroots*). The entries of this matrix are always integers and, in the $\mathfrak{su}(N)$ case, A is symmetric and take the form $A^{ij} = 2\delta_{ij} - \delta_{|i-j|,1}$. For $\mathfrak{su}(N)$ in which all the $N(N - 1)$ roots have equal length (i.e., *simply laced*), it is convenient to choose $|\alpha^{(i)}| = \sqrt{2}$ so that we do not need to distinguish between the roots and the coroots. The lattice spanned by the $r = N - 1$ basis vectors $\alpha^{(i)}$ ($\alpha^{(i)\vee}$) is called the *root lattice* $\Lambda_r(\mathfrak{su}(N))$ [the *coroot lattice* $\Lambda_r^\vee(\mathfrak{su}(N))$].

Fundamental weights. From the set of simple roots $\{\alpha^{(i)}\}$, we can introduce its dual, i.e., the fundamental weights $\omega_{(i)}$ satisfying

$$\alpha^{(i)\vee} \cdot \omega_{(j)} = \delta_j^i, \quad (\text{C5})$$

which can be used as the basis of the weights (*Dynkin basis*):

$$\mu = \sum_{i=1}^{N-1} d(\mu)^i \omega_{(i)}. \quad (\text{C6})$$

The coordinates $d(\mu)^i$ in this basis is called *Dynkin labels*. The lattice spanned by the basis $\{\omega_{(i)}\}$ is called the *weight lattice* $\Lambda_w(\mathfrak{su}(N))$ (see Fig. 15). The relation between the co-root lattice $\Lambda_r^\vee(\mathfrak{su}(N))$ and the weight lattice $\Lambda_w(\mathfrak{su}(N))$ is analogous to that between the lattices in the real space and the reciprocal space. Any irreducible representation \mathcal{R} of $\mathfrak{su}(N)$ is specified by its highest weight $\lambda_{\mathcal{R}}$ or its Dynkin labels $\{d(\mathcal{R})^i\}$

$$\lambda_{\mathcal{R}} = \sum_{i=1}^r d(\mathcal{R})^i \omega_{(i)} \quad (d^i \in \mathbb{Z}, d^i \geq 0) \quad (\text{C7})$$

and, by applying the lowering operators $E_{-\alpha}$ ($\alpha \in \Delta_+$), we can construct the corresponding irreducible representation [see Fig. 16 for $\mathfrak{su}(3)$ examples]. In $\mathfrak{su}(N)$, the representation specified by $(d^1, d^2, \dots, d^{N-1})$ has a Young diagram with d^1 columns with length 1, d^2 columns with length 2, \dots , and d^{N-1} columns with length $N - 1$. For example, the fundamental representations are always specified by the Dynkin

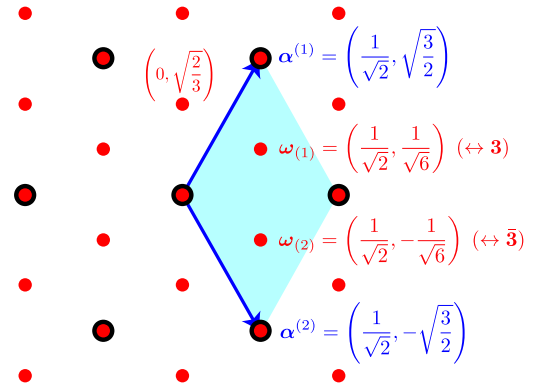


FIG. 15. The (co)root lattice $\Lambda_r(\mathfrak{g})$ (black circles) and the weight lattice $\Lambda_w(\mathfrak{g})$ (red circles) for $\mathfrak{g} = \mathfrak{su}(3)$. The root (weight) lattice is an integer span of two simple (co)roots $\alpha^{(1)}$ and $\alpha^{(2)}$ (two fundamental weights $\omega_{(1)}$ and $\omega_{(2)}$). In $\mathfrak{su}(3)$, $\omega_{(1)}$ and $\omega_{(2)}$ respectively correspond to the highest weights of $\mathbf{3}$ and $\bar{\mathbf{3}}$.

labels $\{d(\mathcal{R})^i\}$ in which only one of d^i is 1 and the others are zero.

2. Affine Lie Algebras and Wess-Zumino-Witten model

The affine Lie algebras are characterized by the following commutation relations which generalize (C1):

$$[J_n^\alpha, J_m^\beta] = if_{\alpha\beta\gamma} J_{n+m}^\gamma + \tilde{k}n\delta_{m+n,0}\delta^{\alpha\beta} \quad (\text{C8})$$

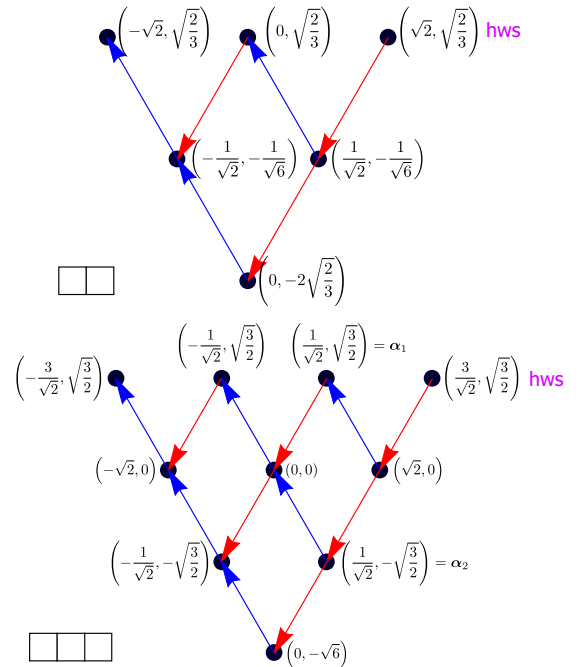


FIG. 16. Weights of **6** and **10**-dimensional representations of $\mathfrak{su}(3)$. The representations **6** and **10** have highest weights (shown as “hws”) with Dynkin labels $(d^1, d^2) = (2, 0)$ and $(3, 0)$, respectively. Red (blue) arrows show the action of the roots (“lowering operators”) $-\alpha^{(1)}$ ($-\alpha^{(2)}$) to the weights (see Fig. 15 for the definitions of $\alpha^{(1,2)}$).

(see, e.g., Refs. [46,93] for physicist-friendly reviews of affine Lie algebras). Physically, (C8) is the algebra of the Fourier modes of the local $SU(N)$ currents $\{J^\alpha(x)\}$ satisfying:

$$[J^\alpha(x), J^\beta(y)] = i f^{\alpha\beta\gamma} J^\gamma(y) \delta(x-y) + \frac{i}{2\pi} \tilde{k} \delta^{\alpha\beta} \partial_x \delta(x-y),$$

$$J^\alpha(x) = \frac{1}{L} \sum_{n \in \mathbb{Z}} e^{-i \frac{2\pi}{L} nx} J_n^\alpha. \quad (C9)$$

The above are anomalous in that the right-hand side contains the central term [which is proportional to $\delta'(x)$] on top of the term expected from the Lie algebra. Obviously, the coefficient \tilde{k} of the central term depends on the normalization of J_n^α and it is convenient to introduce the normalization-independent integer k called the *level* of the affine Lie algebra by

$$\tilde{k} = \frac{|\theta|^2}{2} k,$$

where $|\theta|$ is the length of the highest root (the quantization of k follows, e.g., from the consistency of the path-integral representation of the WZW model). The $|\theta|$ depends on the normalization of the generators and, in $\mathfrak{su}(N)$, a convenient choice is to normalize the N -dimensional hermitian generators $\{J^\alpha\}$ as $\text{Tr}(J^\alpha J^\beta) = \delta^{\alpha\beta}$ which amounts to setting $|\theta| = \sqrt{2}$. Then, we do not have to distinguish between the coefficient \tilde{k} of the central term and the level k ($\in \mathbb{Z}$). The special case $m = n = 0$ of (C8) reduces to (C1), which means that the zero modes $\{J_0^\alpha\}$ form the usual $\mathfrak{su}(N)$ Lie algebra (called the *horizontal subalgebra*).

As a class of CFT with Lie-algebra symmetry, the WZW CFT has the Virasoro generators $\{L_n\}$ which are bilinear in J_n^α (*Sugawara form*) [93,94]:

$$L_n = \frac{1}{|\theta|^2(g^\vee + k)} \sum_\alpha \sum_{m \in \mathbb{Z}} :J_m^\alpha J_{n-m}^\alpha: \quad (C10)$$

where the normal-ordering $:\dots:$ is defined by

$$:J_m^\alpha J_n^\alpha: = \begin{cases} J_m^\alpha J_n^\alpha & \text{when } m < 0 \\ J_n^\alpha J_m^\alpha & \text{when } m \geq 0 \end{cases}.$$

The number g^\vee (the *dual Coxeter number*), which is peculiar to a given Lie algebra, is given by the structure constants as $-f^{\alpha\beta\mu} f^{\alpha\mu\gamma} = |\theta|^2 g^\vee \delta^{\beta\gamma}$ and is equal to N in $\mathfrak{su}(N)$. By a direct calculation, we can show that the above $\{L_n\}$ satisfy the Virasoro algebra

$$[L_m, L_n] = (m-n)L_{m+n} + \frac{1}{12} c(\mathfrak{g}, k) m(m^2 - 1) \delta_{m+n,0} \quad (C11)$$

with the central charge given by

$$c(\mathfrak{g}, k) = \frac{k \dim(\mathfrak{g})}{k + g^\vee} \quad (k = 1, 2, \dots), \quad (C12)$$

which, for $\mathfrak{su}(N)$, reads

$$c(\mathfrak{su}(N), k) = \frac{k(N^2 - 1)}{N + k}. \quad (C13)$$

On top of Eq. (C11), $\{L_n\}$ satisfy the following commutation relations with the generators $\{J_n^\alpha\}$:

$$[L_m, J_n^\alpha] = -n J_{m+n}^\alpha. \quad (C14)$$

In particular,

$$[L_0, J_n^\alpha] = -n J_n^\alpha, \quad [L_0, J_0^\alpha] = 0 \quad (C15)$$

implies that not only L_{-n} ($n > 0$) but also J_{-n}^α increase the eigenvalue of L_0 and that for each eigenvalue of L_0 (i.e., for each level of conformal towers) we have a *reducible* representation of $\mathfrak{su}(N)$ (formed by $\{J_0^\alpha\}$).

In CFTs with extended symmetries, it is convenient to define the *primary states* $|\phi\rangle$ as those annihilated by all J_n^α with positive n :

$$J_n^\alpha |\phi\rangle = 0 \quad (n > 0). \quad (C16)$$

Then, from (C10), $|\phi\rangle$ automatically satisfy the primary condition with respect to the Virasoro algebra [the converse is not true; in that sense, (C16) is stronger than (C17)]:

$$L_n |\phi\rangle = 0 \quad (n > 0),$$

$$L_0 |\phi\rangle = \frac{1}{|\theta|^2(g^\vee + k)} \sum_\alpha J_0^\alpha J_0^\alpha |\phi\rangle$$

$$= \frac{1}{|\theta|^2(g^\vee + k)} \mathcal{C}_2 |\phi\rangle = h_\phi |\phi\rangle, \quad (C17)$$

where J_ϕ^α is a matrix representation of J^α and \mathcal{C}_2 is the quadratic Casimir of $\mathfrak{su}(N)$. All these mean that the primary states of the WZW model transform under the irreducible representations \mathcal{R} of the ordinary $\mathfrak{su}(N)$ spanned by the subset $\{J_0^\alpha\}$:

$$|\phi\rangle = |\mathcal{R}; \mu(\mathcal{R})\rangle \quad (\mu(\mathcal{R}) : \text{weights of } \mathcal{R}),$$

$$J_0^\alpha |\mathcal{R}; \mu(\mathcal{R})\rangle = -J^\alpha(\mathcal{R}) |\mathcal{R}; \mu(\mathcal{R})\rangle$$

$$\times [J^\alpha(\mathcal{R}) : J^\alpha \text{ in representation } \mathcal{R}], \quad (C18)$$

and that the conformal weights h_ϕ are given essentially by the quadratic Casimir \mathcal{C}_2 of \mathcal{R} :

$$h(\mathcal{R}) = \frac{\mathcal{C}_2(\mathcal{R})}{|\theta|^2(g^\vee + k)} \quad (g^\vee = N \text{ for } \mathfrak{su}(N)). \quad (C19)$$

As in other CFTs, these are the lowest states in a given \mathcal{R} -sector and the higher-lying states are generated by applying J_{-n}^α ($n > 0$).

There is a selection rule about the allowed \mathcal{R} for a given level k , which, in terms of the Dynkin labels (d^1, \dots, d^r) [see Eq. (C7)], reads for $\mathfrak{su}(N)$

$$\sum_{i=1}^{N-1} d(\mathcal{R})^i \leq k. \quad (C20)$$

In the level-1 ($k = 1$) $SU(N)$ WZW model which is relevant in this paper, only the vacuum $[1; SU(N)\text{-singlet with } \mathbf{d} = (0, \dots, 0)]$ and the $N - 1$ antisymmetric representations $\mathfrak{aIR}_N(r_0)$ [rank- r_0 antisymmetric tensor with $\mathbf{d} = (0, \dots, 0, \underbrace{1}_{r_0}, 0, \dots, 0)$; $r_0 = 1, \dots, N - 1$] in Sec. II C are

allowed for primary states:

$$C_2 \left(r_0 \left\{ \begin{array}{c} \square \\ \square \\ \square \end{array} \right\} \right) = \frac{N+1}{2N} r_0 (N-r_0) |\boldsymbol{\theta}|^2,$$

$$h \left(r_0 \left\{ \begin{array}{c} \square \\ \square \\ \square \end{array} \right\} \right) = \frac{1}{2N} r_0 (N-r_0) \quad (r_0 = 0, \dots, N-1).$$
(C21)

These N different primary states (fields) correspond to N topologically degenerate ground states of $SU(N)_1$ CSL on a torus. For the selection rule for general \mathfrak{g} , see, e.g., Sec. 3.4 of Ref. [93].

3. Finite-size spectrum

For the clarity of the explanation, we assume $\mathfrak{g} = \mathfrak{su}(N)$ and normalize the generator as $|\boldsymbol{\theta}| = \sqrt{2}$ in this section. In this normalization, the coefficient k of the central term is equal to the level k , and C_2 is given simply by

$$C_2(\mathcal{R}) = \sum_{i,j=1}^{N-1} (\mathbf{d}(\mathcal{R}) + \mathbf{e})_i (A^{-1})^{ij} (\mathbf{d}(\mathcal{R}) + \mathbf{e})_j - \frac{1}{12} N(N^2 - 1),$$

$$\mathbf{e} \equiv \underbrace{(1, 1, \dots, 1)}_{N-1},$$
(C22)

where the matrix A is the Cartan matrix defined in (C4) and $\mathbf{d}(\mathcal{R})$ is the Dynkin labels that characterizes the highest weight $\lambda_{\mathcal{R}}$ of the representation \mathcal{R} by Eq. (C7). When we normalize the N -dimensional generators as $\text{Tr}(J^\alpha J^\beta) = \kappa \delta^{\alpha\beta}$, we need to multiply the right-hand side by κ .

The Hamiltonian of the chiral CFT is given by [46,95]

$$H_{\text{chiral}} = \frac{2\pi}{l} v \left(L_0 - \frac{c}{24} \right) \quad (l : \text{system size}),$$
(C23)

where v is the velocity parameter of the system. As L_0 and c in the level- k $SU(N)$ WZW CFT are given respectively by (C10) and (C13), we obtain

$$H_{\text{chiral}}^{\text{su}(N)} = \frac{2\pi v}{l} \frac{1}{2(N+k)} \sum_{\alpha \in \text{SU}(N)} \left\{ J_0^\alpha J_0^\alpha + 2 \sum_{n=1}^{\infty} J_{-n}^\alpha J_n^\alpha \right\}$$

$$- \frac{\pi v}{12l} \frac{(N^2 - 1)k}{N+k}.$$
(C24)

The results in the previous section show that the Hilbert space in the sector specified by an irreducible representation \mathcal{R} of $\mathfrak{su}(N)$ [\mathcal{R} obeys the selection rule (C20)] consists of the ground (lowest) states with energy

$$\frac{2\pi v}{l} \frac{C_2(\mathcal{R})}{2(N+k)} - \frac{\pi v}{12l} \frac{(N^2 - 1)k}{N+k}$$

and the equally spaced excited states (with the level spacing $2\pi/l$). All these states are labeled by the eigenvalues of L_0 (energy) and $\{H_0^1, \dots, H_0^{N-1}\}$ (weight $\boldsymbol{\mu}$ of horizontal subalgebra $\{J_0^\alpha\}$). As the action of the $\mathfrak{su}(N)$ -generators J_0^α does not change the value of L_0 (i.e., energy) [see Eq. (C15)], each excited level decomposes into a direct sum of several irreducible representations of $\mathfrak{su}(N)$ (Tables IV–XXV shown below give such decompositions).

TABLE IV. $SU(2)_1$ WZW model-tower of states starting from $\mathbf{1}$.

L_0	Order	Irreps / Multiplicities
0	q^0	$\mathbf{1}$ $\mathbf{1}$
1	q^1	$\mathbf{1}$ \square \square
2	q^2	$\mathbf{1}$ $\mathbf{1}$ \oplus $\mathbf{1}$ \square \square
3	q^3	$\mathbf{1}$ $\mathbf{1}$ \oplus $\mathbf{2}$ \square \square
4	q^4	$\mathbf{2}$ $\mathbf{1}$ \oplus $\mathbf{2}$ \square \square \oplus $\mathbf{1}$ \square \square \square
5	q^5	$\mathbf{2}$ $\mathbf{1}$ \oplus $\mathbf{4}$ \square \square \oplus $\mathbf{1}$ \square \square \square
6	q^6	$\mathbf{4}$ $\mathbf{1}$ \oplus $\mathbf{5}$ \square \square \oplus $\mathbf{2}$ \square \square \square
7	q^7	$\mathbf{4}$ $\mathbf{1}$ \oplus $\mathbf{8}$ \square \square \oplus $\mathbf{3}$ \square \square \square

There is a compact way of encoding the information on the structure (i.e., energy, degeneracy, and the Lie-algebraic structure) of the Hilbert space of the WZW CFT. Consider the finite-temperature (T) partition function of the system:

$$Z = \text{Tr}_{\mathcal{R}} e^{-\frac{2\pi}{l} v (L_0 - \frac{c}{24})} = q^{-\frac{c}{24}} \text{Tr}_{\mathcal{R}} q^{L_0} \equiv Z_{\mathcal{R}}(q)$$

$$\times (q \equiv e^{-\frac{2\pi}{l} v}),$$
(C25)

where the subscript \mathcal{R} means that the trace is taken over all the excited states within the \mathcal{R} -sector. Since L_0 takes values $h(\mathcal{R}) + N$ (with N being non-negative integers), if we expand $Z_{\mathcal{R}}(q)$ in a power-series

$$Z_{\mathcal{R}}(q) = q^{h(\mathcal{R}) - \frac{c}{24}} \sum_{N=0}^{\infty} D(N) q^N,$$
(C26)

it immediately gives the degeneracy $D(N)$ of the N th excited state.

In order to know the Lie-algebraic structure, it is convenient to introduce the “fugacities” $\{z_i\}$ for the weight and

TABLE V. $SU(2)_1$ WZW model-tower of states starting from \square .

L_0	Order	Irreps / Multiplicities
0	$q^{1/4}$	$\mathbf{1}$ \square
1	$q^{5/4}$	$\mathbf{1}$ \square
2	$q^{9/4}$	$\mathbf{1}$ \square \oplus $\mathbf{1}$ \square \square
3	$q^{13/4}$	$\mathbf{2}$ \square \oplus $\mathbf{1}$ \square \square
4	$q^{17/4}$	$\mathbf{3}$ \square \oplus $\mathbf{2}$ \square \square
5	$q^{21/4}$	$\mathbf{4}$ \square \oplus $\mathbf{3}$ \square \square
6	$q^{25/4}$	$\mathbf{6}$ \square \oplus $\mathbf{4}$ \square \square \oplus $\mathbf{1}$ \square \square \square
7	$q^{29/4}$	$\mathbf{8}$ \square \oplus $\mathbf{6}$ \square \square \oplus $\mathbf{1}$ \square \square \square

TABLE VI. $SU(3)_1$ WZW model—tower of states starting from \bullet^1 .

L_0	Order	Irreps / Multiplicities
0	q^0	$1 \bullet^1$
1	q^1	$1 \begin{array}{ c c } \hline & 8 \\ \hline \end{array}$
2	q^2	$1 \bullet^1 \oplus 2 \begin{array}{ c c } \hline & 8 \\ \hline \end{array}$
3	q^3	$2 \bullet^1 \oplus 3 \begin{array}{ c c } \hline & 8 \\ \hline \end{array} \oplus 1 \begin{array}{ c c c } \hline & & 10 \\ \hline \end{array} \oplus 1 \begin{array}{ c c c } \hline & & \bar{10} \\ \hline \end{array}$
4	q^4	$3 \bullet^1 \oplus 6 \begin{array}{ c c } \hline & 8 \\ \hline \end{array} \oplus 1 \begin{array}{ c c c } \hline & & 10 \\ \hline \end{array} \oplus 1 \begin{array}{ c c c } \hline & & \bar{10} \\ \hline \end{array} \oplus 1 \begin{array}{ c c c c } \hline & & & 27 \\ \hline \end{array}$
5	q^5	$4 \bullet^1 \oplus 10 \begin{array}{ c c } \hline & 8 \\ \hline \end{array} \oplus 3 \begin{array}{ c c c } \hline & & 10 \\ \hline \end{array} \oplus 3 \begin{array}{ c c c } \hline & & \bar{10} \\ \hline \end{array} \oplus 2 \begin{array}{ c c c c } \hline & & & 27 \\ \hline \end{array}$
6	q^6	$8 \bullet^1 \oplus 16 \begin{array}{ c c } \hline & 8 \\ \hline \end{array} \oplus 5 \begin{array}{ c c c } \hline & & 10 \\ \hline \end{array} \oplus 5 \begin{array}{ c c c } \hline & & \bar{10} \\ \hline \end{array} \oplus 5 \begin{array}{ c c c c } \hline & & & 27 \\ \hline \end{array}$
7	q^7	$10 \bullet^1 \oplus 27 \begin{array}{ c c } \hline & 8 \\ \hline \end{array} \oplus 9 \begin{array}{ c c c } \hline & & 10 \\ \hline \end{array} \oplus 9 \begin{array}{ c c c } \hline & & \bar{10} \\ \hline \end{array} \oplus 8 \begin{array}{ c c c c } \hline & & & 27 \\ \hline \end{array} \oplus 1 \begin{array}{ c c c c c } \hline & & & & \bar{35} \\ \hline \end{array} \oplus 1 \begin{array}{ c c c c c } \hline & & & & 35 \\ \hline \end{array}$

consider the following generalized partition function:

$$\tilde{Z}_{\mathcal{R}}(q; \{z_i\}) = q^{-\frac{c}{24}} \text{Tr}_{\mathcal{R}} \left\{ q^{L_0} \prod_{i=1}^{N-1} z_i^{H_0^i} \right\}, \quad (C27)$$

where \prod_i is over all the $N - 1$ Cartan generators $\{H_0^i\}$ of the $su(N)$ subalgebra $\{J_0^\alpha\}$. Now the coefficient of $q^{N+h(\mathcal{R})-\frac{c}{24}}$ is a polynomial of $z_1^{\mu_1} z_2^{\mu_2} \dots z_{N-1}^{\mu_{N-1}}$ that gives the multiplicity of

TABLE VII. $SU(3)_1$ WZW model—tower of states starting from $\begin{array}{|c|c|} \hline & 3 \\ \hline \end{array}$ (respectively $\begin{array}{|c|} \hline 3 \\ \hline \end{array}$ by conjugation of all IRREPs).

L_0	Order	Irreps / Multiplicities
0	$q^{1/3}$	$1 \begin{array}{ c c } \hline & 3 \\ \hline \end{array}$
1	$q^{4/3}$	$1 \begin{array}{ c c } \hline & 3 \\ \hline \end{array} \oplus 1 \begin{array}{ c c } \hline & \bar{6} \\ \hline \end{array}$
2	$q^{7/3}$	$2 \begin{array}{ c c } \hline & 3 \\ \hline \end{array} \oplus 1 \begin{array}{ c c } \hline & \bar{6} \\ \hline \end{array} \oplus 1 \begin{array}{ c c c } \hline & & 15 \\ \hline \end{array}$
3	$q^{10/3}$	$3 \begin{array}{ c c } \hline & 3 \\ \hline \end{array} \oplus 3 \begin{array}{ c c } \hline & \bar{6} \\ \hline \end{array} \oplus 2 \begin{array}{ c c c } \hline & & 15 \\ \hline \end{array}$
4	$q^{13/3}$	$6 \begin{array}{ c c } \hline & 3 \\ \hline \end{array} \oplus 4 \begin{array}{ c c } \hline & \bar{6} \\ \hline \end{array} \oplus 4 \begin{array}{ c c c } \hline & & 15 \\ \hline \end{array} \oplus 1 \begin{array}{ c c c c } \hline & & & 24 \\ \hline \end{array}$
5	$q^{16/3}$	$9 \begin{array}{ c c } \hline & 3 \\ \hline \end{array} \oplus 8 \begin{array}{ c c } \hline & \bar{6} \\ \hline \end{array} \oplus 1 \begin{array}{ c c c } \hline & & 15' \\ \hline \end{array} \oplus 7 \begin{array}{ c c c } \hline & & 15 \\ \hline \end{array} \oplus 2 \begin{array}{ c c c c } \hline & & & 24 \\ \hline \end{array}$
6	$q^{19/3}$	$15 \begin{array}{ c c } \hline & 3 \\ \hline \end{array} \oplus 12 \begin{array}{ c c } \hline & \bar{6} \\ \hline \end{array} \oplus 1 \begin{array}{ c c c } \hline & & 15' \\ \hline \end{array} \oplus 13 \begin{array}{ c c c } \hline & & 15 \\ \hline \end{array} \oplus 4 \begin{array}{ c c c c } \hline & & & 24 \\ \hline \end{array} \oplus 1 \begin{array}{ c c c c c } \hline & & & & 42 \\ \hline \end{array}$
7	$q^{22/3}$	$22 \begin{array}{ c c } \hline & 3 \\ \hline \end{array} \oplus 21 \begin{array}{ c c } \hline & \bar{6} \\ \hline \end{array} \oplus 3 \begin{array}{ c c c } \hline & & 15' \\ \hline \end{array} \oplus 21 \begin{array}{ c c c } \hline & & 15 \\ \hline \end{array} \oplus 8 \begin{array}{ c c c c } \hline & & & 24 \\ \hline \end{array} \oplus 2 \begin{array}{ c c c c c } \hline & & & & 42 \\ \hline \end{array}$

TABLE VIII. $SU(4)_1$ WZW model—tower of states starting from $\begin{smallmatrix} 1 \\ \bullet \end{smallmatrix}$.

L_0	Order	Irreps / Multiplicities
0	q^0	$\begin{smallmatrix} 1 \\ \bullet \end{smallmatrix}$
1	q^1	$\begin{smallmatrix} 15 \\ 1 \end{smallmatrix}$
2	q^2	$\begin{smallmatrix} 15 \\ 1 \end{smallmatrix} \oplus \begin{smallmatrix} 20' \\ 1 \end{smallmatrix}$
3	q^3	$\begin{smallmatrix} 15 \\ 2 \end{smallmatrix} \oplus \begin{smallmatrix} 20' \\ 1 \end{smallmatrix} \oplus \begin{smallmatrix} 45 \\ 1 \end{smallmatrix} \oplus \begin{smallmatrix} 45 \\ 1 \end{smallmatrix}$
4	q^4	$\begin{smallmatrix} 15 \\ 4 \end{smallmatrix} \oplus \begin{smallmatrix} 20' \\ 4 \end{smallmatrix} \oplus \begin{smallmatrix} 45 \\ 2 \end{smallmatrix} \oplus \begin{smallmatrix} 45 \\ 2 \end{smallmatrix} \oplus \begin{smallmatrix} 84 \\ 1 \end{smallmatrix}$

the weight μ in the N th excited level. In fact, the generalized partition function $\tilde{Z}_{\mathcal{R}}(T, L)$ is nothing but the character of the affine Lie algebra and its expression using the generalized theta function is known explicitly (see, e.g., section 14.4 of Ref. [46] for more details). Tables IV–XXV, which show the contents of irreducible representations appearing at the excited levels of a given \mathcal{R} sector, are obtained in this manner. For example, Table V shows the structure of the Hilbert space of the level-1 $SU(2)$ WZW CFT in the sector of spin-1/2 representation [$h(j = 1/2) = 1/4$] and “Order” denotes q^{L_0} . The degeneracy 2 of the first entry ($q^{1/4}$) is a direct consequence of the doublet level (primary states) constitutes the $j = 1/2$ representation of $\mathfrak{su}(2)$. The third entry from the top implies that the second excited level ($q^{9/4} = q^{1/4+2}$) is sixfold degenerate and decomposes into one $j = 1/2$ ($\begin{smallmatrix} \square \end{smallmatrix}$) and one

TABLE IX. $SU(4)_1$ WZW model—tower of states starting from $\begin{smallmatrix} 4 \\ \square \end{smallmatrix}$ (respectively $\begin{smallmatrix} 4 \\ \square \end{smallmatrix}$ by conjugation of all IRREPs).

L_0	Order	Irreps / Multiplicities
0	$q^{3/8}$	$\begin{smallmatrix} 4 \\ 1 \end{smallmatrix}$
1	$q^{11/8}$	$\begin{smallmatrix} 4 \\ 1 \end{smallmatrix} \oplus \begin{smallmatrix} 20 \\ 1 \end{smallmatrix}$
2	$q^{19/8}$	$\begin{smallmatrix} 4 \\ 2 \end{smallmatrix} \oplus \begin{smallmatrix} 20 \\ 2 \end{smallmatrix} \oplus \begin{smallmatrix} 36 \\ 1 \end{smallmatrix}$
3	$q^{27/8}$	$\begin{smallmatrix} 4 \\ 4 \end{smallmatrix} \oplus \begin{smallmatrix} 20' \\ 1 \end{smallmatrix} \oplus \begin{smallmatrix} 20 \\ 2 \end{smallmatrix} \oplus \begin{smallmatrix} 36 \\ 2 \end{smallmatrix} \oplus \begin{smallmatrix} 60 \\ 1 \end{smallmatrix}$
4	$q^{35/8}$	$\begin{smallmatrix} 4 \\ 7 \end{smallmatrix} \oplus \begin{smallmatrix} 20' \\ 1 \end{smallmatrix} \oplus \begin{smallmatrix} 20 \\ 8 \end{smallmatrix} \oplus \begin{smallmatrix} 36 \\ 5 \end{smallmatrix} \oplus \begin{smallmatrix} 60 \\ 2 \end{smallmatrix} \oplus \begin{smallmatrix} 140 \\ 1 \end{smallmatrix}$

TABLE X. $SU(4)_1$ WZW model—tower of states starting from $\begin{smallmatrix} 6 \\ \square \end{smallmatrix}$.

L_0	Order	Irreps / Multiplicities
0	$q^{1/2}$	$\begin{smallmatrix} 6 \\ 1 \end{smallmatrix}$
1	$q^{3/2}$	$\begin{smallmatrix} 6 \\ 1 \end{smallmatrix} \oplus \begin{smallmatrix} 10 \\ 1 \end{smallmatrix} \oplus \begin{smallmatrix} 10 \\ 1 \end{smallmatrix}$
2	$q^{5/2}$	$\begin{smallmatrix} 6 \\ 3 \end{smallmatrix} \oplus \begin{smallmatrix} 10 \\ 1 \end{smallmatrix} \oplus \begin{smallmatrix} 10 \\ 1 \end{smallmatrix} \oplus \begin{smallmatrix} 64 \\ 1 \end{smallmatrix}$
3	$q^{7/2}$	$\begin{smallmatrix} 6 \\ 4 \end{smallmatrix} \oplus \begin{smallmatrix} 10 \\ 3 \end{smallmatrix} \oplus \begin{smallmatrix} 10 \\ 3 \end{smallmatrix} \oplus \begin{smallmatrix} 64 \\ 3 \end{smallmatrix}$
4	$q^{9/2}$	$\begin{smallmatrix} 6 \\ 9 \end{smallmatrix} \oplus \begin{smallmatrix} 10 \\ 5 \end{smallmatrix} \oplus \begin{smallmatrix} 10 \\ 5 \end{smallmatrix} \oplus \begin{smallmatrix} 50 \\ 1 \end{smallmatrix} \oplus \begin{smallmatrix} 64 \\ 6 \end{smallmatrix} \oplus \begin{smallmatrix} 70 \\ 1 \end{smallmatrix} \oplus \begin{smallmatrix} 70 \\ 1 \end{smallmatrix}$

TABLE XI. $SU(5)_1$ WZW model—tower of states starting from $\begin{smallmatrix} 1 \\ \bullet \end{smallmatrix}$.

L_0	Order	Irreps / Multiplicities
0	q^0	$\begin{smallmatrix} 1 \\ \bullet \end{smallmatrix}$
1	q^1	$\begin{smallmatrix} 24 \\ 1 \end{smallmatrix}$
2	q^2	$\begin{smallmatrix} 24 \\ 1 \end{smallmatrix} \oplus \begin{smallmatrix} 75 \\ 2 \end{smallmatrix}$
3	q^3	$\begin{smallmatrix} 24 \\ 2 \end{smallmatrix} \oplus \begin{smallmatrix} 75 \\ 4 \end{smallmatrix} \oplus \begin{smallmatrix} 126 \\ 2 \end{smallmatrix} \oplus \begin{smallmatrix} 126 \\ 1 \end{smallmatrix}$

TABLE XII. $SU(5)_1$ WZW model—tower of states starting from $\begin{smallmatrix} 5 \\ \square \end{smallmatrix}$ (respectively $\begin{smallmatrix} 5 \\ \square \end{smallmatrix}$ by conjugation of all IRREPs).

L_0	Order	Irreps / Multiplicities
0	$q^{2/5}$	$\begin{smallmatrix} 5 \\ 1 \end{smallmatrix}$
1	$q^{7/5}$	$\begin{smallmatrix} 5 \\ 1 \end{smallmatrix} \oplus \begin{smallmatrix} 45 \\ 1 \end{smallmatrix}$
2	$q^{12/5}$	$\begin{smallmatrix} 5 \\ 2 \end{smallmatrix} \oplus \begin{smallmatrix} 45 \\ 2 \end{smallmatrix} \oplus \begin{smallmatrix} 50 \\ 1 \end{smallmatrix} \oplus \begin{smallmatrix} 70 \\ 1 \end{smallmatrix}$
3	$q^{17/5}$	$\begin{smallmatrix} 5 \\ 4 \end{smallmatrix} \oplus \begin{smallmatrix} 45 \\ 5 \end{smallmatrix} \oplus \begin{smallmatrix} 50 \\ 1 \end{smallmatrix} \oplus \begin{smallmatrix} 70 \\ 2 \end{smallmatrix} \oplus \begin{smallmatrix} 105 \\ 1 \end{smallmatrix} \oplus \begin{smallmatrix} 280 \\ 1 \end{smallmatrix}$

TABLE XIII. $SU(5)_1$ WZW model—tower of states starting

from $\begin{matrix} 10 \\ \square \end{matrix}$ (respectively $\begin{matrix} \bar{10} \\ \square \end{matrix}$ by conjugation of all IRREPs).

L_0	Order	Irreps / Multiplicities
0	$q^{3/5}$	$\begin{matrix} 10 \\ \square \end{matrix}$
1	$q^{8/5}$	$\begin{matrix} 10 \\ \square \end{matrix} \oplus \begin{matrix} 15 \\ \square \end{matrix} \oplus \begin{matrix} 40 \\ \square \end{matrix}$
2	$q^{13/5}$	$\begin{matrix} 10 \\ \square \end{matrix} \oplus \begin{matrix} 15 \\ \square \end{matrix} \oplus \begin{matrix} 40 \\ \square \end{matrix} \oplus \begin{matrix} 175 \\ \square \end{matrix}$
3	$q^{18/5}$	$\begin{matrix} 10 \\ \square \end{matrix} \oplus \begin{matrix} 15 \\ \square \end{matrix} \oplus \begin{matrix} 35 \\ \square \end{matrix} \oplus \begin{matrix} 40 \\ \square \end{matrix} \oplus \begin{matrix} 175 \\ \square \end{matrix} \oplus \begin{matrix} 210 \\ \square \end{matrix}$

$j = 3/2$ ($\begin{matrix} \square & \square & \square \end{matrix}$) representations:

$$2(\begin{matrix} \square & \square & \square \end{matrix}) \oplus 4(\begin{matrix} \square & \square & \square \end{matrix}).$$

For level-1 $\mathfrak{su}(N)$ WZW CFT (for level-1 simply laced \mathfrak{g} , in general), there is a simple way of constructing the Hilbert space in terms of $N - 1$ (i.e., rank- \mathfrak{g}) free bosons (*Frenkel-Kac construction*). First we note that the central charge (C13) of level-1 ($k = 1$) $\mathfrak{su}(N)$ WZW CFT is $c = N - 1$, which clearly suggests its close relation to a system of $N - 1$ free bosons. Below, we quickly sketch how we derive the partition function of the $SU(N)_1$ WZW CFT. To begin with, we prepare a set of $N - 1$ bosons $\phi_i(z)$ ($i = 1, \dots, N - 1$) which are normalized as

$$\langle \phi_i(z)\phi_j(w) \rangle \sim -\delta_{ij} \ln(z - w). \quad (C28)$$

TABLE XIV. $SU(6)_1$ WZW model—tower of states starting from \bullet .

L_0	Order	Irreps / Multiplicities
0	q^0	\bullet
1	q^1	$\begin{matrix} 35 \\ \square \end{matrix}$
2	q^2	$\begin{matrix} 1 \\ \bullet \end{matrix} \oplus \begin{matrix} 2 \\ \square \end{matrix} \oplus \begin{matrix} 35 \\ \square \end{matrix} \oplus \begin{matrix} 189 \\ \square \end{matrix}$
3	q^3	$\begin{matrix} 2 \\ \bullet \end{matrix} \oplus \begin{matrix} 4 \\ \square \end{matrix} \oplus \begin{matrix} 35 \\ \square \end{matrix} \oplus \begin{matrix} 175 \\ \square \end{matrix} \oplus \begin{matrix} 189 \\ \square \end{matrix} \oplus \begin{matrix} 280 \\ \square \end{matrix} \oplus \begin{matrix} 280 \\ \square \end{matrix}$

TABLE XV. $SU(6)_1$ WZW model—tower of states starting from

$\begin{matrix} 6 \\ \square \end{matrix}$ (respectively $\begin{matrix} \bar{6} \\ \square \end{matrix}$ by conjugation of all IRREPs).

L_0	Order	Irreps / Multiplicities
0	$q^{5/12}$	$\begin{matrix} 6 \\ \square \end{matrix}$
1	$q^{17/12}$	$\begin{matrix} 6 \\ \square \end{matrix} \oplus \begin{matrix} 84 \\ \square \end{matrix}$
2	$q^{29/12}$	$\begin{matrix} 6 \\ \square \end{matrix} \oplus \begin{matrix} 84 \\ \square \end{matrix} \oplus \begin{matrix} 120 \\ \square \end{matrix} \oplus \begin{matrix} 210 \\ \square \end{matrix}$
3	$q^{41/12}$	$\begin{matrix} 6 \\ \square \end{matrix} \oplus \begin{matrix} 84 \\ \square \end{matrix} \oplus \begin{matrix} 120 \\ \square \end{matrix} \oplus \begin{matrix} 210 \\ \square \end{matrix} \oplus \begin{matrix} 336 \\ \square \end{matrix} \oplus \begin{matrix} 840 \\ \square \end{matrix}$

The key properties of these bosons are the following operator-product expansions (OPE) [46,95]:

$$\partial_z \phi_i(z) \partial_w \phi_j(w) \sim \frac{-\delta_{ij}}{(z - w)^2},$$

$$\partial_z \phi_i(z) : e^{i v \cdot \phi(w)} : = \partial_z \phi_i(z) : e^{i \sum_j v_j \phi_j(w)} : \sim \frac{-i v_i}{z - w} : e^{i v \cdot \phi(w)} :,$$

$$T(z) : e^{i v \cdot \phi(w)} : = -\frac{1}{2} \sum_{i=1}^{N-1} : (\partial_z \phi_i(z))^2 : e^{i v \cdot \phi(w)} :$$

TABLE XVI. $SU(6)_1$ WZW model—tower of states starting

from $\begin{matrix} 15 \\ \square \end{matrix}$ (respectively $\begin{matrix} \bar{15} \\ \square \end{matrix}$ by conjugation of all IRREPs).

L_0	Order	Irreps / Multiplicities
0	$q^{2/3}$	$\begin{matrix} 15 \\ \square \end{matrix}$
1	$q^{5/3}$	$\begin{matrix} 15 \\ \square \end{matrix} \oplus \begin{matrix} 21 \\ \square \end{matrix} \oplus \begin{matrix} 105 \\ \square \end{matrix}$
2	$q^{8/3}$	$\begin{matrix} 15 \\ \square \end{matrix} \oplus \begin{matrix} 21 \\ \square \end{matrix} \oplus \begin{matrix} 105' \\ \square \end{matrix} \oplus \begin{matrix} 105 \\ \square \end{matrix} \oplus \begin{matrix} 384 \\ \square \end{matrix}$
3	$q^{11/3}$	$\begin{matrix} 15 \\ \square \end{matrix} \oplus \begin{matrix} 21 \\ \square \end{matrix} \oplus \begin{matrix} 105' \\ \square \end{matrix} \oplus \begin{matrix} 105 \\ \square \end{matrix} \oplus \begin{matrix} 210' \\ \square \end{matrix} \oplus \begin{matrix} 384 \\ \square \end{matrix} \oplus \begin{matrix} 1050 \\ \square \end{matrix}$

TABLE XVII. $SU(7)_1$ WZW model—tower of states starting from $\mathbf{1}$.

L_0	Order	Irreps / Multiplicities
0	q^0	$\mathbf{1}$
1	q^1	$\mathbf{48}$
2	q^2	$\mathbf{1} \oplus \mathbf{2} \oplus \mathbf{48} \oplus \mathbf{392}$
3	q^3	$\mathbf{2} \oplus \mathbf{4} \oplus \mathbf{48} \oplus \mathbf{392} \oplus \mathbf{540} \oplus \mathbf{540} \oplus \mathbf{784}$

$$\sim \frac{v^2/2}{(z-w)^2} :e^{iv\cdot\phi(w)}: + \frac{1}{z-w} \partial_w :e^{iv\cdot\phi(w)}: + \dots, \quad (C29)$$

where $v = (v_1, \dots, v_{N-1})$ and $\phi = (\phi_1, \dots, \phi_{N-1})$. Therefore, if we identify

$$H^i(z) = i\partial_z \phi_i(z), \quad E^\alpha(z) = :e^{i\alpha\cdot\phi(w)}: \quad (C30)$$

TABLE XVIII. $SU(7)_1$ WZW model—tower of states starting

from $\mathbf{7}$ (respectively $\bar{\mathbf{7}}$ by conjugation of all IRREPs).

L_0	Order	Irreps / Multiplicities
0	$q^{3/7}$	$\mathbf{7}$
1	$q^{10/7}$	$\mathbf{7} \oplus \mathbf{140}$
2	$q^{17/7}$	$\mathbf{2} \oplus \mathbf{7} \oplus \mathbf{140} \oplus \mathbf{180} \oplus \mathbf{588}$
3	$q^{24/7}$	$\mathbf{4} \oplus \mathbf{7} \oplus \mathbf{5} \oplus \mathbf{140} \oplus \mathbf{180} \oplus \mathbf{490} \oplus \mathbf{588} \oplus \mathbf{840} \oplus \mathbf{2016}$

TABLE XIX. $SU(7)_1$ WZW model—tower of states starting

from $\mathbf{21}$ (respectively $\bar{\mathbf{21}}$ by conjugation of all IRREPs).

L_0	Order	Irreps / Multiplicities
0	$q^{5/7}$	$\mathbf{21}$
1	$q^{12/7}$	$\mathbf{1} \oplus \mathbf{28} \oplus \mathbf{224}$
2	$q^{19/7}$	$\mathbf{3} \oplus \mathbf{28} \oplus \mathbf{224} \oplus \mathbf{490} \oplus \mathbf{735}$
3	$q^{26/7}$	$\mathbf{5} \oplus \mathbf{3} \oplus \mathbf{28} \oplus \mathbf{5} \oplus \mathbf{224} \oplus \mathbf{490} \oplus \mathbf{735} \oplus \mathbf{756} \oplus \mathbf{3402}$

(all the roots α have the length $|\alpha| = \sqrt{2}$), they satisfy the OPEs expected for the generators of $k=1$ $\mathfrak{su}(N)$ (with scaling dimension 1) [46,93]:

$$H^i(z)H^j(w) \sim \frac{\delta_{ij}}{(z-w)^2},$$

$$H^i(z)E^\alpha(w) \sim \frac{\alpha_i}{z-w} E_\alpha(w),$$

$$E^\alpha(z)E^\beta(w) \sim (z-w)^{\alpha\cdot\beta} E^{\alpha+\beta}(w) + i(z-w)^{\alpha\cdot\beta+1} \alpha\cdot\partial_w \phi(w) E^{\alpha+\beta}(w) \quad (C31)$$

[in $\mathfrak{su}(N)$ with $|\alpha| = \sqrt{2}$, $\alpha\cdot\beta = -1$ when $\alpha + \beta$ is a root and $\alpha \neq -\beta$, and $\alpha\cdot\beta = -2$ when $\alpha = -\beta$]. This suggests that we can construct the Hilbert space of the $k=1$ $SU(N)$ WZW CFT by applying $H^i(z) = i\partial_z \phi_i(z)$ ($i = 1, \dots, N-1$) repeatedly to the bosonic primary states $|\mu\rangle \equiv |\mu_1, \dots, \mu_{N-1}\rangle = :e^{i\mu\cdot\phi(0)}: |0\rangle$ [with μ being the weights of $\mathfrak{su}(N)$], that has the eigenvalue $L_0|\mu\rangle = \mu^2/2|\mu\rangle$. The summation over all the possible excited states (with the mode $E_n = (2\pi/l)n$ being occupied with N_n bosons) of the i th linearly dispersive boson above the primary state $|\mu\rangle$ yields the partial partition function

$$e^{-\frac{2\pi v}{7l} \frac{1}{2} \mu_i^2 z_i^{\mu_i}} \prod_{n=1}^{\infty} \left\{ \sum_{N_n=0}^{\infty} e^{-\frac{2\pi v}{7l} n N_n} \right\} = q^{\frac{1}{2} \mu_i^2} z_i^{\mu_i} / \prod_{n=1}^{\infty} (1 - q^n),$$

which is to be combined together for all $N-1$ bosons yielding $q^{\frac{1}{2} \mu^2} \prod_{i=1}^{N-1} z_i^{\mu_i} \prod_{n=1}^{\infty} (1 - q^n)^{N-1}$. As the application of the other generators $E^\alpha(z)$ changes the “weight” of the primary states as $|\mu\rangle \rightarrow |\mu + \alpha\rangle$, all these bosonic conformal towers specified by weights μ that are related to each other by translation by α must be regarded as belonging to the same WZW conformal tower. In $\mathfrak{su}(3)$, for instance, the weights μ on the root lattice all together constitute a *single* WZW tower of the identity representation $\mathbf{1}$ (see Fig. 15). Summing up the partial

TABLE XX. $SU(7)_1$ WZW model—tower of states starting from $\begin{array}{|c|} \hline \square \\ \hline \end{array}$ (respectively $\begin{array}{|c|} \hline \overline{\square} \\ \hline \end{array}$ by conjugation of all IRREPs).

L_0	Order	Irreps / Multiplicities
0	q	$\begin{array}{ c } \hline \square \\ \hline \end{array}$ (35)
1	q	$\begin{array}{ c } \hline \square \\ \hline \end{array}$ (35) \oplus $\begin{array}{ c c } \hline \square & \square \\ \hline \end{array}$ (112) \oplus $\begin{array}{ c c c } \hline \square & \square & \square \\ \hline \end{array}$ (210)
2	q	$\begin{array}{ c } \hline \square \\ \hline \end{array}$ (3) \oplus $\begin{array}{ c c } \hline \square & \square \\ \hline \end{array}$ (2) \oplus $\begin{array}{ c c c } \hline \square & \square & \square \\ \hline \end{array}$ (1) \oplus $\begin{array}{ c c c c } \hline \square & \square & \square & \square \\ \hline \end{array}$ (196) \oplus $\begin{array}{ c c c } \hline \square & \square & \square \\ \hline \end{array}$ (2) \oplus $\begin{array}{ c c c c } \hline \square & \square & \square & \square \\ \hline \end{array}$ (1) \oplus $\begin{array}{ c c c c c } \hline \square & \square & \square & \square & \square \\ \hline \end{array}$ (1323)
3	q	$\begin{array}{ c } \hline \square \\ \hline \end{array}$ (6) \oplus $\begin{array}{ c } \hline \square \\ \hline \end{array}$ (1) \oplus $\begin{array}{ c c c } \hline \square & \square & \square \\ \hline \end{array}$ (84) \oplus $\begin{array}{ c c c c } \hline \square & \square & \square & \square \\ \hline \end{array}$ (4) \oplus $\begin{array}{ c c c } \hline \square & \square & \square \\ \hline \end{array}$ (1) \oplus $\begin{array}{ c c c c } \hline \square & \square & \square & \square \\ \hline \end{array}$ (196) \oplus $\begin{array}{ c c c c } \hline \square & \square & \square & \square \\ \hline \end{array}$ (5) \oplus $\begin{array}{ c c c c } \hline \square & \square & \square & \square \\ \hline \end{array}$ (1) \oplus $\begin{array}{ c c c c c } \hline \square & \square & \square & \square & \square \\ \hline \end{array}$ (378) \oplus $\begin{array}{ c c c c c } \hline \square & \square & \square & \square & \square \\ \hline \end{array}$ (1) \oplus $\begin{array}{ c c c c c c } \hline \square & \square & \square & \square & \square & \square \\ \hline \end{array}$ (1260) \oplus $\begin{array}{ c c c c c } \hline \square & \square & \square & \square & \square \\ \hline \end{array}$ (3) \oplus $\begin{array}{ c c c c c } \hline \square & \square & \square & \square & \square \\ \hline \end{array}$ (1) \oplus $\begin{array}{ c c c c c c c } \hline \square & \square & \square & \square & \square & \square & \square \\ \hline \end{array}$ (3024)

partition functions for those “equivalent” μ , we obtain the partition function of $k = 1$ $SU(N)$ WZW CFT (see Sec. 15.6 of Ref. [46] for more details):

$$\tilde{Z}_{\mathcal{R}}(q; \{z_i\}) \equiv \frac{q^{-\frac{N-1}{24}}}{\prod_{n=1}^{\infty} (1 - q^n)^{N-1}}$$

$$\times \left\{ \sum_{\mu \in \lambda_{\mathcal{R}} + \Lambda_r} q^{\frac{1}{2}\mu^2} \left(\prod_{i=1}^{N-1} z_i^{\mu_i} \right) \right\}, \quad (C32)$$

where $\lambda_{\mathcal{R}}$ is the highest weight of the representation \mathcal{R} and the summation is taken over all the points μ of the weight lattice Λ_w which are equivalent to $\lambda_{\mathcal{R}}$ modulo the root lattice

TABLE XXI. $SU(8)_1$ WZW model—tower of states starting from \bullet .



L_0	Order	Irreps / Multiplicities
0	q^0	\bullet (1)
1	q^1	$\begin{array}{ c } \hline \bullet \\ \hline \end{array}$ (63)
2	q^2	\bullet (1) \oplus $\begin{array}{ c } \hline \bullet \\ \hline \end{array}$ (2) \oplus $\begin{array}{ c } \hline \bullet \\ \hline \end{array}$ (1) \oplus $\begin{array}{ c } \hline \bullet \\ \hline \end{array}$ (63) \oplus $\begin{array}{ c } \hline \bullet \\ \hline \end{array}$ (720)
3	q^3	\bullet (2) \oplus \bullet (1) \oplus $\begin{array}{ c } \hline \bullet \\ \hline \end{array}$ (4) \oplus $\begin{array}{ c } \hline \bullet \\ \hline \end{array}$ (2) \oplus $\begin{array}{ c } \hline \bullet \\ \hline \end{array}$ (1) \oplus $\begin{array}{ c } \hline \bullet \\ \hline \end{array}$ (1) \oplus $\begin{array}{ c } \hline \bullet \\ \hline \end{array}$ (1) \oplus $\begin{array}{ c } \hline \bullet \\ \hline \end{array}$ (63) \oplus $\begin{array}{ c } \hline \bullet \\ \hline \end{array}$ (720) \oplus $\begin{array}{ c } \hline \bullet \\ \hline \end{array}$ (945) \oplus $\begin{array}{ c } \hline \bullet \\ \hline \end{array}$ (1) \oplus $\begin{array}{ c } \hline \bullet \\ \hline \end{array}$ (1) \oplus $\begin{array}{ c } \hline \bullet \\ \hline \end{array}$ (945) \oplus $\begin{array}{ c } \hline \bullet \\ \hline \end{array}$ (1) \oplus $\begin{array}{ c } \hline \bullet \\ \hline \end{array}$ (2352)






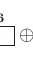



TABLE XXII. $SU(8)_1$ WZW model—tower of states starting from \square (respectively $\overline{\square}$ by conjugation of all IRREPs).

$\begin{array}{|c|} \hline \square \\ \hline \end{array}$ (8) (respectively $\begin{array}{|c|} \hline \overline{\square} \\ \hline \end{array}$ by conjugation of all IRREPs).

L_0	Order	Irreps / Multiplicities
0	$q^{7/16}$	$\begin{array}{ c } \hline \square \\ \hline \end{array}$ (8)
1	$q^{23/16}$	$\begin{array}{ c } \hline \square \\ \hline \end{array}$ (1) \oplus $\begin{array}{ c } \hline \square \\ \hline \end{array}$ (8) \oplus $\begin{array}{ c } \hline \square \\ \hline \end{array}$ (1) \oplus $\begin{array}{ c } \hline \square \\ \hline \end{array}$ (216)
2	$q^{39/16}$	$\begin{array}{ c } \hline \square \\ \hline \end{array}$ (2) \oplus $\begin{array}{ c } \hline \square \\ \hline \end{array}$ (8) \oplus $\begin{array}{ c } \hline \square \\ \hline \end{array}$ (2) \oplus $\begin{array}{ c } \hline \square \\ \hline \end{array}$ (1) \oplus $\begin{array}{ c } \hline \square \\ \hline \end{array}$ (1) \oplus $\begin{array}{ c } \hline \square \\ \hline \end{array}$ (216) \oplus $\begin{array}{ c } \hline \square \\ \hline \end{array}$ (280) \oplus $\begin{array}{ c } \hline \square \\ \hline \end{array}$ (1) \oplus $\begin{array}{ c } \hline \square \\ \hline \end{array}$ (1344)

TABLE XXIII. $SU(8)_1$ WZW model—tower of states starting

from  (respectively  by conjugation of all IRREPs).



L_0	Order	Irreps / Multiplicities
0	$q^{3/4}$	
1	$q^{7/4}$	 \oplus  \oplus 
2	$q^{11/4}$	 \oplus  \oplus  \oplus  \oplus 

Λ_r spanned by the simple roots $\{\alpha^{(i)}\}$. Since such μ are given explicitly as

$$\mu = \lambda_{\mathcal{R}} + \sum_{i=1}^{N-1} n_i \alpha^{(i)}, \quad (\text{C33})$$

we can trade the sum over $\mu \in \lambda_{\mathcal{R}} + \Lambda_r$ with that over the $N - 1$ integers $\{n_i\}$. By construction, the representations \mathcal{R} allowed as primary in the $SU(N)_1$ WZW CFT, which is

 TABLE XXIV. $SU(8)_1$ WZW model—tower of states starting

from  (respectively  by conjugation of all IRREPs).



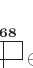
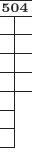




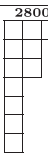






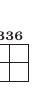
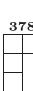
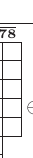
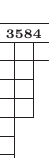
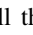
L_0	Order	Irreps / Multiplicities
0	$q^{15/16}$	
1	$q^{31/16}$	 \oplus  \oplus 
2	$q^{47/16}$	 \oplus  \oplus  \oplus  \oplus 

 TABLE XXV. $SU(8)_1$ WZW model—tower of states starting

from .

L_0	Order	Irreps / Multiplicities
0	q^1	
1	q^2	 \oplus  \oplus 
2	q^3	 \oplus  \oplus  \oplus  \oplus  \oplus 

relevant in this paper, are restricted to the points of Λ_w within the unit cell of Λ_r . As all those \mathcal{R} have the Dynkin labels $\sum_{i=1}^{N-1} d(\mathcal{R})^i = 0, 1$, this selection rule is consistent with the general one (C20). For instance, in order to obtain the partition function for $\mathcal{R} = \mathbf{3}$ () of $\mathfrak{su}(3)$, we sum over all the red points in Fig. 15 connected to the point $\omega_{(1)}$ (i.e., the highest weight of $\mathbf{3}$) by the translation generated by two simple roots $\alpha^{(1)}$ and $\alpha^{(2)}$ (red and blue arrows, respectively); the three inequivalent points in the hatched “unit cell” correspond to the three primary fields ϕ_1 (singlet vacuum), ϕ_3 , and $\phi_{\bar{3}}$ allowed in level-1 $\mathfrak{su}(3)$.

APPENDIX D: NOTES ON FINITE SIZE EFFECTS IN ED OF PERIODIC CLUSTERS

1. Antisymmetric vs completely symmetric IRREPS

In the range $\phi \in [0, \pi]$, both J_1 and J_2 couplings are antiferromagnetic but the amplitude J_R of the (real) three-site permutation changes sign, from positive to negative, at $\phi = \pi/2$. Although a negative J_R equally favors both, the completely symmetric multiplet (ferromagnetic) as well as the *completely* antisymmetric multiplet on any triangle (see Appendix A), on finite (periodic) clusters (with $N_s > N$), it strongly favors the ferromagnetic state with respect to the antisymmetric (antiferromagnetic) states of $aLR_N(r_0)$. In fact, a three-site permutation on a triangle with $J_R < 0$ cannot accommodate the complicated sign structure of antiferromagnetic states. Note also that the energy difference is *macroscopic*, in the sense that it scales with the number of sites N_s . At $\phi = \pi/2$ where J_R vanishes and the antiferromagnetic couplings J_1 and J_2 are finite, we observe the reverse, namely, a macroscopic energy penalty for the ferromagnetic state with respect to the antiferromagnetic states.

TABLE XXVI. $SU(3)_1$ WZW model—the direct product of the conformal tower of the $\begin{smallmatrix} 3 \\ \square \end{smallmatrix}$ primary (left: see Table VII in Appendix C) with $\begin{smallmatrix} 3 \\ \square \end{smallmatrix}$ gives a new tower (right) with a tripling of the number of states in each Virasoro level indexed by L_0 .

L_0	$\begin{smallmatrix} 3 \\ \square \end{smallmatrix}$ tower	$\begin{smallmatrix} 3 \\ \square \end{smallmatrix}$ tower \otimes $\begin{smallmatrix} 3 \\ \square \end{smallmatrix}$
0	$\begin{smallmatrix} 1 & 3 \\ \square & \square \end{smallmatrix}$	$\begin{smallmatrix} 1 & 1 & 1 \\ \bullet & \oplus & 1 \\ \square & \oplus & \square \end{smallmatrix}$
1	$\begin{smallmatrix} 1 & 3 \\ \square & \square \end{smallmatrix} \oplus \begin{smallmatrix} 1 & 6 \\ \square & \square \end{smallmatrix}$	$\begin{smallmatrix} 1 & 1 & 2 \\ \bullet & \oplus & 2 \\ \square & \oplus & \square \end{smallmatrix} \oplus \begin{smallmatrix} 1 & 10 \\ \square & \square \end{smallmatrix}$
2	$\begin{smallmatrix} 2 & 3 \\ \square & \square \end{smallmatrix} \oplus \begin{smallmatrix} 1 & 6 \\ \square & \square \end{smallmatrix} \oplus \begin{smallmatrix} 1 & 15 \\ \square & \square \end{smallmatrix}$	$\begin{smallmatrix} 2 & 1 & 4 \\ \bullet & \oplus & 4 \\ \square & \oplus & \square \end{smallmatrix} \oplus \begin{smallmatrix} 1 & 10 \\ \square & \square \end{smallmatrix} \oplus \begin{smallmatrix} 1 & 10 \\ \square & \square \end{smallmatrix} \oplus \begin{smallmatrix} 1 & 27 \\ \square & \square \end{smallmatrix}$
3	$\begin{smallmatrix} 3 & 3 \\ \square & \square \end{smallmatrix} \oplus \begin{smallmatrix} 3 & 6 \\ \square & \square \end{smallmatrix} \oplus \begin{smallmatrix} 2 & 15 \\ \square & \square \end{smallmatrix}$	$\begin{smallmatrix} 3 & 1 & 8 \\ \bullet & \oplus & 8 \\ \square & \oplus & \square \end{smallmatrix} \oplus \begin{smallmatrix} 2 & 10 \\ \square & \square \end{smallmatrix} \oplus \begin{smallmatrix} 3 & 10 \\ \square & \square \end{smallmatrix} \oplus \begin{smallmatrix} 2 & 27 \\ \square & \square \end{smallmatrix}$

This is clearly evidenced in Fig. 17, showing the energy difference $E_a(N_s) - E_F(N_s)$ versus N_s , for $\theta = \pi/4$, and $N = 4$ and $N = 8$. Then, one can argue that a transition from a spin liquid phase (or several spin liquid phases) and the ferromagnetic phase should occur between $\phi = \pi/2$ and $\phi = \pi$.

2. Finite size effects in low-energy spectra

As seen in Appendix A, for a given system size N_s (multiple of N), the spectrum of the $SU(N)$ model includes all $SU(N')$ spectra, $N' < N$. In the frustrated antiferromagnetic regime where a $SU(N)$ chiral spin liquid (or a singlet cluster state) is expected, $SU(M)$ singlets (forming a higher quadratic

TABLE XXVII. $SU(4)_1$ WZW model—the direct product of the conformal tower of the $\begin{smallmatrix} 4 \\ \square \end{smallmatrix}$ primary (left: see Table IX in Appendix C) with $\begin{smallmatrix} 4 \\ \square \end{smallmatrix}$ gives a new tower (right) with a quadrupling of the number of states in each Virasoro level indexed by L_0 .

L_0	$\begin{smallmatrix} 4 \\ \square \end{smallmatrix}$ tower	$\begin{smallmatrix} 4 \\ \square \end{smallmatrix}$ tower \otimes $\begin{smallmatrix} 4 \\ \square \end{smallmatrix}$
0	$\begin{smallmatrix} 1 & 4 \\ \square & \square \end{smallmatrix}$	$\begin{smallmatrix} 1 & 1 & 1 \\ \bullet & \oplus & 1 \\ \square & \oplus & \square \end{smallmatrix}$
1	$\begin{smallmatrix} 1 & 4 \\ \square & \square \end{smallmatrix} \oplus \begin{smallmatrix} 1 & 20 \\ \square & \square \end{smallmatrix}$	$\begin{smallmatrix} 1 & 1 & 2 \\ \bullet & \oplus & 2 \\ \square & \oplus & \square \end{smallmatrix} \oplus \begin{smallmatrix} 1 & 20' \\ \square & \square \end{smallmatrix} \oplus \begin{smallmatrix} 1 & 45 \\ \square & \square \end{smallmatrix}$
2	$\begin{smallmatrix} 2 & 4 \\ \square & \square \end{smallmatrix} \oplus \begin{smallmatrix} 2 & 20 \\ \square & \square \end{smallmatrix} \oplus \begin{smallmatrix} 1 & 36 \\ \square & \square \end{smallmatrix}$	$\begin{smallmatrix} 2 & 1 & 5 \\ \bullet & \oplus & 5 \\ \square & \oplus & \square \end{smallmatrix} \oplus \begin{smallmatrix} 2 & 20' \\ \square & \square \end{smallmatrix} \oplus \begin{smallmatrix} 1 & 45 \\ \square & \square \end{smallmatrix} \oplus \begin{smallmatrix} 2 & 45 \\ \square & \square \end{smallmatrix} \oplus \begin{smallmatrix} 1 & 84 \\ \square & \square \end{smallmatrix}$
3	$\begin{smallmatrix} 4 & 4 \\ \square & \square \end{smallmatrix} \oplus \begin{smallmatrix} 1 & 20' \\ \square & \square \end{smallmatrix} \oplus \begin{smallmatrix} 4 & 20 \\ \square & \square \end{smallmatrix} \oplus \begin{smallmatrix} 2 & 36 \\ \square & \square \end{smallmatrix}$ $\oplus \begin{smallmatrix} 1 & 60 \\ \square & \square \end{smallmatrix}$	$\begin{smallmatrix} 4 & 1 & 10 \\ \bullet & \oplus & 10 \\ \square & \oplus & \square \end{smallmatrix} \oplus \begin{smallmatrix} 5 & 20' \\ \square & \square \end{smallmatrix} \oplus \begin{smallmatrix} 1 & 35 \\ \square & \square \end{smallmatrix} \oplus \begin{smallmatrix} 3 & 45 \\ \square & \square \end{smallmatrix} \oplus \begin{smallmatrix} 5 & 45 \\ \square & \square \end{smallmatrix}$ $\oplus \begin{smallmatrix} 2 & 84 \\ \square & \square \end{smallmatrix} \oplus \begin{smallmatrix} 1 & 175 \\ \square & \square \end{smallmatrix}$

TABLE XXVIII. $SU(4)_1$ WZW model—the direct product of the conformal tower of the $\begin{array}{|c|} \hline 6 \\ \hline \end{array}$ primary (left: see Table X in Appendix C) with $\begin{array}{|c|} \hline 6 \\ \hline \end{array}$ gives a new tower (right) with a multiplicative factor 6 of the number of states in each Virasoro level indexed by m .

L_0	$\begin{array}{ c } \hline 6 \\ \hline \end{array}$ tower	$\begin{array}{ c } \hline 6 \\ \hline \end{array}$ tower \otimes $\begin{array}{ c } \hline 6 \\ \hline \end{array}$
0	$\begin{array}{ c } \hline 1 \\ \hline \end{array}$	$\begin{array}{ c } \hline 1 \\ \hline \end{array} \oplus \begin{array}{ c } \hline 1 \\ \hline \end{array} \oplus \begin{array}{ c } \hline 1 \\ \hline \end{array}$
1	$\begin{array}{ c } \hline 1 \\ \hline \end{array} \oplus \begin{array}{ c } \hline 1 \\ \hline \end{array} \oplus \begin{array}{ c } \hline 1 \\ \hline \end{array}$	$\begin{array}{ c } \hline 1 \\ \hline \end{array} \oplus \begin{array}{ c } \hline 3 \\ \hline \end{array} \oplus \begin{array}{ c } \hline 1 \\ \hline \end{array} \oplus \begin{array}{ c } \hline 1 \\ \hline \end{array} \oplus \begin{array}{ c } \hline 1 \\ \hline \end{array}$
2	$\begin{array}{ c } \hline 3 \\ \hline \end{array} \oplus \begin{array}{ c } \hline 1 \\ \hline \end{array} \oplus \begin{array}{ c } \hline 1 \\ \hline \end{array} \oplus \begin{array}{ c } \hline 1 \\ \hline \end{array} \oplus \begin{array}{ c } \hline 1 \\ \hline \end{array}$	$\begin{array}{ c } \hline 3 \\ \hline \end{array} \oplus \begin{array}{ c } \hline 6 \\ \hline \end{array} \oplus \begin{array}{ c } \hline 4 \\ \hline \end{array} \oplus \begin{array}{ c } \hline 2 \\ \hline \end{array} \oplus \begin{array}{ c } \hline 2 \\ \hline \end{array} \oplus \begin{array}{ c } \hline 1 \\ \hline \end{array} \oplus \begin{array}{ c } \hline 1 \\ \hline \end{array}$
3	$\begin{array}{ c } \hline 4 \\ \hline \end{array} \oplus \begin{array}{ c } \hline 3 \\ \hline \end{array} \oplus \begin{array}{ c } \hline 3 \\ \hline \end{array} \oplus \begin{array}{ c } \hline 3 \\ \hline \end{array}$	$\begin{array}{ c } \hline 4 \\ \hline \end{array} \oplus \begin{array}{ c } \hline 13 \\ \hline \end{array} \oplus \begin{array}{ c } \hline 7 \\ \hline \end{array} \oplus \begin{array}{ c } \hline 6 \\ \hline \end{array} \oplus \begin{array}{ c } \hline 6 \\ \hline \end{array} \oplus \begin{array}{ c } \hline 3 \\ \hline \end{array} \oplus \begin{array}{ c } \hline 3 \\ \hline \end{array}$

Casimir $SU(N)$ IRREP, $M < N$ also divider of N_s , may compete with the expected $SU(N)$ singlet GS of the $SU(N)$ model. We have observed this effect in Fig. 2 for $N = 8, 9, 10$ (with $N_s = 16, 18, 20$ and $M = 4, 6, 5$, respectively) for $\theta = \pi/4$ and small ϕ . For instance, for $N_s = 16$ and $N = 8$, the high Casimir IRREP [44440000] has energy given by Fig. 2(c) which is smaller at $\phi = 0$ than the one of the $SU(8)$ singlet subspace in Fig. 2(g).

Here we argue that such a behavior is in fact a finite size effect occurring when $N_s < N^2$. To illustrate it we compare in Fig. 18 the low-energy spectra of the $N = 4$ model at $\theta = \pi/4$, versus ϕ , on 8-site and 16-site clusters. For $N_s = 8$, we observe that the lowest energies of the $SU(4)$ singlets and those of the higher Casimir IRREP [4400] (also $SU(2)$ singlets) are comparable. In contrast, for $N_s = 16$, a clear

energy separation is seen between the lowest energy states of the higher Casimir [8800] IRREP (also $SU(2)$ singlets) and the lowest $SU(4)$ singlets.

APPENDIX E: DETAILS ON MPO-MPS IMPLEMENTATION

This section describes how to cast a Slater determinant, $|\Psi\rangle = \prod_{k,\sigma} d_{k\sigma}^\dagger |0\rangle$, into an MPS with conserved spin symmetry. We elaborate our implementation for $N = 2$; the generalization to larger N is straightforward. For spin-1/2 fermions, the standard approach to express a single-particle

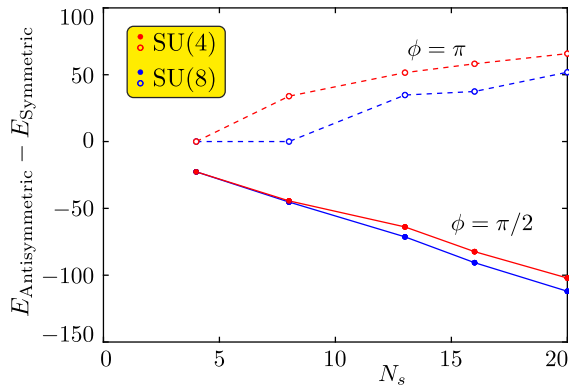


FIG. 17. Energy difference between the ground state of the antisymmetric IRREP $aR_N(r_0)$ and the completely symmetric (ferromagnetic) state for $\theta = \pi/4$, $N = 4$ (red) and $N = 8$ (blue), $\phi = \pi/2$ (filled symbols) and $\phi = \pi$ (open symbols). In all cases, the energy difference scales approximately linearly with N_s , revealing a macroscopic energy difference.

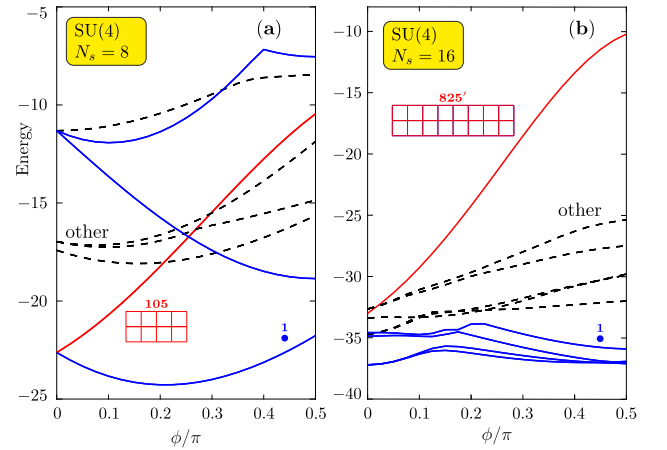


FIG. 18. Low-energy spectra of the $SU(4)$ model computed on 8-site (a) and 16-site (b) periodic clusters at $\theta = \pi/4$, plotted vs ϕ . A few of the lowest energies of the $SU(4)$ singlet subspace are shown (in blue) on both panels as well as the lowest energy (in red) within the subspace of the higher Casimir [4400] (or **105**) (a) and [8800] (or **825'**) (b) IRREPs, which can also be viewed as $SU(2)$ singlets. Other lowest-energy excitations are also shown for completeness.

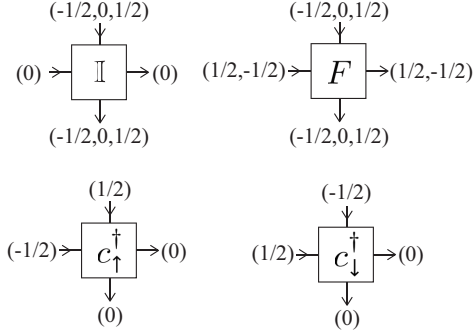


FIG. 19. Graphical representation of MPO matrix elements with U(1) spin symmetry for spin-1/2 fermions. Numbers in brackets indicate the possible values of S_z quantum numbers, 0, $-1/2$ and $1/2$ representing the $|\uparrow\rangle$, $|\downarrow\rangle$ and $|\uparrow\rangle$ at each physical site, respectively. Double occupancy, $|\uparrow\downarrow\rangle$, is excluded.

$$d_{k\sigma}^\dagger = (0 \quad 1) \left[\prod_{j=1}^L \left(\tilde{A}_{k\sigma, 2j-1} \sigma_{2j-1}^+ \otimes \mathbb{1}_{2j} + \tilde{A}_{k\sigma, 2j} \sigma_{2j}^+ \otimes \sigma_{2j-1}^z \right) \right] \begin{pmatrix} 1 \\ 0 \end{pmatrix}. \quad (\text{E3})$$

We can identify $\sigma_{2j-1}^+ \otimes \mathbb{1}_{2j}$ with $c_{j,\uparrow}^\dagger$, $\sigma_{2j-1}^z \otimes \sigma_{2j}^+$ with $c_{j,\downarrow}^\dagger$, and $F_j = \sigma_{2j-1}^z \otimes \sigma_{2j}^z$ with the parity operator to account for anticommutation of different sites. In fact, we can always write the MPO in this spinful fermion basis, regardless of the number of fermion species, i.e.,

$$d_{k\sigma}^\dagger = (0 \quad 1) \left[\prod_{j=1}^L \left(\tilde{A}_{k\sigma, j} c_{j\sigma}^\dagger \quad F \right) \right] \begin{pmatrix} 1 \\ 0 \end{pmatrix}. \quad (\text{E4})$$

This facilitates working with U(1) or SU(N) spin symmetry as each tensor index can be associated with a specific quantum number (see Fig. 19). With U(1) spin symmetry, one can fuse the virtual indices at boundaries of each pair of MPOs to be $S_z = 0$ (see Fig. 20), the resulting MPS $|\Psi\rangle$ also has $S_z = 0$. In the same way, one can easily impose SU(2) spin symmetry to target spin-singlet states, provided an efficient tensor network implementation to handle Clebsch-Gordan coefficients [76,98–100]. We use QSpace for this purpose [76,77].

In Figs. 21(b) and 21(c), we plot the ESs obtained from the parton construction on a 4×12 cylinder. This demonstrates the efficacy of our parton approach, as we are able to prepare trial states in distinct topological sectors for iDMRG using a relatively small size cylinder. Additionally,

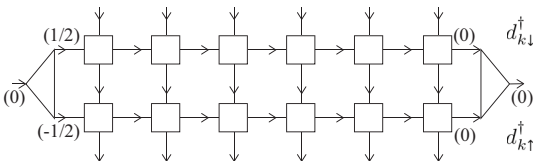


FIG. 20. Graphical representation of fusing edge virtual indices of two MPOs, d_{k1}^\dagger and d_{k2}^\dagger .

operator $d_{k\sigma}^\dagger$ is to map the L -site spinful fermions onto a $2L$ -site pseudospin-1/2 chain using the Jordan–Wigner transformation [63,96,97], namely,

$$\begin{aligned} c_{\ell,\uparrow}^\dagger &\rightarrow \sigma_1^z \cdots \sigma_{2\ell-2}^z \sigma_{2\ell-1}^+, \\ c_{\ell,\downarrow}^\dagger &\rightarrow \sigma_1^z \cdots \sigma_{2\ell-2}^z \sigma_{2\ell-1}^z \sigma_{2\ell}^+. \end{aligned} \quad (\text{E1})$$

And, $d_{k\sigma}^\dagger = \sum_{m,n} A_{m,n}(k) c_{m,n,\sigma}^\dagger = \sum_{\ell} \tilde{A}_{k\sigma,\ell} c_{\ell\sigma}^\dagger$ can be read as an MPO acting on the spin-1/2 chain

$$d_{k\sigma}^\dagger = (0 \quad 1) \left[\prod_{\ell=1}^{2L} \left(\tilde{A}_{k\sigma,\ell} \sigma_{\ell}^+ \quad \sigma_{\ell}^z \right) \right] \begin{pmatrix} 1 \\ 0 \end{pmatrix}. \quad (\text{E2})$$

For our purpose, we would like to block $2\ell - 1$ and 2ℓ sites together, which leads to

imposing SU(2) symmetry constraint leads to an intriguing consequence: if the state is in the topologically nontrivial sector, there are multiple degenerate branches in the ES [see Fig. 21(c)]. This has also been observed in the SU(2) iPEPS simulations previously [44,49,83], and was attributed to the

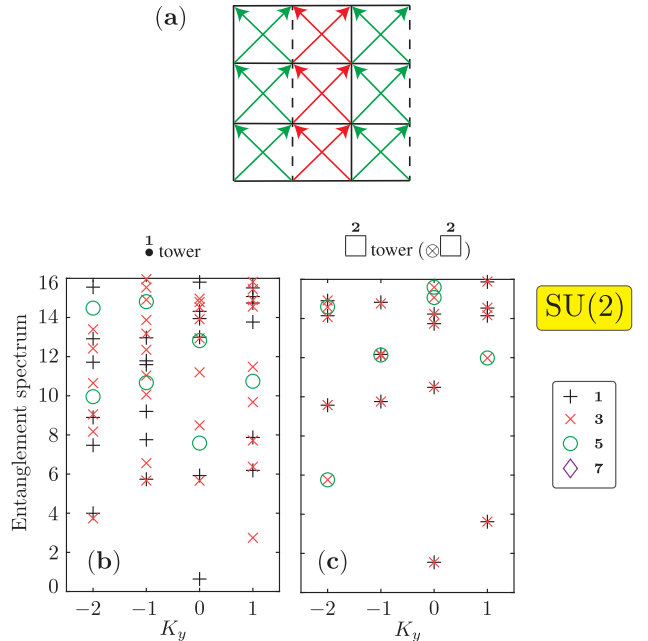


FIG. 21. (a) Illustration of the parton Hamiltonian of the SU(2) CSL. The phase of nearest neighbor hopping is 0 (π) along the solid (dashed) edges. The phase of next-nearest-neighbor hopping is $\pi/2$ ($-\pi/2$) along the green (red) arrows. [(b) and (c)] The entanglement spectra on a 4×12 cylinder for the parton wave function.

so-called “dressed mirror symmetry” within the virtual degrees of freedom [83]. The parton approach offers a more direct understanding—the degeneracy equals to the number of parton states required to form a singlet superposition state.

APPENDIX F: MODIFIED WZW $SU(N)_1$ CHIRAL TOWERS OF STATES

We list here, for $N = 3$ and 4, the predicted ToS corresponding to the $SU(N)$ DMRG cylinders investigated and discussed in the main text.

-
- [1] G. Misguich and C. Lhuillier, Two-dimensional quantum anti-ferromagnets, in *Frustrated Spin Systems*, edited by H. T. Diep (World Scientific, Singapore, 2005), pp. 229–306.
- [2] L. Savary and L. Balents, Quantum spin liquids: A review, *Rep. Prog. Phys.* **80**, 016502 (2016).
- [3] Y. Zhou, K. Kanoda, and T.-K. Ng, Quantum spin liquid states, *Rev. Mod. Phys.* **89**, 025003 (2017).
- [4] X. G. Wen, Topological orders in rigid states, *Int. J. Mod. Phys. B* **04**, 239 (1990).
- [5] D. Poilblanc, N. Schuch, D. Pérez-García, and J. I. Cirac, Topological and entanglement properties of resonating valence bond wave functions, *Phys. Rev. B* **86**, 014404 (2012).
- [6] V. Kalmeyer and R. B. Laughlin, Equivalence of the Resonating-Valence-Bond and Fractional Quantum Hall States, *Phys. Rev. Lett.* **59**, 2095 (1987).
- [7] V. Kalmeyer and R. B. Laughlin, Theory of the spin liquid state of the heisenberg antiferromagnet, *Phys. Rev. B* **39**, 11879 (1989).
- [8] R. B. Laughlin, Spin hamiltonian for which quantum hall wavefunction is exact, *Ann. Phys.* **191**, 163 (1989).
- [9] X. G. Wen, F. Wilczek, and A. Zee, Chiral spin states and superconductivity, *Phys. Rev. B* **39**, 11413 (1989).
- [10] R. B. Laughlin and Z. Zou, Properties of the chiral-spin-liquid state, *Phys. Rev. B* **41**, 664 (1990).
- [11] X.-G. Wen, Quantum orders and symmetric spin liquids, *Phys. Rev. B* **65**, 165113 (2002).
- [12] D. C. Tsui, H. L. Stormer, and A. C. Gossard, Two-Dimensional Magnetotransport in the Extreme Quantum Limit, *Phys. Rev. Lett.* **48**, 1559 (1982).
- [13] B. I. Halperin, Statistics of Quasiparticles and the Hierarchy of Fractional Quantized Hall States, *Phys. Rev. Lett.* **52**, 1583 (1984).
- [14] X. G. Wen, Gapless boundary excitations in the quantum Hall states and in the chiral spin states, *Phys. Rev. B* **43**, 11025 (1991).
- [15] D. F. Schroeter, E. Kapit, R. Thomale, and M. Greiter, Spin Hamiltonian for Which the Chiral Spin Liquid is the Exact Ground State, *Phys. Rev. Lett.* **99**, 097202 (2007).
- [16] R. Thomale, E. Kapit, D. F. Schroeter, and M. Greiter, Parent hamiltonian for the chiral spin liquid, *Phys. Rev. B* **80**, 104406 (2009).
- [17] A. E. B. Nielsen, J. I. Cirac, and G. Sierra, Laughlin Spin-Liquid States on Lattices Obtained from Conformal Field Theory, *Phys. Rev. Lett.* **108**, 257206 (2012).
- [18] M. Greiter, D. F. Schroeter, and R. Thomale, Parent Hamiltonian for the non-Abelian chiral spin liquid, *Phys. Rev. B* **89**, 165125 (2014).
- [19] B. Bauer, L. Cincio, B. P. Keller, M. Dolfi, G. Vidal, S. Trebst, and A. W. W. Ludwig, Chiral spin liquid and emergent anyons in a kagome lattice Mott insulator, *Nat. Commun.* **5**, 5137 (2014).
- [20] A. E. B. Nielsen, G. Sierra, and J. I. Cirac, Local models of fractional quantum Hall states in lattices and physical implementation, *Nat. Commun.* **4**, 2864 (2013).
- [21] A. Wietek and A. M. Läuchli, Chiral spin liquid and quantum criticality in extended $s = \frac{1}{2}$ Heisenberg models on the triangular lattice, *Phys. Rev. B* **95**, 035141 (2017).
- [22] S.-S. Gong, W. Zhu, J.-X. Zhu, D. N. Sheng, and K. Yang, Global phase diagram and quantum spin liquids in a spin- $\frac{1}{2}$ triangular antiferromagnet, *Phys. Rev. B* **96**, 075116 (2017).
- [23] A. Yu. Kitaev, Fault-tolerant quantum computation by anyons, *Ann. Phys.* **303**, 2 (2003).
- [24] A. Kitaev, Anyons in an exactly solved model and beyond, *Ann. Phys.* **321**, 2 (2006).
- [25] H. Yao and S. A. Kivelson, Exact Chiral Spin Liquid with Non-Abelian Anyons, *Phys. Rev. Lett.* **99**, 247203 (2007).
- [26] M. Greiter and R. Thomale, Non-Abelian Statistics in a Quantum Antiferromagnet, *Phys. Rev. Lett.* **102**, 207203 (2009).
- [27] A. V. Gorshkov, M. Hermele, V. Gurarie, C. Xu, P. S. Julienne, J. Ye, P. Zoller, E. Demler, M. D. Lukin, and A. M. Rey, Two-orbital $SU(N)$ magnetism with ultracold alkaline-earth atoms, *Nat. Phys.* **6**, 289 (2010).
- [28] M. Hermele, V. Gurarie, and A. M. Rey, Mott Insulators of Ultracold Fermionic Alkaline Earth Atoms: Underconstrained Magnetism and Chiral Spin Liquid, *Phys. Rev. Lett.* **103**, 135301 (2009).
- [29] P. Nataf, M. Lajkó, A. Wietek, K. Penc, F. Mila, and A. M. Läuchli, Chiral Spin Liquids in Triangular-Lattice $SU(N)$ Fermionic Mott Insulators with Artificial Gauge Fields, *Phys. Rev. Lett.* **117**, 167202 (2016).
- [30] G. Chen, K. R. A. Hazzard, A. M. Rey, and M. Hermele, Synthetic-gauge-field stabilization of the chiral-spin-liquid phase, *Phys. Rev. A* **93**, 061601(R) (2016).
- [31] Y.-C. He, D. N. Sheng, and Y. Chen, Chiral Spin Liquid in a Frustrated Anisotropic Kagome Heisenberg Model, *Phys. Rev. Lett.* **112**, 137202 (2014).
- [32] S.-S. Gong, W. Zhu, and D. N. Sheng, Emergent chiral spin liquid: Fractional quantum Hall effect in a kagome Heisenberg model, *Sci. Rep.* **4**, 6317 (2014).
- [33] A. Wietek, A. Sterdyniak, and A. M. Läuchli, Nature of chiral spin liquids on the kagome lattice, *Phys. Rev. B* **92**, 125122 (2015).
- [34] C. Boos, C. J. Ganahl, M. Lajkó, P. Nataf, A. M. Läuchli, K. Penc, K. P. Schmidt, and F. Mila, Time-reversal symmetry breaking abelian chiral spin liquid in mott phases of three-component fermions on the triangular lattice, *Phys. Rev. Research* **2**, 023098 (2020).
- [35] G. Pagano, M. Mancini, G. Cappellini *et al.*, A one-dimensional liquid of fermions with tunable spin, *Nat. Phys.* **10**, 198 (2014).

- [36] Y.-H. Zhang, D. N. Sheng, and A. Vishwanath, An $su(4)$ chiral spin liquid and quantized dipole hall effect in moiré bilayers, [arXiv:2103.09825](#) [cond-mat.str-el].
- [37] F. Verstraete and J. I. Cirac, Renormalization algorithms for Quantum-Many Body Systems in two and higher dimensions, [arXiv:cond-mat/0407066](#) [cond-mat.str-el].
- [38] H. J. Liao, Z. Y. Xie, J. Chen, Z. Y. Liu, H. D. Xie, R. Z. Huang, B. Normand, and T. Xiang, Gapless Spin-Liquid Ground State in the $s = 1/2$ Kagome Antiferromagnet, *Phys. Rev. Lett.* **118**, 137202 (2017).
- [39] H.-Y. Lee, R. Kaneko, T. Okubo, and N. Kawashima, Gapless Kitaev Spin Liquid to Classical String Gas Through Tensor Networks, *Phys. Rev. Lett.* **123**, 087203 (2019).
- [40] W.-Y. Liu, S.-S. Gong, Y.-B. Li, D. Poilblanc, W.-Q. Chen, and Z.-C. Gu, Gapless quantum spin liquid and global phase diagram of the spin-1/2 J_1 - J_2 square antiferromagnetic Heisenberg model, [arXiv:2009.01821](#) [cond-mat.str-el].
- [41] N. Schuch, J. I. Cirac, and D. Pérez-García, PEPS as ground states: Degeneracy and topology, *Ann. Phys.* **325**, 2153 (2010).
- [42] N. Schuch, D. Poilblanc, J. I. Cirac, and D. Pérez-García, Resonating valence bond states in the PEPS formalism, *Phys. Rev. B* **86**, 115108(R) (2012).
- [43] J.-Y. Chen and D. Poilblanc, Topological \mathbb{Z}_2 resonating-valence-bond spin liquid on the square lattice, *Phys. Rev. B* **97**, 161107(R) (2018).
- [44] D. Poilblanc, J. I. Cirac, and N. Schuch, Chiral topological spin liquids with projected entangled pair states, *Phys. Rev. B* **91**, 224431 (2015).
- [45] J.-Y. Chen, L. Vanderstraeten, S. Capponi, and D. Poilblanc, Non-abelian chiral spin liquid in a quantum antiferromagnet revealed by an iPEPS study, *Phys. Rev. B* **98**, 184409 (2018).
- [46] P. Francesco, P. Mathieu, and D. Sénéchal, *Conformal Field Theory* (Springer-Verlag, New York, 1997).
- [47] J.-Y. Chen, S. Capponi, A. Wietek, M. Mambrini, N. Schuch, and D. Poilblanc, $SU(3)_1$ Chiral Spin Liquid on the Square Lattice: A View From Symmetric Projected Entangled Pair States, *Phys. Rev. Lett.* **125**, 017201 (2020).
- [48] D. Poilblanc, Investigation of the chiral antiferromagnetic Heisenberg model using projected entangled pair states, *Phys. Rev. B* **96**, 121118(R) (2017).
- [49] D. Poilblanc, N. Schuch, and I. Affleck, $SU(2)_1$ chiral edge modes of a critical spin liquid, *Phys. Rev. B* **93**, 174414 (2016).
- [50] P. Nataf and F. Mila, Exact Diagonalization of Heisenberg $SU(n)$ Models, *Phys. Rev. Lett.* **113**, 127204 (2014).
- [51] K. Wan, P. Nataf, and F. Mila, Exact diagonalization of $SU(N)$ Heisenberg and Affleck-Kennedy-Lieb-Tasaki chains using the full $SU(N)$ symmetry, *Phys. Rev. B* **96**, 115159 (2017).
- [52] A. Alex, M. Kalus, A. Huckleberry, and J. von Delft, A numerical algorithm for the explicit calculation of $SU(N)$ and $SL(n, \mathbb{C})/sl(n, \mathbb{C})$ ClebschGordan coefficients, *J. Math. Phys.* **52**, 023507 (2011).
- [53] R. Haghshenas, W.-W. Lan, S.-S. Gong, and D. N. Sheng, Quantum phase diagram of spin-1 J_1 - J_2 Heisenberg model on the square lattice: An infinite projected entangled-pair state and density matrix renormalization group study, *Phys. Rev. B* **97**, 184436 (2018).
- [54] J.-Y. Chen, S. Capponi, and D. Poilblanc, Discrete lattice symmetry breaking in a two-dimensional frustrated spin-1 Heisenberg model, *Phys. Rev. B* **98**, 045106 (2018).
- [55] B. Estienne and B. A. Bernevig, Spin-singlet quantum hall states and jack polynomials with a prescribed symmetry, *Nucl. Phys. B* **857**, 185 (2012).
- [56] A. Sterdyniak, C. Repellin, B. A. Bernevig, and N. Regnault, Series of abelian and non-abelian states in $c > 1$ fractional chern insulators, *Phys. Rev. B* **87**, 205137 (2013).
- [57] Y. Zhang, T. Grover, A. Turner, M. Oshikawa, and A. Vishwanath, Quasiparticle statistics and braiding from ground-state entanglement, *Phys. Rev. B* **85**, 235151 (2012).
- [58] A. A. Abrikosov, Electron scattering on magnetic impurities in metals and anomalous resistivity effects, *Phys. Phys. Fiz.* **2**, 5 (1965).
- [59] X. G. Wen, Non-Abelian Statistics in the Fractional Quantum Hall States, *Phys. Rev. Lett.* **66**, 802 (1991).
- [60] A. Auerbach, *Interacting Electrons and Quantum Magnetism* (Springer, Berlin, 1998).
- [61] H.-H. Tu, Y. Zhang, and X.-L. Qi, Momentum polarization: An entanglement measure of topological spin and chiral central charge, *Phys. Rev. B* **88**, 195412 (2013).
- [62] J.-W. Mei and X.-G. Wen, Modular matrices from universal wave-function overlaps in Gutzwiller-projected parton wave functions, *Phys. Rev. B* **91**, 125123 (2015).
- [63] Y.-H. Wu, L. Wang, and H.-H. Tu, Tensor Network Representations of Parton Wave Functions, *Phys. Rev. Lett.* **124**, 246401 (2020).
- [64] H. Li and F. D. M. Haldane, Entanglement Spectrum as a Generalization of Entanglement Entropy: Identification of Topological Order in Non-Abelian Fractional Quantum Hall Effect States, *Phys. Rev. Lett.* **101**, 010504 (2008).
- [65] H.-K. Jin, H.-H. Tu, and Y. Zhou, Density matrix renormalization group boosted by gutzwiller projected wave functions, *Phys. Rev. B* **104**, L020409 (2021).
- [66] W. Li, A. Weichselbaum, and J. von Delft, Identifying symmetry-protected topological order by entanglement entropy, *Phys. Rev. B* **88**, 245121 (2013).
- [67] L. Cincio and G. Vidal, Characterizing Topological Order by Studying the Ground States on an Infinite Cylinder, *Phys. Rev. Lett.* **110**, 067208 (2013).
- [68] S. Yan, D. A. Huse, and S. R. White, Spin-liquid ground state of the $s = 1/2$ kagome heisenberg antiferromagnet, *Science* **332**, 1173 (2011).
- [69] M. P. Zaletel, R. S. K. Mong, and F. Pollmann, Topological Characterization of Fractional Quantum Hall Ground States from Microscopic Hamiltonians, *Phys. Rev. Lett.* **110**, 236801 (2013).
- [70] S. N. Saadatmand and I. P. McCulloch, Symmetry fractionalization in the topological phase of the spin- $\frac{1}{2}$ J_1 - J_2 triangular Heisenberg model, *Phys. Rev. B* **94**, 121111(R) (2016).
- [71] S. Hu, W. Zhu, S. Eggert, and Y.-C. He, Dirac Spin Liquid on the Spin-1/2 Triangular Heisenberg Antiferromagnet, *Phys. Rev. Lett.* **123**, 207203 (2019).
- [72] A. Szasz, J. Motruk, M. P. Zaletel, and J. E. Moore, Chiral Spin Liquid Phase of the Triangular Lattice Hubbard Model: A Density Matrix Renormalization Group Study, *Phys. Rev. X* **10**, 021042 (2020).
- [73] S. R. White, Density Matrix Formulation for Quantum Renormalization Groups, *Phys. Rev. Lett.* **69**, 2863 (1992).

- [74] I. P. McCulloch, Infinite size density matrix renormalization group, revisited, [arXiv:0804.2509](https://arxiv.org/abs/0804.2509) [cond-mat.str-el].
- [75] This is similar to the AKLT state with periodic boundary conditions, which has fourfold degeneracy in the entanglement spectrum rather than the twofold degeneracy suggested by the $D = 2$ MPS representation [66].
- [76] A. Weichselbaum, Non-abelian symmetries in tensor networks: A quantum symmetry space approach, *Ann. Phys.* **327**, 2972 (2012).
- [77] A. Weichselbaum, X-symbols for non-abelian symmetries in tensor networks, *Phys. Rev. Research* **2**, 023385 (2020).
- [78] M. Mambrini, R. Orús, and D. Poilblanc, Systematic construction of spin liquids on the square lattice from tensor networks with $SU(2)$ symmetry, *Phys. Rev. B* **94**, 205124 (2016).
- [79] T. Nishino and K. Okunishi, Corner transfer matrix renormalization group method, *J. Phys. Soc. Jpn.* **65**, 891 (1996).
- [80] R. Orús and G. Vidal, Simulation of two-dimensional quantum systems on an infinite lattice revisited: Corner transfer matrix for tensor contraction, *Phys. Rev. B* **80**, 094403 (2009).
- [81] D. Poilblanc and M. Mambrini, Quantum critical phase with infinite projected entangled paired states, *Phys. Rev. B* **96**, 014414 (2017).
- [82] J. I. Cirac, D. Poilblanc, N. Schuch, and F. Verstraete, Entanglement spectrum and boundary theories with projected entangled-pair states, *Phys. Rev. B* **83**, 245134 (2011).
- [83] A. Hackenbroich, A. Sterdyniak, and N. Schuch, Interplay of $SU(2)$, point group, and translational symmetry for projected entangled pair states: Application to a chiral spin liquid, *Phys. Rev. B* **98**, 085151 (2018).
- [84] J. Dubail and N. Read, Tensor network trial states for chiral topological phases in two dimensions and a no-go theorem in any dimension, *Phys. Rev. B* **92**, 205307 (2015).
- [85] O. Gauthé, S. Capponi, M. Mambrini, and D. Poilblanc, Quantum spin liquid phases in the bilinear-biquadratic two- $SU(4)$ -fermion hamiltonian on the square lattice, *Phys. Rev. B* **101**, 205144 (2020).
- [86] A. Weichselbaum, S. Capponi, P. Lecheminant, A. M. Tsvelik, and A. M. Läuchli, Unified phase diagram of antiferromagnetic $su(n)$ spin ladders, *Phys. Rev. B* **98**, 085104 (2018).
- [87] B. I. Halperin, Theory of the quantized hall conductance, *Helv. Phys. Acta* **56**, 75 (1983).
- [88] H.-H. Tu, A. E. B. Nielsen, and G. Sierra, Quantum spin models for the $SU(n)_1$ Wess-Zumino-Witten model, *Nucl. Phys. B* **886**, 328 (2014).
- [89] R. Bondesan and T. Quella, Infinite matrix product states for long-range $SU(N)$ spin models, *Nucl. Phys. B* **886**, 483 (2014).
- [90] N. Regnault and B. A. Bernevig, Fractional Chern Insulator, *Phys. Rev. X* **1**, 021014 (2011).
- [91] B. A. Bernevig and N. Regnault, Emergent many-body translational symmetries of Abelian and non-Abelian fractionally filled topological insulators, *Phys. Rev. B* **85**, 075128 (2012).
- [92] H. Georgi, *Lie Algebras in Particle Physics From Isospin to Unified Theories* (Westview Press, Paris, Perseus Books Group, 1999).
- [93] P. Goddard and D. Olive, Kac-Moody and Virasoro algebras in relation to quantum physics, *Int. J. Mod. Phys. A* **1**, 303 (1986).
- [94] V. G. Knizhnik and A. B. Zamolodchikov, Current algebra and Wess-Zumino model in two dimensions, *Nucl. Phys. B* **247**, 83 (1984).
- [95] P. Ginsparg, Applied conformal field theory, in *Fields, Strings and Critical Phenomena*, edited by E. Brézin and J. Zinn-Justin, Les Houches Summer School (North-Holland, Amsterdam, 1988).
- [96] H.-K. Jin, H.-H. Tu, and Y. Zhou, Efficient tensor network representation for Gutzwiller projected states of paired fermions, *Phys. Rev. B* **101**, 165135 (2020).
- [97] G. Petrica, B.-X. Zheng, G. K.-L. Chan, and B. K. Clark, Finite and infinite matrix product states for gutzwiller projected mean-field wave functions, *Phys. Rev. B* **103**, 125161 (2021).
- [98] S. Singh and G. Vidal, Tensor network states and algorithms in the presence of a global $su(2)$ symmetry, *Phys. Rev. B* **86**, 195114 (2012).
- [99] C. Hubig, Abelian and non-abelian symmetries in infinite projected entangled pair states, *SciPost Phys.* **5**, 047 (2018).
- [100] P. Schmoll, S. Singh, M. Rizzi, and R. Ors, A programming guide for tensor networks with global $SU(2)$ symmetry, *Ann. Phys.* **419**, 168232 (2020).

U(1)-symmetric Gaussian fermionic projected entangled paired states and their Gutzwiller projection

Jheng-Wei Li,¹ Jan von Delft,¹ and Hong-Hao Tu²

¹*Arnold Sommerfeld Center for Theoretical Physics, Center for NanoScience, and Munich Center for Quantum Science and Technology, Ludwig-Maximilians-Universität München, 80333 Munich, Germany*

²*Institut für Theoretische Physik, Technische Universität Dresden, 01062 Dresden, Germany*

(Dated: August 12, 2022)

We develop a formalism for constructing particle-number-conserving Gaussian fermionic projected entangled pair states [U(1)-GfPEPS] and show that these states can describe ground states of band insulators and gapless fermions with band touching points. When using them as variational Ansätze for two Dirac fermion systems (π -flux model on the square lattice and $[0, \pi]$ -flux model on the kagome lattice), we find that the U(1)-GfPEPS, even with a relatively small bond dimension, can accurately approximate the Dirac Fermi sea ground states. By applying Gutzwiller projectors on top of these U(1)-GfPEPS, we obtain PEPS representation of U(1)-Dirac spin liquid states for spin-1/2 systems. With state-of-the-art tensor network numerics, the critical exponent in the spin-spin correlation function of the Gutzwiller-projected π -flux state is estimated to be $\eta \approx 1.7$.

I. INTRODUCTION

The idea of the Gutzwiller wave function plays a crucial role in the study of strongly correlated systems. Its original formulation considers a Slater determinant wave function for electrons and supplements that with a Gutzwiller operator accounting for electron correlations [1, 2]. Since its invention, the scope of the Gutzwiller wave function has been considerably broadened. For instance, Anderson has proposed a Gutzwiller projected BCS state for high- T_c cuprates [3]. In the modern context, the Gutzwiller wave function evolves into the framework of a systematic approach called “parton construction”, which includes three main steps: (i) the constituent particles (fermions, bosons, or spins) of an interacting system are split into fermionic or bosonic “partons” with enlarged Hilbert spaces; (ii) the fermionic or bosonic partons are placed into certain non-interacting (quadratic) mean-field Hamiltonians with fermionic or bosonic Gaussian ground states; (iii) the Gutzwiller projection, taking the form of a local projector, is applied to Gaussian ground states of partons to remove unphysical states introduced by the parton construction. For paradigmatic examples like the Haldane-Shastry model [4, 5] and the Kitaev’s honeycomb model [6], Gutzwiller wave functions are exact ground states and provide invaluable insight into exotic states emerging from strong correlations.

From a numerical perspective, the variational Monte Carlo method using Gutzwiller projected fermionic wave functions has been one of the key methods for strongly correlated systems [7–9]. Recently, several methods have been developed for converting fermionic Gaussian states into matrix product states (MPSs) [10–16]. In the MPS representation, the Gutzwiller projection can be implemented easily. This provides not just a new approach for evaluating physical quantities in Gutzwiller wave functions, but also physically motivated MPSs for initializing density matrix renormalization group (DMRG) calculations [17–20]. Such a strategy has already seen success

in accelerating DMRG calculations and, for topologically ordered phases, targeting degenerate ground states in different topological sectors [21–24].

For two-dimensional (2D) systems, too, it is highly desirable to develop a method converting Gutzwiller projected wave functions into projected entangled pair states (PEPSs) [25]. Similar to the benefits for DMRG, Gutzwiller wave functions can serve as good initial inputs in PEPS-based variational methods [26–30]. For concrete Hamiltonians, the comparison of Gutzwiller wave functions with brute-force PEPS numerical results would also become possible. Furthermore, for 2D systems, the PEPS representation of Gutzwiller wave functions has two advantages over its MPS counterpart: (i) infinite-size PEPS algorithms [31–35] work directly in the thermodynamic limit, whereas the MPS approach using a cylindrical boundary condition suffers from finite-size effects; (ii) for topological systems, the local tensor of PEPS usually exhibits a symmetry [36–39], which can be used to characterize topological properties.

In this work, we develop a systematic approach to convert Gutzwiller projected Fermi sea states into PEPSs. This is based on a specification of the Gaussian fermionic PEPS (GfPEPS) formalism [40] to a particle-number-conserving setting (referred to as U(1)-GfPEPS hereafter). We show that the U(1)-GfPEPS can describe band insulators whose filled valence bands and empty conduction bands are separated by a gap, as well as semimetals with band-touching points (e.g., Dirac points) between valence and conduction bands. The case of an open Fermi surface is beyond the scope of U(1)-GfPEPS. Furthermore, we develop a variational algorithm that starts with a particle-number-conserving free fermionic Hamiltonian and approximates its ground state with U(1)-GfPEPS. This complements previous works focusing on analytical constructions [41–46] and a related numerical work which does not impose particle-number conservation [47]. For two Dirac fermion systems (π -flux model on the square lattice and $[0, \pi]$ -flux model on the

kagome lattice), the benchmark calculations with U(1)-GfPEPS accurately reproduce the filled band dispersions with a relatively small bond dimension. The application of additional Gutzwiller projectors to these U(1)-GfPEPS provides PEPS Ansätze for U(1)-Dirac spin liquids. From these we calculate their spin-spin correlation functions with state-of-the-art tensor network algorithms and obtain a critical exponent $\eta \approx 1.7$ for the Gutzwiller-projected π -flux state.

The rest of this paper is organized as follows. In Sec. II we describe our methods, including the construction of U(1)-GfPEPS and its correlation matrix formalism, the variational optimization algorithm for U(1)-GfPEPS, the implementation of Gutzwiller projection, and the contraction method for computing physical quantities. In Sec. III, we apply these methods to two benchmark examples, i.e., the π -flux model on the square lattice and the $[0, \pi]$ -flux model on the kagome lattice. The U(1)-Dirac spin liquid states obtained after Gutzwiller projection are also studied. Sec. IV provides a summary and gives some outlook. Appendix A includes technical details on particle-number-conserving fermionic Gaussian states.

II. METHODS

A. U(1)-symmetric Gaussian fermionic projected entangled-paired state

We use the square lattice to illustrate the construction of U(1)-GfPEPS; the extension to other lattices is straightforward. Each site of the lattice hosts P physical fermionic modes, with creation operators $c_{\mathbf{r},\mu}^\dagger$ ($\mu = 1, \dots, P$), as well as $4M$ virtual fermionic modes, with creation operators $c_{\mathbf{r},\nu,\alpha}^\dagger$ ($\nu = l, r, d, u$ and $\alpha = 1, \dots, M$), where l, r, d, u denote left, right, down, and up, respectively.

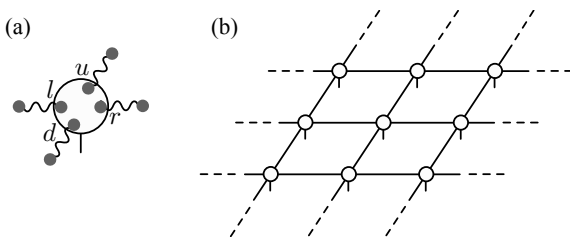


FIG. 1. (a) Schematic of a U(1)-GfPEPS projector $|T_{\mathbf{r}}\rangle$ together with the maximally entangled virtual bonds between neighboring sites. (b) The resulting fermionic PEPS on a square lattice by tiling the local tensors together.

To define a U(1)-GfPEPS (see Fig. 1), virtual fermions between every two neighboring sites form M maximally

entangled bonds,

$$|I\rangle = \prod_{\mathbf{r}} \prod_{\alpha=1}^M (c_{\mathbf{r},r,\alpha}^\dagger + c_{\mathbf{r}+\mathbf{x},l,\alpha}^\dagger)(c_{\mathbf{r},u,\alpha}^\dagger + c_{\mathbf{r}+\mathbf{y},d,\alpha}^\dagger)|0\rangle_{\mathbf{v}}, \quad (1)$$

where, for an $L \times L$ lattice with periodic or antiperiodic boundary conditions, virtual fermions have a fixed particle number $N_{\mathbf{v}} = 2ML^2$. $|0\rangle_{\mathbf{v}}$ is the vacuum of virtual fermions. A fermionic PEPS is defined by $|\Psi\rangle = \langle I|T\rangle$ [40, 44], where $|T\rangle$ is the PEPS projector

$$|T\rangle = \prod_{\mathbf{r}} T_{\mathbf{r}}|0\rangle_{\mathbf{p},\mathbf{v}}. \quad (2)$$

Here $|0\rangle_{\mathbf{p},\mathbf{v}}$ is the shared vacuum of physical and virtual fermions, and $T_{\mathbf{r}}$ creates a local state of physical and virtual fermions at site \mathbf{r} . For illustrating the construction, we shall focus on the translationally invariant case and consider the same $T_{\mathbf{r}}$ for all sites [48]. The PEPS is hence fully characterized by the local state $T_{\mathbf{r}}|0\rangle_{\mathbf{p},\mathbf{v}}$. Generally, $T_{\mathbf{r}}$ is parametrized as

$$T = \sum_{\{m_{\mu}\}, \{n_{\nu,\alpha}\}} T_{\{m_{\mu}\}, \{n_{\nu,\alpha}\}}^{\{m_{\mu}\}} \times \left[\prod_{\mu=1}^P (c_{\mu}^\dagger)^{m_{\mu}} \right] \left[\prod_{\nu=l,r,d,u} \prod_{\alpha=1}^M (c_{\nu,\alpha}^\dagger)^{n_{\nu,\alpha}} \right], \quad (3)$$

where, here and hereafter, the site index \mathbf{r} is dropped when we refer to a local site. m_{μ} ($n_{\nu,\alpha}$) is understood as the collection of occupation numbers of physical (virtual) modes. The conserved fermion parity of $|\Psi\rangle$, known as the “fermion superselection rule”, is imposed by requiring that $T_{\{m_{\mu}\}, \{n_{\nu,\alpha}\}}^{\{m_{\mu}\}}$ vanishes if $\sum_{\mu} m_{\mu} + \sum_{\nu,\alpha} n_{\nu,\alpha}$ is odd (or even).

For describing the ground state of fermionic systems with a fixed particle number, the \mathbb{Z}_2 parity conservation of the local tensor T should be promoted to the U(1) particle-number conservation, by imposing that $T_{\{m_{\mu}\}, \{n_{\nu,\alpha}\}}^{\{m_{\mu}\}}$ is nonvanishing if and only if $\sum_{\mu} m_{\mu} + \sum_{\nu,\alpha} n_{\nu,\alpha} = Q$, where Q is the total number of physical and virtual fermions at a single site. We henceforth restrict ourselves to free fermionic systems (i.e., ones described by quadratic fermionic Hamiltonians), and require the PEPS projector in Eq. (2) to be a fermionic Gaussian state [40]. Thus, for PEPS describing free fermionic ground states with a fixed particle number, the PEPS projector reduces to a local Slater determinant created by

$$T = \prod_{q=1}^Q d_q^\dagger, \quad (4)$$

where the orbitals d_q^\dagger are linear combinations of physical modes $c_{\mathbf{r},\mu}^\dagger$ and virtual modes $c_{\mathbf{r},\nu,\alpha}^\dagger$ at the same site. The explicit form of d_q^\dagger will be specified in Sec. II B. For

the U(1)-GfPEPS defined as $|\Psi\rangle = \langle I|T\rangle$, the number of physical fermions that remain after contracting the virtual modes is $N_p = QL^2 - N_v = (Q - 2M)L^2$. For a system of spin-1/2 fermions, the half-filling condition $N_p = L^2$ is achieved by choosing $Q = 2M + 1$.

B. Correlation matrix formulation

As for fermionic Gaussian states, the virtual bond state $|I\rangle$ and PEPS projector $|T\rangle$ are characterized by their correlation matrices [49, 50]. This provides an efficient computational tool for U(1)-GfPEPS. Below we provide key results that are relevant for U(1)-GfPEPS and leave further details to Appendix A.

Because of translational invariance, we switch to momentum space with $c_{\mathbf{r},\mu}^\dagger = \frac{1}{L} \sum_{\mathbf{k}} c_{\mathbf{k},\mu}^\dagger e^{-i\mathbf{k}\cdot\mathbf{r}}$ for physical modes (μ replaced by ν, α for virtual modes). $\mathbf{k} = (k_x, k_y)$ is a point in the first Brillouin zone (FBZ) and its allowed values depend on boundary conditions. For instance, antiperiodic or periodic boundary conditions along the x -direction allow $k_x = \frac{2\pi}{L}(n_x + 1/2)$ or $k_x = \frac{2\pi}{L}n_x$, respectively, with $n_x = 0, 1, \dots, L - 1$.

For the virtual bond state $|I\rangle$, we write its density operator as $\rho_{\text{in}} = |I\rangle\langle I|$ (input of U(1)-GfPEPS) and define its correlation matrix as

$$[\mathcal{C}_{\text{in}}(\mathbf{k})]_{(\nu,\alpha),(\nu',\alpha')} = 2\text{tr}_v(\rho_{\text{in}} c_{\mathbf{k},\nu,\alpha}^\dagger c_{\mathbf{k},\nu',\alpha'}) - \delta_{\nu,\nu'} \delta_{\alpha,\alpha'}, \quad (5)$$

where the trace tr_v is with respect to virtual modes. Such a correlation matrix is called a complex correlation matrix in Appendix A. To calculate this correlation matrix, one may express $|I\rangle$ in momentum space as

$$|I\rangle = \prod_{\mathbf{k}} \prod_{\alpha=1}^M (c_{\mathbf{k},r,\alpha}^\dagger + c_{\mathbf{k},l,\alpha}^\dagger e^{-ik_x}) (c_{\mathbf{k},u,\alpha}^\dagger + c_{\mathbf{k},d,\alpha}^\dagger e^{-ik_y}) |0\rangle_v. \quad (6)$$

The explicit form of the $4M \times 4M$ correlation matrix $\mathcal{C}_{\text{in}}(\mathbf{k})$ is then obtained as:

$$\mathcal{C}_{\text{in}}(\mathbf{k}) = \begin{pmatrix} 0 & e^{ik_x} \mathbb{1}_M \\ e^{-ik_x} \mathbb{1}_M & 0 \end{pmatrix} \oplus \begin{pmatrix} 0 & e^{ik_y} \mathbb{1}_M \\ e^{-ik_y} \mathbb{1}_M & 0 \end{pmatrix}, \quad (7)$$

where $\mathbb{1}_M$ is an $M \times M$ identity matrix.

As the PEPS projector $|T\rangle$ assumes a translationally invariant onsite form [see Eq. (2)], its correlation matrix is block diagonal in both real and momentum space, and all blocks are the same. Thus, it is sufficient to parameterize this block by considering a single site \mathbf{r} (or momentum \mathbf{k}):

$$\mathcal{C}_T = \begin{pmatrix} A & B \\ B^\dagger & D \end{pmatrix}. \quad (8)$$

The submatrices encode two-point correlators between two physical modes ($P \times P$ matrix A), two virtual modes ($4M \times 4M$ matrix D), and one physical and one virtual

mode ($P \times 4M$ matrix B):

$$\begin{aligned} A_{\mu,\mu'} &= 2\text{tr}_{p,v}(\rho_T c_{\mathbf{r},\mu}^\dagger c_{\mathbf{r},\mu'}) - \delta_{\mu,\mu'}, \\ D_{(\nu,\alpha),(\nu',\alpha')} &= 2\text{tr}_{p,v}(\rho_T c_{\mathbf{r},\nu,\alpha}^\dagger c_{\mathbf{r},\nu',\alpha'}) - \delta_{\nu,\nu'} \delta_{\alpha,\alpha'}, \\ B_{\mu,(\nu',\alpha')} &= 2\text{tr}_{p,v}(\rho_T c_{\mathbf{r},\mu}^\dagger c_{\mathbf{r},\nu',\alpha'}), \end{aligned} \quad (9)$$

where ρ_T is the Gaussian density operator for $|T\rangle$ and $\text{tr}_{p,v}$ is with respect to both physical and virtual modes. It is transparent that Eq. (9) has the same form in momentum space (i.e., \mathbf{r} replaced by \mathbf{k}). Further important information utilizing the results in Appendix A is as follows: As $|T\rangle$ is a pure state, \mathcal{C}_T is Hermitian and can be diagonalized as

$$U^\dagger \mathcal{C}_T U = \begin{pmatrix} \mathbb{1}_Q & 0 \\ 0 & -\mathbb{1}_{P+4M-Q} \end{pmatrix}, \quad (10)$$

where the identity block $\mathbb{1}_Q$ corresponds to occupied single-particle orbitals d_q^\dagger [see Eq. (4)]. Their explicit form is given by

$$d_q^\dagger = \sum_{\mu=1}^P U_{q,\mu}^\dagger c_\mu^\dagger + \sum_{\nu=l,r,d,u} \sum_{\alpha=1}^M U_{q,(\nu,\alpha)}^\dagger c_{\nu,\alpha}^\dagger \quad (11)$$

with $q = 1, \dots, Q$.

For the U(1)-GfPEPS $|\Psi\rangle = \langle I|T\rangle$, its Gaussian density operator ρ_{out} is obtained from $\rho_{\text{out}} \propto \text{tr}_v(\rho_T \rho_{\text{in}})$ as the output. The correlation matrix of ρ_{out} is block diagonal in momentum space and can be defined as

$$[\mathcal{C}_{\text{out}}(\mathbf{k})]_{\mu,\mu'} = 2\text{tr}_p(\rho_{\text{out}} c_{\mathbf{k},\mu}^\dagger c_{\mathbf{k},\mu'}) - \delta_{\mu,\mu'}. \quad (12)$$

It is related to $\mathcal{C}_{\text{in}}(\mathbf{k})$ and \mathcal{C}_T via

$$\mathcal{C}_{\text{out}}(\mathbf{k}) = A - B[D + \mathcal{C}_{\text{in}}(\mathbf{k})]^{-1} B^\dagger, \quad (13)$$

as shown in Appendix A. This expression is the main formal result of this paper.

Before moving on to numerical optimization, we comment on which systems the U(1)-GfPEPS Ansatz is suitable for. Eq. (6) shows that each \mathbf{k} point in the FBZ accommodates $2M$ virtual modes. These virtual modes should be contracted with virtual modes in the U(1)-GfPEPS projector $|T\rangle$, where the latter has Q physical and virtual modes at each \mathbf{k} point. Thus, after contracting the virtual modes, the U(1)-GfPEPS has $Q - 2M$ physical modes for each \mathbf{k} point. This means that, for U(1)-GfPEPS, the number of occupied physical modes must be the *same* at each \mathbf{k} point. While gapped band insulators and gapless semimetals (e.g., those with Dirac points) fulfill this requirement, the possibility of describing a Fermi surface is ruled out. Although gapless fermions with a Fermi surface are known to violate the entanglement area law [51, 52] and cannot be described by PEPS with a fixed bond dimension in the thermodynamic limit, our explicit construction nevertheless puts a stronger constraint on U(1)-GfPEPS: If translational symmetry is preserved, U(1)-GfPEPS cannot have a Fermi surface even on finite-size systems.

C. Optimization

Consider a quadratic Hamiltonian of fermions

$$H = \sum_{\mathbf{k}} \sum_{\mu, \mu'=1}^P c_{\mathbf{k}, \mu}^\dagger [\mathcal{H}(\mathbf{k})]_{\mu, \mu'} c_{\mathbf{k}, \mu'}, \quad (14)$$

where $\mathcal{H}(\mathbf{k})$ is the single-particle Hamiltonian matrix. We use the U(1)-GfPEPS as a variational ansatz to approximate its ground state. We note that the U(1)-GfPEPS has $Q - 2M$ occupied physical modes at each \mathbf{k} point, so it will approximate the Fermi sea ground state of Eq. (14) with $Q - 2M$ occupied bands, implying a filling factor $(Q - 2M)/P$. The variational energy of the U(1)-GfPEPS with correlation matrix \mathcal{C}_{out} [see Eq. (12)] is given by

$$E = \frac{1}{2} \sum_{\mathbf{k}} \text{Tr}[(\mathcal{C}_{\text{out}}(\mathbf{k}) + \mathbb{1}_P) \mathcal{H}(\mathbf{k})^T], \quad (15)$$

where Tr is the usual matrix trace. The variational space is the correlation matrix \mathcal{C}_T for the U(1)-GfPEPS projector (8), which relates to $\mathcal{C}_{\text{out}}(\mathbf{k})$ via Eq. (13) [$\mathcal{C}_{\text{in}}(\mathbf{k})$ is fixed; see Eq. (7)].

For the energy minimization, we observe that the unitary matrix U in Eq. (10) can be parameterized as $U = (W, W_\perp)$, with W corresponding to the occupied modes and W_\perp , the orthogonal complement of W , to the unoccupied ones. By that, we can express \mathcal{C}_T in terms of W ,

$$\mathcal{C}_T = WW^\dagger - W_\perp W_\perp^\dagger = 2WW^\dagger - \mathbb{1}_{P+4M}. \quad (16)$$

Combining Eqs. (8), (13) and (15), our task boils down to numerically optimize W to minimize the ground-state energy in Eq. (15) under the isometry constraint $W^\dagger W = \mathbb{1}_Q$.

We obtain the optimal W by gradient based optimization schemes developed in Refs. [53–57]. First, we compute the numerical gradient $g^* = \frac{\partial E}{\partial W}$, which can be evaluated by finite difference or auto-differentiation. The gradients with respect to the unoccupied modes are always zero as they do not participate in the energetics.

Second, we project g onto the tangent space of $U = (W, W_\perp)$, which yields

$$G = (g - Wg^\dagger W, -Wg^\dagger W_\perp). \quad (17)$$

Note that the equation defining tangent vectors Δ of U can be obtained by differentiating $UU^\dagger = \mathbb{1}$, which gives $\Delta U^\dagger + U \Delta^\dagger = 0$ (i.e., ΔU^\dagger is skew-symmetric), and we can verify that G indeed satisfies such a constraint.

Next, we minimize the energy along the geodesic defined by G , i.e., $E(\alpha)$, with $W(\alpha) = e^{-\alpha Q_G} W$, where

$$Q_G = GU^\dagger = gW^\dagger - Wg^\dagger. \quad (18)$$

The isometry W is then updated according to the optimal value of α via the Wolfe line search [58]. This procedure

is repeated until the norm of the gradient is sufficiently small. To accelerate the convergence of such gradient descent minimization, one can modify the line search direction by combining the current gradient with the previous ones; commonly used methods include the nonlinear conjugate gradient [53, 55], the Limited-memory Broyden–Fletcher–Goldfarb–Shanno [57], and the direct inversion in the iterative subspace [59]. To reduce the numerical noise, one can anti-symmetrize Q_G manually at the end, after adding up the gradients. All methods improve the convergence rate comparing to gradient descent. In this work, we adopt the nonlinear conjugate gradient algorithm, and to reduce the numerical noise, we manually anti-symmetrize Q_G at the end, after adding up the gradients.

Once the optimal \mathcal{C}_T and \mathcal{C}_{out} have been obtained, it is also possible to compare the exact band dispersions obtained by diagonalizing $\mathcal{H}(\mathbf{k})$ with the variational ones obtained from U(1)-GfPEPS. One can diagonalize $\mathcal{C}_{\text{out}}(\mathbf{k})$ to obtain

$$V(\mathbf{k})^\dagger \mathcal{C}_{\text{out}}(\mathbf{k}) V(\mathbf{k}) = \begin{pmatrix} \mathbb{1}_{Q-2M} & 0 \\ 0 & -\mathbb{1}_{P-Q+2M} \end{pmatrix}. \quad (19)$$

Then, the occupied physical orbitals are given by $f_{\mathbf{k}, q}^\dagger = \sum_{\mu=1}^P V(\mathbf{k})_{q, \mu}^\dagger c_{\mathbf{k}, \mu}^\dagger$ with $q = 1, \dots, Q - 2M$. The single-particle Hamiltonian $\mathcal{H}(\mathbf{k})$ is then projected into this one-particle-occupied subspace by defining

$$[\mathcal{H}(\mathbf{k})]_{q, q'} = [V(\mathbf{k})^\dagger \mathcal{H}(\mathbf{k}) V(\mathbf{k})]_{q, q'} \quad (20)$$

with $q, q' = 1, \dots, Q - 2M$. Its eigenvalues give the variational dispersions for the *filled* bands.

D. Gutzwiller projection and tensor network contraction

The Gutzwiller projection is implemented by a product of local operators. For simplicity, we illustrate its implementation for spin-1/2 fermions at each site ($P = 2$). The full Gutzwiller projection is defined by $P_G = \prod_{\mathbf{r}} (n_{\mathbf{r}, \uparrow} - n_{\mathbf{r}, \downarrow})^2$ with $n_{\mathbf{r}, \mu} = c_{\mathbf{r}, \mu}^\dagger c_{\mathbf{r}, \mu}$ ($\mu = \uparrow, \downarrow$). P_G deletes empty and doubly occupied states and keeps two singly occupied states $|\mu\rangle = c_\mu^\dagger |0\rangle$ that are identified as spin-1/2 degrees of freedom.

Once the U(1)-GfPEPS projector $\prod_{\mathbf{r}} T_{\mathbf{r}} |0\rangle_{\text{p}, \text{v}}$ is obtained, the Gutzwiller projection results in a (fermionic) PEPS with projector $\prod_{\mathbf{r}} (n_{\mathbf{r}, \uparrow} - n_{\mathbf{r}, \downarrow})^2 T_{\mathbf{r}} |0\rangle_{\text{p}, \text{v}}$, and the virtual bond state $|I\rangle$ is unchanged. Utilizing this idea, it becomes possible to convert a Gutzwiller-projected Fermi sea state into PEPS, where the unprojected Fermi sea is approximated by optimizing U(1)-GfPEPS with respect to some quadratic Hamiltonians of fermions.

The remaining task is to derive the explicit tensor form of the U(1)-GfPEPS projector. If we write the occupied orbitals in Eq. (11) in a more compact form $d_q^\dagger = \sum_{\zeta=1}^{P+4M} U_{q, \zeta}^* c_\zeta^\dagger$ with ζ enumerating all physical

and virtual modes, the U(1)-GfPEPS local projector in Eq. (4) can be expressed in a Slater determinant form

$$T = \sum_{\zeta_1 < \dots < \zeta_Q} \det(U_{(1, \dots, Q), (\zeta_1, \dots, \zeta_Q)}^\dagger) c_{\zeta_1}^\dagger \cdots c_{\zeta_Q}^\dagger, \quad (21)$$

where local tensor coefficients [see Eq. (3)] can be read out from the determinants. Gutzwiller projection simply removes some configurations in Eq. (21). Other local operators can be applied in a similar way.

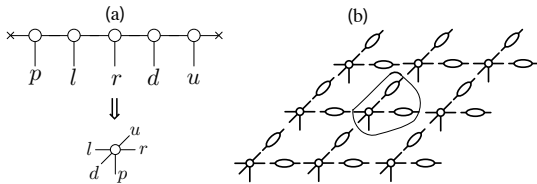


FIG. 2. Schematics of (a) converting the MPS form of $T_{\mathbf{r}}$ to a PEPS local tensor and (b) contracting $T_{\mathbf{r}}$ with entangled bond states (in oval shapes) to obtain a PEPS represented by a single local tensor.

Alternatively, one can also construct the U(1)-GfPEPS projector via the MPO–MPS approach [11]. This is most convenient when working with tensor network libraries supporting U(1) or non-Abelian symmetries. For the local projector $T|0\rangle_{p,v} = \prod_{q=1}^Q d_q^\dagger |0\rangle_{p,v}$, the vacuum $|0\rangle_{p,v}$ is treated as an MPS with bond dimension $D = 1$. Each occupied orbital d_q^\dagger is then represented as an MPO with bond dimension $D = 2$ (see Refs. [11, 22]). After applying all Q MPOs for occupied orbitals, $T|0\rangle_{p,v}$ is represented as an MPS with bond dimension $D = 2^Q$. The local tensor in Eq. (3) is obtained by contracting all virtual indices of this MPS [see Fig. 2(a)]. The advantage of the MPO–MPS approach is that the tensor entries of $T|0\rangle_{p,v}$ as well as the corresponding symmetry structure, including the quantum numbers of the symmetric tensors and the corresponding Clebsch–Gordan coefficients, can be automatically generated.

After the Gutzwiller projection, it is practical to contract the virtual bonds in Eq. (1) into the PEPS local tensors [see Fig. 2(b)]. As the optimization of U(1)-GfPEPS is very efficient and the system size that can be reached is quite large, we can tile up to the resulting Gutzwiller-projected U(1)-GfPEPS tensor to approximate the state on an infinite lattice. Such infinite PEPS involves a single tensor at each site and is ready for computing physical quantities with fermionic tensor network contraction algorithms [60]. For this work, we adopt the corner transfer matrix renormalization group (CTMRG) method [31, 33] to perform tensor network contractions. To achieve higher accuracy and reduce computational cost in CTMRG calculations, we impose both the U(1) particle-number and the SU(2) spin symmetry provided by the QSpace library [61, 62].

III. RESULTS

A. Dirac fermion models on square and kagome lattices

As benchmark examples, we use U(1)-GfPEPS to approximate the Fermi sea ground states of two spinless fermion models with a Dirac spectrum: the π -flux model on the square lattice [63] and the $[0, \pi]$ -flux model on the kagome lattice [64, 65]. Both models have nearest-neighbor hoppings with the Hamiltonian

$$H = \sum_{\langle \mathbf{r}, \mathbf{r}' \rangle} t_{\mathbf{r}, \mathbf{r}'} c_{\mathbf{r}}^\dagger c_{\mathbf{r}'}, \quad (22)$$

where the square-lattice model has π -flux within each plaquette, and the kagome model has zero flux through each triangle and π -flux through each hexagon. The hoppings realizing these flux choices are depicted in Figs. 3(a) and (b).

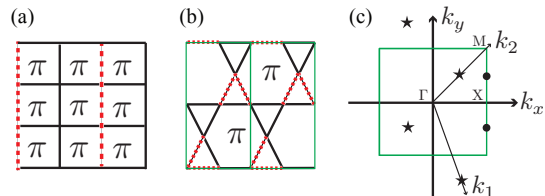


FIG. 3. Schematics of (a) the π -flux model on the square lattice and (b) the $[0, \pi]$ -flux model on the kagome lattice. The solid (red dashed) lines are the bonds with hopping $t = 1$ ($t = -1$). (c) The first Brillouin zone (in green) of the effective square lattices for (a) and (b) with $\Gamma = (0, 0)$, $X = (\pi, 0)$ and $M = (\pi, \pi)$. The black dots denote two Dirac nodes at $(\pi, \pm\pi/2)$ for the π -flux model, and the black stars at $(\pi/2, -3\pi/2)$ and $(\pi/2, \pi/2)$ for the $[0, \pi]$ -flux model along k_1 and k_2 directions, respectively.

The π -flux square-lattice ($[0, \pi]$ -flux kagome) model has a two-site (six-site) unit cell. We group all sites in the same unit cell together and treat them as a single site in an effective square lattice. This allows us to use a translationally invariant U(1)-GfPEPS ansatz with $P = 2$ ($P = 6$) for the π -flux square-lattice ($[0, \pi]$ -flux kagome) model. At half filling, both models have two Dirac nodes in the FBZ, as shown in Fig. 3(c). For the numerical optimization, the effective square lattice has size $L \times L$ and the boundary condition (periodic or antiperiodic) is adjusted such that exact zero-energy modes at the Dirac nodes are avoided to ensure a unique ground state. The optimal U(1)-GfPEPS is determined numerically for each fixed number of virtual mode M , when the averaged norm of its energy gradient with respect to the Hamiltonian in Eq. (22) is smaller than 10^{-6} .

For the π -flux square-lattice model, we observe that the relative error in the ground-state energy density δE decreases exponentially when increasing the number of

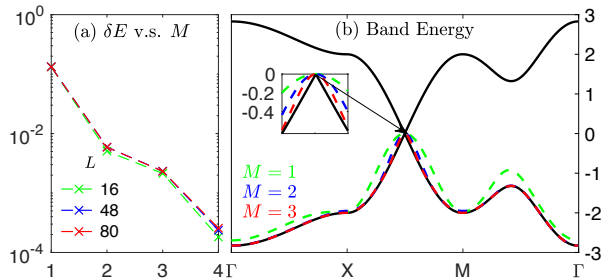


FIG. 4. Results of optimized U(1)-GfPEPS for the π -flux state on the square lattice. (a) Relative error in the energy density of U(1)-GfPEPS versus the number of virtual modes, M . (b) Plots of the exact band structure (solid lines) and the variationally obtained occupied band at half filling (dashed lines).

virtual modes M [see Fig. 4(a)]. Furthermore, the finite-size effect in the energy density error appears to be small. As shown in Fig. 4(b), the U(1)-GfPEPS with $M = 2$ (bond dimension $D = 4$), which is variationally optimized on a 80×80 lattice, reproduces the band dispersion in the thermodynamic limit very well.

For the $[0, \pi]$ -flux kagome model, the relative error of the ground-state energy density δE in Fig. 5(a) follows the same trend as the π -flux square-lattice model. At half filling, the low-energy physics is dictated by two Dirac nodes [Fig. 5(b)]. The band dispersions along k_1 and k_2 directions (cutting two Dirac nodes) are plotted in Figs. 5(b) and (c). With that, we examine the results due to the U(1)-GfPEPS approximation at small M . We again find a good agreement between the variational results with $M = 2$ and the exact solution in the thermodynamic limit.

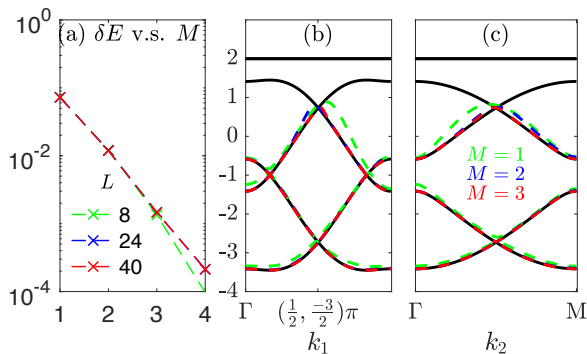


FIG. 5. Results of optimized U(1)-GfPEPS for the $[0, \pi]$ -flux model on the kagome lattice. (a) Relative error in the energy density of U(1)-GfPEPS versus the number of virtual modes, M . (b), (c) Plots of the exact band structure (solid lines) and the variationally obtained lower occupied bands (dashed lines), as functions of k_1 and k_2 .

B. U(1)-Dirac spin liquids on square and kagome lattices

The optimized U(1)-GfPEPS for Dirac Fermi sea states in Sec. III A are then used to build PEPS representing U(1)-Dirac spin liquids. To this end, we attach a spin index $\sigma = \uparrow, \downarrow$ to the physical modes in Eq. (22) and interpret them as fermionic partons for a spin-1/2 system. The spin-1/2 operators are written as $\mathbf{S}(\mathbf{r}) = \frac{1}{2} \sum_{\sigma\sigma'} c_{\mathbf{r}\sigma}^\dagger \boldsymbol{\tau}_{\sigma\sigma'} c_{\mathbf{r}\sigma'}$, where $\boldsymbol{\tau}$ are Pauli matrices. The single-occupancy constraint $\sum_{\sigma} c_{\mathbf{r}\sigma}^\dagger c_{\mathbf{r}\sigma} = 1$ ensures the physical spin-1/2 Hilbert space and is imposed by the full Gutzwiller projection.

Starting from a U(1)-GfPEPS $|\Psi\rangle$ for spinless fermions, we just need two copies of it (with different spins) and apply the Gutzwiller projection to obtain a PEPS for spin-1/2 system, i.e., $|\Phi\rangle = P_G |\Psi_\uparrow\rangle \otimes |\Psi_\downarrow\rangle$. For $|\Psi\rangle$ with virtual bonds and projector defined in Eqs. (1) and (4), $|\Psi_\uparrow\rangle \otimes |\Psi_\downarrow\rangle$ is obtained by attaching a spin index σ to both virtual and physical modes, e.g., the projector with $T = \prod_{q=1}^Q \prod_{\sigma=\uparrow,\downarrow} d_{q,\sigma}^\dagger$ (similar for the virtual bonds). If $|\Psi\rangle$ has bond dimension $D = 2^M$, the Gutzwiller-projected PEPS $|\Phi\rangle$ has bond dimension $D = 4^M$. The method for determining the local tensor of $|\Phi\rangle$ is described in Sec. II D.

As the U(1)-GfPEPSs obtained in Sec. III A represent Dirac Fermi sea states, it is possible to obtain U(1)-Dirac spin liquids after the Gutzwiller projection [65, 66]. The field theory governing the large-distance behavior of U(1)-Dirac spin liquids is quantum electrodynamics in 2+1 dimensions (QED₃), with N_f -flavor Dirac fermions coupled to a U(1) gauge field. The calculation of critical exponents in QED₃ is, however, very challenging, especially when the fermion flavor N_f is not large [67]. As our setups in Sec. III A have two Dirac nodes, the Gutzwiller-projected U(1)-GfPEPSs should be relevant to QED₃ with $N_f = 4$. It is thus an interesting task to compute their critical exponents with PEPS techniques in the thermodynamic limit.

We focus in this work on the staggered spin-spin correlation function $C(r) = (-1)^r \langle \mathbf{S}(0) \cdot \mathbf{S}(\mathbf{r}) \rangle$, where two spins, with distance $r = |\mathbf{r}|$, are placed on the same row of the effective square lattice. Due to the large computational cost, we have only performed calculations using Gutzwiller-projected U(1)-GfPEPSs with $D = 4$ and 16 ($M = 1$ and 2). For a given D , we compute the environment of PEPS via CTMRG method with a fixed number of symmetry multiplets χ^* , which roughly corresponds to a typical bond dimension of $\chi = 2\chi^*$ if symmetries are not used. The CTMRG environment constitutes the bulk part of the infinite lattice, and its accuracy can be examined by varying χ^* .

For the PEPS representing Gutzwiller projected π -flux state, the results are plotted in Figs. 6(a) and (b). For $D = 4$, $C(r)$ has a fast exponential decay, which is almost unchanged when varying χ^* . However, such exponential decay gets slowed down as we increase the bond

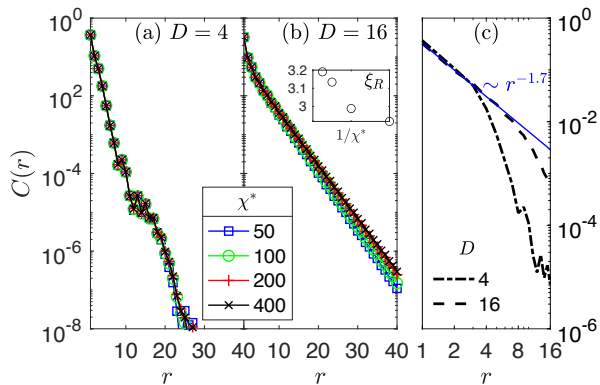


FIG. 6. Staggered spin correlations for Gutzwiller-projected U(1)-GfPEPS from the π -flux state on the square lattice. Semilogarithmic plots for (a) $D = 4$ and (b) $D = 16$ with different environmental bond dimensions χ^* . (c) Log-log plots with $\chi^* = 400$, and the blue solid line shows a powerlaw decay with an exponent $\eta = 1.7$.

dimension to $D = 16$. We also observe an increase of the correlation length ξ_R at large distance ($C(r) \sim e^{-r/\xi_R}$) by increasing χ^* . Overall, our results suggest that the spin gap imposed by the finite bond dimensions (D and χ^*) can be further reduced. However, at this stage, we cannot predict to which value of D one may achieve an algebraic decay at large distance. Turning to the short distance regime [Fig. 6(c)], we observe a buildup of a powerlaw decay $C(r) \sim r^{-\eta}$ with exponent $\eta \approx 1.7$. This is in rough agreement with previous Monte Carlo estimates ($\eta \approx 1.6$ [68] and $\eta \approx 2$ [69]) on finite-size clusters, but smaller than the extrapolation of the large- N_f result $\eta = 4 - 64/(3\pi^2 N_f) + \mathcal{O}(1/N_f^2)$ [70] to $N_f = 4$, which gives $\eta \approx 3.46$.

For the kagome-lattice case, the calculation with the Gutzwiller-projected U(1)-GfPEPS is very challenging, since the physical index of each PEPS local tensor contains six spin-1/2's (physical dimension $d = 32$). This makes it difficult to contract double layer tensors in CTMRG. Therefore, for $D = 16$, we only report results with small environmental bond dimensions $\chi^* = 20$ and 40. Nevertheless, in Fig. 7(a), one can still observe an increase in the correlation length when going from $D = 4$ to 16. This entails a rather severe finite D effect, similar to the square-lattice case. From the plot in log-log scale [Fig. 7(b)], we see a quick deviation from the powerlaw behavior. Thus, for the Gutzwiller projected $[0, \pi]$ -flux state, reliable conclusions cannot be made from these results. This issue, instead, should be further investigated with even larger bond dimensions, which is beyond our current computational capability.

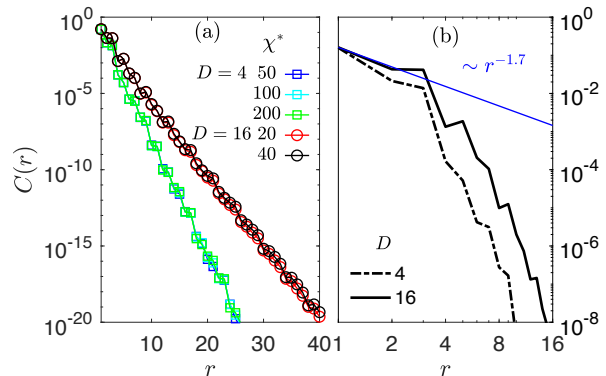


FIG. 7. Staggered spin correlations for Gutzwiller-projected U(1)-GfPEPS from the $[0, \pi]$ -flux state on the kagome lattice. (a) Semilogarithmic plots for $D = 4$ and $D = 16$ with different environmental bond dimension χ^* . (b) Log-log plots with the largest possible χ^* . The blue solid line showing the powerlaw decay with exponent $\eta = 1.7$ is a guide to the eye.

IV. SUMMARY AND OUTLOOK

To summarize, we have put forward a formalism for constructing particle-number-conserving Gaussian fermionic projected entangled pair states. These states are suitable for describing the ground states of gapped band insulators and gapless fermions with band touching points, but incapable of describing gapless fermions with a Fermi surface. We further develop a systematic method using these states as variational Ansatz for approximating the Fermi sea ground states of free fermionic Hamiltonians. Benchmark calculations on the π -flux square-lattice model and the $[0, \pi]$ -flux kagome-lattice model have shown excellent results. The implementation of additional Gutzwiller projection on top of these variationally obtained U(1)-GfPEPS provides PEPS representation of U(1)-Dirac spin liquid states for spin-1/2 systems. Using the CTMRG method to calculate spin-spin correlation functions in the thermodynamic limit, we have obtained a critical exponent $\eta \approx 1.7$ from the Gutzwiller-projected U(1)-GfPEPS representing π -flux U(1)-Dirac spin liquid state on the square lattice.

Computationally, the optimization of the U(1)-GfPEPS using correlation matrix is efficient, as the number of parameters scales linearly with respect to the number of virtual modes M . The size of real-space PEPS tensor, on the other hand, grows exponentially when increasing M . This turns out to be the bottleneck for constructing the Gutzwiller-projected U(1)-GfPEPS with larger bond dimensions.

For future works, one interesting direction is to use our method to test the quality of Gutzwiller projected wave functions for challenging strongly correlated systems, such as the kagome Heisenberg antiferromagnet and the t - J model. It is also a promising direction to use them as initial Ansatz to improve the performance

of PEPS variational algorithms.

ACKNOWLEDGMENTS

We thank Nick Bultinck, Meng Cheng, and Jutho Haegeman for helpful discussions. H.-H.T. is grateful to Lei Wang and Qi Yang for collaborations and stimulating discussions on a closely related topic. The numerical simulations in this work are based on the QSpace tensor library [61, 62]. J.-W.L. and J.v.D. are supported by the Deutsche Forschungsgemeinschaft under Germany's Excellence Strategy EXC-2111 (Project No. 390814868), and are part of the Munich Quantum Valley, supported by the Bavarian state government through the High-tech Agenda Bayern Plus. H.-H.T. is supported by the Deutsche Forschungsgemeinschaft through project A06 of SFB 1143 (project-id 247310070).

Appendix A: Particle-number-conserving fermionic Gaussian states

In this Appendix, we provide further details on particle-number-conserving fermionic Gaussian states. The proof of Eq. (13) is also given.

To begin with, we briefly review the formalism of fermionic Gaussian states [50]. Consider a system of n fermionic modes with creation (annihilation) operators c_j^\dagger (c_j), $j = 1, \dots, n$. Their linear combinations

$$\gamma_{2j-1} = c_j^\dagger + c_j, \quad \gamma_{2j} = (-i)(c_j^\dagger - c_j) \quad (\text{A1})$$

define $2n$ Majorana operators satisfying $\{\gamma_a, \gamma_b\} = 2\delta_{ab}$ ($a, b = 1, \dots, 2n$). The density operator ρ , for both pure and mixed states, can be written as a polynomial in γ_a :

$$\rho = \frac{1}{2^n} \left(\mathbb{1} + \frac{i}{2} \gamma^T G \gamma + \dots \right), \quad (\text{A2})$$

where $\gamma = (\gamma_1, \gamma_2, \dots, \gamma_{2n})^T$, $\mathbb{1}$ is the identity operator in the 2^n -dimensional Hilbert space, and the ellipsis stands for terms with more than two (but even number of) Majorana operators. The real skew-symmetric matrix G encodes two-point correlators in ρ , i.e., $G_{ab} = \frac{i}{2} \text{tr}(\rho[\gamma_a, \gamma_b])$. This so-called correlation matrix G satisfies $G^T G \leq \mathbb{1}_{2n}$ with $\mathbb{1}_{2n}$ being the $2n \times 2n$ identity matrix, and $G^T G = \mathbb{1}_{2n}$ is achieved if and only if ρ describes a pure state. An operational definition of *fermionic Gaussian state* is through the Grassmann representation of ρ in Eq. (A2): If one replaces each γ_a by its corresponding Grassmann variable θ_a (and the identity operator I by 1), the Grassmann representation for a fermionic Gaussian state ρ , denoted by $\omega(\rho, \theta)$, takes the following Gaussian form:

$$\omega(\rho, \theta) = \frac{1}{2^n} \exp\left(\frac{i}{2} \theta^T G \theta\right), \quad (\text{A3})$$

where $\theta = (\theta_1, \theta_2, \dots, \theta_{2n})^T$. The expansion of the exponential in Eq. (A3) gives all multipoint correlators in ρ , which are just coefficients of the respective Grassmann monomials and can be easily verified to be determined by Wick's theorem.

For our purpose, we would like to restrict ourselves to fermionic Gaussian states with a *fixed particle number*. That means, the density operator ρ in Eq. (A2), apart from being Gaussian, should also commute with the total fermion number operator

$$N = \sum_{j=1}^n c_j^\dagger c_j = \frac{n}{2} \mathbb{1} - \frac{i}{2} \gamma^T Q \gamma \quad (\text{A4})$$

with $Q = \mathbb{1}_n \otimes i\sigma^y$. For $[\rho, N] = 0$ to hold, the correlation matrix G must take the following form:

$$G = G_1 \otimes \mathbb{1}_2 + G_2 \otimes i\sigma^y, \quad (\text{A5})$$

where the $n \times n$ matrix G_1 (G_2) is real and skew-symmetric (symmetric). This structure can also be seen by requiring that there are no pairing correlations in ρ , i.e., $\text{tr}(\rho c_i^\dagger c_j^\dagger) = \text{tr}(\rho c_i c_j) = 0 \forall i, j$. It is then more natural to use a $n \times n$ "complex" correlation matrix

$$C_{ij} \equiv 2\text{tr}(\rho c_i^\dagger c_j) - \delta_{ij}, \quad (\text{A6})$$

which relates to the "real" one in Eq. (A5) via $C = -G_2 - iG_1$. The complex correlation matrix C is Hermitian and has eigenvalues $\lambda_q \in [-1, 1] \forall q = 1, \dots, n$. If all $\lambda_q = \pm 1$, ρ is a pure state and the complex correlation matrix satisfies $C^{-1} = C$. The diagonalization of C with a unitary matrix U via $(U^\dagger C U)_{qq'} = \lambda_q \delta_{qq'}$ defines the eigenmodes of ρ :

$$d_q^\dagger = \sum_{j=1}^n U_{qj}^\dagger c_j^\dagger. \quad (\text{A7})$$

This brings ρ into a simple form

$$\rho = \prod_{q=1}^n \left(\frac{1 + \lambda_q}{2} d_q^\dagger d_q + \frac{1 - \lambda_q}{2} d_q d_q^\dagger \right), \quad (\text{A8})$$

where $d_q^\dagger d_q$ ($d_q d_q^\dagger$) is a projector onto an occupied (empty) state of d_q -mode. Thus, the eigenmodes d_q^\dagger associated with $\lambda_q = 1$ (-1) correspond to occupied (empty) single-particle orbitals in ρ . For a pure state ρ , the number of eigenvalues with $\lambda_q = 1$ is equal to the total number of occupied fermions.

The Grassmann representation is a convenient tool for fermionic Gaussian states [50]. To adjust this tool for the particle-number-conserving case, we define n pairs of "complex" Grassmann variables

$$\bar{\xi}_j = \frac{1}{\sqrt{2}}(\theta_{2j-1} - i\theta_{2j}), \quad \xi_j = \frac{1}{\sqrt{2}}(\theta_{2j-1} + i\theta_{2j}) \quad (\text{A9})$$

with $j = 1, \dots, n$. After substituting them into Eq. (A3) and using the relation between real and complex correlation matrices [Eqs. (A5) and (A6)], we arrive at the

following ‘‘complex’’ Grassmann representation of ρ :

$$\omega(\rho, \bar{\xi}, \xi) = \frac{1}{2^n} \exp(-\bar{\xi}^T \mathcal{C} \xi), \quad (\text{A10})$$

where $\xi = (\xi_1, \xi_2, \dots, \xi_n)^T$ and $\bar{\xi}$ is similarly defined.

For constructing GfPEPS, one needs to deal with both *physical* and *virtual* fermionic modes. Let us consider n physical and m virtual modes whose creation operators are c_j^\dagger ($j = 1, \dots, n$) and b_l^\dagger ($l = 1, \dots, m$), respectively. The input is a Gaussian density operator ρ_{in} residing solely in the virtual Hilbert space. The GfPEPS projector, formulated as another Gaussian density operator ρ_{T} , lives in the composite Hilbert space of physical and virtual modes. The Gaussian density operator of GfPEPS is written as

$$\rho_{\text{out}} \propto \text{tr}_v(\rho_{\text{T}} \rho_{\text{in}}), \quad (\text{A11})$$

where the partial trace tr_v is with respect to the virtual Hilbert space. It is shown in Ref. [71] that the correlation matrix of ρ_{out} can be calculated by using the Grassmann representation of $\text{tr}_v(\rho_{\text{T}} \rho_{\text{in}})$. We can readily generalize this approach to the particle-number-conserving setting by converting ‘‘real’’ Grassmann variables to ‘‘complex’’

ones [see Eq. (A9)] and obtain

$$\begin{aligned} \text{tr}_v(\rho_{\text{T}} \rho_{\text{in}})(\bar{\xi}, \xi) &= 2^m \int D\bar{\eta} D\eta D\bar{\mu} D\mu e^{\bar{\eta}^T \mu - \bar{\mu}^T \eta} \\ &\times \omega(\rho_{\text{T}}, \bar{\xi}, \xi, \bar{\eta}, \eta) \omega(\rho_{\text{in}}, \bar{\mu}, \mu), \end{aligned} \quad (\text{A12})$$

where $\bar{\xi}, \xi$ ($\bar{\eta}, \eta, \bar{\mu}, \mu$) are Grassmann variables for physical (virtual) modes and $D\bar{\eta} D\eta = d\bar{\eta}_1 d\eta_1 \dots d\bar{\eta}_m d\eta_m$ (similar for $D\bar{\mu} D\mu$). By using the Grassmann representation of ρ_{T} and ρ_{in} , namely,

$$\begin{aligned} \omega(\rho_{\text{T}}, \bar{\xi}, \xi, \bar{\eta}, \eta) &= \frac{1}{2^{n+m}} \exp \left[-(\bar{\xi}^T \ \bar{\eta}^T) \begin{pmatrix} A & B \\ B^\dagger & D \end{pmatrix} \begin{pmatrix} \xi \\ \eta \end{pmatrix} \right], \\ \omega(\rho_{\text{in}}, \bar{\mu}, \mu) &= \frac{1}{2^m} \exp(-\bar{\mu}^T \mathcal{C}_{\text{in}} \mu), \end{aligned}$$

and performing Gaussian integrations in Eq. (A12), we obtain

$$\begin{aligned} \text{tr}_v(\rho_{\text{T}} \rho_{\text{in}})(\bar{\xi}, \xi) &= \frac{1}{2^{n+m}} \det(\mathcal{C}_{\text{in}}) \det(D + \mathcal{C}_{\text{in}}^{-1}) \\ &\times \exp(-\bar{\xi}^T \mathcal{C}_{\text{out}} \xi), \end{aligned} \quad (\text{A13})$$

where the correlation matrix of ρ_{out} reads

$$\mathcal{C}_{\text{out}} = A - B(D + \mathcal{C}_{\text{in}}^{-1})^{-1} B^\dagger, \quad (\text{A14})$$

For $U(1)$ -GfPEPS, ρ_{in} is a pure state and satisfies $\mathcal{C}_{\text{in}}^{-1} = \mathcal{C}_{\text{in}}$. This completes the proof of Eq. (13).

-
- [1] M. C. Gutzwiller, *Phys. Rev. Lett.* **10**, 159 (1963).
[2] M. C. Gutzwiller, *Phys. Rev.* **137**, A1726 (1965).
[3] P. W. Anderson, *Science* **235**, 1196 (1987).
[4] F. D. M. Haldane, *Phys. Rev. Lett.* **60**, 635 (1988).
[5] B. S. Shastry, *Phys. Rev. Lett.* **60**, 639 (1988).
[6] A. Kitaev, *Ann. Phys.* **321**, 2 (2006).
[7] C. Gros, R. Joynt, and T. M. Rice, *Phys. Rev. B* **36**, 381 (1987).
[8] H. Yokoyama and H. Shiba, *J. Phys. Soc. Jpn* **56**, 1490 (1987).
[9] C. Gros, *Ann. Phys.* **189**, 53 (1989).
[10] M. T. Fishman and S. R. White, *Phys. Rev. B* **92**, 075132 (2015).
[11] Y.-H. Wu, L. Wang, and H.-H. Tu, *Phys. Rev. Lett.* **124**, 246401 (2020).
[12] H.-K. Jin, H.-H. Tu, and Y. Zhou, *Phys. Rev. B* **101**, 165135 (2020).
[13] A. M. Aghaei, B. Bauer, K. Shtengel, and R. V. Mishmash, [arXiv:2009.12435](https://arxiv.org/abs/2009.12435).
[14] G. Petrica, B.-X. Zheng, G. K.-L. Chan, and B. K. Clark, *Phys. Rev. B* **103**, 125161 (2021).
[15] N. G. Jones, J. Bibo, B. Jobst, F. Pollmann, A. Smith, and R. Verresen, *Phys. Rev. Research* **3**, 033265 (2021).
[16] H.-K. Jin, R.-Y. Sun, Y. Zhou, and H.-H. Tu, *Phys. Rev. B* **105**, L081101 (2022).
[17] S. R. White, *Phys. Rev. Lett.* **69**, 2863 (1992).
[18] S. Östlund and S. Rommer, *Phys. Rev. Lett.* **75**, 3537 (1995).
[19] F. Verstraete, V. Murg, and J. I. Cirac, *Adv. Phys.* **57**, 143 (2008).
[20] U. Schollwöck, *Ann. Phys.* **326**, 96 (2011).
[21] H.-K. Jin, H.-H. Tu, and Y. Zhou, *Phys. Rev. B* **104**, L020409 (2021).
[22] J.-Y. Chen, J.-W. Li, P. Nataf, S. Capponi, M. Mambri, K. Totsuka, H.-H. Tu, A. Weichselbaum, J. von Delft, and D. Poilblanc, *Phys. Rev. B* **104**, 235104 (2021).
[23] H.-K. Jin, R.-Y. Sun, H.-H. Tu, and Y. Zhou, *Sci. Bull.* (2022).
[24] R.-Y. Sun, H.-K. Jin, H.-H. Tu, and Y. Zhou, [arXiv:2203.07321](https://arxiv.org/abs/2203.07321).
[25] F. Verstraete and J. I. Cirac, [arXiv: cond-mat/0407066](https://arxiv.org/abs/cond-mat/0407066).
[26] H. C. Jiang, Z. Y. Weng, and T. Xiang, *Phys. Rev. Lett.* **101**, 090603 (2008).
[27] J. Jordan, R. Orús, G. Vidal, F. Verstraete, and J. I. Cirac, *Phys. Rev. Lett.* **101**, 250602 (2008).
[28] P. Corboz, *Phys. Rev. B* **94**, 035133 (2016).
[29] L. Vanderstraeten, J. Haegeman, P. Corboz, and F. Verstraete, *Phys. Rev. B* **94**, 155123 (2016).
[30] H.-J. Liao, J.-G. Liu, L. Wang, and T. Xiang, *Phys. Rev. X* **9**, 031041 (2019).
[31] T. Nishino and K. Okunishi, *J. Phys. Soc. Jpn* **65**, 891 (1996).
[32] M. Levin and C. P. Nave, *Phys. Rev. Lett.* **99**, 120601 (2007).
[33] R. Orús and G. Vidal, *Phys. Rev. B* **80**, 094403 (2009).
[34] Z. Y. Xie, J. Chen, M. P. Qin, J. W. Zhu, L. P. Yang,

- and T. Xiang, *Phys. Rev. B* **86**, 045139 (2012).
- [35] M. T. Fishman, L. Vanderstraeten, V. Zauner-Stauber, J. Haegeman, and F. Verstraete, *Phys. Rev. B* **98**, 235148 (2018).
- [36] N. Schuch, I. Cirac, and D. Pérez-García, *Ann. Phys.* **325**, 2153 (2010).
- [37] O. Buerschaper, *Ann. Phys.* **351**, 447 (2014).
- [38] D. J. Williamson, N. Bultinck, M. Mariën, M. B. Şahinoğlu, J. Haegeman, and F. Verstraete, *Phys. Rev. B* **94**, 205150 (2016).
- [39] M. B. Şahinoğlu, D. Williamson, N. Bultinck, M. Mariën, J. Haegeman, N. Schuch, and F. Verstraete, *Ann. Henri Poincaré* **22**, 563 (2021).
- [40] C. V. Kraus, N. Schuch, F. Verstraete, and J. I. Cirac, *Phys. Rev. A* **81**, 052338 (2010).
- [41] T. B. Wahl, H.-H. Tu, N. Schuch, and J. I. Cirac, *Phys. Rev. Lett.* **111**, 236805 (2013).
- [42] J. Dubail and N. Read, *Phys. Rev. B* **92**, 205307 (2015).
- [43] D. Poilblanc, P. Corboz, N. Schuch, and J. I. Cirac, *Phys. Rev. B* **89**, 241106 (2014).
- [44] T. B. Wahl, S. T. Hafler, H.-H. Tu, J. I. Cirac, and N. Schuch, *Phys. Rev. B* **90**, 115133 (2014).
- [45] S. Yang, T. B. Wahl, H.-H. Tu, N. Schuch, and J. I. Cirac, *Phys. Rev. Lett.* **114**, 106803 (2015).
- [46] A. Hackenbroich, B. A. Bernevig, N. Schuch, and N. Regnault, *Phys. Rev. B* **101**, 115134 (2020).
- [47] Q. Mortier, N. Schuch, F. Verstraete, and J. Haegeman, *arXiv:2008.11176*.
- [48] This can be straightforwardly generalized to the case of a larger unit cell, where different sites in the same unit cell have different T_i .
- [49] I. Peschel, *J. Phys. A* **36**, L205 (2003).
- [50] S. Bravyi, *Quantum Inf. and Comp.* **5**, 216 (2005).
- [51] M. M. Wolf, *Phys. Rev. Lett.* **96**, 010404 (2006).
- [52] D. Gioev and I. Klich, *Phys. Rev. Lett.* **96**, 100503 (2006).
- [53] A. Edelman, T. A. Arias, and S. T. Smith, *SIAM J. Matrix Anal. Appl.* **20**, 303 (1998).
- [54] T. V. Voorhis and M. Head-Gordon, *Mol. Phys.* **100**, 1713 (2002).
- [55] T. Abrudan, J. Eriksson, and V. Koivunen, *Signal Process.* **89**, 1704 (2009).
- [56] X. Zhu, *Comput. Optim. Appl.* **67**, 73 (2016).
- [57] M. Hauru, M. V. Damme, and J. Haegeman, *SciPost Phys.* **10**, 40 (2021).
- [58] J. Nocedal and S. J. Wright, *Numerical Optimization* (Springer New York, 2006).
- [59] P. Császár and P. Pulay, *J. Mol. Struct.* **114**, 31 (1984).
- [60] P. Corboz, R. Orús, B. Bauer, and G. Vidal, *Phys. Rev. B* **81**, 165104 (2010).
- [61] A. Weichselbaum, *Ann. Phys.* **327**, 2972 (2012).
- [62] A. Weichselbaum, *Phys. Rev. Research* **2**, 023385 (2020).
- [63] I. Affleck and J. B. Marston, *Phys. Rev. B* **37**, 3774 (1988).
- [64] M. B. Hastings, *Phys. Rev. B* **63**, 014413 (2000).
- [65] Y. Ran, M. Hermele, P. A. Lee, and X.-G. Wen, *Phys. Rev. Lett.* **98**, 117205 (2007).
- [66] M. Hermele, Y. Ran, P. A. Lee, and X.-G. Wen, *Phys. Rev. B* **77**, 224413 (2008).
- [67] M. Hermele, T. Senthil, M. P. A. Fisher, P. A. Lee, N. Nagaosa, and X.-G. Wen, *Phys. Rev. B* **70**, 214437 (2004).
- [68] D. A. Ivanov, *On the $SU(2)$ theory of the t - J model*, Ph.D. thesis, MIT (1999).
- [69] F. Ferrari, A. Parola, and F. Becca, *Phys. Rev. B* **103**, 195140 (2021).
- [70] W. Rantner and X.-G. Wen, *Phys. Rev. B* **66**, 144501 (2002).
- [71] Q. Yang, X.-Y. Zhang, H.-J. Liao, H.-H. Tu, and L. Wang, *arXiv:2208.xxxxx*.

5 Conclusion and outlook

This thesis demonstrates that while tensor network methods have been making much progress over the past three decades, there is still room for new ideas and methodological improvement in simulating correlated quantum many-body systems. Here we close with a summary of what we have achieved and an outlook of future research directions.

Matrix product states For MPS, we put forward a new approach to improve the accuracy of one-site algorithms for both ground state search and real-time evolution. The importance of this is that for an MPS with physical dimensions of d and virtual bond dimensions of D , the commonly used two-site algorithms run in $\mathcal{O}(D^3 d^2)$ time with reliable accuracy, while one-site algorithms run in $\mathcal{O}(D^3 d)$ time with less control. Nonetheless, the factor of d is crucial. To this end, we proposed a bond expansion approach using tangent space methods to fix the accuracy problem. Now, for the one-band Hubbard model with $d = 4$, a one-month calculation using the two-site scheme can be done in one week by our modified one-site scheme that yields the same accuracy.

Going beyond, we realize that the concept of dissecting the parameter space of MPS via tangent space methods in a sense is very general. The conventional one-site projector \mathcal{P}^{1s} that leads to the typical one-site algorithms confines the variational space within the subspace \mathbb{V}^{1s} of the full Hilbert space. Extending the tangent space construction, we can easily define the n -site projector \mathcal{P}^{ns} , which corresponds to an enlarged MPS manifold \mathbb{V}^{ns} . We have so far devised a method to enrich \mathbb{V}^{1s} using a small portion of \mathbb{V}^{2s} to improve the one-site algorithms. As $\mathbb{V}^{1s} \subseteq \mathbb{V}^{2s} \dots \subseteq \mathbb{V}^{zs}$ is always true and does not depend on the specifics of algorithms, we, therefore, foresee that our idea will also be applicable for computing low energy excitations, spectral functions and finite temperature density matrices in the future.

Projected entangled-pair states Following the technical advance on non-abelian iPEPS by Benedikt Bruognolo, we focused on applying the existing iPEPS algorithms to study the ground states of two-dimensional quantum systems.

We have worked on the two-dimensional t - J model, which is related to the Hubbard model through the second order approximation in the large U/t limit. Close to half-filling, we found a phase transition from the spin stripe order to the d -wave superconducting order around hole doping $\delta \sim 0.2$. We have also studied the two-dimensional Kitaev- Γ model, a relevant spin model to the α - RuCl_3 material. While the Kitaev- Γ model has been extensively studied, its magnetic properties are poorly understood. We use iPEPS to simulate its quantum phase diagram, in which we found evidence of an exotic magnetic ordering in line with the classical spin simulations.

Looking ahead, we would like to push forward our iPEPS research to simulate the two-dimensional Hubbard model with next-nearest-neighbor hoppings or nearest-neighbor repulsions [Rie89, dS89, TTR⁺93, WS99, ZC16, IOI18, JD19, PTIG19]. These two terms are prime candidates to introduce further frustrations that could potentially stabilize the d -wave superconducting order at doping close to $1/8$, relevant

to the cuprate materials. Besides the ground state search problem, iPEPS simulations for finite temperatures [CDC19, KREO19, CRCD21] and excitation spectra [VMVH15, VHV19, PC20, PAC22] are also very much desirable. So far, several interesting experimental observations at finite temperature on cuprate materials, such as the pseudogap phase, the melting of charge-density-waves in $\text{La}_{2-x}\text{Ba}_x\text{CuO}_4$, and the giant phonon anomalies in $\text{YBa}_x\text{Cu}_y\text{O}_{7-x}$, remain terra incognita for tensor network simulations [RJRT19, Tra20]. We look forward to addressing these challenges in the future.

Parton construction of tensor network states In this research direction, we combine two pivotal methods, tensor network methods and parton construction, to study quantum spin liquid in two dimensions.

First, we have used the parton construction of MPSs to study $\text{SU}(N)$ chiral spin liquids. We first generalized the parton fermionic model for $\text{SU}(2)$ chiral spin liquids to $\text{SU}(N)$ chiral spin liquids. We then used the parton approach we developed to construct a complete, orthonormal set of topological states as MPSs on narrow cylinders to benchmark against the conformal field theory predictions. Lastly, we numerically testified that the spin Hamiltonian we proposed can indeed stabilize these MPSs as its ground states. Together with exact diagonalizations and iPEPS, we hence put forward a new type of short-ranged Hamiltonian that supports $\text{SU}(N)$ chiral spin liquids from $N = 2$ to 4.

Second, we have developed a method to achieve the parton construction of iPEPSs. To demonstrate its practical use, we focused on parton models that could potentially give rise to $\text{U}(1)$ Dirac spin liquids after the Gutzwiller projection. The two fermionic parton models we have studied are the π -flux model on the square lattice and the $[0, \pi]$ -flux model on the kagome lattice. Using iPEPS, we show that first, we are able to simulate the Dirac Fermi sea accurately using only small bond dimensions. And upon applying the Gutzwiller projector, we observe an algebraic decay of spin-spin correlations in the short-range that gives a critical exponent $\eta \approx 1.7$.

We envision such parton construction of tensor network states will be useful for studying correlated spin systems. An immediate application is to use these projected parton states as initial inputs for ground-state search to accelerate the convergence of tensor network simulations. Another potential research direction is how to represent “gapless” parton mean-field states faithfully as tensor network states in two dimensions. A gapless parton state with a finite Fermi surface violates the entropic area law and cannot be simulated using MPS or PEPS. To overcome this, one could consider other types of tensor network states, such as tree tensor networks or multi-scale entanglement renormalization ansatz that are designed to handle gapless systems [HSW⁺18, LGSF21]. We believe these ideas are also worth investigating.

Bibliography

- [P1] Andreas Gleis, Jheng-Wei Li and Jan von Delft, *Controlled bond expansion for DMRG ground state search at single-site costs*, arXiv:2207.14712 (2022).
- [P2] Jheng-Wei Li, Andreas Gleis and Jan von Delft, *Time-dependent variational principle with controlled bond expansion for matrix product states*, arXiv:2208.10972 (2022).
- [P3] Andreas Gleis, Jheng-Wei Li and Jan von Delft, *Projector formalism for kept and discarded spaces of matrix product states*, arXiv:2207.13161 (2022).
- [P4] Benedikt Bruognolo, Jheng-Wei Li, Jan von Delft, Andreas Weichselbaum, *A beginner's guide to non-abelian iPEPS for correlated fermions*, SciPost Phys. Lect. Notes 25 (2021)
- [P5] Jheng-Wei Li, Benedikt Bruognolo, Andreas Weichselbaum, Jan von Delft, *Study of spin symmetry in the doped t - J model using infinite projected entangled pair states*, Phys. Rev. B **103** (2021), 075127
- [P6] Jheng-Wei Li, Nihal Rao, Jan von Delft, Lode Pollet, and Ke Liu, *Tangle of Spin Double Helices in the Honeycomb Kitaev- Γ Model* arXiv:2206.08946 (2022)
- [P7] Ji-Yao Chen, Jheng-Wei Li, Pierre Nataf, Sylvain Capponi, Matthieu Mambrini, Keisuke Totsuka, Hong-Hao Tu, Andreas Weichselbaum, Jan von Delft, Didier Poilblanc, *Abelian $SU(N)_1$ chiral spin liquids on the square lattice*, Phys. Rev. B **104** (2021), 235104
- [P8] Jheng-Wei Li, Jan von Delft and Hong-Hao Tu, *$U(1)$ -symmetric Gaussian fermionic projected entangled-paired states and their Gutzwiller projection* arXiv:2208.04623 (2022)
- [AA88] Daniel P. Arovas and Assa Auerbach, *Functional integral theories of low-dimensional quantum Heisenberg models*, Phys. Rev. B **38** (1988), 316–332.
- [Aid16] Monika Aidelsburger, *Cold atoms twisting spin and momentum*, Science **354** (2016), no. 6308, 35–36.
- [AKLT87] Ian Affleck, Tom Kennedy, Elliott H. Lieb, and Hal Tasaki, *Rigorous results on valence-bond ground states in antiferromagnets*, Phys. Rev. Lett. **59** (1987), no. 7, 799–802.
- [AM88] Ian Affleck and J. Brad Marston, *Large- N limit of the Heisenberg-Hubbard model: Implications for high- T_c superconductors*, Phys. Rev. B **37** (1988), 3774–3777.

- [And07] P. W. Anderson, *PHYSICS: Is there glue in cuprate superconductors?*, Science **316** (2007), no. 5832, 1705–1707.
- [BBY⁺16] A. Banerjee, C. A. Bridges, J. Q. Yan, A. A. Aczel, L. Li, M. B. Stone, G. E. Granroth, M. D. Lumsden, Y. Yiu, J. Knolle, S. Bhattacharjee, D. L. Kovrizhin, R. Moessner, D. A. Tennant, D. G. Mandrus, and S. E. Nagler, *Proximate Kitaev quantum spin liquid behaviour in a honeycomb magnet*, Nat. Mater. **15** (2016), no. 7, 733–740.
- [BC17] Jacob C Bridgeman and Christopher T Chubb, *Hand-waving and interpretive dance: an introductory course on tensor networks*, J. Phys. A: Math. Theor. **50** (2017), no. 22, 223001.
- [BCK⁺14] B. Bauer, L. Cincio, B. P. Keller, M. Dolfi, G. Vidal, S. Trebst, and A. W. W. Ludwig, *Chiral spin liquid and emergent anyons in a kagome lattice Mott insulator*, Nat. Commun. **5** (2014), no. 1, 5137.
- [BCOT11] B. Bauer, P. Corboz, R. Orús, and M. Troyer, *Implementing global abelian symmetries in projected entangled-pair state algorithms*, Phys. Rev. B **83** (2011), 125106.
- [BFK⁺07] E. Berg, E. Fradkin, E.-A. Kim, S. A. Kivelson, V. Oganesyan, J. M. Tranquada, and S. C. Zhang, *Dynamical layer decoupling in a stripe-ordered high- T_c superconductor*, Phys. Rev. Lett. **99** (2007), 127003.
- [BH14] Fernando G. S. L. Brandão and Michał Horodecki, *Exponential decay of correlations implies area law*, Commun. Math. Phys. **333** (2014), no. 2, 761–798.
- [BLKL88] J. Broeckhove, L. Lathouwers, E. Kesteloot, and P. Van Leuven, *On the equivalence of time-dependent variational principles*, Chem. Phys. Lett. **149** (1988), no. 5-6, 547–550.
- [BYK⁺17] Arnab Banerjee, Jiaqiang Yan, Johannes Knolle, Craig A. Bridges, Matthew B. Stone, Mark D. Lumsden, David G. Mandrus, David A. Tennant, Roderich Moessner, and Stephen E. Nagler, *Neutron scattering in the proximate quantum spin liquid α - RuCl_3* , Science **356** (2017), no. 6342, 1055–1059.
- [CCG⁺21] Bin-Bin Chen, Ziyu Chen, Shou-Shu Gong, D. N. Sheng, Wei Li, and Andreas Weichselbaum, *Quantum spin liquid with emergent chiral order in the triangular-lattice Hubbard model*, arXiv:2102.05560 (2021).
- [CDC19] Piotr Czarnik, Jacek Dziarmaga, and Philippe Corboz, *Time evolution of an infinite projected entangled pair state: An efficient algorithm*, Phys. Rev. B **99** (2019), 035115.
- [CKL22] Gianluca Ceruti, Jonas Kusch, and Christian Lubich, *A rank-adaptive robust integrator for dynamical low-rank approximation*, BIT Numer. Math. (2022).
- [CNA⁺11] Yu-Ao Chen, Sylvain Nascimbène, Monika Aidelsburger, Marcos Atala, Stefan Trotzky, and Immanuel Bloch, *Controlling correlated tunneling and superexchange interactions with ac-driven optical lattices*, Phys. Rev. Lett. **107** (2011), 210405.

- [COBV10] Philippe Corboz, Román Orús, Bela Bauer, and Guifré Vidal, *Simulation of strongly correlated fermions in two spatial dimensions with fermionic projected entangled-pair states*, Phys. Rev. B **81** (2010), 165104.
- [CPGSV21] J. Ignacio Cirac, David Pérez-García, Norbert Schuch, and Frank Verstraete, *Matrix product states and projected entangled pair states: Concepts, symmetries, theorems*, Rev. Mod. Phys. **93** (2021), 045003.
- [CRCD21] Piotr Czarnik, Marek M. Rams, Philippe Corboz, and Jacek Dziarmaga, *Tensor network study of the $m = \frac{1}{2}$ magnetization plateau in the shastry-sutherland model at finite temperature*, Phys. Rev. B **103** (2021), 075113.
- [CRT14] Philippe Corboz, T. M. Rice, and Matthias Troyer, *Competing states in the t - J model: Uniform d -wave state versus stripe state*, Phys. Rev. Lett. **113** (2014), 046402.
- [CS00] Matteo Calandra and Sandro Sorella, *From antiferromagnetism to d -wave superconductivity in the two-dimensional t - J model*, Phys. Rev. B **61** (2000), R11894–R11897.
- [CSZ20] Titas Chanda, Piotr Sierant, and Jakub Zakrzewski, *Time dynamics with matrix product states: Many-body localization transition of large systems revisited*, Phys. Rev. B **101** (2020), 035148.
- [CV13] L. Cincio and G. Vidal, *Characterizing topological order by studying the ground states on an infinite cylinder*, Phys. Rev. Lett. **110** (2013), 067208.
- [CYW⁺18] Andrei Catuneanu, Youhei Yamaji, Gideon Wachtel, Yong Baek Kim, and Hae-Young Kee, *Path to stable quantum spin liquids in spin-orbit coupled correlated materials*, npj Quantum Materials **3** (2018), no. 1, 23.
- [Dag94] Elbio Dagotto, *Correlated electrons in high-temperature superconductors*, Rev. Mod. Phys. **66** (1994), 763–840.
- [DC21] Angus J. Dunnett and Alex W. Chin, *Efficient bond-adaptive approach for finite-temperature open quantum dynamics using the one-site time-dependent variational principle for matrix product states*, Phys. Rev. B **104** (2021), 214302.
- [Dir30] P. A. M. Dirac, *Note on exchange phenomena in the Thomas atom*, Math. Proc. Camb. Philos. Soc. **26** (1930), no. 3, 376–385.
- [DM88] Elbio Dagotto and Adriana Moreo, *Zero-temperature properties of the two-dimensional Heisenberg antiferromagnet: A numerical study*, Phys. Rev. B **38** (1988), 5087–5090.
- [DR92] E. Dagotto and J. Riera, *Superconductivity in the two-dimensional t - J model*, Phys. Rev. B **46** (1992), 12084–12087.

- [DRV21] Alec Dektor, Abram Rodgers, and Daniele Venturi, *Rank-adaptive tensor methods for high-dimensional nonlinear PDEs*, J. Sci. Comput. **88** (2021), no. 2, 36.
- [dS89] Raimundo R. dos Santos, *Enhanced pairing in the repulsive hubbard model with next-nearest-neighbor hopping*, Phys. Rev. B **39** (1989), 7259–7262.
- [DW89] B. Douçot and X. G. Wen, *Instability of the Nagaoka state with more than one hole*, Phys. Rev. B **40** (1989), 2719–2722.
- [EBHA02] E. Eisenberg, R. Berkovits, David A. Huse, and B. L. Altshuler, *Breakdown of the Nagaoka phase in the two-dimensional t - J model*, Phys. Rev. B **65** (2002), 134437.
- [ECP10] J. Eisert, M. Cramer, and M. B. Plenio, *Colloquium: Area laws for the entanglement entropy*, Rev. Mod. Phys. **82** (2010), 277–306.
- [Edi13] Editorial, *The Hubbard model at half a century*, Nat. Phys. **9** (2013), no. 9, 523–523.
- [EKL90] V. J. Emery, S. A. Kivelson, and H. Q. Lin, *Phase separation in the t - J model*, Phys. Rev. Lett. **64** (1990), 475–478.
- [EOS22] Lukas Einkemmer, Alexander Ostermann, and Carmen Scalone, *A robust and conservative dynamical low-rank algorithm*, arXiv:2206.09374 (2022).
- [FPB21] Francesco Ferrari, Alberto Parola, and Federico Becca, *Gapless spin liquids in disguise*, Phys. Rev. B **103** (2021), 195140.
- [GCKK20] Matthias Gohlke, Li Ern Chern, Hae-Young Kee, and Yong Baek Kim, *Emergence of nematic paramagnet via quantum order-by-disorder and pseudo-Goldstone modes in Kitaev magnets*, Phys. Rev. Res. **2** (2020), 043023.
- [GD19] Shimpei Goto and Ippei Danshita, *Performance of the time-dependent variational principle for matrix product states in the long-time evolution of a pure state*, Phys. Rev. B **99** (2019), 054307.
- [GJR87] C. Gros, R. Joynt, and T. M. Rice, *Antiferromagnetic correlations in almost-localized Fermi liquids*, Phys. Rev. B **36** (1987), 381–393.
- [GKNB⁺18] F. Grusdt, M. Kánasz-Nagy, A. Bohrdt, C. S. Chiu, G. Ji, M. Greiner, D. Greif, and E. Demler, *Parton theory of magnetic polarons: Mesonic resonances and signatures in dynamics*, Phys. Rev. X **8** (2018), 011046.
- [GLHF14] Fabian Grusdt, Fabian Letscher, Mohammad Hafezi, and Michael Fleischhauer, *Topological growing of Laughlin states in synthetic gauge fields*, Phys. Rev. Lett. **113** (2014), 155301.
- [GP20] Fabian Grusdt and Lode Pollet, *z_2 parton phases in the mixed-dimensional $t - J_z$ model*, Phys. Rev. Lett. **125** (2020), 256401.
- [Gro89] Claudius Gros, *Physics of projected wavefunctions*, Ann. Phys. **189** (1989), no. 1, 53–88.

- [Gut63] Martin C. Gutzwiller, *Effect of correlation on the ferromagnetism of transition metals*, Phys. Rev. Lett. **10** (1963), 159–162.
- [GWY⁺18] Matthias Gohlke, Gideon Wachtel, Youhei Yamaji, Frank Pollmann, and Yong Baek Kim, *Quantum spin liquid signatures in Kitaev-like frustrated magnets*, Phys. Rev. B **97** (2018), 075126.
- [GZSD18] Fabian Grusdt, Zheng Zhu, Tao Shi, and Eugene Demler, *Meson formation in mixed-dimensional t - J models*, SciPost Phys. **5** (2018), 57.
- [Has00] M. B. Hastings, *Dirac structure, RVB, and Goldstone modes in the kagomé antiferromagnet*, Phys. Rev. B **63** (2000), 014413.
- [Has07] M B Hastings, *An area law for one-dimensional quantum systems*, J. Stat. Mech. Theory Exp. **2007** (2007), no. 08, 08024–08024.
- [HCO⁺11] Jutho Haegeman, J. Ignacio Cirac, Tobias J. Osborne, Iztok Pižorn, Henri Verschelde, and Frank Verstraete, *Time-dependent variational principle for quantum lattices*, Phys. Rev. Lett. **107** (2011), 070601.
- [HLO⁺16] Jutho Haegeman, Christian Lubich, Ivan Oseledets, Bart Vandereycken, and Frank Verstraete, *Unifying time evolution and optimization with matrix product states*, Phys. Rev. B **94** (2016), 165116.
- [HLW06] Ernst Hairer, Christian Lubich, and Gerhard Wanner, *Geometric numerical integration*, Springer-Verlag, 2006.
- [HM97] C. Stephen Hellberg and E. Manousakis, *Phase separation at all interaction strengths in the t - J model*, Phys. Rev. Lett. **78** (1997), 4609–4612.
- [HM99] ———, *Stripes and the t - J model*, Phys. Rev. Lett. **83** (1999), 132–135.
- [HMSW15] C. Hubig, I. P. McCulloch, U. Schollwöck, and F. A. Wolf, *Strictly single-site DMRG algorithm with subspace expansion*, Phys. Rev. B **91** (2015), 155115.
- [HOV13] Jutho Haegeman, Tobias J. Osborne, and Frank Verstraete, *Post-matrix product state methods: To tangent space and beyond*, Phys. Rev. B **88** (2013), 075133.
- [HSC14a] Yin-Chen He, D. N. Sheng, and Yan Chen, *Chiral spin liquid in a frustrated anisotropic kagome Heisenberg model*, Phys. Rev. Lett. **112** (2014), 137202.
- [HSC14b] ———, *Obtaining topological degenerate ground states by the density matrix renormalization group*, Phys. Rev. B **89** (2014), 075110.
- [HSW⁺18] Jutho Haegeman, Brian Swingle, Michael Walter, Jordan Cotler, Glen Evenbly, and Volkher B. Scholz, *Rigorous free-fermion entanglement renormalization from wavelet theory*, Phys. Rev. X **8** (2018), 011003.
- [Hub63] J. Hubbard, *Electron correlations in narrow energy bands*, Proc. Math. Phys. Eng. Sci. P Roy Soc A-Math Phys **276** (1963), no. 1365, 238–257.

- [HZOP17] Yin-Chen He, Michael P. Zaletel, Masaki Oshikawa, and Frank Pollmann, *Signatures of Dirac cones in a DMRG study of the kagome Heisenberg model*, Phys. Rev. X **7** (2017), 031020.
- [IFT98] Masatoshi Imada, Atsushi Fujimori, and Yoshinori Tokura, *Metal-insulator transitions*, Rev. Mod. Phys. **70** (1998), 1039–1263.
- [IOI18] Kota Ido, Takahiro Ohgoe, and Masatoshi Imada, *Competition among various charge-inhomogeneous states and d -wave superconducting state in hubbard models on square lattices*, Phys. Rev. B **97** (2018), 045138.
- [JD19] Hong-Chen Jiang and Thomas P. Devereaux, *Superconductivity in the doped Hubbard model and its interplay with next-nearest hopping t'* , Science **365** (2019), no. 6460, 1424–1428.
- [JDJ19] Yi-Fan Jiang, Thomas P. Devereaux, and Hong-Chen Jiang, *Field-induced quantum spin liquid in the Kitaev-Heisenberg model and its relation to α -RuCl₃*, Phys. Rev. B **100** (2019), 165123.
- [JOV⁺08] J. Jordan, R. Orús, G. Vidal, F. Verstraete, and J. I. Cirac, *Classical simulation of infinite-size quantum lattice systems in two spatial dimensions*, Phys. Rev. Lett. **101** (2008), 250602.
- [JWB12] Hong-Chen Jiang, Zhenghan Wang, and Leon Balents, *Identifying topological order by entanglement entropy*, Nat. Phys. **8** (2012), no. 12, 902–905.
- [JWK18] Hong-Chen Jiang, Zheng-Yu Weng, and Steven A. Kivelson, *Superconductivity in the doped t - J model: Results for four-leg cylinders*, Phys. Rev. B **98** (2018), 140505.
- [JWX08] H. C. Jiang, Z. Y. Weng, and T. Xiang, *Accurate determination of tensor network state of quantum lattice models in two dimensions*, Phys. Rev. Lett. **101** (2008), 090603.
- [JXK⁺21] Geoffrey Ji, Muqing Xu, Lev Haldar Kendrick, Christie S. Chiu, Justus C. Brüggenjürgen, Daniel Greif, Annabelle Bohrdt, Fabian Grusdt, Eugene Demler, Martin Lebrat, and Markus Greiner, *Coupling a mobile hole to an antiferromagnetic spin background: Transient dynamics of a magnetic polaron*, Phys. Rev. X **11** (2021), 021022.
- [KEL90] S. A. Kivelson, V. J. Emery, and H. Q. Lin, *Doped antiferromagnets in the weak-hopping limit*, Phys. Rev. B **42** (1990), 6523–6530.
- [Kit06] Alexei Kitaev, *Anyons in an exactly solved model and beyond*, Ann. Phys. **321** (2006), no. 1, 2–111.
- [KL87] V. Kalmeyer and R. B. Laughlin, *Equivalence of the resonating-valence-bond and fractional quantum Hall states*, Phys. Rev. Lett. **59** (1987), 2095–2098.
- [KL88] Gabriel Kotliar and Jialin Liu, *Superexchange mechanism and d -wave superconductivity*, Phys. Rev. B **38** (1988), 5142–5145.

- [KL89] Vadim Kalmeyer and R. B. Laughlin, *Theory of the spin liquid state of the Heisenberg antiferromagnet*, Phys. Rev. B **39** (1989), 11879–11899.
- [KL07] Othmar Koch and Christian Lubich, *Dynamical low-rank approximation*, SIAM J. Matrix Anal. Appl. **29** (2007), no. 2, 434–454.
- [KL10] ———, *Dynamical tensor approximation*, SIAM Journal on Matrix Analysis and Applications **31** (2010), no. 5, 2360–2375.
- [Koh64] Walter Kohn, *Theory of the insulating state*, Phys. Rev. **133** (1964), A171–A181.
- [KREO19] A. Kshetrimayum, M. Rizzi, J. Eisert, and R. Orús, *Tensor network annealing algorithm for two-dimensional thermal states*, Phys. Rev. Lett. **122** (2019), 070502.
- [KRS87] Steven A. Kivelson, Daniel S. Rokhsar, and James P. Sethna, *Topology of the resonating valence-bond state: Solitons and high- T_c superconductivity*, Phys. Rev. B **35** (1987), 8865–8868.
- [LCBn14] Michael Lubasch, J. Ignacio Cirac, and Mari-Carmen Bañuls, *Algorithms for finite projected entangled pair states*, Phys. Rev. B **90** (2014), 064425.
- [LGL⁺22] Wen-Yuan Liu, Shou-Shu Gong, Yu-Bin Li, Didier Poilblanc, Wei-Qiang Chen, and Zheng-Cheng Gu, *Gapless quantum spin liquid and global phase diagram of the spin-1/2 J_1 - J_2 square antiferromagnetic Heisenberg model*, Sci. Bull. **67** (2022), no. 10, 1034–1041.
- [LGSF21] Peter Lunts, Antoine Georges, E. Miles Stoudenmire, and Matthew Fishman, *Hubbard model on the Bethe lattice via variational uniform tree states: Metal-insulator transition and a Fermi liquid*, Phys. Rev. Res. **3** (2021), 023054.
- [LKC⁺20] Hyun-Yong Lee, Ryui Kaneko, Li Ern Chern, Tsuyoshi Okubo, Youhei Yamaji, Naoki Kawashima, and Yong Baek Kim, *Magnetic field induced quantum phases in a tensor network study of Kitaev magnets*, Nat. Commun. **11** (2020), no. 1, 1639.
- [LNW06] Patrick A. Lee, Naoto Nagaosa, and Xiao-Gang Wen, *Doping a Mott insulator: Physics of high-temperature superconductivity*, Rev. Mod. Phys. **78** (2006), 17–85.
- [LO13] Christian Lubich and Ivan V. Oseledets, *A projector-splitting integrator for dynamical low-rank approximation*, BIT Numer. Math. **54** (2013), no. 1, 171–188.
- [LOV15] Christian Lubich, Ivan V. Oseledets, and Bart Vandereycken, *Time integration of tensor trains*, SIAM J. Numer. Anal. **53** (2015), 917–941.
- [LPB⁺17] Eyal Leviatan, Frank Pollmann, Jens H. Bardarson, David A. Huse, and Ehud Altman, *Quantum thermalization dynamics with matrix-product states*, arXiv:1702.08894 (2017).

- [LRSV13] Christian Lubich, Thorsten Rohwedder, Reinhold Schneider, and Bart Vandereycken, *Dynamical approximation by hierarchical Tucker and tensor-train tensors*, SIAM J. Matrix Anal. Appl. **34** (2013), no. 2, 470–494.
- [Lub15] Christian Lubich, *Time integration in the multiconfiguration time-dependent Hartree method of molecular quantum dynamics*, Appl. Math. Res. eXpress **2015** (2015), no. 2, 311–328.
- [LW06] Michael Levin and Xiao-Gang Wen, *Detecting topological order in a ground state wave function*, Phys. Rev. Lett. **96** (2006), 110405.
- [LXC⁺17] H. J. Liao, Z. Y. Xie, J. Chen, Z. Y. Liu, H. D. Xie, R. Z. Huang, B. Normand, and T. Xiang, *Gapless spin-liquid ground state in the $S = 1/2$ kagome antiferromagnet*, Phys. Rev. Lett. **118** (2017), 137202.
- [LZP21] Sheng-Hsuan Lin, Michael Zaletel, and Frank Pollmann, *Efficient simulation of dynamics in two-dimensional quantum spin systems with isometric tensor networks*, arXiv:2112.08394 (2021).
- [MB20] Rocco Martinazzo and Irene Burghardt, *Local-in-time error in variational quantum dynamics*, Phys. Rev. Lett. **124** (2020), 150601.
- [McL64] A.D. McLachlan, *A variational solution of the time-dependent Schrodinger equation*, Mol. Phys. **8** (1964), no. 1, 39–44.
- [MMC90] H.-D. Meyer, U. Manthe, and L.S. Cederbaum, *The multi-configurational time-dependent Hartree approach*, Chem. Phys. Lett. **165** (1990), no. 1, 73–78.
- [Mot68] Nevill Francis Mott, *Metal-insulator transition*, Rev. Mod. Phys. **40** (1968), no. 4, 677–683.
- [Nag66] Yosuke Nagaoka, *Ferromagnetism in a narrow, almost half-filled s band*, Phys. Rev. **147** (1966), 392–405.
- [NO96] Tomotoshi Nishino and Kouichi Okunishi, *Corner transfer matrix renormalization group method*, J. Phys. Soc. Jpn. **65** (1996), 891–894.
- [NO97] ———, *Corner transfer matrix algorithm for classical renormalization group*, J. Phys. Soc. Jpn. **66** (1997), no. 10, 3040–3047.
- [OR95] Stellan Östlund and Stefan Rommer, *Thermodynamic limit of density matrix renormalization*, Phys. Rev. Lett. **75** (1995), 3537–3540.
- [OV09] Román Orús and Guifré Vidal, *Simulation of two-dimensional quantum systems on an infinite lattice revisited: Corner transfer matrix for tensor contraction*, Phys. Rev. B **80** (2009), 094403.
- [PAC22] Boris Ponsioen, Fakher F. Assaad, and Philippe Corboz, *Automatic differentiation applied to excitations with Projected Entangled Pair States*, SciPost Phys. **12** (2022), 6.
- [PBT⁺15] Ho N. Phien, Johann A. Bengua, Hoang D. Tuan, Philippe Corboz, and Román Orús, *Infinite projected entangled pair states algorithm improved: Fast full update and gauge fixing*, Phys. Rev. B **92** (2015), 035142.

- [PC20] Boris Ponsioen and Philippe Corboz, *Excitations with projected entangled pair states using the corner transfer matrix method*, Phys. Rev. B **101** (2020), 195109.
- [PCC19] Boris Ponsioen, Sangwoo S. Chung, and Philippe Corboz, *Period 4 stripe in the extended two-dimensional Hubbard model*, Phys. Rev. B **100** (2019), 195141.
- [PcvZ93] P. Prelovšek and X. Zotos, *Hole pairing and clustering in the two-dimensional t - J model*, Phys. Rev. B **47** (1993), 5984–5991.
- [PKH98] Leonid P. Pryadko, Steven Kivelson, and Daniel W. Hone, *Instability of charge ordered states in doped antiferromagnets*, Phys. Rev. Lett. **80** (1998), 5651–5654.
- [PMTM09] Frank Pollmann, Subroto Mukerjee, Ari M. Turner, and Joel E. Moore, *Theory of finite-entanglement scaling at one-dimensional quantum critical points*, Phys. Rev. Lett. **102** (2009), 255701.
- [PTBO10] Frank Pollmann, Ari M. Turner, Erez Berg, and Masaki Oshikawa, *Entanglement spectrum of a topological phase in one dimension*, Phys. Rev. B **81** (2010), 064439.
- [PTIG19] Joseph Paki, Hanna Terletska, Sergei Isakov, and Emanuel Gull, *Charge order and antiferromagnetism in the extended hubbard model*, Phys. Rev. B **99** (2019), 245146.
- [QCS⁺20] Mingpu Qin, Chia-Min Chung, Hao Shi, Ettore Vitali, Claudius Hubig, Ulrich Schollwöck, Steven R. White, and Shiwei Zhang, *Absence of superconductivity in the pure two-dimensional Hubbard model*, Phys. Rev. X **10** (2020), 031016.
- [Rie89] J. A. Riera, *Binding of holes in the Hubbard model with next-nearest-neighbor hopping*, Phys. Rev. B **40** (1989), 833–836.
- [RJRT19] Neil J Robinson, Peter D Johnson, T Maurice Rice, and Alexei M Tsvelik, *Anomalies in the pseudogap phase of the cuprates: competing ground states and the role of umklapp scattering*, Rep. Prog. Phys. **82** (2019), no. 12, 126501.
- [RS91] N. Read and Subir Sachdev, *Large- N expansion for frustrated quantum antiferromagnets*, Phys. Rev. Lett. **66** (1991), 1773–1776.
- [RW06] Ying Ran and Xiao-gang Wen, *Continuous quantum phase transitions beyond Landau’s paradigm in a large- N spin model*, arXiv:0609620 (2006).
- [RY88] J. D. Reger and A. P. Young, *Monte Carlo simulations of the spin-1/2 Heisenberg antiferromagnet on a square lattice*, Phys. Rev. B **37** (1988), 5978–5981.
- [RY89] J. A. Riera and A. P. Young, *Binding of holes in one-band models of oxide superconductors*, Phys. Rev. B **39** (1989), 9697–9700.

- [San97] Anders W. Sandvik, *Finite-size scaling of the ground-state parameters of the two-dimensional Heisenberg model*, Phys. Rev. B **56** (1997), 11678–11690.
- [Sch89] HJ Schulz, *Domain walls in a doped antiferromagnet*, Journal de Physique **50** (1989), no. 18, 2833–2849.
- [Sch11] Ulrich Schollwöck, *The density-matrix renormalization group in the age of matrix product states*, Ann. Phys. **326** (2011), 96–192.
- [SCW96] D. N. Sheng, Y. C. Chen, and Z. Y. Weng, *Phase string effect in a doped antiferromagnet*, Phys. Rev. Lett. **77** (1996), 5102–5105.
- [SRF⁺13] Pietro Silvi, Davide Rossini, Rosario Fazio, Giuseppe E. Santoro, and Vittorio Giovannetti, *Matrix product state representation for Slater determinants and configuration interaction states*, Int. J. Mod. Phys. B **27** (2013), no. 01n03, 1345029.
- [SSB⁺20] Tomohiro Soejima, Karthik Siva, Nick Bultinck, Shubhayu Chatterjee, Frank Pollmann, and Michael P. Zaletel, *Isometric tensor network representation of string-net liquids*, Phys. Rev. B **101** (2020), 085117.
- [STG99] Horst L. Stormer, Daniel C. Tsui, and Arthur C. Gossard, *The fractional quantum Hall effect*, Rev. Mod. Phys. **71** (1999), S298–S305.
- [STG⁺19] Pietro Silvi, Ferdinand Tschirsich, Matthias Gerster, Johannes Jünemann, Daniel Jaschke, Matteo Rizzi, and Simone Montangero, *The tensor networks anthology: Simulation techniques for many-body quantum lattice systems*, SciPost Phys. Lect. Notes (2019), 8.
- [Tra20] J. M. Tranquada, *Cuprate superconductors as viewed through a striped lens*, Adv. Phys. **69** (2020), no. 4, 437–509.
- [Tru88] S. A. Trugman, *Interaction of holes in a Hubbard antiferromagnet and high-temperature superconductivity*, Phys. Rev. B **37** (1988), 1597–1603.
- [TSG82] D. C. Tsui, H. L. Stormer, and A. C. Gossard, *Two-dimensional magnetotransport in the extreme quantum limit*, Phys. Rev. Lett. **48** (1982), 1559–1562.
- [TTR⁺93] M. Troyer, H. Tsunetsugu, T. M. Rice, J. Riera, and E. Dagotto, *Spin gap and superconductivity in the one-dimensional t - J model with coulomb repulsion*, Phys. Rev. B **48** (1993), 4002–4013.
- [UV20] André Uschmajew and Bart Vandereycken, *Geometric methods on low-rank matrix and tensor manifolds*, pp. 261–313, Springer International Publishing, 2020.
- [Van17] Laurens Vanderstraeten, *Tensor network states and effective particles for low-dimensional quantum spin systems*, Springer International Publishing, 2017.
- [VC06] F. Verstraete and J. I. Cirac, *Matrix product states represent ground states faithfully*, Phys. Rev. B **73** (2006), 094423.

- [VDVH⁺21] Maarten Van Damme, Robijn Vanhove, Jutho Haegeman, Frank Verstraete, and Laurens Vanderstraeten, *Efficient matrix product state methods for extracting spectral information on rings and cylinders*, Phys. Rev. B **104** (2021), 115142.
- [VHV19] Laurens Vanderstraeten, Jutho Haegeman, and Frank Verstraete, *Simulating excitation spectra with projected entangled-pair states*, Phys. Rev. B **99** (2019), 165121.
- [Vid03] Guifré Vidal, *Efficient classical simulation of slightly entangled quantum computations*, Phys. Rev. Lett. **91** (2003), 147902.
- [VMC08] F. Verstraete, V. Murg, and J.I. Cirac, *Matrix product states, projected entangled pair states, and variational renormalization group methods for quantum spin systems*, Adv. Phys. **57** (2008), no. 2, 143–224.
- [VMVH15] Laurens Vanderstraeten, Michaël Mariën, Frank Verstraete, and Jutho Haegeman, *Excitations and the tangent space of projected entangled-pair states*, Phys. Rev. B **92** (2015), 201111.
- [VWPGC06] F. Verstraete, M. M. Wolf, D. Perez-Garcia, and J. I. Cirac, *Criticality, the area law, and the computational power of projected entangled pair states*, Phys. Rev. Lett. **96** (2006), 220601.
- [Wen91a] X. G. Wen, *Mean-field theory of spin-liquid states with finite energy gap and topological orders*, Phys. Rev. B **44** (1991), 2664–2672.
- [Wen91b] ———, *Non-abelian statistics in the fractional quantum Hall states*, Phys. Rev. Lett. **66** (1991), 802–805.
- [WH93] Steven R. White and David A. Huse, *Numerical renormalization-group study of low-lying eigenstates of the antiferromagnetic $S = 1$ Heisenberg chain*, Phys. Rev. B **48** (1993), 3844–3852.
- [Whi92] Steven R. White, *Density matrix formulation for quantum renormalization groups*, Phys. Rev. Lett. **69** (1992), 2863–2866.
- [Whi05] ———, *Density matrix renormalization group algorithms with a single center site*, Phys. Rev. B **72** (2005), 180403.
- [Wil75] Kenneth G. Wilson, *The renormalization group: Critical phenomena and the Kondo problem*, Rev. Mod. Phys. **47** (1975), no. 4, 773–840.
- [WN92] S. R. White and R. M. Noack, *Real-space quantum renormalization groups*, Phys. Rev. Lett. **68** (1992), 3487–3490.
- [WNL19] Jiucui Wang, B. Normand, and Zheng-Xin Liu, *One proximate Kitaev spin liquid in the K - J - Γ model on the honeycomb lattice*, Phys. Rev. Lett. **123** (2019), 197201.
- [WS98] Steven R. White and D. J. Scalapino, *Density matrix renormalization group study of the striped phase in the 2d t - J model*, Phys. Rev. Lett. **80** (1998), 1272–1275.
- [WS99] ———, *Competition between stripes and pairing in a t - t' - J model*, Phys. Rev. B **60** (1999), R753–R756.

- [WSCT97] Z. Y. Weng, D. N. Sheng, Y.-C. Chen, and C. S. Ting, *Phase string effect in the t - J model: General theory*, Phys. Rev. B **55** (1997), 3894–3906.
- [Wu20] Yantao Wu, *Time-dependent variational principle for mixed matrix product states in the thermodynamic limit*, Phys. Rev. B **102** (2020), 134306.
- [WWT20] Ying-Hai Wu, Lei Wang, and Hong-Hao Tu, *Tensor network representations of parton wave functions*, Phys. Rev. Lett. **124** (2020), 246401.
- [XXX⁺22] Yihe Xu, Zhaoxuan Xie, Xiaoyu Xie, Ulrich Schollwöck, and Haibo Ma, *Stochastic adaptive single-site time-dependent variational principle*, JACS Au **2** (2022), no. 2, 335–340.
- [YW20] Mingru Yang and Steven R. White, *Time-dependent variational principle with ancillary Krylov subspace*, Phys. Rev. B **102** (2020), 094315.
- [ZC16] Bo-Xiao Zheng and Garnet Kin-Lic Chan, *Ground-state phase diagram of the square lattice hubbard model from density matrix embedding theory*, Phys. Rev. B **93** (2016), 035126.
- [ZCC⁺17] Bo-Xiao Zheng, Chia-Min Chung, Philippe Corboz, Georg Ehlers, Ming-Pu Qin, Reinhard M. Noack, Hao Shi, Steven R. White, Shiwei Zhang, and Garnet Kin-Lic Chan, *Stripe order in the underdoped region of the two-dimensional Hubbard model*, Science **358** (2017), 1155.
- [ZG89] Jan Zaanen and Olle Gunnarsson, *Charged magnetic domain lines and the magnetism of high- T_c oxides*, Phys. Rev. B **40** (1989), 7391–7394.
- [ZGT⁺12] Yi Zhang, Tarun Grover, Ari Turner, Masaki Oshikawa, and Ashvin Vishwanath, *Quasiparticle statistics and braiding from ground-state entanglement*, Phys. Rev. B **85** (2012), 235151.
- [ZMP13] Michael P. Zaletel, Roger S. K. Mong, and Frank Pollmann, *Topological characterization of fractional quantum Hall ground states from microscopic hamiltonians*, Phys. Rev. Lett. **110** (2013), 236801.
- [ZMPR15] Michael P. Zaletel, Roger S. K. Mong, Frank Pollmann, and Edward H. Rezayi, *Infinite density matrix renormalization group for multicomponent quantum Hall systems*, Phys. Rev. B **91** (2015), 045115.
- [ZP20] Michael P. Zaletel and Frank Pollmann, *Isometric tensor network states in two dimensions*, Phys. Rev. Lett. **124** (2020), 037201.
- [ZR88] F. C. Zhang and T. M. Rice, *Effective hamiltonian for the superconducting Cu oxides*, Phys. Rev. B **37** (1988), 3759–3761.
- [ZSVF⁺18] V. Zauner-Stauber, L. Vanderstraeten, M. T. Fishman, F. Verstraete, and J. Haegeman, *Variational optimization algorithms for uniform matrix product states*, Phys. Rev. B **97** (2018), 045145.

Acknowledgements

I would like to express my deep gratitude to my advisor Jan von Delft for giving me this wonderful opportunity to pursue my PhD study in his group. During these four years, Jan not only gave me the utmost freedom to work and explore at my own pace, indulged my idiosyncrasy, but also gently advised me, and shared his knowledge and experiences whenever I needed him. I cannot thank him enough for his infinite patience, constructive criticism, and being always cheerful and supportive throughout my PhD study. Without his continuous support, it would be in many ways unthinkable for me to sit here writing this sentence.

I would also like to thank Hong-Hao Tu at Dresden for his intellectual stimulation and constant help. The last part of this thesis would not be materialized without his sharp insight and patient guidance. I profited a lot from his experience and knowledge in tensor networks. I have also learned a great deal from his way of thinking and conveying complicated ideas through simple but precise words.

I am thankful to Frank Pollmann for referring this thesis.

I want to also thank Andreas Weichselbaum, Andreas Gleis, Ke Liu and Ji-Yao Chen for fruitful collaborations, and Didier Poilblanc for initiating and letting me participate in the joint project on $SU(N)$ chiral spin liquids. In addition, I want to extend my warm thanks to my office mates and colleagues on the fourth floor. I particularly appreciate occasional discussions with Seung-Sup Lee, Fabian Kugler, Elias Walter, Andreas Gleis, Wei Li and Bin-Bin Chen. Their expertise in their own fields and quantum many-body physics in general always held me in awe.

I want to further thank Toru Shiozaki for introducing me to the field of tensor networks during my stay at the Chemistry department at Northwestern. I also thank Hai-Anh Le, Aysenur Iscen, Liang-Yan Hsu, and Cheng-Tsung Lai for their friendly support through the most challenging time at Northwestern.

I want to address my special thanks to Jer-Lai Kuo at Academia Sinica for his continuous caring and encouragement through my academic study.

Lastly, I am eternally grateful to my parents, to whom I owe everything.

